

Copyright is owned by the Author of the thesis. Permission is given for a copy to be downloaded by an individual for the purpose of research and private study only. The thesis may not be reproduced elsewhere without the permission of the Author.

# Approaches to forecast volcanic hazard in the Auckland Volcanic Field, New Zealand

A thesis presented in partial fulfilment of the requirements for the  
degree of Doctor of Philosophy in Earth Science

At Massey University, Palmerston North, New Zealand



**MASSEY UNIVERSITY**  
**TE KUNENGA KI PŪREHUROA**  
**UNIVERSITY OF NEW ZEALAND**

Gabor Kereszturi

2014



# No Telling Where Next

## But Signs Expected

When any of the 50 volcanic centres in Auckland next erupts, there is likely to be some warning to allow evacuation.

"Unlike with earthquakes, it is possible to see something coming," the senior lecturer in geology at the University of Auckland, Dr Ian Smith, told a civil defence seminar yesterday.

The next eruption could occur anywhere in metropolitan Auckland, but is likely to be of short duration.

The last eruption to affect people in New Zealand was Tarawera, 100 years ago.

Dr Smith said yesterday: "What we need in this country is a good eruption to remind people about the effects it can have."

Auckland University has established a seismometer on Motutapu Island and the Auckland Regional Authority is siting others at dams in the Hunua and Waitakere ranges.

Dr Smith said these would give between 24 hours and a week's

warning of coming volcanic activity.

The threat to life would not be great but destruction of property could be considerable.

The last local eruption was on Rangitoto about 800 years ago.

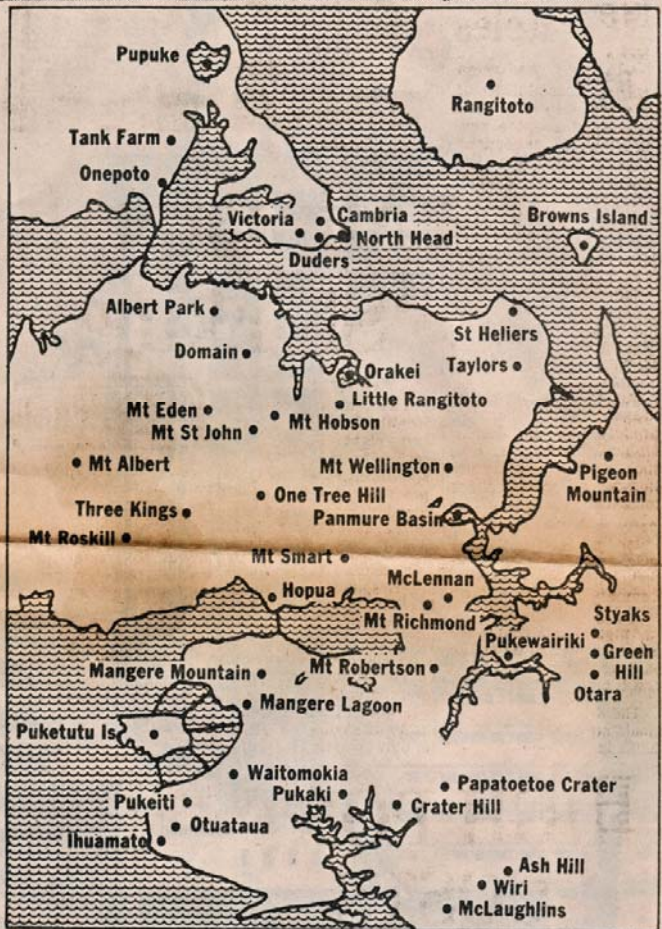
Explosive outbursts could be expected from areas like the Orakei or Panmure basins, Lake Pupuke or the Onepoto basin.

The blasts would cause destruction up to three kilometres away with damage extending several kilometres. Such eruptions had produced 160 km/h surges, removing trees for up to a kilometre.

In addition, wet ash would clog drains, affect water supplies and disrupt traffic. The weight of it could cause buildings to collapse.

The more visible cones such as Mt Eden, Mt Wellington or Mangere could throw up lava, producing heat damage up to a kilometre away.

Dr Smith said that there was no way of predicting where a future eruption would be.



The main volcanic areas in Auckland.



## Abstract

Monogenetic basaltic volcanism is characterised by a complex array of behaviours in the spatial distribution of magma output and also temporal variability in magma flux and eruptive frequency. For understanding monogenetic volcanoes different topographic and remote sensing-based information can be used, such as Digital Surface Models (DSMs). These data are most appropriately analysed in a Geographic Information System (GIS). In this study a systematic dataset of the Auckland Volcanic Field (AVF), New Zealand, was collected and pre-processed to extract quantitative parameters, such as eruptive volumes, sedimentary unit thicknesses, areas affected, spatial locations, and topographic positions. The topographic datasets available for the AVF were Shuttle Radar Topography Mission (SRTM), Advanced Spaceborne Thermal Emission and Reflection Radiometer (ASTER), contour-based Digital Elevation Models, and Light Detection And Range (LiDAR) datasets. These were validated by comparing their elevations to high accuracy ground control reference data from multiple Real-Time-Kinematic (RTK) Global Positioning System and Terrestrial Laser Scanning surveys. The attribute extraction was carried out on the LiDAR DSM, which had the best vertical accuracy of  $\leq 0.3$  m. The parameterisation of monogenetic volcanoes and their eruptive products included the extraction of eruptive volumes, areas covered by deposits, identification of eruptive styles based on their sedimentary characteristics and landform geomorphology. A new conceptual model for components of a monogenetic volcanic field was developed for standardising eruptive volume calculations and tested at the AVF. In this model, a monogenetic volcano is categorised in six parts, including diatremes beneath phreatomagmatic volcanoes, or crater infills, scoria/spatter cones, tephra rings and lava flows. The most conservative estimate of the total Dense Rock Equivalent eruptive volume for the AVF is  $1.704 \text{ km}^3$ . The temporal-volumetric evolution of the AVF is characterised by a higher magma flux over the last 40 ky, which may have been triggered by plate tectonic processes (e.g. increased asthenospheric shearing and back-arc spreading underneath the Auckland region). The eruptive volumes were correlated with the sequences of eruption styles preserved in the pyroclastic record, and environmental influencing factors, such as distribution and thickness of water-saturated post-Waiemata sediments, topographic position, distance from the sea and known fault lines. The past eruptive sequences are characterised by a large scatter without any initially obvious trend in relation to any of the four influencing factors. The influencing factors, however, showed distinct differences between sub-domains of the field, i.e. North Shore, Central Auckland and Manukau Lowlands. Based on the spatial variability of these environmental factors, a susceptibility conceptual model was provided for the AVF. Based on the comparison of area affected by eruption styles and eruptive volume, lava flow inundation is the most widespread hazard of the field. To account for this, a topographically adaptive numerical method was developed to model the susceptibility for lava flow inundation in the AVF. This approach distinguished two different hazard profiles for the valley-dominated Central Auckland and North Shore regions, and the flat Manukau Lowlands. A numerical lava flow simulation code, MAGFLOW, was applied to understand the eruption and rheological properties of the past AVF lava flow in the Central Auckland area. Based on the

simulation of past lava flows, three eruptive volume-based effusive eruption scenarios were developed that best characterise the range of hazards expected.

To synthesise, susceptibility mapping was carried out to reveal the patterns in expected future eruption styles of the AVF, based on the eruptive volumes and environmental factors. Based on the susceptibility map, the AVF was classified as highly susceptible to phreatomagmatic vent-opening eruptions caused by external environmental factors. This susceptibility map was further combined with eruptive volumes of past phreatomagmatic phases in order to provide an eruption sequence forecasting technique for monogenetic volcanic fields. Combining numerical methods with conceptual models is a new potential direction for producing the next generation of volcanic hazard and susceptibility maps in monogenetic volcanic fields. These maps could improve and standardise hazard assessment of monogenetic volcanic fields, raising the preparedness for future volcanic unrest.

## Acknowledgements

I would like to express my great thanks for the many people whom I have interacted in the last few years, and who helped me to complete my PhD thesis. First of all, I am thankful to my chief-supervisors, Károly Németh and Jonathan Procter, for guiding me through the PhD process. I am also thankful for the contributions from my co-supervisors, Shane J. Cronin, Jan M. Lindsay (University of Auckland, New Zealand), Mike Tuohy, Mark Bebbington and Győző Jordán (Hungarian Academy of Science, Hungary). Many thanks to Kate Arentsen for helping me to improve the presentation of this thesis. Special thanks go to all the staff and students of the Volcanic Risk Solutions group at Massey University, for their support and help my PhD studies, including Javier Agustin-Flores, Kate Arentsen, Eric Breard, Marco Brenna, Magret Damaschke, Gaby Gomez, Matt Irwin, Emily Kawabata, Gert Lube, Anja Möbis, Adam Neather, Natalia Pardo, Bob Stewart, Rafael Torres-Orozco, Manuela Tost, Georg Zellmer, Anke Zernack and Ting Wang.

For financial help, I would like to thank the Institute of Agriculture and Environment at Massey University for the PhD Research Fellowship. This work was also supported by the Massey University-led FRST-IIOF project “Facing the challenge of Auckland’s volcanism” and the Natural Hazards Research Platform project “Living with Volcanic Risk”, based at Massey University, as well as the DEtermining VOlcanic Risk in Auckland (DEVORA) project, co-funded by the NZ Earthquake Commission (EQC) and the Auckland Council, GNS Science, University of Auckland and Massey University.

I am thankful for the use of LiDAR data, which was provided by Auckland Council. I would also like to thank Tracy Howe, Elaine Smid and Madison Frank (University of Auckland) for their help in requesting the LiDAR data. Special help with the LiDAR dataset and details of its “origin” were given by Carl Ellaway (Auckland Council), Michael De Lacy (Fugro Spatial, Australia) and Jeremy Neilson (NZ Aerial Mapping Ltd). During the GPS and Terrestrial Laser Scanning surveys the important help of Bruce Robinson and Simon Smith (Global Survey, Auckland) was appreciated. In the field and the laboratory, many people have helped me including Anja Möbis, Javier Agustin-Flores, Jonathan Procter, Károly Németh, Hugo Murcia, Jan M. Lindsay, Natalia Pardo, Lucy McGee and Katarina Postekova. Their patience and support are appreciated, especially when they helped me to carry heavy equipment over long-distances. Thank you also to the Department of Conservation/Te Papa Atawhai who helped many times with logistics of field work on Browns Island. During the lava flow modelling, I am grateful for the help of Annalisa Cappello, Gaetana Ganci, Ciro Del Negro, Giuseppe Bilotta and Alexis Hérault (Istituto Nazionale di Geofisica e Vulcanologia, Catania, Italy). They made my stay in Catania wonderful and scientifically fruitful. Financial aid for this visit was made possible through the DEVORA project.

I am grateful to Győző Jordán for encouraging me to pursue research in the field of remote sensing and Geographical Information System (GIS). My former supervisors, György Less, János Földessy and Éva Hartai (University of Miskolc, Hungary), are thanked for supporting me to continue my PhD studies at Massey University in New Zealand.

For the “Thursdays”, I am really thankful to those people who made my stay in Palmerston North beautiful, including Marcela Humphrey, Natalia Pardo, Javier Agustin-Flores, Adimar Lujan, Jimena Rodríguez, Thiago Alves Amaro, Rafael Torres-Orozco, Ana Mar-Sarabia, Gaby Gómez, Hatim El Al, Marco Brenna, Friederike von Schlippe and Daniel Farley.

I wish to thank my parents in Hungary for their support and encouragement throughout my PhD study.

I owe the biggest thanks in the world to my loving wife, Angela, who has supported me over this intense period of my life. Thank you very much for being with me.

## Table of Contents

Abstract .....	i
Acknowledgements.....	iii
Table of Contents.....	v
List of Figures.....	ix
List of Tables.....	xix
Chapter One – Introduction.....	3
1.1. Monogenetic volcanoes and their hazards.....	3
1.2. GIS and remote sensing of monogenetic volcanoes .....	6
1.3. Aims and objectives .....	9
1.4. Thesis outline and structure.....	10
Chapter Two – Geological setting .....	15
2.1. Introduction .....	15
2.2. Basement geology of Auckland.....	15
2.3. Basaltic monogenetic volcanism in Auckland.....	20
2.3.1. Quaternary basaltic volcanism in the North Island.....	20
2.3.2. Melt extraction models and geochemical evolution.....	22
2.3.3. Eruption styles and volcanic landforms .....	25
2.3.4. Volcanic hazard assessment and monitoring system .....	30
Chapter Three – Materials and methods .....	39
3.1. Introduction to Digital Terrain Analysis (DTA).....	39
3.2. Materials and methods .....	41
3.2.1. Input data types available in Auckland .....	41
3.2.2. Data acquisition and pre-processing .....	47
3.2.3. Data interpolation.....	51
3.2.4. Post-processing techniques.....	56
3.2.5. Testing topographic datasets for Auckland .....	57
3.2.5.1. Terrain height and representation.....	58
3.2.5.2. Terrain attributes in 2D and 3D .....	59
3.3. Results: accuracy and variability .....	64
3.4. Which input data should be used? .....	72
Chapter Four – Quantitative parameterization of monogenetic volcanoes: geometry and volumes .....	82
4.1. Introduction .....	82
4.2. Model for volume estimates of monogenetic volcanoes.....	84
4.2.1. Bulk subsurface volume .....	86
4.2.2. Bulk proximal tephra accumulation and lava flows volume .....	88
4.2.3. Bulk medial to distal pyroclastic volume .....	90
4.3. Input data and configuration for the AVF .....	92
4.3.1. Bulk subsurface volume for the AVF .....	92
4.3.2. Bulk proximal tephra accumulation and lava flows volumes for the AVF.....	93
4.3.3. Bulk medial to distal pyroclastic volume for the AVF .....	95
4.4. Converting bulk to Dense Rock Equivalent (DRE) eruptive volumes .....	96

4.5. Results .....	101
4.6. Discussion.....	107
4.6.1. Limits and errors in eruptive volume estimates .....	107
4.6.2. Spatial and temporal magma flux.....	108
4.6.3. Integrating eruptive volumes with the AVF's evolution.....	110
4.6.4. AVF evolution and relationship to neighbouring fields .....	115
4.6.5. Volcanic hazard consequences.....	115
4.7. Conclusions.....	116
 Chapter Five – Linking eruptive volumes to eruptive styles.....	 121
5.1. Introduction.....	121
5.2. Methodology and conceptual framework.....	122
5.2.1. Coding of eruption styles and their eruptive volumes.....	122
5.2.2. Defining area affected in an eruptive history.....	131
5.2.3. Influencing factors on eruption styles .....	132
5.3. Results .....	135
5.3.1. Types and distribution of past eruptive histories .....	135
5.3.2. Influences on AVF eruptive sequences .....	141
5.4. Discussion.....	144
5.4.1. Factors influencing eruption style .....	144
5.4.2. A spatial model for distribution of factors influencing eruption style .....	145
5.5. Conclusion .....	148
 Chapter Six – Lava flow susceptibility mapping.....	 154
6.1. Introduction.....	154
6.2. Materials and methods.....	157
6.2.1. LiDAR survey and DSM preparation.....	157
6.2.2. Lava flow parameters .....	158
6.2.3. Hydrological channel extraction .....	162
6.2.4. Topographic classification of zones subject to lava flow inundation .....	163
6.2.5. Watershed characteristics .....	167
6.3. Results .....	168
6.3.1. Characteristics of past lava flows.....	168
6.3.2. Characteristics of present topography .....	170
6.4. Discussion.....	173
6.4.1. Lava flow susceptibility.....	178
6.4.2. Watershed characteristics .....	179
6.4.3. Evaluation of the method and its limitations .....	181
6.6. Conclusions.....	183
 Chapter Seven – Effusive eruption scenarios based on lava flow simulations .....	 189
7.1. Introduction.....	189
7.2. Materials and methods.....	194
7.2.1. MAGFLOW code.....	194
7.2.2. Input data for simulation of past lava flows .....	197
7.2.3. Matching lava flows with simulation results .....	200
7.3. Results .....	200
7.4. Discussion.....	206
7.4.1. Volume-limited versus cooling-limited flow regimes.....	206
7.4.2. Constraints on magma ascent velocity .....	207

7.4.3. Volcanic hazard consequences .....	210
7.4.4. Creating eruption scenarios for lava flow hazard mapping .....	210
7.4.5. Limits of lava flow simulations in volcanic field settings.....	211
7.5. Conclusions .....	212
Chapter Eight – Discussion and conclusions .....	217
8.1. Discussion.....	217
8.2. A conceptual model for eruption style susceptibility mapping .....	218
8.3. A conceptual model for lava flow susceptibility mapping.....	227
8.4. Towards a GIS-based hazard assessment of monogenetic volcanic fields .....	231
8.5. Conclusions .....	233
8.5.1 Research objectives.....	233
8.5.2. Future directions of research.....	235
8.5.3. Concluding remarks .....	237
References cited.....	242
Appendix A – Pullout map.....	283
Appendix B – Supplementary data (DVD) .....	285
Appendix C – Statement of contribution .....	301



## List of Figures

- Figure 2.1 Simplified geologic and tectonic map of the broader Auckland region, based on Kermode (1992) and Edbrooke (2001). The black rectangle shows the area of the AVF with the locations mentioned in the text (1 – Takapuna Beach, 2 – Cheltenham Beach, 3 – Rangitoto, 4 – Motutapu Island, 5 – Browns Island, 6 – One Tree Hill, 7 – Pukaki maar, 8 – Crater Hill.). The roman numerals show the area of the three domains within the AVF mentioned in the text (I – North Shore, II – Central Auckland, III – Manukau Lowlands). The coordinates are in metres (New Zealand Map Grid). ..... 16
- Figure 2.2 Simplified stratigraphic column with characteristics of the main geologic formations occurring in Auckland. Note that the depth indicated in the sedimentary column varies from region to region. The values used here are based on Edbrooke et al. (1998). Sedimentary characteristics are after Kermode (1992) and Edbrooke et al. (1998). The Dun Mountain–Maitai Terrane has not been penetrated by the drill core described in Edbrooke et al. (1998), but it is inferred to be located underneath Auckland based on magnetic anomalies (e.g. Eccles et al., 2005). ..... 18
- Figure 2.3 Outcropping Waitemata units with an extensive multidirectional fracture system at Takapuna Beach (A) and Cheltenham Beach (B) in the North Shore. For the location map, see Fig. 2.1. .... 19
- Figure 2.4 Oblique view of the basaltic volcanic regions in Northland and Auckland. The coordinates are in metres (New Zealand Transverse Mercator 2000). ..... 21
- Figure 2.5 (A) Location map for the 52 monogenetic vents scattered around the Auckland region overlain on the LiDAR DSM. (B) Location of the 52 eruptive centres (green triangles) within the City of Auckland overlain on a false-colour multispectral SPOT-5 satellite image. Note that the areas in grey to green are the urban and heavily populated parts of Auckland, while the red colour shows distribution of vegetated areas, such as forest or park. The coordinates are in metres (New Zealand Transverse Mercator 2000). ..... 23
- Figure 2.6 Simple and complex magma generation scenarios based on three examples from the AVF. .... 24
- Figure 2.7 Examples of monogenetic volcanoes from the AVF. For the locations of these examples, the reader is referred to Fig. 2.5 and Appendix A. (A) Overview photo of monogenetic volcanoes in the Auckland area. (B) An example of a wide and circular crater formed by extensive phreatomagmatic eruptions, Pukaki volcano. (C) Combination of phreatomagmatic eruption and late stage magmatic eruption forming complex monogenetic volcanoes, such as Browns Island in the Waitemata Harbour. (D) Purely magmatic processes form scoria cone and extensive lava flow fields at Rangitoto. .... 26
- Figure 2.8 Sedimentary structures in tuff deposits formed by phreatomagmatic eruptions in the AVF. For location of these examples, the reader is referred to Fig. 2.5 and Appendix A. (A) Dune- and cross-bedded units with contrasting granulometric characteristics at the Pupuke eruption centre. (B) Close view of an impact sag

- caused by a ballistically ejected basaltic block at Browns Island. (C) Complex sedimentary unit, exposed at the basal parts of Browns Island tuff pyroclastic sequence, revealing the dominant transportation mechanism (e.g. pyroclastic density current and tephra fall) related to the formation of tuff rings. .... 28
- Figure 2.9 Simplified sedimentary log for deposits of a Strombolian eruption style, exposed at the Rangitoto scoria cone (see Fig. 2.5 for location). This log gives examples for the contrasting styles of ejecta transport on the flanks of a growing scoria cone by grain flow processes (e.g. lapilli-sized scoria fragments) and ballistics (e.g. larger broken or fluidal-shaped blocks/bombs). Modified from Kereszturi and Németh (2012a)..... 29
- Figure 2.10 Spatial intensity maps of the AVF based on the vent locations. The spatial intensity is calculated by (A) symmetric Gaussian kernel after Kereszturi et al. (2012b), and (B) asymmetric elliptic kernel after Bebbington and Cronin (2011). .... 33
- Figure 3.1 Overview of topographic data used in this study captured at different spatial scales with different coverage and (vertical) accuracy. For more information about these datasets for Auckland, see text. Note that for accuracy assessment purposes, TLS survey points with 0.5 m average point spacing were used in the present accuracy assessment..... 40
- Figure 3.2 Basic survey concepts of RTK GPS, LiDAR, SRTM and ASTER data acquisition and imaging geometry. The figure is not to scale. The inset shows the vertical and horizontal error in topographic survey after Hodgson and Bresnahan (2004). .... 44
- Figure 3.3 Field photos of the TLS (A) and RTK GPS surveys (B) carried out on the distal segment of a rubbly a'a lava flow near Flax Point, Rangitoto. (C) Perspective view of the TLS point cloud after registration of point from each station. The inset shows the capability of the TLS to resolve detailed features, such as grass (white arrows). Vegetation was removed manually from the point cloud to obtain bare surface points for the DSM..... 50
- Figure 3.4 Structure of data and interpolation from vector-based input data, such as spot heights and contour lines, using (A) Triangulated Irregular Network (TIN) and (B) linear interpolation, implemented in the ILWIS software package. Note that there are two examples provided for comparison to highlight the effect of user-defined horizontal resolution and vertical precision on the resultant DEM. If the horizontal resolution is too large in relation to the average distance between two neighbouring contour lines, a grid cell is created with the average value of the two input contour line elevations. If the vertical precision is too low, then the resultant grid cell might have the same elevation, and consequently a flat grid cell would be created. .... 52
- Figure 3.5 (A) Overview of topographic data available in Auckland with various spatial resolutions. From the top to the bottom: 2 m LiDAR DSM, 4 m topo50 DEM, 30 m ASTER GDEM, 90 m SRTM DTM. (B) Elevation histograms for each dataset. .... 55
- Figure 3.6 (A) Scheme of filtering with moving window of a 3×3 and 5×5 kernel.  $Z1$  to  $Z25$  are the grid cells. (B) Concept of the resampling in a gridded environment by the nearest neighbour method. During nearest neighbour resampling, no additional

- interpolation takes place. During resampling the grid cell value of the new resolution is the value of the cell located the closest to the new grid cell centre (e.g. Wood, 1996). ..... 57
- Figure 3.7 High accuracy reference topographic data from the Auckland region. (A) Spatial location of geodetic survey marks as red triangles. The light yellow and light green polygons represent the available point cloud data from LiDAR surveys with rural and urban settings, respectively. The green rectangles are the location of the RTK GPS profiles and TLS DSM data. Numbered test sites in green triangles are: 1 – Onepoto, 2 – Rangitoto, 3 – Browns Island, 4 – Panmure Basin, 5 – Pukewairiki, 6 – Mt. Mangere, 7 – Mangere Lagoon, 8 – Pukeiti and Otutataua, 9 – Crater Hill. (B) RTK GPS profiles from Auckland used in this study. (C) Location of the RTK GPS profiles and the TLS survey site on the Rangitoto volcano. On the right hand-side the TLS-based DSM shown here is with spatial resolution of 0.5 m. .... 60
- Figure 3.8 Overview of the calculation of zero-order derivatives such as area (A), standard deviation of elevation (B), and volumes (C). .... 63
- Figure 3.9 Overview of the calculation of first-order derivatives, such as slope angle and slope aspect, in 2D and 3D environment. Note that the examples are used here with a linear, unweighted Prewitt filter (Prewitt, 1970). (A) An example for calculating slope angle along a 2D profile. (B) Perspective view of a 3×3 grid cell kernel, which was used to calculate slope angle and aspect by numerical differentiation in (C). .... 63
- Figure 3.10 Point-based error assessments using the geodetic survey marks. Note that negative and positive values show places where elevation values are underestimated and overestimated, respectively. .... 66
- Figure 3.11 Profile-based error assessments for the three test sites. The upper row of graphs shows the elevation of different topographic datasets from the Auckland region. The bottom row of graphs shows the error along the control profile. The insets are the error distribution histograms for each topographic dataset. The bins are 1 m for SRTM DTM, ASTER GDEM and topo50 DEM, and 0.05 m for 10 m and 2 m for LiDAR DSMs. .... 67
- Figure 3.12 Surface-based error assessment based a TLS acquired reference surface on the distal part of the Rangitoto lava flow field. Note the multimodal (arrows) error distributions for the topo50 DEM, ASTER GDEM and SRTM DTMs. These are due to the dominance of under- and overestimation of the real topography. .... 68
- Figure 3.13 Variability of zero and first derivatives, calculated from the DSM/DTM/DEMs, along the RTK GPS control profiles for three test sites: Browns Island (first column), Pukaki (second column), and Rangitoto (third column). .... 69
- Figure 3.14 Error in eruptive volume estimations due to resampling and different input data types, including LiDAR DSM 2m (blue), topo50 DEM (orange), ASTER GDEM (yellow) and SRTM DTM (green). For the location of each evaluation site see Fig. 3.7. This graph shows the overall inaccuracy of ASTER and SRTM DTM products in resolving the fine-details of the topography on monogenetic volcanoes. .... 71

- Figure 3.15 Graph shows two profiles through the youngest volcanic edifice, Rangitoto, with all the available topographic data from Auckland. The summit crater with a diameter of 200 m is not resolved by the coarser topographic data sources, such as SRTM DTM or ASTER GDEM. The surface roughness on a dm-scale is shown in the inset. This example surface is based on the TLS DSM data on the distal parts of Rangitoto a'ā lava flow. The blue line is the LiDAR 2m data, while the black line is the much higher resolution TLS DSM data. .... 75
- Figure 4.1 Geology of the AVF after Hayward et al. (2011). The whole area shown in this map coincides with the area of City of Auckland. The inset map shows the location of the AVF and other Quaternary basaltic volcanic fields in the North Island, New Zealand. .... 83
- Figure 4.2 (A) Diagram of the volcano-sedimentary parts of a conceptualised monogenetic volcano for volume estimation. (B) Methods applied for volume estimation from the different volcano parts. The pie charts represent the DRE correction scheme applied in this study. As the first step of the DRE corrections, a proportion of juvenile, non-juvenile (lithics) and interparticle void space in the volcano parts were used (shown as large pie charts). In the second step, the juvenile content left was corrected for vesicularity (shown as smaller pie charts). .... 85
- Figure 4.3 Outcrop photos of volcanic deposits from the AVF. (A) Photos showing the well to poorly sorted deposits in one of the scoria cones of Three Kings volcanic complex. The inter-particle void space can be large. (B) Contrasts between juvenile-rich and juvenile-poor units exposed in the succession at Browns Island. Note the large diversity of accidental lithic clasts from the underlying Miocene Waitemata sediments, such as sandstone (black horizontal arrows). (C) A typical lava flow surface from the youngest eruption site, Rangitoto. The lava flows in Rangitoto usually range from shelly pahoehoe to rubbly a'ā lava flow morphotypes. The measuring tape is 50 cm long. .... 89
- Figure 4.4 (A and B) Microphotographs of pyroclastic rocks from the phreatomagmatic ejecta ring of Orakei Basin. S – sideromelane glass shards and T – tachylite glass shards. (C) Point counting results of a typical thin-section from the Browns Island ejecta ring, showing the maximum 35 vol% of juvenile content. The graph is the evaluation plot for the counts. (D) Closer view of two juvenile fragments with contrasting vesicularity. .... 91
- Figure 4.5 (A) Scan of a scoria hand specimen from the Rangitoto scoria cone. (B) Binary image of the same sample, showing the distribution of vesicles in white. The red box is the area considered in the 2D vesicularity calculations. (C) Field photo of a moderately vesiculated lava flow texture from the lava flow field of Rangitoto. (D) Thresholded binary image showing the distribution of largest vesicularity population. (E) Graph showing the results of density measurements on scoria (n = 48) and lava rock (n = 42) samples from Rangitoto and Browns Island volcanoes. The densities were measured as envelope density by Micrometrics Geo PyC1360 density analyser. Due to the small diameter (i.e. 2 cm in diameter) of the samples measured in the density analyser, these density and vesicularity values are considered as minimum values. The vesicularity is calculated proportional to  $2.8 \text{ g/cm}^3$ . .... 94

- Figure 4.6 Results of the new DRE eruptive volume estimates for the AVF. (A) The results of minimum estimates, including those volcanic parts where the volumes can be estimated with a relatively high accuracy. (B and C) Overall DRE eruptive volumes change if distal tephra blankets and diatreme volumes are considered. 102
- Figure 4.7 (A) DRE eruptive volume as a function of time during the evolution of the AVF for each estimate. The ages are based on the most likely simulated eruption history based on the probabilistic analysis of Bebbington and Cronin (2011). The ages are simulated based on 1000 Monte Carlo simulations of the existing event-order of the AVF. Therefore, individual volcanoes might have a slightly different order (Bebbington and Cronin, 2011). (B) Number of volcanic events over the evolution of AVF, showing a decreasing trend since 32 ka..... 103
- Figure 4.8 (A) Spatial distribution of volcanic centres formed during the older (blue triangles within the blue polygon) and younger stages (red triangles within the red polygon) in the AVF with the geometric, areal and volumetric characteristics. The blue, red and black crosses are the geometric centre of older, younger stages and the all ( $n = 52$ ) volcanoes from the AVF, respectively. (B) Spatial distribution of eruptive volume per volcanoes (blue dots) scaled by their volumetric size in the AVF, revealing a couple of exceptionally large volcanic centres (black arrows with names). The numbered red arrows show the distribution of those “paired-volcanoes”. These paired-volcanoes could have formed from the same eruptive event, involving a lateral vent migration. Red numbers with arrows are: 1 – Tank Farm and Onepoto, 2 – Mt. Victoria and Mt. Cambia, 3 – Grafton volcano and Auckland Domain, 4 – Purchas Hill and Mt. Wellington, 5 – Mt. Richmond and McLennan Hills, 6 – Styaks Swamp, Green Mt., Otara Hill and Hampton Park, 7 – Mt. Mangere and Mangere Lagoon, 8 – Wiri Mt. and Ash Hill..... 109
- Figure 4.9 Histograms showing the eruptive volumes of each volcano in the AVF (first column), older stage ( $\geq 40$  ka; second column) and younger stage ( $\leq 40$  ka; third column), using bulk (A) and DRE-corrected volumetric data (B). Bin size is  $0.01 \text{ km}^3$  on all histograms. Outliers, such as Rangitoto and One Tree Hill, are not shown on the histograms..... 110
- Figure 4.10 (A) Distribution of monogenetic volcanics in the broader Auckland region. The black ellipses show the location of Auckland (AVF), South Auckland (SAVF) and Ngatutura (NVF) volcanic fields, with the duration of volcanic activity and distance from location of the recent manifestation of volcanism. For scale, the average spatial extent of a monogenetic volcanic field is given, based on data from Le Corvec et al. (2013c). (B) Age distribution for the monogenetic volcanic eruptions in the last 2.5 My in the broader Auckland region. The K-Ar radiometric ages are from Briggs et al. (1994)..... 113
- Figure 5.1 Eruptive histories (E) of monogenetic volcanoes can be defined as an array of numbers ordered chronologically. The numerical codes include 1 – fire-fountaining, 2 – Strombolian, 3 – violent Strombolian, 4 – phreatomagmatic, 5 – Surtseyan and 6 – magmatic effusive activity. Modified from Kereszturi and Németh (2012a). ..... 128
- Figure 5.2 Area-equivalent circles of Browns Island, calculated from the delimited area of each differentiated eruption style type..... 131
- Figure 5.3 Overview of the AVF and two cross-sections through the Manukau Lowlands. The drill core data are from the PETLAB database ([www.pet.gns.cri.nz](http://www.pet.gns.cri.nz)).

Geographic divisions on the left of the map include: North Shore, which includes areas now occupied by sea water in the Waitemata Harbour; Central Auckland, which encompasses the elevated parts of the Auckland Isthmus; and the Manukau Lowlands including the Manukau Harbour and the alluvial plain areas with the western slopes of the Hunua Range. The size of the green dots is scaled to the eruptive volume of the phreatomagmatic phase (in  $\times 10^6 \text{ m}^3$ ) of past volcanoes. 133

- Figure 5.4 Area-equivalent circles revealing eruptive histories with either increasing (e.g. One Tree Hill) or decreasing (e.g. Crater Hill) footprints of volcanic hazard during the course of the eruptions..... 136
- Figure 5.5 Histogram of area affected by different volcanic processes forming ejecta rings (A), scoria cones (B) and lava flow (C) in the AVF. The bin size is  $0.5 \text{ km}^2$  for all histograms. .... 137
- Figure 5.6 Contribution of different eruption styles to the total eruptive volumes of each volcano in the AVF. The colouring indicates phreatomagmatic (green), magmatic explosive (yellow) and the magmatic effusive volume (red). The chronological order is a simulated event order from Bebbington and Cronin (2011). ..... 137
- Figure 5.7 Ternary diagram for proportional volumes for three types of eruption styles in the AVF, with those affected by phreatomagmatic and Surtseyan eruptions, magmatic explosive eruptions (fire-fountaining and Strombolian types), and magmatic effusive eruptions. The data were normalised to the mean of each eruptive unit. .... 138
- Figure 5.8 (A) Proportions of single, compound and complex eruptive histories in the AVF, and their dominant eruption styles. (B) Box plot graphs for the area affected (left) and eruptive volumes (right graph) in relation to eruptive histories. The lower quartile ( $Q_1$ ), median ( $m$ ), upper quartile ( $Q_3$ ), and outliers' values are shown. .... 139
- Figure 5.9 Spatial distributions of single (A), compound (B), and complex eruption histories (C), as well as the number of eruption styles (D) in the AVF..... 140
- Figure 5.10 Scatter graphs of phreatomagmatic vent-opening volumes of the AVF's volcanoes in relation to the (A) thickness of post-Waitemata non-volcanic sediments, (B) pre-eruptive elevation, (C) distance from the present coastline, and (D) distance from known fault lines. .... 141
- Figure 5.11 Box plots showing the three sub-areas of the AVF and the total AVF in relation to (A) thickness of post-Waitemata non-volcanic sediments, (B) pre-eruptive elevation, (C) distance from the present coastline, and (D) distance from known fault lines. Note that in graph A, the thickness is inferred to be  $\leq 5 \text{ m}$  under volcanoes in the Central Auckland region. .... 142
- Figure 5.12 Box plots showing the distance from the coast to the volcanoes from three distinct sub-areas of the AVF and the total field in relation to (A) a sea level higher than the present day by 10 m, and (B) 5 m, as well as (C) a sea level lower than the present day by 5 m and (D) by 10 m. .... 143
- Figure 5.13 A model for internal (red circles) and external (green circles) factors influencing eruption styles in the AVF. Future hypothesised eruption site examples are shown as black dots with the four environmental factors ( $d_{\text{sea}}$  – distance from sea;  $d_{\text{fault}}$  – distance from known fault lines;  $Z_{\text{topo}}$  – topographic

- position, as well as  $h_{\text{wat}}$  – thickness of water-bearing units). The significance of each environmental factor varies between parts of the field, and there is no sole controlling factor for eruption styles and histories. The listed external environmental factors are in the order of inferred importance. Note the excavation depth of the maar volcanoes is not constrained well, but it is inferred to be very shallow, 50-100 m (Cassidy et al., 2007; Agustin-Flores et al., 2014). The fault location data are after Kenny et al. (2012)..... 146
- Figure 5.14 The relationship between thickness of post-Waitemata non-volcanic sediments and the eruptive volumes of ejecta rings and crater infills for all volcanoes in the Manukau Lowlands (A), and with the largest volume volcanoes of the area (B). Note that all volcanoes located under the predicted line have extremely small erupted volumes, with large extents of anthropogenic modification..... 148
- Figure 6.1 (A) An overview LiDAR-based DSM of the Auckland region with the location of studied volcanic centres. Note that a phreatomagmatic maar volcano, Orakei Basin, and a complex monogenetic volcano with initial phreatomagmatic and late magmatic stage, Crater Hill, both mentioned in the text, are indicated by the dashed arrows. The dashed ellipsoid shows the extent of the Auckland Volcanic Field (after Spörli and Eastwood, 1997). The coordinates are given in New Zealand Transverse Mercator (NZTM2000). The solid boxes indicate the location of Figs. 6.3, 6.4 and 6.8. (B) Location of the 52 eruptive centres (green triangles) within the AVF overlaid on a false-colour multispectral SPOT-5 satellite image. Note that the areas in grey to green are the urban and heavily populated parts of Auckland, while the red colour shows distribution of vegetated areas, such as forest or park. .... 156
- Figure 6.2 Flow diagram for input data, data processing and results ..... 159
- Figure 6.3 Perspective (A) and profile (B) views of morphometric parameters of lava flows applied in this paper visualised on the Mt. Mangere volcano (for the detailed location see Fig. 6.1)..... 161
- Figure 6.4 Definitions of susceptibility zones (sea, depressions, low-lying area, buffer and ridges/peaks) identified in the AVF visualised on an area from North Shore (for the detailed location see Fig. 6.1). The largest depression in the figure is the Lake Pupuke, generated by series of phreatomagmatic eruptions..... 163
- Figure 6.5 Field photographs illustrating examples of preserved lava flow surfaces and their source scoria cones (black arrows). (A) A'a lava flow surface preserved in the coastal area of Browns Island. (B) Pahoehoe surface related to the Mt. Mangere scoria cone. (C) Fresh a'a lava flow from the youngest eruption centre, Rangitoto. (D) Overview photo of the Mt. Wellington scoria cone and its basaltic lava flow exposed due to extensive quarrying. Note that the white arrow indicates the direction of the lava flow..... 169
- Figure 6.6 Graphs of the main morphometric parameters of lava flows. Age estimates are from Bebbington and Cronin (2011). Note that the black arrows indicate the morphometric values of Rangitoto volcano. .... 170
- Figure 6.7 Figure showing the spatial density of the entire field (green background on each map) based on the location of the 50 eruption centres (triangles in A). A 400 m wide zone at the coastline is indicated by black-grey-white lines, see text for

- explanation. (A) Watershed ranking based on the averaged kernel density. The contour lines (black lines) represent the 25%, 50% and 75% percentage of input point used to estimate the probability density distribution. (B) Watershed ranking based on cumulative bulk volume. (C and D) These two maps show the area portion (pie diagrams) of zones within watersheds for the Scenario 1 (C) and Scenario 2 (D). The colouring of the watershed boundaries shows the ratio between the total areas of buffer (light green) and ridge/peaks (dark green) as well as depressions (red) and low-lying areas (pink). The colours used here are the same as on the lava flow susceptibility map in Fig. 6.9..... 177
- Figure 6.8 Cross-section through the central, elevated part, of the AVF, illustrating the channelised lava flows by valley eroded into the Waitemata sandstone. For the detailed location see Fig. 6.1. .... 180
- Figure 6.9 Lava flow susceptibility map based on Scenario 1 (without Rangitoto) for the AVF showing the susceptibility zones with the major hydrological and topographical characteristics (A) and with major infrastructures (B). .... 182
- Figure 7.1 Overview of the AVF and its volcanoes (black dots) and the location of the simulated lava flows (numbered black dots). .... 193
- Figure 7.2 Graph shows three effusion curves of Little Rangitoto (A), Mt. Roskill (B) and Three Kings (C) and their comparison (D). .... 199
- Figure 7.3 Lava flow simulation results of Little Rangitoto (left-hand side) and comparison with the mapped extent of the flow (right-hand side). On the left-hand side, the histogram insets show the distribution of thickness values for the simulations. .... 201
- Figure 7.4 Lava flow simulation results of Mt. Roskill (left-hand side) and comparison with the mapped extent of the flow (right-hand side). On the left-hand side, the histogram insets show the distribution of thickness values for the simulations; the smaller histograms are the original flow thickness distributions. .... 202
- Figure 7.5 Lava flow simulation results of Three Kings (left-hand side) and comparison with the mapped extent of the flow (right-hand side). On the left-hand side, the histogram insets show the distribution of thickness values for the simulations; the smaller histograms are the original flow thickness distributions. .... 203
- Figure 7.6 Dyke widths as a function of ascent velocity for a fissure length of 50, 100 and 150 m. The magma flux is estimated at  $40 \text{ m}^3/\text{s}$ , in accordance with the value of best simulation. .... 207
- Figure 7.7 Envisaged feeder dyke geometries of the three eruption centres. Abbreviated parameters are U – ascent velocity, L – flow length, F – fissure length, and V – bulk eruptive volume. .... 209
- Figure 8.1 Classified maps of features used for eruption style susceptibility mapping in the AVF. (A) Combined thickness map of post-Waitemata uncompacted non-volcanic sediments. (B) Topographic elevation. (C) Distance from the present shore line, (D) Distance from known faults. .... 220
- Figure 8.2 Susceptibility map (red = high, green = low) for phreatomagmatic vent-opening phase in future eruptions in the AVF, based on combining the maps shown in Fig. 8.1. The inset shows the distribution of each susceptibility class. The areas below sea level (white) were not considered. .... 222

- Figure 8.3: Scatter graph showing the relationship between susceptibility classes for phreatomagmatic eruptions (Fig. 8.2) and the median volume estimated from the interpolated raster of phreatomagmatic phases. .... 224
- Figure 8.4 Eruption sequence forecast map based on the eruption style susceptibility map (Fig. 8.2) and interpolated values of the phreatomagmatic volumes of the 52 volcanoes in the AVF. The likely eruption sequences and eruptive volume percentages (blue column = phreatomagmatic volume; light yellow column = magmatic explosive and effusive volume) of three example volcanoes are shown for a magma supply of  $8 \times 10^6 \text{ m}^3$  (e.g. Panmure Basin; Chapter 4). .... 225
- Figure 8.5 A model of proximal and distal zones in lava flow simulations in a monogenetic volcanic field setting. A hypothetical vent (red dot) is characterised by a radius ( $r$ ), which is 1 km here. The circle with radius  $r$  shows the potential area that might be modified by initial cratering and ejecta ring formation during a phreatomagmatic eruption. This might be coupled with an eruption taking place on a watershed boundary (e.g. Mt. Albert). Lava flow modelling within proximal areas thus has a higher degree of uncertainty. Accuracy of prediction of potential lava flow path and length increases towards distal zones, where topographic modification from the eruption is not extensive. .... 228
- Figure 8.6 Maps showing different methods of modelling lava flow susceptibility in the North Shore area, including (A) stochastic lava flow inundation map from a hypothesised vent (blue triangle), and (B) thickness map simulated by MAGFLOW using the Mt. Roskill effusive curve and magma supply volumes (e.g. Chapter 7). The insets shown in (B) are topographic profiles with the simulated lava flows (under red curve). The valley-confined (C) and unconfined (UC) flow zones of each simulation are marked. .... 230
- Figure 8.7 Structure of spatial attribute based hazard assessment designed for the AVF. The layers of the database can be separated into input (I), hazard (H) and risk (R) components. .... 232



## List of Tables

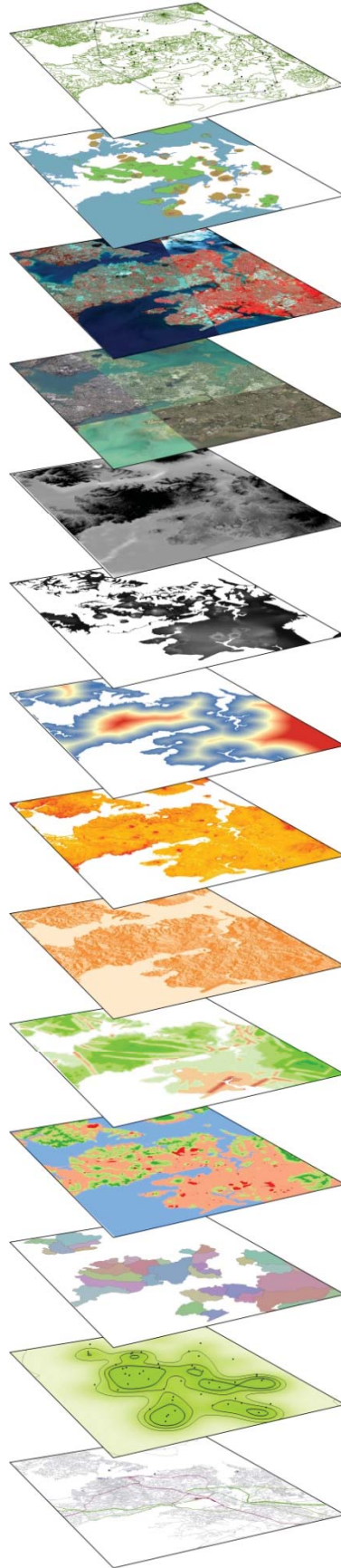
Table 2.1 Summary of simulated ages (from Bebbington and Cronin, 2011; 2012), eruption styles (from Hayward et al., 2011) and eruptive volumes (from Allen and Smith, 1994) of the AVF volcanoes. ....	32
Table 3.1 Results of the error assessment of the topographic data for Auckland. ....	65
Table 4.1 Summary of physical properties used to establish the input data for DRE corrections. ....	98
Table 4.2 Summary of the DRE correction values used in this study. ....	100
Table 4.3 Summary of DRE-corrected, minimum eruptive volumes estimate for each monogenetic volcano in the AVF. The underlined eruptive volumes are based on the bulk volume data published in Allen and Smith (1994), recalculated with our DRE correction scheme. The chronology shown here is based on simulated ages adapted from Bebbington and Cronin (2011). Notes: 1 – Pupuke and North Head bulk volumes was corrected for a higher amount of juvenile contents (Allen and Smith, 1994), 2 – In the case of Maungataketake, the bulk ejecta rings volume has been corrected for erosion, 3 – Bulk lava flow volumes has been updated since Kereszturi et al. (2012b) due to more information about the pre-eruptive surface, 4 – The bulk volume for St. John volcano is estimated using the inferred areal extent of the flow and a constant thickness of 10 m, 5 – The bulk volume of McLaughlin Mt. includes the bulk volume of the three small, Puhinui craters’ as well, 6 – Lava flow from Mt. Eden and Three Kings flowed partially on top of one of the earliest lava flows of Central Auckland are from the St. John volcano (Eade, 2009). As a result of this stratigraphy, the area proportional bulk volume of St. John lava flow has been substrate from the bulk volumes of Mt. Eden and Three Kings volcanoes, 7 – Mt. Eden’s bulk volume contains the ejecta ring and magmatic crater infill of Te Pou Hawaiki volcano (Fig. 4.1), 8 – In the case of Mt. Mangere 0 m a.s.l. plane were used as the pre-eruptive surface, however, it is possible that the contact between lava flow and the Tauranga Formation is a couple of m below the present sea-stand. Therefore, this is a minimum volume, 9 – The initial phreatomagmatic phase of Rangitoto is approximated using a volume of a crater with diameter of 800 m and depth of 30 m, as well as the ejecta rings volume equivalent to the Panmure Basin. The selection of this approximation was based on the available geophysical surveys of Rangitoto, after Milligan (1977), 10 – Note that the bulk volume estimate for Rangitoto contains the eruptive products from both phase of activities. ....	104
Table 4.4 Summary of field-scale and edifice-scale characteristics of the AVF for the older (250–40 ka) and younger (<40 ka) stages and for the whole field. The duration is based on an average of 10 m <sup>3</sup> /s eruption rate. Note: ph – phreatomagmatic eruptions, mag – magmatic explosive eruptions, eff – effusive activity. ....	114
Table 5.1 Summary of the DRE-corrected eruptive volumes and eruption styles inferred from the pyroclastic deposits preserved at each monogenetic volcano in the AVF. The chronology shown here is based on simulated ages adapted from Bebbington and Cronin (2011). The underlined eruptive volumes are based on the bulk	

volume data published in Allen and Smith (1994), recalculated with our DRE correction scheme (Chapter 4). Key: “L” – sub-region within the AVF in which “N” is North Shore, “C” is Central Auckland and “M” is Manukau Lowlands; “ph.” – phreatomagmatic phase; “mag.” – magmatic explosive phase; “eff.” – magmatic effusive phase; “E” – refers to eruption history or eruption sequence with the eruption styles as 1 – phreatomagmatic, 2 – magmatic explosive, 3 – magmatic effusive; “ $T_{sed}$ ” – thickness of the post-Waitemata non-volcanic sediments; “ $d_{sea}$ ” – distance from coastline; “+10 m” and “+5m” – distance from the coastline in the case of a higher sea level by 10 m and 5 m respectively; “pr. day” – distance from the present day coastline; “-10 m” and “-5m” – distance from the coastline in the case of a lower sea level by 10 m and 5 m respectively; “ $Z_{topo}$ ” – elevation of pre-eruptive topography at vent location, in which zero indicates that the vent is on the shore or submarine; “ $d_{fault}$ ” – distance from known fault line..... 124

Table 6.1 Summary of morphometric parameters for the studied fifteen lava flows. $Z$ – is the pre-eruptive basement elevation in meter a.s.l. that was used in the bulk volume calculations. ....	165
Table 6.2 Differences in the area of hazard zones using two simulated scenarios.....	172
Table 6.3 Properties of large (larger than 2 km <sup>2</sup> ) watersheds. The values in bold represent either the smaller topographical differences between catchment rims and drainage than a lava flow with average thickness or those catchment that are limited (i.e. smaller than average lava flow) in volume capacities.....	174
Table 7.1 Summary of the input physical parameters of the lava flows ( $L_{max}$ – maximum length, $A_{lava}$ – area, $T_{max}$ and $T_{mean}$ – maximum and average thickness, bulk and DRE-corrected eruptive volumes). ....	194
Table 7.2 Overview of MAGFLOW input parameters for the simulation in the AVF.	197
Table 7.3 Comparison of properties of simulated lava flow scenarios of Little Rangitoto, Mt. Roskill and Three Kings examples. The best-fit scenarios are highlighted in green. ....	204
Table 8.1 List of cities and infrastructure located on or near monogenetic volcanic fields. In such settings susceptibility mapping could be useful to improve hazard assessment. Key: M – monogenetic; P – polygenetic; pop. – population (in million) in the metropolitan area; VF – volcanic field.....	226







Chapter **1**  
Introduction

# 01 / introduction

This Chapter introduces the scientific background to research on monogenetic volcanic fields and their associated volcanic processes, especially studies aided by remote sensing and Geographic Information System (GIS). This introductory chapter begins to examine monogenetic volcanism as a whole before zooming down into the edifice- and eruption-scales. Eruptive processes in the formation of a monogenetic volcano result in a range of volcanic hazards, which are discussed in relation to the Auckland Volcanic Field (AVF), New Zealand. This Chapter concludes by introducing the main hypotheses and aims of the thesis and presenting a conceptual framework for methods to test and achieve these, respectively.

## Chapter contents

1.1. Monogenetic volcanoes and their hazards.....	3
1.2. GIS and remote sensing of monogenetic volcanoes .....	6
1.3. Aims and objectives .....	9
1.4. Thesis outline and structure.....	10

## Chapter One – Introduction

### 1.1. Monogenetic volcanoes and their hazards

Monogenetic volcanoes are typically small in eruptive volume ( $\leq 1 \text{ km}^3$ ) and can form within a timeframe of days to month, and rarely years (Valentine and Gregg, 2008; Németh, 2010; White and Ross, 2011). This type of volcanism occurs relatively far ( $>200 \text{ km}$ ) from active plate boundaries, normally in an intracontinental setting (e.g. Cebriá and López-Ruiz, 1995; Demidjuk et al., 2007). In this tectonic setting, their origin is related to successful melt extraction from the mantle at depths between 60 to 90 km (e.g. Brenna et al., 2012b) that can be induced by tectonic strain (e.g. Valentine and Hirano, 2010) and/or asthenospheric upwelling (e.g. Konecny et al., 2002; McGee et al., 2013). Monogenetic volcanoes are not limited to intraplate settings; they may also occur on polygenetic volcanoes as a product of flank eruptions (e.g. Mazzarini and Armienti, 2001; Germa et al., 2010). In such geologic settings they are often called flank/parasitic cones or satellite cones (Settle, 1979; Mazzarini and Armienti, 2001; Favalli et al., 2009c). Monogenetic volcanoes seldom occur individually, but tend to form spatially closely-located groups of cones or vents, forming clusters, such as the SP cluster in the San Francisco Volcanic Field in Arizona (Conway et al., 1998). If dispersed monogenetic volcanism occupies a broader geographic area of  $>10 \text{ km}$  in diameter, it is often called a volcanic field (Connor and Conway, 2000; Valentine and Gregg, 2008; Németh, 2010). A monogenetic volcanic field comprises tens to thousands of individual volcanic edifices, formed as a result of a series of eruptive events that can vary in style (White, 1991; Aranda-Gómez and Luhr, 1996; Guilbaud et al., 2009; Pardo et al., 2009), fed by single or multiple batches of magma (Brenna et al., 2010; Jankovics et al., 2012; McGee et al., 2012; Le Corvec et al., 2013a). Each volcano has its own dyke/feeding network and eruptive location. Rejuvenation of volcanic activity within an already established conduit/vent area is not common (Connor et al., 2000; Keating et al., 2008; Lefebvre et al., 2012). However, overlapping volcanic edifices are common, due to the closely spaced magma ascent pathways or individual focal eruptive sites along a long dyke (Auer et al., 2007; Kereszturi et al., 2010; Shaw et al., 2010; Needham et al., 2011). Monogenetic eruptions are mostly fed by single or multiple batches of magma

where the residence time in the lithosphere is limited (Németh et al., 2003; Smith et al., 2008; Valentine and Hirano, 2010). The rapid magma ascent and brief eruptive history of these volcanoes mean they record both mantle/source and near-surface environmental conditions well (Németh et al., 2001; Valentine and Perry, 2007; Geyer and Martí, 2010; Kereszturi et al., 2011; Brenna et al., 2012a).

Tectonic strain-induced melting in the mantle, especially under low magma-flux volcanic fields, can lead to “time-predictability” in the patterns and cycles of eruptions in monogenetic fields (Sandri et al., 2005; Valentine and Perry, 2007). Thus, monogenetic volcanic fields may in some cases operate periodically in relation with tectonic processes (Bacon, 1982; Valentine and Perry, 2007; Valentine and Hirano, 2010). This has most commonly been seen at million-year time scales (Aranda-Gómez et al., 2003; Wijbrans et al., 2007; Guilbaud et al., 2012). Between volcanic pulses in long-lived fields, absence of any volcanism or related volcanic signatures is common (e.g. Bacon, 1982; Kereszturi et al., 2011). Knowing the long-term trends (e.g. time-predictable) and controls (e.g. tectonically-controlled) of any monogenetic volcanic field does not necessarily mean that volcanic hazard can be forecast accurately. Knowledge of the evolution of a magmatic system does not provide enough information to allow the location of individual future volcanic events to be forecast. Unlike polygenetic volcanoes, in which there are geographic areas with elevated volcanic hazard (e.g. central vent zone or extensional volcanic rift), the spatial location of volcanic hazards related to monogenetic eruptions are often difficult to predict. The uncertainty in both spatial and temporal eruption forecast is due to the lack of knowledge of the location and processes involved in magma extraction in the mantle, along with controls on ascent (Rubin, 1995; Watanabe et al., 1999; Németh et al., 2003; Katz et al., 2006; O'Neill and Spiegelman, 2010). The location of melt extraction is thought to be the primary control on eruption location (e.g. Valentine and Perry, 2006). En-route to the surface, the buoyancy-driven ascending magma may be influenced by geological boundaries, faults and joints, along with near-surface country rock or groundwater (White, 1991; Connor et al., 2000; Valentine and Krogh, 2006; Suiting and Schmincke, 2009; White and Ross, 2011; Németh et al., 2012). These interactions, however, are expected to be confined within the magmatic footprint of the magma (e.g. Valentine and Perry, 2006). In such context the magmatic footprint is defined as the dimensions of the area of the magma extraction zone, projected to the surface

(Valentine and Perry, 2006). Preferred eruption locations may be forecast from major crustal faults and structural weakness zones (Connor et al., 2000; Valentine and Krogh, 2006; Le Corvec et al., 2013b), from horizontal density contacts between country rocks (Németh et al., 2003; Taisne and Jaupart, 2009), and from the orientation of the overall regional- and local-scale stress fields (Nakamura, 1977; Delaney et al., 1986; Takada, 1994; Watanabe et al., 1999). The interaction between magma and country rock, and its effect on magma propagation, is dependent on magma composition and supply pressure (Valentine and Perry, 2006; Le Corvec et al., 2013b), as well as the tectonic/geologic structures of the country rock physical properties (Connor et al., 2000; Aranda-Gómez et al., 2003; Valentine and Krogh, 2006; Gaffney et al., 2007). Long-term eruption forecasts from volcanic fields require detailed information on the geological setting.

Ascending magma feeding monogenetic eruptions on the surface may be detectable shortly (hours to weeks) before an eruption by monitoring systems, such as remotely sensed Interferometric Synthetic Aperture Radar (InSAR) data (Samsonov et al., 2010), networks of seismographs (Sherburn et al., 2007; Ashenden et al., 2011; de la Cruz-Reyna and Yokoyama, 2011), or by monitoring CO<sub>2</sub> degassing (Mazot et al., 2013). Once nearing the surface, magmas supplying monogenetic eruptions may undergo volatile-driven volcanic eruptions, such as Strombolian style eruptions or fire-fountaining (Vespermann and Schmincke, 2000; Bertotto et al., 2006; Cabrera and Caffè, 2009; Németh et al., 2011; Cashman and Sparks, 2013) and/or effusion activity, i.e. lava flows (Thordarson and Self, 1993; Kilburn, 2000; Rowland et al., 2005; Dietterich et al., 2012; Cashman et al., 2013). If magma interacts with groundwater, or any water-saturated sediment, it may lead to phreatomagmatic eruptions (Sheridan and Wohletz, 1981; Wohletz, 1986; Zimanowski et al., 1997; Büttner et al., 1999). Phreatomagmatic eruptions result in a highly dynamic and violent hazard within monogenetic volcanic fields, with associated tephra dispersion and pyroclastic density currents (Sohn and Chough, 1989; Chough and Sohn, 1990; Aranda-Gómez and Luhr, 1996; Vazquez and Ort, 2006; Gençalioglu-Kuşcu et al., 2007; Sandri et al., 2011). Rapid variations from “wet” phreatomagmatic or Surtseyan to “dry” magmatic activity are common in monogenetic volcanoes, such as Lathrop Wells scoria cone in Nevada (Valentine et al., 2007), or Tihany volcanic complex in Bakony-Balaton Highland volcanic field in Hungary (Németh et al., 2001), as well as in historic, eye-witnessed

eruptions, such as Surtsey (Thorarinsson, 1966; Kokelaar, 1983), or Ukinrek maars in Alaska (Self et al., 1980; Büchel and Lorenz, 1993).

Monogenetic eruptions and their hazards have been more difficult to quantify due to their overall small magma supply ( $\leq 1 \text{ km}^3$ ) and localised spatial (e.g. limited extent of 1 to  $10^3 \text{ km}^2$ ) and temporal (e.g. hours to years) impacts in relation to other volcanic phenomena, e.g. Plinian eruptions from stratovolcanoes (e.g. Pardo et al., 2012). The volcanic hazard of monogenetic fields is often exacerbated when towns/cities or power plant are built around them – a common occurrence due to their large areal extent and their low overall activity levels. The potential for a small-volume eruption to occur anywhere in the large areal extent of a volcanic field can be of significant consequence particularly when the entire area is populated or is the location of any valuable assets, e.g. Auckland in North Island, New Zealand (Allen and Smith, 1994), Yucca Mountain nuclear waste repository, Nevada (Spera et al., 2009), Medina, Kingdom of Saudi Arabia (Moufti et al., 2012), SW Armenia (Karakhanian et al., 2003), or Mexico City, Mexico (Siebe et al., 2004). In such volcanic settings an effective geophysical monitoring system, good hazard planning and education, as well as forecasting of eruption size and type, are necessary.

## 1.2. GIS and remote sensing of monogenetic volcanoes

The Geographic Information System (GIS) is an integrated package of tools especially developed and designed for the analysis of spatial data ( $x$  and  $y$  coordinates) with associated attribute values ( $z_1, z_2, \dots z_n$ ) contained in a related database. Hence, it is capable for handling, mapping and analyzing quantitative data in the field of Earth Science (e.g. Burrough and McDonnell, 1998). GIS can help to merge various data types from remotely sensed to field-based geodetic surveying data. The most common data used are quantitative, such as elevation values describing terrain morphology (e.g. Li et al., 2005). Geology/geomorphology data can be analyzed, including: eruptive volume, geometry, as well as vent distribution, and vent density. Quantitative data of this type can be considered on many scales, with the possibility of determining inter-scale relationships with related geomorphic and volcanic processes. In geology/volcanology, these working scales can range from the grain- ( $\mu\text{m}$  to  $\text{cm}$ ) to field-scales (tens of  $\text{km}$ ). On the grain-scale, GIS is often used in isopach and isopleths

mapping to visualize tephra dispersal and calculate eruptive volumes (e.g. Bisson and Del Carlo, 2013). On the edifice-scale, quantitative measures could be eruptive volumes of monogenetic volcanoes (e.g. Kiyosugi et al., 2010; Kereszturi et al., 2011) or polygenetic volcanoes (e.g. Grosse et al., 2009; Karátson et al., 2012), the volcano's geometric parameters, such as height, width, slope angle (e.g. Favalli et al., 2009c; Kereszturi et al., 2012a), and remotely sensed thermal data of volcanic deposits, such as from the Moderate Resolution Imaging Spectro-radiometer (MODIS) (e.g. Wright et al., 2004; Ganci et al., 2012), and Multispectral Infrared and Visible Imaging Spectrometer (MIVIS) (e.g. Lombardo et al., 2009). A range of satellite-based images has been used for mapping volcanic edifices and fields (e.g. Csatho et al., 2008; Wantim et al., 2011), detecting volcano deformation via InSAR images (e.g. Fernández et al., 2009; Samsonov et al., 2010), or characterising surface roughness of volcanic terrains (e.g. Shepard et al., 2001; Mazzarini et al., 2008). On a larger field-scale, quantitative data associated with individual eruption centres can be analyzed, including the spatial distribution of volcanic edifices by average nearest neighbour methods (e.g. Baloga et al., 2007; Bishop, 2007; Hamilton et al., 2010), or by kernel density approaches (e.g. Lutz and Gutmann, 1995; Condit and Connor, 1996; Weller et al., 2009; Bebbington, 2013). The analysis of the spatial and temporal distribution of volcanic landform types (e.g. Bishop, 2009) provides valuable information about the evolution of a monogenetic volcanic field.

The techniques and applications of GIS and remote sensing listed above have been applied on active polygenetic volcanoes, such as Mt. Etna in Italy (Wright et al., 2001; Vicari et al., 2009), Mt. Ruapehu in New Zealand (Joyce et al., 2009; Procter et al., 2010) and Kilauea in Hawaii (Mouginis-Mark and Garbeil, 2005). The resolution of such remotely sensed data ranges from coarse [1 km in the case of MODIS data (e.g. Vicari et al., 2009)], to 15 m for the Advanced Spaceborne Thermal Emission and Reflection Radiometer (ASTER) images (e.g. Stevens et al., 2004). This limits the capability for some of the data types to be applied to monogenetic volcanoes, which are often edifices with areas  $\leq 1\text{--}2 \text{ km}^2$ . The Shuttle Radar Topography Mission Digital Terrain Models (Rabus et al., 2003; Wright et al., 2006; Karátson et al., 2012), with spatial resolutions of 30 m and 90 m, are too coarse to analyze volcanic edifices, such as scoria cones (e.g. Kervyn et al., 2008; Fornaciai et al., 2012), but could be used on a field-scale ( $10^2\text{--}10^4 \text{ km}^2$ ). High-resolution ( $\leq 10 \text{ m}$ ) topographic data, including contour

line based Digital Elevation Models (e.g. Rodriguez-Gonzalez et al., 2011), Light Detection And Ranging (LiDAR) data (e.g. Favalli et al., 2009c), TOPSAR airborne interferometric radar data (e.g. Mouginis-Mark and Garbeil, 2005), or the recently tested TanDEM-X (Gruber et al., 2012), are increasingly available and well-suited to individual edifice-scale work. A key point to note is that results computed from high-resolution data may not be more accurate than those from coarser resolution datasets, depending on the scale used. For example, topographic data with resolutions down to 0.5 m, such as airborne LiDAR (e.g. Anderson et al., 2006) or even 0.01 m for terrestrial LiDAR (e.g. Pollyea and Fairley, 2012), make processing very computationally difficult. Some patterns and trends in such detailed surface data may throw up features that cannot be explained by earlier studies (e.g. Kereszturi et al., 2013a). Therefore, an adequate choice of working resolution (as a proxy for scale) is essential (Gallant and Hutchinson, 1997; Jordan, 2007b; Dragut et al., 2009; Goodchild, 2011).

In monitoring volcanoes, remote sensing techniques are popular, including degassing measurements (e.g. Carn et al., 2008), and deformation detection (e.g. Lowry et al., 2001). These can be readily integrated in a GIS-based environment (e.g. Arana et al., 2000; Pareschi et al., 2000; Felpeto et al., 2001; 2007; Bisson et al., 2010). These data sources and techniques are also increasingly popular for supporting decisions during volcanic unrest (e.g. Pareschi et al., 2000). As introduced earlier, limited information on the spatial location of the next eruption in a volcanic field reduces the vent location-specific application of remote sensing or GIS in volcanic hazard assessment of monogenetic volcanic fields. Considering the complexity of processes involved in a monogenetic eruption, it is a mostly interaction-driven environment, similar to natural hazards such as landslides. Landslide hazard mapping (e.g. Chau et al., 2004) can be modelled as a function of deterministic components, such as lithological and structural settings of country rock, hydrologic properties, geomorphology, soil category and type of vegetation canopy (Chau et al., 2004; Ayalew and Yamagishi, 2005; Guzzetti et al., 2005; Fell et al., 2008), as well as stochastic components, such as an extreme weather event or a seismic event (Del Gaudio and Wasowski, 2004; Guzzetti et al., 2004; Shakoor and Smithmyer, 2005). Monogenetic volcanic events and eruption styles also tend to occur in spatial heterogeneity and are also likely to be a function of deterministic and stochastic components. Deterministic

components could be topography, substrate geology, hydrology, or tectonic settings (Takada, 1994; Sohn, 1996; Connor et al., 2000; Dahm, 2000; Lorenz, 2003; Gaffney et al., 2007), while stochastic components are the temporal recurrence rate, and magma extraction likelihood in the mantle (Condit and Connor, 1996; Conway et al., 1998; Cronin et al., 2001; Valentine and Perry, 2007; Bebbington and Cronin, 2011). For susceptibility mapping of landslides, GIS-based techniques are well-suited to the required multi-criteria decision analysis (e.g. Chau et al., 2004). This should also be the case for making the most of a variety of information for improving the hazard assessment at monogenetic volcanic fields.

### 1.3. Aims and objectives

Combining the potential of remote sensing data and GIS platform, along with physical volcanology and geology datasets, the present study is centred on demonstrating the usefulness of such numerical methods, through specific examples from the Auckland Volcanic Field (AVF), New Zealand (for location information hereafter see Appendix A). Besides point pattern analysis of eruptive vents and conduits (Connor, 1990; Mazzarini, 2004; Bishop, 2007; Bebbington and Cronin, 2011; Kiyosugi et al., 2012) and stochastic hazard assessment (Lindsay et al., 2010; Marzocchi et al., 2010; Bartolini et al., 2013), gaps in monogenetic volcanic hazard research include the quantitative analysis of eruptive volumes, landforms and eruption styles on a field-scale. GIS-based methods offer an ideal means of improving the evaluation of short- and long-term hazard in a monogenetic volcanic field. Therefore, the main aims of this study are:

- To investigate how systematic analysis of spatial location, area affected, edifice geometry, eruptive volume and eruptive sequences of the past eruptive centres of the AVF can be used to improve the understanding of the volcanic field's structure and hazard profile.
- To quantify the typical combination of eruption styles and sequences during AVF eruptions, as well as exploring the range of external and internal factors that influence eruption styles in monogenetic volcanic fields.

- To evaluate lava flow hazard and emplacement processes for a monogenetic field, via susceptibility mapping, and with a rheology-based lava flow simulation approach.
- To use GIS to apply physical volcanological data, such as eruptive volumes, to develop new hazard mapping techniques for monogenetic volcanic fields.

Achieving the collective goals will help to improve the understanding of volcanic hazard in the AVF, but also provide tools and approaches that can be exported to other monogenetic volcanic fields worldwide. Monogenetic volcanism is a common igneous process on Earth, and thus this thesis will contribute towards a better preparedness for potential future volcanic unrest in such areas, particularly in urban settings.

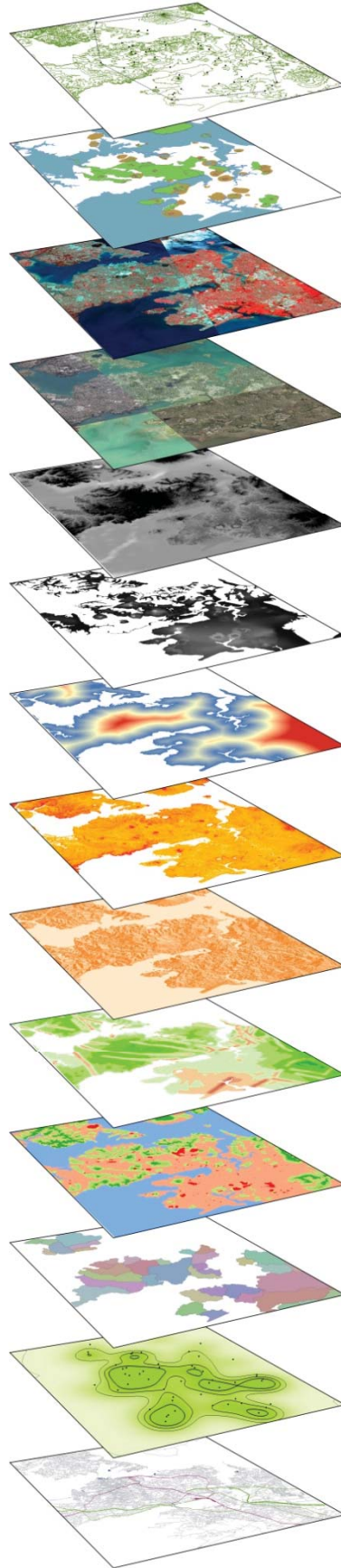
## 1.4. Thesis outline and structure

This thesis consists of eight chapters, which can be subdivided into three parts. In the first three chapters, after the introduction (Chapter 1), a geologic setting and literature review for the broader region of the AVF is provided (Chapter 2). Chapter 2 includes a brief review of the geologic and tectonic history of the basement under the AVF, as well as previous research on the basaltic volcanism in the study area. In Chapter 3, the geospatial methods applied are introduced and topographic data available for Auckland are presented. Chapter 3 further explores the variety of datasets and their validity as input data for integration into spatial analysis within a GIS environment.

Within the body of the thesis, Chapter 4 presents results of the quantitative analysis of volcanoes and volcanic products from the AVF by reanalysing the overall magma output of the field and eruptive volumes of individual volcanoes. Chapter 5 presents spatial characteristics of the eruptive volumes associated with eruption styles of different genetic origins. These data are then used to unravel influencing factors on the eruption styles occurred in AVF. Chapter 6 shows the development of lava flow hazard maps for the AVF, with a spatial susceptibility mapping approach using the present topography as a major controlling factor on the lava flow emplacement mechanism. Chapter 7 tests the MAGFLOW rheology-based lava flow simulation code in monogenetic volcanic field settings, to develop eruption scenarios.

The final section of the thesis, Chapter 8, provides a discussion on monogenetic volcanism in the AVF, including two conceptual models developed for eruption style susceptibility mapping and lava flow hazard mapping in volcanic fields as well as the role of GIS in assessing volcanic hazard in such geological settings. In the conclusion, a summary is provided of this study in the context of research objectives along with future direction of research in the field of monogenetic volcanism.





Chapter **2**  
Geological setting

# 02 / geological setting

This Chapter presents an overview of the geologic, tectonic and volcanic context for the broader Auckland area based on the literature. The major focus in this Chapter is on understanding the importance of the local environmental controls on the location and type of volcanism experienced by the Auckland Volcanic Field (AVF), New Zealand, and to introduce the previous methods and techniques applied here to understand spatial and temporal aspects of volcanic hazards.

## Chapter contents

2.1. Introduction.....	15
2.2. Basement geology of Auckland .....	15
2.3. Basaltic monogenetic volcanism in Auckland.....	20
2.3.1. Quaternary basaltic volcanism in the North Island.....	20
2.3.2. Melt extraction models and geochemical evolution.....	22
2.3.3. Eruption styles and volcanic landforms.....	25
2.3.4. Volcanic hazard assessment and monitoring system .....	30

## Chapter Two – Geological setting

### 2.1. Introduction

The broader Auckland area, New Zealand, has a spatial dimension of about 90×60 km, and it is defined for the present study in Fig. 2.1. Within the broader Auckland area, the youngest volcanic field, the Auckland Volcanic Field (AVF), occupies an area of about 35×25 km (black rectangle in Fig. 2.1). The AVF can be defined using the distribution of past volcanoes, by fitting either an ellipse (Spörli and Eastwood, 1997) or a convex hull (Kereszturi et al., 2013b). The former has an area of 375 km<sup>2</sup>, while the latter has an area of 336 km<sup>2</sup>. The area of the AVF coincides with the outskirts of the City of Auckland, the largest economic centre of both the North Island and New Zealand as a whole, with a rapidly increasing population of 1.415 million people (2013 Census, [www.stats.govt.nz](http://www.stats.govt.nz)). The potentially active status of the field has been known for many decades (e.g. Searle, 1964), and due to the high population density, special attention is paid to understanding its volcanic history.

### 2.2. Basement geology of Auckland

The basement beneath the AVF consists of indurated marine sedimentary units, including greywacke, chert, quartzite and crystalline limestone, deposited between Late Paleozoic to Early Mesozoic (e.g. Kermode, 1992). Such sedimentary rocks were deposited in coastal to marine environments, associated with a continental margin and subduction zone in the Mesozoic (Isaac et al., 1994). They are subdivided into two NNW-trending terranes: the Murihiku Supergroup and the Waipapa Group (Figs. 2.1 and 2.2), based on their componentry, as well as textural and structural characteristics. The basement of the AVF is predominantly Waipapa Group units, outcropping on the western flanks of Hunua Ranges and on Motutapu Island at the eastern margin of the volcanic field (Fig. 2.1). Below the AVF, there is also thought to be a 6–8 km wide band of variably serpentinised ultramafic ophiolitic rocks, termed the Dun Mountain–Maitai Terrane (Coombs et al., 1976; Woollaston, 1996; Eccles et al., 2005; Cassidy and Locke, 2010). This narrow zone is interpreted to be the source of the regionally

dominant NNW-trending gravity and magnetic anomaly, known as the Junction Magnetic Anomaly (e.g. Woollaston, 1996; Cassidy and Locke, 2010). Tectonically, the basement is characterised by a series of uplifted and subsided blocks formed during extension periods between Late Miocene to Pleistocene, forming dominantly N, NE and NNW trending sets of normal faults (Spörl, 1978; Boedihardi, 1990; Wise et al., 2003; Kenny et al., 2012). This age range, however, is poorly constrained (Wise et al., 2003; Kenny et al., 2012).

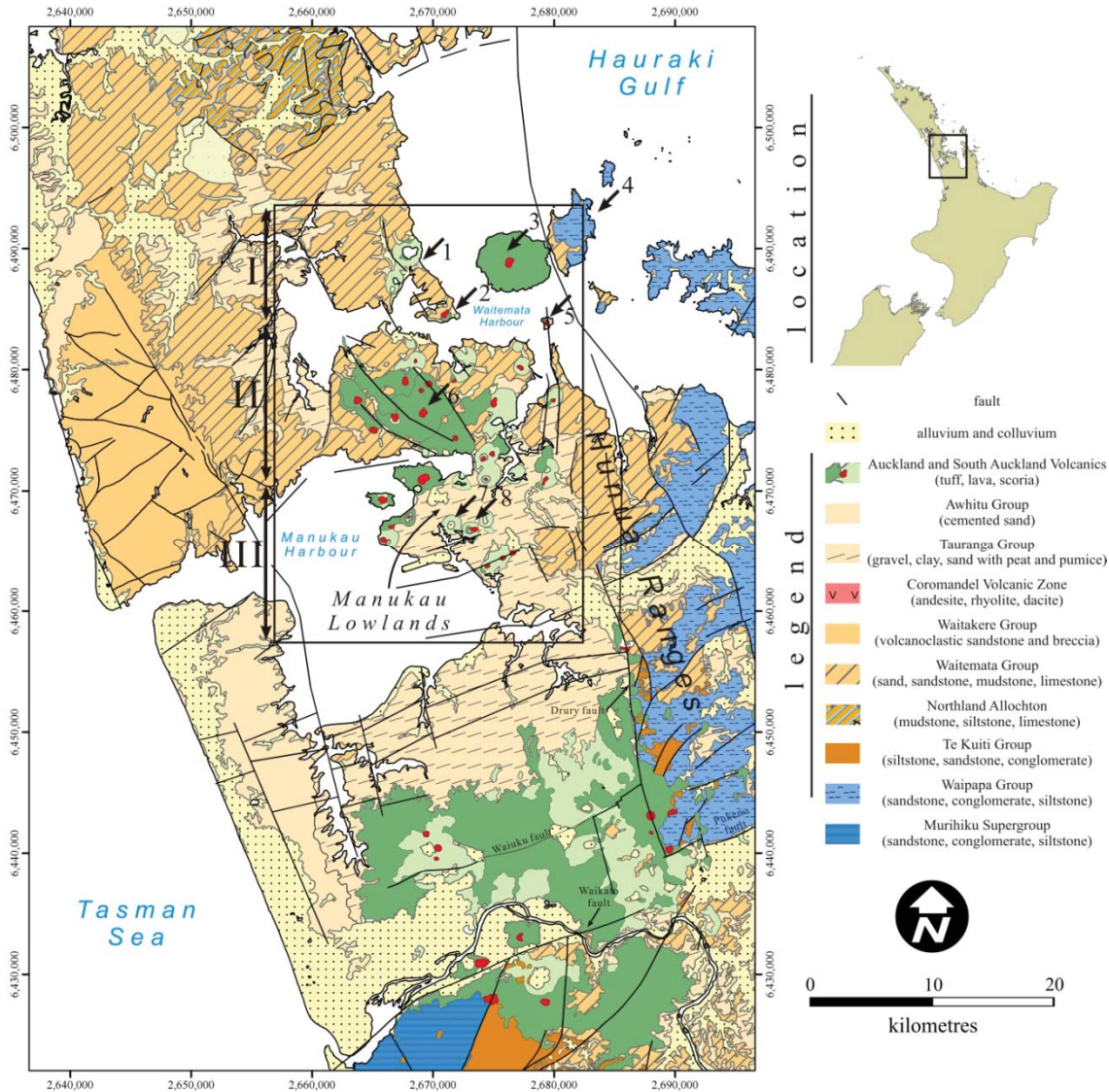


**Figure 2.1** Simplified geologic and tectonic map of the broader Auckland region, based on Kermod (1992) and Edbrooke (2001). The black rectangle shows the area of the AVF with the locations mentioned in the text (1 – Takapuna Beach, 2 – Cheltenham Beach, 3 – Rangitoto, 4 – Motutapu Island, 5 – Browns Island, 6 – One Tree Hill, 7 – Pukaki maar, 8 – Crater Hill.). The roman numerals show the area of the three domains within the AVF mentioned in the text (I – North Shore, II – Central Auckland, III – Manukau Lowlands). The coordinates are in metres (New Zealand Map Grid).

After the depositional unit of Murihiku and Waipapa Groups, there is erosion discordance in the stratigraphic column, corresponding to a hypothesised uplift and erosional period between Cretaceous and Early Eocene (Kermode, 1992; Raza et al., 1999). In the Late Eocene, terrestrial deposition and erosion was gradually overwhelmed by marine transgression, forming basin-wide deposition of sediments of the Te Kuiti Group (e.g. Kear and Schofield, 1959). The resultant sequence of the Te Kuiti Group comprises, from the base, Waikato Coal Measures, Mangakotuku and Glen Massey Formations (Fig. 2.2), with the latter reflecting the full marine incursion, from the Late Eocene to Oligocene (Nelson, 1978; Nelson and Hume, 1987; Edbrooke et al., 1998). The Waikato Coal Measures have been penetrated by drill cores in the AVF at a depth of >500 m below sea level (Edbrooke et al., 1998), and are capped by marine silt-, mud- and sandstones of Mangakotuku and Glen Massey Formations (Kermode, 1992).

The majority of the pre-eruptive terrain in the AVF is dominated by deposits of a volcanogenic flysch and marine sandstones, known collectively as the Waitemata Group (Figs. 2.2 and 2.3). This sequence was formed about 20 Ma ago (Spörli and Browne, 1982; Hayward and Brook, 1984; Spörli, 1989; Shane et al., 2010). These deposits accumulated within a former elongated Waitemata Basin (130×60 km) located between two active southeast-trending volcanic arcs from Late Oligocene to Late Miocene (Ballance, 1976; Spörli and Browne, 1982; Kermode, 1992). However, the stratigraphy, dating and geochemistry of volcanogenic clasts from the Waitemata sequences have shown a lack of subduction signatures and more of an ocean island basalt chemical affinity (Shane et al., 2010). The up to 2 km-thick deposits include variously consolidated silt, mud and sand, along with consolidated varieties of sandstone, limestone and breccias/conglomerates from volcanic and non-volcanic origins (Ballance, 1964; Carter, 1971; Ballance, 1974; 1976; Hayward and Brook, 1984; Ricketts et al., 1989; Hayward, 1993; Shane et al., 2010).

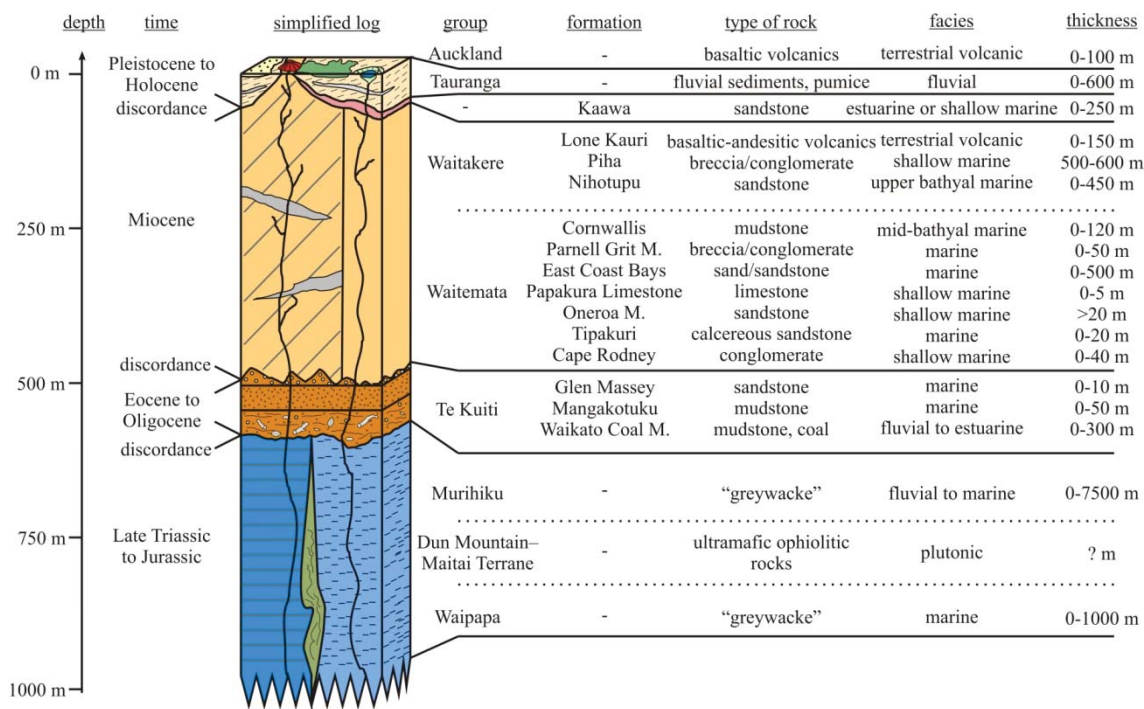


**Figure 2.2** Simplified stratigraphic column with characteristics of the main geologic formations occurring in Auckland. Note that the depth indicated in the sedimentary column varies from region to region. The values used here are based on Edbrooke et al. (1998). Sedimentary characteristics are after Kermode (1992) and Edbrooke et al. (1998). The Dun Mountain–Maitai Terrane has not been penetrated by the drill core described in Edbrooke et al. (1998), but it is inferred to be located underneath Auckland based on magnetic anomalies (e.g. Eccles et al., 2005).

The silt and mud beds of the Waitemata Formation were deposited in a marine setting, along with intercalated coarser deposits from turbidites bearing sediments from terrestrial and volcanic rocks from the proximal two active volcanic arcs (Ricketts et al., 1989; Spörli, 1989; Kermode, 1992; Davidson and Black, 1994). Due to the turbidite origin, syn-depositional slumping and sliding is common (Gregory, 1969; Spörli, 1989; Spörli and Rowland, 2007); however, their discrimination from the post-Miocene faulting is often complicated (e.g. Gregory, 1969). In proximal position to the volcanoes, the formation of the Waitakere Group was contemporaneous with the Waitemata Group (Fig. 2.2), and contains volcanic-rich sediments from the nearby volcanoes (Allen, 2004; Shane et al., 2010). These form lenses within the thick Waitemata sequences, such as the Parnell Grit Member, found within a few tuff ring deposits in the AVF, including Orakei Basin (Németh et al., 2012), or Maungataketake (Conybeer, 1995; Agustín-Flores et al., 2014).

Deposition within the Waitemata Basin ceased about 8 Ma ago, due to slow continuous uplift. Following this, erosion and tectonic dissection began, associated with block faulting (Barter, 1976; Anderson, 1977; Berry, 1986; Wise et al., 2003; Irwin,

2009; Kenny et al., 2012). A block of the Waitemata Group subsided to form the Manukau Lowlands (Figs 2.1) and is characterised by multiple sets of fault orientations (Hayward, 1975; Berry, 1986). These include NE–SW and WNW–ESE striking normal and reverse faults with some minor bedding-parallel thrusts, and N–S striking extensional normal faults (Berry, 1986). These faults are not expressed in the younger, post-Waitemata sedimentary units (Berry, 1986).

Most of the subsided Waitemata blocks were transgressed again, forming an estuarine environment (e.g. Kermode, 1992). During this time, the deposition of the Kaawa Formation took place (Fig. 2.2), followed by the Tauranga Group, which includes terrestrial fluvial sediments (e.g. Kermode, 1992; Edbrooke, 2001).

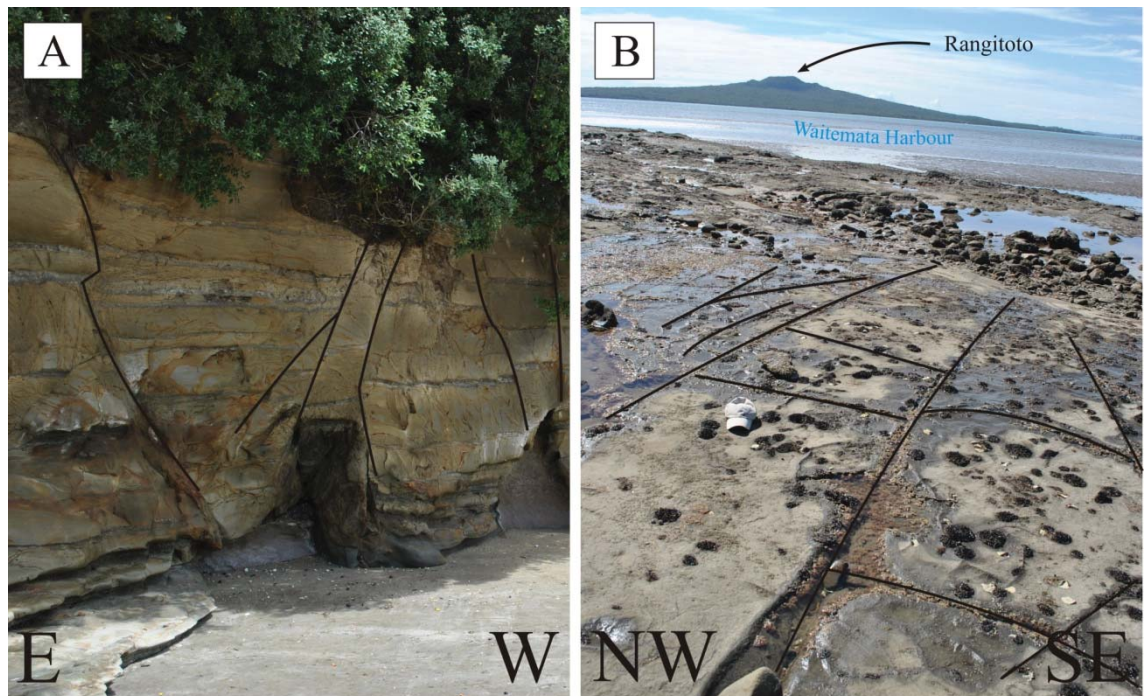


**Figure 2.3** Outcropping Waitemata units with an extensive multidirectional fracture system at Takapuna Beach (A) and Cheltenham Beach (B) in the North Shore. For the location map, see Fig. 2.1.

Most recent sedimentary units, formed in the Pleistocene to Holocene, have been grouped into the Tauranga and Kaihu Groups (Fig. 2.2). Their deposits accumulated mostly on top of the low-lying, subsided basement blocks, such as those forming the Manukau Lowlands (Kermode, 1992; Edbrooke, 2001). These deposits interfinger with the basaltic volcanic products of the AVF (Kermode, 1992; Edbrooke, 2001). The sediments of Kaihu Group are exposed along the coastline, and include present day beach deposits (Kermode, 1992). The sedimentary units of the Tauranga Group

comprise silt, mud, sand and gravel with intercalated organic materials (e.g. peat, organic-rich clay) and pumiceous volcanics from the Taupo Volcanic Zone (Kermode, 1992). They indicate mostly fluvio-lacustrine depositional settings, and rare shallow marine conditions (Nelson, 1978; Nelson and Hume, 1987).

## 2.3. Basaltic monogenetic volcanism in Auckland

### 2.3.1. Quaternary basaltic volcanism in the North Island

Quaternary alkaline and subalkaline basaltic volcanism was focused two distinctive areas in the North Island in New Zealand: Northland and the broader Auckland regions (Figs. 2.1 and 2.4). These volcanics were proposed originally to be the results of an active mantle convection behind an active volcanic arc system (Rafferty and Heming, 1979; Heming, 1980b). This was later revised for Northland (Smith et al., 1993; Huang et al., 2000) and for the broader Auckland region as well (Briggs et al., 1994; Cook et al., 2005), and replaced by a melting model based on a vertically layered mantle source, where the upper parts carry geochemical signatures from an earlier subduction event (Smith et al., 1993; Cook et al., 2005; McGee et al., 2013). These volcanic fields erupt alkaline to subalkaline basaltic magmas (Heming, 1980b; Smith et al., 1993; Huang et al., 1997; Huang et al., 2000; Cook et al., 2005; McGee et al., 2011). Basaltic volcanism in the northern North Island (Fig. 2.4) ranges from 10 Ma to recent in Northland (Kear and Thompson, 1964; Smith et al., 1993), while significantly younger volcanism occurred in the broader Auckland region, where it started about 2–2.5 Ma ago until the present day (Briggs et al., 1989; Briggs et al., 1994; Shane and Sandiford, 2003; Lindsay et al., 2011; Needham et al., 2011).

The broader Auckland region has hosted a series of basaltic volcanic fields formed over the last 2–2.5 My. These geographically confined zones of volcanism are known as the Auckland, the South Auckland (SAVF), the Ngatutura and the Okete Volcanic Fields (Briggs et al., 1990; Briggs et al., 1994; Huang et al., 1997; Cook et al., 2005; Smith et al., 2009). This basaltic magmatic system is situated about 150–250 km behind the active Taupo Volcanic Zone, and about 350–450 km behind the active subduction of the Pacific plate beneath the North Island (e.g. Wilson et al., 1995; Stern et al., 2010). Volcanism in Auckland is seemingly the continuation of volcanism towards the north, given the fact that the first basaltic activity started about 2.5 Ma in

the southern extremity of the area, Ngatutura and Okete (Briggs et al., 1990; 1994). The melting at depth associated with the basaltic magmatic system of South Auckland has been envisaged at a depth of 65–70 km (i.e. 2.0–2.5 GPa), and originated from a spinel/garnet peridotite parental source (Rafferty and Heming, 1979; Briggs et al., 1990; Cook et al., 2005). The sequence of basaltic volcanism was simultaneously fed from magmas characterised by geochemically different, alkaline and subalkaline, suites (e.g. Cook et al., 2005).

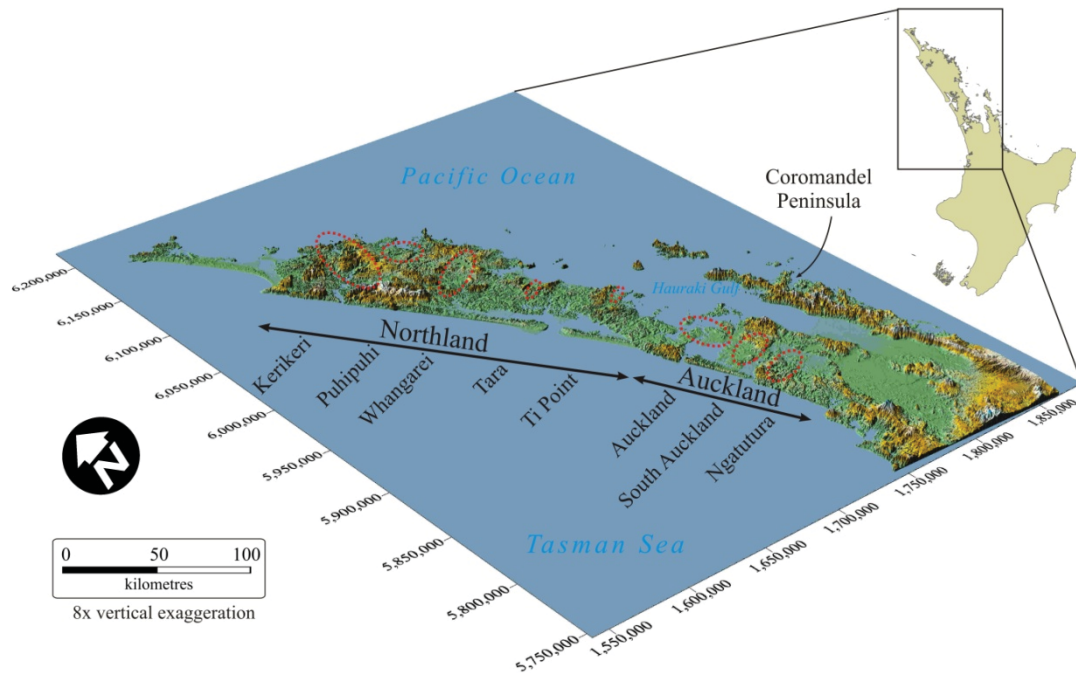


**Figure 2.4** Oblique view of the basaltic volcanic regions in Northland and Auckland. The coordinates are in metres (New Zealand Transverse Mercator 2000).

Spatially, the monogenetic volcanoes in the volcanic fields of the broader Auckland region have slightly different clustering. The SAVF is characterised by significant clustering, while the vent distribution in the AVF is consistent with a Poisson (or random) distribution (Le Corvec et al., 2013c). On the other hand, temporally, there are distinct phases that are characterised by higher rates of volcanic activity, based on the number of dated eruption centres (Briggs et al., 1994). The volcanism migrated northwards from the Okete and Ngatutura Volcanic Fields to the AVF at a rate of 5 cm/yr (Briggs et al., 1994). The depth of Moho over this continental crust varies between  $29\pm 1$  and  $26\pm 1$  km, shallowing toward the north, to 27–28 km beneath the AVF (e.g. Stern et al., 1987; Horspool et al., 2006).

A structural control on volcanic locations has been recognised widely in the SAVF, because the majority of the volcanic vents are located along normal faults (e.g.

Briggs et al., 1994). The ENE fault-controlled vent alignments are parallel with the major Waiuku and Pokeno faults (Fig. 2.1) (Briggs et al., 1994). Other sets of vent alignments include a NNW trend, which coincides with the striking of the Drury fault (Fig. 2.1) (e.g. Al-Salim, 2000). Each of these volcanoes included both phreatomagmatic and magmatic phases, forming maars, tuff rings and scoria cones (Heming, 1980a; Briggs et al., 1989; Rosenberg, 1991; Briggs et al., 1994).

### 2.3.2. Melt extraction models and geochemical evolution

Volcanism in the AVF is the northernmost of the fields of the broader Auckland region. It began to be active 0.25 Ma ago (Shane and Sandiford, 2003; Lindsay et al., 2011). The AVF includes about 52 monogenetic volcanoes (Fig. 2.5). The current magma generation model is of slow upwelling (0.5–1.5 cm/yr) of the asthenosphere, based on major and trace elements together with isotope studies (Huang et al., 1997; McGee et al., 2011; 2013). Both alkaline and subalkaline basaltic composition magmas are erupted, as in the SAVF (Briggs et al., 1994; Huang et al., 1997; Cook et al., 2005; Smith et al., 2008; McGee et al., 2011; Needham et al., 2011). These magmas originate from three different mantle sources located at different depths (Fig. 2.6). Two are asthenospheric in origin (e.g. eclogite vein-dominated domain and fertile garnet-dominated peridotite) and one is a shallower lithospheric, spinel-dominated peridotite source (McGee et al., 2012).

Some of the AVF eruptions (Figs 2.5 and 2.6) are fed by a single batch of magma from a single melt source with a primitive geochemical signature, such as Crater Hill (Smith et al., 2008). This represents melt extraction from a partially molten media and subsequent limited fractional crystallization during ascent above the Moho, ca. 28 km depth (Smith et al., 2008). In other cases, multiple magma sources are expressed by variable erupted compositions (Fig. 2.6), such as at Browns Island (McGee et al., 2012) and Rangitoto (McGee et al., 2011; Needham et al., 2011). Browns Island (Figs 2.5 and 2.6) was constructed from two distinct magma batches with similar degrees of partial melting of 1–2 % (one early magma batch was nephelinite, while the latter batch was alkaline basalt). The separate magma batches were erupted with no significant time gap between them (McGee et al., 2012), and also appear to have used the same conduit system (Fig. 2.6).

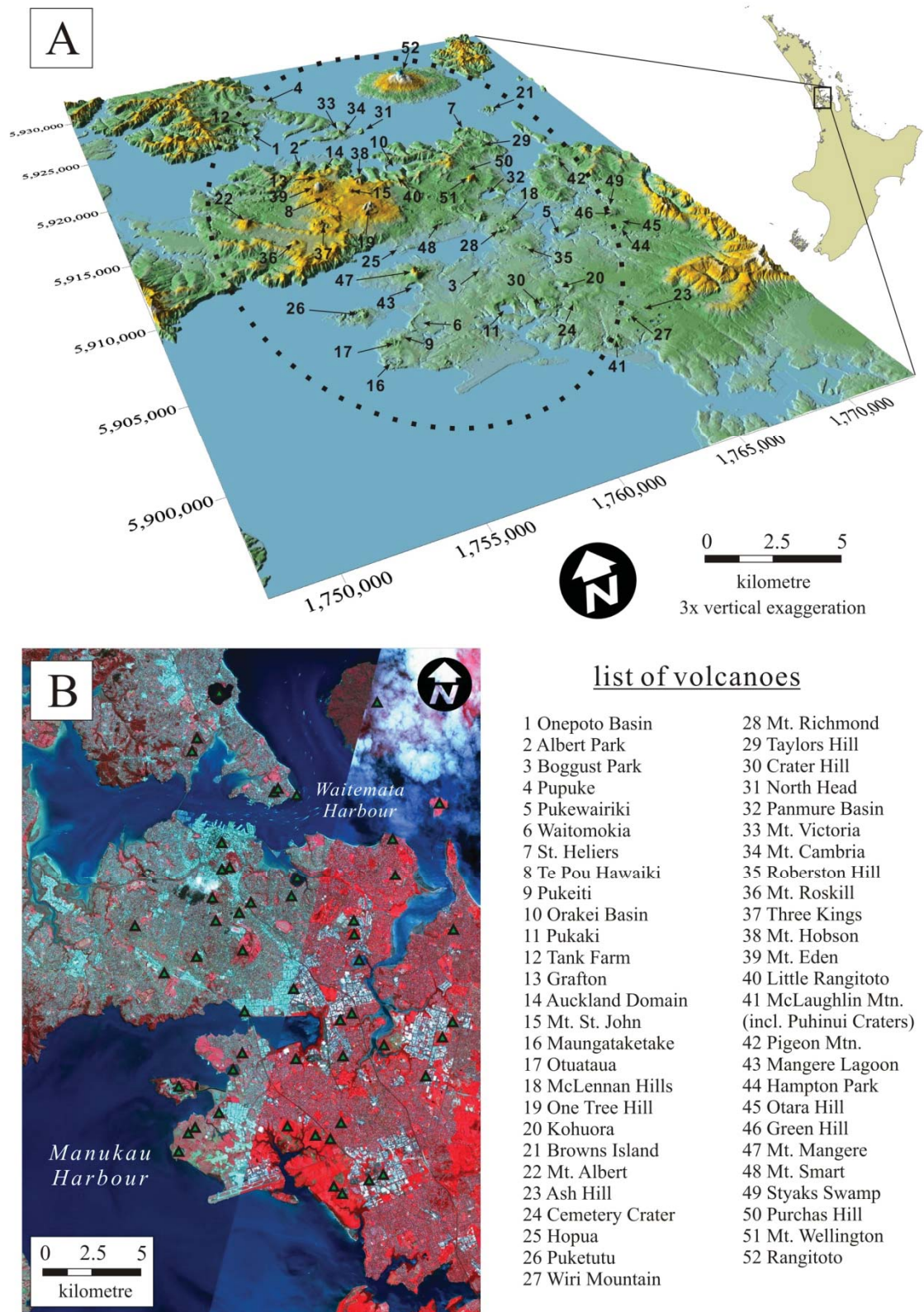


**Figure 2.5** (A) Location map for the 52 monogenetic vents scattered around the Auckland region overlain on the LiDAR DSM. (B) Location of the 52 eruptive centres (green triangles) within the City of Auckland overlain on a false-colour multispectral SPOT-5 satellite image. Note that the areas in grey to green are the urban and heavily populated parts of Auckland, while the red colour shows distribution of vegetated areas, such as forest or park. The coordinates are in metres (New Zealand Transverse Mercator 2000).

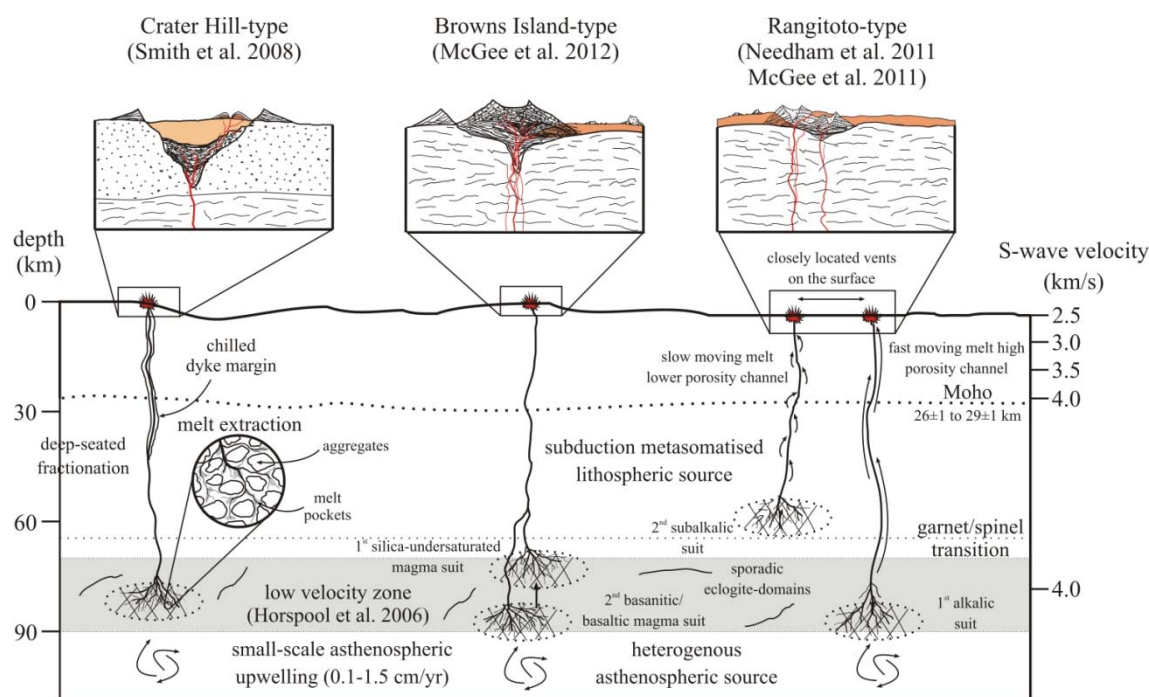


**Figure 2.6** Simple and complex magma generation scenarios based on three examples from the AVF.

The youngest and volumetrically largest eruption centre of the AVF, Rangitoto (Figs. 2.5 and 2.6), also formed from at least two geochemically distinctive magmas from different sources (McGee et al., 2011; Needham et al., 2011). In this case, the magma batches feeding the eruption reached the surface with a possible 50 years gap between them, based on the distal tephra records on the nearby Motutapu Island (Fig. 2.1) (Lindsay et al., 2011; Needham et al., 2011). At Rangitoto, the alkaline magma suite was generated at greater depth and at a lower degree of partial melting of a fertile heterogeneous garnet peridotite source than the later subalkaline magma (McGee et al., 2011; Needham et al., 2011). The alkaline suite is modelled to be the result of about 2–3 % partial melting (McGee et al., 2011). The more volumetric subalkaline magmas were generated by higher degrees of partial melting (~3–6%) at shallower depths around the garnet-spinel transition zone, and they moved to the surface as diffuse porosity melts (McGee et al., 2011). In this case the second batch of magma probably opened a new dyke to rise, and did not use the previous one (Milligan, 1977; McGee et al., 2011; Needham et al., 2011). Therefore, the construction of Rangitoto is the result of two closely spaced monogenetic vents, forming a volumetrically large centre by superposition (Figs. 2.3B and 2.6).

### 2.3.3. Eruption styles and volcanic landforms

The monogenetic volcanism in the AVF is concentrated in a very small area, underlying the City of Auckland (Figs. 2.1 and 2.5). The time span of volcanism is not well-constrained (e.g. Lindsay et al., 2011). The oldest known volcanic rock occurs at the Pupuke and Onepoto volcanoes in the North Shore, which are dated at around 250 ka (Shane and Hoverd, 2002; Lindsay et al., 2011). The monogenetic volcanism in the AVF is characterised by a large variety of eruptions styles, based on the sedimentary, stratigraphic architecture and geomorphology of the volcanic edifices (Figs. 2.7–2.9). As in a typical monogenetic volcanic field (e.g. Németh, 2010), eruption styles associated with past eruptions in AVF include phreatomagmatic, Surtseyan, Strombolian, fire-fountaining and effusive styles (e.g. Allen and Smith, 1994; Németh et al., 2012; Agustín-Flores et al., 2014). However, most volcanoes were produced by only two eruption styles: phreatomagmatic and/or fire-fountaining and Strombolian eruptions with or without effusive activity (Searle, 1962; Searle, 1964; Searle, 1981; Rout et al., 1993; Allen and Smith, 1994; Allen et al., 1996; Cassidy et al., 2007; Hayward et al., 2011; Németh et al., 2012; Agustín-Flores et al., 2014). Initial eruptions were mostly characterised by various degrees of magma-water interactions, producing phreatomagmatic eruptions. In the initial phreatomagmatic eruptions, pyroclastic transportation and deposition were mostly from pyroclastic density currents and associated pyroclastic fall (Allen et al., 1996; Smith et al., 2008; McGee et al., 2012; Németh et al., 2012). The accumulated volcano-sedimentary units (Fig. 2.8) are abundant in cross- to dune-bedded units, containing poorly sorted, accidental-lithic-rich ash and lapilli beds (Allen et al., 1996; Németh et al., 2012). Sedimentation from a phreatomagmatic eruption is expected to be important in about a 1–2 km radius from pyroclastic density currents (Allen and Smith, 1994; Allen et al., 1996; Sandri et al., 2011; Németh et al., 2012), and about a 2–5 km, or sometimes larger, radius from pyroclastic fall, based on tephra preserved in many maar lakes during the evolution of the field (Shane and Smith, 2000; Sandiford et al., 2001; Shane and Hoverd, 2002; Horrocks et al., 2005; Houghton et al., 2006; Molloy et al., 2009).

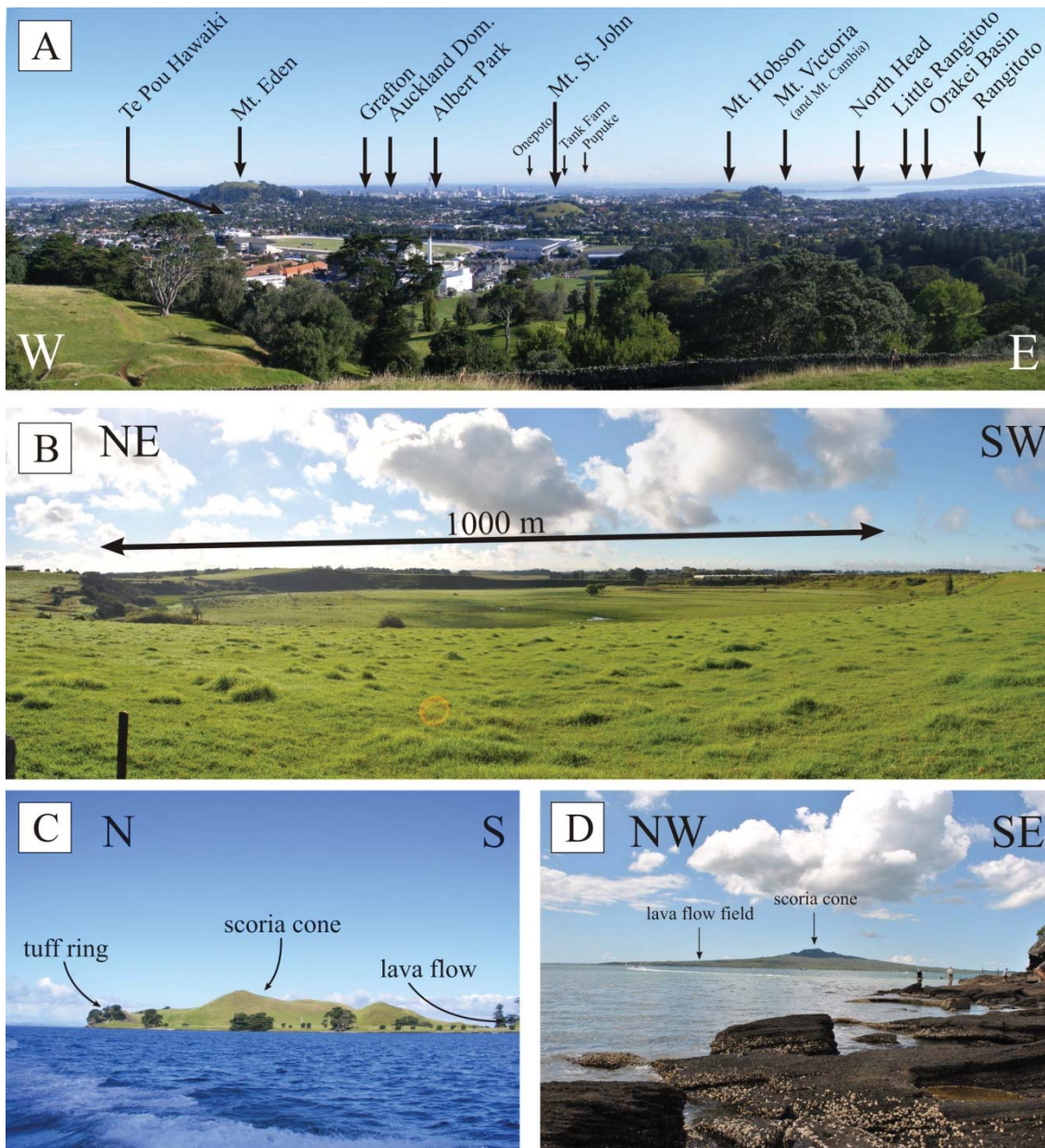


**Figure 2.7** Examples of monogenetic volcanoes from the AVF. For the locations of these examples, the reader is referred to Fig. 2.5 and Appendix A. (A) Overview photo of monogenetic volcanoes in the Auckland area. (B) An example of a wide and circular crater formed by extensive phreatomagmatic eruptions, Pukaki volcano. (C) Combination of phreatomagmatic eruption and late stage magmatic eruption forming complex monogenetic volcanoes, such as Browns Island in the Waitemata Harbour. (D) Purely magmatic processes form scoria cone and extensive lava flow fields at Rangitoto.

In comparison with violent magma-water driven phreatomagmatic eruptions (Wohletz, 1986), an order of magnitude smaller area ( $\leq 1 \text{ km}^2$ ) is normally affected by the products of magmatic eruptions in the AVF, such as fire-fountaining and Strombolian type eruptions (e.g. Németh et al., 2012). Such eruptions are responsible for the formation of scoria cones with a range of geomorphologies. These eruption

styles produce coarsely fragmented, lapilli-sized fragments of scoria/reticulite (Fig. 2.9) that accumulate proximally (<1 km) to the erupting vents, forming cones (e.g. Mangan and Cashman, 1996; Riedel et al., 2003; Németh et al., 2011). The main difference between fire-fountaining activity and Strombolian eruptions is the magma flux (Parfitt and Wilson, 1995; Parfitt, 2004; Valentine and Gregg, 2008). When the magma flux is high (e.g.  $\geq 0.1$  m/s) fire-fountaining takes place (e.g. Parfitt, 2004), where molten clots of lava are ejected from the fissures or central vents (e.g. Parfitt, 2004; Valentine and Gregg, 2008). These lava clots, when falling rapidly, remain hot and fluid enough to be agglutinated after landing (Head and Wilson, 1989; Sumner et al., 2005). On the other hand, a slow magma ascent rate of  $\leq 0.1$  m/s can lead to Strombolian activity, in which magma fragmentation occurs when gas forms large bubbles, breaking bubble walls at shallow depth in the conduit (Chouet et al., 1974; Cashman et al., 2000; Taddeucci et al., 2012). Violent Strombolian eruptions occur when there is a larger magma viscosity and sustained eruption plumes can be formed (Valentine et al., 2007; Pioli et al., 2008; Valentine and Gregg, 2008; Courtland et al., 2013; Kiyosugi et al., 2013). This eruption style has not been identified from the AVF, but it is common from basaltic-andesitic scoria cones, such as Paricutin in Mexico (e.g. Pioli et al., 2008). For the AVF, the first two types, fire-fountaining and Strombolian activity, are the most dominant explosive magmatic eruption styles described (Houghton et al., 1991; Allen and Smith, 1994; Houghton et al., 1996).

The eruption styles introduced above often occur together or successively during any single eruption, forming volcanoes with complex pyroclastic successions and morphologies. One of the most common sequences in the AVF is an initial phreatomagmatic eruption followed by a transition to magmatic activity. This generates tuff rings with intra-crater scoria cones and lava flows or crater lava infills (e.g. Browns Island in Fig. 2.7), commonly documented in the AVF (Allen and Smith, 1994; Houghton et al., 1996; Hayward et al., 2011; McGee et al., 2012; Agustín-Flores et al., 2014). These transitions are the results of flux changes in the conduit system caused by either restriction of groundwater or increase in magma flux (Houghton et al., 1999; Németh et al., 2001; Valentine and White, 2012; Agustín-Flores et al., 2014).

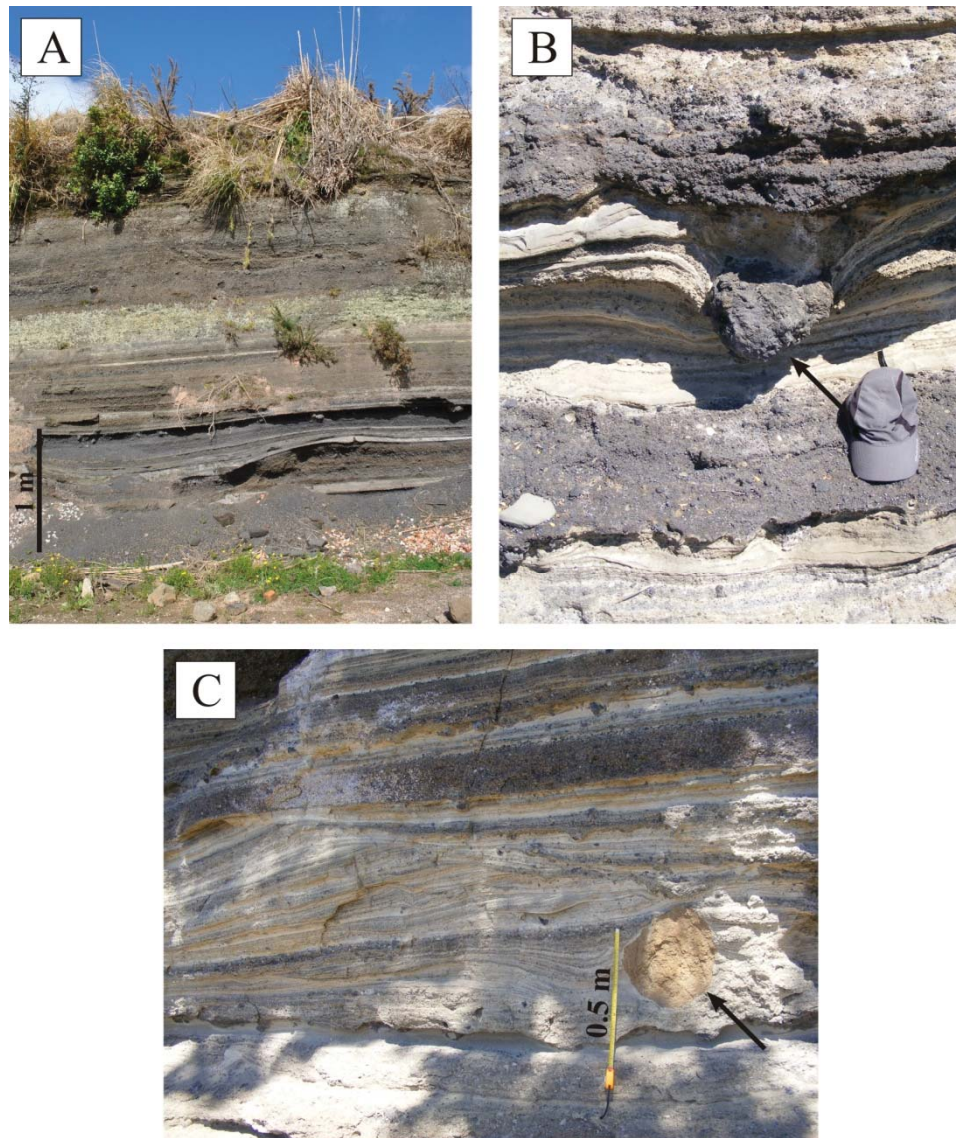


**Figure 2.8** Sedimentary structures in tuff deposits formed by phreatomagmatic eruptions in the AVF. For location of these examples, the reader is referred to Fig. 2.5 and Appendix A. (A) Dune- and cross-bedded units with contrasting granulometric characteristics at the Pupuke eruption centre. (B) Close view of an impact sag caused by a ballistically ejected basaltic block at Browns Island. (C) Complex sedimentary unit, exposed at the basal parts of Browns Island tuff pyroclastic sequence, revealing the dominant transportation mechanism (e.g. pyroclastic density current and tephra fall) related to the formation of tuff rings.

The occurrence of effusive eruptions, producing lava flows, usually follows scoria cone producing eruptions (Thordarson and Self, 1993; Rossi, 1997; Valentine and Keating, 2007; Pioli et al., 2008; Németh et al., 2011; Deardorff and Cashman, 2012). Lava either ponds in a crater, such as at Crater Hill (Fig. 2.5) (Houghton et al., 1999), or flows radially away from the base of a scoria cone, such as at Rangitoto (Fig. 2.5) (Needham et al., 2011). If lava flows encounter no significant topographic barriers, they often show a distinct facies distribution due to down-slope transport and cooling

(Hulme, 1974; Rossi and Gudmundsson, 1996; Rossi, 1997; Calvari and Pinkerton, 1999; Mazzarini et al., 2005; Dietterich et al., 2012). At Rangitoto (Fig. 2.5), most of the known/described lava flow morpho-types can be recognised (Nowak, 1995). The lava flows range from proximal pahoehoe sheets to distal rubbly a’ā lava flows with lateral break-outs, showing toothpaste lava surface textures (Allen and Smith, 1991; Sano, 1991; 1994; Nowak, 1995; Hayward et al., 2011), following a similar evolutionary pattern as documented in the fire-fountaining 1984 eruptions of Krafla volcano, Iceland (e.g. Rossi, 1997).

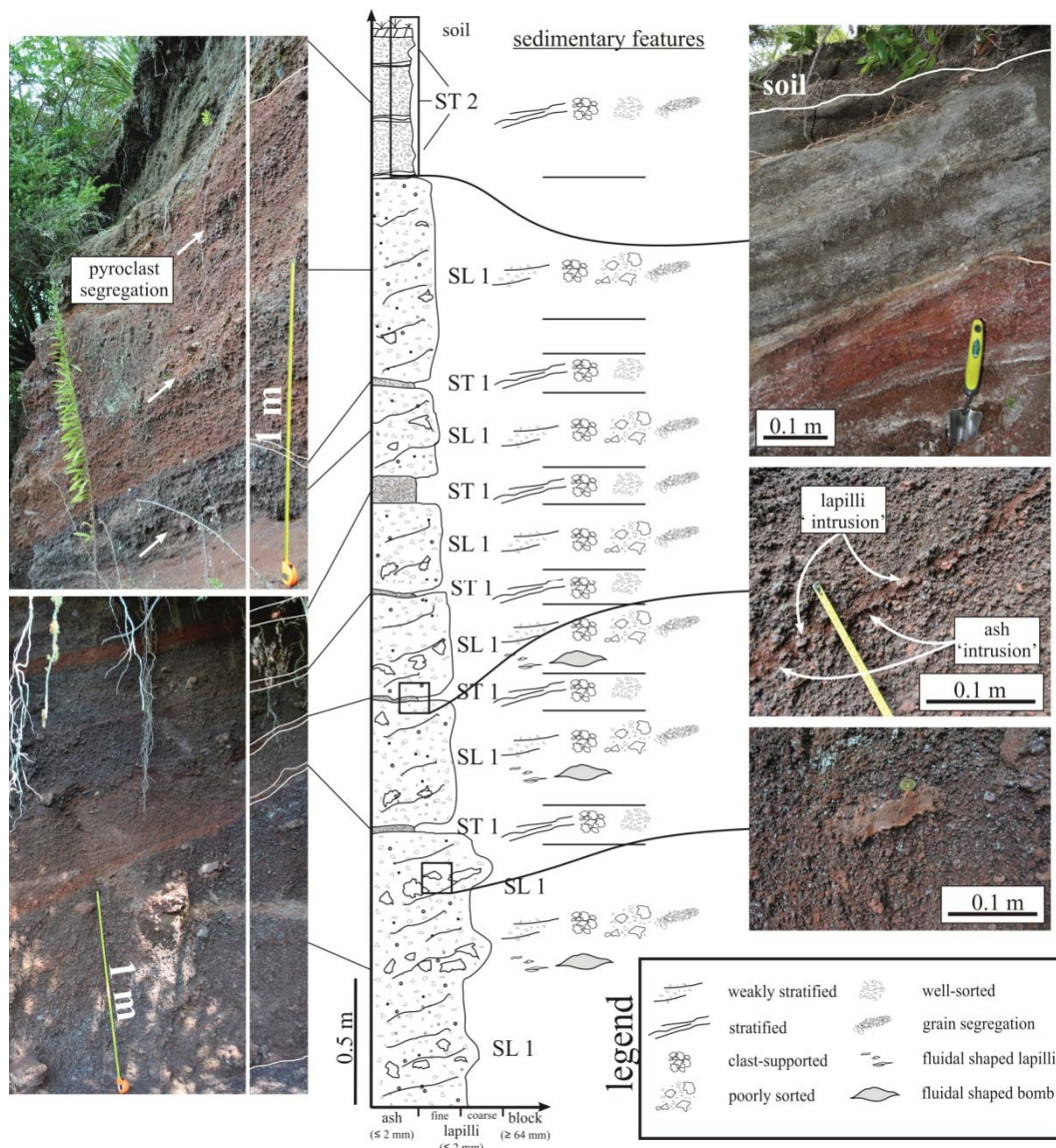


**Figure 2.9** Simplified sedimentary log for deposits of a Strombolian eruption style, exposed at the Rangitoto scoria cone (see Fig. 2.5 for location). This log gives examples for the contrasting styles of ejecta transport on the flanks of a growing scoria cone by grain flow processes (e.g. lapilli-sized scoria

fragments) and ballistics (e.g. larger broken or fluidal-shaped blocks/bombs). Modified from Kereszturi and Németh (2012a).

Volcanoes of the AVF are typical small-volume examples of monogenetic volcanoes, with eruptive volumes  $<1 \text{ km}^3$  (e.g. Allen and Smith, 1994). According to previous volume calculations, based on geometric approximation, the Dense Rock Equivalent (DRE) corrected magma output at the AVF is estimated between 3.4 to  $7 \text{ km}^3$  over the last 0.25 My (e.g. Houghton et al., 1991; Allen and Smith, 1994; Huang et al., 1997). Allen and Smith (1994) calculated the average volcano size at about  $69.9 \times 10^6 \text{ m}^3$ , while the median is only  $4.71 \times 10^6 \text{ m}^3$  (Table 2.1). This distribution is skewed by a single eruption (Rangitoto) that the study states represents 59% of the total eruptive products of the field (Allen and Smith, 1994).

#### 2.3.4. Volcanic hazard assessment and monitoring system

For volcanic hazard assessment, the spatial and temporal distribution of past eruption centres are commonly used (Conway et al., 1998; Connor and Connor, 2009; Weller et al., 2009; Bebbington and Cronin, 2011; Bebbington, 2013). The locations of volcanic events in the AVF have been analyzed by several studies by applying nearest neighbour-based point pattern analysis (Le Corvec et al., 2013c), kernel density estimates (Fig. 2.10) (Bebbington and Cronin, 2011; Bebbington, 2013), the Hough Transform method (von Veh and Németh, 2009), a geometrical approach (Spörli and Eastwood, 1997) and cluster analysis (Magill et al., 2005b). Some of these studies have shown that the spatial distribution of past volcanoes is consistent with Poisson-type (i.e. random) distribution, while others have shown spatial patterns, but none that could be related to temporal processes (Bebbington and Cronin, 2011; Bebbington, 2013; Le Corvec et al., 2013c). The most significant spatial control found is the location and geometry of the AVF itself, which can be best approximated by an ellipse with axis of 28.9 km and 16.5 km (Spörli and Eastwood, 1997), aligned with the direction of the Junction Magnetic Anomaly (Eccles et al., 2005). At the edifice-scale, there is only very limited knowledge on actual spatial controls on vent positioning. This is hampered by erosion processes, or overlapping of eruptive products as well as human landscape modifications (e.g. Kermodé, 1992). There is some evidence of linear features, interpreted as normal faults, based on the offsets and steps of the Waitemata

depositional surface from drill core data (Kenny et al., 2011; 2012). Some of these features pass right beneath volcanoes, such as Three Kings (Fig. 2.5) (Harding et al., 2010; Kenny et al., 2012), while other volcanoes are located far (e.g. 1–2 km) from known or inferred faults, such as Rangitoto or One Tree Hill (Fig. 2.5) (Kenny et al., 2012). Systematic volcano offsets from faults could be explained by the spreading of magma along any plane of weaknesses found in the uppermost 400–500 m of Waitemata country rocks (Kenny et al., 2012). Theoretically, either tectonic elements, such as faults and joints (e.g. Connor et al., 2000), and/or the regional and local stress fields (e.g. Takada, 1994) could influence the direction of propagating magma, and therefore the location of eruptive centres on the surface. Nevertheless, structural controls are only effective in near-surface settings (e.g. upper 1–2 km) and if tectonic lineaments are within the magmatic footprint of the propagating magma (Valentine and Perry, 2006). The magmatic footprint is defined as the area where the melt extraction occurred in the source zone, usually in the mantle (Valentine and Perry, 2006). The magmatic footprint concept is based on the assumption that the magma, once it is extracted from its source media, propagates vertically (e.g. Lister and Kerr, 1991; Rubin, 1995).

The temporal controls on monogenetic volcanism usually depend on tectonic factors (Németh et al., 2003; Valentine and Perry, 2007) or melt productivity in the source region (Kuntz et al., 1986). The total AVF volcanic activity spans a narrow time period from 250 to 0.5 ka (Bebbington and Cronin, 2011; Lindsay et al., 2011; Needham et al., 2011). This is shorter than some other dated volcanic fields, such as the 1.8 My Springerville Volcanic Field in Arizona (Condit and Connor, 1996) or the 5.6 My Bakony-Balaton Highland Volcanic field in the Western Pannonian Basin (Wijbrans et al., 2007). Based on its short life so far, high eruption rates and very recent last eruption, the AVF is considered an active system (e.g. Molloy et al., 2009). According to the present eruption age model, the volcanism shows “pulsing” or “flare-up” in rates of activity (e.g. Molloy et al., 2009). Based on tephra chronostratigraphy and existing dates from single eruption centres, Bebbington and Cronin (2011) estimated the current hazard in the AVF equates to 0.0002 events/yr if quiescence continues. In their renewal-based model, the hazard is decreasing with increasing time elapsed since the last eruption (Bebbington and Cronin, 2011).

**Table 2.1** Summary of simulated ages (from Bebbington and Cronin, 2011; 2012), eruption styles (from Hayward et al., 2011) and eruptive volumes (from Allen and Smith, 1994) of the AVF volcanoes.

location		age		eruptive volumes					landforms		
		mean age	error	scoria cone	ejecta ring	lava flow	total bulk	total DRE	ejecta ring	scoria cone	lava flow
		ka	ka	×10 <sup>6</sup> m <sup>3</sup>					yes/no	yes/no	yes/no
1	Onepoto Basin	246.9	27.3		13		13	3.9	y	n	n
2	Albert Park	227.2	40.7	0.07	3.92	0.59	4.58	1.79	y	y	y
3	Boggust Park*	203.6	41	recently recognised volcanoes					y	n	n
4	Pupuke	200	7.3		33.96	26.4	60.36	45.46	y	y	y
5	Pukewairiki	198.7	42.5		15.7		15.7	4.71	y	n	y
6	Waitomokia	193.8	55.7	0.54	9.64		10.18	3.32	y	y	y
7	St. Heliers	179.7	53.4		5.87		5.87	1.761	y	n	n
8	Te Pou Hawaiki	153.3	69.9	0.4			0.4	0.32	y	y	y
9	Pukeiti	114.4	54.1	0.13		3.87	4	3.78	n	y	y
10	Orakei Basin	102.9	10.1		32.5		32.5	9.75	y	n	n
11	Pukaki	83.5	5.1		19		19	5.7	y	n	n
12	Tank Farm	74.4	5.7		11.64		11.64	3.49	y	n	n
13	Grafton*	69.7	5.2	recently recognised volcanoes					y	y	y
14	Auckland Domain	69.6	5.2	0.28	19.33	6.3	26.41	12.16	y	y	y
15	Mt. St. John	54.5	4.5	2.21	2.8		5.01	2.61	n	y	y
16	Maungataketake	41.4	0.4	4.36	7.2	2.03	13.59	7.58	y	y	y
17	Otuataua	41.4	0.4	1.02		3.62	4.64	4.26	n	y	y
18	McLennan Hills	40.1	1.2	1.1		11.00	12.1	11.33	y	y	y
19	One Tree Hill	35	0.6	24.87		325.46	350.33	329.08	n	y	y
20	Kohuora	34	0.3		4.71		4.71	1.413	y	n	n
21	Browns Island	33.8	0.8	3.89	44.22	4.95	53.06	21.08	y	y	y
22	Mt. Albert	32.8	0.4	5.72	1.67	24.99	32.38	28.8175	y	y	y
23	Ash Hill	32.3	0.1		0.25		0.25	0.08	y	n	n
24	Hopua	32.2	0.3		12.83		12.83	3.85	y	n	n
25	Cemetery Hill*	32.1	0.4	recently recognised volcanoes					y	n	n
26	Puketutu	31.9	0.3	14	14.3	10.88	39.18	25.83	y	y	y
27	Wiri Mountain	31.9	0.3	4.32	0.4	28.38	33.1	30.537	y	y	y
28	Mt. Richmond	31.7	0.3	1.81	8.98		10.79	4.14	y	y	n
29	Taylor's Hill	31.7	0.3	1.95	2.23	0.51	4.69	2.71	y	y	y
30	Crater Hill	31.6	0.3	3.82	22.4	2.62	28.84	12.27	y	y	y
31	North Head	31.2	0.1	2.67	2	0.03	4.7	2.76	y	y	y
32	Panmure Basin	31.2	0.1		30.68		30.68	9.2	y	y	n
33	Mt. Victoria	31.1	0.1	1.47		1.00	2.47	2.13	n	y	y
34	Mt. Cambria	31.1	0.1	0.25			0.25	0.2	n	y	y
35	Roberston Hill	31.1	0.1	1.2	4.43		5.63	2.29	y	y	n
36	Mt. Roskill	30.4	1.2	1.36	0.08	6.27	7.71	7.07	y	y	y
37	Three Kings	28.8	0.3	12	89.35	99.84	201.19	131.25	y	y	y
38	Mt. Hobson	28.6	0.3	5.07	2.8	0.25	8.12	5.13	n	y	y
39	Mt. Eden	28.4	0.3	21.73		162.16	183.89	183.89	n	y	y
40	Little Rangitoto	27.8	0.5	0.17		0.15	0.32	0.28	n	y	y
41	McLaughlin Mnt.	27.1	0.6	1.89		5.94	7.83	7.16	y	y	y
42	Pigeon Mountain	26.8	0.5	1.06	6.33	0.14	7.53	2.88	y	y	y
43	Mangere Lagoon	26.2	0.4	0.1	6.49		6.59	2.02	y	y	n
44	Hampton Park	25.3	0.7	0.08		2.1	2.18	2.06	y	y	y
45	Otara Hill	25.3	0.7	4.43	0.53	4.38	9.34	7.86	y	y	y
46	Green Hill	23.4	3.9	3.3	1.71	15.46	20.47	17.84	y	y	y
47	Mt. Mangere	22.1	0.4	21.5		165.85	187.35	174.76	n	y	y

48	Mt. Smart	21.3	0.6	3.81		89.55	93.36	88.12	y	y	y
49	Styaks Swamp	17.1	1		1.17		1.17	0.36	y	n	n
50	Purchas Hill	10.8	0.1	0.13			0.13	0.1	y	y	y
51	Mt. Wellington	10.5	0.1	20.91	9.2	159.98	190.09	171.47	y	y	y
52	Rangitoto	0.5	0	33.79	19.16	2341.21	2394.16	2022.81	y	y	y
53	Puhinui craters*	?	?	recently recognised volcanoes					y	n	n

In the AVF, continuous seismic monitoring of the field was started in 1986 (Cassidy, 1990), using five telemetered, vertical-component, short-period (1 Hz) seismographs (Cassidy, 1990; Cassidy and Daly, 1995; Sherburn et al., 2007), run by the Auckland Volcano-Seismic Network (AVSN). The estimated warning time ranges from days to a maximum 1–2 weeks, depending on the size of the ascending magma batch (Blake et al., 2006; Sherburn et al., 2007; Ashenden et al., 2011). Historically, only 81 earthquakes were detected between 1960 to 1983, thus the AVF is a low seismicity area (Cassidy and Daly, 1995; Sherburn et al., 2007).

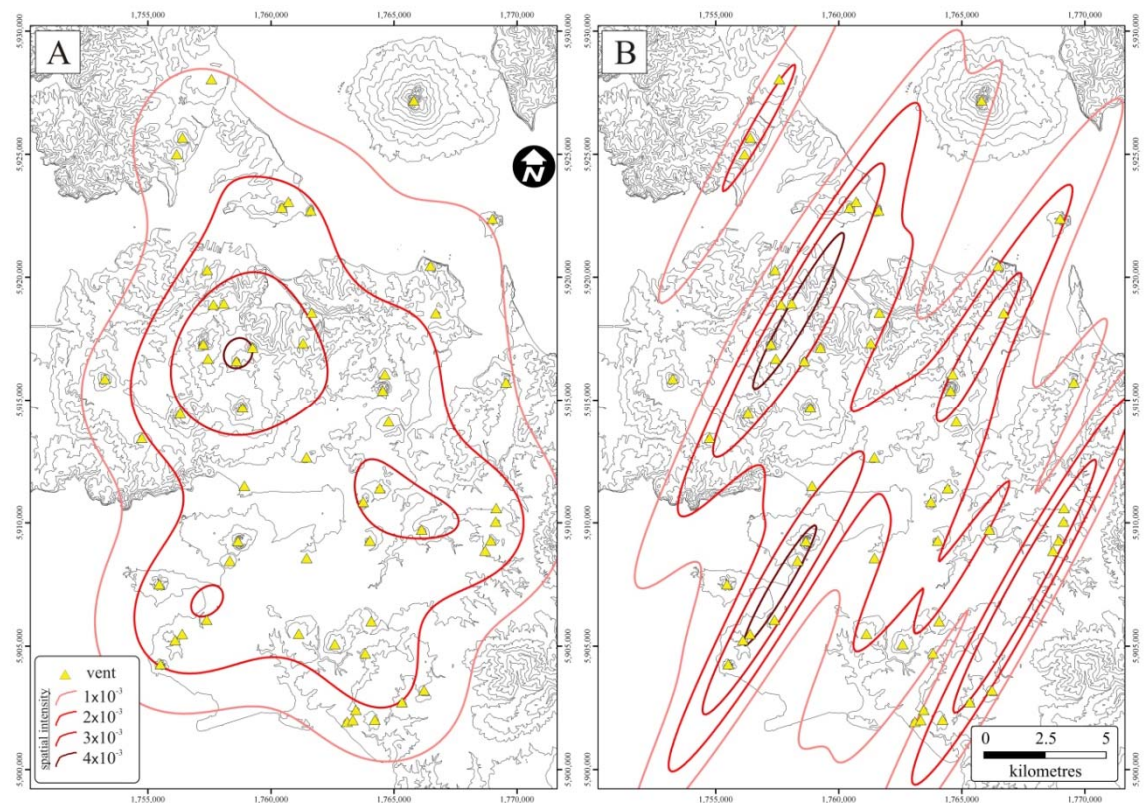


**Figure 2.10** Spatial intensity maps of the AVF based on the vent locations. The spatial intensity is calculated by (A) symmetric Gaussian kernel after Kereszturi et al. (2012b), and (B) asymmetric elliptic kernel after Bebbington and Cronin (2011).

Geodetic monitoring systems are also in use at Auckland, including Global Positioning System (GPS) and spaceborne ground deformation detection using

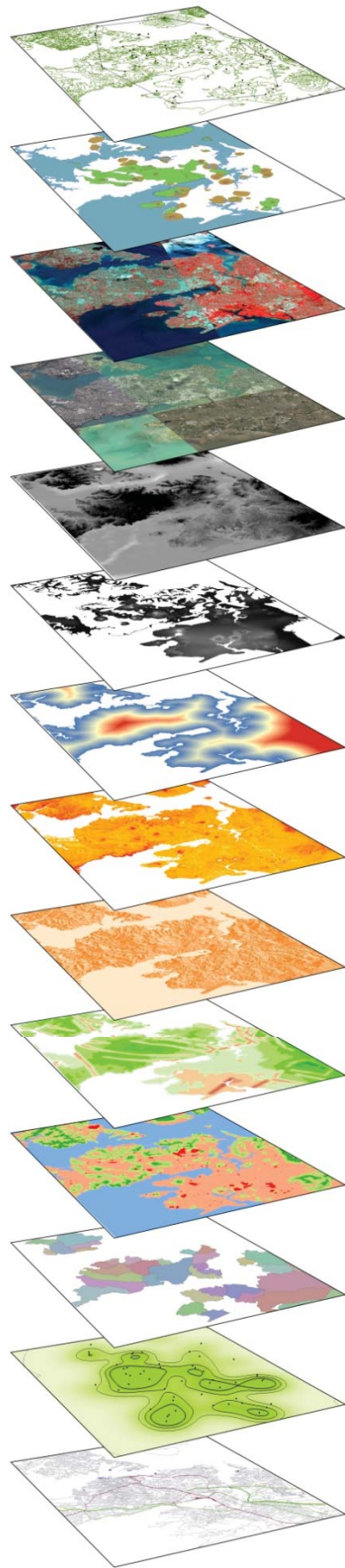
interferometric synthetic aperture radar (InSAR) data (Latimer et al., 2010; Samsonov et al., 2010). These techniques have been found to be effective in detecting even small-scale deformation events that might be associated with rising magma (Samsonov et al., 2010). Although, the low frequency of observation (e.g. weeks to month) due to satellite orbiting could be a significant limitation during a volcanic unrest in Auckland (Samsonov et al., 2010).

Recent attempts were also made to establish the background CO<sub>2</sub> release and locations of underlying fractures and faults in the AVF (e.g. Mazot et al., 2013).

Probabilistic forecasting of event onsets have been carried out based on known eruption locations and timing (Magill et al., 2005b; Bebbington and Cronin, 2011; Bebbington, 2013). The most complex probabilistic model employed in the AVF is the Bayesian Event Tree for Eruption Forecasting (BET\_EF), which was tested in the *Exercise Ruaumoko* in March 2008 (Lindsay et al., 2010). This was a test of New Zealand's nation-wide preparedness for responding to a major disaster resulting from a volcanic eruption in Auckland City (Lindsay et al., 2010). Other work has gone into volcanic scenarios, to characterise the impact of volcanic eruptions on properties, infrastructure and the economy (Johnston et al., 1997; Paton et al., 1999; Magill and Blong, 2005a; Houghton et al., 2006; Lindsay et al., 2010). Based on various eruption scenarios some volcanic loss and hazard models for the AVF have been published, including volcanic impacts from outside of Auckland [e.g. tephra fall from the Taupo Volcanic Zone (Magill and Blong, 2005a; 2005b; Magill et al., 2005a; Houghton et al., 2006; Magill et al., 2006)].







Chapter **3**  
Materials and methods

# 03 / materials and methods

This Chapter introduces the main types of input data, methods and techniques used to accomplish the outlined goals. The Digital Terrain Analysis (DTA) is described, which was a major part of this investigation. As part of the DTA, an extensive comparison is made between a range of existing topographic datasets from Auckland. The validity of input data was tested by on examining terrain attributes (e.g. elevation, standard deviation of elevation, volume, slope angle etc.) and calculating their variability as a function of input data properties (e.g. grid cell size, surveying technique and data structure, etc.). Based on the terrain attribute testing, the most suitable input data were chosen for further analysis.

Supplementary data for this Chapter are in Appendix B.

## Chapter contents

3.1. Introduction to Digital Terrain Analysis (DTA).....	39
3.2. Materials and methods.....	41
3.2.1. Input data types available in Auckland.....	41
3.2.2. Data acquisition and pre-processing.....	47
3.2.3. Data interpolation.....	51
3.2.4. Post-processing techniques.....	56
3.2.5. Testing topographic datasets for Auckland.....	57
3.2.5.1. Terrain height and representation.....	58
3.2.5.2. Terrain attributes in 2D and 3D.....	59
3.3. Results: accuracy and variability.....	64
3.4. Which input data should be used?.....	72

## Chapter Three – Materials and methods

### 3.1. Introduction to Digital Terrain Analysis (DTA)

Spatial data can be stored in discrete or continuous forms (Burrough and McDonnell, 1998; Li et al., 2005). The former is vector data (e.g. points, line, polygons) in which all geometric shapes and curves are defined by points (i.e. nodes) of given  $x$  and  $y$  coordinates (Burrough and McDonnell, 1998; Li et al., 2005; Hengl and Evans, 2008). The accuracy of vector data is defined by the accuracy of its coordinates. Continuous data are raster-based and are represented by individual grid cells in a regularly spaced array (Burrough and McDonnell, 1998; Li et al., 2005; Hengl and Evans, 2008). The distance between these grid cells is the resolution (Goodchild, 2011). The continuous distribution of data, such as elevation values over digital terrain, is often the result of various interpolation methods and not a result of homogeneous sampling of the object of interest (e.g. Aguilar et al., 2005). Due to the gridded representation of data, the capability to resolve fine details (e.g. topography) requires close spacing between sampling locations (e.g. Hengl and Evans, 2008).

Most topographic data are based on discrete point observations of elevation values from geodetic, photogrammetric or laser-based surveys (Axelsson, 1999; Maas and Vosselman, 1999; Mazzarini et al., 2008). Space-borne techniques, such as Shuttle Radar Topography Mission (SRTM) data (Rabus et al., 2003), are based on Radio Detection And Ranging (RADAR) technology. In this technique the topography is created from interferometry of image pairs (i.e. phase difference map of electromagnetic waves), and it is also processed in a raster-based environment. The final product of each type of topographic survey is an equally ordered array of data, which is continuous over the studied terrain. In the case of discrete, point-based surveying, continuous data over an area of interest are only achieved by applying various interpolation methods (Wood and Fisher, 1993; Burrough and McDonnell, 1998; Aguilar et al., 2005; Jordan, 2007b; Yilmaz, 2007). The smallest entity of such continuous raster-based data is the grid cell, which represents the smallest mappable unit. This grid cell is strongly related to the scale of survey (e.g. Goodchild, 2011). Each grid point is characterised by an  $x$ ,  $y$  and a location-specific attribute value,  $z$ . The attribute data over the area of study can be of a

wide variety, including elevation (e.g. Hengl and Evans, 2008), chemical contamination data (e.g. Praharaj et al., 2002), land-use categories (e.g. Szilassi et al., 2006), forest productivity (e.g. Payn et al., 1999), hazard susceptibility (Conoscenti et al., 2008), or soil type data (e.g. Debella-Gilo and Etzelmüller, 2009).

The most basic type of attribute associated with  $x$  and  $y$  coordinate pairs is topographic elevation of a surface. These are referred to as a Digital Elevation Model (DEM), Digital Terrain Model (DTM) or Digital Surface Model (DSM). All of these models contain an ordered array of elevation values referenced to an arbitrary level surface, such as either a global (e.g. World Geodetic System or WGS84) or a local reference datum (e.g. New Zealand Geodetic Datum 2000 or NZGD2000). These models are also defined in a horizontal space, thus they are geodetically projected (e.g. New Zealand Transverse Mercator 2000).

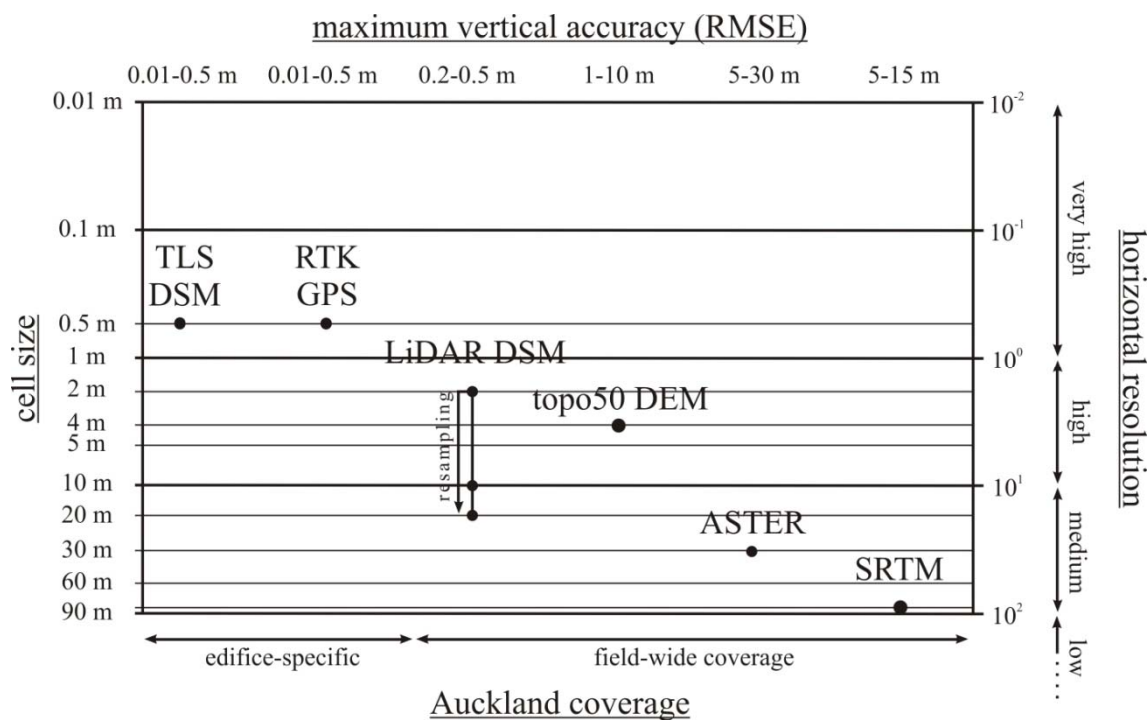


**Figure 3.1** Overview of topographic data used in this study captured at different spatial scales with different coverage and (vertical) accuracy. For more information about these datasets for Auckland, see text. Note that for accuracy assessment purposes, TLS survey points with 0.5 m average point spacing were used in the present accuracy assessment.

DEMs are commonly produced from digitised contour lines that were originally acquired by photogrammetric techniques with field-based verification and support (e.g. Nelson et al., 2008). Therefore, a DEM is limited to elevation values without anthropogenic features. On the other hand, DTMs and DSMs are based on ground-, air-

or spaceborne data acquisition techniques, using satellites or space-/aircraft (e.g. Mouginiis-Mark and Garbeil, 2005; Anderson et al., 2006). A DTM is a broad term for all types of digital surface that includes vegetation cover and buildings [e.g. Shuttle Radar Topography Mission DTM or “raw” unfiltered Light Detection And Range DTM (e.g. Rabus et al., 2003)]. A specific subset of DTMs is the DSM, in which only ground-surface elevation data are represented (e.g. Zhang and Whitman, 2005; Meng et al., 2009).

All kinds of topographic data are characterised by a scale that corresponds to the survey type and sampling used (e.g. Goodchild, 2011). However, the topography is infinitely complex, so it is ascribed by reducing its details. This is called cartographic generalisation in mapping. In cartographic generalisation the resampling of details is carried out to extract/capture the larger and most important features (Goodchild, 2011). Defining scale for digital data is not straightforward (Goodchild, 2011). In a GIS environment the scale of the input data is analogous to grid cell size (e.g. Zhang and Montgomery, 1994; Dragut et al., 2011). The grid cell size is determined based on a combination of sampling and terrain properties, including terrain morphology (Florinsky and Kuryakova, 2000; Shepard et al., 2001), input data type and data organisation (Tsai, 1993; Hengl and Evans, 2008), sampling intervals (Aguilar et al., 2005) and the interpolation techniques applied to create the continuous raster surface (Wise, 2007; Yilmaz, 2007; Wise, 2011). Topographic data can be sorted by their corresponding resolution into three larger categories (Fig. 3.1): low ( $\geq 100$  m), medium (10–100 m) and high-resolution ( $< 10$  m) and very high resolution ( $< 1$  m).

In this study, multiple types of topographic data are compared using different basic terrain attributes (e.g. elevation and its standard deviation, slope angle). Based on the variability of the topographic parameters, the most suitable topographic data are chosen to provide the basis for this and also future analysis.

## 3.2. Materials and methods

### 3.2.1. Input data types available in Auckland

Topographic data types can be grouped based on their coverage into two: edifice-scale data (e.g. results of a survey over a  $\leq 2$  km<sup>2</sup> area) and field-scale data (e.g. captured topographic data encompassing the Auckland Volcanic Field, as defined in Chapter 2).

The data used are presented in increasing horizontal resolution from high to low: Terrestrial Laser Scanning (TLS) DSM, Real-Time-Kinematic (RTK) Global Positioning System (GPS) profiles, Light Detection And Range (LiDAR) DSM, contour-based topo50 DEM, Advanced Spaceborne Thermal Emission and Reflection Radiometer (ASTER) Global DEM, and the Shuttle Radar Topography Mission (SRTM) DTM (Fig. 3.1).

The **Real-Time-Kinematic (RTK) Global Positioning System (GPS)** is a satellite-based positioning system (Parkinson and Spilker, 1996; Farrel and Barth, 1998), based on a rover unit, a base-station unit and a satellite navigation system, such as the United States' NAVSTAR Global Navigation Satellite System (GNSS) or Russia's Global'naya Navigatsionnaya Sputnikovaya Sistema (GLONASS) (Fig. 3.2). The high (1–2 cm) vertical and horizontal accuracy is obtained by measuring the phase of the signal's carrier (i.e. faster than the signal itself) wave and performing a real-time correction of a signal reference station (Gili et al., 2000; Malet et al., 2002). The differentiation can efficiently reduce orbit errors, ionospheric and tropospheric refraction, to achieve cm-scale accuracy (Garrido et al., 2011). Due to its high accuracy, it has an important implication on state-of-the-art topographic mapping and surveying (e.g. Gili et al., 2000; Garrido et al., 2011).

**Laser-based topographic surveys** can be classified based on the distance between the laser sensor and the object detected, including (1) spaceborne (SLS), (2) airborne (ALS), or (3) terrestrial laser scanning (TLS). ALS and TLS are the most common in Earth Sciences (Bellian et al., 2005; Csatho et al., 2008; Mazzarini et al., 2008; Favalli et al., 2009b; Meng et al., 2009).

**Terrestrial Laser Scanning (TLS)** is a ground-based method (Fig. 3.2) for surveying topography (e.g. Dunning et al., 2009), outcrops (e.g. Bellian et al., 2005) and buildings (e.g. Martínez et al., 2012). It is often used for smaller surveys, typically from  $10^1$  to  $10^6$  m<sup>2</sup> due to the limitation of its mobility (Dunning et al., 2009). The tripod-mounted laser sensor emits laser beams in pulses (typically  $10^4$  to  $10^5$  laser emissions/second) towards the object (e.g. building, vegetation or bare ground), and then records their backscatter time. The return time then is converted to distance based on the speed of light. Thus, the laser itself is capable of measuring distance with high vertical and horizontal accuracy of cm to mm-scales in a single measurement. Nevertheless, DSMs-based on TLS data have a realistic accuracy in the range of 0.01 to

0.1 m. The accuracy is dependent on many factors, such as number of stations used, height of the laser scanner, distance to the object, error in co-registration of different scanning swaths, terrain properties (e.g. surface roughness, reflectivity), data occlusion, and accuracy of the GPS tie points (e.g. Pollyea and Fairley, 2012; Brown and Hugenholtz, 2013).

A more effective survey technique for larger survey sites is the aircraft-mounted **Light Detection And Range (LiDAR)** technique (Fig. 3.2). The survey area is typically between  $10^6$ – $10^9$  m<sup>2</sup> (e.g. Aguilar and Mills, 2008; Liu, 2008; Bater and Coops, 2009). Smaller survey areas are often combined for a nation-wide dataset, such as in the United Kingdom (e.g. Gallay, 2013). A LiDAR survey has three major components (Baltsavias, 1999a; Wehr and Lohr, 1999): the laser sensor, RTK GPS and the Inertial Measurement Unit (IMU), which are all mounted to a helicopter or aircraft. The laser scanner fires a laser beam to the surface at an angle (e.g. scanning half-angle). The laser travelling times, geographic position and roll (i.e. rotation around its longitudinal axis), pitch (i.e. rotation around its transverse axis), yaw (i.e. rotation around its vertical axis) of the aircraft are continuously recorded, and then, using the IMU, these data are synchronised to calculate the elevation values of the detected ground-objects. Limitations in the LiDAR technology are that it uses near infra-red lasers, which are unable to penetrate fog, smoke or rain (Baltsavias, 1999b). Some sensors emit multiple laser beams and then record multiple returns and intensities (i.e. reflection), thus the detected sampling location has horizontal  $x$  and  $y$  coordinates with multiple attribute values from  $z_1, z_2, \dots, z_n$ , including first ( $z_1$ ), second ( $z_2$ ) and last returns ( $z_n$ ). The last returns are often called ground returns, due to the signal most likely being scattered back from the ground and not from the top of the vegetation canopy (Bowen and Waltermire, 2002; Hodgson and Bresnahan, 2004; Anderson et al., 2006; Mazzarini et al., 2007; Liu, 2008). Laser-based topographic survey data tend to be noisy (e.g. systematic and random error) due to factors, such as sensor positioning (e.g. Hodgson and Bresnahan, 2004), GPS and IMU errors, errors in determining roll, pitch and heading (e.g. Vosselman and Maas, 2001), topographic variability of the surveyed terrain (Favalli et al., 2009b), classification errors in recognising ground and non-ground points (e.g. Hodgson and Bresnahan, 2004), water/vegetation coverage, and changing reflection properties of the scanned object (e.g. Meng et al., 2009). Some of the systematic errors can be further reduced by applying corrections to the raw laser data (Vosselman and Maas, 2001; Bowen and

Waltermire, 2002; Favalli et al., 2009b). The typical error range for LiDAR-based DSM data is between 0.1 to 2 m both vertically and horizontally (e.g. Hodgson and Bresnahan, 2004; Aguilar and Mills, 2008; Fornaciai et al., 2010).

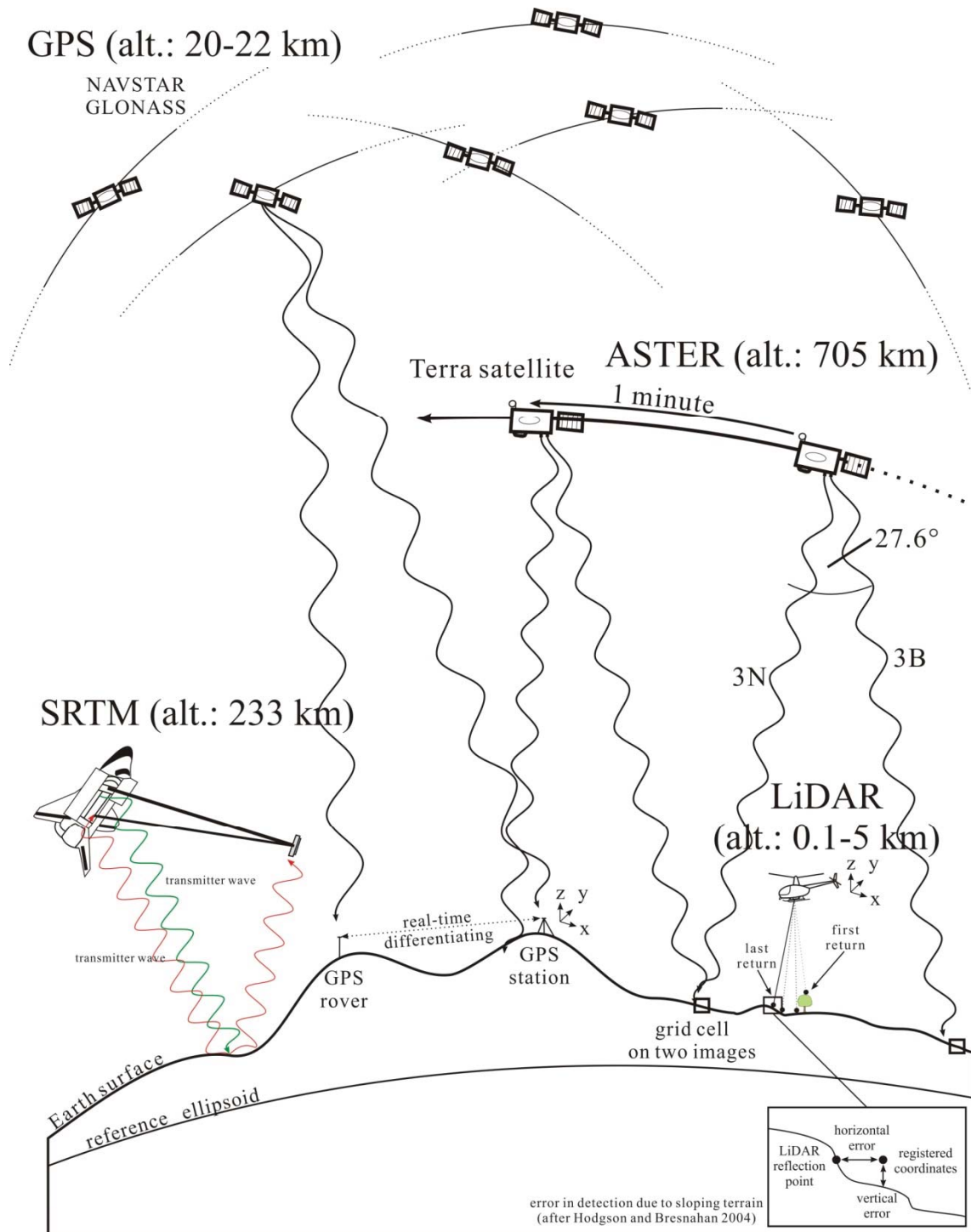


**Figure 3.2** Basic survey concepts of RTK GPS, LiDAR, SRTM and ASTER data acquisition and imaging geometry. The figure is not to scale. The inset shows the vertical and horizontal error in topographic survey after Hodgson and Bresnahan (2004).

**Contour-based Digital Elevation Models (DEMs or topoDEMs)** are usually produced through interpolation from scanned and digitised contour line data. This technique is possibly the most popular given its availability (Robinson, 1994; Taud et al., 1999; Wise, 2000; Bonin and Rousseaux, 2005; Jordan et al., 2005; Hengl, 2006). The original elevation data are created from triangulation surveys and/or alternatively by photogrammetric techniques, using pairs of stereo images (Li et al., 2005; Nelson et al., 2008). The height at a given location, in the case of topographic maps, is usually determined from aerial images taken about the same object, but from two different angles (e.g. Li et al., 2005). The aerial stereo image pairs are then used to reconstruct the object in 3D. This model is used to extract height data. Stereo models of an object can only be generated within the overlapping part of two images shot from a slightly different location. The accuracy of the derived products, such as elevation spot heights, contour lines and DEMs, varies, depending on the scale of the original area mapped, contour intervals, interpolation technique and terrain complexity. The accuracy is typically in the range of 1–5 m vertically and horizontally (e.g. Oky Dicky Ardiansyah and Yokoyama, 2002; Ziadat, 2007; Schumann et al., 2008; Kereszturi and Németh, 2012b).

The **Advanced Spaceborne Thermal Emission and Reflection Radiometer (ASTER)** is an imaging instrument onboard Terra satellite, launched by NASA and METI in December 1999 (Hirano et al., 2003; ASTER GDEM Validation Team, 2009). The ASTER sensor provides imagery in 14 visible, near-infrared, short wavelength infrared and thermal infrared spectral bands (Hirano et al., 2003). The satellite orbit was designed as an along-track, orbiting about 705 km above the Earth's surface (Fig. 3.2). The stereo imagery acquired in Band 3 (near-infrared wavelength), using the nadir and backward-telescopes (aft) Band 3 images (Hirano et al., 2003). Stereo images are captured about 60 s apart, minimising the noise from atmospheric change or lighting and sensor modelling error. Then an automated procedure is used to autoregister the images using SILCAST software, developed to process ASTER imagery (Hirano et al., 2003). The ASTER-based terrain elevation products cover the whole of the Earth's surface between 83°N to 83°S (Hirano et al., 2003). The horizontal resolution of ASTER-based DTMs is approximately 30 m (Hirano et al., 2003; Gilichinsky et al., 2010; Zhao et al., 2011; Bulatović et al., 2012). Vertical and horizontal error is

estimated to be 5–30 m (Hirano et al., 2003; Stevens et al., 2004; ASTER GDEM Validation Team, 2009; Hirt et al., 2010; Zhao et al., 2011; Bulatović et al., 2012).

The **Shuttle Radar Topography Mission (SRTM)** is a spaceborne, space shuttle-based Interferometric Synthetic Aperture Radar (InSAR) product (Rabus et al., 2003; Gorokhovich and Voustianiouk, 2006; Slater et al., 2006; Farr et al., 2007; Reuter et al., 2007). This survey was specifically designed to collect topographic data with global coverage at a resolution of 1 arc second, equivalent to about a 30×30 m grid cell (e.g. Rabus et al., 2003). The SRTM data were surveyed between 11<sup>th</sup> to 20<sup>th</sup> February 2000, using two synthetic aperture radars onboard space shuttle “Endeavour”, including a C-band radar (wavelength of 5.6 cm; C-RADAR) and an X-band radar (wavelength of 3.1 cm; X-RADAR). Subsequently, the DTM products were created based on the difference in the phase of radar wave returns in the SAR images, covering the Earth between 60°N and 57°S (e.g. Rabus et al., 2003). The sensor was an active, microwave-based radar with dual radar antennae that applies the Doppler frequency shift to calculate the distance between the sensor and the object (e.g. Bamler and Hartl, 1998). The intensity of reflection was recorded and stored as a grey-scale image (Bamler and Hartl, 1998). Two images taken above the same area were used to create an image of the phase difference (i.e. interferograms). Image registration and resampling were carried out to generate a terrain interferogram, which in turn was the basis of a DTM pre-processing (Farr et al., 2007). Because it is based on microwaves, this sensor is able to penetrate cloud and fog. However, it cannot penetrate heavy vegetation, but it reflects back from the topmost few metres of the vegetation canopy (e.g. Hofton et al., 2006). The SRTM survey was designed to be one single-pass mission, applying the across-track InSAR configuration (Fig. 3.2) (Farr et al., 2007). Local sharp terrain elements, such as steep cliffs, can cause missing data, or voids, due to radar “shadowing” (e.g. Farr et al., 2007). These data voids need to be filled or interpolated in the data during post-processing (e.g. Grohman et al., 2006; Reuter et al., 2007). Two sets of topographic data have been released based on the same survey: the 1 arc second resolution SRTM for the territory of the United States, and the resampled 3 arc second product for the whole world (Farr et al., 2007). The SRTM mission was designed to achieve vertical absolute and relative height errors of  $\leq 16$  m and  $\leq 6$  m respectively (e.g. Rabus et al., 2003; Farr et al., 2007). However, the SRTM-based DTMs are found to be more accurate than this. The estimated errors vertically are in the range of 1 to 10 m for the

original 30 m resolution SRTM (Rodríguez et al., 2005; Kon Joon et al., 2007; Kervyn et al., 2008; Schumann et al., 2008; Zhao et al., 2011), while somewhat lower ( $\pm 5\text{--}15$  m) for the resampled 90 m version (Gorokhovich and Voustianiouk, 2006).

### 3.2.2. Data acquisition and pre-processing

In this investigation, the **RTK GPS** survey data were collected during multiple field campaigns (e.g. Rangitoto, Browns Island, and Pukaki volcanoes; Appendix A) using a Leica 1200 RTK GPS. In the survey, WGS84 vertical datum (ellipsoidal) and the New Zealand Transverse Mercator 2000 (NZTM2000) projections were used. The ellipsoid heights were post-processed into a geoid-based vertical datum. The conversion was carried out using NZ-standard methods ([www.apps.linz.govt.nz/coordinate-conversion](http://www.apps.linz.govt.nz/coordinate-conversion)). During the surveys, real-time corrections of vertical and horizontal positions were carried out using a base station. The base station was positioned at such a height so as to maintain a direct line of sight between the rover units and the base station. The dataset consists of topographic profiles with closely-spaced measurements (0.5 to 1 m) over various volcanic terrains, such as scoria cones, lava flows and maar craters with different surface coverage (e.g. bare surface and grass-vegetation cover) and geometries. These data were later used to identify the spatial location of error and noise capture in the DSM/DTM/DEM data and used as high accuracy ground control points to assess the accuracy of other topographic data (e.g. LiDAR DSM).

The **TLS** surveys were carried out using a Leica ScanStation C10 laser scanner (Fig. 3.3). This stationary laser scanner has a field of view of  $360^\circ$  horizontally and  $270^\circ$  vertically, with a maximum scanning speed of 50 000 points per second. Due to its capability to scan the surface with near cm accuracy, this technique is able of resolving fine-scale topography, including textural changes on volcanic surfaces, such as rough a'a lava flows (Farr, 1992; Shepard et al., 2001). Therefore, the data acquired by TLS surveys can be used to calibrate the possible loss of information due to highly irregular surfaces and to validate the details captured by the coarser datasets, such as LiDAR DSM, topo50 DEM, SRTM DTM and ASTER GDEM. A TLS survey was carried out on the southernmost part of the Rangitoto Island's a'a lava flow units (Fig. 3.3), covering a total area of  $100 \times 200$  m. The area between survey stations is  $90 \times 60$  m. This test site was chosen due to the absence of vegetation; only individual bushes or grass-

type vegetation occurs. The surveyed site also exhibits lava flow surfaces with contrasting surface roughness properties, which are considered to be representative of the entire flow field. Four survey stations were used that were located on the edges of the survey area. The coordinates of the survey station and backsight points (for later georeferencing and calibrating purposes) were measured using RTK GPS before scanning started. The same backsight point was used from each station point for orientation and co-registration of each survey point cloud. The WGS84 vertical datum and the New Zealand Transverse Mercator 2000 (NZTM2000) projection were used. The survey was set up with a vertical and horizontal scanning point density of 10 cm at 100 m from the station points. The scanning results were processed using Leica Cyclone 8.0 software ([www.leica-geosystems.com/en/Leica-Cyclone\\_6515.htm](http://www.leica-geosystems.com/en/Leica-Cyclone_6515.htm)). Using systematic station and backsight point referencing, the real world coordinate conversion is automatic based on the RTK GPS registration points. Data filtering, such as outlier filtering, was carried out manually using clipping windows. Outliers included reflections from the sky and minor vegetation, such as grass and scrub (Fig. 3.3). For the whole study area, the point cloud was resampled to 0.1 m ( $3800 \times 10^3$  points), 0.5 m ( $198.9 \times 10^3$  points), 1 m ( $61.5 \times 10^3$  points), 2 m ( $16.8 \times 10^3$  points), and 5 m ( $4.3 \times 10^3$  points) average point spacings. These resampled datasets correspond to 0.05 m, 0.1 m, 0.2 m, 0.4 m, 1 m average nearest neighbour distances, respectively. Finally, all of these point clouds were then exported from model space to ASCII files and prepared for interpolation and topographic profile extraction.

The airborne **LiDAR** survey data were obtained by Fugro Spatial Solutions and New Zealand Aerial Mapping Limited for Auckland City Council. Two different types of aircraft-mounted LiDAR sensors were used for data-capturing. A Leica Airborne Laser Scanner 50 (ALS50) and an Optech Airborne Laser Terrain Mapper 3100-EA (ALTM3100) were used in surveys in 2005–2006 and 2008, respectively. Two types of surveys were carried out in each of these periods, for urban/intertidal and for rural areas, with different LiDAR settings. The surveys for the urban and intertidal (captured at low tide) areas were carried out with an average flying height of 1330 m and 1200 m above ground level at 150 (or 77.1 m/s) and 130 knots (or 66.8 m/s), respectively. The two LiDAR sensors operated between 73 kHz and 70 kHz pulse repetition frequencies and 39 and 40 Hz scanning frequencies with scanning half-angles of  $\pm 20^\circ$  and  $\pm 22^\circ$ , resulting swath widths of 960 m and 968 m, respectively. The accuracy of the LiDAR

scanners, without GPS errors, is estimated at  $\pm 0.20$  m at  $1\sigma$  horizontally and  $\pm 0.15$  m at  $1\sigma$  vertically for the Leica ALS50, and  $\pm 0.21$  m at  $1\sigma$  (calculated as  $1/5500 \times \text{flight height in m}$ ) horizontally and  $\pm 0.11$  m at  $1\sigma$  vertically for the Optech ALTM3100. The mean ground point density varied spatially, but has an average of 1 point per  $\text{m}^2$ . The rural survey was carried out with average flight heights of 2000 m above ground level at 150 knots (or 77.1 m/s) using the Leica ALS50. The sensor was set to a 54.8 kHz pulse repetition frequency, 31 Hz scanning frequency with a scanning half-angle of  $\pm 20^\circ$ . This resulted in a 1455 m swath width. The scanning accuracy was  $\pm 0.25$  m at  $1\sigma$  horizontally and  $\pm 0.2$  m at  $1\sigma$  vertically. The mean ground point density ranged between 0.04 to 0.15 point per  $\text{m}^2$  over areas such as Rangitoto, Motutapu and Browns Islands. Post-processing, including filtering and bare-earth point detection of the point cloud, was performed by the data provider, Fugro Spatial Solutions. Both urban and rural LiDAR surveys were completed using the New Zealand Geodetic Datum 2000 (NZGD2000) datum and the New Zealand Transverse Mercator 2000 (NZTM2000) projection.

The **contour map data** of the Auckland area were originally captured by photogrammetry and geodetic surveys and then later digitised at a scale of 1: 50 000 (LINZ, 2010; 2012a; 2012b; 2012c). From the vector-based topographic data only contour lines and shore lines (0 m a.s.l. contour) were extracted and merged into ArcGIS shape files. The topographic data used the New Zealand Geodetic Datum 2000 (NZGD2000) and the New Zealand Transverse Mercator 2000 (NZTM2000) projection. Before interpolation, a visual check of contour data (e.g. elevation attributes) was made to find possible mistyped elevation values.

The **space-based DTMs**, such as ASTER GDEM ([www.gdem.ersdac.jspacesystems.or.jp](http://www.gdem.ersdac.jspacesystems.or.jp)) and SRTM ([www.srtm.usgs.gov](http://www.srtm.usgs.gov)), were readily available online. Originally, these topographic data used WGS84 vertical datum (based on the EGM96 geoid) and the WGS84 horizontal projection. In this study, to allow for better comparison, both ASTER GDEM (1 arc second horizontal resolution, approximately 30 m) and SRTM DTM (3 arc second horizontal resolution, approximately 90 m) data were converted into the New Zealand Transverse Mercator 2000 (NZTM2000) projection, while the WGS84 vertical datum was kept, assuming a minimal vertical difference ( $\leq 0.5$  m) between the elliptical-based New Zealand Geodetic Datum 2000 and the WGS84 datum ([www.linz.govt.nz](http://www.linz.govt.nz)).

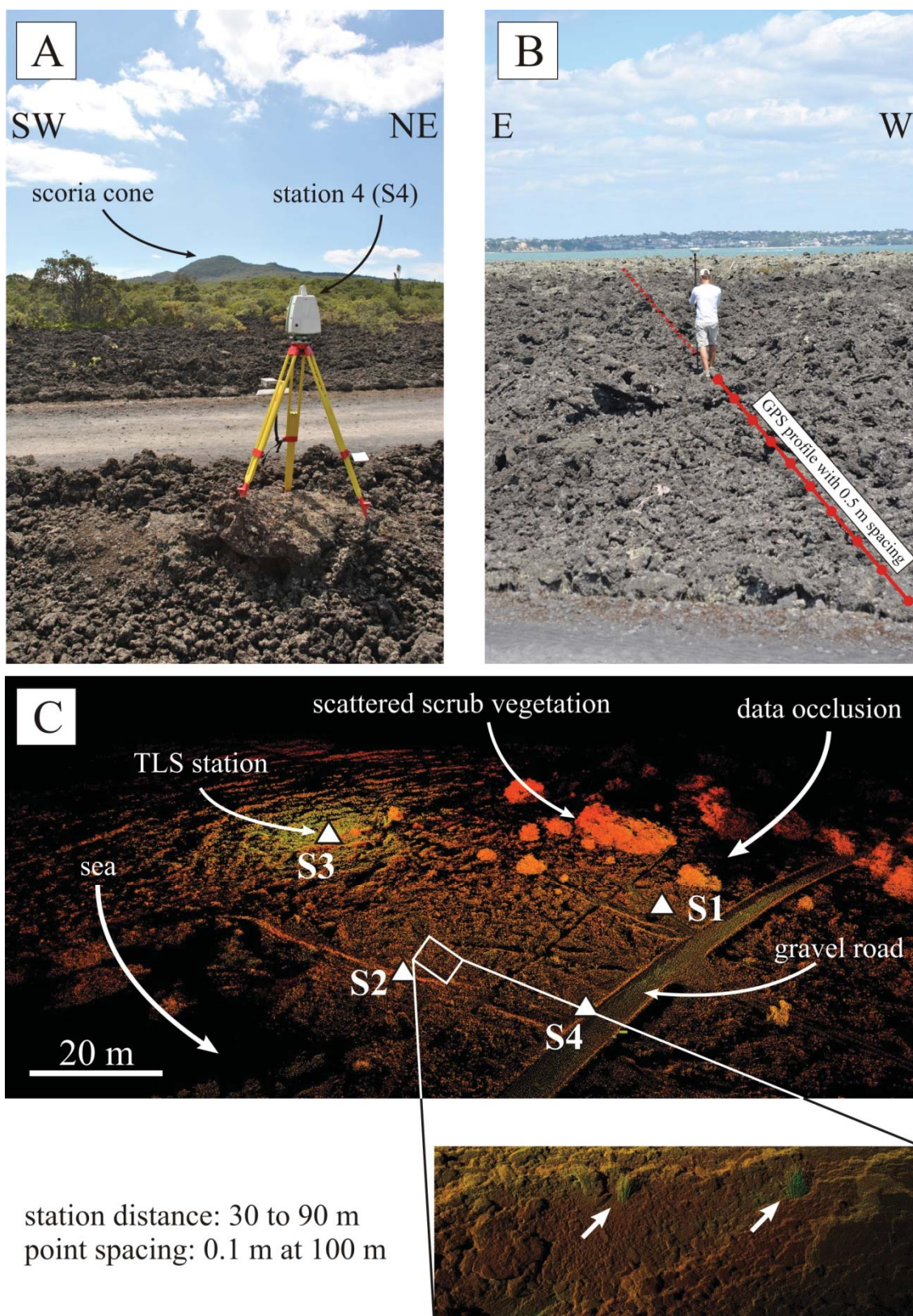


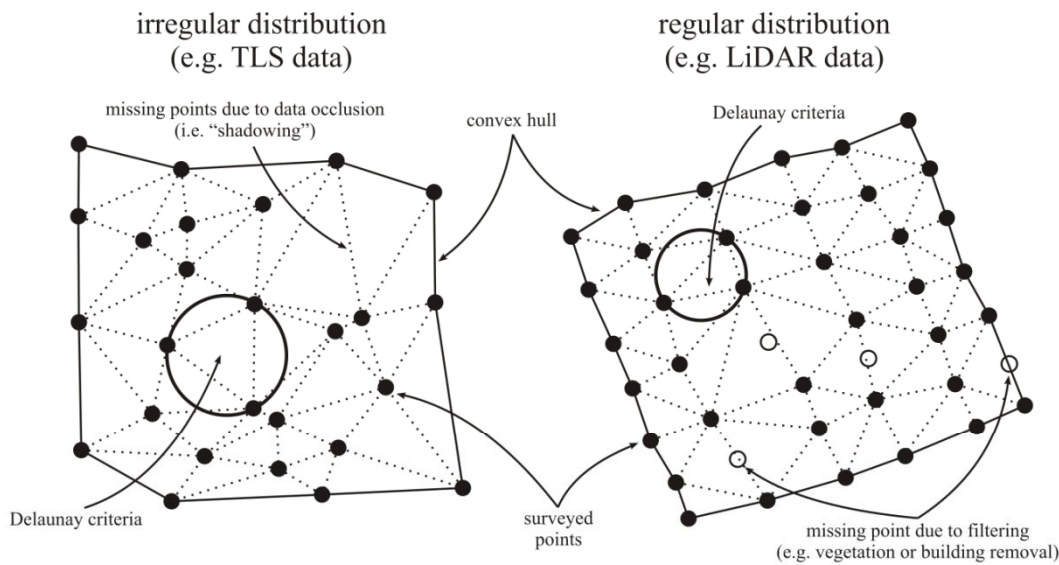
**Figure 3.3** Field photos of the TLS (A) and RTK GPS surveys (B) carried out on the distal segment of a rubbly a’ā lava flow near Flax Point, Rangitoto. (C) Perspective view of the TLS point cloud after registration of point from each station. The inset shows the capability of the TLS to resolve detailed features, such as grass (white arrows). Vegetation was removed manually from the point cloud to obtain bare surface points for the DSM.

### 3.2.3. Data interpolation

In the present dataset comparison, DSMs and DEMs were created by two interpolation methods: Triangulated Irregular Network (TIN) and linear interpolation implemented in the ILWIS software package (Moore et al., 1991; ILWIS, 2001).

The Triangulated Irregular Network (TIN) is a popular interpolation method for vector-based data (Fig. 3.5), such as points and polylines (e.g. Jordan, 2007a; Eastman, 2009). In the triangulation input data, such as points or nodes of isolines, are used with associated elevation attribute data as vertices of the triangle facets (Li et al., 2005; Eastman, 2009). The interpolation works only within the minimum convex area of the input data. The Delaunay criterion is used during TIN construction (Li et al., 2005). It is defined as follows (Fig. 3.5): (1) a circle goes through every three vertices and it does not contain any other input points, (2) no overlapping triangles, and (3) no gaps between the triangles (e.g. Tsai, 1993; Li et al., 2005; Eastman, 2009). This ensures that the angle of the triangles will be maximised; therefore no narrow triangles will be created. All point-source data, such as TSL and LiDAR spot heights, were interpolated using the TIN method. In the construction of the DSM from the LiDAR survey data, only bare-ground spot heights (last returns) were used. Spot heights on buildings and other anthropogenic features were removed, which decreased the original point density to 0.5 points per m<sup>2</sup>. The DSM was created by the data provider ([www.fugrospatial.com.au](http://www.fugrospatial.com.au)). These data were converted from TIN into a grid-based DSM with a 2×2 m grid cell size. The TLS data were gridded with a grid cell size of the average spacing between survey points.

### A Triangulated Irregular Network (TIN)



### B Linear Interpolation

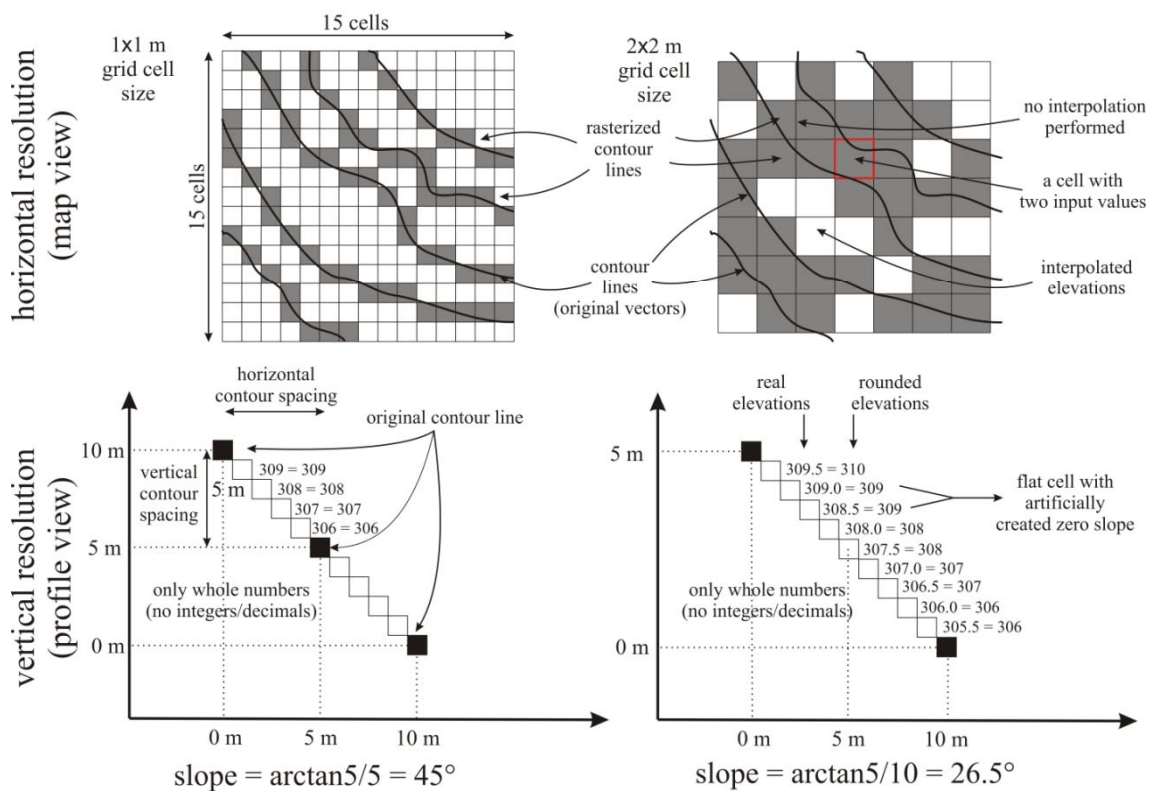


**Figure 3.4** Structure of data and interpolation from vector-based input data, such as spot heights and contour lines, using (A) Triangulated Irregular Network (TIN) and (B) linear interpolation, implemented in the ILWIS software package. Note that there are two examples provided for comparison to highlight the effect of user-defined horizontal resolution and vertical precision on the resultant DEM. If the horizontal resolution is too large in relation to the average distance between two neighbouring contour lines, a grid cell is created with the average value of the two input contour line elevations. If the vertical precision is too low, then the resultant grid cell might have the same elevation, and consequently a flat grid cell would be created.

Contour lines from the 1:50 000 scale topographic maps were interpolated using a Linear Interpolation method (Fig. 3.5), implemented into the ILWIS software package (Gorte and Koolhoven, 1990). This interpolation is the simplest local and exact interpolation method (Hengl and Evans, 2008; Nelson et al., 2008). This interpolation starts with rasterization of the input contour data with the elevation values. Once all contour lines are rasterized, a linear interpolation is carried out between the grid cells with elevation values. To obtain the undefined elevation values, the shortest distances between neighbouring contour lines were measured, based on the Borgefors distance method (Borgefors, 1984; Gorte and Koolhoven, 1990). Thus, the undefined elevation values,  $Z_{grid\ cell}$ , are calculated as (ILWIS, 2001):

$$Z_{grid\ cell} = Z_1 + \left[ \frac{d_1}{d_1 + d_2} (Z_2 - Z_1) \right] \quad (3.1)$$

where  $Z_1$  and  $Z_2$  are the elevation values of the lower and higher contour lines, respectively. Thus,  $Z_2 - Z_1$  is the contour interval of the input data, 5 m in the present study. The terms  $d_1$  and  $d_2$  are the shortest distances between  $Z_{grid\ cell}$  and the lower and higher contour lines. Due to rasterization of the original input data being the first step of data processing, the user-defined grid cell size is crucial. If the user-defined grid cell size is less than the minimum distance between the contour lines, some contour lines will share the same grid cell, leading to inappropriate rasterized representation of the original data. Thus, in the present study, the grid cell size was determined on the basis of contour line properties, such as distance between neighbouring contour lines, i.e. complexity of the terrain modelled (e.g. Hengl, 2006). On a trial-and-error basis, input vector lines were rasterized into 2 m, 4 m, 5 m, 10 m and 15 m horizontal resolutions. Neighbouring contour lines were detected after rasterization by a 3×3 moving window. Based on the number of neighbouring rasterized contour lines, a 4×4 m grid cell size was chosen, because it was small enough to resolve the topography captured by the original contour data. The elevation value for each grid cell was established to a precision of 2 decimal places, to avoid artificially generated flat cells (i.e. neighbouring cells with the same elevation value). On the interpolated DEMs, flat analysis was performed in order to detect interpolation errors derived from, for example, inadequate determination of resolutions (Martz and Garbrecht, 1998). The real flat cells (i.e. ‘no

flow') are those cells that have at least one cell in its 3×3 neighbourhood with the same elevation value (Martz and Garbrecht, 1998; Jordan, 2007b). There are two additional types of flat cells: inflow and outflow cells (Garbrecht and Martz, 1997). An inflow cell is characterised by neighbouring cells in the 3×3 grid kernel with higher or equal elevation values. Thus, the cell can receive inflow from the higher neighbours, but the flow cannot leave the cell. For outflow cells, all neighbours have lower or equal elevations. The importance of flat cell detection is that the first-order derivative of a surface, such as slope angle or aspect, is calculated from the values of the surrounding cells in a 3×3 grid kernel. Thus, the existence of any flat cells may cause errors in the calculations of the derivatives. For example, the slope and aspect value of a real flat cell is zero (Jordan, 2007b). These types of error were systematically removed by a 5×5 (2.5×2.5 m) average moving window.

Cell elevation values within a closed contour line are characterised by a flat surface after interpolation (ILWIS, 2001; Hengl et al., 2008). In order to improve the topographic data of the topo50 DEM, local maxima ( $n = 39$ ) and minima ( $n = 7$ ) spot height data were extracted from places with different lithologies (e.g. volcanic deposits, Waitemata Group) from the LiDAR survey. These spot heights were used as control points when new peaks/pits were extrapolated. In the local maxima and minima construction, various DEMs were created with different slope angles from 1° to 15°, based on Jordan (2007b). The elevation value at a grid cell location  $k$ , within a closed local minimum and maximum contour line, is obtained as:

$$Z_k = Z \pm (\tan\beta d_k) \quad (3.2)$$

where  $Z$  corresponds to the elevation of the last closed contour lines,  $\tan\beta$  is the user-defined degree of slope in the local minima (-) or maxima (+), and the  $d_k$  is the raster distance between the last contour line and grid cell  $k$ . These various local maxima and minima configurations with different slope angles were then compared with the known spot height values obtained from the LiDAR survey. Then, the best fit local minima and maxima DEMs with fewer differences were chosen to proceed and obtain the final topo50 DEM.

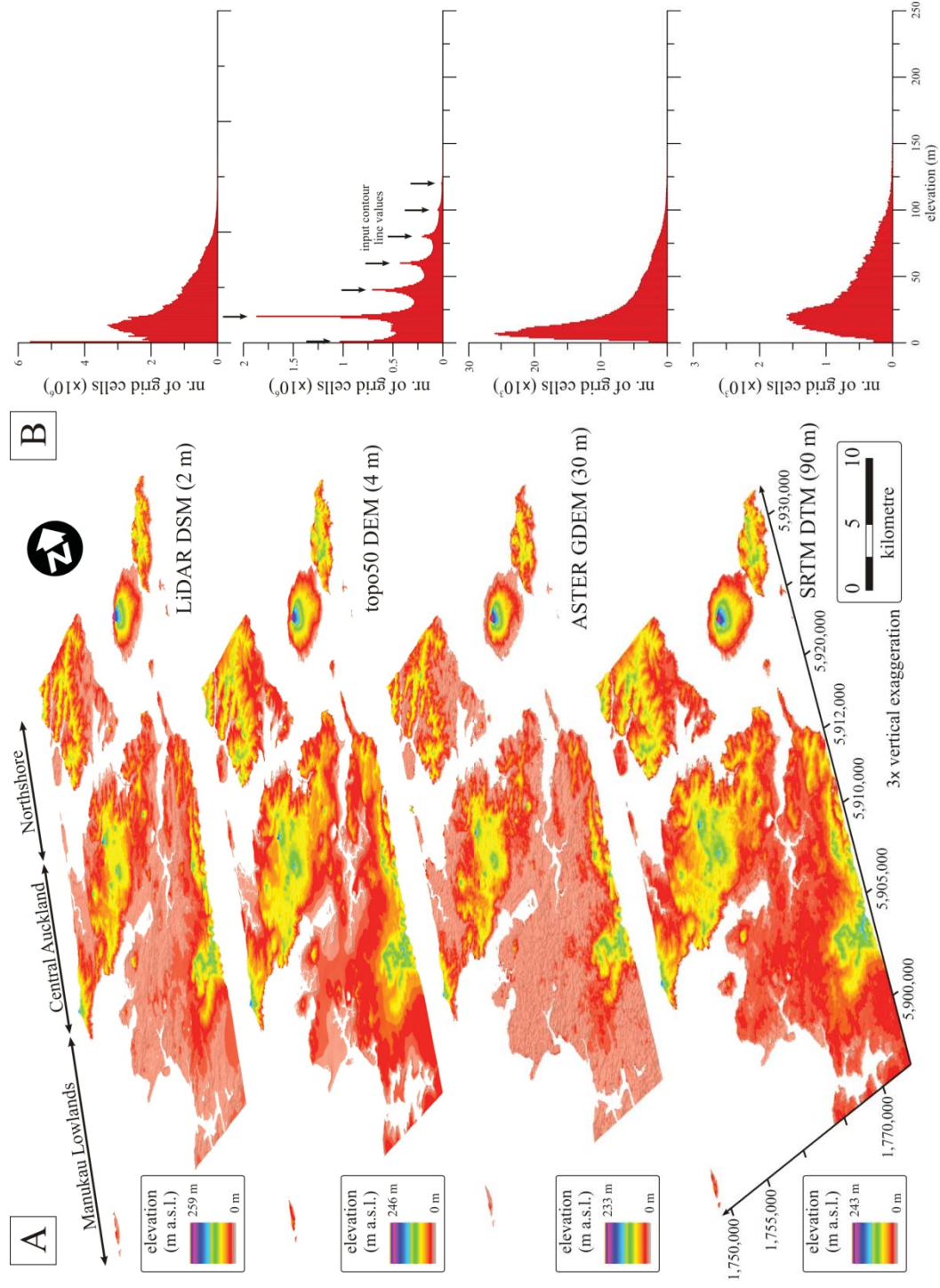


**Figure 3.5** (A) Overview of topographic data available in Auckland with various spatial resolutions. From the top to the bottom: 2 m Lidar DSM, 4 m topo50 DEM, 30 m ASTER GDEM, 90 m SRTM DTM. (B) Elevation histograms for each dataset.

### 3.2.4. Post-processing techniques

The major post-processing data modifications were based on various image filtering techniques, resampling processes and void removal routines from the gridded data (Wood, 1996; Zhang and Whitman, 2005; Reuter et al., 2007; Reuter et al., 2008; Wu et al., 2008; Meng et al., 2009). Among these, the most common techniques operate on different moving windows sizes from  $3 \times 3$  to  $n \times n$  (Fig. 3.6). Filtering is an important step in data preparation for geomorphic analysis and terrain attribute extractions (Nelson et al., 2008; Reuter et al., 2008). The main aim of filtering is to reduce both random and systematic errors in the interpolated DSM/DTM/DEMs (e.g. Reuter et al., 2008). These errors are often due to open water bodies (e.g. Brzank et al., 2008), vegetation (Hutton and Brazier, 2012) or buildings (e.g. Maas and Vosselman, 1999; Zhang and Whitman, 2005).

Resampling was found to be an important and reliable technique to reduce noise and error in the data (e.g. Raaflaub and Collins, 2006). The most commonly used resampling techniques are the cubic, bicubic and nearest neighbour methods (e.g. Wu et al., 2008). From these only nearest neighbours were used (Fig. 3.6) due to the fact that there is no reinterpolation of the existing data during resampling (Wood, 1996; Wu et al., 2008). The nearest neighbour method was used to create coarser resolution datasets for comparison and for further data analysis.

Sinks, flat areas with zero first-derivates and void removal are also important post-processing techniques to remove artificial outlying or missing data from the dataset (Jenson and Domingue, 1988; Garbrecht and Martz, 1997; Martz and Garbrecht, 1998; Temme et al., 2006; Reuter et al., 2007; Kenny et al., 2008). Sinks (i.e. topographic local minima) are grid cells bordered by grid cells with only higher elevation values. The origin of such local minima and flat grid cells could possibly be an interpolation error, such as the inadequate determination of the vertical precision used to calculate the elevation values of a grid cell (Martz and Garbrecht, 1998). These grid cells have an important effect on the accuracy of terrain calculated from the DSM/DTM/DEM (e.g. drainage extraction), thus their correction is essential (Wood, 1996; Martz and Garbrecht, 1998; Jordan, 2007a; Kenny et al., 2008). In the Auckland topographic datasets, voids only occur in the LiDAR DSM; however, their overall proportion is

small ( $\leq 0.1\%$  of the total area). These voids were delimited manually and they were filled by sink functions implemented into the ILWIS software (ILWIS, 2001; Maathuis and Wang, 2006). This algorithm increases the elevation of a void/sink until it reaches the elevation of the lowest outlet point, similar to Jenson and Domingue (1988). The elevations of the filled voids were then extracted and merged with the original LiDAR DSM, except in those areas of natural depressions, such as scoria cone craters.

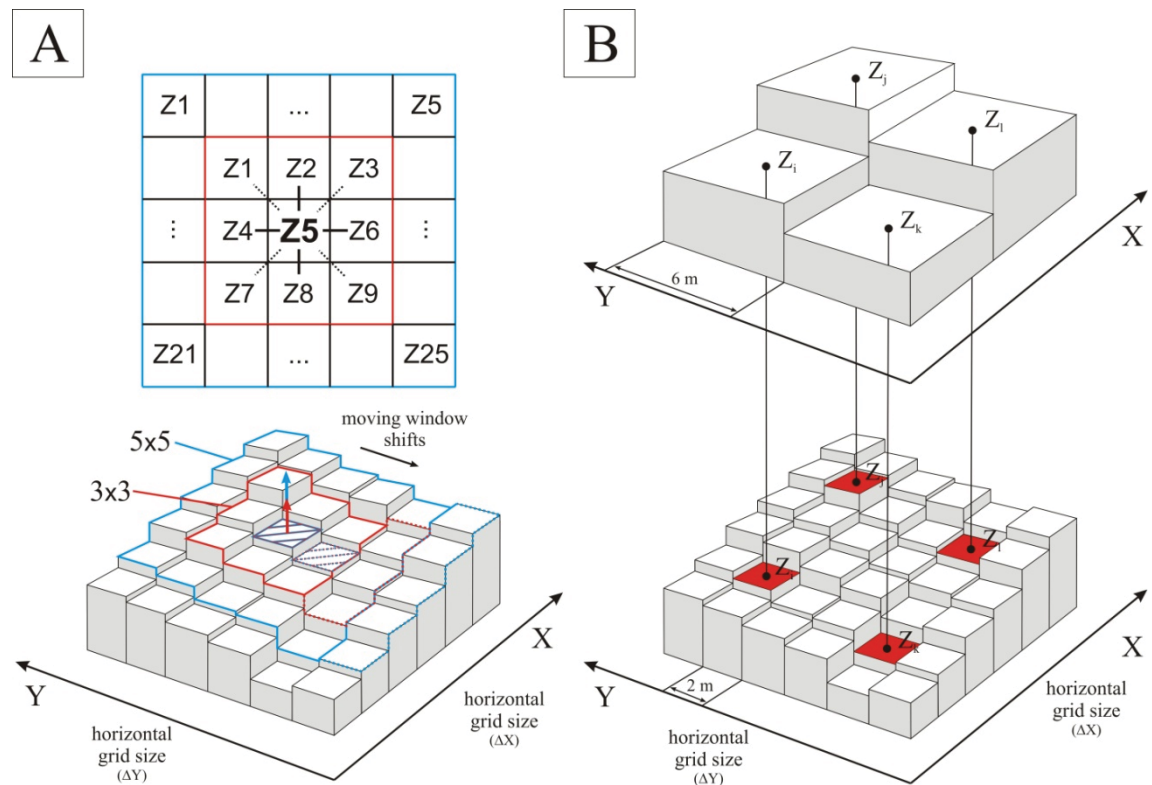


**Figure 3.6** (A) Scheme of filtering with moving window of a  $3 \times 3$  and  $5 \times 5$  kernel. Z1 to Z25 are the grid cells. (B) Concept of the resampling in a gridded environment by the nearest neighbour method. During nearest neighbour resampling, no additional interpolation takes place. During resampling the grid cell value of the new resolution is the value of the cell located the closest to the new grid cell centre (e.g. Wood, 1996).

### 3.2.5. Testing topographic datasets for Auckland

The accuracy of each topographic dataset can be described quantitatively by comparing their terrain parameters to higher accuracy ground control points, profiles or surfaces (Fisher and Tate, 2006; Aguilar and Mills, 2008; Wise, 2011). In the present study, three different high accuracy ground control datasets were used: (1) geodetic survey marks, (2) high accuracy RTK GPS profiles and (3) TLS DSM data. The location of control points, profiles and a surface are given in Fig. 3.7. These higher

accuracy control datasets are different in terms of data structure. The geodetic survey marks are irregularly distributed discrete point features, whereas the RTK GPS profiles and the TLS-based DSM are regularly arrayed points (Fig. 3.7).

### 3.2.5.1. Terrain height and representation

The accuracy of digital terrain data can be evaluated by comparing data with independent, high accuracy ground-control points to calculate the relative error in height (Fisher and Tate, 2006; Wise, 2011). The vertical error assessment was carried out by calculating Mean Error ( $ME$ ), absolute Mean Error ( $|ME|$ ), Standard Deviation Error ( $S$ ) and Root Mean Square Error ( $RMSE$ ) in between the topographic data ( $z_{DEM}$ ) and the higher order ground reference data ( $z_{control}$ ). These error descriptors are defined as (Fisher and Tate, 2006):

$$ME = \frac{\sum(z_{DEM} - z_{control})}{n} \quad (3.3)$$

$$S = \sqrt{\frac{\sum[(z_{DEM} - z_{control}) - ME]^2}{n-1}} \quad (3.4)$$

$$RMSE = \sqrt{\frac{\sum(z_{DEM} - z_{control})^2}{n}} \quad (3.5)$$

where the total number of control points is  $n$ .

In this study, geodetic survey marks and their location, height and accuracy are obtained from Land Information New Zealand ([www.linz.govt.nz](http://www.linz.govt.nz)). Only vertical survey marks with higher vertical accuracy than 0.35 m were selected. This is the accuracy level of the LiDAR-based DSM (e.g. Hodgson and Bresnahan, 2004). In total, there were 859 geodetic reference points in the study area that were used to assess the vertical accuracy of the topographic datasets of Auckland (Fig. 3.7A). The vertical error assessment using geodetic survey marks was performed using the point cloud data, where they were available (Fig. 3.7A), and the gridded LiDAR DSM. In the case of input point data assessment, geodetic survey mark points were used in the immediate adjacency of the survey mark, 5 m in rural areas and 2 m in urban areas (Fig. 3.7A).

The accuracy of DSM/DTM/DEM can also be tested by comparing them to a higher order reference profile or surface (Fig. 3.7B and C). In this investigation, three

test sites were used and compared: 1) a profile of the scoria cones in Browns Island (Fig. 3.7B), 2) a profile of Pukaki maar (Fig. 3.7B), and 3) a profile and a TLS-based surface from the southern part of Rangitoto's bare lava flow (Fig. 3.7C).

### 3.2.5.2. Terrain attributes in 2D and 3D

There are multiple types of parametric descriptors for terrain morphology (Evans, 1972; Speight, 1974; Moore et al., 1991; Wood, 1996; Shary et al., 2002; MacMillan and Shary, 2008; Minár and Evans, 2008). In a 3D digital surface, these terrain attributes can be grouped into three categories: zero-order (e.g. elevation, volume), first-order (slope angle and slope aspect) and second-order derivatives (e.g. curvature). Terrain attributes used in this research were selected and their accuracy tested. These 2D and 3D terrain attributes were then compared and evaluated in terms of their dependence on data types and their variability with respect to grid cell size.

The **elevation data** ( $z$ ) on a DSM/DTM/DEM is associated with each grid cell (Figs. 3.5 and 3.8). The structure of the digital surface can be described by its **standard deviation** ( $\sigma$ ) (e.g. Dragut et al., 2011). The  $\sigma$  is used to measure surface roughness (e.g. Shepard et al., 2001; Morris et al., 2008; Berti et al., 2013) or local variance in remote sensing and GIS (Woodcock and Strahler, 1987; Dragut et al., 2010; 2011). The  $\sigma$  can be calculated for a 2D profile as (Fig. 3.8):

$$\sigma_{2D} = \sqrt{\frac{\sum(x_i - \bar{x})^2}{n-1}} \quad (3.6)$$

where  $x_i$  is the elevation at location  $i$ , while  $\bar{x}$  is the average elevation of the sample points, and  $n$  is the sample number. In 3D, the  $\sigma$  is calculated, by a moving window, as (Fig. 3.8):

$$\sigma_{3D} = \sqrt{\frac{\sum(x_i - \bar{x})^2}{\Delta X_{window} \Delta Y_{window} - 1}} \quad (3.7)$$

where  $x_{window} \times y_{window}$  are the dimensions of the moving window. In this attribute testing, only the smallest window size,  $3 \times 3$ , was used.

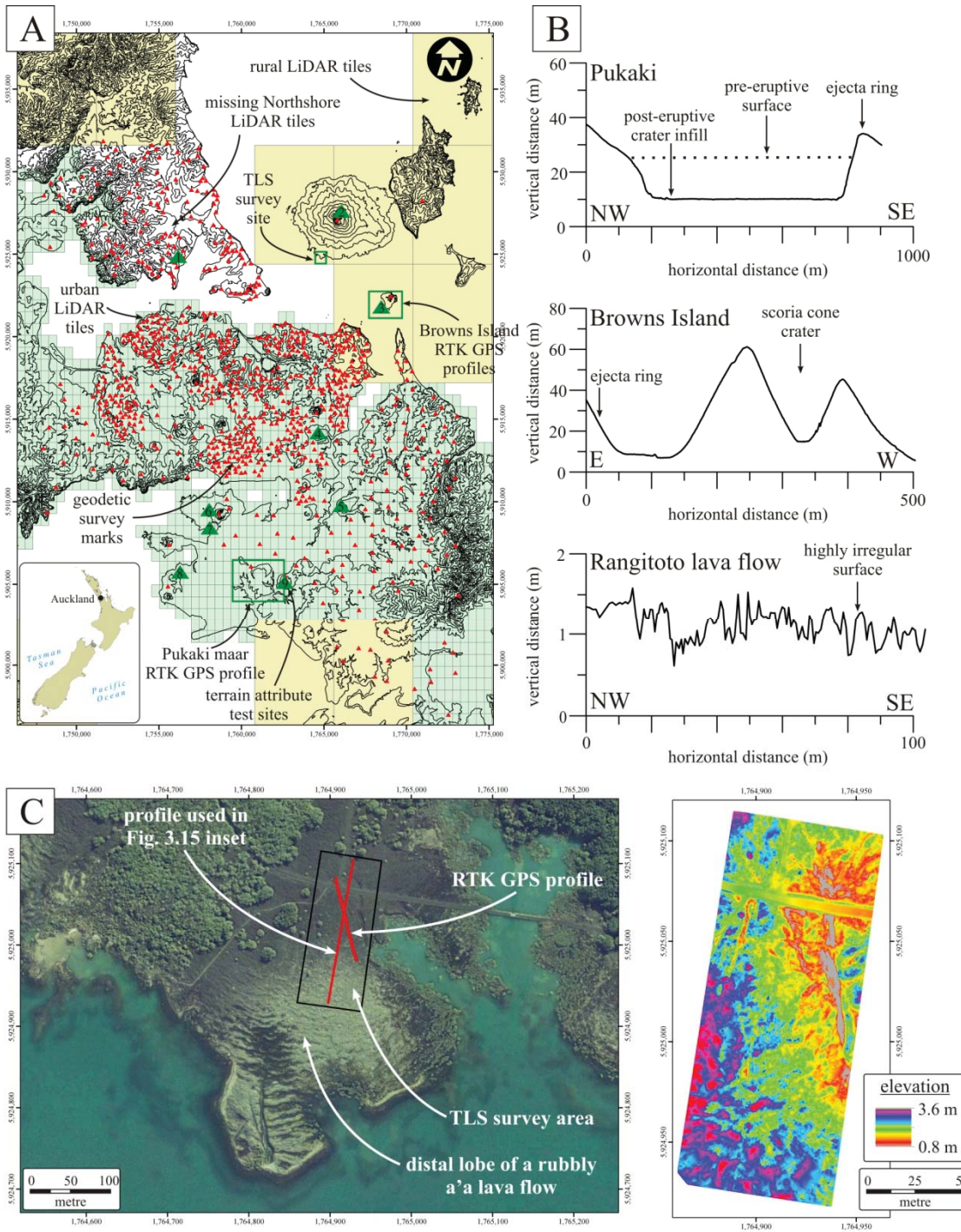


**Figure 3.7** High accuracy reference topographic data from the Auckland region. (A) Spatial location of geodetic survey marks as red triangles. The light yellow and light green polygons represent the available point cloud data from LiDAR surveys with rural and urban settings, respectively. The green rectangles are the location of the RTK GPS surveys and TLS DSM data. Numbered test sites in green triangles are: 1 – Onepoto, 2 – Rangitoto, 3 – Browns Island, 4 – Panmure Basin, 5 – Pukewairiki, 6 – Mt. Mangere, 7 – Mangere Lagoon, 8 – Pukeiti and Otuaatua, 9 – Crater Hill. (B) RTK GPS profiles from Auckland used in this study. (C) Location of the RTK GPS profiles and the TLS survey site on the Rangitoto volcano. On the right hand-side the TLS-based DSM shown here is with spatial resolution of 0.5 m.

The **area (A)** and **volume (V)** describes the 2D area and 3D space enclosed by a geologic or geomorphic unit (e.g. a lava flow or a volcanic edifice) on a profile or surface (Fig. 3.8). The area under a curve can be calculated as an integral of the curve; however, in a topographic profile, it is determined as (Fig. 3.8):

$$A = z_i \frac{(x_h + x_j)}{2} \quad (3.8)$$

where  $z$  is the elevation of a sample point, while  $x$  is the distance between two neighbouring sampling points around location  $i$ . In a 3D grid-based environment, the volumes (in all cases) were determined on a cell basis (Fig. 3.8):

$$V = \sum_i \Delta Z_i x_{cell} y_{cell} \quad (3.9)$$

where  $\Delta Z_i$  is the elevation difference between the DSM/DTM/DEM and the interpolated surface modelling the basement underneath the volcanics at the grid cell location of  $i$ ,  $x_{cell}$  and  $y_{cell}$  correspond to the length of a grid cell in the main direction  $X$  and  $Y$  (i.e. their multiplication is the area of a grid cell). The underlying terrain can be modelled (1) with an equal-elevated plane, (2) an inclined plane or (3) a user interpolated surface (e.g. based on drill core locations or from the outline of the feature).

The **gradient vector (G)** of a digital surface is characterised by its length, slope, and its direction, aspect (Evans, 1972; Zevenbergen and Thorne, 1987; Moore et al., 1991). Both slope and aspect components are based on numerical differentiation of elevation values around sample location  $i$  (e.g. Jordan et al., 2005). Hence it is based on the surrounding grid locations instead of the sample point itself. In 2D the slope angle is considered here as (Fig. 3.9):

$$\text{slope}_{2D} = \arctan\left(\frac{dz_i}{dx_i}\right) \quad (3.10)$$

where  $dz$  and  $dx$  are the vertical and horizontal differences around the sample point  $i$ . In 3D, it changes to (Fig. 3.9):

$$\text{slope}_{3D} = \arctan \sqrt{f_x^2 + f_y^2} \quad (3.11)$$

$$\text{aspect} = 180^\circ - \arctan(f_y/f_x) + 90^\circ (f_x/|f_x|) \quad (3.12)$$

where aspect is the modified directional component of the gradient vector pointing in the down flow direction and measured clockwise from north. The partial derivatives ( $f_x$ ,  $f_y$ ) can be estimated using different filters (Jones, 1998). For simplicity, in the present investigation, only the unweighted eight-point Prewitt operator (Prewitt, 1970) was used (Fig. 3.9):

$$f_x = (Z3+Z6+Z9-Z1-Z4-Z7)/6\Delta X \quad (3.13)$$

$$f_y = (Z1+Z2+Z3-Z7-Z8-Z9)/6\Delta Y \quad (3.14)$$

where  $Z1-Z9$  are the elevation values in a  $3 \times 3$  grid kernel, and  $\Delta X$  and  $\Delta Y$  are the size of the grid cell along the two principal directions.  $Z1$  corresponds to the top left, while  $Z9$  is the bottom right cell. Besides its smoothing effect, this method has the advantage of being identical to a least-squares plane fit to the 9 window elevations (Sharpnack and Akin, 1969), thus the linear Prewitt operators are particularly suitable for linearly interpolated surfaces (Jordan, 2007b). The slope and aspect values of a DEM are highly dependent on the resolution (Zhou and Liu, 2004; Deng et al., 2007; Dragut et al., 2011) and filter used (Jones, 1998; Jordan, 2007b).

Second-order derivatives, such as profile or plan curvature (Moore et al., 1991; Shary et al., 2002; MacMillan and Shary, 2008; Minár and Evans, 2008), as well as third-order derivatives (Florinsky, 2009; Minár et al., 2013), are commonly used and documented parameters in describing surfaces and feature extraction. These higher-order terrain parameters are not considered in the present study.

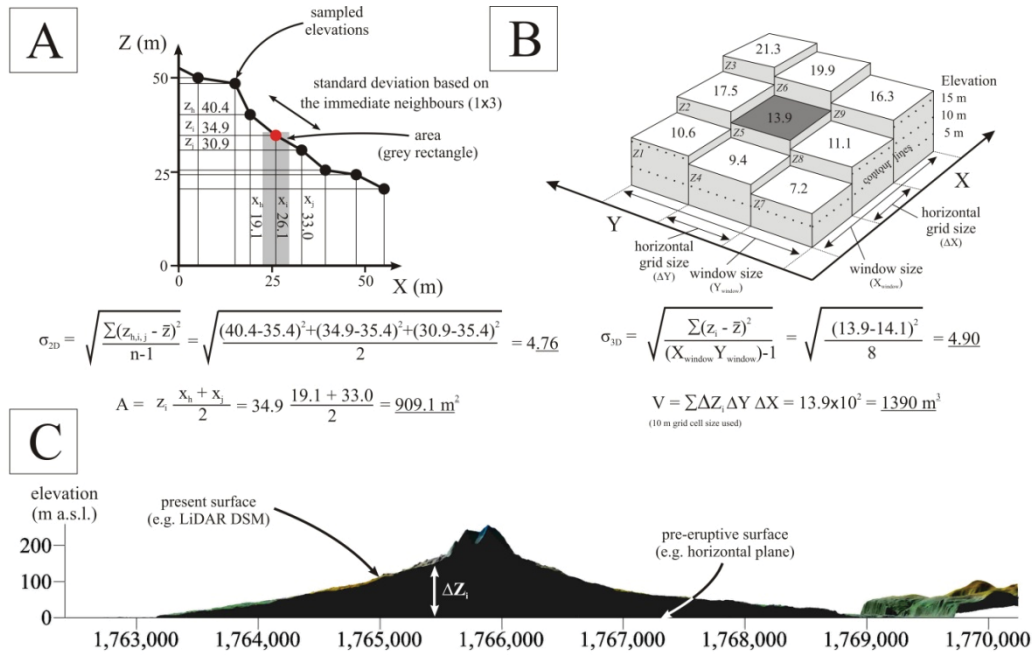


**Figure 3.8** Overview of the calculation of zero-order derivatives such as area (A), standard deviation of elevation (B), and volumes (C).

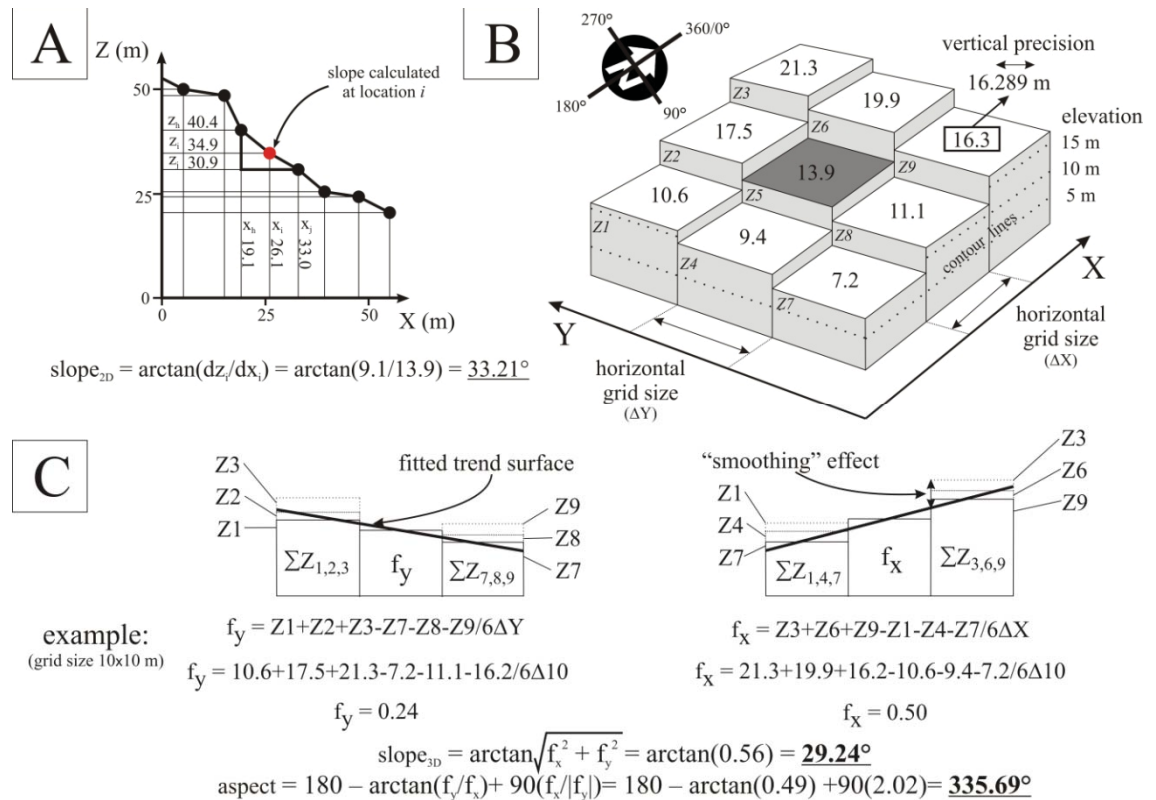


**Figure 3.9** Overview of the calculation of first-order derivatives, such as slope angle and slope aspect, in 2D and 3D environment. Note that the examples are used here with a linear, unweighted Prewitt filter (Prewitt, 1970). (A) An example for calculating slope angle along a 2D profile. (B) Perspective view of a 3x3 grid cell kernel, which was used to calculate slope angle and aspect by numerical differentiation in (C).

In order to analyse multi-scale behaviour of important terrain attributes (e.g. Dragut and Eisank, 2011), the previously introduced topographic datasets (e.g. LiDAR DSM, topo50 DEM, ASTER GDEM, SRTM DTM) were resampled into coarser subsets (2 m, 4 m, 5 m, 10 m, 20 m, 30 m, 60 m and 90m). The resampling was performed by the nearest neighbour method (Fig. 3.6). In 2D the terrain attributes were calculated along the RTK GPS profiles (Fig. 3.7). For testing terrain attributes in 3D, five test sites were selected with different geometries and volumetric sizes, from “small” to “large” for scoria cones, lava flows, and ejecta rings (Fig. 3.7). In the comparison data, there was no smoothing applied. Given that Auckland is located at sea level, the sea (0 m a.s.l.) is an additional source of error in data comparisons. The effect from the representation of the sea in different DSM/DTM/DEMs was minimised by masking all the DSM/DTM/DEMs with the same sea level ( $\leq 0$  m a.s.l.) from the LiDAR DSM.

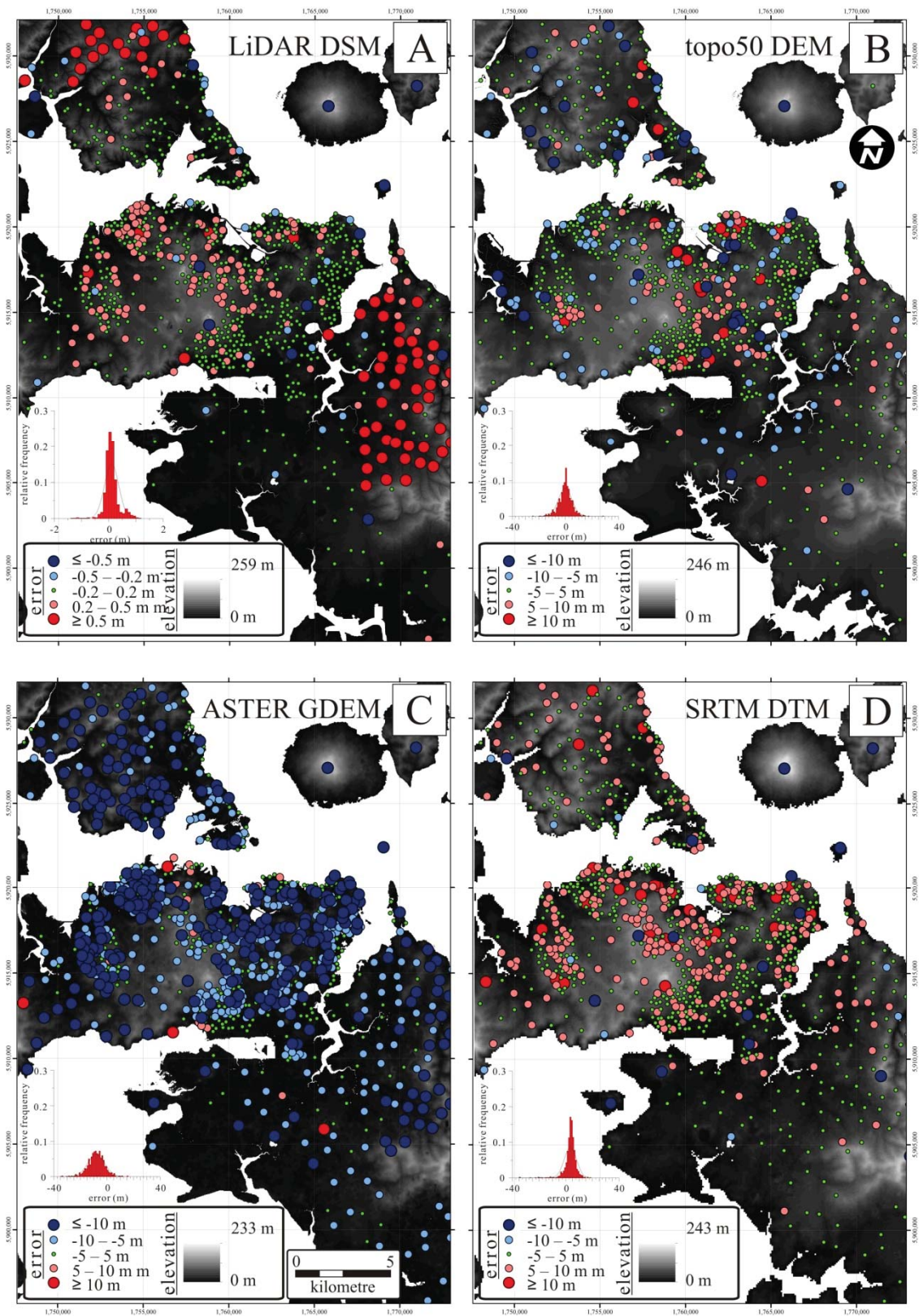
### 3.3. Results: accuracy and variability

The error assessment for the available topographic datasets for Auckland was calculated by comparing these datasets to a finite number of control points, profiles and surfaces (Fig. 3.7). The results of the error assessment are summarised in Table 3.1. The best performing dataset is the LiDAR DSM (Fig. 3.10 and Table 3.1). The LiDAR DSM has a RMSE of  $\pm 0.28$  m, which is comparable to other LiDAR-based studies (e.g. Hodgson and Bresnahan, 2004; Aguilar and Mills, 2008). The elevation differences in the LiDAR DSM ranged from -1.40 m to 1.14 m, with an average of 0.08 m. The absolute average of the difference is 0.26 m (Table 3.1). The error shows a slight decreasing trend over increasing resampling (Table 3.1), although the error stayed in the same order of magnitude as for the original 2 m resolution LiDAR DSM.

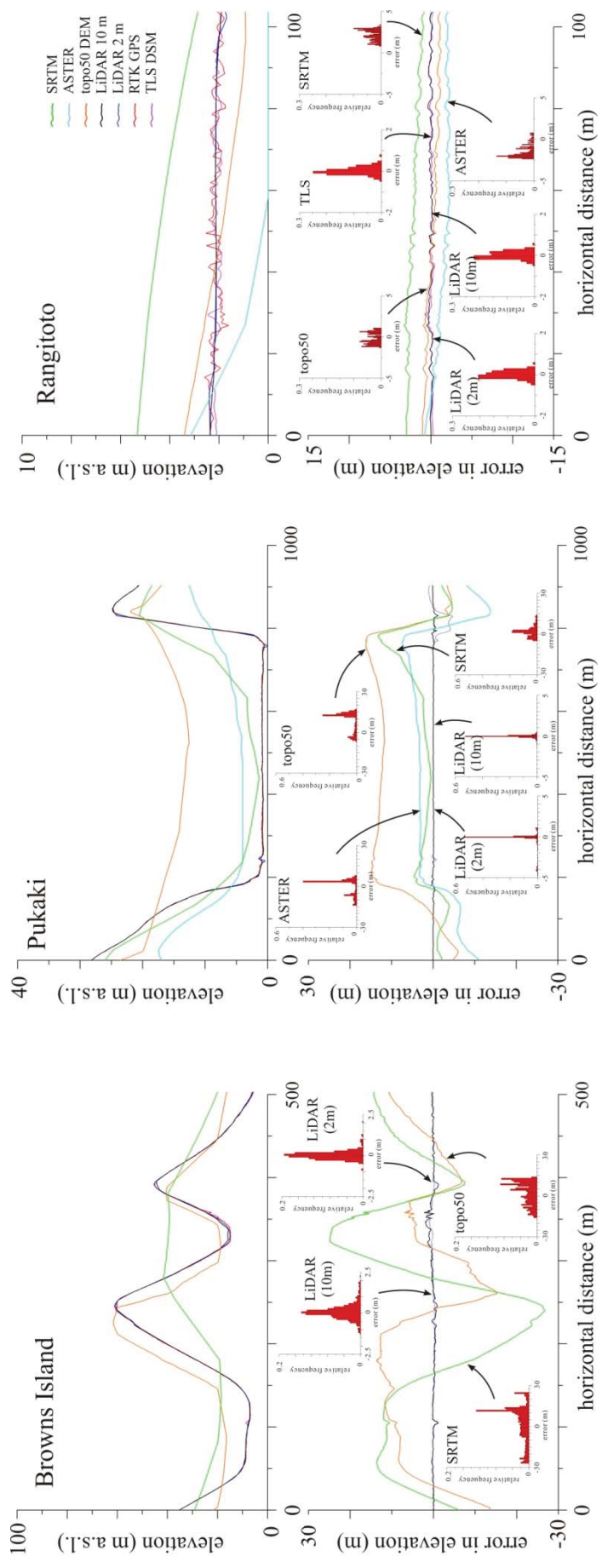
It is worth noting that these error values are identical to the often quoted industrial standard values for the vertical and horizontal properties of LiDAR-derived products,  $\pm 0.1$  to  $\pm 0.5$  m (e.g. Hodgson and Bresnahan, 2004; Gally, 2013). All other topographic datasets have RMSEs in the range of 5 m (e.g. topo50 DEM, SRTM DTM) to 10 m (ASTER GDEM), which is consistent with the range of similar estimates from the same datasets in different locations (e.g. Gorokhovich and Voustianiouk, 2006; Hirt et al., 2010).

Table 3.1 Results of the error assessment of the topographic data for Auckland.

control data	vertical control data				topographic data type						
	location	nr of control points	error descriptor	TLS DSM	LidAR points	LidAR DSM	LidAR DSM	topo50 DEM	ASTER GDEM	SRTM DTM	
point (geodetic network)	field-wide	859	RMSE	0.5 m	-	LidAR DSM 2 m	LidAR DSM 10 m	topo50 DEM 4 m	ASTER GDEM 30 m	SRTM DTM 90 m	
			ME		0.308	0.284	0.407	5.028	10.835	5.764	
			ABS(ME)		0.117	0.081	0.092	-0.148	-8.295	3.442	
			S	-	0.191	0.264	0.267	3.652	8.875	4.652	
			MIN		0.284	0.188	0.397	5.032	6.974	4.625	
			MAX		-1.700	-1.400	-2.755	-24.800	-67.510	-34.766	
					2.420	1.140	1.818	28.530	15.277	18.640	
						0.252	0.453	8.404		13.441	
						0.016	0.079	2.446		2.716	
						0.175	0.309	7.436		11.438	
profile (RTK GPS)	Browns Island scoria cone	773	S	-	-	0.251	0.446	8.045	no coverage	13.172	
			MIN		-0.885	-1.233	-15.213		-26.751		
			MAX		2.028	2.216	13.642		24.872		
						0.995	0.147	11.193		5.737	
						-0.254	-0.048	8.692		0.100	
						0.361	0.089	10.153		5.051	
						0.963	0.139	7.057		5.739	
						-4.760	-1.210	-6.035		-13.792	
						1.105	0.446	16.293		7.519	
						0.170	0.171	0.718		1.695	
surface (TLS data)	Rangitoto lava flow	141	RMSE	0.201		0.006	0.009	-0.180	-1.500	2.165	
			ME		-0.0938						
			ABS(ME)		0.1638		0.137	0.139	0.647	1.561	2.165
			S		0.2044		0.171	0.171	0.698	0.792	0.650
			MIN		-0.5425		-0.415	-0.416	-1.269	-2.350	0.807
			MAX		0.6395		0.515	0.540	1.064	0.797	3.307
						0.256		0.874		2.133	2.444
						-0.061		0.065		-1.523	2.345
						0.198		0.773		2.016	0.691
						0.248		0.712		1.493	2.345
			-1.182		-2.138		-3.327	0.858			
			1.193		1.977		3.971	4.504			



**Figure 3.10** Point-based error assessments using the geodetic survey marks. Note that negative and positive values show places where elevation values are underestimated and overestimated, respectively.



**Figure 3.11** Profile-based error assessments for the three test sites. The upper row of graphs shows the elevation of different topographic datasets from the Auckland region. The bottom row of graphs shows the error along the control profile. The insets are the error distribution histograms for each topographic dataset. The bins are 1 m for SRTM DTM, ASTER GDEM and topo50 DEM, and 0.05 m for 10 m and 2 m for LiDAR DSMs.

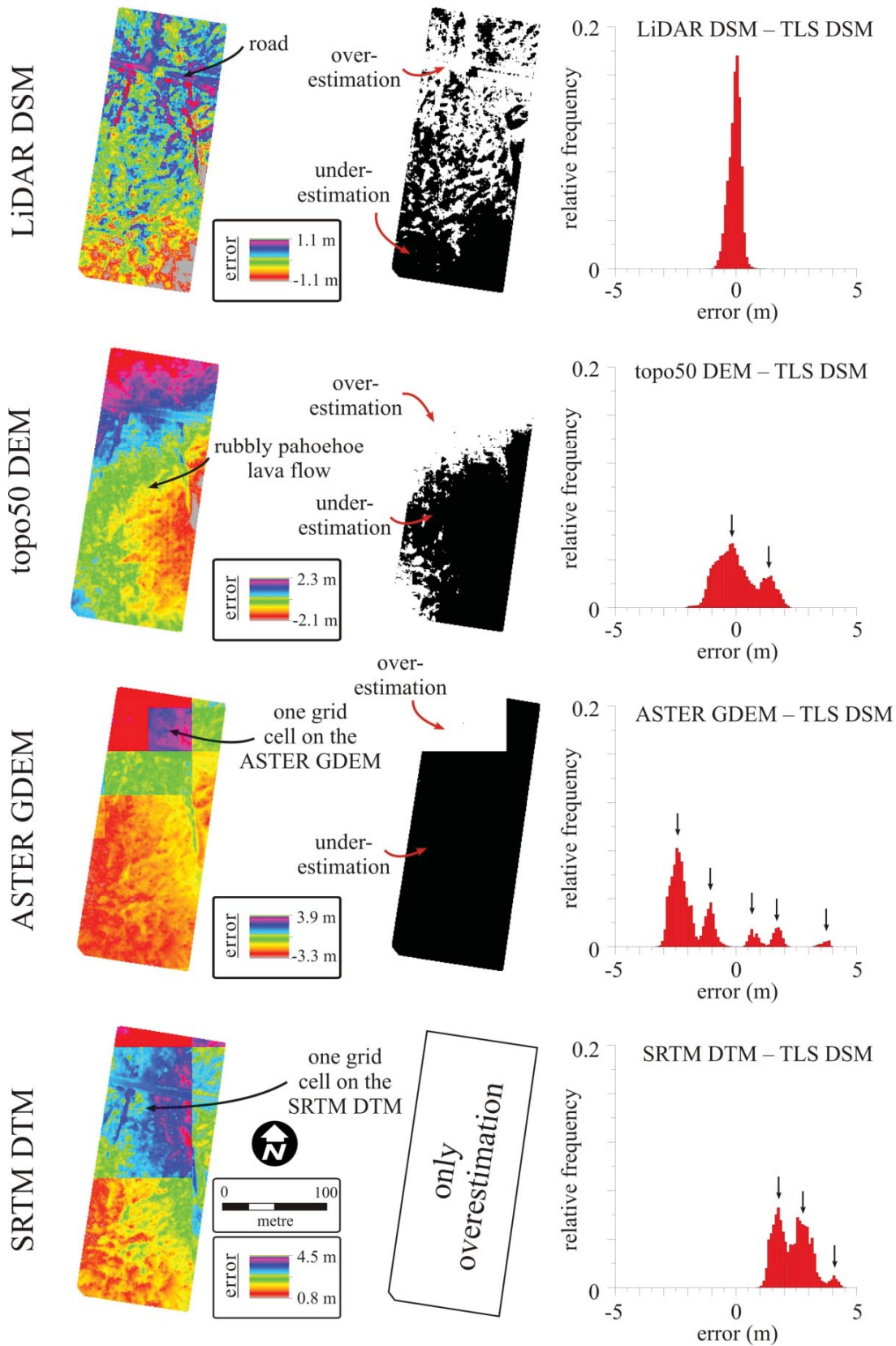


**Figure 3.12** Surface-based error assessment based a TLS acquired reference surface on the distal part of the Rangitoto lava flow field. Note the multimodal (arrows) error distributions for the topo50 DEM, ASTER GDEM and SRTM DTMs. These are due to the dominance of under- and overestimation of the real topography.

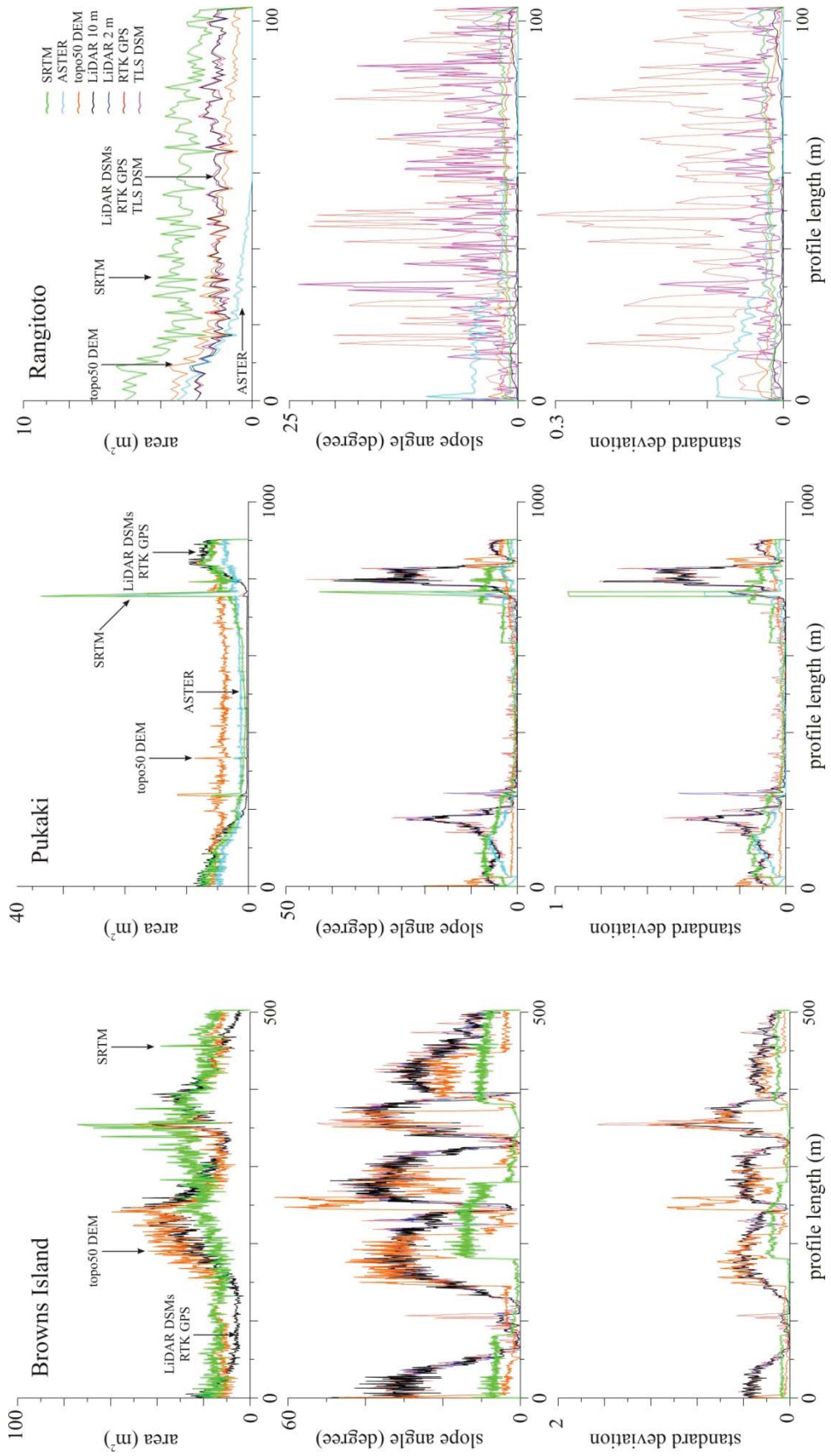


**Figure 3.13** Variability of zero and first derivatives, calculated from the DSM/DTM/DEMs, along the RTK GPS control profiles for three test sites: Browns Island (first column), Pukaki (second column), and Rangitoto (third column).

The error of the topographic data for Auckland was estimated by using RTK GPS profile data for three survey sites: Browns Island scoria cone, Pukaki maar and Rangitoto lava flow (Fig. 3.7). In the Browns Island profile, the accuracy of the LiDAR dataset (including the resampled 10 m version) is identical to the results of the point-based error assessment (Table 3.1 and Fig. 3.11). The RMSE is somewhat better,  $\pm 0.25$  m, while the ME and S are 0.016 m and 0.25 m respectively. The maximum and minimum differences are -0.88 to 2.02 m respectively. The accuracy, measured along profiles, dropped significantly for both the topo50 DEM and the remotely sensed SRTM DTM (Fig. 3.11), showing the insufficient resolution to resolve the details of the changes of the terrain being modelled.

For the Pukaki maar profile, the accuracy of the LiDAR data is slightly worse than in other profiles (e.g. Browns Island) with a RMSE of  $\pm 0.99$  m, ME of -0.25 m and S of 0.36 m (Table 3.1). The resampled LiDAR data showed the best performance in representing the topography along the control profile. In the other topographic datasets, the accuracy improved significantly, with the RMSEs of  $\pm 5.73$  m and  $\pm 4.05$  m for the ASTER GDEM and SRTM DTM, respectively, in contrast to the topo50 DEM, where the accuracy decreased (RMSE of  $\pm 11.19$  m; Table 3.1).

Surprisingly, the accuracy over the highly rough rubbly a'a lava flow area (Figs 3.7 and 3.11) showed the smallest deviation from the control RTK GPS profile. All error descriptors are similar for both LiDAR and resampled LiDAR datasets. Visually, however, the surface representation of the LiDAR DSM was not able to resolve fine-scale ( $\leq 2$  m) topography (Fig. 3.11). The error properties of much coarser datasets are also improved (RMSE of  $\pm 0.78$  to  $\pm 2.25$  m), which is in contrast to their visual appearance in representing the 'true' surface (Fig. 3.11).

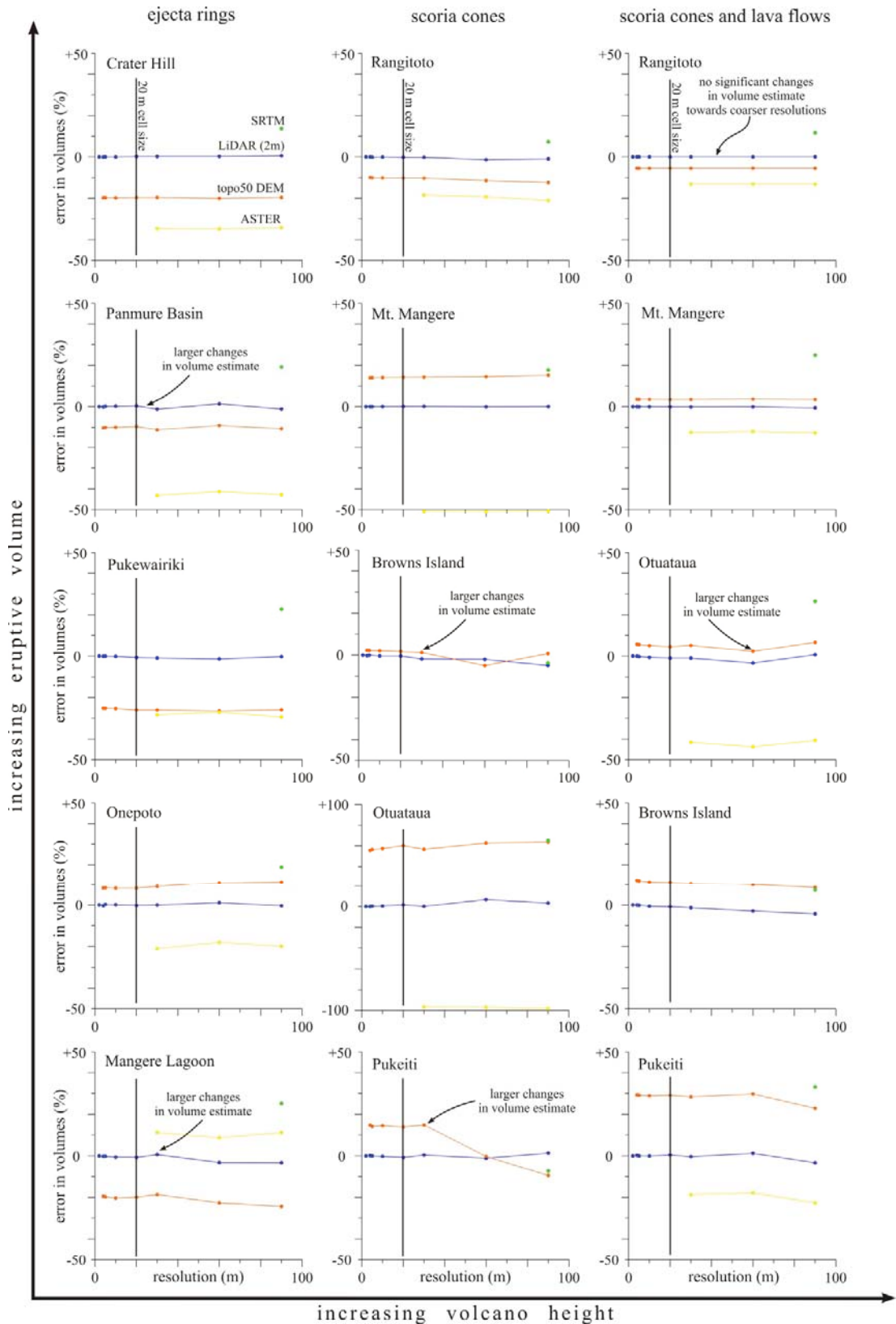


**Figure 3.14** Error in eruptive volume estimations due to resampling and different input data types, including LiDAR DSM 2m (blue), topo50 DEM (orange), ASTER GDEM (yellow) and SRTM DTM (green). For the location of each evaluation site see Fig. 3.7. This graph shows the overall inaccuracy of ASTER and SRTM DTM products in resolving the fine-details of the topography on monogenetic volcanoes.

The results of the comparison of different topographic datasets to a higher accuracy reference surface, such as TLS DSM (Fig. 3.7) for a limited area (100 by 200 m), showed similar error ranges (Table 3.1). The overall elevation differences between the TLS DSM reference surface and the examined DSM/DTM/DEMs are found to be very narrow (-3.6 to 4.2 m; Table 3.1), which in turn results in an apparently better overall accuracy in the values for each of the datasets. In contrast, visually, the surface representation is similar to the RTK GPS profile data (Fig. 3.11). None of the input data can resolve the fine details of the extremely rough lava flow surface; however, it seems that the elevation can be systematically over and underestimated. The LiDAR error over this TLS control data is symmetrically distributed around 0 m (i.e. there is no significant error introduced to the volume calculations, Fig. 3.12). The error descriptors, such as RMSE, ranged from  $\pm 0.25$  m for LiDAR DSM to  $\pm 2.44$  m for SRTM DTM (Table 3.1).

The basic terrain attributes, such as area, standard deviation of elevation, volume or slope angles, were found to be contrasting and highly dependent on the input data types and structure (e.g. Figs. 3.13 and 3.14). The post-processing techniques, such as nearest neighbour resampling, introduced only marginal error ( $\pm 1\%$ ) in the derived attributes (Fig. 3.14). This is consistent with other studies (e.g. Wu et al., 2008). The trend of changing attributes was usually consistent with a slight decrease with decreasing grid cell size from 2 m to 90 m resolutions (Fig. 3.14).

### 3.4. Which input data should be used?

Based on the accuracy of each topographic dataset available for the Auckland region, the best performance is, in decreasing order, the LiDAR DSM, topo50 DEM, SRTM DTM and ASTER GDEM (e.g. Fig. 3.15 and Table 3.1). This is in agreement with the performance of the terrain attributes and their changes as a function of horizontal grid cell size (e.g. Fig. 3.14). Therefore, in subsequent analysis the LiDAR dataset will be used.

This calibration of terrain data available for the Auckland region, and the accuracy of extractable terrain attributes, is important for establishing the overall limits of the input data in terms of terrain representation. Furthermore, the appropriate 'scale' of the subsequent investigation also needs to be determined based on available topographic

data. The working scale (i.e. resolution) for our calculations is between 5 to 20 m, and occasionally less detailed topographic data are acceptable (i.e. 20 to 30 m). This is consistent with the suggested working resolution for any hydrological and geomorphic mapping studies and landform/feature extraction found elsewhere (e.g. Zhang and Montgomery, 1994). Therefore, in the following investigations it is appropriate and acceptable to extract quantitative topographic information, such as eruptive volumes, using a subset of the resampled LiDAR DSM data. In the following chapters, there are two preferred working scales for different investigations: (1) the 10 m LiDAR DSM scale for edifice eruptive volumes, and (2) the 20 m resampled DSM used for modelling the broad-scale properties of the terrain in Auckland.

(1) The first preferred scale is the 10 m LiDAR DSM to be used for detecting edifice-scale eruptive volumes, as an important quantitative parameter for further complex hazard assessments of Auckland (Chapters 4 and 5). Based on the error assessment of terrain features/attributes, resampling by natural neighbour technique has a minimal effect. This post-processing technique introduced a maximum error of  $\pm 1\%$ , but more realistically about  $\pm 0.1\%$  for the 10 m and 20 m resampled datasets (Fig. 3.14). From the example given in Fig. 3.14, the resampling led to underestimation in the bulk eruptive volumes, thus these can be considered as minimum estimates.

On the edifice-scale, there is another important factor limiting the accuracy of eruptive volume estimates, such as surface roughness, including changes of the degree of fine-ash tephra mantling, or rough rubbly a'a lava flow (e.g. Gaddis et al., 1990; Campbell and Shepard, 1996; Shepard et al., 2001; Mazzarini et al., 2008; Morris et al., 2008). Examining how the LiDAR DSM could resolve the topography over the extremely rough lava flow surface at Rangitoto (Figs 3.11 and 3.15 inset), it is evident that the surface roughness of bare lava flows is the largest contributor to the overall uncertainty in the eruptive volume estimates. This roughness is on m to mm scales (e.g. Farr, 1992; Shepard et al., 2001). The overall representation of Rangitoto volcano on a larger scale (i.e. 10 m to km) is fairly consistent for all the available topographic datasets of Auckland (Fig. 3.15). The surface roughness is often found to have a strong correlation with the time elapsed since the emplacement of the lava flow (e.g. Farr, 1992).

Given that the lava flows of the AVF formed in the last tens of thousands of years (Lindsay et al., 2011) and are covered by soil and eroded through weathering, these lava

flows are expected to be well characterised by the 10 m resampled DSM topographic data and show no significant changes in the eruptive volume estimates from coarser DSMs (Figs 3.14). The only exception is the Rangitoto lava flow, which is moderately vegetated and shows an extremely rough lava flow surface with slabs (diameter of 1–2 m) and loose cobbles to boulder sized clasts on the surface (Figs 3.3B and 3.11). The inaccuracy of the terrain representation due to surface roughness can be quantified using the TLS DSM in comparison with the LiDAR data and resampled LiDAR DSMs. Using 2D and 3D reference data, the LiDAR data and its resampled products do not resolve the topography, but they tend to smooth the terrain being modelled on a below m-scale (Fig. 3.15). This smoothing is due to the insufficient point density or sampling intervals used in the LiDAR surveys (Fig. 3.15 inset). Nevertheless, the overall effect is marginal for the present investigation. Based on the high-resolution and accuracy of the reference surface, for instance, volume-loss and volume-gain seem to be equivalently represented (Figs. 3.12 and 3.15 inset). Thus, the possible encountered error (i.e. over- or underestimating due to data limits) is estimated to be of  $\pm 1\text{--}2\%$ . Overall, the LiDAR DSM is found to be an accurate m-scale terrain representation for the entire Auckland area.

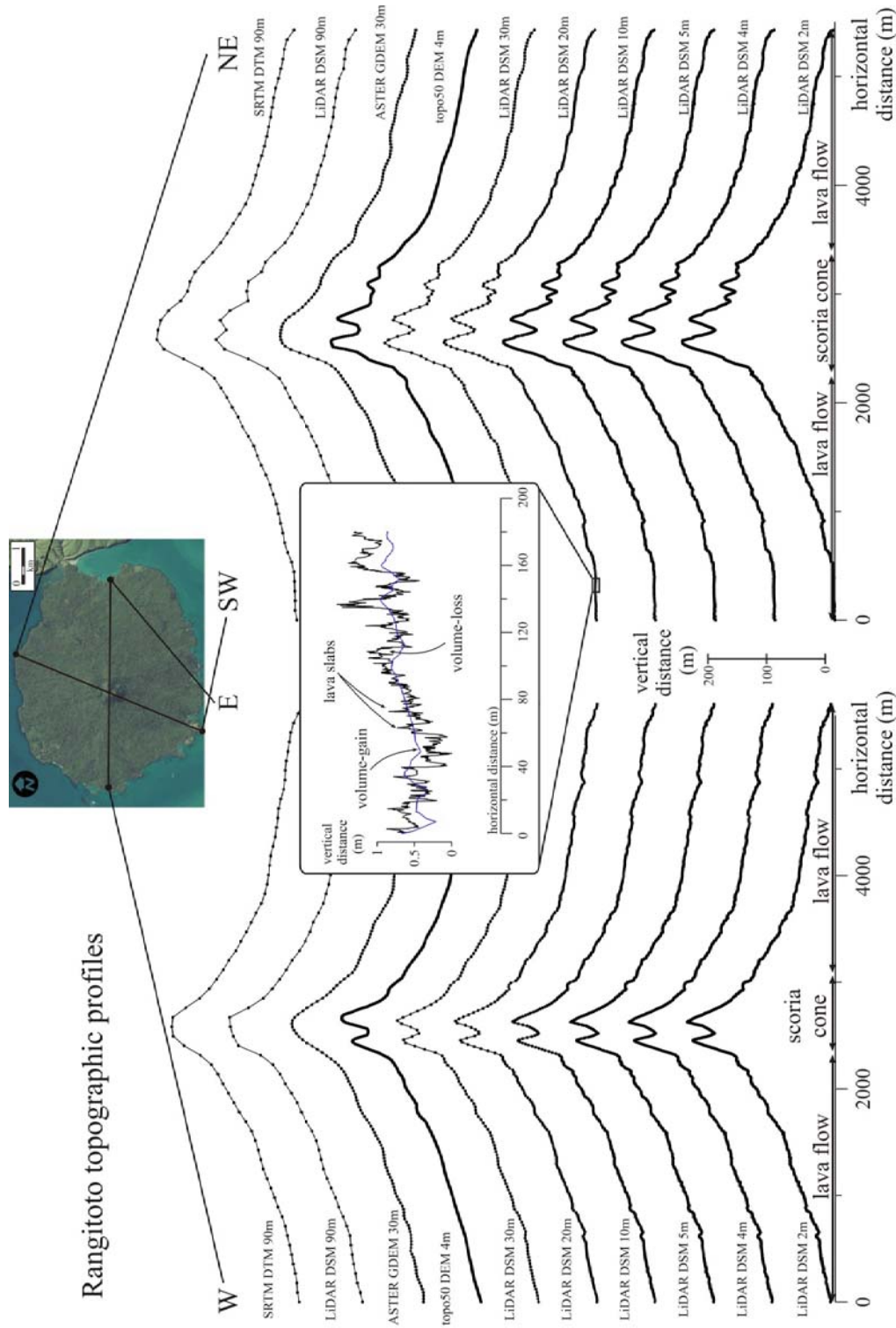


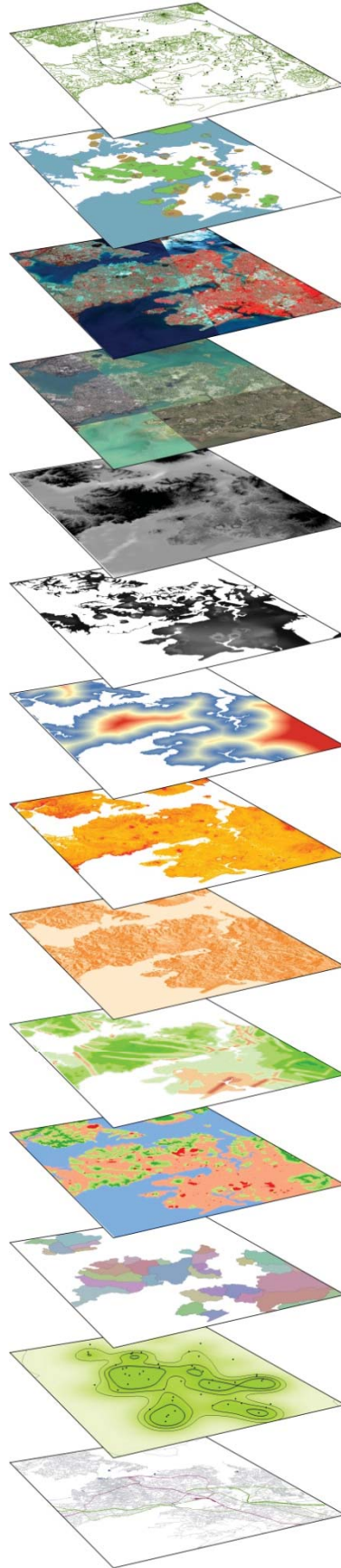
**Figure 3.15** Graph shows two profiles through the youngest volcanic edifice, Rangitoto, with all the available topographic data from Auckland. The summit crater with a diameter of 200 m is not resolved by the coarser topographic data sources, such as SRTM DTM or ASTER GDEM. The surface roughness on a dm-scale is shown in the inset. This example surface is based on the TLS DSM data on the distal parts of Rangitoto a 'lava flow'. The blue line is the LiDAR 2m data, while the black line is the much higher resolution TLS DSM data.

(2) The second scaled dataset is a 20 m resampled DSM that will be used for modelling the large-scale changes of the terrain below Auckland. This resampled LiDAR DSM is coarse enough to minimise the effect of filtering issues (e.g. vegetation filtering and LiDAR labelling error) and voids due to building removals that are common in an urban setting, but it keeps the (coarse) topography accurately represented on a 100 m scale. This 20 m resampled LiDAR DSM was smoothed with an average  $3 \times 3$  or  $5 \times 5$  moving window before further data extractions. This smooth topography was used in the hydrological characterisation of the study area, and as the pre-eruptive topography for the simulation of lava flows (Chapters 6 and 7).

For lava flow simulations and hazard mapping, subaerial regions are preferred (e.g. Felpeto et al., 2007; Rodriguez-Gonzalez et al., 2009b; Cappello et al., 2012). However, in Auckland, about 41% of the area studied is covered by shallow sea water ( $\leq 30$  m deep). Over these areas, the elevation values in the LiDAR DSM are 0 m a.s.l. (i.e. no topographic information was captured by LiDAR). Volcanic eruptions could, however, take place in such areas in the future, thus their hazard assessment is essential, but not possible using the current (above sea level) topographical datasets. There is a rare opportunity to have a DSM/DTM/DEM with both elevation information (Reuter et al., 2008) and bathymetric data (e.g. Robinson and Eakins, 2006). For the Auckland region, bathymetric data are available as contour maps with a scale of 1:100 000, with contour intervals of 10 m. From these bathymetric maps, both contour lines and sea water depth points were digitised for the broader Auckland region. After digitization, the contour lines and points were interpolated by a linear interpolator. The bathymetric DEM then was merged with both 10 m and 20 m resampled DSM datasets, providing combined on- and offshore DSM for hazard assessment.







Chapter 4  
Eruptive volumes

# 04 / eruptive volumes

This Chapter presents the complex issues involved in eruptive volume estimation, and goes on to propose a model for estimating eruptive volumes of small-volume ( $\leq 1 \text{ km}^3$ ) monogenetic volcanoes, using the example of the Auckland Volcanic Field (AVF), New Zealand. This is based on the previously assessed LiDAR topographic datasets of the AVF and their derivatives (e.g. resampled products of the original version). The main aim of this Chapter is to provide a quantitative means for assessing volcanic fields' eruption properties and to develop an extensive database for the AVF for further hazard analysis. The Chapter concludes with a discussion of the edifice-scale and field-scale properties of the AVF.

Supplementary data for this Chapter are in Appendix B.

## Chapter contents

4.1. Introduction.....	82
4.2. Model for volume estimates of monogenetic volcanoes .....	84
4.2.1. Bulk subsurface volume .....	86
4.2.2. Bulk proximal tephra accumulation and lava flows volume .....	88
4.2.3. Bulk medial to distal pyroclastic volume .....	90
4.3. Input data and configuration for the AVF .....	92
4.3.1. Bulk subsurface volume for the AVF.....	92
4.3.2. Bulk proximal tephra accumulation and lava flows volumes for the AVF .....	93
4.3.3. Bulk medial to distal pyroclastic volume for the AVF.....	95
4.4. Converting bulk to Dense Rock Equivalent (DRE) eruptive volumes.....	96
4.5. Results .....	101
4.6. Discussion.....	107
4.6.1. Limits and errors in eruptive volume estimates .....	107
4.6.2. Spatial and temporal magma flux.....	108
4.6.3. Integrating eruptive volumes with the AVF's evolution.....	110
4.6.4. AVF evolution and relationship to neighbouring fields .....	115
4.6.5. Volcanic hazard consequences.....	115
4.7. Conclusions.....	116

This Chapter is based on a published paper (Appendix B):

Kereszturi, G., Németh, K., Cronin, J.S., Agustin-Flores, J., Smith, I.E.M. and Lindsay, J., 2013: A model for calculating eruptive volumes for monogenetic volcanoes – Implication for the Quaternary Auckland Volcanic Field, New Zealand. *Journal of Volcanology and Geothermal Research*, 266: pp. 16-33.  
*[DOI:10.1016/j.jvolgeores.2013.09.003](https://doi.org/10.1016/j.jvolgeores.2013.09.003)*

Participating authors:

**Gabor Kereszturi** (field work, data processing, lab work, volume calculations, manuscript writing and editing)

**Károly Németh** (assisting in the field, manuscript editing and discussion, help to design volume estimation scheme)

**Shane J. Cronin** (manuscript editing and discussion)

**Javier Agustin-Flores** (assisting in the field, manuscript editing and discussion)

**Ian M. Smith** (manuscript editing and discussion)

**Jan M. Lindsay** (manuscript editing and discussion)

## Chapter Four – Quantitative parameterization of monogenetic volcanoes: geometry and volumes

### 4.1. Introduction

A volcanic field is produced by distributed volcanism of a variety of explosive and effusive eruption styles, which is often termed monogenetic (Valentine and Gregg, 2008; Guilbaud et al., 2009; Kereszturi and Németh, 2012a; Németh et al., 2012). Monogenetic eruptions are characterised by episodic short periods of activity (days to years), with each new eruption breaking out in a distinct location, rather than repeatedly from the same site, such as at polygenetic volcanoes. Individual eruptions generally involve low magma volumes ( $<1 \text{ km}^3$ ), but can be complex with many different phases and styles of activity. Basaltic volcanic fields occur in nearly every known tectonic setting, although typically within an extensional regime (Connor and Conway, 2000; Valentine and Gregg, 2008; Németh, 2010; Le Corvec et al., 2013c). Monogenetic eruption behaviour depends on the regional tectonic settings, near-surface geology and hydrology and the magma source processes (Smith et al., 2008; Valentine and Gregg, 2008; Brenna et al., 2012a; Jankovics et al., 2012). Eruptions are typically generated by discrete ascent of magma, forming spatially and temporally focussed eruption centres (Connor et al., 2000; Kereszturi et al., 2011; Guilbaud et al., 2012). Due to the long lifespan of monogenetic fields ( $10^6$ – $10^7$  yr), the volumes of individual volcanoes are often difficult to determine with precision. Erosion modifies the original volcanic edifices and removes most traces of tephra. Consequently, either a volcanic model must be used to quantify the original geometry of each volcano (e.g. Rodriguez-Gonzalez et al., 2009a), or the magmatic volume estimates must be considered minima (e.g. Kereszturi et al., 2011). Understanding the volumetric evolution of volcanic fields and characterising the sizes of magma batches feeding eruptions are essential for understanding regional tectonic evolution and forecasting volcanic hazard.

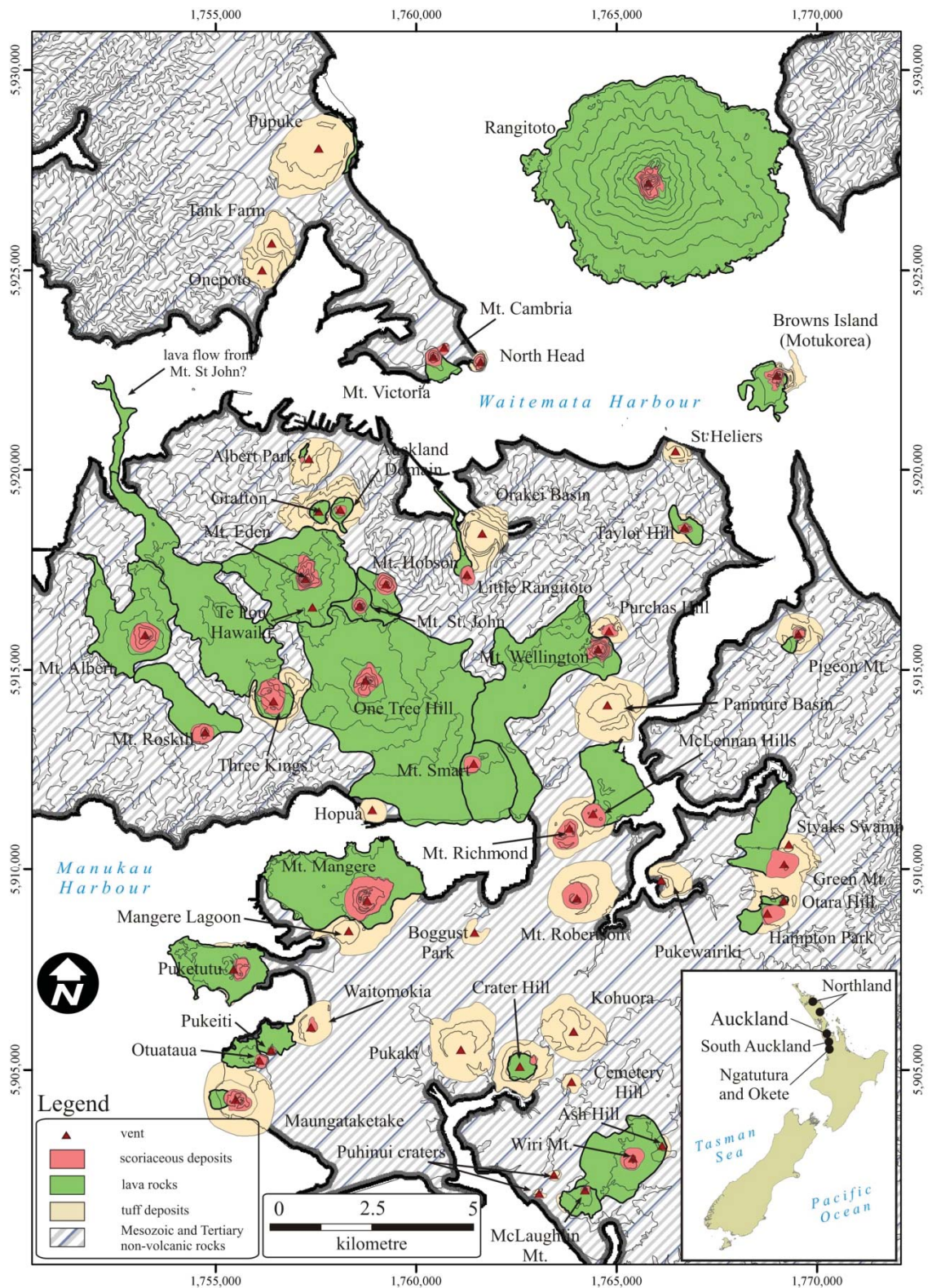


**Figure 4.1** Geology of the AVF after Hayward et al. (2011). The whole area shown in this map coincides with the area of City of Auckland. The inset map shows the location of the AVF and other Quaternary basaltic volcanic fields in the North Island, New Zealand.

The late Quaternary Auckland Volcanic Field (AVF; Fig. 4.1) is located under Auckland, the largest city of New Zealand (1.4 million inhabitants), and is thus the focus of intensive volcanic hazards research (e.g. Sandri et al., 2011; Németh et al., 2012; Mazot et al., 2013). Determining the past magmatic output patterns of this field is challenging due to the wide range of volcanic landforms (Allen and Smith, 1994; Hayward et al., 2011), as well as the humid climate that promotes rapid erosion and weathering. In this study, a volcanic model is developed for volume estimation of individual monogenetic volcanic edifices. It is based on our current knowledge on the volcanic architecture, eruption mechanisms, and geological preservation potential of volcanic landforms and associated volcanoclastic successions. This model is then applied to the AVF in order to estimate its magma output over its evolution, contributing important information for future hazard assessment of the field.

## 4.2. Model for volume estimates of monogenetic volcanoes

A complex monogenetic volcano can be split into several components/parts. In the present study, a six-fold division is used: (1) diatreme/root zone, (2) crater infill, (3) tuff ring, (4) scoria cone, (5) lava flow, and (6) medial–distal tephra blanket. For many volcanoes with multiple vents or craters must be combined. The systematic division of volume elements enables the application of semi-automated techniques based on: Digital Surface Models (DSM, a remotely sensed surface model that includes the bare ground elevation data), Digital Terrain Models (DTM, a remotely sensed terrain model that includes vegetation and anthropogenic feature such as buildings), Digital Elevation Models (DEM, generated from vector-based input data such as contour lines); and geometrical approximations of cone shapes or deposit fans (Fig. 4.2). The volume estimation scheme is included in Appendix B.

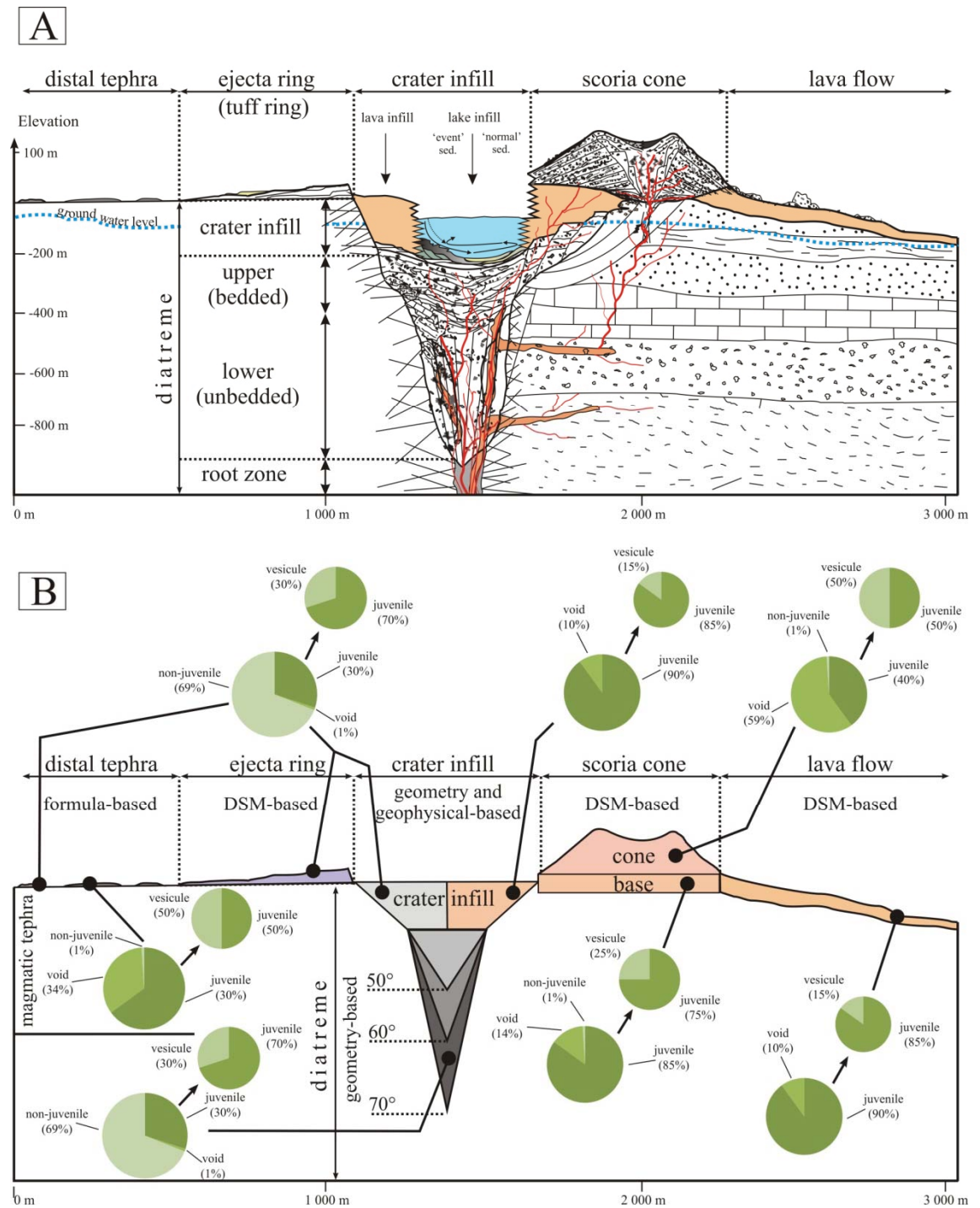


**Figure 4.2** (A) Diagram of the volcano-sedimentary parts of a conceptualised monogenetic volcano for volume estimation. (B) Methods applied for volume estimation from the different volcano parts. The pie charts represent the DRE correction scheme applied in this study. As the first step of the DRE corrections, a proportion of juvenile, non-juvenile (lithics) and interparticle void space in the volcano parts were used (shown as large pie charts). In the second step, the juvenile content left was corrected for vesicularity (shown as smaller pie charts).

### 4.2.1. Bulk subsurface volume

Diatremes (Fig. 4.2) occur beneath many maar volcanoes, as seen in exhumed rock sequences and with geomagnetic and gravimetric surveys (Schulz et al., 2005; Lorenz and Kurszlaukis, 2007; Mrlina et al., 2009; Skácelová et al., 2010; White and Ross, 2011). A diatreme results from the explosive interaction of rising magma and ground-water, excavating a crater that is subsequently filled with a chaotic mixture of sills and dykes, pyroclastic ejecta and debris from collapsing country rock walls (Németh et al., 2001; Lorenz and Kurszlaukis, 2007; Lefebvre et al., 2013). These zones are often “carrot” shaped and may be cut by coherent and clastic dykes as well as being interbedded with pyroclastic breccias (Lorenz and Kurszlaukis, 2007). The shape and depth of a diatreme may depend on the physical properties and strength of the country rock (Lorenz, 2003; Auer et al., 2007; Ross et al., 2011). In general, diatremes formed in “soft” substrate are broad with low-angle walls, whereas those formed in hard rock are narrow with near-perpendicular walls. The diatreme shape and geometry may also be influenced by eruption styles (e.g. Valentine, 2012), and vent migration (e.g. Son et al., 2012). Due to the complex evolution of diatremes and the limited number of exposed examples, methods for calculating their volume have not yet been formalised.

If geophysical imaging and/or drill core data are not available, known volcanic structures can be used as analogues. The diatreme geometry is best approximated by an inverted cone (e.g. White and Ross, 2011; Lefebvre et al., 2013). The wall rock angle between a diatreme and country rock can be measured and/or estimated. Assuming a wall rock dip value,  $\theta$ , from  $0^\circ$  to  $90^\circ$  measured from vertical, the diatreme depth ( $h_{simple}$ ) and volume ( $V_{simple}$ ) can be estimated using simple trigonometric equations (Fig. 4.2):

$$h_{simple} = r_{top} / \tan\theta \quad (4.1)$$

$$V_{simple} = 1/3\pi r_{top}^2 h_{simple} \quad (4.2)$$

where  $r_{top}$  is the minimum crater radius of the crater rim. A minimum crater radius is preferred in order to minimise over-estimation of surface crater width caused by post-eruptive crater wall collapse and erosional widening (e.g. Németh et al., 2012).

Other diatremes can be characterised by a shallow-bowl-shaped crater with a steep and narrow diatreme beneath, i.e. a champagne-glass-shape (Lorenz, 2003). In this case, the upper part, such as the shallow crater infill volume ( $V_{infill}$ ), can be approximated by an inverted truncated cone (Fig. 4.2):

$$V_{infill} = 1/3 \pi h_{infill}(r_{top}^2 + r_{top} r_{bottom} + r_{bottom}^2) \quad (4.3)$$

where  $h_{infill}$  is the height of the crater infill deposits,  $r_{bottom}$  is the lower radius of the crater at the depth (i.e. bottom of the inverted truncated cone). The  $r_{bottom}$  can be expressed considering of crater wall angle,  $\beta$ , between  $0^\circ$  to  $90^\circ$  from vertical, as:

$$r_{bottom} = r_{top} - (2 \tan \beta h_{infill}) \quad (4.4)$$

Combining Eqs. 4.2 and 4.3, the complete bulk volume of a complex diatreme can be expressed as:

$$V_{complex} = [1/3 \pi h_{infill}(r_{top}^2 + r_{top} r_{bottom} + r_{bottom}^2)] + [1/3 \pi r_{bottom}^2 (r_{bottom}/\tan \theta)] \quad (4.5)$$

The upper truncated cone (i.e. crater infill in Fig. 4.2) may host post-eruptive basin fill sediments, late-stage tuff deposits, and/or magmatic infill, such as lava lakes/flows or spatter-, scoria cones (Németh et al., 2001; Suhr et al., 2006; Lorenz, 2007).

In contrast to maar-diatreme volcanoes, plumbing system beneath typical spatter and scoria cones, usually consist of a swarm of radial dykes with thicknesses of <3–5 m (Rappich et al., 2007; Hintz and Valentine, 2012; Kiyosugi et al., 2012) that are clustered within a few tens of metres in horizontal extent. Given a radius of 25 m for a typical shallow magmatic plumbing network with a depth of 100 m (e.g. Valentine, 2012), the maximum bulk volumes are on the order of  $6.5 \times 10^4 \text{ m}^3$  if a conical geometry is assumed.

#### 4.2.2. Bulk proximal tephra accumulation and lava flows volume

The bulk surface eruptive volumes can be derived from topographic/geologic maps, field surveys or DSMs/DTMs/DEMs. These include positive landforms such as ejecta rings, spatter and scoria cones, along with lava flows (Fig. 4.2). The bulk volume of these components is traditionally calculated, using areal and thickness data (e.g. Hasenaka and Carmichael, 1985), geophysical data (e.g. Courtland et al., 2012), remotely sensed DTMs (e.g. Kervyn et al., 2008) or contour-based DEMs (e.g. Kereszturi and Németh, 2012b). If the pre-eruptive surface can be approximated accurately, DSM/DTM/DEM-based volumetric estimates have the highest reliability. However, the pre-eruptive terrain is commonly difficult to constrain. It is often approximated by manual modification of contour lines (e.g. Rodriguez-Gonzalez et al., 2009a), or based on slope angles of the surroundings (e.g. Tarquini et al., 2012), and/or interpolations from drill cores (e.g. Kereszturi et al., 2012b). For positive relief features of monogenetic volcanoes, volume ( $V$ ) can be calculated at every grid cell of a DSM/DTM/DEM as (Fig. 4.2):

$$V = \sum \Delta Z_i \times y \quad (4.6)$$

where  $\Delta Z_i$  is the elevation difference between the DSMs/DTMs/DEMs and the pre-eruptive basement at the grid cell location  $i$ , with  $x$  and  $y$  corresponding to the horizontal grid cell dimensions. Lava flows are commonly associated with scoria cones and cover large areas ( $1-10^3 \text{ km}^2$ ), making reconstruction of a pre-eruptive terrain particularly challenging (Fig. 4.2). This is especially difficult if spatter and/or scoria cone(s) sit on top of lava flow units, creating a ‘missing’ cone base from the eruptive volume calculations (e.g. Rangitoto in the AVF; Figs. 4.1 and 4.2). In this case the volume can be calculated as the area multiplied by its average thickness.

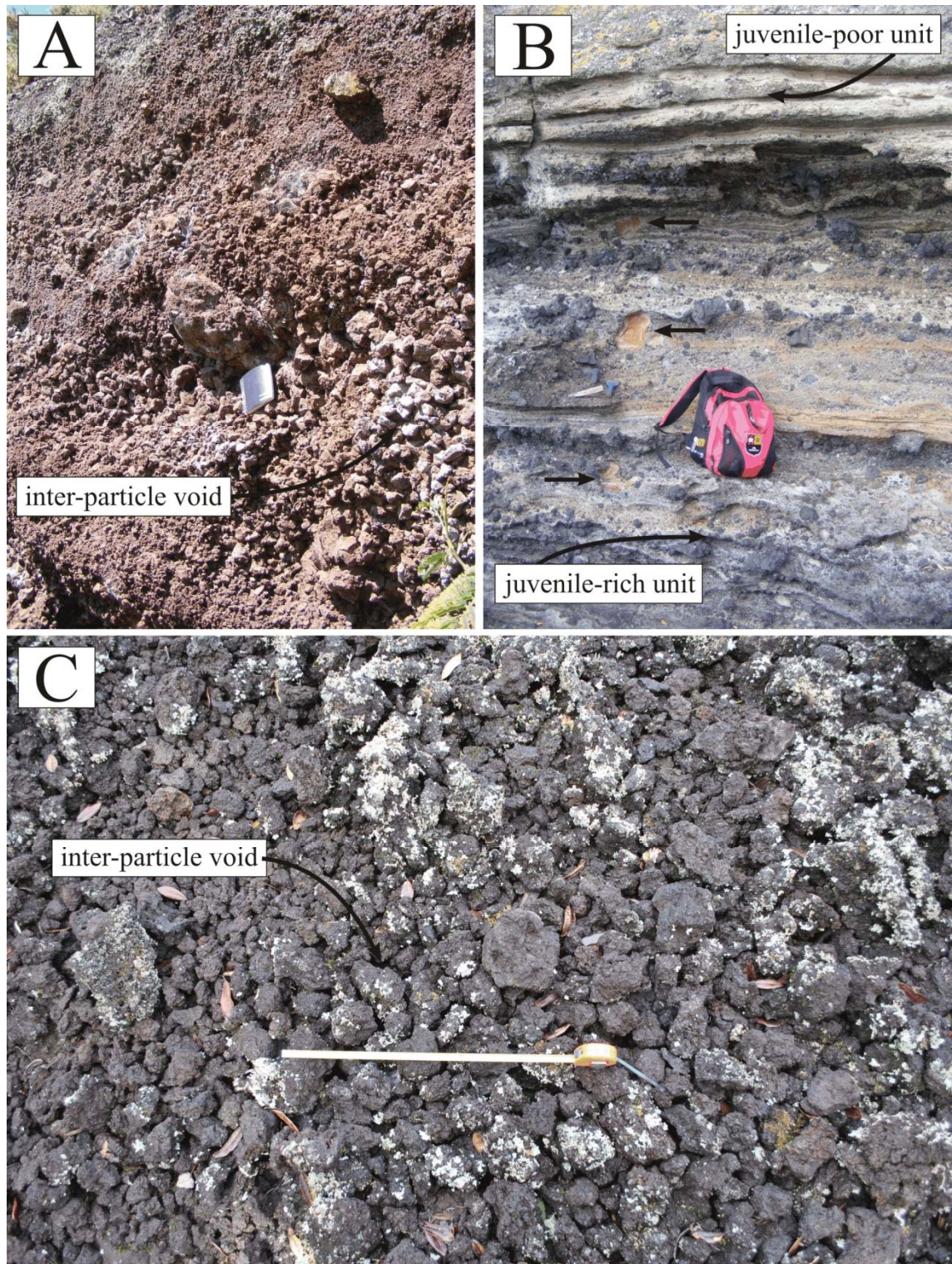


**Figure 4.3** Outcrop photos of volcanic deposits from the AVF. (A) Photos showing the well to poorly sorted deposits in one of the scoria cones of Three Kings volcanic complex. The inter-particle void space can be large. (B) Contrasts between juvenile-rich and juvenile-poor units exposed in the succession at Browns Island. Note the large diversity of accidental lithic clasts from the underlying Miocene Waitemata sediments, such as sandstone (black horizontal arrows). (C) A typical lava flow surface from the youngest eruption site, Rangitoto. The lava flows in Rangitoto usually range from shelly pahoehoe to rubbly a'ā lava flow morphotypes. The measuring tape is 50 cm long.

### 4.2.3. Bulk medial to distal pyroclastic volume

Basaltic tephra fall deposits (Fig. 4.2) downwind of volcanic cones are typically quickly eroded, weathered and vegetated in temperate and tropical climates (e.g. Manville et al., 2009). This makes the standard methods of volume reconstruction via isopach mapping difficult, especially for older volcanoes. One possible approach is to use an empirical relationship between average crater diameter ( $d_{magmatic}$  and  $d_{phreatomagmatic}$ ) and eruptive volume, as estimated by (Sato and Taniguchi, 1997):

$$d_{magmatic} = 0.11 V_{ejecta}^{0.42} \quad (4.7)$$

$$d_{phreatomagmatic} = 0.97 V_{ejecta}^{0.36} \quad (4.8)$$

This assumes that crater size is the result of the largest explosion (Taddeucci et al., 2009), which may not be always fulfilled in the case of maars and tuff rings (e.g. Valentine and White, 2012; Ross et al., 2013). Crater morphology and ejecta volume depend on combination of eruption energy, explosion depth and mass wasting processes during and after the eruption (Self et al., 1980; Lorenz, 1986; White and Ross, 2011; Valentine, 2012). These factors lead to large error margins in estimations.

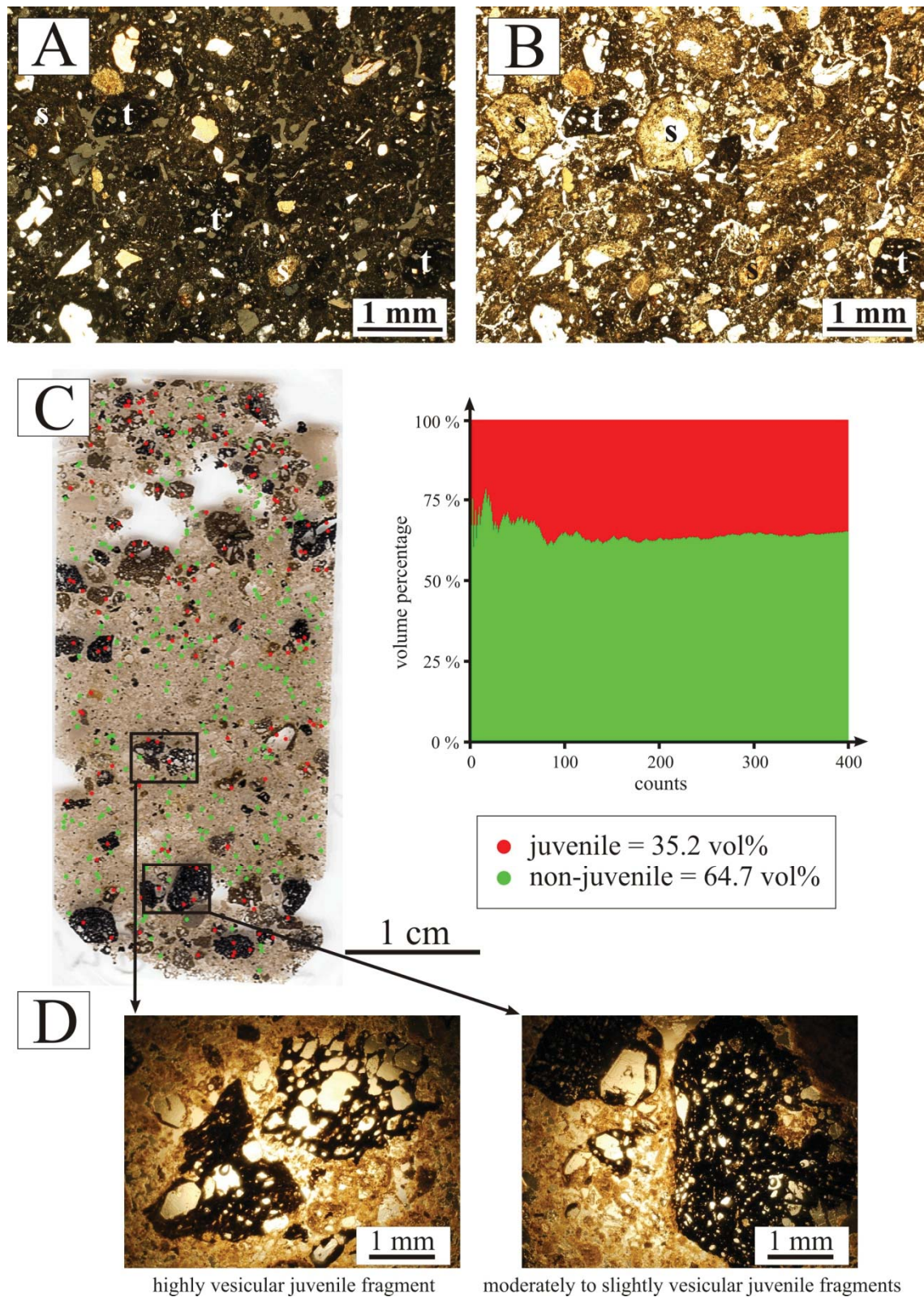


**Figure 4.4** (A and B) Microphotographs of pyroclastic rocks from the phreatomagmatic ejecta ring of Orakei Basin. S – sideromelane glass shards and T – tachylite glass shards. (C) Point counting results of a typical thin-section from the Browns Island ejecta ring, showing the maximum 35 vol% of juvenile content. The graph is the evaluation plot for the counts. (D) Closer view of two juvenile fragments with contrasting vesicularity.

### 4.3. Input data and configuration for the AVF

#### 4.3.1. Bulk subsurface volume for the AVF

Diatremes beneath the phreatomagmatic volcanoes of the AVF have not been geophysically imaged due to weak gravity anomalies (e.g. Cassidy and Locke, 2010), indicating that if they are present, they must have similar density to the Waitemata country rock (2000–2200 kg/m<sup>3</sup>). This is consistent with typical diatremes where 50% of the deposit made of juvenile particles with density of ~2200 kg/m<sup>3</sup>, equivalent to a 20 vol% vesicle content (e.g. Ross and White, 2012) (Table 4.1). The lack of direct diatreme observations and weak geophysical signatures in the AVF result in a significant uncertainty in eruptive volume calculations, because diatremes are usually an order of magnitude larger than the surface volcanic edifices (Lorenz, 1986; White and Ross, 2011). Analogies of similar volcanoes are required. Hence, a shallow inverted cone frustum (e.g. phreatomagmatic crater infill, Fig. 4.2) with a 45° wall angle was assumed for application of Eq. 4.3. For phreatomagmatic crater infills, the depth was estimated as a constant value of 15 m (for small, ≤500 m, eruptive centres), or 30 m (for large, ≥500 m, eruptive centres). This is the same as the average measured ejecta ring thicknesses, and consistent with the depth of the excavated lithic populations in the Maungataketake volcano (Agustín-Flores et al., 2014), as well as gravity and magnetic imaging of phreatomagmatic craters in Auckland (Cassidy et al., 2007). Magmatic crater infills (e.g. lava lakes) were recognised from aeromagnetic survey data (Rout et al., 1993; Cassidy et al., 1999; Affleck et al., 2001; Cassidy et al., 2007). Cassidy and Locke (2010) found that craters with residual magnetic anomalies of >50 nT were filled with lava. In this case, the eruptive volumes were calculated as the area of magnetic anomaly multiplied by the estimated thickness from Cassidy and Locke (2010).

For underlying diatremes beneath the crater infills, wall rock angles of 50°, 60° and 70° were assumed (Fig. 4.2). Their volumes were calculated using a simple inverted cone geometry by Eq. 4.2. Current crater geometries were used to define  $r_{top}$  and  $r_{bottom}$ . The minimum crater radius was used, determined by the shortest distance between the digitised crater rim, based on slope angle and slope aspect maps, and the calculated centre point of the crater.

In the bulk eruptive volume calculations feeder dykes and plumbing systems of scoria and spatter cones were not estimated due to the uncertain dyke and sill geometries.

#### 4.3.2. Bulk proximal tephra accumulation and lava flows volumes for the AVF

For the bulk volume estimates of the positive landforms of the AVF, a Light Detection And Ranging (LiDAR) survey-based DSM was used. The survey was carried out with a Leica Airborne Laser Scanner 50 (ALS50) and an Optech Airborne Laser Terrain Mapper 3100-EA (ALTM3100) in 2005–2006 and 2008. Details of LiDAR processes and survey are reported in Kereszturi et al. (2012b). The mean survey density varied from 0.04 to 1 point per m<sup>2</sup>, corresponding to resolutions of between 5 to 1 m, respectively. The original data have been pre-processed, including height correction, vegetation filtering and artificial infrastructure removal by Fugro Spatial Solutions ([www.fugrospatial.com.au](http://www.fugrospatial.com.au)). The original DSM was interpolated using a Triangulated Irregular Network (TIN) and converted into a gridded model at 2 m resolution. This bare surface DSM was resampled by the nearest neighbour method into a medium resolution DSM (10 m) in order to enhance calculation time and reduce error due to filtering and post-processing. The pre-eruptive terrain beneath volcanoes and lava flows was either: (1) modelled as a flat surface in the southern and northern, low-lying parts of the field, or (2) interpolated from spot heights by the natural neighbour method (Sibson, 1981) in the central elevated areas. The flat base surfaces were created with a constant height (Appendix B), based on the elevation of lowermost outcropping pyroclastic or lava rocks. The sub-surface spot heights were derived from drill core descriptions (n = 488) and field observations (n = 26). Using these two surfaces, the volumes were obtained by Eq. 4.6.

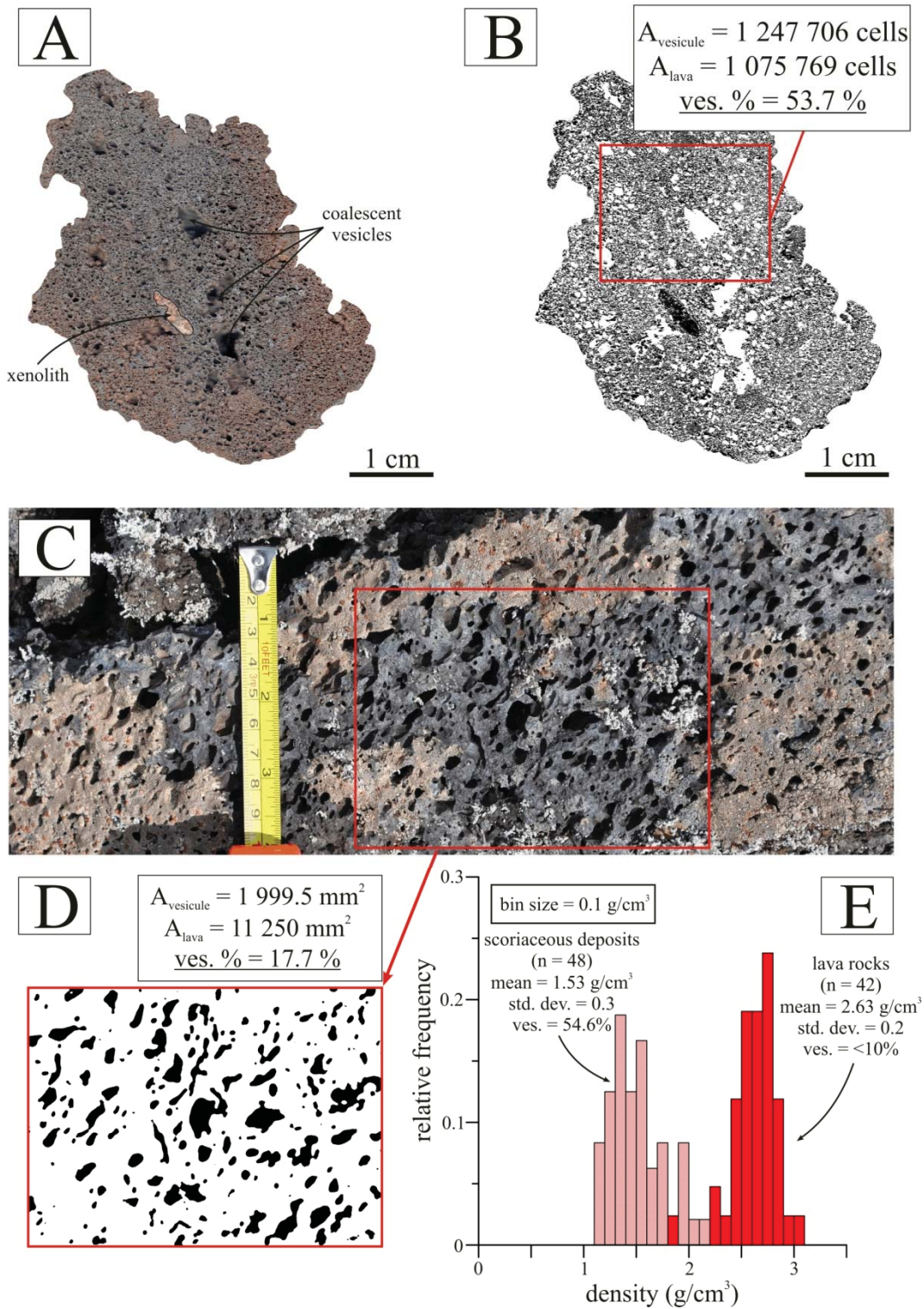


**Figure 4.5** (A) Scan of a scoria hand specimen from the Rangitoto scoria cone. (B) Binary image of the same sample, showing the distribution of vesicles in white. The red box is the area considered in the 2D vesicularity calculations. (C) Field photo of a moderately vesiculated lava flow texture from the lava flow field of Rangitoto. (D) Thresholded binary image showing the distribution of largest vesicularity population. (E) Graph showing the results of density measurements on scoria ( $n = 48$ ) and lava rock ( $n = 42$ ) samples from Rangitoto and Browns Island volcanoes. The densities were measured as envelope density by Micrometrics Geo PyC1360 density analyser. Due to the small diameter (i.e. 2 cm in diameter) of the samples measured in the density analyser, these density and vesicularity values are considered as minimum values. The vesicularity is calculated proportional to  $2.8 \text{ g/cm}^3$ .

The limits of volcanic edifices and lava flows were based on a combination of geological maps (Kermode, 1992; Hayward et al., 2011), high-resolution orthophotos (0.5 m), drill core datasets (e.g. PETLAB database, [www.pet.gns.cri.nz](http://www.pet.gns.cri.nz)) and new field mapping. Where DSM-based bulk volume estimates could not be performed accurately (e.g. smaller volcanic edifices, with ill-defined boundaries), bulk volumes from Allen and Smith (1994) were adopted. Additional details for each volcano examined are contained within Appendix B.

### 4.3.3. Bulk medial to distal pyroclastic volume for the AVF

Erosion and reworking of basaltic tephra, along with the intensive urban modification over the AVF make it impossible to map fall distributions and provide reliable estimates of distal tephra volumes. The youngest volcano, Rangitoto (553–504 yrs BP) has a local tephra blanket that is mapped onshore (Needham et al., 2011), but other tephra falls are preserved only at isolated locations within lacustrine successions (Augustinus et al., 2011; Shane and Zawalna-Geer, 2011). The distal tephra layers associated confidently with their potential source ( $n = 24$ ) have recently been revealed by drilling (Molloy et al., 2009; Augustinus et al., 2011; Shane et al., 2013) and matched via statistical likelihoods (Bebbington and Cronin, 2011).

Due to these sparse data, the range of erupted tephra must be approximated using historical eruption analogues. The typical tephra blankets of various comparable eruption styles are:  $10.3 \times 10^6 \text{ m}^3$  [fire fountaining eruptions of Kilauea Iki, Hawaii (Parfitt, 1998)],  $38 \times 10^6 \text{ m}^3$  [violent Strombolian eruptions of Jorullo scoria cone, Mexico (Rowland et al., 2009)], or  $30 \times 10^6 \text{ m}^3$  [phreatomagmatic eruption of the 1886 AD Rotomahana eruption New Zealand (White and Ross, 2011)]. In order to obtain a systematic bulk volume range for the tephra blankets around the AVF volcanoes, Eqs 7 and 8 were applied, which include proximal deposits, such as scoria cones and ejecta rings. However, these are likely overestimates (Appendix B) and cannot be reliably used for field evolution interpretations.

#### 4.4. Converting bulk to Dense Rock Equivalent (DRE) eruptive volumes

To convert to DRE juvenile volumes (e.g. Houghton and Wilson, 1989), accidental/lithic clast proportions, inter- and intra-particle void spaces were quantified (Figs. 4.3–5). Hawaiian and Strombolian eruptions (Fig. 4.3A) generate coarsely fragmented, juvenile-rich pyroclastic successions, characterised by lapilli and block/bombs with moderate to high vesicularity and welding (Pioli et al., 2008; Perugini et al., 2011). Due to limited fines in the pyroclastic successions, these deposits are characterised by high vol.% of inter-particle void space (Fig. 4.3A). These types of eruptions are often associated with effusive activity, forming lava flows with different surface morphotypes with various inter-particle void-spaces (Fig. 4.3C). By contrast, phreatomagmatic deposits often contain large proportions of non-juvenile fragments (Fig. 4.3B), along with dense juvenile glass shards (Fig. 4.4A) (Németh et al., 2001; White and Ross, 2011). A range of physical characteristics of pyroclastic deposits and lava rocks from the AVF and analogue monogenetic volcanoes were collected (Table 4.1), including new data from the AVF on componentry (e.g. point counting on thin sections), rock-slab derived vesicularity, inter-particle void space and grain density.

Juvenile contents of proximal ejecta rings were estimated at 30 vol.% from the Orakei Basin (Németh et al., 2012), Browns Island (Figs. 4.4B and C and Table 4.1) and Maungataketake (Agustín-Flores et al., 2014) (Fig. 4.2 and Table 4.2). This is consistent with Allen and Smith's (1994) estimates for the AVF. The bulk volumes of diatremes, tuff-crater infills and distal tephra were also corrected to DRE volumes, using 30 vol.% juvenile content (Fig. 4.2 and Table 4.2). These values are, however, slightly lower than from diatremes elsewhere (e.g. Schulz et al., 2005). Vesicularity within the juvenile pyroclastic deposits (Figs. 4.4C and D) was estimated at 30 vol.% for phreatomagmatic glass (Fig. 4.2 and Table 4.2), based on observation from Crater Hill volcano (Houghton et al., 1999) and Browns Island (Allen et al., 1996). Diatreme juvenile particles may have lower vesicularity (e.g. Nitzsche et al., 2006; Suiting and Schmincke, 2009). These values were systematically applied for all ejecta rings bulk volumes, excluding Pupuke and North Head volcanoes, in which higher 60 vol.% and 80 vol.% bulk juvenile content, were used, based on specific observations (Allen and Smith, 1994).

For scoria cones, the eruptive volumes were corrected to DRE volumes by assuming 40 vol.% bulk juvenile content, 60 vol.% combined interparticle void space and xenoliths (Fig. 4.2, Tables 4.1 and 4.2). Interparticle void space was measured on scoriaceous lapilli samples from Rangitoto and Browns Island by packing coarse ash to fine scoria lapilli in 150 ml, 300 ml and 500 ml beakers followed by completely filling with water on a scale. For nine separate measurements were made, a range of 60 to 70 vol.% void space was calculated (Fig. 4.2, Tables 4.1 and 4.2). Somewhat similar values were used to correct bulk distal volumes for the tephra blanket from scoria cones in which bulk juvenile content was estimated to be of 65 vol.%, with about 34 vol.% of interparticle void due to the enrichment of fines over distance (Fig. 4.2 and Table 4.2). The vesicularity was corrected systematically for scoria cone and distal tephra deposits to 50 vol.%, based on density measurements of scoriaceous lapilli from AVF samples (Fig. 4.5E and Table 4.2), Digital Image Analysis on rock-slabs (Fig. 4.5A), and published values from the AVF (e.g. Allen et al., 1996), and elsewhere (e.g. Mangan and Cashman, 1996). The ‘bases’ of scoria cones are approximated with lower interparticle void space (14 vol.%; Fig. 4.2, Tables 4.1 and 4.2). This accounts for the common mechanical welding and agglutination at the core and base of these edifices (e.g. Kereszturi and Németh, 2012b; Barde-Cabusson et al., 2013). Vesicularity is approximated as 25 vol.% for scoria cone bases (Fig. 4.5A and Table 4.2).

**Table 4.1** Summary of physical properties used to establish the input data for DRE corrections.

analogue volcano	analogue part	GPS coordinates	reference	age	juvenile content	vesicle content	inter-particle void	density (kg/m <sup>3</sup> )
Orakei Basin (Auckland, New Zealand)	ejecta ring	36°52'0.45"S and 174°48'48.08"E	Németh et al. 2012	103 ka	30%	20%		
Maungataketake (Auckland, New Zealand)	ejecta ring	36°59'54.69"S and 174°44'50.59"E	Agustin-Flores et al. 2014	41 ka	30-35%	max 35%		
Browns Island (Auckland, New Zealand)	ejecta ring	36°49'46.90"S and 174°53'41.02"E	Allen et al. 1996, this study	34 ka	20-35%	27-48%		
Pupuke (Auckland, New Zealand)	ejecta ring	36°46'51.61"S and 174°45'56.77"E	Allen et al. 1996	200 ka		19-26%		
Crater hill (Auckland, New Zealand)	ejecta ring	36°59'13.93"S and 174°49'39.94"E	Houghton et al. 1999	32 ka		20-50%		1700-2200
Ukinrek (Alaska)	ejecta ring	57°50'1.70"N and 156°30'57.66"W	Self et al. 1980	1977 AD	max 30%			
Asososca (Managua, Nicaragua)	ejecta ring	12° 8'12.36"N and 86°18'58.50"W	Pardo et al. 2009	1245 yr BP	15-20 vol%	usually >20%		
Coombs Hills (Antarctica)	diatreme	76°47'24.17"S and 159°54'40.40"E	Ross and White 2012	Jurassic		max 20%		
Rychnov maar (Czech Republic)	diatreme	50°40'45.41"N and 15° 8'22.61"E	Skacelova et al. 2010	28.3 Ma				2150-2450
Baruth maar-diatreme (Germany)	diatreme	52° 2'10.27"N and 13°32'55.14"E	Schulz et al. 2005	20-28 Ma	40-70%			1200-2100
Messel maar-diatreme (Germany)	diatreme	49°54'57.43"N and 8°45'4.64"E	Schulz et al. 2005, Nitzsche et al. 2006	47 Ma	50-80%	max 10%		2070-2250
Costa Giardini (Iblean Mountains, Italy)	diatreme	37° 8'42.29"N and 15° 3'45.26"E	Suiting and Schmincke 2009	Miocene	20-60%	10-40%		
Kilauea Iki (Kilauea, Hawaii)	scoria cone	19°24'42.16"N and 155°15'13.81"W	Parfitt 1998	1959 AD	99-100%	60-95%		1045-150
Paricutin (Michoacan, Mexico)	scoria cone	19°29'35.83"N and 102°15'4.88"W	Pioli et al. 2008	1943-1952 AD	99-100%	45-68%		
Pu'u 'O'o (Hawaii)	scoria cone	19°23'17.60"N and 155° 6'22.70"W	Mangan and Cashman 1996	1983 to present	99-100%	70-85%		
El Crosat (Olot, Spain)	scoria cone	42° 9'12.82"N and 2°32'6.67"E	Di Traglia et al. 2008	11 ka	99-100%	58-73%		
Crater hill (Auckland, New Zealand)	scoria cone	36°59'13.93"S and 174°49'39.94"E	Houghton et al. 1999	32 ka	95-100%	25-80%		700-2200
Maungataketake (Auckland, New Zealand)	scoria cone	36°59'54.69"S and 174°44'50.59"E	Conybeer 1995	41 ka	99-100%	20-90%		200-2000
Browns Island (Auckland, New Zealand)	scoria cone	36°49'46.90"S and 174°53'41.02"E	Allen et al. 1996, this study	34 ka	99-100%	52-54%	60-70%	1164-2356

Rangitoto (Auckland, New Zealand)	scoria cone	36°47'12.66"S and 174°51'29.11"E	this study	550 yr BP	99-100%	25-70%	60-70%	1113-2287
Pelagatos (Sierra Chichinautzin, Mexico)	scoria cone	19° 5'33.60"N and 98°57'43.27"W	Guilbaud et al. 2009	≤14 ka	99-100%	60-80%		
Kalapana (Kilauea, Hawaii)	lava flow	19°24'24.76"N and 155° 5'6.73"W	Cashman and Kauahikaua 1997	1990-1991 AD	99-100%	10-60%		
Makapuu a'a flow (Oahu, Hawaii)	lava flow	21°18'32.70"N and 157°39'8.84"W	Shea et al. 2010	1.8-2.8 Ma	99-100%	21-41%		2000-2300
Makapuu pahoehoe flow (Oahu, Hawaii)	lava flow	21°18'32.70"N and 157°39'8.84"W	Shea et al. 2010	1.8-2.8 Ma	99-100%	34-53%		1300-1800
Mt. Etna lava flow (Sicily, Italy)	lava flow	37°43'55.93"N and 14°59'21.71"E	Gaonac'h et al. 1996	1985 AD	99-100%	3.8-41.5%		
Pupuke (Auckland, New Zealand)	lava flow	36°46'51.61"S and 174°45'56.77"E	Allen et al. 1996	200 ka	99-100%	20-40%		
Rangitoto (Auckland, New Zealand)	lava flow	36°47'12.66"S and 174°51'29.11"E	this study	550 yr BP	99-100%	0-20%	10-25%	2257-3027
Browns Island (Auckland, New Zealand)	lava flow	36°49'46.90"S and 174°53'41.02"E	this study	34 ka	99-100%	0-10%		1842-2836
Paricutin (Michoacan, Mexico)	distal	19°29'35.83"N and 102°15'4.88"W	Pioli et al. 2008	1943-1952 AD	99-100%	30-68%		1010-1650
Ukinrek (Alaska)	distal	57°50'1.70"N and 156°30'57.66"W	Self et al. 1980	1977 AD	25-35%			

The densest components were the lava flows and magmatic crater infills (Gaonac'h et al., 1996; Cashman and Kauahikaua, 1997; Shea et al., 2010). Both parts were corrected using 10 vol.% for void space (Fig. 4.2 and Table 4.2). For Rangitoto lava flows, a higher void-space correction (24 vol.%) was applied, due to its unique typical shelly pahoehoe to rubbly a'a lava textures with common autobreccia between thin flow units (e.g. Rossi and Gudmundsson, 1996). The vesicularity is estimated as high as 20 vol.% from rock slab analysis of Rangitoto samples (Figs. 4.2, 4.5C, 4.5D and Table 4.2). These measurements are in accordance with previous estimates for Rangitoto (Allen and Smith, 1994). Envelop density measurements using a Micromeritics Geopyc show minimum porosity of 10 vol.% (Fig. 4.5E). Consequently, for vesicularity-corrections an intermediate value of 15 vol.% was used (Fig. 4.2 and Table 4.2).

**Table 4.2** Summary of the DRE correction values used in this study.

volcanic components		inter-particle void space	non-juvenile content	bulk juvenile content	vesicularity	DRE juvenile content
		%	%	%	%	%
ejecta ring	$V_{\text{ejecta}}$	1	69	30	30	70
diatreme	$V_{\text{diatreme}}$	1	69	30	30	70
crater infill (ph)	$V_{\text{infill (ph)}}$	1	69	30	30	70
distal (ph)	$V_{\text{distal (ph)}}$	1	69	30	30	70
scoria cone	$V_{\text{scoria cone}}$	59	1	40	50	50
scoria cone base	$V_{\text{scoria base}}$	14	1	85	25	75
distal (m)	$V_{\text{distal (m)}}$	34	1	65	50	50
lava flow	$V_{\text{lava flow}}$	10	0	90	15	85
crater infill (m)	$V_{\text{infill (m)}}$	10	0	90	15	85

In summary, the DRE eruptive volume corrections were applied using the following formulae (Table 4.2):

$$\text{DRE}_{\text{ejecta ring}} = \text{DRE}_{\text{diatreme}} = \text{DRE}_{\text{distal (ph)}} = \text{DRE}_{\text{infill (ph)}} = V_{\text{bulk}} \times 0.3 \times 0.7 \quad (4.9)$$

$$\text{DRE}_{\text{scoria cone}} = V_{\text{bulk}} \times 0.4 \times 0.5 \quad (4.10)$$

$$\text{DRE}_{\text{scoria cone base}} = V_{\text{bulk}} \times 0.85 \times 0.75 \quad (4.11)$$

$$\text{DRE}_{\text{distal (m)}} = V_{\text{bulk}} \times 0.65 \times 0.5 \quad (4.12)$$

$$\text{DRE}_{\text{lava flow}} = \text{DRE}_{\text{infill (m)}} = V_{\text{bulk}} \times 0.9 \times 0.85 \quad (4.13)$$

where the bulk volumes are denoted as  $V_{\text{bulk}}$  for each part of a monogenetic volcano defined in Fig. 4.2, and  $m$  and  $ph$  correspond to magmatic and phreatomagmatic deposits, respectively.

## 4.5. Results

The estimated bulk eruptive volumes of the six components of monogenetic volcanoes at the AVF are: ejecta rings (0.380 km<sup>3</sup>), phreatomagmatic crater infills (0.322 km<sup>3</sup>), scoria cones (0.314 km<sup>3</sup>), magmatic craters infills (0.146 km<sup>3</sup>) and lava flows (1.971 km<sup>3</sup>). The highly uncertain parts, such as diatremes (50° – 1.902 km<sup>3</sup>, 60° – 2.641 km<sup>3</sup> and 70° – 4.030 km<sup>3</sup>) and distal tephra blankets (4.874 km<sup>3</sup>), have large bulk volumes. After DRE corrections (Figs. 4.6 and 4.7), the eruptive volumes are: 0.090 km<sup>3</sup> for ejecta rings, 0.067 km<sup>3</sup> for phreatomagmatic crater infills, 0.104 km<sup>3</sup> for scoria cones, 0.112 km<sup>3</sup> for magmatic crater infills, and 1.329 km<sup>3</sup> for lava flows. DRE-corrected volumes of distal tephra (1.141 km<sup>3</sup>), diatremes (0.399–0.846 km<sup>3</sup> using wall rock angles from 50° to 70°), are still significantly higher than the rest of the components. The volume estimates for each eruption centre and for components of lava flows, scoria cones, ejecta rings and crater infills are given in Table 4.3.

The cumulative minimum DRE-corrected eruptive magma output of Auckland is estimated at 1.704 km<sup>3</sup> (Table 4.3), excluding distal tephra and diatreme volumes. Adding these components results in a volume of 3.692 km<sup>3</sup> (Figs. 4.6 and 4.7). The 1.704 km<sup>3</sup> calculation is the same as Allen and Smith (1994) who estimated 3.42 km<sup>3</sup>. The largest volume discrepancy is associated with Rangitoto; here it is estimated at 0.698 km<sup>3</sup> (Table 4.3), rather than 2.02 km<sup>3</sup> by Allen and Smith (1994). This is because Rangitoto was approximated as a truncated cone in previous estimates and was precisely defined by the LiDAR DSM here. Previously, Rangitoto was thought to comprise 59% of the entire magmatic output of the AVF, whereas the new estimates indicate it was 41%.

Despite a range of methods applied, reliable ages are known only for a small number of the eruption centres (summarised in Lindsay et al., 2011). An attempt was carried out to develop a most-probable order of volcanic eruptions using a combination of known dates, stratigraphic relationships and a statistical correlation of dated tephras to source vents in the field (Bebbington and Cronin, 2011). When this age model was combined with our eruptive volumes, it indicated that there were volumetrically two distinct periods in the development of the AVF; an older period from 250 to 40 ka and younger period between 40 ka to the present (Fig. 4.7). In the early phase smaller

volume eruptions emplaced a total DRE volume of  $0.204 \text{ km}^3$ , while the latter, shorter phase produced a far greater magma output of  $1.499 \text{ km}^3$  (Fig. 4.7).

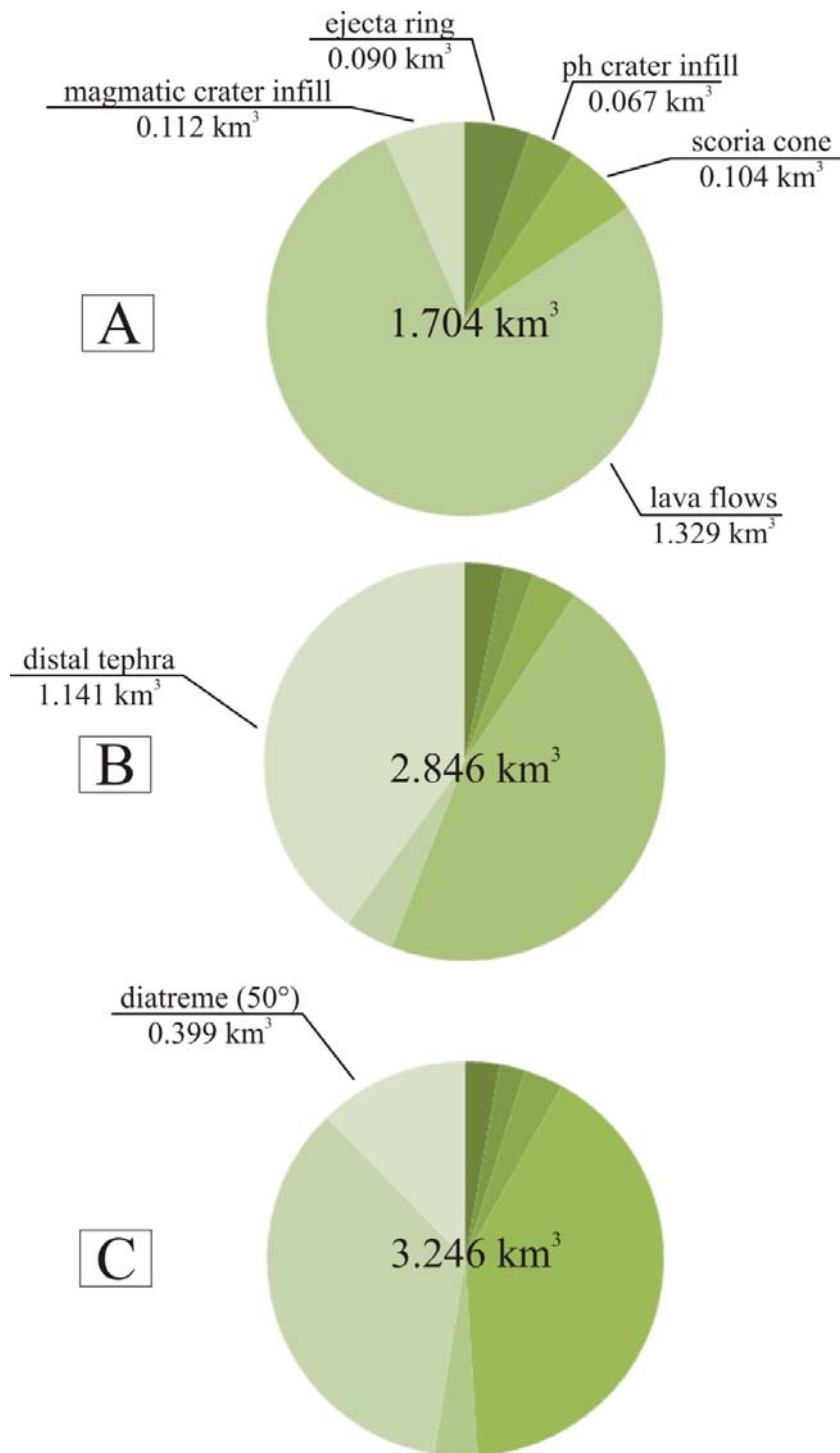


**Figure 4.6** Results of the new DRE eruptive volume estimates for the AVF. (A) The results of minimum estimates, including those volcanic parts where the volumes can be estimated with a relatively high accuracy. (B and C) Overall DRE eruptive volumes change if distal tephra blankets and diatreme volumes are considered.

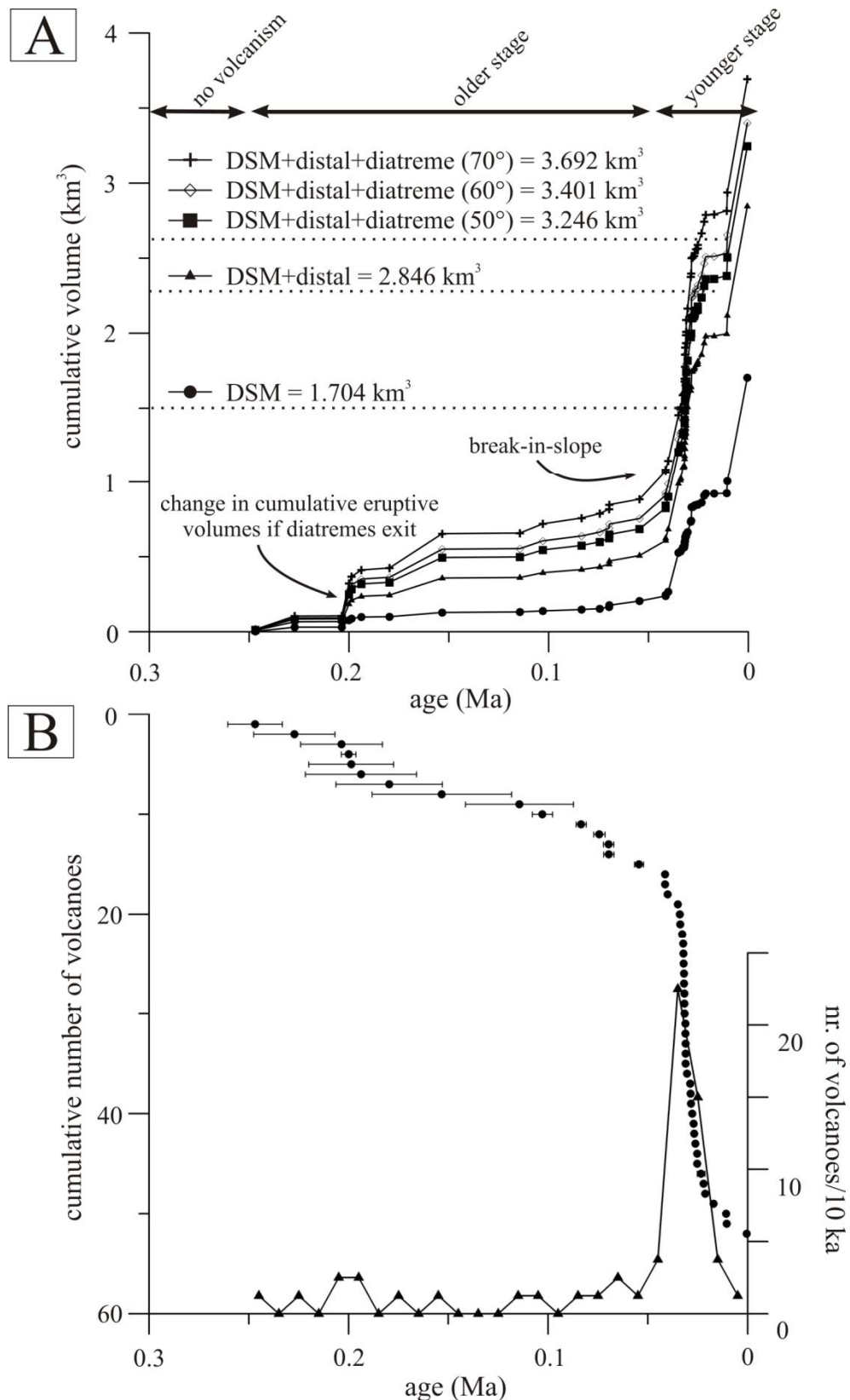


**Figure 4.7** (A) DRE eruptive volume as a function of time during the evolution of the AVF for each estimate. The ages are based on the most likely simulated eruption history based on the probabilistic analysis of Bebbington and Cronin (2011). The ages are simulated based on 1000 Monte Carlo simulations of the existing event-order of the AVF. Therefore, individual volcanoes might have a slightly different order (Bebbington and Cronin, 2011). (B) Number of volcanic events over the evolution of AVF, showing a decreasing trend since 32 ka.

**Table 4.3** Summary of DRE-corrected, minimum eruptive volumes estimate for each monogenetic volcano in the AVF. The underlined eruptive volumes are based on the bulk volume data published in Allen and Smith (1994), recalculated with our DRE correction scheme. The chronology shown here is based on simulated ages adapted from Bebbington and Cronin (2011). Notes: 1 – Pupuke and North Head bulk volumes was corrected for a higher amount of juvenile contents (Allen and Smith, 1994), 2 – In the case of Maungataketake, the bulk ejecta rings volume has been corrected for erosion, 3 – Bulk lava flow volumes has been updated since Kereszturi et al. (2012b) due to more information about the pre-eruptive surface, 4 – The bulk volume for St. John volcano is estimated using the inferred areal extent of the flow and a constant thickness of 10 m, 5 – The bulk volume of McLaughlin Mt. includes the bulk volume of the three small, Puhinui craters’ as well, 6 – Lava flow from Mt. Eden and Three Kings flowed partially on top of one of the earliest lava flows of Central Auckland are from the St. John volcano (Eade, 2009). As a result of this stratigraphy, the area proportional bulk volume of St. John lava flow has been substrate from the bulk volumes of Mt. Eden and Three Kings volcanoes, 7 – Mt. Eden’s bulk volume contains the ejecta ring and magmatic crater infill of Te Pou Hawaiiki volcano (Fig. 4.1), 8 – In the case of Mt. Mangere 0 m a.s.l. plane were used as the pre-eruptive surface, however, it is possible that the contact between lava flow and the Tauranga Formation is a couple of m below the present sea-stand. Therefore, this is a minimum volume, 9 – The initial phreatomagmatic phase of Rangitoto is approximated using a volume of a crater with diameter of 800 m and depth of 30 m, as well as the ejecta rings volume equivalent to the Panmure Basin. The selection of this approximation was based on the available geophysical surveys of Rangitoto, after Milligan (1977), 10 – Note that the bulk volume estimate for Rangitoto contains the eruptive products from both phase of activities.

nr	Location	simulated age		DRE-corrected minimum eruptive volumes							TOTAL	note	
		mean age	error	tuff ring	phreatom. crater infill	scoria cone	lava flow	magmatic crater infill					
		ka	ka	m <sup>3</sup>	m <sup>3</sup>	m <sup>3</sup>	m <sup>3</sup>	m <sup>3</sup>	m <sup>3</sup>				
1	Onepoto Basin	247	27	1,536,946	1,085,961							2,622,907	
2	Albert Park	227	41	<u>823,200</u>	1,467,579	14,000	450,968		25,020,147			27,775,893	
3	Boggust Park	204	41	184,032	137,835							321,866	
4	Pupuke	200	7	20,110,730	6,357,569		<u>20,196,000</u>					46,664,298	1
5	Pukewairiki	199	43	2,292,673	1,049,581				7,646,950			10,989,204	
6	Waitomokia	194	56	2,299,366	1,028,920	108,000			6,352,772			9,789,057	
7	St. Heliers	180	53	<u>1,232,700</u>	963,872							2,196,572	
8	Te Pou Hawaiiki	153	70		3,387,407	<u>80,000</u>			24,679,676			28,147,083	
9	Pukeiti	114	54			436,904	3,262,880					3,699,784	
10	Orakei Basin	103	10	3,774,695	2,928,453							6,703,147	
11	Pukaki	84	5	7,102,770	2,084,842							9,187,613	
12	Tank Farm	74	6	4,127,422	1,745,358							5,872,780	

13	Grafton	70	5	<u>4,059,300</u>	1,448,777				5,861,694	11,369,770	
14	Auckland Domain	70	5	<u>4,059,300</u>	1,448,777	56,552			5,861,694	11,426,323	
15	Mt. St. John	55	5			400,979	27,664,782			28,065,762	4
16	Maungataketake	41.4	0.4	4,396,305	2,857,490	<u>872,000</u>	4,688,150		20,818,859	33,632,804	2
17	Otuataua	41.4	0.4			990,198	5,307,367			6,297,566	
18	McLennan Hills	40.1	1.2	420,000	1,467,579	3,792,071	16,242,020			21,921,671	
19	One Tree Hill	35	0.6			5,703,834	254,735,864			260,439,698	
20	Kohuora	34	0.3	5,101,061	2,137,063					7,238,124	
21	Browns Island	33.8	0.8	657,229	313,149	1,311,839	2,272,855			4,555,073	
22	Mt. Albert	32.8	0.4	<u>350,700</u>	1,467,579	3,026,882	18,098,393			22,943,555	3
23	Ash Hill	32.3	0.1	<u>52,500</u>	23,070					75,570	
24	Hopua	32.2	0.3	308,414	547,250					855,664	
25	Cemetery Hill	32.1	0.4	137,626	104,509					242,136	
26	Puketutu	31.9	0.3	<u>3,003,000</u>	1,467,579	2,147,429	10,926,298			17,544,307	3
27	Wiri Mountain	31.9	0.3	<u>84,000</u>	339,433	864,000	<u>15,068,557</u>			16,355,990	
28	Mt. Richmond	31.7	0.3	1,170,039	1,467,579	3,037,026				5,674,644	
29	Taylor's Hill	31.7	0.3	<u>468,300</u>	3,497,252	182,866	<u>925,551</u>			5,073,969	
30	Crater Hill	31.6	0.3	5,881,637	1,765,387	764,000		16,067,063		24,478,087	
31	North Head	31.2	0.1	<u>1,120,000</u>	1,467,579	36,198	<u>22,950</u>			2,646,727	1
32	Panmure Basin	31.2	0.1	4,645,434	2,499,542	300,000				7,444,975	
33	Mt. Victoria	31.1	0.1			2,582,535	2,222,939			4,805,474	
34	Mt. Cambria	31.1	0.1			294,591				294,591	
35	Roberston Hill	31.1	0.1	1,010,793	1,467,579	<u>240,000</u>				2,718,373	
36	Mt. Roskill	30.4	1.2	<u>16,800</u>	1,467,579	1,373,086	11,573,221			14,430,686	3

37	Three Kings	28.8	0.3	-	6,436,369	3,004,030	59,871,292		69,311,692	3,6
38	Mt. Hobson	28.6	0.3			1,199,818	5,475,451		6,675,269	
39	Mt. Eden	28.4	0.3			5,944,328	83,833,340		89,777,668	6,7
40	Little Rangitoto	27.8	0.5			499,355	1,206,979		1,706,334	
41	McLaughlin Mt.	27.1	0.6	509,724	36,368	430,828	6,608,069		7,584,989	5
42	Pigeon Mountain	26.8	0.5	<u>1,329,300</u>	963,872	276,577	<u>744,536</u>		3,314,285	
43	Mangere Lagoon	26.2	0.4	708,335	1,319,868	12,971			2,041,174	
44	Hampton Park	25.3	0.7	<u>105,000</u>	254,080	398,957	<u>1,652,491</u>		2,410,528	
45	Otara Hill	25.3	0.7	<u>111,300</u>	547,250	697,314	<u>943,250</u>		2,299,114	
46	Green Hill	23.4	3.9	<u>359,100</u>	1,467,579	1,501,827	<u>8,789,695</u>		12,118,201	
47	Mt. Mangere	22.1	0.4			15,005,533	31,200,303		46,205,837	3,8
48	Mt. Smart	21.3	0.6		1,467,579	2,344,811	9,608,102		13,420,492	
49	Styaks Swamp	17.1	1	<u>245,700</u>	120,484				366,184	
50	Purchas Hill	10.8	0.1	<u>210,000</u>	1,448,777	<u>26,000</u>			1,684,777	
51	Mt. Wellington	10.5	0.1	<u>1,932,000</u>	1,467,579	3,016,917	75,864,318		82,280,815	3
52	Rangitoto	0.5	0	4,645,434	2,715,467	41,604,798	649,938,412		698,904,111	9,10
<b>SUM</b>				<b>90,582,865</b>	<b>67,737,401</b>	<b>104,579,054</b>	<b>1,329,395,033</b>	<b>112,308,855</b>	<b>1,704,603,213</b>	
<b>MIN</b>				<b>16,800</b>	<b>23,070</b>	<b>12,971</b>	<b>22,950</b>	<b>5,861,694</b>	<b>75,570</b>	
<b>MAX</b>				<b>20,110,730</b>	<b>6,436,369</b>	<b>41,604,798</b>	<b>649,938,412</b>	<b>25,020,147</b>	<b>698,904,111</b>	

## 4.6. Discussion

### 4.6.1. Limits and errors in eruptive volume estimates

Uncertainties and limitations in eruptive volume-estimates for monogenetic volcanoes include: (1) erosion from both anthropogenic and natural processes; (2) accuracy of topographic data; (3) geological unit-determination; (4) data available for pre-eruptive surface reconstruction; (5) uncertainty in bulk juvenile, vesicle and void space content in the deposits; (6) missing distal tephra blankets; and (7) unknown geometry of crater infills, diatremes and plumbing systems.

Ejecta rings and tephra blankets are often rapidly eroded during and immediately post eruption, especially in high-rainfall regimes (e.g. Segerstrom, 1950). Scoria cone erosion is an order of magnitude slower process (e.g. Kereszturi and Németh, 2012a), leading to better preservation potential. Erosion is greatest in the first few thousand years (e.g. Kereszturi and Németh, 2012a). Over the first thousands of years, volume-loss is estimated to be a maximum of 1–10%/ky for scoria cones and 1–5%/ky for lava flows (Rodriguez-Gonzalez et al. (2011). In a dry climate in the Mojave Desert in California these can be as low as 0.01%/ky (Dohrenwend et al., 1986). Since 37 of the 52 AVF volcanoes are <40 ka, the total expected volume-loss could be as high as 10% for scoria cones and ejecta rings, and  $\leq 5\%$  for lava flows.

The accuracy of topographic data includes the original vertical and horizontal precision of acquisition, interpolation methods, pre- and post-processing, and data available for reconstruction of the pre-volcanic surface. In this case the LiDAR accuracy was 0.15 to 0.25 m  $\pm 1 \sigma$  both vertically and horizontally (Kereszturi et al., 2012b). The root mean square error (RMSE) of the LiDAR DSM is estimated at about  $\leq 0.5$  m, based on high-accuracy Real Time Kinematic GPS points collected through volcanic edifices with various geometries (G. Kereszturi, unpublished data). Given that the volume calculations were performed on a resampled LiDAR DSM dataset, the estimated error due to resampling is modelled as  $\pm 0.02\%$  for volume estimates, based on a small (Pukeiti) and large volcano (Rangitoto) (Kereszturi et al., 2012b). The largest error is derived from the geological mapping and reconstruction of pre-eruptive terrains using sparse drill core data especially in the flat-lying Manukau Lowlands and Waitemata Harbour (Fig. 4.1).

The DRE correction assumes overall average values, although it is known that vesicularity, juvenile content can change unit by unit within a pyroclastic succession and certainly between volcanoes (e.g. Cashman and Kauahikaua, 1997). For visualizing changes due to DRE-corrections, both bulk and DRE-corrected volumetric data were used in the Fig. 4.8.

The unknown geometries of the unexposed plumbing system under the young scoria cones and of diatremes under phreatomagmatic craters in the AVF introduce further uncertainties. A minimal volume-loss is introduced by unaccounted plumbing beneath scoria cones (about  $6.5 \times 10^4 \text{ m}^3$ ), which is only fraction (usually  $\leq 1\%$ ) of most of the edifice's volumes in the AVF.

The dimensions of distal tephra blankets are also difficult to accurately quantify. These potentially large contributors to volume, along with that of diatremes were not used in temporal and spatio-temporal analyses. The AVF volumes reported here are hence minima. An overall error of the minimum eruptive volumes from the above considerations is likely to be around 10–15%.

#### 4.6.2. Spatial and temporal magma flux

The overall spatial and temporal magma flux of the AVF is calculated as  $0.005 \text{ km}^3/\text{km}^2$  and  $0.007 \text{ km}^3/\text{ky}$ , respectively (Table 4.4). This is comparable with  $0.003 \text{ km}^3/\text{km}^2$  for Bakony-Balaton Highland Volcanic Field, Hungary (Kereszturi et al., 2011) and the  $0.03 \text{ km}^3/\text{km}^2$  for Tacámbaro-Puruarán area in Michoacán, México (Guilbaud et al., 2012). The temporal magma flux is higher than the lowest known  $0.0005 \text{ km}^3/\text{ky}$  for the Southwest Nevada Volcanic Field (Valentine and Perry, 2007). However, it is not as high as some fields, such as the  $0.18 \text{ km}^3/\text{ky}$  for the San Francisco Volcanic Field in Arizona (Tanaka et al., 1986). The spatio-temporal flux can be further calculated for the two stages in the field's life span (Fig. 4.8A). The area defined by a minimum bounding polygon drawn around the outermost vents is  $181 \text{ km}^2$  for the older period  $>250 \text{ ka}$  to ca.  $40 \text{ ka}$  and  $285 \text{ km}^2$  for the younger period  $\leq 40 \text{ ka}$  (Table 4.4). The older stage of the AVF had a total magma output of  $0.204 \text{ km}^3$  from 15 volcanoes, equating to  $0.001 \text{ km}^3/\text{km}^2$  and  $0.001 \text{ km}^3/\text{ky}$ . After  $40 \text{ ka}$ , a higher frequency of eruptions is recorded by tephra layers (e.g. Molloy et al., 2009), including multiple eruptions during the  $<1000$  year Mono Lake paleomagnetic excursions (e.g. Cassata et

al., 2008). Thus the 37 post 40 ka eruption centres produced  $1.499 \text{ km}^3$  (Fig. 4.7), with an average spatial and temporal magma flux of this period of  $0.005 \text{ km}^3/\text{km}^2$  and  $0.037 \text{ km}^3/\text{ky}$ , respectively (Table 4.4).

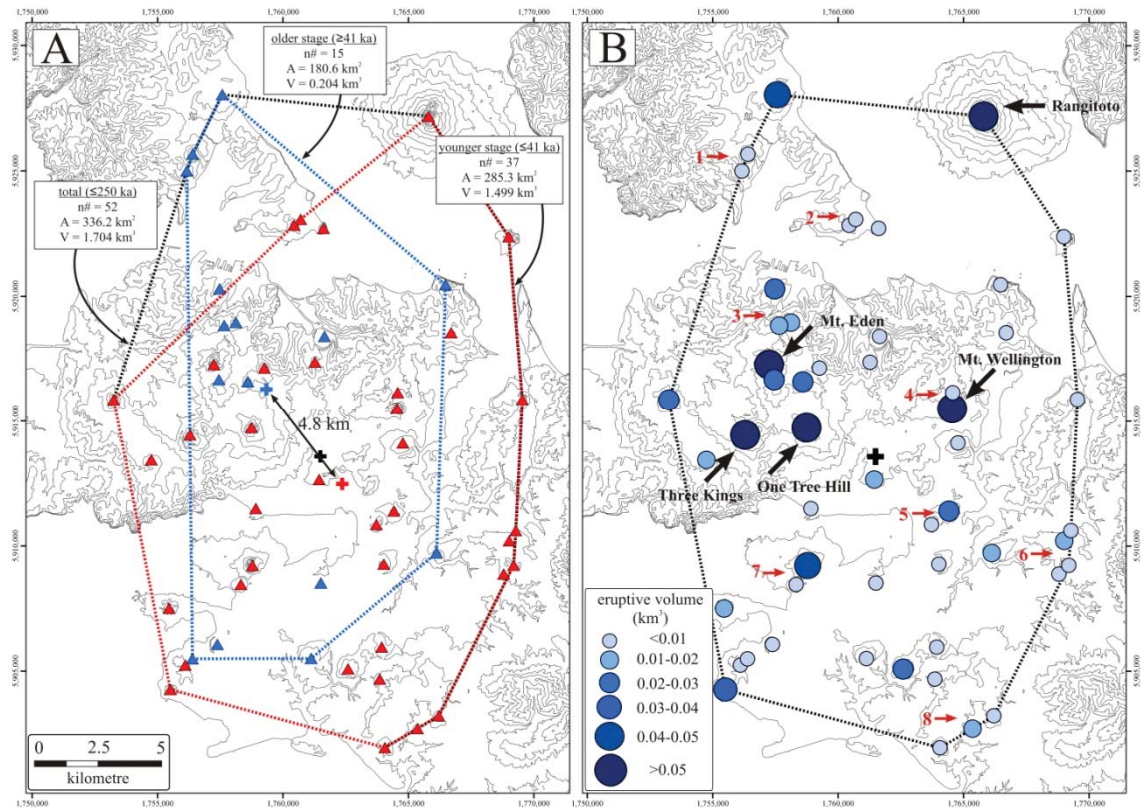


**Figure 4.8** (A) Spatial distribution of volcanic centres formed during the older (blue triangles within the blue polygon) and younger stages (red triangles within the red polygon) in the AVF with the geometric, areal and volumetric characteristics. The blue, red and black crosses are the geometric centre of older, younger stages and the all ( $n = 52$ ) volcanoes from the AVF, respectively. (B) Spatial distribution of eruptive volume per volcanoes (blue dots) scaled by their volumetric size in the AVF, revealing a couple of exceptionally large volcanic centres (black arrows with names). The numbered red arrows show the distribution of those “paired-volcanoes”. These paired-volcanoes could have formed from the same eruptive event, involving a lateral vent migration. Red numbers with arrows are: 1 – Tank Farm and Onepoto, 2 – Mt. Victoria and Mt. Cambia, 3 – Grafton volcano and Auckland Domain, 4 – Purchas Hill and Mt. Wellington, 5 – Mt. Richmond and McLennan Hills, 6 – Styaks Swamp, Green Mt., Otara Hill and Hampton Park, 7 – Mt. Mangere and Mangere Lagoon, 8 – Wiri Mt. and Ash Hill.

Distinct volume concentrations occur in two locations, one at Rangitoto and the other in the central field, encompassing One Tree Hill, Mt. Eden, Mt. Wellington and Three Kings (Fig 4.8B). This also correlates with the location of the Junction Magnetic Anomaly defining a weakness in the crust beneath Auckland (e.g. Cassidy and Locke, 2010). The central concentration of volume is common to intraplate volcanic fields formed on continental crust, such as Jeju Island, Korea (Brenna et al., 2012a) or Pinacate Volcanic Field, Sonora, Mexico (e.g. Lynch et al., 1993). Also in Jeju, large

young eruptions on a similar scale as Rangitoto have also occurred on the field outskirts [e.g. Udo volcano (Brenna et al., 2010)]. In Jeju's case, the volumetric distribution of volcanism is explained by higher heat flows and longer periods of melt extraction from the central parts of the magmatic system, as well as crustal storage and evolution of magmas (Brenna et al., 2012a). There is, however, no evidence for crustal storage of any AVF magmas.

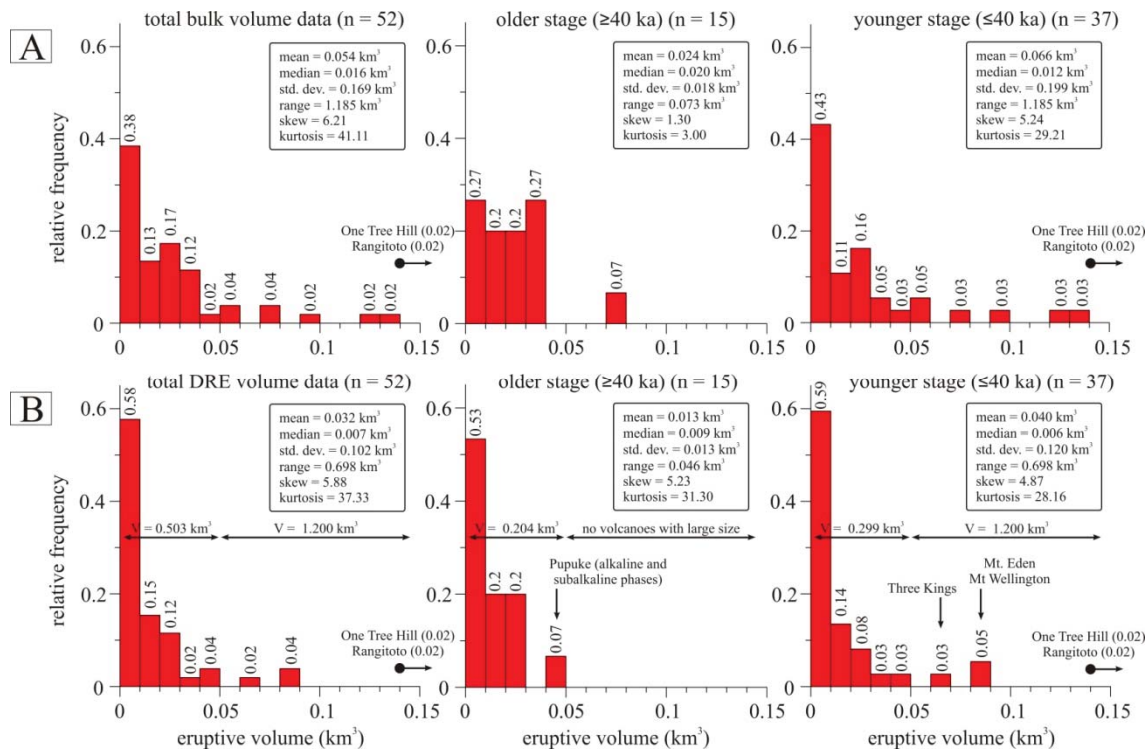


**Figure 4.9** Histograms showing the eruptive volumes of each volcano in the AVF (first column), older stage ( $\geq 40$  ka; second column) and younger stage ( $\leq 40$  ka; third column), using bulk (A) and DRE-corrected volumetric data (B). Bin size is  $0.01 \text{ km}^3$  on all histograms. Outliers, such as Rangitoto and One Tree Hill, are not shown on the histograms.

#### 4.6.3. Integrating eruptive volumes with the AVF's evolution

Individual eruption centres in monogenetic fields normally have volumes between  $0.0001$  and a few  $\text{km}^3$  (e.g. Guilbaud et al., 2012) and the AVF is no exception. The bulk and DRE-corrected eruptive volumes have highly dispersed distributions, but with a strong positive skew (Fig. 4.9). Around 58% have volumes of  $\leq 0.01 \text{ km}^3$ , with 33% between  $0.01$ – $0.05 \text{ km}^3$  and 10% being extremely large. The older period of volcanism of the AVF shows a small range of eruptive volumes ( $0.0003$ – $0.046 \text{ km}^3$ ), while the latter stage had a much greater span ( $0.00007$ – $0.698 \text{ km}^3$ ). Thus, the largest eruptions

occurred only in the younger stage of the field's evolution, including five volcanoes that alone produced 1.2 km<sup>3</sup> of magma (Fig. 4.9). The lack of as large-volume volcanoes in the older stage of the field's evolution could reflect magma-source processes or possibly external tectonic settings.

Geochemically, the AVF is characterised by magma sources at different depths and with different parental compositions (e.g. Needham et al., 2011; McGee et al., 2013). The youngest eruption, Rangitoto, includes a first eruption from a 1% partial melt deep source (~2.5–3 GPa, ~80–90 km depth) within fertile garnet-bearing mantle. The secondary source produced larger magma volumes, derived from ~3% partial melts at ~2 GPa, or ~60–70 km depth (McGee et al., 2011). In the other volcanoes of the field, there is a strong correlation between eruptive volumes and compositional variation, reflecting the depth of the melting column involved in producing magmas (e.g. Le Corvec et al., 2013a; McGee et al., 2013). The initiation of melting is normally deep in the asthenosphere with a rapid rise to the surface (e.g. Sprung et al., 2007; Smith et al., 2008). This may trigger or mobilise melts from shallower levels to produce larger eruptions from two or more magma sources, with consequently increasing volumes. This geochemical data thus indicates that the larger eruptions in the latter part of the AVF's existence were the result of the presence and eruption of a longer column of melt extraction and the eruption of magmas from multiple levels, especially from the lithospheric source.

The triggering of eruptions in monogenetic fields could either be conceived of as a change in conditions that may induce sudden melt formation, or the sudden release of already formed melts. The coincidence of five or more eruptions within the short time around the Mono Lake paleomagnetic excursion in the AVF (Cassidy, 2006), points to the latter mechanism being more likely. The eruptive activity and magma output of volcanic fields have often been described as episodic (e.g. Connor and Conway, 2000), with intense periods of volcanism lasting 10<sup>3</sup>–10<sup>5</sup> yr separated by quiescence for 10<sup>5</sup>–10<sup>6</sup> yr (e.g. Kereszturi et al., 2011). This pattern is hard to define for the very young AVF whose whole life span is only 250 ky. Nonetheless, episodic eruption frequency behaviour is often interpreted as a coupling with regional tectonics (e.g. Aranda-Gómez et al., 2003; Valentine and Hirano, 2010). Plate motion, rotation and mantle density heterogeneities induce asthenospheric shearing that focuses and induces melt extraction (e.g. Conrad et al., 2011). Large-scale plate deformation can also induce melt collection

and forming melt pockets (e.g. Valentine and Hirano, 2010). Both mechanisms may occur at AVF and the older volcanic fields (e.g. Le Corvec et al., 2013a).

The notable increase in large-volume volcanoes in the young AVF ( $\leq 40$  ka) indicates a significant change in state of the system. This has been termed before a “flare up” (Molloy et al., 2009), but is actually an enduring change in behaviour. This could indicate a change in tectonic setting that subsequently allowed accumulation and/or injection of more frequent and larger magma batches. An increase in asthenosphere shearing, coupled with increased crustal extension behind the active North Island subduction zone, could cause this. Coincidental with this change in state at the AVF was the onset of a period of major caldera eruptions in the Taupo Volcanic Zone, starting with a series of 12 large eruptions from the Okataina Caldera from ca. 45–30 ka (Charlier and Wilson, 2010), and proceeding southward to a series of major eruptions of Taupo Caldera in ca. 26.5 ka B.P., coincident also with major upsurges in the rate and magnitudes of activity at the andesitic Ruapehu and Taranaki volcanoes (Alloway et al., 1995; Donoghue et al., 1995). Thus, clearly the change in behaviour of the AVF was coincident with tectonic stress regime changes in the North Island of New Zealand.

A finding of episodic basaltic volcanism with varying rates, is consistent with other fields in the region (e.g. Briggs et al., 1994), erupted from compositionally similar characteristics and sources (Cook et al., 2005; Sprung et al., 2007; McGee et al., 2013). The AVF volcanoes also show no apparent clustering or preferred alignments over time, suggesting spatio-temporal independency (e.g. Bebbington and Cronin, 2011; Le Corvec et al., 2013a). If some degree of relationship exists between spatio and temporal processes that would imply a dominant source control (i.e. magmatic source-control, c.f., Valentine and Perry, (2007)). This is usually manifested as waxing and waning phases of monogenetic volcanism (e.g. Condit and Connor, 1996), responding to a systematic tapping followed by depletion of fertile mantle zones and migration of volcanism towards undepleted mantle sources over time. If AVF magma supply rates are controlled by a random (Poisson) process (e.g. Le Corvec et al., 2013a), a higher post-40 ka eruption rate and greater volumes can only be explained by a secondary control, i.e., tectonic regime. This should be investigated in the future, by an integrated analysis of DRE-corrected eruptive volumes of the AVF with the knowledge of magma

source regions (especially the vertical depth over which magmas are sourced) and the tectonic evolution of the broader region.

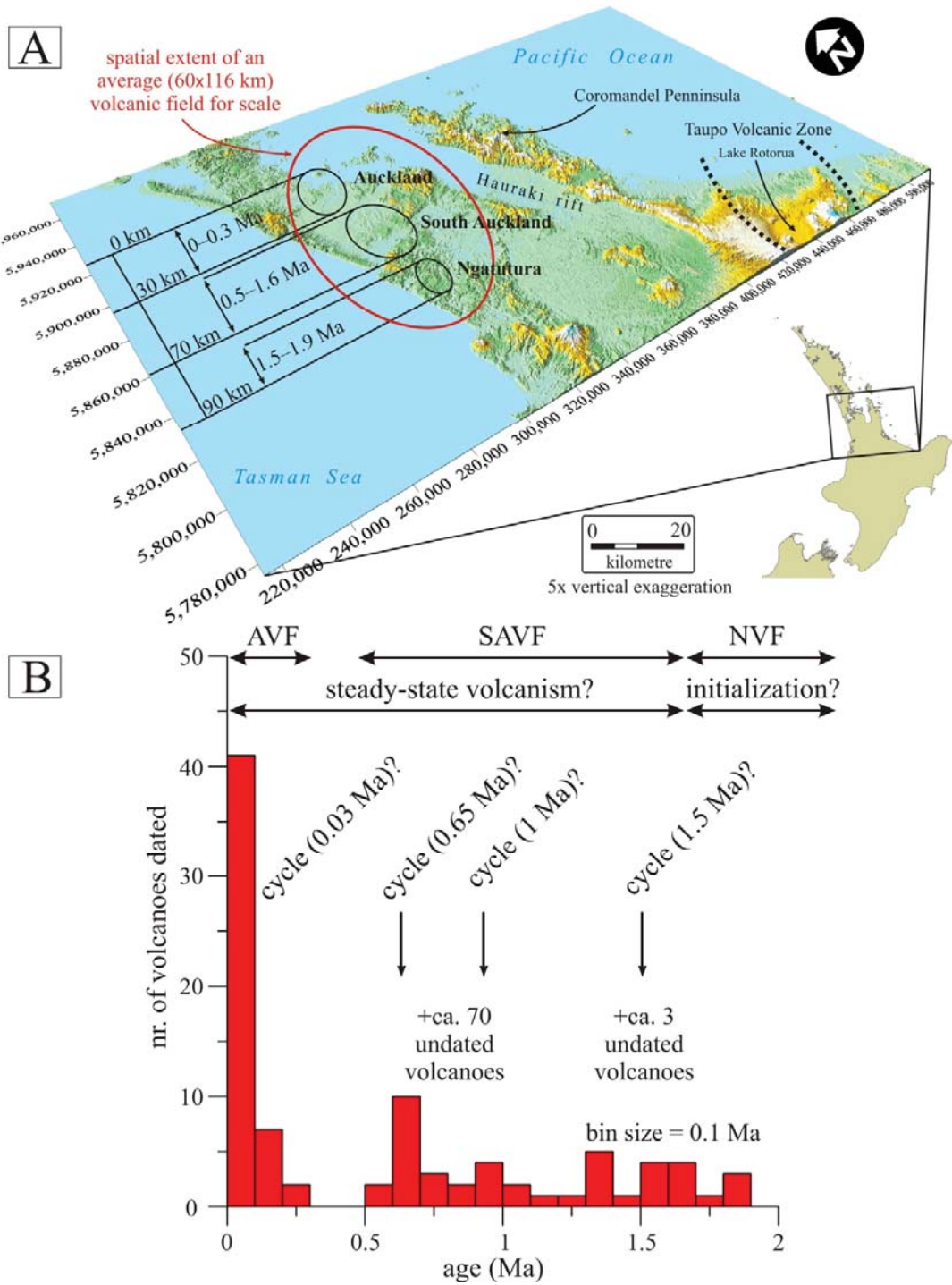


**Figure 4.10** (A) Distribution of monogenetic volcanics in the broader Auckland region. The black ellipses show the location of Auckland (AVF), South Auckland (SAVF) and Ngatutura (NVF) volcanic fields, with the duration of volcanic activity and distance from location of the recent manifestation of volcanism. For scale, the average spatial extent of a monogenetic volcanic field is given, based on data from Le Corvec et al. (2013c). (B) Age distribution for the monogenetic volcanic eruptions in the last 2.5 My in the broader Auckland region. The K-Ar radiometric ages are from Briggs et al. (1994).

**Table 4.4** Summary of field-scale and edifice-scale characteristics of the AVF for the older (250–40 ka) and younger (<40 ka) stages and for the whole field. The duration is based on an average of 10 m<sup>3</sup>/s eruption rate. Note: ph – phreatomagmatic eruptions, mag – magmatic explosive eruptions, eff – effusive activity.

scale	parameter			unit	stage of evolution			
					initial stage	peak	TOTAL	
					>40 ka	<40 ka	246 to present	
field-scale	duration			ka	207	40	247	
	area			km <sup>2</sup>	180.6	285.3	336.2	
	eruptive volume			km <sup>3</sup>	0.204	1.499	1.704	
	temporal magma flux			km <sup>3</sup> /ky	0.001	0.037	0.007	
	spatial magma flux			km <sup>3</sup> /km <sup>2</sup>	0.001	0.005	0.005	
edifice-scale	duration	ph	all data	range	day	30.6	8.9	30.6
			no large volc.	range	day	30.6	8.9	30.6
		mag+eff	all data	range	day	32.5	800.4	800.4
			no large volc.	range	day	32.5	53.5	53.5
	edifice/unit area	ph		mean	km <sup>2</sup>	1.25	1.13	1.17
		mag		mean	km <sup>2</sup>	0.08	0.25	0.23
		eff		mean	km <sup>2</sup>	1.05	3.25	2.72
	eruptive volume	ph		min	m <sup>3</sup>	321,866	75,570	75,570
				max	m <sup>3</sup>	26,468,298	7,647,024	26,468,298
		mag		min	m <sup>3</sup>	14,000	12,971	12,971
				max	m <sup>3</sup>	436,904	41,604,798	698,904,111
		eff		min	m <sup>3</sup>	3,262,880	22,950	22,950
				max	m <sup>3</sup>	27,664,782	649,938,412	649,938,412

#### 4.6.4. AVF evolution and relationship to neighbouring fields

The physical parameters of a volcanic field, such as spatial and temporal magma flux, recurrence rate, spatial-volumetric and temporal-volumetric properties are the basis for hazard assessment (e.g. Connor et al., 2000; Bebbington and Cronin, 2011; Guilbaud et al., 2012; Le Corvec et al., 2013a). In some cases, these properties allow classification of fields into so called “volume-predictable” (i.e. supply-controlled) or “time-predictable” (controlled by external forces operating on a regular or predictable timescale) (e.g. Valentine and Perry, 2007). The AVF behaviour as a whole does not fit either model and it may be a hybrid between the two. The older sparse activity with a limited range in volume and poor age control does not allow clear evidence for either type of activity, however, in the post 40 ka history, the longest pauses are followed by the largest eruptions – indicative of a possible volume-predictable relationship (e.g. One Tree Hill, Mt Wellington, Rangitoto). This case thus shows a field may be classified differently throughout its evolution.

Viewing the AVF in relation to earlier monogenetic volcanism Auckland region (Fig. 4.10), it is of similar scale and composition to the South Auckland and Ngatutura Volcanic Fields (Fig. 4.10). The AVF dimensions (16×35 km or 336 km<sup>2</sup>) (Spörli and Eastwood, 1997) is comparable in size to “volcanic clusters” documented within larger volcanic fields elsewhere, including the SP cluster (250 km<sup>2</sup>) in Arizona (Conway et al., 1998), or the Mt. Gambier cluster (489 km<sup>2</sup>) within the Newer Volcanic Province in Victoria, Australia (Bishop, 2007). A global average monogenetic volcanic field defines a 60×116 km ellipse (Fig. 4.10), based on data from Le Corvec et al. (2013c). These characteristics indicate that the AVF could be a “cluster” within a larger magmatic system below the Auckland region, however because the AVF is so young compared to most global field examples, it may be too early to classify it accurately.

#### 4.6.5. Volcanic hazard consequences

Assuming similar controls on melt extraction and ascent characteristics of future eruptions, the volumetric data presented here can be used for hazard assessment of the AVF and help define a range in likely eruptive scenarios. For this purpose the post-40 ka range in eruption sizes and compositions is the most relevant (e.g. Fig. 4.9), which

includes the largest range in eruption volumes. The eruptive volumes, or magma supply scenarios, control both the potential duration of eruptions and many hazard processes appear to be volume-controlled, such as large-volumes being most likely to involve complex multi-phase eruptions with initial phreatomagmatism, followed by scoria/spatter cones and widespread lava flows. By contrast, under the low-volume scenario ranges, lava flows are unlikely.

The eruption rate of analogue volcanoes varies between 1 and 10 m<sup>3</sup>/s for the (e.g. Tokarev, 1983; Hill et al., 1998; Parfitt, 2004). Comparable Strombolian eruptions at Cerro Negro, Nicaragua, between 22 November to 2 December 1995 had a magma discharge rate of 3–5 m<sup>3</sup>/s (Hill et al., 1998), while the Great Tolbachik eruptions, Kamchatka, produced at the rate of 8.6 m<sup>3</sup>/s (Tokarev, 1983). The total eruption of Ukinrek maars, Alaska, occurred with an average of 2.8 m<sup>3</sup>/s magma discharge (Self et al., 1980). Commonly, magma discharge rates are higher at the beginning and less intense at the waning stages of eruptions (e.g. Wadge, 1981). For the example case of a discharge of 10 m<sup>3</sup>/s at the AVF, initial phreatomagmatic phases of past eruptions may have lasted between 0.1 and 30.6 days and if scoria and lava were erupted, this could have lasted between 0.1 and 800.4 days of spatter/scoria cone and lava flow formation (Table 4.4). Examining only the <0.05 km<sup>3</sup> eruptions, event duration ranges of 0.1–53.5 days are estimated. For long-lived, large-supply (>0.05 km<sup>3</sup>) eruptions, the construction of a volcanic edifice and associated lava flows could have lasted from months to maximum a year in duration, such as Three Kings, Mt. Eden, One Tree Hill, Mt. Wellington and Rangitoto. These are needed to be considered as worst-case scenarios in future volcanic hazard assessment.

## 4.7. Conclusions

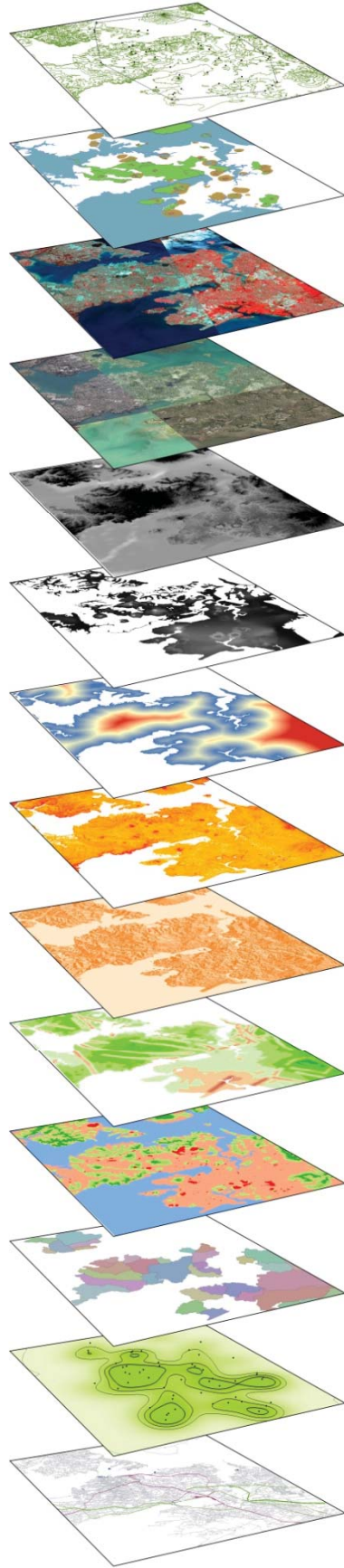
A monogenetic volcano can be modelled by six components for the purposes of systematic volume calculation (Fig. 4.2). Some components can be estimated reliably, such as: ejecta rings, scoria cones and lava flows. These provide good estimation of minimum eruptive volumes. It is more difficult to calculate volumes for crater fills, distal tephra deposits or diatremes (Fig. 4.2). Without drilling, intense geophysical exploration or deep exposures, sub-surface eruptive volume estimates will always be fraught with uncertainty. For a field, such as the AVF, where over two-thirds of the

volcanoes have phreatomagmatic phases, the uncertainty around diatreme structures is potentially the major uncertainty in event magma volume estimations. Based on a conservative estimate, the AVF has produced at least 1.704 km<sup>3</sup> DRE-corrected eruptive volumes over its 250 ky evolution. If additional subsurface components and estimates of distal tephra falls are included, this magma output could be doubled.

The systematic calculation of AVF erupted volumes presented here shows that the field underwent two distinctive periods of behaviour. The early field, from 250–40 ka produced eruptions that were dominantly of small-volume (<0.046 km<sup>3</sup>). From ~40 ka to the present day, eruptions were more frequent and included a greater range in volumes (0.00007–0.698 km<sup>3</sup>). This appears to represent a major change in the tectonic setting, magma supply or both. Interestingly, the largest-volume eruptions of the post ~40 ka field were preceded by the longest pauses, which may indicate an element of volume or source-supply control of the extreme volcanism. Future unrest in the AVF must be modelled on this latter high-rate and highly variable volume volcanism. For forecasting eruption styles a wide range of eruptive volume scenarios must be used. Future studies should investigate relationship between eruptive volumes and geochemical evolution of spatially and temporally over the evolution of the AVF, including its relationship to its southern older siblings, the South Auckland and Ngatutura Volcanic Fields (Fig. 4.10).

Success in understanding long-term behaviour of the monogenetic basaltic volcanism in any region rests upon the understanding of volumetric eruption rates and spatio-temporal patterns. Integrating volume information with the understanding of the source regions (depths, range of melting conditions and degrees of partial melting) from the geochemistry of erupted products may be the key to explain volcanic cycles and future eruptive potential of the AVF and volcanic fields like it.





Chapter **5**  
Eruption styles



# 05 / eruption styles

This Chapter builds on the quantitative data of monogenetic volcanoes, by combining the eruptive volume dataset from Chapter 4 with analysis of the location and timing of different eruptive styles in the Auckland Volcanic Field (AVF), New Zealand, with an aim of developing a complete catalogue for its volcanoes. This catalogue will help to develop eruption scenarios for the AVF, and identify the influencing factors (e.g. geological, topographic, hydrologic and climatic) on eruption styles that can be used for forecasting future volcanic hazard in the AVF and other similar volcanic fields.

Supplementary data for this Chapter are in Appendix B.

## Chapter contents

5.1. Introduction.....	121
5.2. Methodology and conceptual framework.....	122
5.2.1. Coding of eruption styles and their eruptive volumes.....	122
5.2.2. Defining area affected in an eruptive history.....	131
5.2.3. Influencing factors on eruption styles .....	132
5.3. Results .....	135
5.3.1. Types and distribution of past eruptive histories .....	135
5.3.2. Influences on AVF eruptive sequences .....	141
5.4. Discussion.....	144
5.4.1. Factors influencing eruption style.....	144
5.4.2. A spatial model for distribution of influencing factors.....	145
5.5. Conclusion .....	148

## Chapter Five – Linking eruptive volumes to eruptive styles

### 5.1. Introduction

A monogenetic volcanic eruption is initiated by successful tapping and focussing of magma into dykes in the mantle (e.g. Rubin, 1995; Katz et al., 2006). After extraction, the magma may not stop until it reaches the surface, allowing only minor crustal assimilation and fractional crystallisation to occur in most cases (e.g. McGee et al., 2012). In some cases, however, chemical evidence shows that magma ascent can be complex and involve multiple pauses en-route (Shaw, 2004; Jankovics et al., 2012). In the uppermost few kilometres, magmas may also intrude and interact intimately with the host environment, leading to dyke-wall interactions and erosion of the host rock, sill formation, and/or stalling of the ascending magma (e.g. Valentine and Krogh, 2006). Near the surface ( $\leq 1$  km), magmas may also intersect the groundwater table and water-saturated sediments. Under the right conditions, interaction of ascending magma with water/water-bearing sediment may result in explosive eruptions, driving phreatomagmatism (e.g. White, 1996; Zimanowski, 1998). Phreatomagmatic explosions generate low eruption columns (up to 10 km in height), but commonly violent, laterally radiating pyroclastic density currents, distributing tephra horizontally across the landscape. These eruptions lead to the formation of maar craters surrounded by ejecta rings (e.g. Németh et al., 2001; Lorenz and Kurszlauskis, 2007; White and Ross, 2011). When groundwater is not a major factor, eruption explosivity and resultant hazard processes relate to magma flux, volatile content and viscosity, as well as the conduit setting (Cashman et al., 2000; Rust and Cashman, 2011). These “dry” eruption styles are characterised by fire-fountaining activity (or Hawaiian eruptions) or Strombolian-type explosions (e.g. Head and Wilson, 1989; Parfitt, 2004; Valentine and Gregg, 2008; Németh et al., 2011). Such eruption styles result in the formation of scoriaceous pyroclastic deposits that accumulate in close proximity to the vent area, building scoria cones or spatter cones (Head and Wilson, 1989; Riedel et al., 2003; Martin and Németh, 2006; Valentine and Gregg, 2008). These eruptions are generally low in eruption energy and produce both tephra falls and potentially widespread lava flows (Houghton et al., 2006; Németh et al., 2012). Quantification of the widely contrasting eruption styles and

eruptive processes in monogenetic volcanic fields remains the great challenge in comprehensive hazard assessment.

One way of viewing monogenetic volcanic hazards is through internal versus external environmental influences on eruptive style. Internal (or magmatic) influences include the properties of the ascending magma, such as composition, volatile content, decompression, and degassing (Mangan and Cashman, 1996; Cashman et al., 2000; Di Traglia et al., 2009; Pioli et al., 2009; Rust and Cashman, 2011). The external environmental influences include the broad environment hosting the eruption, such as topography, groundwater depth, faults and the properties of the substrate geology (Connor et al., 2000; Gaffney and Damjanac, 2006; Auer et al., 2007; Ross et al., 2011; van Otterloo and Cas, 2013). When examining final eruption products, discrimination of magma fragmented by internal gas expansion versus that fragmented by magma-water interactions may help understand monogenetic volcanism. Similarly, the proportion of country-rock materials with pyroclastic deposits is a key factor to understand magma-environment interactions (Valentine, 2012; Agustín-Flores et al., 2014). This classification of eruptive products can give snapshots of eruption-site conditions at the time of the eruption at each specific location within a monogenetic volcanic field. Combining the spatial and temporal attributes of these data will help to quantify the susceptibility of certain areas to any particular eruption style, feeding into a potential eruption style forecast model. In this study, the eruptive volume catalogue (Chapter 4) of the Quaternary Auckland Volcanic Field (AVF), New Zealand, is compared to catalogue of eruptive histories and a series of external environmental features, such as the geology, hydrogeology and topography of the eruption centres (Table 5.1). From this, the potential features that influence eruption styles are explored and a conceptual model developed for spatial distribution of factors influencing eruption styles in the AVF.

## 5.2. Methodology and conceptual framework

### 5.2.1. Coding of eruption styles and their eruptive volumes

For cross-comparison of eruptive volumes with eruptive histories in the AVF, the overall or dominant eruption style should be defined. This is difficult in many fields, including the AVF, because major transitions in eruption styles occurred during many

past eruptions (Houghton et al., 1999; McGee et al., 2012). Hence, to define eruption styles and sequences, the geomorphology of the final volcanic landform with sedimentological-constraints was used in combination with the observed and mapped pyroclastic rock units associated with each of the analysed volcanoes. Based on the primary morphological criteria, there are six broad genetic classifications of monogenetic volcanoes: (1) eruptive fissures, (2) spatter cones, (3) scoria or cinder cones, (4) maars or maar-diatremes, (5) tuff rings and (6) tuff cones (e.g. Wood, 1979; Head et al., 1981; Wohletz and Sheridan, 1983; Valentine and Gregg, 2008; Németh, 2010; Kereszturi and Németh, 2012a). These volcanic landforms correspond to dominant eruption styles. In this classification scheme, a large group of volcanoes, such as maars with late stage magmatic infills and scoria cones (Chough and Sohn, 1990; White, 1991; Auer et al., 2007; Németh et al., 2008; Martí et al., 2011), cannot be distinguished from their simpler variants. To accurately reflect volcanic hazard, the transitions in eruption styles must be better quantified. By combining eruptive style, eruptive transitions and eruptive volumes, a broad genetic classification of eruption sequences can be proposed (Table 5.1).





31	North Head	31	N	785,000	12,100	10,000	807,100	2,587,579	36,198	22,950	y	y	y	123	0	120	131	130	166	528	-2	2,450
32	Panmure Basin	31	C	1,132,201			1,132,201	7,144,976	300,000		y	y	n	12	15	0	0	0	2,278	7,714	0	1,117
33	Mt. Victoria	31	N		136,800	304,800	441,600		2,582,535	2,222,939	n	y	y	23	0	283	374	560	563	923	0	1,377
34	Mt. Cambria	31	N		51,600		51,600		294,591		n	y	y	23	0	80	151	589	618	1,123	6	1,729
35	Roberston Hill	31	M	2,009,600	17,000		2,026,600	2,478,372	240,000		y	y	n	12	26	543	697	810	6,128	11,600	10	2,409
36	Mt. Roskill	30	C	1,130,400	241,100	1,833,000	3,204,500	1,484,379	1,373,086	11,573,221	y	y	y	123	5	2,235	2,255	2,282	2,298	6,932	52	553
37	Three Kings	29	C	1,648,900	479,200	6,086,600	8,214,700	6,436,369	3,004,030	59,871,292	y	y	y	123	5	2,329	2,438	2,688	3,509	7,132	37	340
38	Mt. Hobson	29	C		214,400	715,745	930,145		1,199,818	5,475,451	n	y	y	23	5	796	1,077	1,865	3,703	3,971	74	397
39	Mt. Eden	28	C		404,300	4,772,400	5,176,700		5,944,328	83,833,340	n	y	y	23	5	2,196	2,439	2,911	3,813	4,136	65	1,065
40	Little Rangitoto	28	C		144,400	315,550	459,950		499,355	1,206,979	n	y	y	23	5	575	594	646	3,412	3,624	40	136
41	McLaughlin Mt.	27	M	1,130,400	30,800	542,200	1,703,400	546,092	430,828	6,608,069	y	y	y	123	43	155	445	891	4,746	12,252	5	481
42	Pigeon Mountain	27	C	1,130,400	109,400	97,325	1,337,125	2,293,172	276,577	744,536	y	y	y	123	23	332	551	714	1,418	6,524	14	92
43	Mangere Lagoon	26	M	388,353	28,600		416,953	2,028,203	12,971		y	y	n	12	53	0	0	0	3,242	5,883	0	2,270
44	Hampton Park	25	M	1,130,400	181,000	332,326	1,643,726	359,080	398,957	1,652,491	y	y	y	123	17	475	1,102	2,259	5,847	13,442	19	2,232
45	Otara Hill	25	M	1,130,400	469,000	168,905	1,768,305	658,550	697,314	943,250	y	y	y	123	17	931	1,476	2,532	5,631	13,012	25	1,822
46	Green Hill	23	M	1,130,400	464,800	1,665,188	3,260,388	1,826,679	1,501,827	8,789,695	y	y	y	123	14	1,077	1,277	1,583	4,654	12,100	23	1,560
47	Mt. Mangere	22	M		873,600	5,111,800	5,985,400		15,005,533	31,200,303	y	y	y	123	42	531	566	566	3,113	6,569	0	1,600
48	Mt. Smart	21	C	502,400	528,500	1,809,800	2,840,700	1,467,579	2,344,811	9,608,102	y	y	y	123	23	292	598	1,394	5,580	8,344	15	708
49	Styaks Swamp	17	M	1,130,400			1,130,400	366,184			y	n	n	1	11	599	883	1,438	4,396	11,642	10	1,183
50	Purchas Hill	11	C	1,130,400			1,130,400	1,658,777	26,000		y	y	y	12	5	1,254	1,698	1,785	1,971	5,764	31	874
51	Mt. Wellington	11	C	1,130,400	263,500	6,642,600	8,036,500	3,399,579	3,016,917	75,864,318	y	y	y	123	5	1,063	1,102	1,146	2,058	6,339	22	314



The construction of a monogenetic volcano is envisaged as a function of (1) eruption style and (2) number of eruption phases (Fig. 5.1). To put this into a quantitative context, considering only a basaltic composition range ( $\text{SiO}_2 \leq 52\%$  w.t.), the eruption styles and their combinations can be expressed as set of matrices, similar to Bishop (2009).

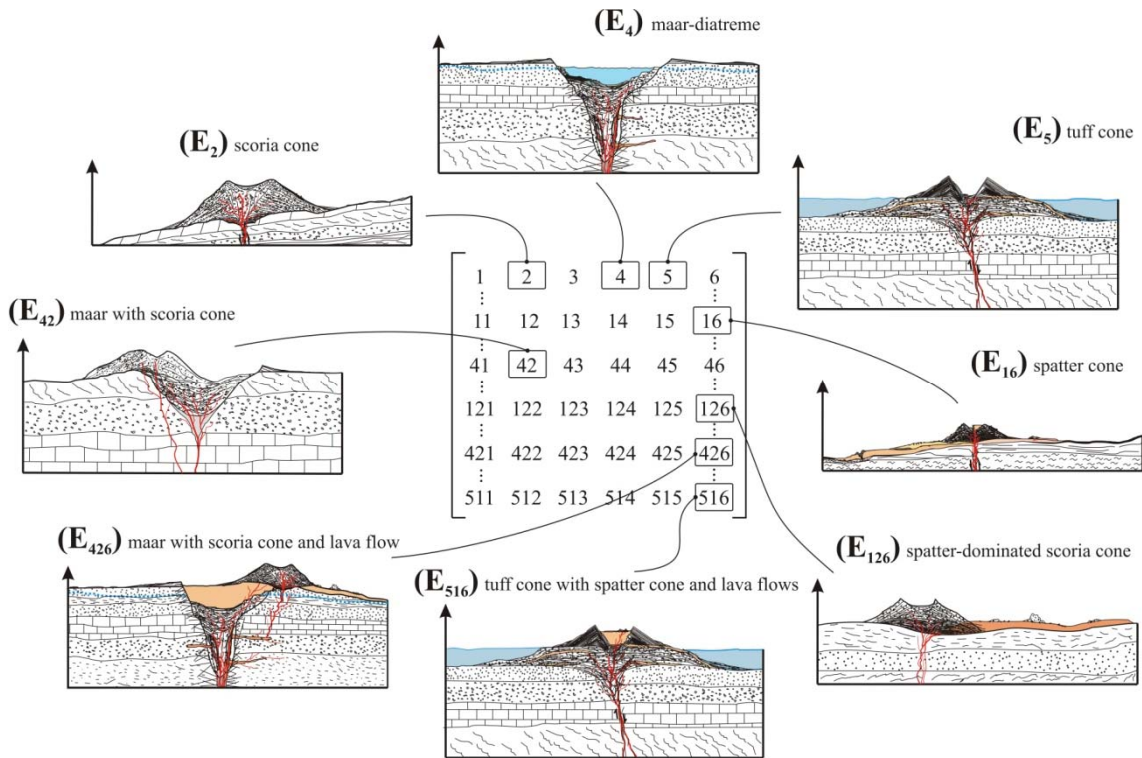


**Figure 5.1** Eruptive histories ( $E$ ) of monogenetic volcanoes can be defined as an array of numbers ordered chronologically. The numerical codes include 1 – fire-fountaining, 2 – Strombolian, 3 – violent Strombolian, 4 – phreatomagmatic, 5 – Surtseyan and 6 – magmatic effusive activity. Modified from Kereszturi and Németh (2012a).

The six basic eruption styles common to monogenetic volcanoes are: fire-fountaining, Strombolian, violent Strombolian, phreatomagmatic and Surtseyan eruptions, along with effusive processes (e.g. Kokelaar, 1983; Valentine and Gregg, 2008; White and Ross, 2011). These six eruption styles can be combined as  $6 \times 6^0$ ,  $6 \times 6^1$ ,  $6 \times 6^2$  or  $6 \times 6^n$  matrices, depending on the number of phases involved in the course of any particular eruption (Kereszturi and Németh, 2012a). This means that an eruptive sequence ( $E$ ) of a simple volcano ( $E_{simple}$ ) could be written as:

$$E_{simple} = [1 \quad 2 \quad 3 \quad 4 \quad 5 \quad 6] \tag{5.1}$$

where the elements 1, 2, 3, 4 and 5 correspond to explosive phases, such as Hawaiian, Strombolian, violent Strombolian, phreatomagmatic and Surtseyan-type eruptions, respectively, while 6 represents effusive eruptive activity. A more complex eruptive sequence involving two ( $E_{compound}$ ) or multiple ( $E_{complex}$ ) eruption styles can be written as:

$$E_{compound} = \begin{bmatrix} 11 & 12 & 13 & 14 & 15 & 16 \\ 21 & 22 & 23 & 24 & 25 & 26 \\ 31 & 32 & 33 & 34 & 35 & 36 \\ 41 & 42 & 43 & 44 & 45 & 46 \\ 51 & 52 & 53 & 54 & 55 & 56 \\ 61 & 62 & 63 & 64 & 65 & 66 \end{bmatrix} \quad (5.2)$$

$$E_{complex} = \begin{bmatrix} 111 & 112 & 113 & 114 & 115 & 116 \\ \cdot & & & & & \cdot \\ \cdot & & & & & \cdot \\ \cdot & & & & & \cdot \\ 661 & 662 & 663 & 664 & 665 & 666 \end{bmatrix} \quad (5.3)$$

For instance, a monogenetic volcano with an eruptive sequence involving fire-fountain activity and associated lava effusion could be described as having a “compound” eruptive history (or  $E_{16}$  in Fig. 5.1). A complex eruptive history could be evidenced by a volcanic edifice with a wide, ‘maar-crater-like’ morphology, but built up from variously welded or agglutinated scoriaceous pyroclastic rock units (e.g.  $E_{1264}$  in Fig. 5.1), similar to the wide craters in Al Haruj al Abyad, Libya (Németh, 2004; Martin and Németh, 2006), and Crater Elegante in Pinacate volcanic field, Sonora, Mexico (Gutmann, 1976). In some cases, gaps, paucity of eruptions, multiple vents or vent migration can increase the complexity of a volcanic landform. These can be identified based on reconstructed stratigraphy (e.g. Ort and Carrasco-Núñez, 2009; Kereszturi and Németh, 2011) and/or geochemistry (Brenna et al., 2011; Sohn et al., 2012). In this classification system, eruptions fed by more than one batch of magma with distinct geochemical signatures (Brenna et al., 2010; Németh et al., 2010; Shaw and Woodland, 2012) can be integrated. The volcano could be, for example,  $E_{44}$  if the influencing factors on eruption style remained the same, or  $E_{42}$  if chemical change were associated with changes in eruption style. The number of rows and columns in these matrices could be increased until all reasonable variations in eruption style are described numerically,

thus an  $n \times m$  matrix is created. The likelihood of various eruptive combinations described by these matrices varies considerably, including ‘highly unlikely combinations’ (e.g.  $E_{665}$ ) versus very ‘common’ scenarios (e.g.  $E_{412}$ ).

To avoid complexity in the analysis, a simpler classification scheme and coding of volcanoes were applied to the AVF, based on just three major types of eruption styles denoted as:

$$E_{\text{auckland}} = \begin{bmatrix} 1 & 2 & 3 \\ 11 & 12 & 13 \\ 21 & 22 & 23 \\ 31 & 32 & 33 \\ 111 & 112 & 113 \\ 121 & 122 & 123 \\ 131 & 132 & 133 \\ 211 & 212 & 213 \\ 221 & 222 & 223 \\ 231 & 232 & 233 \\ 311 & 312 & 313 \\ 321 & 322 & 323 \\ 331 & 332 & 333 \end{bmatrix} \quad (5.4)$$

This classification still allows for 39 combinations of eruption styles. Externally influenced eruption styles include both phreatomagmatism driven by magma-groundwater interaction and Surtsey-type eruptions in shallow subaqueous sites (both coded as 1). In addition, no distinction is made between cone-building Hawaiian/fire-fountaining, Strombolian and violent-Strombolian eruption styles (all coded as 2). Lava flow effusion is coded separately (as 3). There are subtle variations in style that will be missed in this analysis. For example, the single scoriaceous beds within the ejecta ring sequences of Browns Island (McGee et al., 2012) or Crater Hill (Houghton et al., 1996) are classified along with their host deposits as ‘phreatomagmatic’. These brief and volumetrically insignificant parts of the much thicker pyroclastic succession (e.g. 1–3 m thick beds within a  $\geq 30$  m volcanic succession) represent only minor fluctuations, rather than sustained change in the eruptive environment.

The coded eruption sequences were paired with the eruption style differentiated volumes. The Dense Rock Equivalent-corrected (DRE), minimum eruptive volumes of AVF volcanoes from Chapter 4 were classified into three components: phreatomagmatic volumes (e.g. tuff/ejecta rings around maar craters, phreatomagmatic crater infill),

magmatic explosive volumes (e.g. scoria cones), as well as magmatic effusive volumes (e.g. lava flows and magmatic crater infills). Recognising that phreatomagmatic eruptions are more environmentally influenced than magmatic explosive and effusive styles, the phreatomagmatic volumes were used to assess whether or not they can provide an environmental proxy.

### 5.2.2. Defining area affected in an eruptive history

The area impacted or covered by each eruptive unit (e.g. ejecta ring, scoria cone, lava flow) was estimated for the AVF using mapped extents, digitised from geological maps, orthophotos and LiDAR DSM-based derivative maps, such as slope angle and aspect maps. The plan-view area for ejecta rings and scoria cones tends to be circular (Fig. 5.2), whereas it varies largely for lava flows, from radial (e.g. Rangitoto) to elongated flows, such as those from Three Kings.

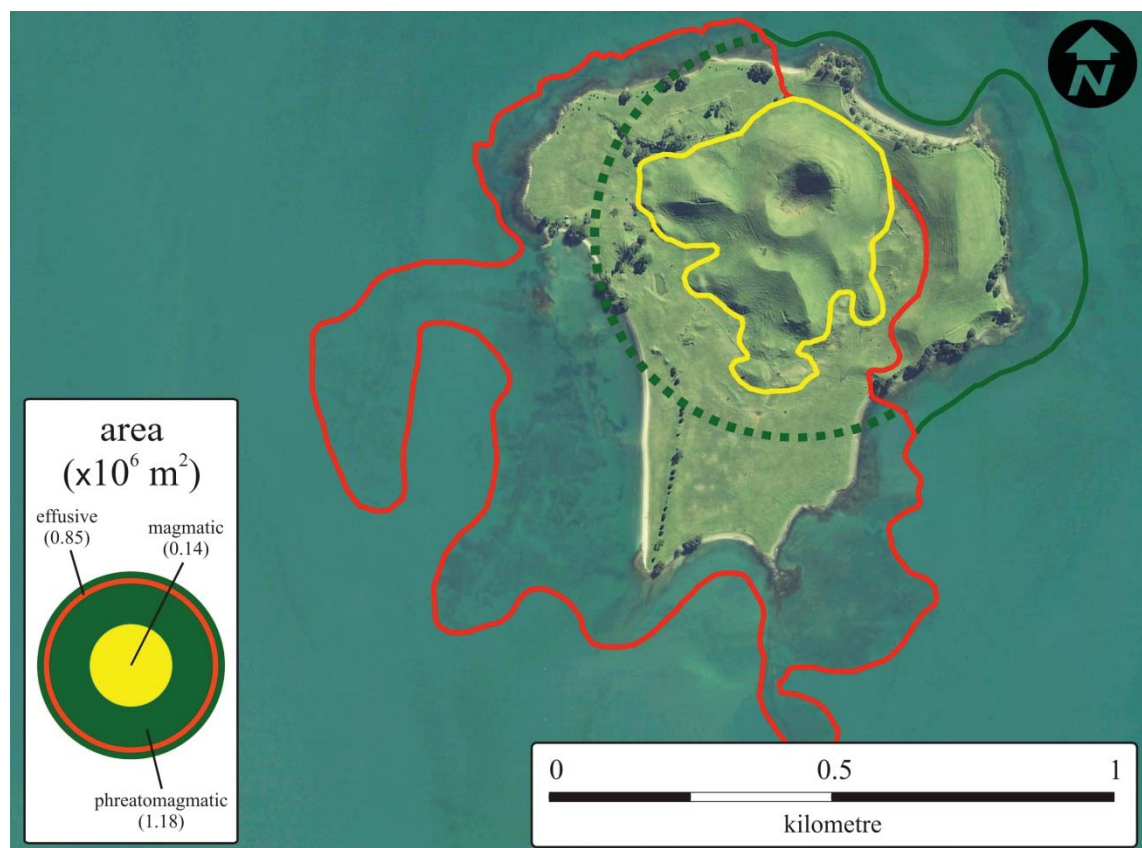


**Figure 5.2** Area-equivalent circles of Browns Island, calculated from the delimited area of each differentiated eruption style type.

In order to visualise and normalise areal data, a circle-equivalent area was calculated. The circle-based approach allows direct comparison of volcanic units with different areal extents. The radius of the area-equivalent circle ( $r$ ) is given as:

$$r = \sqrt{\frac{A}{\pi}} \quad (5.5)$$

where the  $A$  is equivalent to the area of an ejecta ring, scoria cone or lava flow.

### 5.2.3. Influencing factors on eruption styles

In the early stages of past AVF eruptions, rising magma often encountered groundwater or wet sediments, and fragmented phreatomagmatically during vent opening (Allen and Smith, 1994; Houghton et al., 1999). Magmatic explosive or effusive phases were most common later in the course of the eruption. The volcanic hazard posed by compound (two phases) and complex (three or more phases) eruptions is strongly dependent on the order of processes. For example, during an eruption onset, before effective evacuation is possible highly explosive phases are likely to be of largest threat to populations. Hydro-geologic factors have a large impact on the eruption style at the onset of a monogenetic volcanic eruption (Chough and Sohn, 1990; Németh et al., 2001; Sohn and Yoon, 2010; Agustín-Flores et al., 2014). Since the AVF encompasses an area that is either below seawater or with a high groundwater table in soft sedimentary substrates (e.g. Kaawa Formation and Tauranga Group), the potential for phreatomagmatic eruptions is very high (Németh et al., 2012; Agustín-Flores et al., 2014). To examine the potential influence of the external environmental conditions at eruption sites in the AVF, four hypothesised influencing factors were considered: (1) substrate geological units and their thicknesses; (2) sea level and its changes; (3) topographic position within the volcanic field; and (4) distance from known faults and fractures in the hosting country rock. These influencing factors were compared to the phreatomagmatic volumes, as well as to the spatial sub-areas of the field (e.g. North Shore, Central Auckland, Manukau Lowlands; Fig. 5.3).

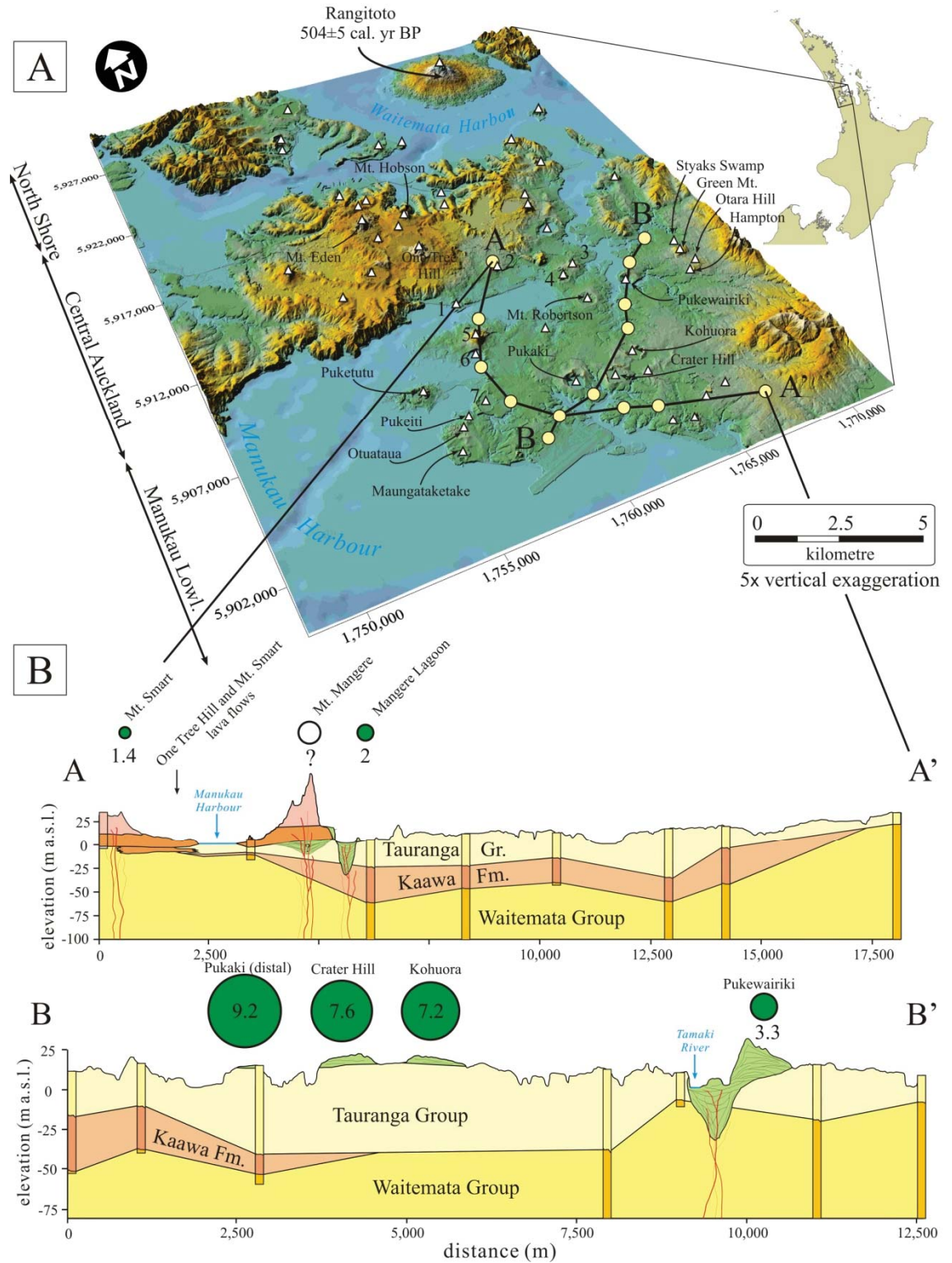


**Figure 5.3** Overview of the AVF and two cross-sections through the Manukau Lowlands. The drill core data are from the PETLAB database ([www.pet.gns.cri.nz](http://www.pet.gns.cri.nz)). Geographic divisions on the left of the map include: North Shore, which includes areas now occupied by sea water in the Waitemata Harbour; Central Auckland, which encompasses the elevated parts of the Auckland Isthmus; and the Manukau Lowlands including the Manukau Harbour and the alluvial plain areas with the western slopes of the Hunua Range. The size of the green dots is scaled to the eruptive volume of the phreatomagmatic phase (in  $\times 10^6 \text{ m}^3$ ) of past volcanoes.

(1) The most important substrate properties are: the thickness of the water-saturated sediments; the hydrological properties; and the degree of compaction/cementation. Many phreatomagmatic eruptions occurred in the Manukau Lowlands in the southern part of the AVF (Agustín-Flores et al., 2014). The substrate thickness for the Manukau Lowlands was modelled using available deep borehole data from the PETLAB website ([www.pet.gns.cri.nz](http://www.pet.gns.cri.nz)). The maximum depth of the loose sediment cover (e.g. Tauranga Group and Kaawa Formation) at each drill core location ( $n = 421$ ) was used to create an interpolated surface using natural neighbour interpolation method (Sibson, 1981). In the AVF, the Manukau Lowlands hosts the largest thickness of post-Waitemata soft-sediment cover within a basin morphology (Fig. 5.3 and Table 5.1).

(2) The present coastline was defined as 0 m a.s.l. on the LiDAR DSM. In addition, four paleosea level scenarios (i.e. -10 m, -5 m and +5 m and +10 m) were created, based on the LiDAR DSM, with bathymetric data to model the coastlines in this area over the last 250 ky (Searle, 1981; Sandiford et al., 2003; Marra et al., 2006; Agustín-Flores et al., 2014). In all sea-level scenarios, Euclidean distances between the shoreline and all volcanic centres were measured (Table 5.1) and compared with the eruptive volumes of phreatomagmatic products (i.e. ejecta rings and crater infill).

(3) Vent elevation was calculated from the lowest contact of the volcanic rocks and the pre-eruptive country rocks (Table 5.1). This was achieved by combining drill core based sub-surface models for the Central Auckland area (Chapter 4), as well as field- and LiDAR DSM-based observations for volcanoes of the Manukau Lowlands and North Shore areas.

(4) Faults and fracture zones can enhance the permeability of the country rocks (e.g. Evans et al., 1997); hence it increases the likelihood of a phreatomagmatic eruption occurring (Gevrek and Kazanci, 2000; Pedrazzi et al., 2014). Tectonic lineaments, such as faults, in the AVF were compiled by Kenny et al. (2012) based on topographic analysis, drill core datasets and vertical offset of the Waitemata paleosurface. These lines of evidence were frequently missing for the Manukau Lowlands, due to the thick soft-sediment cover within the basin (Fig. 5.3). The Euclidian distance was measured between the vent locations and the known faults (Table 5.1).

## 5.3. Results

### 5.3.1. Types and distribution of past eruptive histories

Of the 52 eruptive centres of the AVF, at least 43 (82.7%) show phreatomagmatic phases, 40 (76.9%) experienced explosive magmatic phases, while 37 (71.1%) produced effusive lava flows (Table 5.1). Volcanic products of the field (excluding distal tephtras) cover a total area of 148.8 km<sup>2</sup>. Lava flows cover 92.4 km<sup>2</sup> (62%) of their total area. Pyroclastic deposits from phreatomagmatic eruptions cover at least 48.9 km<sup>2</sup> (32.9%), while magmatic explosive products are minor, covering only 7.4 km<sup>2</sup> (5%, Table 5.1). These data are equivalent to the proximal to medial sedimentation zones (i.e. 0.1 to 2 km in radius) recognised from scoria/spatter fall and pyroclastic density currents (Houghton et al., 2006; Agustín-Flores et al., 2014).

Two patterns were observed in the AVF eruptive histories: those with increasing and those with decreasing areas of impact throughout the event (Fig. 5.4). Small-volume volcanoes that experienced phreatomagmatic vent opening phases mostly had a decreasing pattern, such as Crater Hill (Fig. 5.4). Footprints of successive volcanic hazards did not always superpose earlier deposits, especially lava flows spread over the surrounding landscape (e.g. Browns Island; Fig. 5.2).

The large volume volcanic centres show a pattern of increasing hazard footprint during the eruption, such as Three Kings (Fig. 5.4). The areas affected by lava flows show the largest range, while scoria cones were tightly limited in size (Fig. 5.5). Ejecta ring areas range from 0.1 to 3 km<sup>2</sup> with a mode of 1–1.5 km<sup>2</sup> (Fig. 5.5). Overall, the area affected by magmatic explosive and effusive processes appears to be magma-supply dependent, consequently their distribution is similar to the distribution of the total DRE-corrected eruptive volumes (Fig. 4.9).

There is no clear pattern in the proportion of various eruption types in the AVF through time (Fig. 5.6). From event 15 onward, a larger proportion of lava flows occur, coinciding with larger erupted volumes (e.g. One Tree Hill, Three Kings, Mt. Eden, Mt. Wellington, Rangitoto, Chapter 4). The phreatomagmatic volumes have not changed over time, and they were distributed mostly  $\leq 10 \times 10^6$  m<sup>3</sup>, except Pupuke (Fig. 5.6).

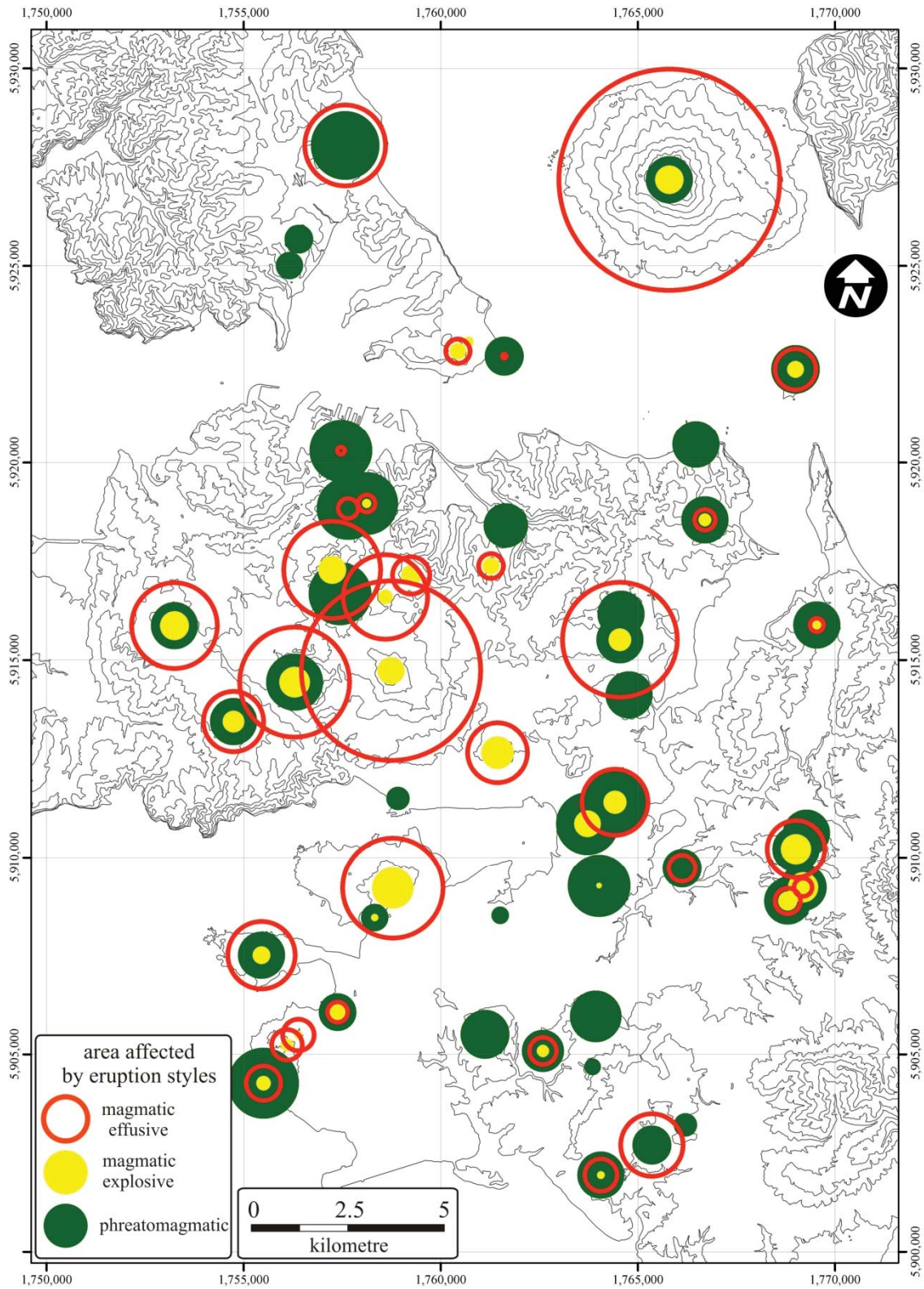


**Figure 5.4** Area-equivalent circles revealing eruptive histories with either increasing (e.g. One Tree Hill) or decreasing (e.g. Crater Hill) footprints of volcanic hazard during the course of the eruptions.

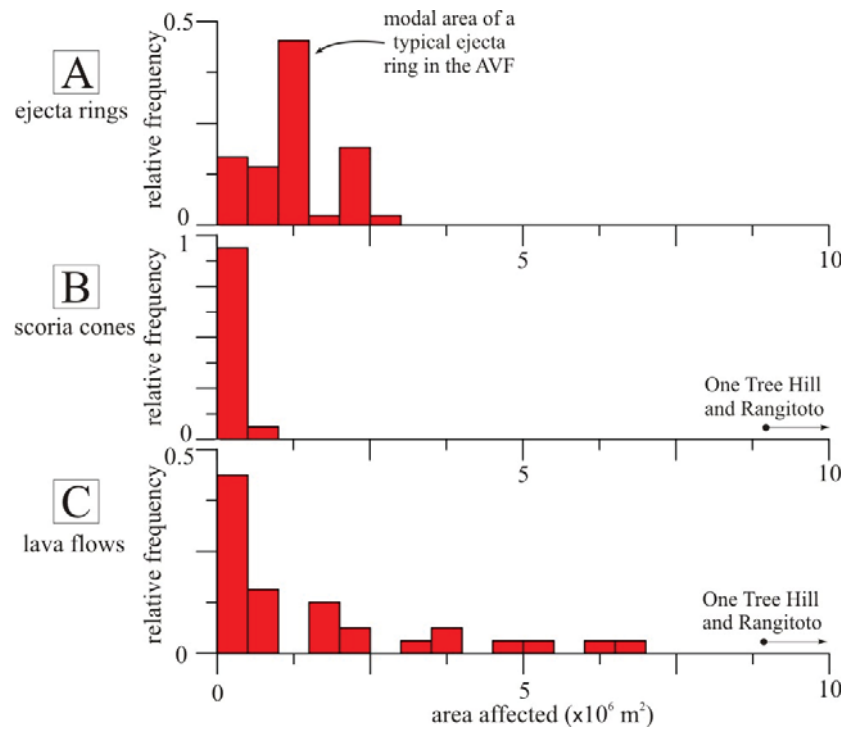


**Figure 5.5** Histogram of area affected by different volcanic processes forming ejecta rings (A), scoria cones (B) and lava flow (C) in the AVF. The bin size is  $0.5 \text{ km}^2$  for all histograms.

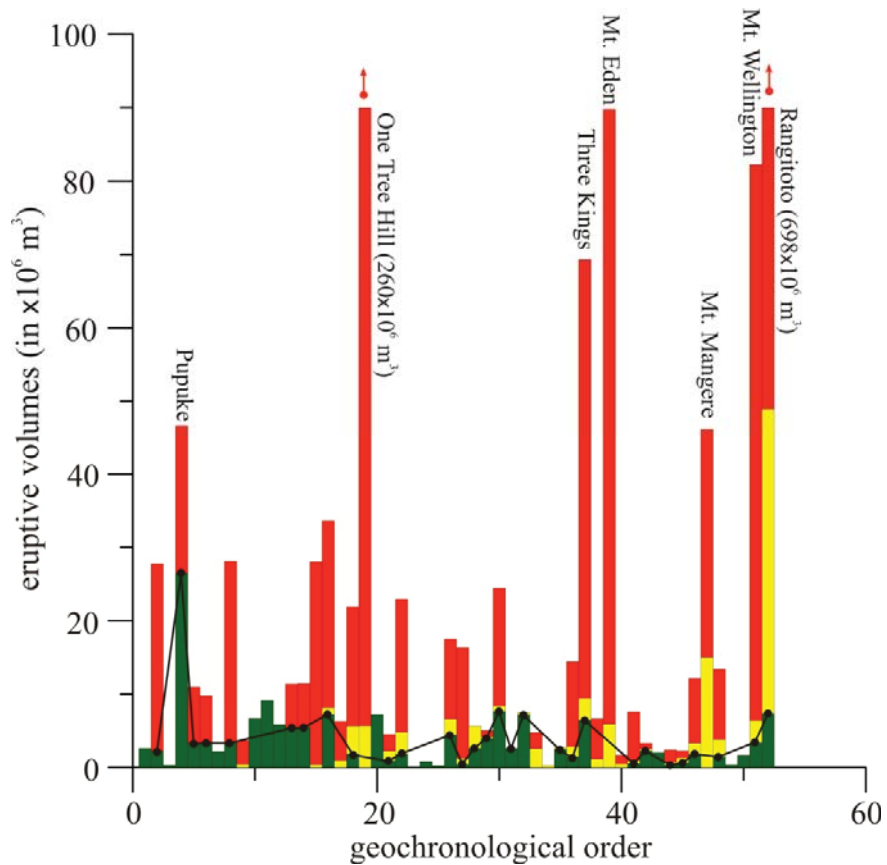


**Figure 5.6** Contribution of different eruption styles to the total eruptive volumes of each volcano in the AVF. The colouring indicates phreatomagmatic (green), magmatic explosive (yellow) and the magmatic effusive volume (red). The chronological order is a simulated event order from Bebbington and Cronin (2011).

The AVF eruption event histories show three distinct populations (Fig. 5.7): magmatic explosive + effusive dominated, phreatomagmatic dominated, and a broad group with a range of all eruptive types (Fig. 5.7).

Overall, 21.2% of the AVF volcanoes had simple, single-type eruptions, 28.8% were compound eruptions; and 50% were complex (Fig. 5.8A). With larger complexity, larger areas were affected. The median areas affected by single, compound and complex eruptive histories were 0.42 km<sup>2</sup>, 1.13 km<sup>2</sup> and 2.48 km<sup>2</sup>, respectively (Fig. 5.8B). There is also a trend of increasing volume and increasing variability of eruption style in the course of volcanic activity. The median volumes were  $2.20 \times 10^6$  m<sup>3</sup>,  $5.67 \times 10^6$  m<sup>3</sup> and  $15.39 \times 10^6$  m<sup>3</sup> for single, compound and complex eruption histories, respectively (Fig. 5.8B).

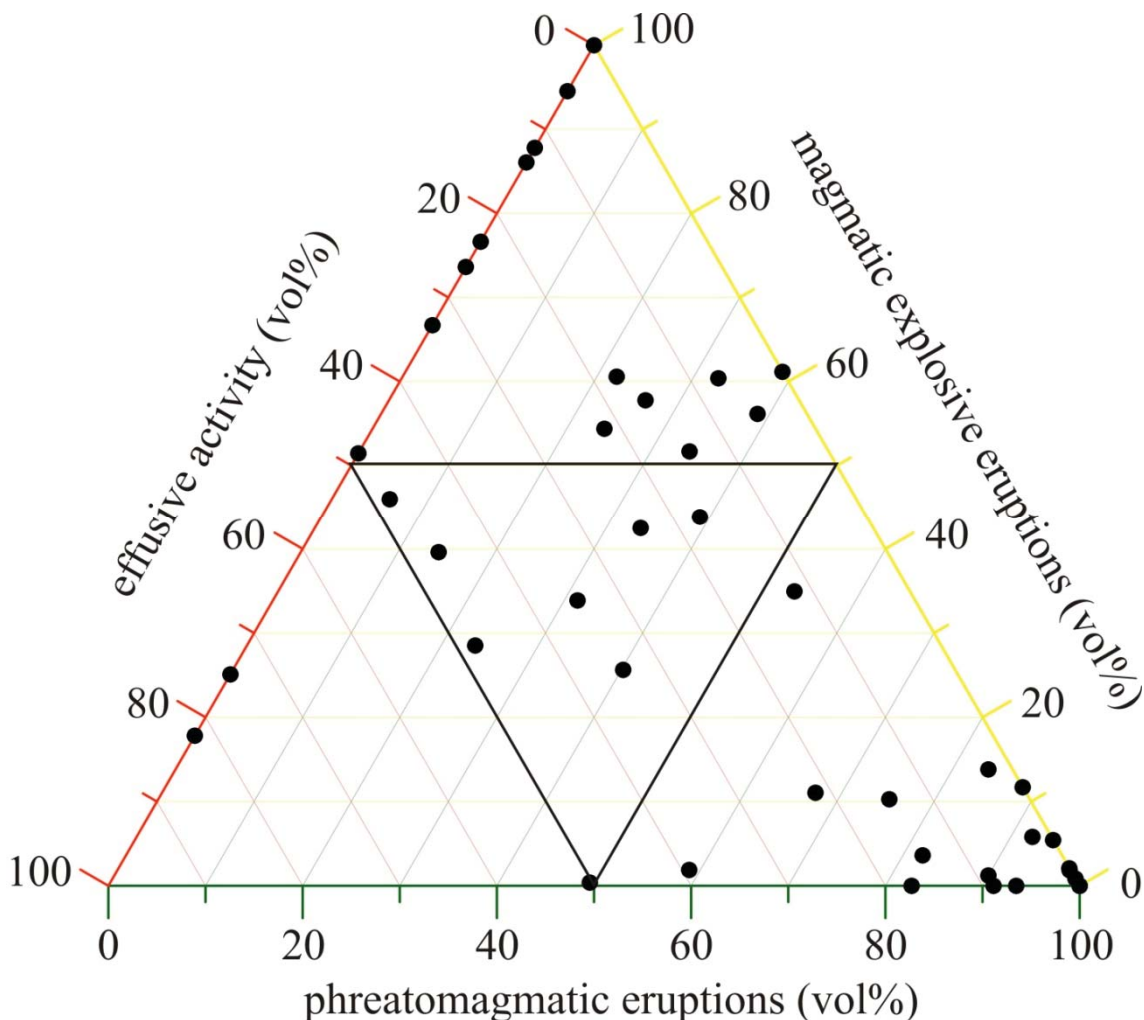


**Figure 5.7** Ternary diagram for proportional volumes for three types of eruption styles in the AVF, with those affected by phreatomagmatic and Surtseyan eruptions, magmatic explosive eruptions (fire-fountaining and Strombolian types), and magmatic effusive eruptions. The data were normalised to the mean of each eruptive unit.

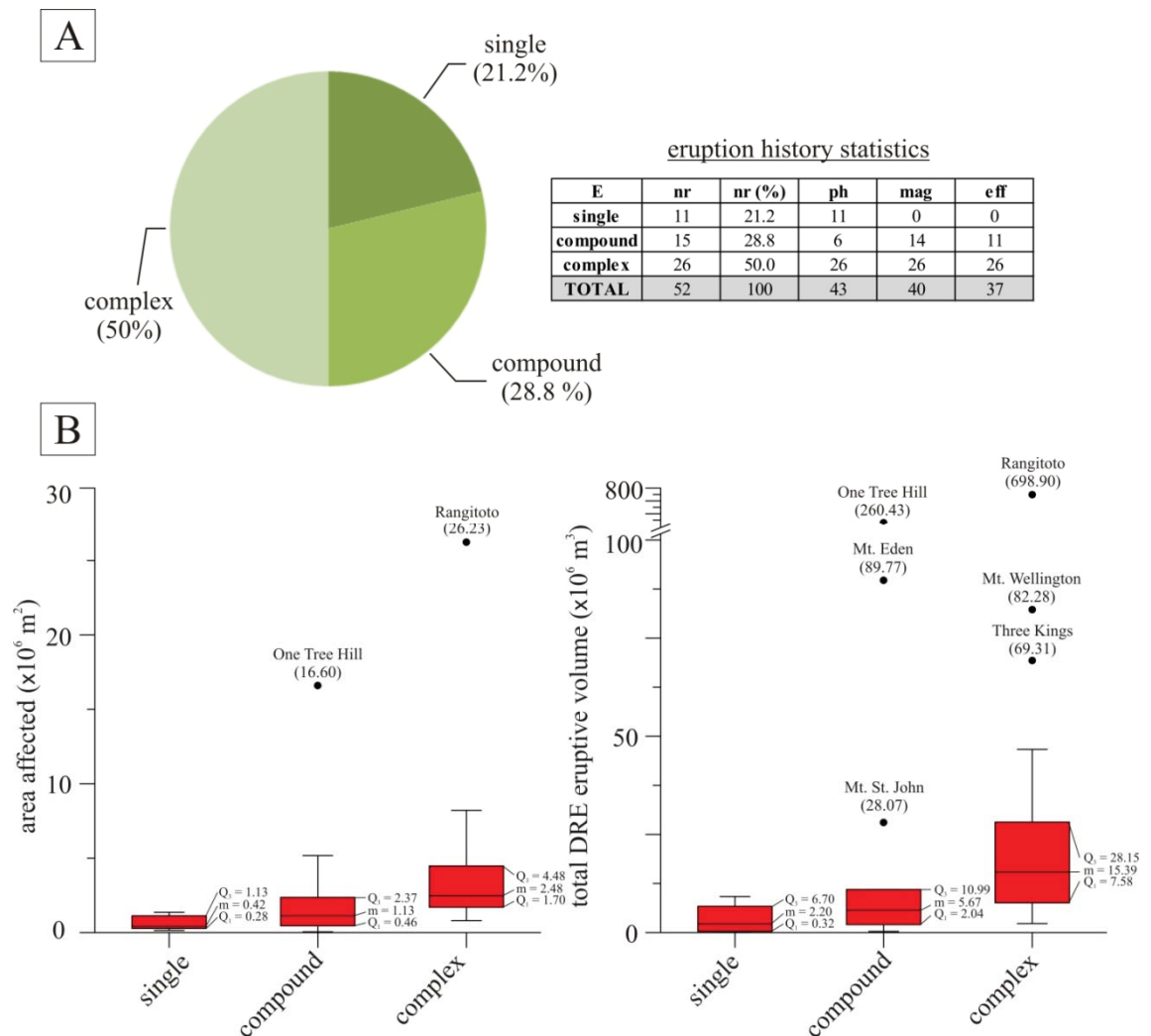


**Figure 5.8** (A) Proportions of single, compound and complex eruptive histories in the AVF, and their dominant eruption styles. (B) Box plot graphs for the area affected (left) and eruptive volumes (right graph) in relation to eruptive histories. The lower quartile ( $Q_1$ ), median ( $m$ ), upper quartile ( $Q_3$ ), and outliers' values are shown.

Most AVF eruptions had initial phreatomagmatic vent opening phases, especially volcanoes located in the southern part of the Manukau Lowlands (Fig. 5.9). Neither magmatic nor effusive eruption styles occurred alone, but were the last phases of compound or complex eruptive histories (Figs. 5.4, 5.8 and 5.9). Explosive magmatic eruptions occurred over most parts of the AVF, except in the centre of the Manukau Lowlands (Figs. 5.4 and 5.9). Complex eruptive histories were also found throughout the whole field (Fig. 5.9).

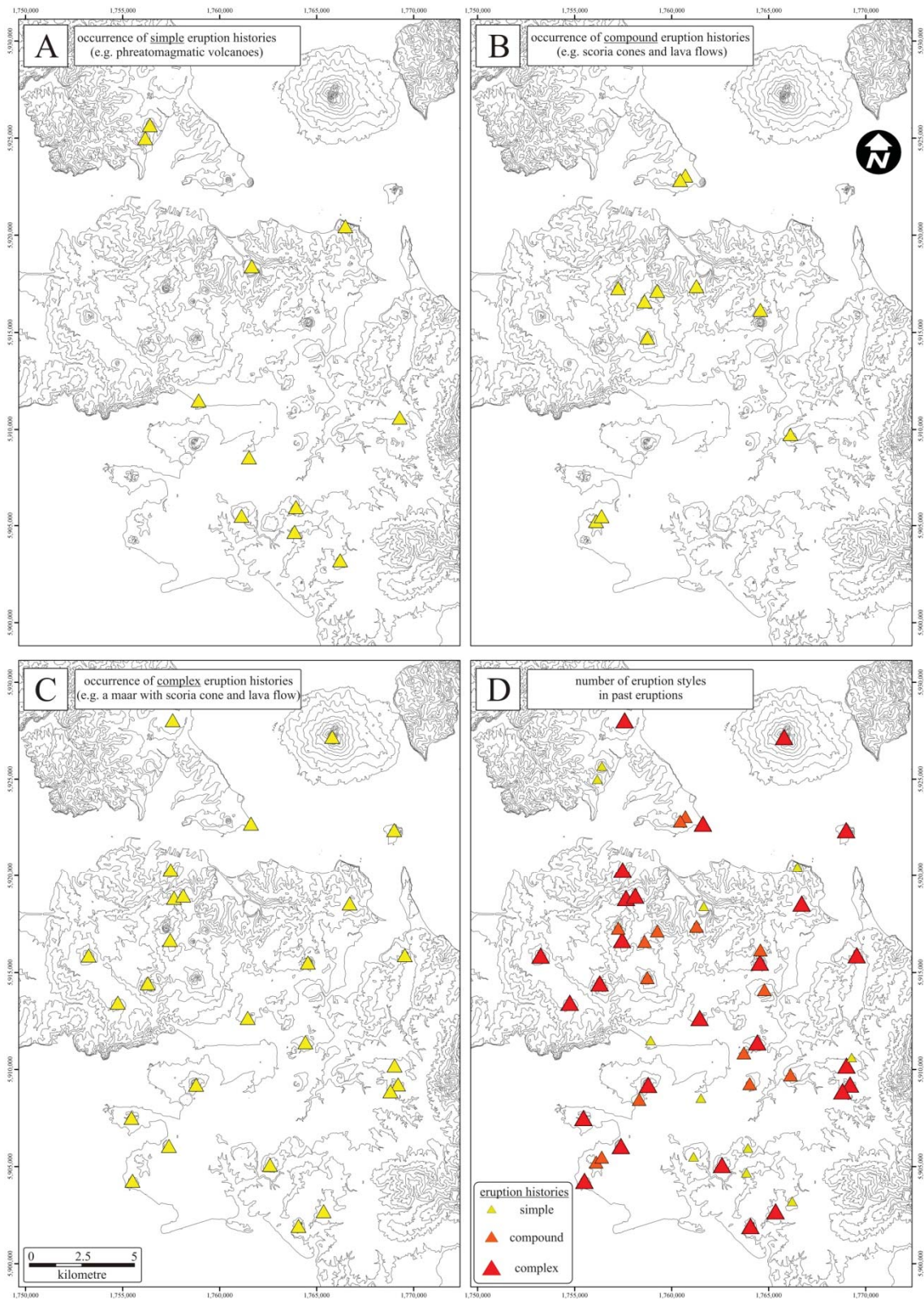


**Figure 5.9** Spatial distributions of single (A), compound (B), and complex eruption histories (C), as well as the number of eruption styles (D) in the AVF.

## 5.3.2. Influences on AVF eruptive sequences

The phreatomagmatic eruption style is influenced to the largest degree by environmental factors; hence the volumes of this phase in the AVF eruptions were plotted as a function of four hypothesised environmental influencing factors: (1) the thickness of the inferred water-saturated host sediments, (2) distance from the coastline, (3) distance from faults, as well as (4) the pre-eruptive topographic elevation (Figs. 5.10). The phreatomagmatic component volumes of most eruptive centres lie within a narrow range ( $\leq 0.01 \text{ km}^3$ ; except Pupuke which is an outlier), but show a large scatter without any initially obvious trend in relation to any of the four influencing factors (Figs. 5.10).

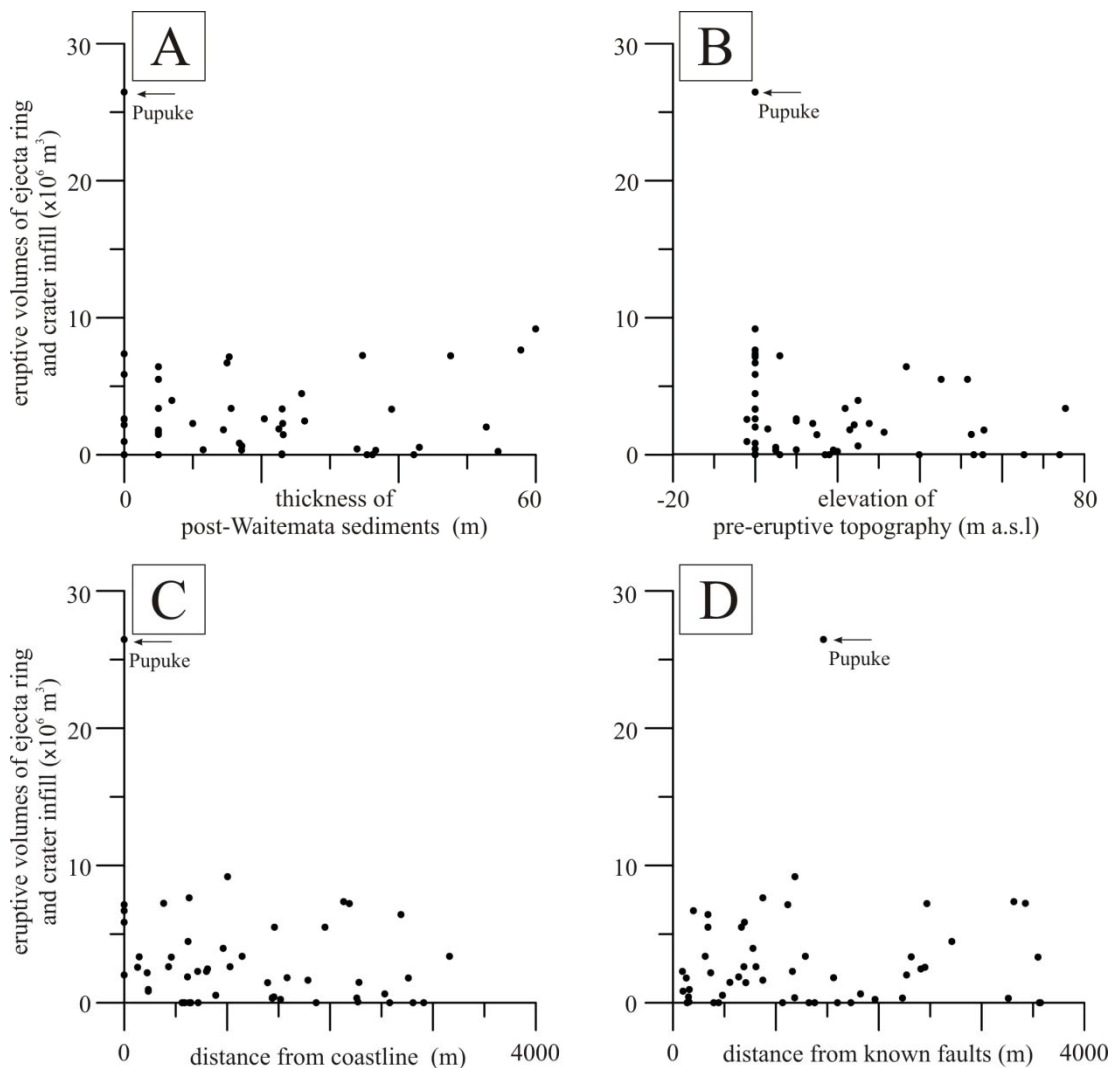


**Figure 5.10** Scatter graphs of phreatomagmatic vent-opening volumes of the AVF's volcanoes in relation to the (A) thickness of post-Waiemata non-volcanic sediments, (B) pre-eruptive elevation, (C) distance from the present coastline, and (D) distance from known fault lines.

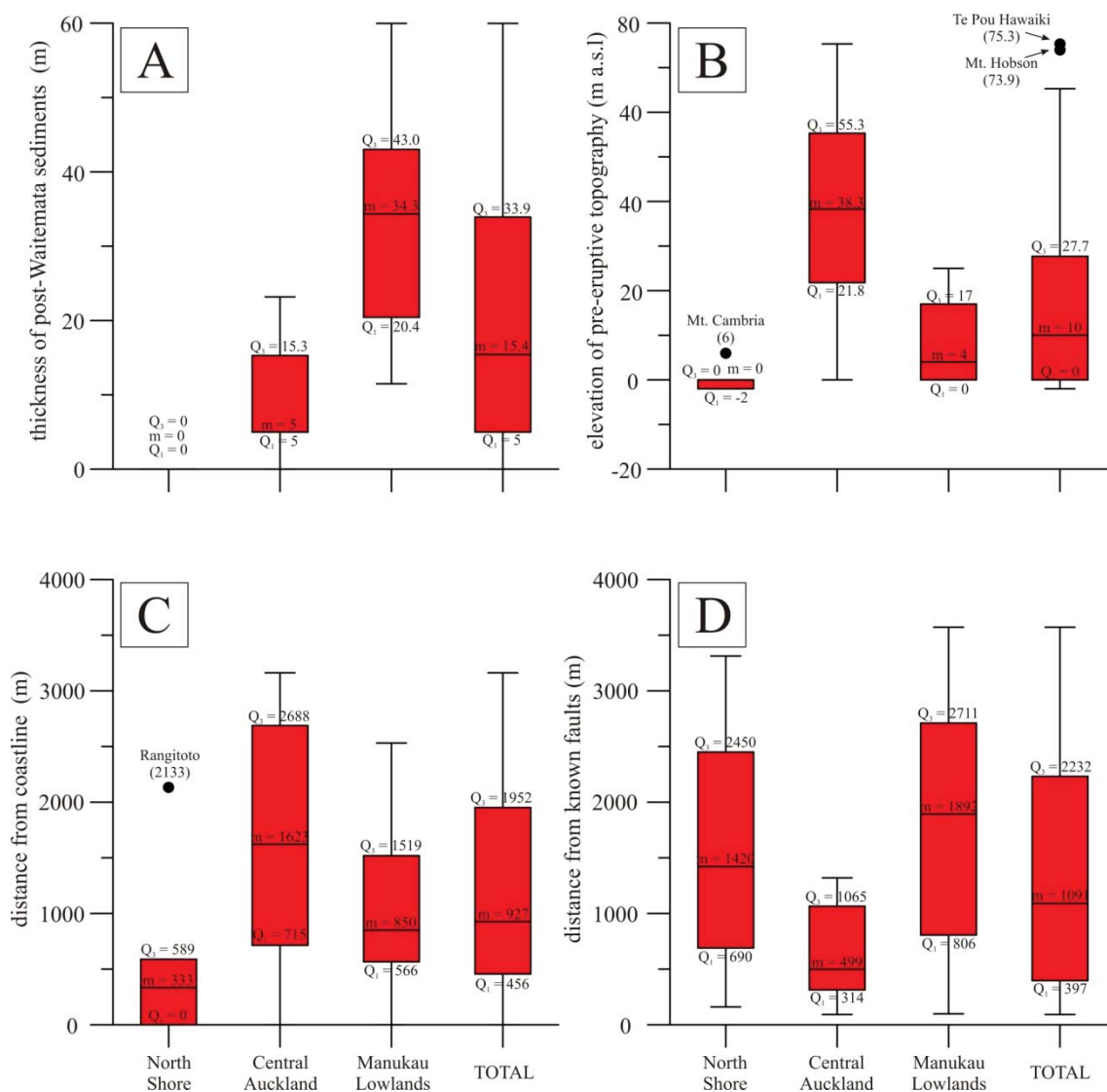


**Figure 5.11** Box plots showing the three sub-areas of the AVF and the total AVF in relation to (A) thickness of post-Waitemata non-volcanic sediments, (B) pre-eruptive elevation, (C) distance from the present coastline, and (D) distance from known fault lines. Note that in graph A, the thickness is inferred to be  $\leq 5$  m under volcanoes in the Central Auckland region.

There is a greater difference seen in the factors when the phreatomagmatic volume data are analysed with respect to the three geologically and topographically distinct parts of the AVF (Figs. 5.11 and 5.12; and Table 5.1). The thickness of the post-Waitemata saturated and poorly to unconsolidated sediment cover clearly differs in the three geographical divisions (Fig. 5.11A), in addition to the pre-eruptive elevation (Fig. 5.11B), the distance to the coastline (Fig. 5.11C) and fault lines (Fig. 5.11D).

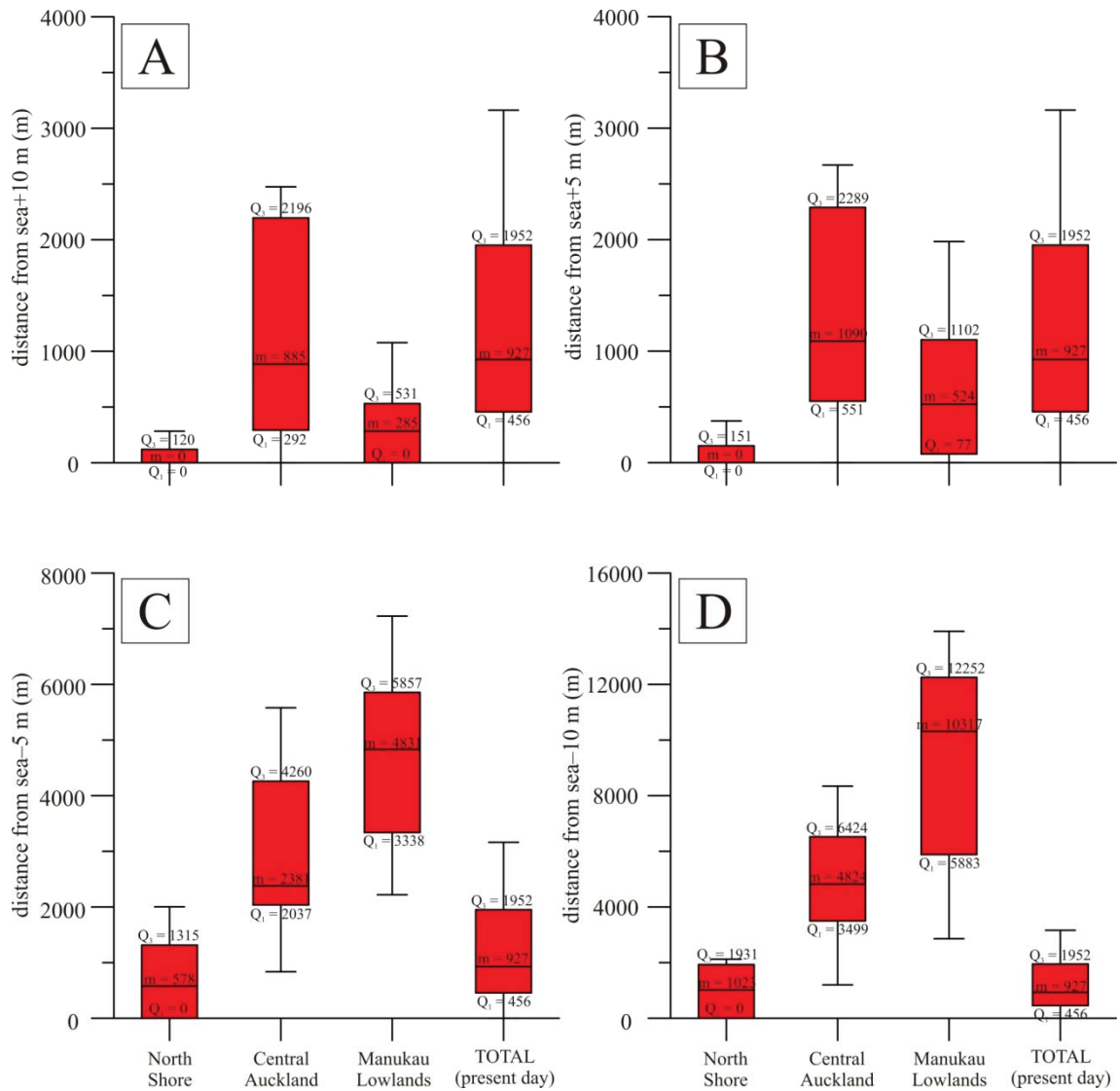


**Figure 5.12** Box plots showing the distance from the coast to the volcanoes from three distinct sub-areas of the AVF and the total field in relation to (A) a sea level higher than the present day by 10 m, and (B) 5 m, as well as (C) a sea level lower than the present day by 5 m and (D) by 10 m.

The current sea level is higher than the level throughout the formation of most, if not all, of the AVF’s volcanoes. Modelled paleo-sea levels during glacial periods (e.g. -5 and -10 m) show that the proximity to the coastline could have been much larger ( $\leq 16$  km; Fig. 5.12).

The distances between vents and known fault lines reveal similar differences between the sub-areas of the AVF (Fig. 5.11D), although in the Manukau Lowlands some of the faults may be masked by the thick post-Waitemata sediment cover. Some volcanoes are located very close to known fault lines, such as Orakei Basin (ca. 200 m; Table 5.1), while others are located as far as 3.6 km away, such as Pukeiti (Table 5.1).

## 5.4. Discussion

### 5.4.1. Factors influencing eruption style

The AVF volcanoes have erupted a confined range of basaltic magmas; however, within the alkaline basalt field, each volcanic centre has erupted a broad range of basalt compositions, sourced from variable depths, including in two cases, alkaline to subalkaline compositions (Huang et al., 1997; Smith et al., 2008; Needham et al., 2011; McGee et al., 2013). Increasing compositional variability correlates with increasing eruptive volume (McGee et al., 2013), suggesting a possible internal influence on eruption styles. McGee et al. (2013) observed patterns of trace element and Sr–Nd–Pb isotopic trends that can be explained by an interplay between asthenospheric and subduction-metasomatised lithospheric mantle sources. This leads to a correlation between the degree of melting and total eruptive volumes (McGee et al., 2013). A larger volume of erupted magma not only leads to a greater range of compositions, but it also increases the likelihood of an eruption moving from a phreatomagmatic phase into magmatic explosive and effusive phases. An example of this sequence can be seen in a comparison of simple phreatomagmatic Pukaki (ca. 84 ka), involving only  $9.2 \times 10^6 \text{ m}^3$  DRE magma (Table 5.1), with its larger neighbour, Crater Hill ( $24 \times 10^6 \text{ m}^3$ ), with transitional phreatomagmatic to magmatic eruption phases (Houghton et al., 1999). With larger magma volumes, there is an increased likelihood of conduit sealing over the course of an eruption, which leads to scoria-cone formation and lava flows. Conduit sealing may be coupled with increase of magma flux (Lorenz, 1986; Németh et al., 2008; Valentine and White, 2012). Additional influences on eruption continuity from geochemical variability or compositional changes (e.g. Brenna et al., 2011) cannot be ruled out in the AVF, but this needs further analysis, beyond the scope of this study.

The environmental influencing factors, such as the availability of groundwater, water saturated sediment, or faulting, have been frequently described as influencing the eruption styles of monogenetic volcanoes (Chough and Sohn, 1990; White, 1991; 1996; Connor et al., 2000). For the AVF, external factors including the abundance of water saturated soft-sediment cover, proximity of sea water, tectonic settings, as well as the overall topography, were investigated. These may readily modify the eruption styles, with several AVF volcanoes showing very different eruption sequences, despite having similar erupted volumes (e.g. compare Mt. Hobson, Mt. Roskill and Pukaki; Table 5.1).

This suggests that the external environmental factors most strongly influenced the initial vent opening phases of eruptions (e.g. Mt. Hobson vs. Pukaki), and the potential water-supply to a vent site may have strongly influenced the duration of the highly explosive phreatomagmatic phases (e.g. Mt. Roskill vs. Pukaki).

#### 5.4.2. A spatial model for distribution of factors influencing eruption style

The examined external environmental factors that may influence eruptive style correlate only poorly with the style-partitioned erupted volumes, mostly due to the small sample number and the variability in overall erupted volumes (Figs. 5.10). More robust trends may emerge when examining larger volcanic fields with more vents. For the AVF, however, this variability also highlights the lack of any single factor influencing the dominant eruption styles. It may be that all potential factors correlate to some degree. Many of the factors treated separately here are in fact related, including topography with coastline and fault patterns and hydrology with elevation. Consequently, these vent-environment and geological features must be considered in volcanic hazard assessment collectively.

At the volcanic edifice-scale, there are examples in which there might have been only a single influencing condition over the course of construction, such as Pukaki. However, these are the exception rather than the rule. Based on the past volcanoes in the AVF, the environmental factors show more distinctive differences in their influence between sub-regions of the field (e.g. Fig. 5.11 and 5.12). The general features that emerge from a comparison of these conditions in the three distinct areas were used to define a simple model for the spatial distribution of potential eruption styles in the AVF (Fig. 5.13).

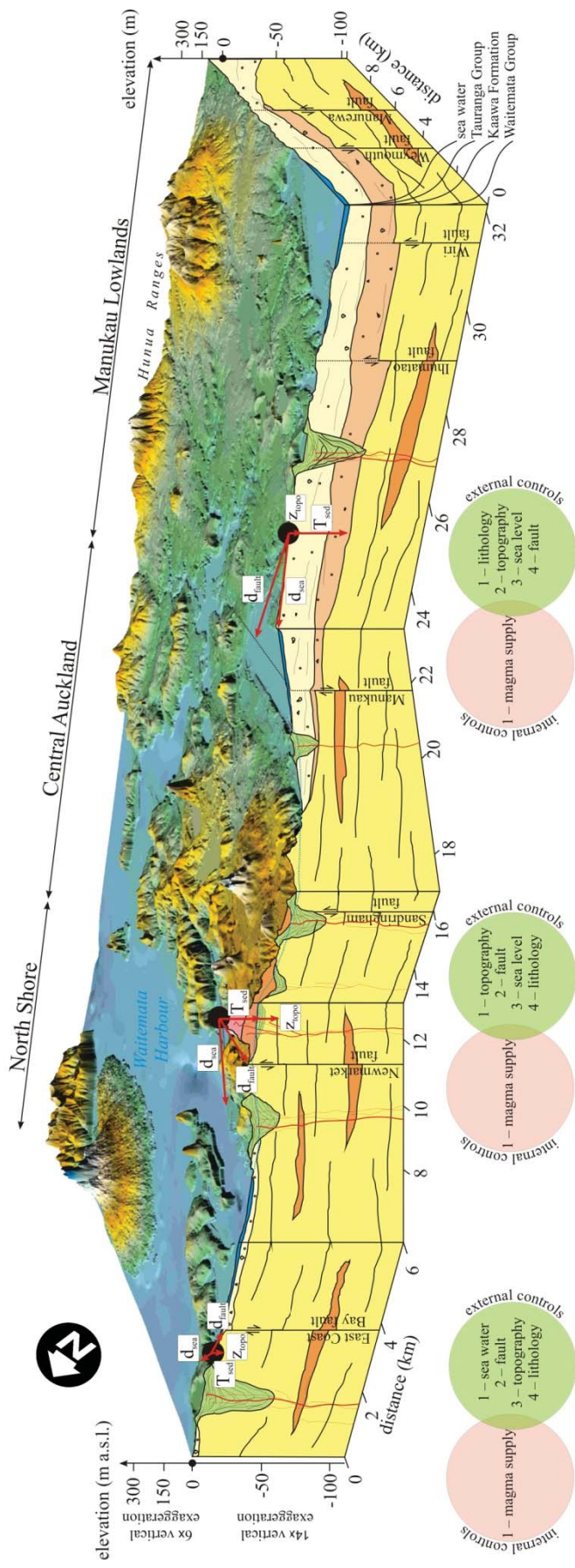


**Figure 5.13** A model for internal (red circles) and external (green circles) factors influencing eruption styles in the AVF. Future hypothesised eruption site examples are shown as black dots with the four environmental factors ( $d_{\text{sea}}$  – distance from sea;  $d_{\text{fault}}$  – distance from known fault lines;  $Z_{\text{topo}}$  – topographic position, as well as  $h_{\text{wat}}$  – thickness of water-bearing units). The significance of each environmental factor varies between parts of the field, and there is no sole controlling factor for eruption styles and histories. The listed external environmental factors are in the order of inferred importance. Note the excavation depth of the maar volcanoes is not constrained well, but it is inferred to be very shallow, 50-100 m (Cassidy et al., 2007; Agustín-Flores et al., 2014). The fault location data are after Kenny et al. (2012).

In this model, the areas covered by sea water have not been accounted for, and future iterations of this work will require specific inputs of the influence of surface water depth on eruption style. In the North Shore, the coastal, low-elevation influence is largest, along with fractured and faulted Waitemata country rocks (Fig. 5.13).

In the Central Auckland area, the higher elevation, due to block faulting of the Waitemata country rocks (Kenny et al., 2012), is the primary influence, leading to more magmatic explosive and effusive eruptions (Fig. 5.13). Exceptions in this region are eruptions sited in areas of thick alluvium [e.g. Orakei Basin (Németh et al., 2012)] and close proximity to the coastline.

In the Manukau Lowlands, excluding the Hunua Ranges (Fig. 5.13), the soft-sediment and high groundwater table, coupled with low elevation, are the largest influencing factors, leading dominantly to eruptions that had at least phreatomagmatic vent-opening phases, if not entirely phreatomagmatic. In the Manukau Lowlands, the eventual erupted volume of pyroclastic materials during phreatomagmatic eruptions correlates strongly with the depth of loose to semi-consolidated soft-sediments, such as Tauranga Group and Kaawa Formation (e.g. Agustín-Flores et al., 2014). This can be further seen in the relationship between some of the phreatomagmatic volumes from the Manukau Lowlands as a function of the thickness of post-Waitemata soft-sediment basin infill beds (Fig. 5.14). Plotting these variables, the equation of the line is expressed as (Fig. 5.14):

$$V_{\text{ejecta+crater}} = 0.163h_{\text{alluvium}} - 0.968 \quad (5.6)$$

where  $h_{\text{alluvium}}$  is the thickness of post-Waitemata sediments. This linear relationship shows an  $R^2$  value of 0.8, but several exceptions must be taken into account. Some volcanoes do not fit the trend despite being erupted over thick post-Waitemata sediments, simply because too little magma was erupted (e.g. Mangere Lagoon; Fig. 5.14). Acknowledging the outliers to this relationship does not stop it being useful as an indicator of the potential of a given location to sustain phreatomagmatic eruptions, assuming enough magma is available.

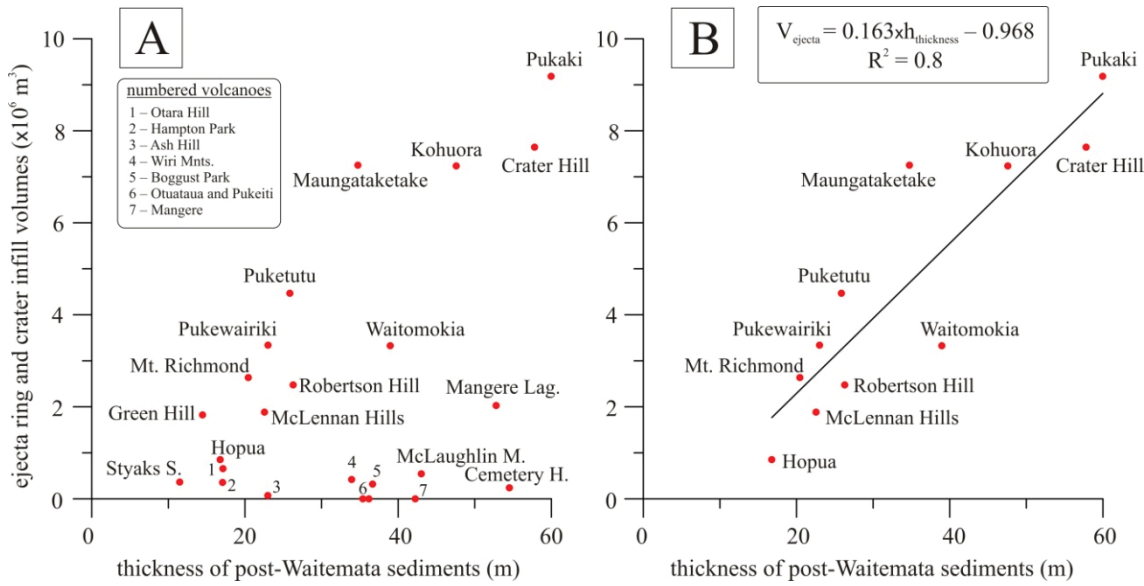


**Figure 5.14** The relationship between thickness of post-Waitemata non-volcanic sediments and the eruptive volumes of ejecta rings and crater infills for all volcanoes in the Manukau Lowlands (A), and with the largest volume volcanoes of the area (B). Note that all volcanoes located under the predicted line have extremely small erupted volumes, with large extents of anthropogenic modification.

### 5.5. Conclusion

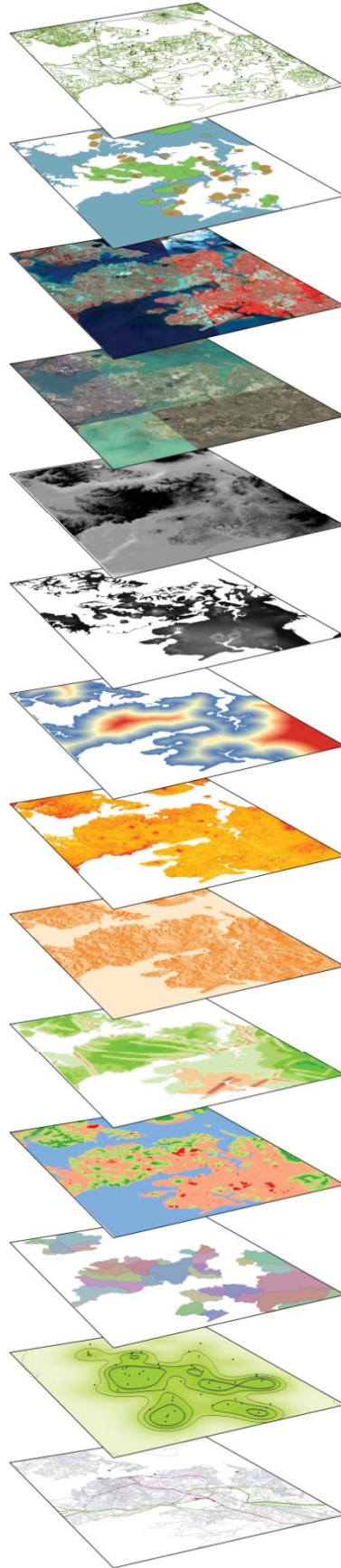
The spatial distribution of different eruption styles or eruptive histories can be systematically related to the landscape, tectonic setting, climate change and shallow geo-hydrology in the AVF (e.g. Fig. 5.13). Despite a great deal of scatter in relationships due to the small event numbers and the large variability in erupted volumes, the AVF data show that there are significant differences in the site-specific geological and hydrological factors between three segments of the field (North Shore, Central Auckland and the Manukau Lowlands). Of the eruption products, lava flows cover the largest area in the AVF, but these are more likely to be a function of magma volume, with larger eruptions ( $\geq 0.05 \text{ km}^3$ ) most readily transitioning from phreatomagmatic to magmatic explosive and effusive phases.

Individual AVF eruption centre histories show a clear dual influence from internal and external environmental factors. The internal factors (e.g. magma supply) mostly determine whether a simple one-phase eruption occurs, or if a complex eruption with multiple phases and styles ensues. On the other hand, the external factors (e.g. lithology, sea water level, faulting of the basement, topographic position) influence the form of at least the vent-opening phase, and possibly the entire duration of the eruption. In the case

of the AVF, the external influences on the eruption styles are seemingly more prominent than the internal ones, but this does not mean external influences work alone. This information shows that by evaluating pre-eruption conditions across a volcanic field such as the AVF, the susceptibility for eruptions of various styles and hazard potential can be mapped.

Forecasting the location of a monogenetic volcanic event is challenging, due to the unique nature of melt extraction at the source. In the AVF, the spatial distribution of past volcanoes is random (e.g. Bebbington, 2013; Le Corvec et al., 2013c). Consequently, forecasting hazard could be improved by developing field-specific conceptual models for eruption style susceptibility, based on geological, hydrological and topographic parameters. These factors need to be taken into account with time-varying features of the area, including sea-level changes due to climate change, or long-term evolution in processes such as rainfall, uplift and faulting/stress regimes.





Chapter 6  
susceptibility mapping

# 06 / lava flow susceptibility

This Chapter aims to demonstrate some practical aspects of quantitative analysis of monogenetic volcanoes. In this Chapter a vent-independent lava flow hazard mapping method is developed using adaptive topographic characterisation in order to reveal spatial susceptibility to lava flow inundation in a future effusive event. The previously calculated quantitative data (e.g. eruptive volumes, lava flow thicknesses) are used as inputs to seek topographic barriers higher than an average lava flow thickness.

Supplementary data for this Chapter are in Appendix B.

## Chapter contents

6.1. Introduction.....	154
6.2. Materials and methods.....	157
6.2.1. LiDAR survey and DSM preparation.....	157
6.2.2. Lava flow parameters .....	158
6.2.3. Hydrological channel extraction .....	162
6.2.4. Topographic classification of zones subject to lava flow inundation .....	163
6.2.5. Watershed characteristics .....	167
6.3. Results .....	168
6.3.1. Characteristics of past lava flows.....	168
6.3.2. Characteristics of present topography .....	170
6.4. Discussion.....	173
6.4.1. Lava flow susceptibility.....	178
6.4.2. Watershed characteristics .....	179
6.4.3. Evaluation of the method and its limitations .....	181
6.6. Conclusions.....	183

This Chapter is based on a published paper (Appendix B):

Kereszturi, G., Procter, J., Cronin, J.S., Németh, K., Bebbington, M. and Lindsay, J., 2012. LiDAR-based quantification of lava flow susceptibility in the City of Auckland (New Zealand). *Remote Sensing of Environment*, 125: pp. 198-213.  
*DOI:10.1016/j.rse.2012.07.015*

Participating authors:

**Gabor Kereszturi** (field work, data processing, method development, manuscript writing and editing)

**Jonathan Procter** (manuscript editing and discussion)

**Shane J. Cronin** (manuscript editing and discussion)

**Károly Németh** (manuscript editing and discussion)

**Mark Bebbington** (manuscript editing and discussion, help in the kernel density calculations)

**Jan M. Lindsay** (manuscript editing and discussion)

## Chapter Six – Lava flow susceptibility mapping

### 6.1. Introduction

Basaltic, monogenetic volcanoes often produce lava flows with a wide range in length and volumetric size (Felpeto et al., 2001; Harris and Rowland, 2001; Tucker and Scott, 2009; Kereszturi et al., 2013b). The length of lava flows is mostly dependent on the rate of effusion (Walker, 1973; Harris et al., 2007b), the total volume (Stasiuk and Jaupart, 1997), the crystallinity and viscosity (Dragoni and Tallarico, 1994; Griffiths, 2000), the slope angle of the substratum (Favalli et al., 2009d) and other topographic features, such as valleys (Rodriguez-Gonzalez et al., 2011). To quantify and express such controlling conditions on lava flow emplacement, which are the basic inputs required of lava flow simulation codes, remotely sensed data are commonly used. For detection of active lava flows, the thermal bands of various satellites, such as MODerate resolution Imaging Spectroradiometer (MODIS), Advanced Spaceborne Thermal Emission and Reflection radiometer (ASTER) and LANDSAT Thematic Mapper are used (Harris et al., 1998; Wright et al., 2004; Pieri and Abrams, 2005; Lombardo and Buongiorno, 2006; Ganci et al., 2012). These remote sensing data can provide information about the time-averaged discharge rates of a lava flow, which is one of the major requirements of lava flow simulations.

Lava flows related to monogenetic eruptions are commonly small in volume ( $\leq 1 \text{ km}^3$ ) and affect small areas (a few  $\text{km}^2$ ). This small size requires at least medium (10–50 m) to high resolution ( $\leq 10 \text{ m}$ ) imagery to map them accurately. Many types of topographic data in the form of Digital Surface Models (DSM) or Digital Terrain Model (DTM) can be used to calculate lava flow volumes, including Light Detection And Ranging (LiDAR) DSM (Harris et al., 2010), Interferometric Synthetic Aperture Radar (InSAR) (Mouginis-Mark and Garbeil, 2005), ASTER stereo image-based DTM (Hirano et al., 2003) and Shuttle Radar Topography Mission (SRTM) derived DTM (Kervyn et al., 2008) or contour-based Digital Elevation Model (DEM) (Kereszturi and Németh, 2012b). These volumes could also be converted into time-averaged discharge rates (Harris and Baloga, 2009; Favalli et al., 2010; Harris et al., 2010), but the exact duration of the volcanic activity is required. In the case of monogenetic volcanic fields,

where volcanic eruptions are less frequent than at polygenetic volcanoes, there is no information about the exact duration of past eruptions, posing some problems for the use of time-averaged discharge rates as a calibrator of lava flow simulations.

Apart from the lava flow parameterization, the topography (represented digitally in a DSM or DEM) plays an important role in the emplacement of lava flows (Favalli et al., 2009d). The topography may modify the flow emplacement mechanism and channelise lava flows if the eruptive vent is located in a highly dissected topography, such as the flank of a polygenetic volcano (Mazzarini et al., 2005). The techniques to quantify and simulate lava flow behaviour described above used various algorithms to model the hazard related to lava flows from thermorheological- to topographic-dominated models. The thermorheological-dependent models require many input parameters including density, heat-preservation and composition (Harris and Rowland, 2001; Crisci et al., 2004; Hidaka et al., 2005; Vicari et al., 2007; Del Negro et al., 2008). More topography-centred codes, such as DOWNFLOW and LAZSLO are based on the probabilistic methods to establish lava flow pathways over a DSM/DTM/DEM (Felpeto et al., 2001; Favalli et al., 2005; Bonne et al., 2008; Tarquini and Favalli, 2011; Connor et al., 2012).

Typically, lava flow simulations are performed for locations with a known vent on the flanks of a large, polygenetic volcano, e.g. Etna in Italy, or Kilauea in Hawaii (Harris and Rowland, 2001; Favalli et al., 2009e; Herault et al., 2009). On the flanks of a polygenetic volcano, the likelihood of vent-formation is significantly higher along extensional rift zones (Favalli et al., 2009e) making volcanic eruption forecasting in a particular location more accurate than in many monogenetic volcanic fields. The volcanism in Auckland in New Zealand differs from large, polygenetic volcanoes because future eruptions will likely take place within a densely populated city, there are no rift zones that indicate areas of elevated hazard, and the future vent area is therefore unknown, and due to the generally low-lying topography, there are few opportunities to use mitigation options, such as artificial dams (Barberi et al., 1993; Scifoni et al., 2010). The Auckland Volcanic Field (AVF) consists of at least 52 monogenetic maars, tuff rings and scoria cones that erupted over the last 250 ky (Molloy et al., 2009; Bebbington and Cronin, 2011). The entire field (336 km<sup>2</sup>) is located within the area of the City of Auckland, with a total population of ~1.4 million (Fig. 6.1). Hence, future vent forming eruptions will very likely occur within the city limits or its outskirts, allowing few

mitigation or preparation options. The majority of previous scoria cones and lava flows are located in the heart of the city, upon a presently slightly elevated ridge-system (Fig. 6.1).

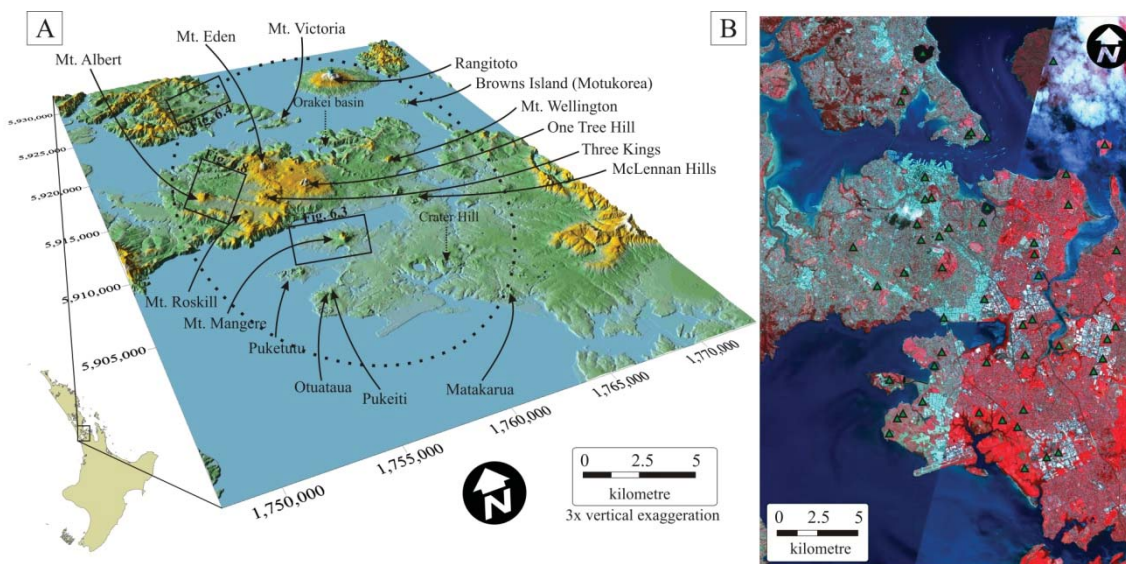


**Figure 6.1** (A) An overview LiDAR-based DSM of the Auckland region with the location of studied volcanic centres. Note that a phreatomagmatic maar volcano, Orakei Basin, and a complex monogenetic volcano with initial phreatomagmatic and late magmatic stage, Crater Hill, both mentioned in the text, are indicated by the dashed arrows. The dashed ellipsoid shows the extent of the Auckland Volcanic Field (after Spörli and Eastwood, 1997). The coordinates are given in New Zealand Transverse Mercator (NZTM2000). The solid boxes indicate the location of Figs. 6.3, 6.4 and 6.8. (B) Location of the 52 eruptive centres (green triangles) within the AVF overlaid on a false-colour multispectral SPOT-5 satellite image. Note that the areas in grey to green are the urban and heavily populated parts of Auckland, while the red colour shows distribution of vegetated areas, such as forest or park.

Previous studies have mostly focused on determining the location, nature and the possible effect of the future eruptions on the city (Edbrooke et al., 2003; Magill and Blong, 2005a; Lindsay et al., 2010; Bebbington and Cronin, 2011). Detailed evaluation of lava flow hazards and delimitation of potentially safe places from lava flow inundation have not yet been attempted, in spite of the relatively high level of their potential risk (Magill and Blong, 2005b). Due the high uncertainty in the location of a new vent in Auckland, the simulation of lava flow pathways from a single source is not appropriate for monogenetic field hazard analysis. In the present investigation, a vent-location independent lava flow susceptibility mapping technique is presented. This method requires only two types of information: morphometry of past lava flows, such as area, bulk volume and length characteristics, and digital representation of the underlying terrain (i.e. DSM/DTM/DEM). In the present study, a resampled airborne-based LiDAR

DSM was used to calculate morphometric parameters of lava flows and delimit those areas which are in relatively safe positions from lava flows using adaptive topographic classification. Based on this vent-location-independent input data, a generalised lava flow susceptibility map was created for the AVF using Geographical Information System (GIS).

## 6.2. Materials and methods

### 6.2.1. LiDAR survey and DSM preparation

Spot heights were obtained by Fugro Spatial Solutions and New Zealand Aerial Mapping Limited companies for the Auckland City Council using two different types of aircraft-mounted LiDAR sensors. A Leica Airborne Laser Scanner 50 (ALS50) and an Optech Airborne Laser Terrain Mapper 3100-EA (ALTM3100) were used in surveys in 2005–2006 and 2008, respectively. Two types of surveys were carried out in each of these years, for urban/intertidal and for rural areas, with different LiDAR settings. The survey for the urban and intertidal (captured at low tide) areas was carried out with an average flight height of 1330 m and 1200 m above ground level at 150 (or 77.1 m/s) and 130 knots (or 66.8 m/s), respectively. These two LiDAR sensors operated between 73 kHz and 70 kHz pulse repetition frequency and 39 and 40 Hz scanning frequency with scanning half-angle of  $\pm 20^\circ$  and  $\pm 22^\circ$  resulting swath widths of 960 m and 968 m, respectively. The accuracy of the LiDAR scanners, without GPS errors, are estimated at 0.20 m at 1  $\sigma$  horizontally and 0.15 m at 1  $\sigma$  vertically for the Leica ALS50, while 0.21 m at 1  $\sigma$  (calculated as  $1/5500 \times \text{flight height in m}$ ) horizontally and 0.11 m at 1  $\sigma$  vertically for the Optech ALTM3100. The mean ground point density was about 1 point per  $\text{m}^2$ . The rural survey was carried out with average flight heights of 2000 m above ground level at 150 knots (or 77.1 m/s) using the Leica ALS50. The sensor setting was 54.8 kHz pulse repetition frequency, 31 Hz scanning frequency with a scanning half-angle of  $\pm 20^\circ$ . This resulted in a 1455 m swath width. The scanning accuracy was 0.25 m at 1  $\sigma$  horizontally and 0.2 m at 1  $\sigma$  vertically. The mean ground point density ranged between 0.04 to 0.15 point per  $\text{m}^2$  over areas, such as Rangitoto, Motutapu and Motukorea Islands (Fig. 6.1). Post-processing including filtering and bare-earth point detection of the point cloud was performed by the data provider, Fugro Spatial Solutions ([www.fugrospatial.com.au](http://www.fugrospatial.com.au)).

In the construction of the DSM, only bare-ground spot heights (last returns) were used. Spot heights on buildings and other anthropogenic features were removed, which decreased the original point density to 0.5 point per m<sup>2</sup>. The DSM was created by the Triangulated Irregular Network (TIN) method and subsequently converted into a grid-based DSM with a 2×2 m grid cell size (Fig. 6.2). To enable ready calculations on this dataset, the original 2 m resolution LiDAR DSM (12 785 × 18 366 cells) was resampled into a 10 m resolution for the bulk volume calculations and 20 m resolution for the hydrologic channel extraction by the nearest neighbour method (Fig. 6.2). Before hydrologic channel extraction, the DSM was smoothed by an average 3×3 (60×60 m) moving window in order to avoid noise, such as due to vegetation filtering, and enhance computation time (Fig. 6.2).

### 6.2.2. Lava flow parameters

During a monogenetic eruption, multiple lava flows (or smaller lava lobes) can form which usually pile on top of each other forming sequences of lava flows (Self et al., 1998; Wantim et al., 2011). In the present study, the final size and dimension of lava flows were measured and treated as a single unit, regardless of whether or not they were formed from multiple smaller lava flows (Fig. 6.3). In addition, just those lava flows were considered which are visible in the field, having mappable boundaries. There are a few buried lava flows by Holocene sediments and/or volcanics, such as lava flow from Mt. St. John or Green Mountain, but they are discarded from the calculation because of the high uncertainty in their parameterization.

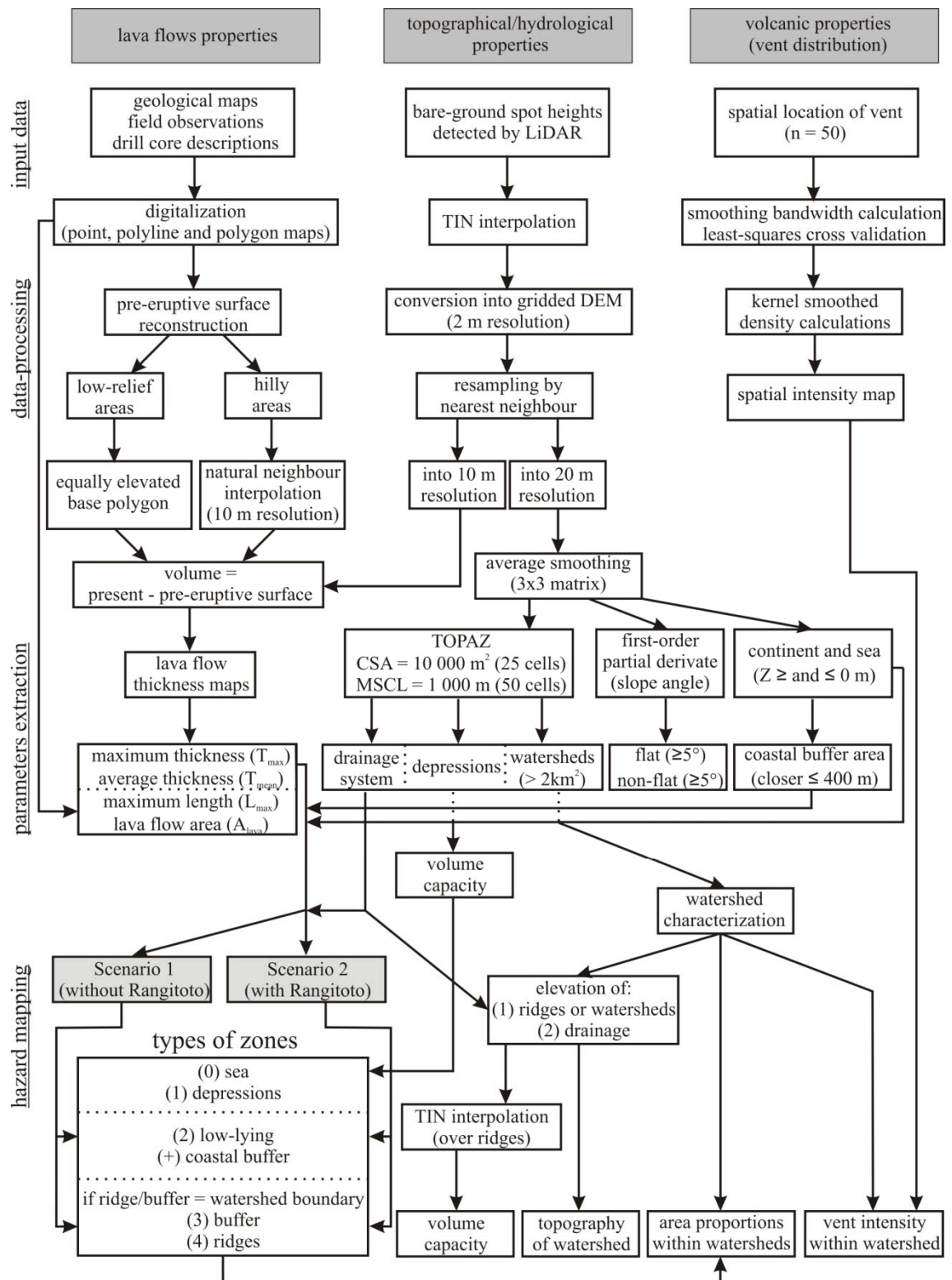


Figure 6.2 Flow diagram for input data, data processing and results

The polygon of each lava flow was determined on the basis of previously published geological maps (Kermode, 1992; Hayward et al., 2011), aerial photographs and field observations (Figs. 6.2 and 6.3). The area of the lava flow ( $A_{lava}$ ) was derived

directly from the area of the digitised polygon (Fig. 6.3). The length of the lava flows ( $L_{max}$ ) was calculated from the point maps at equal spacings of 0.5 m, which were converted from the boundary lines of each lava flow. The centre point of each source volcano was defined as a centre point of the local minima (i.e. last closed contour line at the crater bottom of each edifice) or edifice centre if a crater is not present. This was digitised manually from the contour maps with 1 m intervals derived from LiDAR DSM (Fig. 6.3). The  $L_{max}$  was calculated between the source point and the lava flow maximum extremity as a vector (Figs. 6.2 and 6.3). The bulk volume ( $V_{lava}+V_{cone}$ ) for those volcanoes located on flat areas or forming individual islands/peninsulas such as Mt. Mangere, Rangitoto, Motukorea (Browns Island), Puketutu, Pukeiti, Otuaataua, McLaughlin Mt. and Mt. Victoria was calculated as a difference between the present DSM and an equal base height (i.e. plane). For the rest of the cones, Mt. Roskill, Mt. Eden, Three Kings, Mt. Albert, One Tree Hill and Mt. Wellington, the bulk volume was defined as the difference between the present 10 m DSM and a reconstructed pre-eruptive surface beneath the volcanics (Fig. 6.3 and Table 6.1). The pre-eruptive surface was interpolated from spot heights with elevation of the contact of lava flow and the underlying non-volcanic strata derived from drill core points ( $n = 488$ ) and field observations ( $n = 26$ ). The spot height data were used to interpolate a 10 m resolution DEM by using natural neighbour interpolator. The bulk volumes in both cases were determined on a cell basis:

$$V = \sum[(Z_{present} - Z_{bottom}) \times A_{cell}] \quad (6.1)$$

where  $Z_{present}$  is the elevation of the LiDAR DSM (i.e. present surface), the  $Z_{bottom}$  is the reconstructed pre-eruptive surface DEM beneath the lava flows, the  $A_{cell}$  corresponds to the grid cell's area (in this case  $10 \times 10 \text{ m} = 100 \text{ m}^2$ ). From the residual maps, the maximum ( $T_{max}$ ) and mean thickness ( $T_{mean}$ ) of the lava flow were calculated (Figs. 6.2 and 6.3).

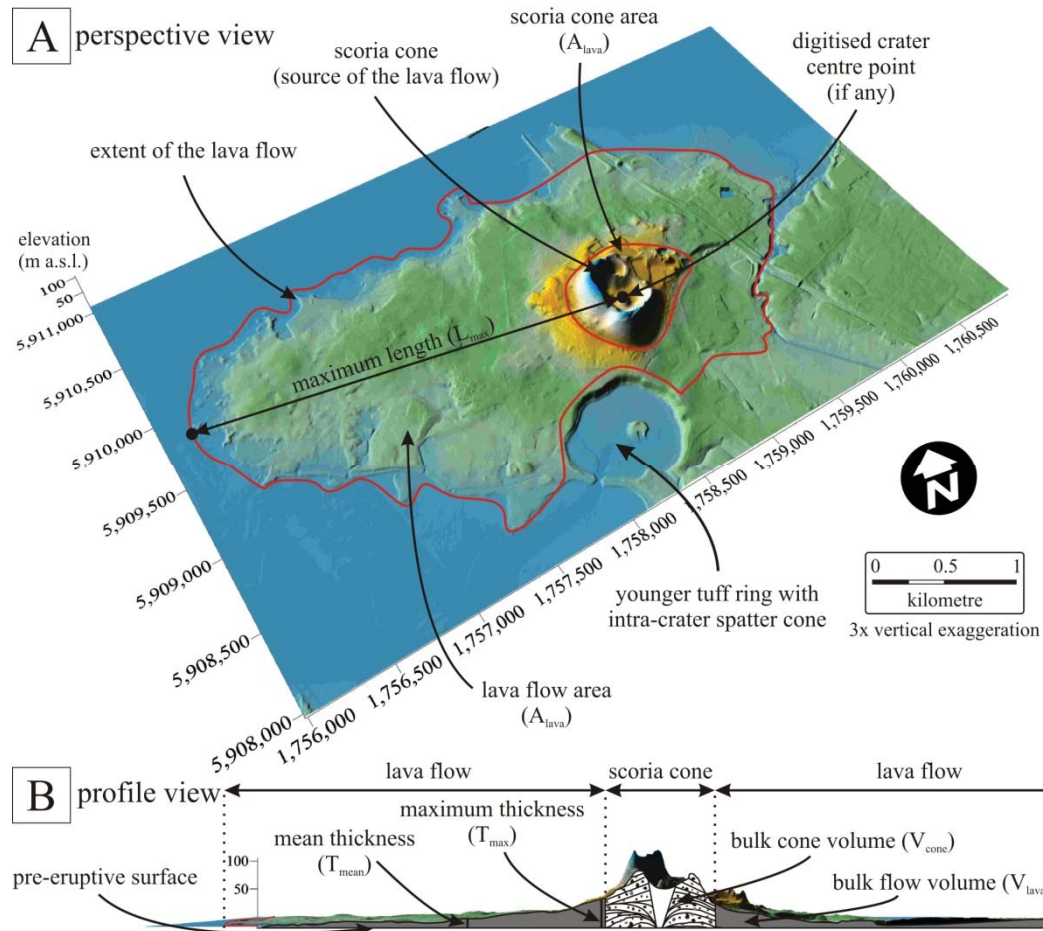


**Figure 6.3** Perspective (A) and profile (B) views of morphometric parameters of lava flows applied in this paper visualised on the Mt. Mangere volcano (for the detailed location see Fig. 6.1)

Error in the bulk volume calculations can be associated with (1) surface processes including erosion after the formation of the lava flows and anthropogenic activity, such as quarrying, (2) data capturing techniques, such as laser positioning, angle of view, distance from the surface and the laser and topography (Aguilar et al., 2005; Su and Bork, 2006; Favalli et al., 2009b; Pollyea and Fairley, 2012) as well as (3) processing of the raw data including systematic correction, gridding, subsequent smoothing or resampling (Aguilar and Mills, 2008; Favalli et al., 2010). In this study, the applied low, average smoothing and resampling from 2 m to 10 m resolution may introduce some modification of the bulk volume and thickness calculations. To express the expected differences and data modification introduced by these post-processing techniques, the parameters derived from these two data sets were crosschecked. The smallest (Pukeiti) and largest (Rangitoto) volcanoes were selected for comparison. The differences between the 2 m and 10 m resolution DSMs were  $\leq 16\,429\text{ m}^3$  (0.001%) and  $903\text{ m}^3$

(0.02%) for the bulk volume and 0.01 m (0.1%) for thickness, respectively (e.g. Chapter 3). Finally, the overall accuracy of the LiDAR DSM is in the dm range, thus only one decimal place was considered in the calculations and results, except for the bulk volume calculations because there were converted from  $\text{m}^3$  into  $\text{km}^3$ .

### 6.2.3. Hydrological channel extraction

Hydrological characteristics and associated features, such as valleys and ridges and their orientations, can be used to describe the terrain (Moore et al., 1991; Jordan, 2003; Székely and Karátson, 2004; Jordan and Schott, 2005; Bonne et al., 2008; Favalli et al., 2009d). The theoretical drainage system (Fig. 6.2) was extracted from the resampled, 20 m resolution LiDAR DSM using TOPographic PArameteriZation (TOPAZ) application developed by Garbrecht and Martz (1995). The methods behind the TOPAZ include the D8 method (Douglas, 1986), the down-slope flow routing (Morris and Heerdegen, 1988) and the critical source area method (Mark, 1984). Interpolation noise, such as isolated pits or depression cells or flat cells, may distort the final results of drainage extraction (Jenson and Domingue, 1988; Costa-Cabral and Burges, 1994; Garbrecht and Martz, 1997). TOPAZ uses a breaching algorithm that detects local minima in a DSM/DTM/DEM on a  $5 \times 5$  cell matrix (Garbrecht and Martz, 1995). This algorithm systematically lowers the elevation along the rim of the depression and then fills depressions by modification of cell elevation (Martz and Garbrecht, 1999). To extract drainage patterns from a DSM or from a DEM by the TOPAZ, two input parameters are required (Fig. 6.2). The Critical Source Area (CSA) defines the drainage channel as raster cells that have an upstream area greater than the user-defined threshold value (Mark, 1984; Martz and Garbrecht, 1992; Garbrecht and Martz, 1995). The Minimum Source Channel Length (MSCL) defines the minimum length of individual channels extracted from the DSM or DEM (Garbrecht and Martz, 1995). In the present study, the CSA chosen was  $10\,000 \text{ m}^2$  (25 cells), and the MSCL chosen was 1 000 m (50 cells), respectively (Fig. 6.2).

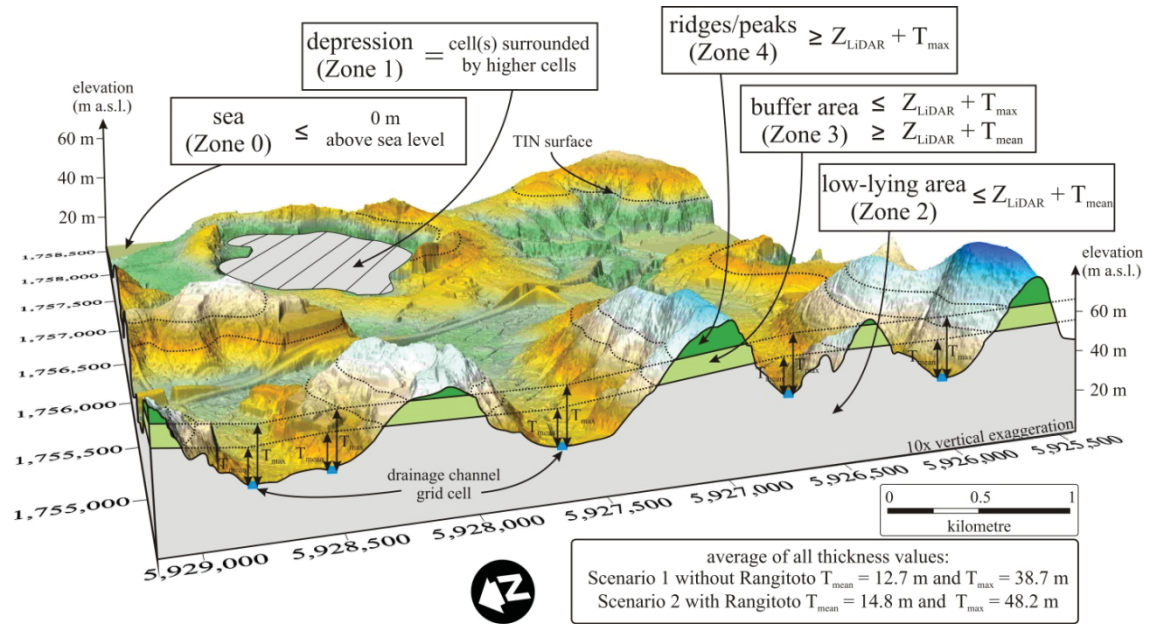


**Figure 6.4** Definitions of susceptibility zones (sea, depressions, low-lying area, buffer and ridges/peaks) identified in the AVF visualised on an area from North Shore (for the detailed location see Fig. 6.1). The largest depression in the figure is the Lake Pupuke, generated by series of phreatomagmatic eruptions.

These values are high enough to extract a dense drainage which is a good basis of further re-interpolation (see details later), while the 1000 m MSCL value allows extracting only longer channels which are potentially large enough to control the pathway(s) of future lava flows.

#### 6.2.4. Topographic classification of zones subject to lava flow inundation

The present topography was classified as (1) sea, (2) depressions, (3) low-lying areas, (4) a buffer zone and (5) ridges (Figs. 6.2 and 6.4). Due to the coastal location of Auckland, the total area covered by sea is also an important class, but the proper lava flow pathway prediction under this area is uncertain due to the lack of high-resolution bathymetric data. In this investigation, the sea was defined in a raster-based environment as those areas that are characterised by elevation  $\leq 0$  m a.s.l. (Figs. 6.2 and 6.3).

The local minima (i.e. topographic depressions), in which a cell has surrounding cells with higher elevation values, are most likely to be filled by lava flows. To identify and delimit them, a sink-filling algorithm was used (Jenson and Domingue, 1988). These areas are assumed to be the most susceptible to inundation by a lava flow sourced

from a distance  $\leq L_{max}$  (6.5 km; Fig. 6.4). The low-lying areas are referred to here as those parts of the field which are currently characterised by smooth surfaces with low elevation differences ( $< T_{mean}$ ; 12–14 m), hence they could be buried easily by a lava flow sourced  $\leq L_{max}$  (6.5 km) and having an average thickness (Fig. 6.4). To delimit these areas, the theoretical drainage system was used as a basis with the assumption that future lava flows will follow the topography and therefore the drainage system. To delimit zones, such as low-lying, buffer and ridges, the cell elevation values along drainage channels as local lowest points, were increased by the values of  $T_{mean}$  (Fig. 6.4), similar to Jordan (2007a). The cell values (present elevation +  $T_{mean}$ ) were then converted into points which were used to construct a new surface by TIN interpolation (Fig. 6.4). The constructed TIN surface was converted into gridded DEM with 10 m resolution and extracted from the original DSM. Those areas below the interpolated TIN surface are defined as low-lying areas that could be affected by a future lava flow from a source closer than  $L_{max}$ . The delimitation of the buffer zone was constructed using the same technique, but substituting  $T_{mean}$  with  $T_{max}$  values (38–48 m; Fig. 6.4). The rest of the area (i.e. above the buffer zone), is locally above the valley bottoms by  $T_{max}$ , therefore they are characterised as ridges. The advantage of this method is that it is adaptive, and uses the local lowest values of the surface as a basis to construct topographic classification/hazard zonation.

The definitions of this classification are based on (1) the topographical properties and (2) the lava flow parameters introduced above. The morphometric parameters of the lava flows, such as thickness, lie within a narrow range, but there is an outlier value associated with the massive lava field of Rangitoto (Figs. 6.2 and 6.5). Thus, this asymmetry of the thickness data means that the definitions of the low-lying, buffer and ridge zones could differ significantly. To handle this asymmetry, two scenarios were calculated. Scenario 1 uses the morphometric parameters without Rangitoto values, while Scenario 2 contains all of the morphometric values of the field (Fig. 6.2 and Table 6.1).

**Table 6.1** Summary of morphometric parameters for the studied fifteen lava flows.  $Z_c$  – is the pre-eruptive basement elevation in meter a.s.l. that was used in the bulk volume calculations.

n#	location	length		thickness		area			bulk eruptive volume				
		$L_{min}$	$L_{max}$	$T_{max}$	$T_{mean}$	cone	flow	TOTAL	$Z_{cone}$	$Z_{flow}$	$V_{lava\ flow}$	$V_{cone}$	TOTAL
-	-	m	m	m	m	$m^2$	$m^2$	$m^2$	m	m	$m^3$	$m^3$	$m^3$
1	Pukeiti	106.7	762.7	20.7	8.4	35,900	501,800	537,700	18	0	4,265,202	770,959	5,036,161
2	Otuataua	149.4	964.5	30.8	14.3	81,500	482,100	563,600	17	0	6,937,735	1,920,211	8,857,946
3	McLennan Hills	263.2	1,730.1	29.2	10.3	261,800	1,582,800	1,844,600	20	0	16,333,328	7,077,218	23,410,546
4	One Tree Hill	1,359.1	4,403.7	80.8	22.7	374,800	15,292,800	15,667,600	surface		347,362,933	28,456,852	375,819,785
5	Browns Island	150.4	1,155.6	18.3	3.4	144,800	852,900	997,700	8	-2	2,971,052	4,314,795	7,285,847
6	Mt. Albert	596.9	2,320.6	34.3	8.3	425,700	3,322,700	3,748,400	surface		27,647,490	15,339,485	42,986,975
7	Puketutu	230.0	1,793.7	30.1	6.1	163,600	1,677,200	1,840,800	16	0	9,077,513	5,011,146	14,088,659
8	Mt. Victoria	188.7	754.7	29.4	10.8	136,800	304,800	441,600	23	0	2,905,802	6,029,926	8,935,728
9	Mt. Roskill	219.1	2,463.2	29.3	8.2	241,100	1,392,500	1,633,600	surface		11,513,967	6,865,428	18,379,395
10	Three Kings	411.7	5,723.8	46.3	14.1	480,300	6,086,600	6,566,900	surface		85,008,373	14,308,042	99,316,415
11	Mt. Eden	902.6	2,175.8	76.3	26.9	405,000	5,136,000	5,541,000	surface		138,656,128	29,804,539	168,460,667
12	McLaughlin Mt.	90.6	732.6	38.6	15.9	30,800	542,200	573,000	17	0	8,637,999	1,008,765	9,646,764
13	Mt. Mangere	557.6	2,699.3	29.3	8.5	873,600	4,344,900	5,218,500	21	0	36,099,442	34,896,667	70,996,109
14	Mt. Wellington	369.9	6,525.8	48.8	20.2	262,600	5,981,000	6,243,600	surface		127,521,507	15,130,206	142,651,713
15	Rangitoto	2,241.8	3,677.0	180.5	43.8	416,400	24,686,000	25,102,400	140	-3	1,083,230,686	81,750,692	1,164,981,378
<b>MEAN without Rangitoto (Scenario 1)</b>		<b>2,443.3</b>	<b>2,443.3</b>	<b>38.7</b>	<b>12.7</b>	<b>279,879</b>	<b>3,392,879</b>	<b>3,672,757</b>			<b>58,924,176</b>	<b>12,209,589</b>	<b>71,133,765</b>
<b>MEAN (Scenario 2)</b>		<b>2,525.5</b>	<b>2,525.5</b>	<b>48.2</b>	<b>14.8</b>	<b>288,980</b>	<b>4,812,420</b>	<b>5,101,400</b>		<b>SUM</b>	<b>1,908,169,157</b>	<b>252,684,931</b>	<b>2,160,854,088</b>

Additional, significant features of the present topography (e.g. flat areas) were also detected using slope-angle maps (Fig. 6.2). Here, flat areas were defined as having a  $\leq 5^\circ$  slope angle (Fig. 6.2). Generally, these flat areas would favour the broad spread of lava flows over the topography (Favalli et al., 2009d). Slope was calculated by using an unweighted, third order finite difference filter (“Prewitt” filter), which gives more general “smoothed” slope values. This linear filter applies a first-order trend surface fitted to the cell values on a  $3 \times 3$  moving window by least-squares method (Sharpnack and Akin, 1969; Jones, 1998; Jordan, 2007b). The slope angle in a grid-based environment is formally written as (e.g. Fig. 3.9):

$$\text{SLOPE} = \arctan \sqrt{f_x^2 + f_y^2} \quad (6.2)$$

in which the first derivatives are calculated as  $f_x = (Z_3+Z_6+Z_9-Z_1-Z_4-Z_7)/6\Delta X$  and  $f_y = (Z_1+Z_2+Z_3-Z_7-Z_8-Z_9)/6\Delta Y$ , where  $Z_1-Z_9$  correspond to the cell elevation read from the top left corner to the bottom right corner in a  $3 \times 3$  matrix, and  $\Delta X$  and  $\Delta Y$  are the grid cell size along the two main principal directions.

Other point-like features, such as valley conjunctions and watershed outlets, were also digitised manually, with the value of upstream areas taken from the theoretical drainage system map. The valley conjunctions possibly represent an increased likelihood of lava inundation from multiple directions (i.e. from different valleys), if the eruption takes place within the upstream area. An outlet point along the coastal area may represent a location with increased likelihood of explosive sea water/lava interaction associated with littoral cone formation (Mattox and Mangan, 1997). A 400 m-wide coastal-hazard zone was thus created around the coastal regions (Fig. 6.2) based on the dimensions of littoral cones [up to 400 m in width (Jurado-Chichay et al., 1996)]. The sea was defined in a raster-based environment as those areas that are characterised elevation  $\leq 0$  m a.s.l. Thus, the coastal buffer zone was constructed from this boundary between the land and sea using raster-based distance calculation.

### 6.2.5. Watershed characteristics

Topography, especially ridges that divide watersheds, is highly effective in controlling lava flow emplacement (Bonne et al., 2008). Adapting this concept, the watersheds that are large enough to host a future eruption ( $\geq 2 \text{ km}^2$ ) were extracted, noting that small watersheds can be easily overtopped or destroyed by vent opening eruptions or vent migrations (Fig. 6.2). Taking the fact that an average monogenetic eruption (excluding tephra fall) rarely impacts a circular area larger than  $\sim 0.75 \text{ km}$  in radius (Magill and Blong, 2005a), the minimum area of each event would be  $\geq 2 \text{ km}^2$  (i.e.  $\geq 4 \text{ 500 cells}$ ). Each watershed defined can be evaluated in terms of its future susceptibility to eruptions by calculating the number of past eruption onsets that occurred in it (Fig. 6.2). Kernel smoothed density methods, based on the location of all past eruption centres including all eruption centres ( $n = 50$ ) were used to evaluate a spatial intensity. Two-dimensional, symmetric Gaussian kernel density estimates were used (Connor and Hill, 1995):

$$\lambda(s) = \frac{1}{2\pi h^2} \sum_{i=1}^n \exp\left[-\frac{1}{2}\left(\frac{d_i}{h}\right)^2\right] \quad (6.3)$$

where  $d_i$  is the distance from the point of interest,  $s$ , to the vent location,  $n$  is the number of vents, and  $h$  ( $=2.42 \text{ km}$ ) is the smoothing bandwidth. The bandwidth was determined by least squares cross validation (Duong, 2007). To approximate probabilities of future eruptions and possible lava flows within watersheds, the spatial intensity values were averaged within the area of each watershed and ranked (Fig. 6.2).

Other characteristics were calculated for each watershed, such as area of depressions, low-lying, buffer and ridge areas (in  $\text{km}^2$  and %) for the scenarios, average number and bulk volume of lava flows within a watershed, perimeter and average elevation of drainage as well as watershed border and bulk volume capacity (Fig. 6.2). The raster-based maps of each watershed were converted into vector-based polygon and subsequently polylines. Such polylines were rasterized with the same spatial resolution (i.e.  $20 \text{ m}$ ), in order to extract elevation values along the watershed boundaries. The elevation values were also extracted along the drainage systems. For both cases, mean, median and standard deviations were calculated in order to characterise the

topographical variations within a watershed and between watersheds (Fig. 6.2). The hosting capacities of the watersheds were established by Eq. 6.1 between present LiDAR DSM and a surface constructed by TIN interpolation from the elevation values along the present ridgelines, similar to Jordan (2007a).

## 6.3. Results

### 6.3.1. Characteristics of past lava flows

The lava flows examined in the present study are  $\leq 0.1$  Ma old, thus the erosion-related modification is negligible as the rocks are still relatively fresh and erosion resistant. Some modifications may be expected from anthropogenic processes, such as quarrying (Fig. 6.5). The largest portion of lava flow was quarried away from the Mt. Wellington reducing the original bulk volume by  $0.008 \text{ km}^3$  (Fig. 6.5). From the fifteen preserved lava flows (Fig. 6.1 and Table 6.1), the maximum length of the AVF lava flows range between 0.7 km (McLaughlin Mt.) and 6.5 km (Mt. Wellington; Fig. 6.5), while the average is 2.5 km (Table 6.1). The longest flow of Auckland is, however, from the Mt. St. John volcano with the total length of about 10 km (Eade, 2009). Due to the limited knowledge about its exact path, it was discarded from the calculations. Interestingly, the exceptionally large eruptive centre of Rangitoto did not produce the longest flows (Table 6.1) because they were concentrically emplaced around the vent and flowed over a flat basal topography. The average area invaded by a single AVF eruption centre (from the fifteen studied centres) is around  $5.1 \text{ km}^2$ , including  $4.8 \text{ km}^2$  lava flow and  $0.3 \text{ km}^2$  scoria cone area. These areas range from  $<0.5 \text{ km}^2$ , (e.g. at Mt. Victoria and Pukeiti) to  $24.6 \text{ km}^2$  and  $15.2 \text{ km}^2$  for the Rangitoto and One Tree Hill centres, respectively (Table 6.1).

Bulk total edifice bulk volumes (cone + lava flow), excluding basal phreatomagmatic deposits and distal tephra, show high variability from  $0.005 \text{ km}^3$  (Pukeiti) up to  $\sim 1 \text{ km}^3$  (Rangitoto) (Table 6.1). From these, the most significant portions are preserved as lava flows. Other large lava flows include: One Tree Hill ( $0.34 \text{ km}^3$ ), Mt Eden ( $0.13 \text{ km}^3$ ), Mt. Wellington ( $0.12 \text{ km}^3$ ) and Three Kings ( $0.08 \text{ km}^3$ ). The maximum and mean thicknesses of lava flows from individual centres are between 18.3–180.5 m and 3.4–43.8 m, (from Motukorea to Rangitoto) (Table 6.1). Based on the past effusive activity, an average AVF lava flow is characterised by a mean thickness of

14.8 m, while the mean maximum thickness is 48.2 m. If the fact that the Rangitoto is an outlier volcano in terms of eruption duration (Needham et al., 2011), geochemistry (McGee et al., 2011) as well as size were considered, and it was excluded from the calculations, the mean and mean maximum thickness values decrease to 12.7 m and 38.7 m, respectively (Table 6.1). The average bulk volume of the fifteen lava flows measured here is  $0.127 \text{ km}^3$  which can be related to an average edifice with a bulk volume of  $0.016 \text{ km}^3$  measured from the basement.

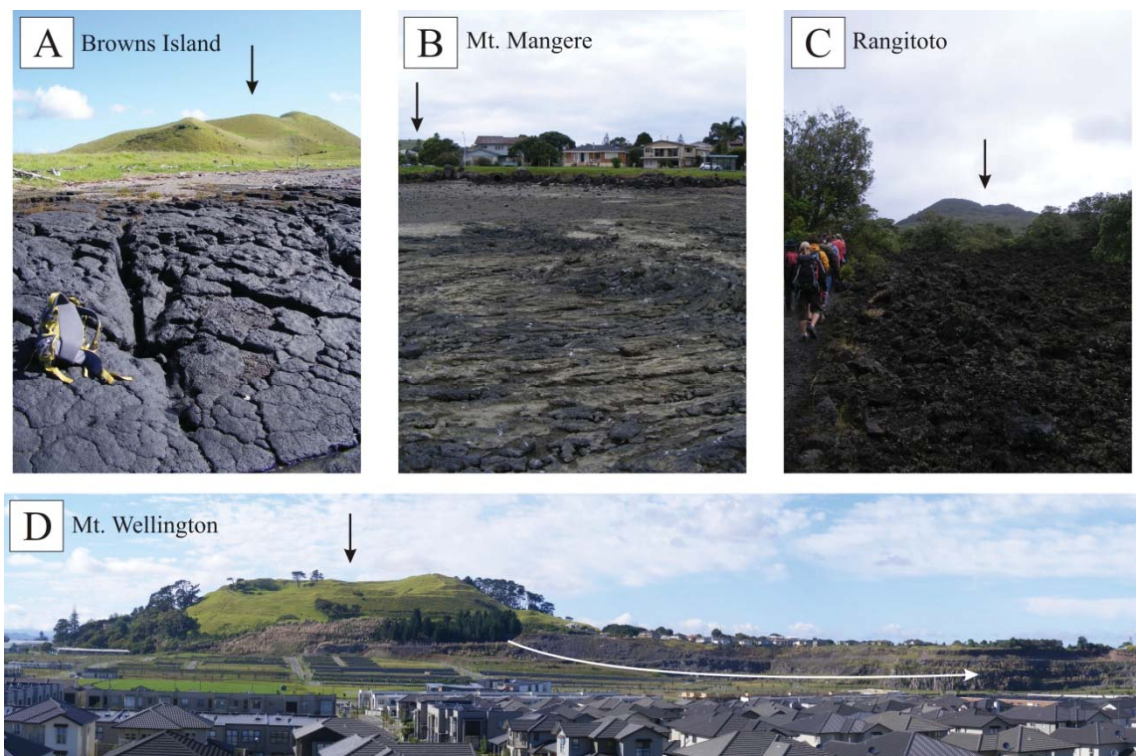


**Figure 6.5** Field photographs illustrating examples of preserved lava flow surfaces and their source scoria cones (black arrows). (A) A'a lava flow surface preserved in the coastal area of Browns Island. (B) Pahoehoe surface related to the Mt. Mangere scoria cone. (C) Fresh a'a lava flow from the youngest eruption centre, Rangitoto. (D) Overview photo of the Mt. Wellington scoria cone and its basaltic lava flow exposed due to extensive quarrying. Note that the white arrow indicates the direction of the lava flow.

No distinct trends can be seen in bulk lava flow volume as a function of lava flow length (Fig 6.6), because many large flows related to the Rangitoto eruption spread widely on flat topography, thus the maximum length is only 3.6 km (Table 6.1). On the other hand, there is a correlation between bulk flow volumes and their areal extent meaning that the lava flows were mostly emplaced freely over the topography (Fig. 6.6). Volumetric evolution in the field considers total bulk lava flow and scoria cone volumes

(excluding the eruption products of phreatomagmatic eruption and tephra dispersion) shows a rapid increase due to the large size of the last eruption, Rangitoto.

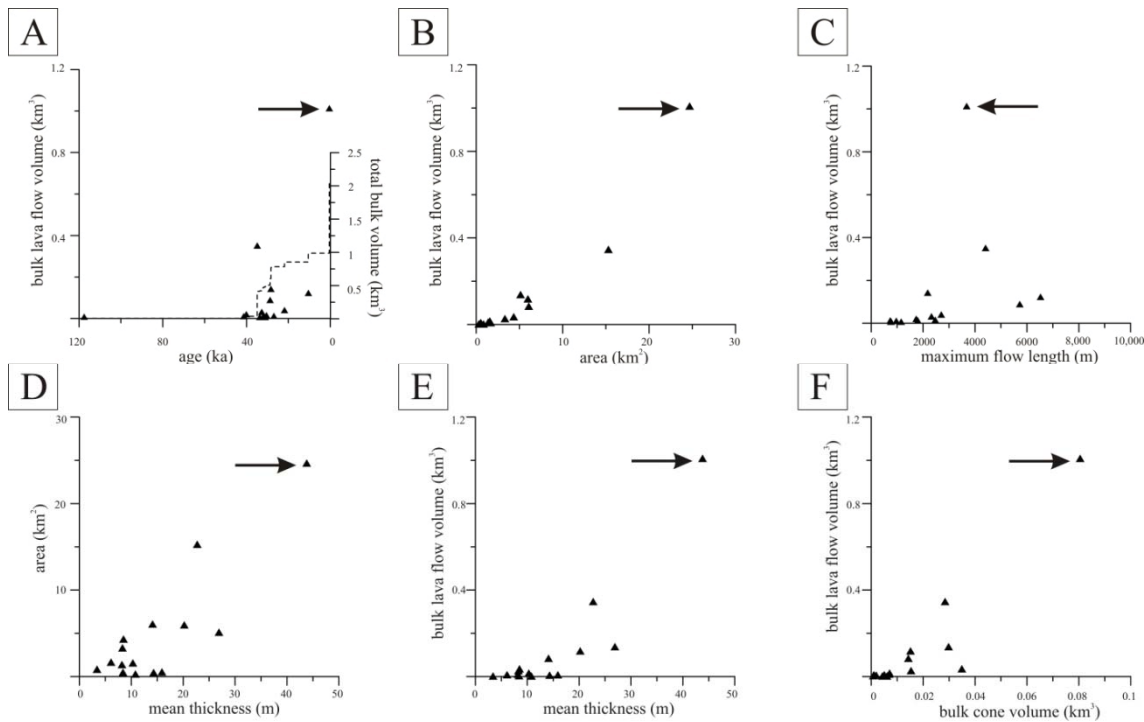


**Figure 6.6** Graphs of the main morphometric parameters of lava flows. Age estimates are from Bebbington and Cronin (2011). Note that the black arrows indicate the morphometric values of Rangitoto volcano.

### 6.3.2. Characteristics of present topography

The area examined (793 km<sup>2</sup>; Fig. 6.1) is slightly more than twice that of the area of the AVF, about 336 km<sup>2</sup> (Spörl and Eastwood, 1997). From the study area, around 40% is covered by the sea or is intertidal (326 km<sup>2</sup>), and because this is not inhabited, it was excluded from our analysis. Based on present topography, the study area can be subdivided into two significantly different areas: (1) a valley–ridge-dominated northern/central region; and (2) the plain-dominated southern region (Fig. 6.1). The northern part is characterised by low ridges composed of sandstone (Waitemata Fm.), whereas the southern part is mostly covered by Late Pleistocene-Holocene alluvium, peat and marine sands and mud (Kermode, 1992; Edbrooke, 2001). The extracted drainage system is characterised by having a dense channel system (0.7 km/km<sup>2</sup>). The average distance between individual channels is 374 m (median = 321 m) and 73% of the channels are <500 m away from their neighbouring ones. This dense drainage

provides a good detailed basis to re-model the topography during the secondary TIN interpolation and thus to calculate inundated areas by an average lava flow.

As described above, the classification of the topography into zones (sea, depressions, low-lying areas, buffer area and ridges) is based on the mean thickness of past lava flows. Due to the outlier values of Rangitoto, two scenarios were used (Scenario 1 without, while Scenario 2 with Rangitoto). From the zones above, the sea and depressions are the same for both scenarios.

The depressions (Fig. 6.4) have a maximum depth of 49.4 m, e.g. the quarry near Three Kings (Fig. 6.1). The rest of the depressions are shallower (average depth of 1.8 m) and 70% of them are <1.5 m deep. Most of these are small-scale pits due to rapid changes in topography, detection error or interpolation noise. There are very few natural depressions, such as maar craters. The total area of depressions is around 45.2 km<sup>2</sup>, but from these only 9 km<sup>2</sup> (1.1% of the total area) is inferred to represent 'real' depressions (i.e. areas larger than a few grid cells in width; Fig. 6.4). The total bulk volume of these depressions that can be invaded by future lava flows is about 0.062 km<sup>3</sup>.

The low-lying zone (Fig. 6.4) covers an area of 300 km<sup>2</sup> (38 %) and 319 km<sup>2</sup> (40 %), without and with Rangitoto lavas, respectively (Table 6.2). Consequently, an overwhelming proportion of the AVF is characterised by indistinct topographical difference, thus a future flow with an average thickness cannot be fully channelised by the topography. In both scenario cases, this zone has slope angle dominantly <5° (253/265 km<sup>2</sup> or 84/83% of the area). The flat areas are mostly located in the southern part of the volcanic field.

The 'buffer' zone (Fig. 6.4), between low-lying and ridge zones encompasses 121 km<sup>2</sup> and 118 km<sup>2</sup>, with and without Rangitoto (Table 6.2), respectively, or ~15% of the total study area. This area mostly coincides with sandstone ridges made up by Waitemata sediments and minor areas of scoria cones. The largest differences in area between scenarios can be found in the case of the most elevated parts, i.e. ridges (Table 6.2), with 35 km<sup>2</sup> (4 %) excluding Rangitoto and 19.7 km<sup>2</sup> (2%) including it. These areas should be relatively safe, unless a future eruption takes place on the ridges.

**Table 6.2** Differences in the area of hazard zones using two simulated scenarios

Scenario 1 (without Rangitoto)				
zone	N# of pixels	area (m <sup>2</sup> )	area (%)	volume capacity (m <sup>3</sup> )
sea	815,280	326,112,000	41.1	-
1   depressions	23,044	9,217,600	1.2	62,622,601
2   low-lying	751,696	300,678,400	37.9	-
3   buffer	304,371	121,748,400	15.3	-
4   ridge	88,872	35,548,800	4.5	-

Scenario 2 (with Rangitoto)				
zone	N# of pixels	area (m <sup>2</sup> )	area (%)	volume capacity (m <sup>3</sup> )
sea	815,280	326,112,000	41.1	-
1   depressions	23,183	9,217,600	1.2	62,622,601
2   low-lying	798,124	319,249,600	40.2	-
3   buffer	297,206	118,938,000	15.0	-
4   ridge	49,470	19,788,000	2.5	-
	1,983,263	793,305,200		

In parallel with the lava susceptibility zone classification, the largest watersheds (i.e. 2 km<sup>2</sup>), were also extracted in order to characterise their properties, such as size, hosting capacity and boundary heights, and then ranked based on the spatial intensity of past eruptions. The total number of ‘large’ watersheds is 40, but only 38 have outflow points in the study area (Fig. 6.7 and Table 6.3). They range in area between 1.9 km<sup>2</sup> and 30 km<sup>2</sup>. The elevation of cells on the ridges versus those along the drainage channels were extracted from each other to detect those watersheds that are surrounded by low or less significant ridges (possibly  $\leq T_{mean}$  or  $T_{max}$ ). These differences were generally larger than an average lava flow thickness (i.e. 14.7 m; Table 6.1). Nevertheless, there are only 13 watersheds, mostly in the southern part of the field, which are characterised by low watershed boundaries. The bulk volume capacities range from 0.006 km<sup>3</sup> up to 0.475 km<sup>3</sup>, with an average of 0.088 km<sup>3</sup> (Table 6.3). This number is significantly smaller than an average bulk lava flow volume (0.127 km<sup>3</sup>), in the study area. Only 10 valleys are significantly larger than the average bulk lava flow volume. The averaged spatial intensity within watersheds range from zero (e.g. watershed *IDI*) to 0.25 (e.g. watershed *IDI2*) vents per km<sup>2</sup> (Fig. 6.7 and Table 6.3).

## 6.4. Discussion

In the case of active monogenetic volcanic fields, such as the AVF, forecasting of future hazards can be challenging due to the unknown location of the next event, lack of well defined orientation of previous vents, or inapplicability of classical volcano monitoring techniques, such as geochemical or geodetic/deformation (Lindsay et al., 2010; Ashenden et al., 2011). Even with seismology, real-time observation and identification of small-volume magma as it travels towards the surface can be challenging in Auckland due to large anthropogenic background noise and the coarse resolution of monitoring sites (Ashenden et al., 2011). This means that localisation of a future eruption site is only likely to occur within a few hours or days of an eruption. Hence there is a need for establishing a vent location-independent view of lava flow susceptibility that can be applied in any future scenario or modelling study. There have been many recent efforts to understand the nature and behaviour of potential future hazard from a volcanic eruption, earthquakes, tsunamis and landslides, within New Zealand's most densely populated urban area (Smith and Allen, 1993; Allen and Smith, 1994; Edbrooke et al., 2003; Magill and Blong, 2005a; Magill et al., 2005a; Molloy et al., 2009; Bebbington and Cronin, 2011; Needham et al., 2011). Most of these studies focused on the impacts of initial vent-opening processes, such as base surge or ash fall, within the city. Knowledge of lava flow susceptibility is an essential addition, because over half of the eruptions in Auckland have produced lava flows or lakes (Allen and Smith, 1994). For example, in the central part of the field, there are remnants of 12 monogenetic volcanoes, of which 10 have lava flows with relatively large dimensions. These parts of the field are also the most densely populated areas of the city.

**Table 6.3** Properties of large (larger than 2 km<sup>2</sup>) watersheds. The values in bold represent either the smaller topographical differences between catchment rims and drainage than a lava flow with average thickness or those catchment that are limited (i.e. smaller than average lava flow) in volume capacities.

ID	N# of pixels	area													
		TOTAL	on the map			Scenario 1				Scenario 2					
			km <sup>2</sup>	km <sup>2</sup>	km <sup>2</sup>	Zone 1	Zone 2	Zone 3	Zone 4	Zone 1	Zone 2	Zone 3	Zone 4		
<b>1</b>	6,193	2,477,200	2,477,600	0	606,800	960,800	909,200	0	720,000	1,144,000	612,800	0	720,000	1,144,000	612,800
<b>2</b>	6,404	2,561,600	2,562,000	0	475,200	969,600	1,116,400	0	554,800	1,233,600	772,800	0	554,800	1,233,600	772,800
<b>3</b>	38,419	15,367,600	14,364,400	1,259,200	7,030,400	5,081,600	990,800	1,259,200	7,630,400	5,067,600	404,800	1,259,200	7,630,400	5,067,600	404,800
<b>4</b>	12,098	4,839,200	4,839,600	18,000	2,740,800	1,681,600	399,200	18,000	3,045,200	1,588,400	188,000	18,000	3,045,200	1,588,400	188,000
<b>5</b>	17,201	6,880,400	6,880,800	0	1,457,600	3,043,600	2,379,200	0	1,696,000	3,794,400	1,390,000	0	1,696,000	3,794,400	1,390,000
<b>6</b>	4,764	1,905,600	1,906,000	1,600	422,000	970,000	512,400	1,600	518,800	1,099,200	286,400	1,600	518,800	1,099,200	286,400
<b>7</b>	5,458	2,183,200	2,183,600	0	814,400	1,067,600	301,600	0	894,800	1,204,800	84,000	0	894,800	1,204,800	84,000
<b>8</b>	4,938	1,975,200	1,975,600	0	926,800	966,800	80,800	0	1,022,400	952,000	0	0	1,022,400	952,000	0
<b>9</b>	8,074	3,229,600	3,230,000	2,800	1,082,800	1,811,600	332,800	2,800	1,192,000	1,947,200	88,000	2,800	1,192,000	1,947,200	88,000
<b>10</b>	8,169	3,267,600	3,268,000	0	1,220,000	1,905,200	142,800	0	1,392,400	1,875,600	0	0	1,392,400	1,875,600	0
<b>11</b>	20,980	8,392,000	8,392,400	405,600	4,742,800	3,042,800	201,200	405,600	5,131,600	2,763,200	92,000	405,600	5,131,600	2,763,200	92,000
<b>12</b>	21,701	8,680,400	8,680,800	116,400	4,148,400	3,488,800	927,200	117,200	4,483,200	3,690,400	390,000	117,200	4,483,200	3,690,400	390,000
<b>13</b>	5,010	2,004,000	2,004,400	0	807,600	1,101,200	95,600	0	902,800	1,101,600	0	0	902,800	1,101,600	0
<b>14</b>	28,817	11,526,800	11,527,200	218,000	8,028,800	3,011,200	266,400	267,200	8,482,400	2,634,000	140,800	267,200	8,482,400	2,634,000	140,800
<b>15</b>	31,834	12,733,600	12,734,000	63,200	7,897,600	4,139,600	633,600	63,200	8,526,800	3,920,000	224,000	63,200	8,526,800	3,920,000	224,000
<b>16</b>	34,414	13,765,600	12,527,600	13,600	7,135,600	4,714,400	663,200	13,600	7,703,200	4,617,600	192,400	13,600	7,703,200	4,617,600	192,400
<b>17</b>	10,862	4,344,800	4,345,200	268,000	2,499,200	1,325,200	252,400	268,000	2,732,800	1,214,400	129,600	268,000	2,732,800	1,214,400	129,600
<b>18</b>	51,174	20,469,600	20,470,000	1,654,000	13,472,800	4,636,400	706,800	1,654,000	14,052,800	4,472,000	291,200	1,654,000	14,052,800	4,472,000	291,200
<b>19</b>	5,206	2,082,400	2,082,800	0	609,200	1,233,600	240,000	0	687,200	1,374,400	21,200	0	687,200	1,374,400	21,200
<b>20</b>	8,457	3,382,800	3,383,200	44,000	1,610,000	1,614,000	114,400	44,000	1,861,200	1,472,000	5,200	44,000	1,861,200	1,472,000	5,200
<b>21</b>	17,073	6,829,200	6,829,600	660,400	4,345,200	1,525,600	298,400	660,400	4,727,200	1,325,600	116,400	660,400	4,727,200	1,325,600	116,400
<b>22</b>	5,863	2,345,200	2,345,600	146,000	1,836,400	326,400	36,800	146,000	1,923,200	250,000	26,400	146,000	1,923,200	250,000	26,400
<b>23</b>	7,929	3,171,600	3,172,000	0	2,056,400	1,097,200	13,600	0	2,310,800	856,400	0	0	2,310,800	856,400	0
<b>24</b>	34,763	13,905,200	12,041,200	42,000	7,066,800	4,326,400	600,000	42,000	7,902,800	3,879,600	210,800	42,000	7,902,800	3,879,600	210,800
<b>25</b>	7,143	2,857,200	2,857,600	8,800	2,210,400	620,000	18,000	8,800	2,358,400	490,000	0	8,800	2,358,400	490,000	0
<b>26</b>	12,154	4,861,600	4,862,000	173,200	4,087,200	563,600	37,200	173,200	4,182,000	500,400	5,600	173,200	4,182,000	500,400	5,600
<b>27</b>	18,294	7,317,600	7,318,000	30,400	5,434,400	1,207,200	622,800	30,400	5,632,000	1,202,400	430,000	30,400	5,632,000	1,202,400	430,000
<b>28</b>	no outlet	-	1,307,600	0	21,200	317,200	969,200	0	30,000	506,400	771,200	0	30,000	506,400	771,200
<b>29</b>	77,268	30,907,200	26,655,600	133,600	21,762,400	3,695,200	1,063,600	133,600	22,494,000	3,387,200	640,000	133,600	22,494,000	3,387,200	640,000
<b>30</b>	19,946	7,978,400	7,978,800	202,000	7,752,400	22,000	0	0	202,000	7,764,800	9,600	0	202,000	7,764,800	9,600
<b>31</b>	11,860	4,744,000	4,744,400	2,400	4,739,600	1,200	0	2,400	4,739,600	1,200	0	2,400	4,739,600	1,200	0
<b>32</b>	17,550	7,020,000	7,020,400	410,400	6,054,000	399,200	156,000	410,400	6,147,200	370,400	91,600	410,400	6,147,200	370,400	91,600
<b>33</b>	14,688	5,875,200	5,875,600	0	5,522,800	99,600	0	0	5,583,200	39,200	0	0	5,583,200	39,200	0
<b>34</b>	8,399	3,359,600	3,360,000	46,800	3,296,000	17,200	0	46,800	3,313,200	0	0	46,800	3,313,200	0	0

35	10,989	4,395,600	4,396,000	962,800	3,171,200	262,000	0	962,800	3,321,200	112,000	0
36	55,868	22,347,200	22,048,000	972,400	14,896,400	4,391,600	1,787,200	972,400	15,498,800	4,677,600	898,800
37	7,924	3,169,600	3,170,000	59,200	3,007,600	103,200	0	59,200	3,098,800	12,000	0
38	5,642	2,256,800	2,257,200	0	1,971,600	285,600	0	0	2,196,400	60,800	0
39	15,993	6,397,200	6,397,600	3,200	5,160,800	1,229,600	0	3,200	5,639,600	750,800	0
40	no outlet	-	17,480,440	226,800	15,170,400	1,727,600	314,800	226,800	15,460,000	1,659,200	93,600

Table 6.3 (continued)

ID	N# of vents	lava volume		perimeter on the map	average spatial intensity	average height of watershed boundary (ridge)				average height of drainage system				difference		volume capacity
		km <sup>3</sup>	within a watershed			mean	median	std dev	mean	median	std dev	mean	median	m	m	
1	0	0	8,680	0.00	72.54	77.74	25.80	14.83	16.26	6.98	57.71	61.48	67,448,589			
2	0	0	8,960	0.02	80.88	88.02	22.97	14.67	15.65	8.30	66.21	72.37	73,222,025			
3	1	(unmeasured)	21,640	0.37	54.18	59.14	26.93	17.96	17.33	6.53	36.22	41.81	259,637,000			
4	0	0	13,560	0.88	43.87	34.55	27.44	15.24	17.83	10.17	28.63	16.72	57,590,928			
5	0	0	15,080	0.13	76.55	83.47	22.47	14.50	14.68	9.15	62.05	68.79	177,746,866			
6	0	0	8,600	0.02	57.00	59.64	28.17	15.21	12.45	8.08	41.79	47.19	23,584,874			
7	1	(unmeasured)	8,280	0.87	47.66	47.71	22.77	8.27	4.67	7.80	39.39	43.04	33,073,636			
8	0	0	7,880	1.26	39.40	46.92	24.22	5.07	4.08	2.77	34.33	42.84	19,609,298			
9	2	(unmeasured)	11,120	2.01	45.98	50.17	30.05	5.50	3.73	3.76	40.48	46.44	33,245,378			
10	0	0	10,360	0.71	48.21	51.25	16.68	11.34	11.30	6.60	36.87	39.95	44,224,369			
11	2	92,625,870	21,320	1.32	55.51	49.28	34.47	25.22	24.80	12.40	30.29	24.48	94,930,518			
12	4	93,373,840	19,400	2.57	79.96	85.71	34.58	45.14	56.69	29.66	34.82	29.02	195,929,114			
13	2	(unmeasured)	7,360	1.87	46.32	47.79	23.19	9.60	6.33	7.79	36.72	41.46	16,867,823			
14	2	80,034,090	25,800	1.19	57.14	57.84	30.27	35.79	39.12	18.77	21.35	18.72	158,501,042			
15	2	25,171,120	28,680	0.83	64.50	68.04	25.09	39.95	46.47	16.56	24.55	21.57	202,682,174			
16	0	0	27,880	0.25	53.95	57.42	23.14	18.68	17.11	11.57	35.27	40.31	205,096,408			
17	1	52,020,000	14,000	1.55	76.14	81.16	36.44	38.44	54.17	25.28	37.70	26.99	51,242,497			
18	4	307,467,100	31,000	1.52	56.27	52.12	34.92	31.40	30.86	19.39	24.87	21.26	466,590,181			
19	0	0	8,320	0.85	39.27	42.69	18.83	3.90	3.44	1.01	35.37	39.25	22,264,479			
20	2	(unmeasured)	11,000	1.04	40.59	43.09	14.15	16.23	14.71	6.86	24.36	28.38	33,184,163			
21	2	9,338,770	15,440	1.29	42.31	42.91	25.07	14.69	13.94	10.02	27.62	28.97	78,930,672			
22	2	24,359,770	9,520	1.53	38.72	38.64	20.65	19.91	16.65	8.13	18.81	21.99	6,209,318			
23	0	0	10,720	0.45	26.24	23.95	12.73	6.62	7.07	3.15	19.62	16.88	25,605,477			
24	1	(unmeasured)	21,360	0.31	35.61	30.38	20.45	16.03	16.32	8.21	19.58	14.06	70,992,050			
25	1	1,921,990	10,720	1.57	24.17	22.60	12.25	7.89	8.27	1.78	16.28	14.33	14,354,005			
26	1	33,815,100	18,600	1.42	26.76	28.06	12.59	12.21	6.29	9.04	14.55	21.77	34,154,080			
27	2	(unmeasured)	15,800	1.15	41.52	30.01	32.99	15.07	15.54	8.07	26.45	14.47	72,872,974			

<b>28</b>	0	0	8,960	0.26	78.19	77.72	29.77	16.75	13.27	13.05	61.44	64.45	<b>7,685,945</b>
<b>29</b>	2	(unmeasured)	29,920	0.73	53.57	33.42	39.24	22.46	19.45	13.75	<b>31.11</b>	<b>13.97</b>	475,496,577
<b>30</b>	0	0	20,000	1.15	19.44	20.21	5.74	7.53	6.97	4.16	<b>11.91</b>	<b>13.24</b>	<b>25,563,064</b>
<b>31</b>	0	(unmeasured)	13,560	0.95	12.67	11.97	4.78	4.75	4.80	2.53	<b>7.92</b>	<b>7.17</b>	<b>12,510,351</b>
<b>32</b>	1	5,585,270	16,840	1.19	20.96	16.05	17.34	7.94	7.04	2.27	<b>13.02</b>	<b>9.01</b>	<b>22,370,090</b>
<b>33</b>	3	1,205,530	14,640	1.62	16.16	16.02	4.03	5.27	5.04	2.88	<b>10.89</b>	<b>10.98</b>	<b>24,694,262</b>
<b>34</b>	0	0	12,360	0.52	10.05	6.62	5.73	5.17	5.03	1.37	<b>4.88</b>	<b>1.59</b>	<b>6,348,976</b>
<b>35</b>	2	(unmeasured)	15,240	1.33	23.83	24.54	4.60	12.69	15.56	5.53	<b>11.14</b>	<b>8.98</b>	<b>29,670,382</b>
<b>36</b>	3	8,637,990	37,840	0.69	47.28	27.37	37.76	25.06	20.91	16.19	<b>22.22</b>	<b>6.46</b>	219,321,351
<b>37</b>	0	0	10,640	1.09	24.61	26.01	8.38	9.53	9.01	6.79	15.08	17.00	<b>11,093,630</b>
<b>38</b>	0	0	9,720	0.38	25.34	28.84	8.81	12.66	13.88	7.85	12.68	14.96	<b>6,053,654</b>
<b>39</b>	0	0	18,960	0.14	27.03	28.25	15.23	12.14	11.62	9.98	14.89	16.63	<b>24,463,943</b>
<b>40</b>	0	0	21,242	0.00	36.12	24.38	33.22	13.78	10.02	14.99	<b>22.34</b>	<b>14.36</b>	141,708,902
										MEAN	28.29	27.58	88,669,277
										MAX	66.21	72.37	475,496,577
										MIN	4.88	1.59	6,053,654

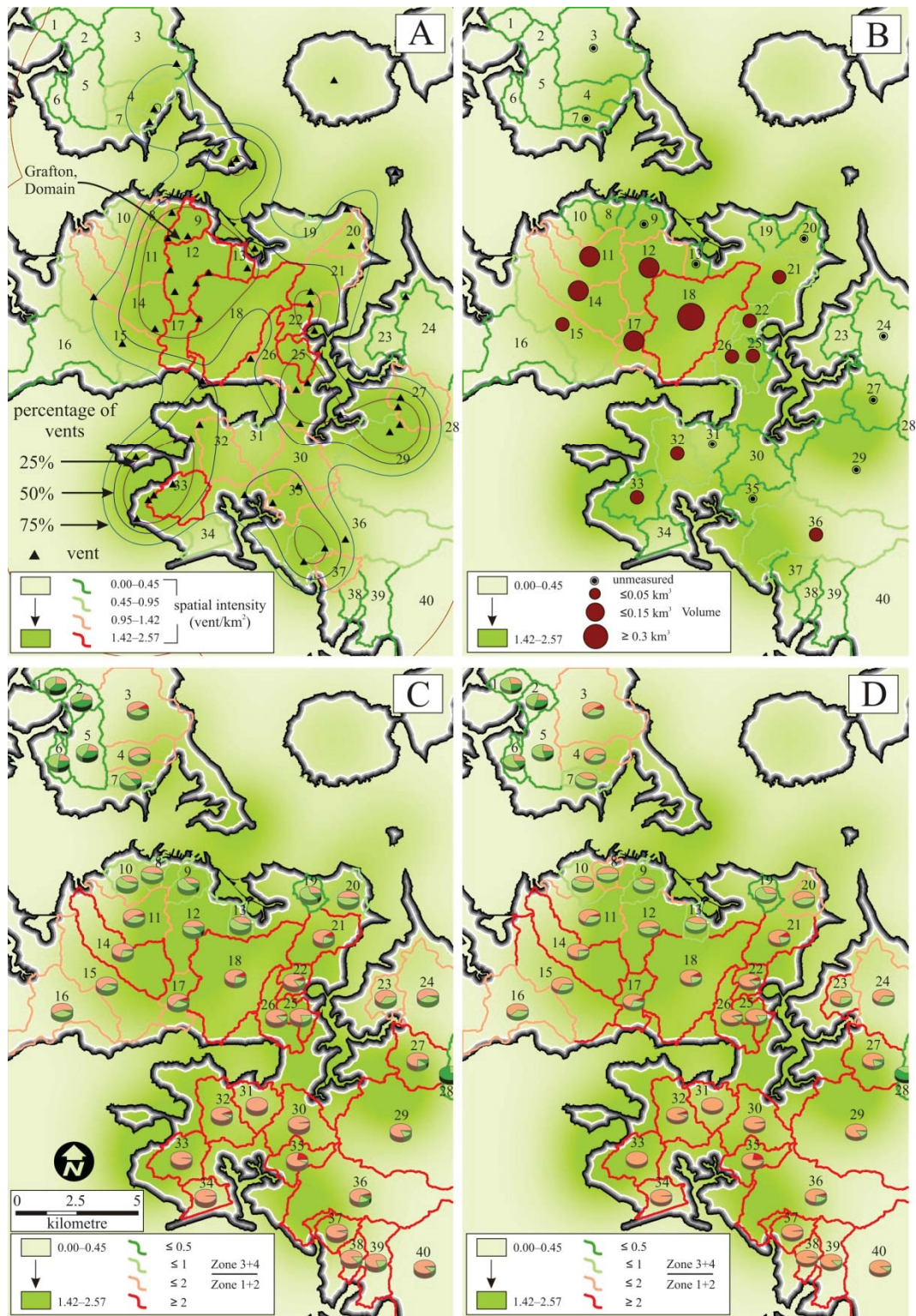


**Figure 6.7** Figure showing the spatial density of the entire field (green background on each map) based on the location of the 50 eruption centres (triangles in A). A 400 m wide zone at the coastline is indicated by black-grey-white lines, see text for explanation. (A) Watershed ranking based on the averaged kernel density. The contour lines (black lines) represent the 25%, 50% and 75% percentage of input point used to estimate the probability density distribution. (B) Watershed ranking based on cumulative bulk volume. (C and D) These two maps show the area portion (pie diagrams) of zones within watersheds for the Scenario 1 (C) and Scenario 2 (D). The colouring of the watershed boundaries shows the ratio between the total areas of buffer (light green) and ridge/peaks (dark green) as well as depressions (red) and low-lying areas (pink). The colours used here are the same as on the lava flow susceptibility map in Fig. 6.9.

### 6.4.1. Lava flow susceptibility

In this study, the topography and morphometry of past lava flows were used to generate a simple map that outlines relative susceptibility to inundation by lava flow associated with a future monogenetic eruption (Fig. 6.9). One of the major advantages of this assessment is that it is completely vent-location independent, preferable for hazard prediction in less-frequently erupting monogenetic volcanic fields. The main assumption of this technique to produce lava flow susceptibility maps is that the topography will play the major role in controlling the distribution of lava flows, which has been widely documented elsewhere (Bonne et al., 2008; Favalli et al., 2009d). Based on the lava flow susceptibility map, the potentially safe areas were identified as buffer and ridge zones. The zones in the Fig. 6.9 only depict lava flow susceptibility from distal sources (closer than  $L_{max}$ , <6.5 km), because near vent accumulation of lava can produce thicker lava accumulations (e.g. Rangitoto) and the vent opening eruption may truncate the topography merging watersheds. A future lava flow may not travel as far as in past examples, up to 10 km (Eade, 2009), because of the high density of buildings especially in the central parts of Auckland, thus the 6.5 km flow distance is a maximum estimate.

In the AVF, there are two distinct parts of the lava flow susceptibility map (Fig. 6.9), a northern-central hilly region and a southern flat region. Thus, different flow behaviour is expected over these two areas. The southern parts of the AVF are characterised by watersheds that lack natural topographical boundaries and that have small differences in elevation between the watershed boundaries and channels (Fig. 6.9). This implies that future lava flows can easily flow over the topography, affecting multiple watersheds. On this flat terrain dominated by anthropogenic features, such as houses, bridges or roads, the topography-based lava flow forecasting codes could forecast incorrect and unrealistic pathways for future lava flows due to the minimal elevation difference between neighbouring cell values. Such a minimal elevation difference may also be caused by differences in anthropogenic features (e.g. houses), vegetation, errors in the data acquisition or subsequent raw-data processing, such as vegetation filtering and noise reduction. If a future eruption takes place in the southern region of the field, it will likely result in either a landform similar to Rangitoto and/or a phreatomagmatic crater filled by lava flows (Fig. 6.1). However, its size and

geographical extent over the flat topography will vary as a function of total volume of magma and effusion rates involved in the eruptions. To model such distribution a more effusion rate or viscosity-governed lava flow simulation is needed.

In contrast, most lava flows that have been emplaced during the last 50 ky are situated in the northern and central part of the field, within valleys on the Waitemata paleosurface (Fig. 6.1). In these regions, the size (i.e. thickness, length, or area) and shape (i.e. elongated or circular) of past lava flows were strongly governed by the properties of hosting valleys (Fig. 6.8). The elevation difference between the topographic lows (depressions and valley bottoms) and highs (ridges or hill tops) are large enough to stop or force future lava flows to change direction, and therefore control their geographical extent (Fig. 6.9). The North Shore and Central Auckland host the majority of the ridges that can be interpreted as relatively safe places from a distal ( $<L_{max}$ ) future lava flow. Overall, due to the generally low volume host capacity (i.e. lack of depressions) of these watersheds, future lava flows are inferred to either fill their initially hosting watershed rapidly and spill out to neighbouring ones (especially in the southern region), or flow down to the coastal area and enter into the sea, possibly forming littoral cones. The likelihood of overspill of lava from a watershed to another may be low because the volumes beneath the present ridge lines are high, mostly  $>0.12 \text{ km}^3$ , which is larger than 96% of the total population of the past bulk volumes of the AVF (Table 6.3) (Kereszturi et al., 2013b).

#### 6.4.2. Watershed characteristics

The lava flow susceptibility map (Fig. 6.9) does not provide information about the location of future eruption(s), but the spatial intensity of past eruptions may give us a general picture of vent concentrations. These higher intensity regions may be the likely locations of future vents if the spatial controls, such as stress field, faulting or location of melt source in the mantle, still remain the same as they were in the past (Fig. 6.7). Nevertheless, not all of the vents in Auckland produced lava flows, making spatial intensity values somewhat unreliable for lava flow hazard assessment. For instance, some vents located in both the northern and southern parts, were formed by hydromagmatic eruptions and are presented by tuff rings, maars and tuff cones (Allen and Smith, 1994; Allen et al., 1996; Smith et al., 2008). A consequence of the negative,

crater-like shape of such volcanic features is that any late-stage effusive activity was generally emplaced within the previously formed crater, creating lava lakes rather than flows, e.g. Crater Hill (Allen et al., 1996). Thus, they did not cover an extended area. A similar outcome is expected during a future eruption where lava effusion follows phreatomagmatic activity. The volume distribution of the lava flows examined within watersheds coincides with the spatial intensity peaks, because the centrally located watersheds hosted the majority of the large bulk lava flow volumes, excluding Rangitoto (Fig. 6.7). The largest bulk volume ( $0.3 \text{ km}^3$ ) hosted by a single watershed is observed in the case *ID18*, containing One Tree Hill (Figs. 6.1 and 6.7). This watershed (*ID18*) also has a large volume-capacity ( $0.46 \text{ km}^3$ ), which means that if a future eruption does not exceed this volume; the flows will be controlled by the topographical extent of this watershed.

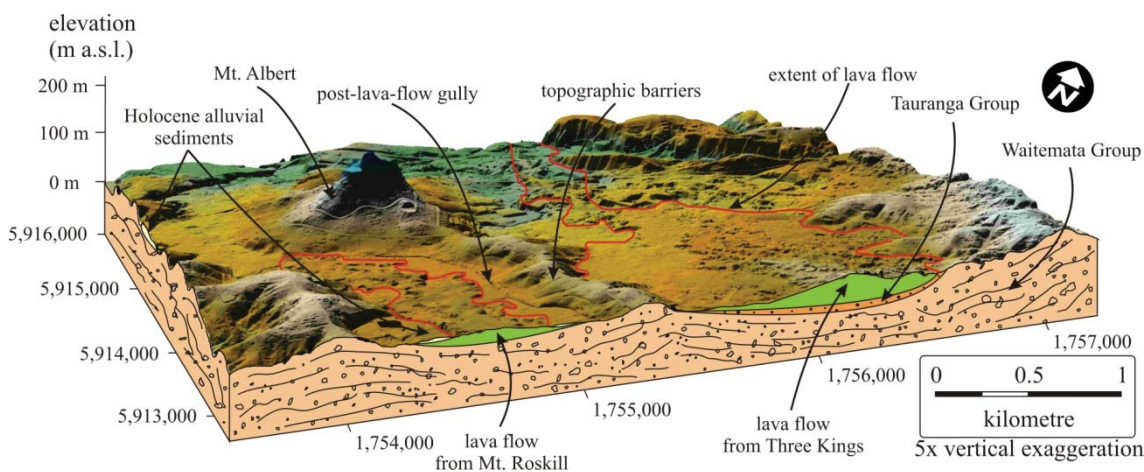


**Figure 6.8** Cross-section through the central, elevated part, of the AVF, illustrating the channelised lava flows by valley eroded into the Waitemata sandstone. For the detailed location see Fig. 6.1.

The proportion of susceptibility zones within watersheds reveals that the geographical locations of safe zones are highly scattered and mostly concentrated in the central and northern part of the field (Fig. 6.7). The difference between the scenarios (i.e. without and with Rangitoto), causes only a slight decrease in the area of buffer zone and ridges in Scenario 2. The majority of the centrally located watersheds also have a significant proportion of predominantly flat areas, which favours the spreading of a lava flow over the topography in some cases  $>50\%$  of the watershed. Nevertheless, the elevation of the rim of each watershed is high enough ( $\geq T_{mean}$  or  $\geq 15 \text{ m}$ ) to hinder the overspill of lava flows to neighbouring watersheds. The larger watersheds, such as *ID*

14 or *ID18* in the central area, have a high proportion of depressions and low-lying areas (Fig. 6.7). Finally, the highest likelihood of future topographically-controlled lava flow emplacement occurs at the northern edge of the AVF. In this area the total proportion of buffer and ridge zones within a watershed is generally >50%. In contrast, the southern parts are almost completely lacking in topographically elevated ridges or hill tops (Figs. 6.7 and 6.9).

### 6.4.3. Evaluation of the method and its limitations

There are a few limitations of the mapping technique presented. For instance, future eruptions may occur on a ridge, possibly feeding multiple watersheds (the only example is Mt. Albert; Fig. 6.8). The possibility of an eruption on a ridge (or local topographical highs) is likely when the magma supply is high enough to generate faulting. This is possibly expected in the case of high-magma-flux volcanic fields that are often magmatically-controlled (Valentine and Krogh, 2006; Valentine and Perry, 2007). The bulk magma supply of most of the eruptive centres in the AVF was in the range of  $\leq 0.1 \text{ km}^3$ , excluding One Tree Hill and Rangitoto (Table 6.1). This is in the range of the typical, intraplate monogenetic eruptive volume values (e.g. Valentine and Perry, 2006). In addition, the central part of Auckland, where watershed-controlled behaviour of a future lava flow is expected, a few normal faults have been identified (e.g. Kenny et al., 2011). The combination of the limited magma supply with the presence of large-scale faulting means, the propagation of magma related to a future eruption is expected to be captured by the pre-existing structural features. This means that vent-position of a future eruption is more likely to be situated within the valleys (or watershed) and not on the ridges if the magma supply of a future eruption remains in the same range as it was in the past eruptions. On this theoretical basis, the delimited ridges could be interpreted as the safest places during a future effusive eruption. This is in further agreement with the fact that most of the past eruptive centres are located within valleys and not on the ridges. Thus, in the localization of the monogenetic volcanism, the topography may have played a major role.

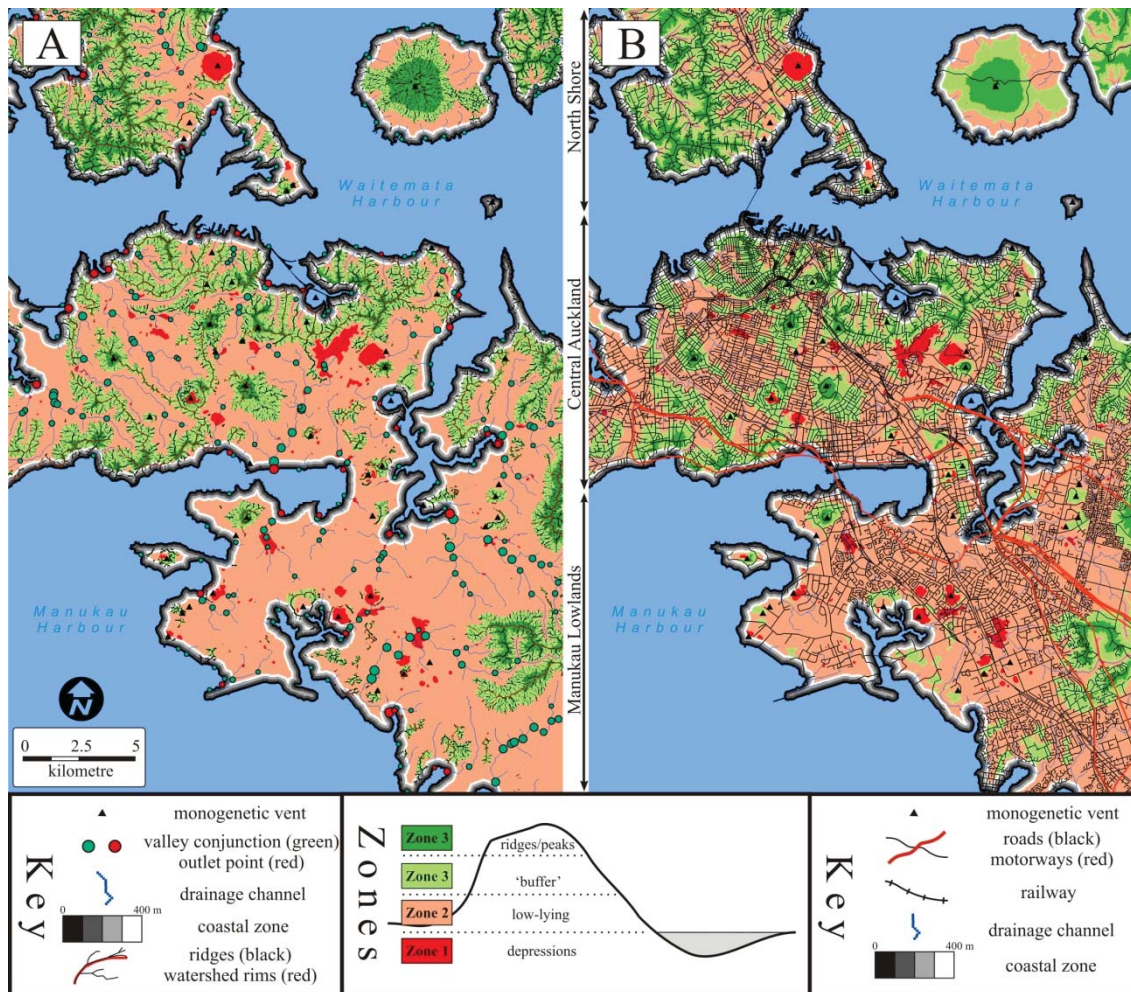


**Figure 6.9** Lava flow susceptibility map based on Scenario 1 (without Rangitoto) for the AVF showing the susceptibility zones with the major hydrological and topographical characteristics (A) and with major infrastructures (B).

Another limitation of the method (and all such methods) is the possibility of phreatomagmatic explosion forming craters that can control the subsequent lava flow emplacement. This scenario is especially important in the southern, low-lying area, where porous-controlled, water-saturated alluvial sediments are common (Kermode, 1992), which are able to fuel phreatomagmatic eruptions (Houghton et al., 1996). There is also possibility in future events that the topography will be altered or watersheds become truncated by various large-scale eruptive processes that will require a dynamic lava flow modelling approach and/or a continuous update of topographically delimited hazard zones.

Finally, some limitation and uncertainty in the delimited susceptibility zones may derive from the under- or overestimate of lava flow thickness preserved in the past lava

flows due to accuracy of the basement reconstructed beneath the volcanic edifices and lava flows.

## 6.6. Conclusions

The AVF is highly susceptible to lava flows, which are likely to travel further, and be more destructive to infrastructure over longer periods, than the products of explosive opening phases of monogenetic eruptions at Auckland. Past lava flows in Auckland totalled  $>2 \text{ km}^3$  in bulk volume (mostly produced during the last 40 ky), with average flows reaching 2.5 km (up to 6.5 km) and with a mean thickness of  $\sim 14.8 \text{ m}$ . They covered areas up to  $>25 \text{ km}^2$ , but on average  $5.1 \text{ km}^2$ .

Two scenarios were tested using two different lava-thickness threshold values calculated directly from the flow properties. These scenarios showed that the study area can be split into two regions, south and north: the southern part lacks large-scale topographical boundaries (ridges) that can significantly control the pathways of future lava flows, whereas in the north, ridges of underlying sandstone are prominent enough to potentially control the distribution and shape of future lava flows. The field also lacks large depressions that can be lava depocentres. Extremely long lava flows are hence only expected from future Auckland eruptions located in topographically constrained portions of the central/northern region of the field.

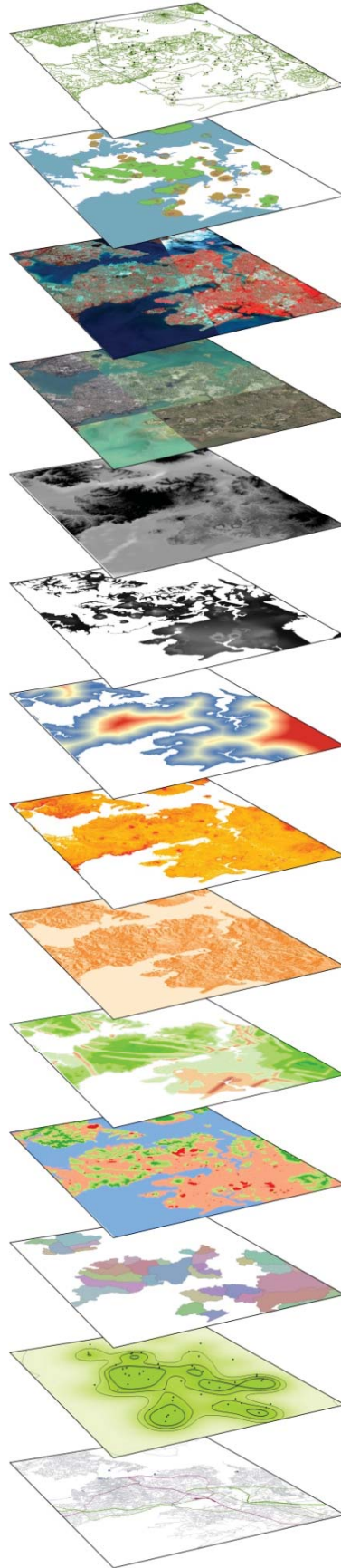
The range of methods applied here are available in free or commercial GIS software packages, and when combined they provide valuable results that can be used for lava flow susceptibility mapping. In addition, freely available remotely-sensed DSMs or DTMs, such as 30 m or 90 m STRM, provide opportunities giving place for increasing lava flow susceptibility modelling over monogenetic volcanic fields worldwide.

The major advantage of this method is that it is suitable for modelling lava flow susceptibility for monogenetic volcanic fields, where no eye-witnessed eruption was recorded. This method is also vent-location independent because it is based on morphometric characteristics of past lava flows and the present state of the topography. The compiled lava flow susceptibility map is based on detecting relative topographic difference as compared to the local low point (bottom of drainage channels), improving the adaptive nature of this technique. This method can be used as an input map for

detailed dynamic lava flow simulations. Due to the very flat morphology of the southern part of Auckland, thermorheological-dependent models rather than topography-dependent models are more favourable for modelling lava flow pathways.







Chapter **7**  
lava flow simulations

# 07 / lava flow simulations

This Chapter aims to examine the suitability of using the rheology-based numerical lava flow simulation code, MAGFLOW, to understand factors behind lava flow emplacement in the Auckland Volcanic Field (AVF), New Zealand, specifically eruption durations and speed of lava flow inundation from past eruptions. In this Chapter, eight past lava flows were simulated using a set of input parameters, such as lava flow rheological estimates and eruptive volumes measured from Digital Surface Models (DSMs). The successful validation of a lava flow simulation code for the AVF is a starting point in understanding the lava flow hazard of the field, and for creating eruption scenarios for magmatic effusive activity.

Supplementary data for this Chapter are in Appendix B.

## Chapter contents

7.1. Introduction.....	189
7.2. Materials and methods.....	194
7.2.1. MAGFLOW code.....	194
7.2.2. Input data for simulation of past lava flows .....	197
7.2.3. Matching lava flows with simulation results .....	200
7.3. Results .....	200
7.4. Discussion.....	206
7.4.1. Volume-limited versus cooling-limited flow regimes.....	206
7.4.2. Constraints on magma ascent velocity .....	207
7.4.3. Volcanic hazard consequences.....	210
7.4.4. Creating eruption scenarios for lava flow hazard mapping .....	210
7.4.5. Limits of lava flow simulations in volcanic field settings.....	211

## Chapter Seven – Effusive eruption scenarios based on lava flow simulations

### 7.1. Introduction

Apart from distal tephra fall, lava flow is the largest-distributed volcanic product of the Auckland Volcanic Field (AVF), New Zealand, and lava flows affected double the area of phreatomagmatic eruption products. In Chapter 6 a vent-independent lava flow susceptibility map for ‘average’ lava flow thickness was produced based on the assumption of the important role of topography on the lava flow emplacement mechanism, leading to topographically confined and unconfined types of lava flows. A hindrance to the next step of vent-dependent hazard modelling is the uncertainty in forecasting eruption sites. However, modelling lava flows from specific vent sites in the AVF remains a highly useful approach for better understanding the effect of lava flow on the infrastructure and economy. In addition, modelling past lava-producing eruptions is not only useful for calibrating models for the AVF, but also provides information, such as flow durations and speeds of inundation, that is critical for emergency management planning. For lava flow simulations, a large variety of models/codes have been developed (e.g. Proietti et al., 2009). These codes are increasingly popular, due to the greater availability of freely available Digital Surface Models from volcanic areas, such as Mt. Etna, Italy (Del Negro et al., 2005), and Mauna Loa, Hawaii (Harris and Rowland, 2001), and an increase in computing capacity. Fundamentally, there are two kinds of simulation codes: stochastic and deterministic codes.

Stochastic codes calculate the probability of a cell being inundated by lava during emplacement (Arana et al., 2000; Felpeto et al., 2001; Favalli et al., 2005; Damiani et al., 2006; Felpeto et al., 2007; Favalli et al., 2009d; Tarquini and Favalli, 2011; 2013), without modelling the lava’s fluid-dynamic processes (Hulme, 1974; Dragoni, 1989; Gregg and Fink, 2000; Griffiths, 2000; Harris et al., 2000; 2007c). These codes determine lava flow paths by either following the steepest descent path on a stochastically perturbed topography (e.g. Favalli et al., 2005), or by choosing the descent path from a 3×3 cell moving window using Monte Carlo algorithms, weighted by maximum slope angles (e.g. Felpeto et al., 2001). Such approaches are based on an important assumption that the major influence on lava flow emplacement is the pre-

existing topography, i.e. the relative elevation of a grid cell in a 3×3 cell moving window (Felpeto et al., 2001; Favalli et al., 2005; 2009d).

The code DOWNFLOW was developed based on stochastic perturbation of the topography (Favalli et al., 2005; 2012a). The DOWNFLOW code determines the maximum slope (i.e. steepest terrain path) at each step of the inundation simulation. In each iteration, a stochastic perturbation of the topography is added within a predefined range of  $\pm h$  (Favalli et al., 2005). Then, on the perturbed topography, the maximum slope descent path is calculated. This iteration is repeated thousands and thousands of times, and a probability of inundation is determined based on the number of times the grid cell received the steepest descent path (e.g. Favalli et al., 2005). The range of perturbations of topography is used as an analogue for the maximum height (i.e. absolute elevation difference at a location on a digital terrain) that a lava flow can overpass (Favalli et al., 2005). Therefore, in DOWNFLOW, there is no need to predefine the total volume or effusion curves. Although, this code does not determine the length of the flow; therefore, it is a user-defined parameter in DOWNFLOW. Thus, the validation of such stochastic codes is based on empirical relationships (Favalli et al., 2005; 2009e; Tarquini and Favalli, 2011; 2013), such as the relationship found between the vent height above sea level and the maximum length of past lava flows from Etna volcano (e.g. Guest, 1982). Nevertheless, it has been validated and used at many other composite volcanoes, such as Mt. Nyiragongo, Democratic Republic of Congo (Favalli et al., 2009a) and Mt. Cameroon, Cameroon (Favalli et al., 2012b). Other codes, such as that developed in Felpeto et al. (2001), use similar techniques to assess the likelihood of a cell being inundated, using Monte Carlo simulations, where the probability is higher with steeper slope angle values (Arana et al., 2000; Felpeto et al., 2001; Damiani et al., 2006).

Some deterministic lava flow simulation codes and approaches consider the lava flow rheological behaviour and cooling conditions at a unit area (i.e. grid cell) along with the topography (Ishihara et al., 1990; Young and Wadge, 1990; Miyamoto and Sasaki, 1997; Harris and Rowland, 2001; Crisci et al., 2004; Del Negro et al., 2005; Hidaka et al., 2005; Proietti et al., 2009; Vicari et al., 2011). Others use the topography (Guest and Murray, 1979; Kauahikaua et al., 1995a; Gomez-Fernandez, 2000; Bonne et al., 2008). In the physics-based simulation codes, the rheological properties of lava flow are dependent on many factors, as are their spatial and temporal interactions, including

the composition of lava, crystallinity and temperature (Pinkerton, 1987; Pinkerton and Stevenson, 1992; Calvari and Pinkerton, 1999; Harris and Allen Iii, 2008). These input variables determine viscosity and yield strength of a propagating lava flow (Dragoni et al., 1986; Dragoni, 1989; Dragoni and Tallarico, 1994). These codes account for various degrees of complexity in known lava processes in three dimensions and over time. In 1D, the FLOWGO numerical model can be used to evaluate maximum expected run-out distances for a cooling-limited, channelised lava flow (Harris and Rowland, 2009). This code was developed based on lava flow examples from Hawaii (Harris and Rowland, 2001; Rowland et al., 2005) and later adapted to Mt. Etna (Harris et al., 2007a; Wright et al., 2008). This numerical model, however, requires a large range of input data, such as composition, initial and solidification temperature, microlite content, crystallinity, vesicularity, density, surface thermal structure (e.g. solidified lava crust proportion), crust temperature and basal crust thickness (Harris and Rowland, 2001; Rowland et al., 2005). This extensive range of input data is not available for most volcanic regions, especially for fields with no historical eruptions. Thus, the applicability of this flow model is limited in older volcanic terrains. As a consequence of the 1D calculation environment, the results of the FLOWGO code are the maximum run-out distance and the changes of input parameters over distance from the source vent (Harris and Rowland, 2001). The vast majority of other available numerical codes for lava flow simulations operate in 2D, including FLOWFRONT (Young and Wadge, 1990; Wadge et al., 1994), MAGFLOW (Del Negro et al., 2008; Herault et al., 2009), and SCIARA (Crisci et al., 2004; Avolio et al., 2006). The latter two codes are both based on the Cellular Automata (CA) method of solving complex patterns of solidification processes and heat conditions (Ishihara et al., 1990; Barca et al., 1994; Miyamoto and Sasaki, 1997; Crisci et al., 2004; Avolio et al., 2006; Vicari et al., 2007; Del Negro et al., 2008; Herault et al., 2009). The only model for lava flows in a 3D environment is LavaSIM, which was developed by Hidaka et al (2005).

Other deterministic approaches use topography characteristics, such as hydrologic watershed (e.g. Guest and Murray, 1979) or elevation distribution on a moving window (Gomez-Fernandez, 2000), as the major control on the spatial distribution of lava flows. These approaches are often termed the “lavashed” concept (Kauahikaua et al., 1995a; Favalli et al., 2009d). This method has been applied to Hawaii (Kauahikaua et al., 1995a; Kauahikaua et al., 1995b), Mt. Etna (Guest and Murray, 1979) and Mt.

Cameroon (Bonne et al., 2008). These approaches describe the long-term susceptibility and hazard from lava flow, rather than short-term factors, such as run-out distance, and area affected. Fundamentally, this topographic concept is similar to the method developed in Chapter 6.

‘Hybrid’ numerical codes and techniques for lava flow simulations use both deterministic and probabilistic components (e.g. Wright et al., 2008). For instance, the deterministic 1D FLOWGO and the stochastic DOWNFLOW can be used together in order to assess the maximum expected run-out distance constraint on all the steepest descent paths simulated by DOWNFLOW (e.g. Wright et al., 2008; Harris et al., 2011). Another approach is to combine deterministic and stochastic components in identifying lava flow hazard with numerical codes, such as was introduced in Connor et al. (2012). The deterministic component is the lava distribution over a DEM that is based on an iterative grid cell filling routine if the effective elevation (i.e. pre-defined lava thickness+DEM elevation) is less than the source cell’s elevation (Connor et al., 2012). This algorithm is similar to other methods used in drainage analysis and DEM processing (e.g. Planchon and Darboux, 2002). The input data are field-derived because the code requires the modal thickness data of past lava flows. The stochastic part of this approach is the simulation of the spatial distribution of future monogenetic vents and their volumetric characteristics (Connor et al., 2012).

No earlier lava flow simulations have been attempted in the AVF. In this investigation, lava flow simulations were applied in order to assess emplacement conditions and eruption scenarios for future hazard assessment of the AVF. Considering the generally flat terrain in the AVF, a rheology and physics-based lava flow simulation code was chosen due to its ability to model detailed lava flow emplacement processes (e.g. solidification, inflation, bifurcation, depression/valley filling and pressure-driven flow spreading). Alternative probabilistic approaches, such as codes by Felpeto et al. (2001) and DOWNFLOW (Favalli et al., 2005), are dependent strongly on the volcanic terrain’s morphology; therefore, they are less feasible for forecasting lava flow paths in low-relief areas. FLOWGO is useful to identify the maximum length of channelised lava flows (Harris and Rowland, 2001; Rowland et al., 2005), but it does not provide information on the area affected and thickness. For this study, a 2D deterministic code, MAGFLOW, was chosen for the AVF, due to its capability to run on the available input data (eruptive volumes, density and vent distributions, Digital Surface Model). A

validation exercise was carried out on MAGFLOW based on simulating eight past eruptions in the AVF, including: Little Rangitoto, Mt. Hobson, Mt. Roskill, Mt. St. John, Three Kings, Mt. Wellington, and Mt. Eden. These sites were chosen based on the high quality of data for reconstructing the pre-eruptive topography (Fig. 7.1).

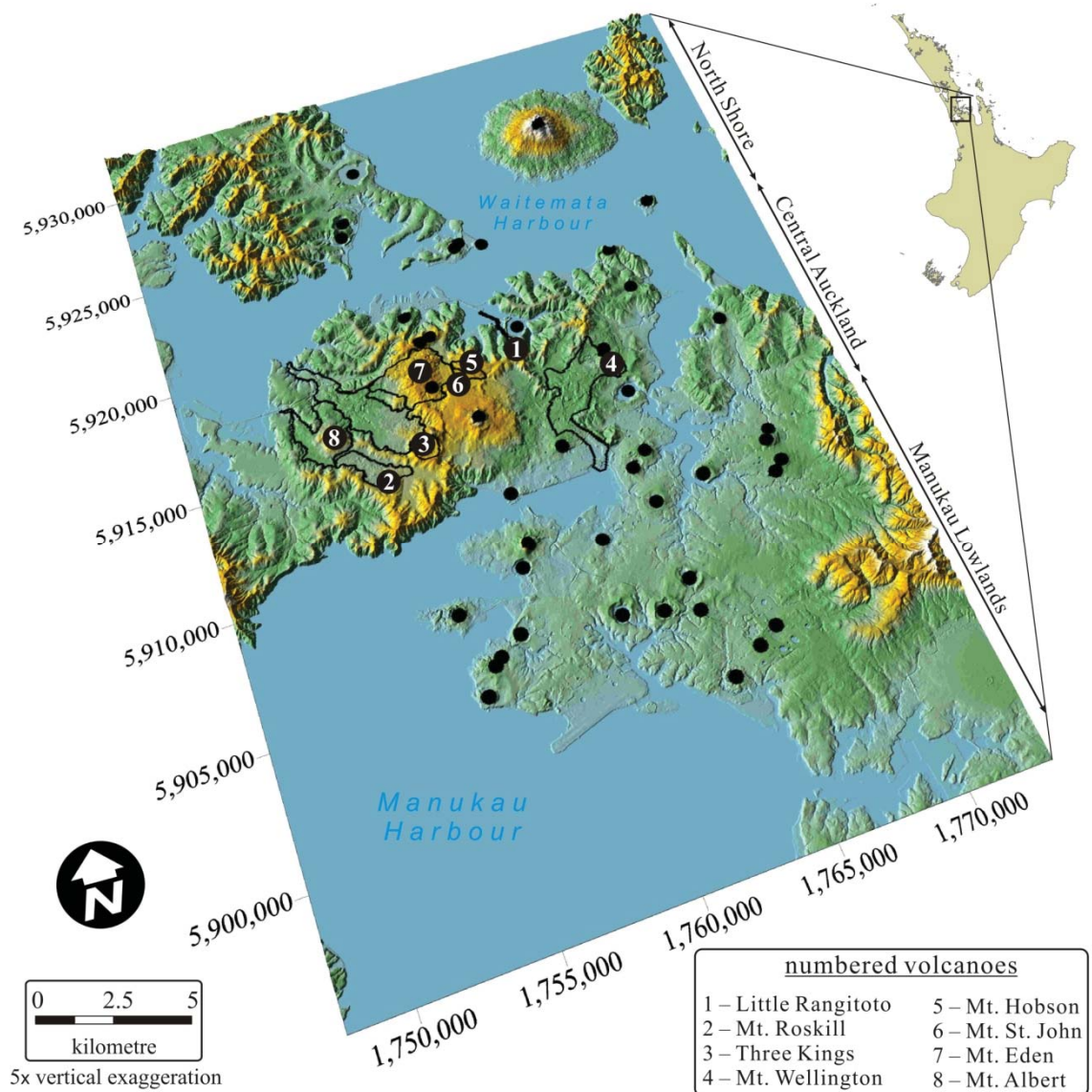


**Figure 7.1** Overview of the AVF and its volcanoes (black dots) and the location of the simulated lava flows (numbered black dots).

**Table 7.1** Summary of the input physical parameters of the lava flows ( $L_{\max}$  – maximum length,  $A_{\text{lava}}$  – area,  $T_{\max}$  and  $T_{\text{mean}}$  – maximum and average thickness, bulk and DRE-corrected eruptive volumes).

location	$L_{\max}$	$A_{\text{lava}}$	thickness		eruptive volume	
			$T_{\max}$	$T_{\text{mean}}$	bulk	DRE
	m	m <sup>2</sup>	m	m	m <sup>3</sup>	m <sup>3</sup>
<b>Little Rangitoto</b>	ca. 2.5 km	315,550	-	5	1,577,750	1,206,979
<b>Mt. Hobson</b>	750	715,745	-	10.0	7,157,452	5,475,451
<b>Mt. Roskill</b>	2,463.2	1,833,000	29.5	8.2	15,128,393	11,573,221
<b>Mt. Albert</b>	2,320.6	3,705,500	29.7	6.4	23,658,031	18,098,393
<b>Mt. St. John</b>	ca. 11 km	3,616,311	-	10	36,163,114	27,664,782
<b>Three Kings</b>	5,723.8	6,086,600	49.4	12.6	78,263,127	59,871,292
<b>Mt. Wellington</b>	6,525.8	6,642,600	49.3	14.7	99,169,044	75,864,318
<b>Mt. Eden</b>	2,175.8	4,772,400	77.5	25.8	109,586,065	83,833,340

## 7.2. Materials and methods

### 7.2.1. MAGFLOW code

The MAGFLOW code is based on the Cellular Automata (or Cellular Automaton abbreviated as CA hereafter) technique originally developed during the 1940s in the Manhattan Project, Los Alamos National Laboratory, New Mexico (e.g. Von Neumann, 1966). CA requires gridded input data where each cell has a ‘state’ that is simultaneously updated by applying local, mostly mathematical/physical rules. In each iteration, the grid cell state is updated based on the grid cell itself and the neighbour cell’s state. This property of CA allows simulation of complex evolutionary patterns in accordance with the local rule, usually on a 3×3 matrix or moving window (e.g. John Conway's Game of Life). CA is very sensitive to distance variation between the central cell and its neighbours on a 3×3 kernel. This is due to the rectangular-based grid cell representation, in which the Euclidian distance between the centre cell ( $Z5$ ) and its neighbours ( $Z2$ ,  $Z4$ ,  $Z6$  and  $Z8$ ; Fig 3.6) in the  $X$  and  $Y$  principal direction is 1. However, the distance to the neighbours ( $Z1$ ,  $Z3$ ,  $Z7$  and  $Z9$ ; Fig 3.6) located in the orthogonal directions is usually approximated as  $\sqrt{2}$  (i.e. using Pythagorean Theorem). This sensitivity of CA can be overcome by using Monte Carlo simulations for determining neighbourhood distances (Vicari et al., 2007). This approach allows the

code to create neighbours that are randomly distributed within a given radius from the central cell (Vicari et al., 2007). The state detail of each randomised point around the cell of being updated is derived from the grid-based surface. In practice, this approach helps to cut out anisotropy in simulation results. This problem is solved elsewhere by applying hexagonal cell geometries (e.g. Crisci et al., 2004), instead of the conventionally used rectangle-based geometry (e.g. Garbrecht and Martz, 1994).

In the CA-based MAGFLOW code, each grid cell has two attributes, the thickness and heat of lava that are calculated iteratively (Del Negro et al., 2005; Vicari et al., 2007). The motion of the lava flow evolves in accordance with Bingham fluid dynamics and is subject to pressure forces (i.e. variation in lava thickness and topography) (Miyamoto and Sasaki, 1997; Del Negro et al., 2005). In the case of Bingham behaviour, a viscous fluid will flow once the specific yield strength exceeds a threshold value (e.g. Dragoni et al., 1986). Consequently, the lava flow is characterised by a yield strength ( $s$ ) and plastic viscosity ( $\mu$ ) (Dragoni et al., 1986). In MAGFLOW, this motion is calculated at each grid cell by solving the Navier-Stokes equation, which determines the lava flux (Del Negro et al., 2005; Vicari et al., 2007). Numerically, this lava flux ( $q$ ) is:

$$q = \frac{sh_{cr}^2\Delta x}{3\mu} \left( a^3 - \frac{3}{2}a^2 + \frac{1}{2} \right) \quad (7.1)$$

where  $a = h/h_{cr}$ ,  $h_{cr}$  is the critical thickness, and  $\Delta x$  is the distance between two neighbouring grid cells. The critical thickness is:

$$h_{cr} = \frac{s}{\rho g (\sin \alpha - \frac{dh}{dx} \cos \alpha)} \approx \frac{s\sqrt{\Delta z^2 + \Delta x^2}}{\rho g (\Delta z - \Delta h)} \quad (7.2)$$

where the  $\rho$  is the density of lava,  $g$  is the acceleration due to gravity,  $\Delta z$  is the difference in height between the neighbour cells, and  $\Delta h$  is the thickness increase in the receiver cell. The viscosity and yield strength is approximated by the temperature of the lava (Pinkerton and Stevenson, 1992; Harris and Rowland, 2001). The yield strength in the MAGFLOW code is formulated after Ishihara et al. (1990):

$$\log_{10} s(T_{cell}) = 13.00997 + 0.0089T_{cell} \quad (7.3)$$

while the viscosity is after Giordano and Dingwell (2003):

$$\log_{10} \mu(T_{cell}) = -4.643 \frac{5812.44 - 427.04 \times H_2O}{T_{cell} - 499.31 + 28.74 \ln(H_2O)} \quad (7.4)$$

where the  $T_{cell}$  is the temperature in Kelvin, while the water content ( $H_2O$ ) is in weight percentage.

The heat quality ( $Q$ ) of each grid cell is evaluated using the following heat budget:

$$Q_{t+\Delta t} = Q_t + \Delta Q_{t,m} - \Delta Q_{t,r} \quad (7.5)$$

where

$$\Delta Q_{t,m} = \left( \sum_{q_n > 0} q_n T_n + \sum_{q_n < 0} q_n T_{cell} \right) \rho c_v \Delta t \quad (7.6)$$

$$\Delta Q_{t,r} = \varepsilon A_{cell} \sigma T_{cell}^4 \Delta t \quad (7.7)$$

where  $T_{cell}$  is the temperature of the central cell,  $T_n$  is the neighbour cell's temperature,  $q_n$  is the flux between the cells to cell  $n$ ,  $c_v$  is the specific heat,  $\varepsilon$  is the emissivity of lava,  $\sigma$  is the Stefan-Boltzmann's constant ( $5.68 \times 10^{-8} \text{ J/m}^2/\text{s/K}^4$ ),  $\Delta t$  is the iteration timestep, and  $A_{cell}$  is the area of the cell. The heat at each grid cell then is calculated as:

$$T_{t+\Delta t} = \frac{Q_{t+\Delta t}}{\rho c_v h_{t+\Delta t} A} \quad (7.8)$$

where the  $h_{t+\Delta t}$  is the thickness of lava.

A limitation of MAGFLOW is that it does not account for heat loss into the ground, and convection with the atmosphere. These two can cause “heat-gain” at each grid cell during simulations. Wind and rain are also not considered, but will affect the cooling of lava flows (e.g. Garel et al., 2013). These limitations could result in an overestimation of the simulated lava flow.

### 7.2.2. Input data for simulation of past lava flows

The required input data for MAGFLOW include some physical properties of lava flow, such as initial and solidification temperatures ( $T_i$  and  $T_s$ ), specific heat ( $c_v$ ), emissivity ( $\epsilon$ ), water content (H<sub>2</sub>O vol%), density ( $\rho$ ), and pre-eruptive terrain (DEM). In addition, before simulations with MAGFLOW, effusion curves and vent locations must be defined. Locating a vent in this study was based on an obvious source scoria cone or cones. The effusion curves should be based on geologically well-constrained models or observed analogues. These values were determined using AVF eruptive volumes and similar basaltic examples elsewhere. The MAGFLOW code was developed for modelling lava flows on Mt. Etna, and this model was adopted for the AVF in the first instance. This is supported by similar basaltic compositions (e.g. Andronico et al., 2005), eruptive volumes (e.g. Vicari et al., 2011), lava morphotypes (e.g. Calvari and Pinkerton, 1999), and inferred rheological properties (e.g. Pinkerton and Norton, 1995).

**Table 7.2** Overview of MAGFLOW input parameters for the simulation in the AVF.

input parameters	symbol	unit	value used
density	$\rho$	kg/m <sup>3</sup>	2650
initial temperature	$T_i$	K	1473
solidification temperature	$T_s$	K	1100
emissivity	$\epsilon$	-	0.9
specific heat	$c_v$	J/Kg/K	1150
H <sub>2</sub> O content	-	wt. %	0.07

The **initial and solidification temperatures ( $T_i$  and  $T_s$ )** were adapted from the literature. Based on the dominant proportion of olivine as a phenocryst, the maximum temperature of the eruption of ca. 1493 K can be constrained, similar to Eade (2009). Other mineral assemblages, such as clinopyroxene, often comprise the groundmass; consequently, they formed during the eruption. The solidus temperature of clinopyroxene is around 1443 K, considering a predominantly low-silica, basaltic compositional range (Smith et al., 2008). This shows that the initial temperature varied between 1493 to 1443 K (Eade, 2009). In the simulation, an average value of 1473 K was used (Table 7.1). The solidus temperature of 1100 K was chosen to be similar to

other lava flow simulation studies (Harris and Rowland, 2001; Hidaka et al., 2005; Vicari et al., 2007; Herault et al., 2009).

The **emissivity ( $\epsilon$ )** and **specific heat ( $c_v$ )** were defined as 0.9 and 1150 J/Kg/K, respectively. These values were determined on the basis of empirical estimates on historical lava flows of Mt. Etna (Del Negro et al., 2005; Herault et al., 2009; Vicari et al., 2011). This value for emissivity and specific heat are close to those used in other physics-based lava flow simulation codes, such as 0.95 and 1225 J/Kg/K (e.g. Harris and Rowland, 2001), 0.66 and 1260 J/Kg/K (Hidaka et al., 2005), as well as 0.7–0.95 and 840 J/Kg/K (Proietti et al., 2009).

The **water content ( $H_2O$  wt%)** was chosen to be 0.07 wt%, which is lower than the 0.6 wt% documented in Mt. Cameroon, Cameroon (e.g. Wantim et al., 2013), but larger than some alkali basaltic lava rock from Mt. Etna (e.g. Giordano and Dingwell, 2003).  $H_2O$  can have a significant influence on the viscosity and liquidus temperature of the flowing lava (e.g. Pinkerton and Stevenson, 1992), and it has been found to be sensitive input data for MAGFLOW (Bilotta et al., 2012).

The **density ( $\rho$ )** is fixed as 2650 kg/m<sup>3</sup>, which is in agreement with the analysed samples from lava units of Rangitoto and Browns Island (Chapter 4). This density value includes 10 vol% vesicles, in agreement with independent measurements from Rangitoto (e.g. Nowak, 1995), and the accepted “standard” value of lava rock of basaltic composition (e.g. Cashman et al., 1994; Cashman and Kauahikaua, 1997; Kilburn, 2000).

The **effusion flux and curve ( $Q$ )** are estimated from analogue lava flows elsewhere. The lava flow simulations are based on the bulk lava flow volume data of the AVF. Bulk lava flow volumes were used, rather than Dense Rock Equivalent-corrected (DRE) values, because the former have a direct link with the physical resulting flow. For the effusion curve, a linear increase with a break in slope by an exponential decay was used (Fig. 7.2). The effusion curves were created with their maximum flux occurring at a quarter of the total duration, similar to Cappello et al. (2011). The total lava effusion durations were fixed between 50h and 2500h (Fig. 7.2). The shape of the effusion curves are in agreement with the observed trend from the 1256 AD Al Madinah eruptions, Kingdom of Saudi Arabia (Camp et al., 1987), 1981 AD, 2001 AD and 2011 AD flank eruptions of Mt. Etna, Italy (Marsella et al., 2011; Vicari et al., 2011; Ganci et al., 2012), 1980 AD and 1984 AD eruption of Krafla, Iceland (Harris et al., 2000), as

well as the total eruption rates documented from the Paricutin eruption, Mexico (Fries, 1953; Luhr and Simkin, 1993).

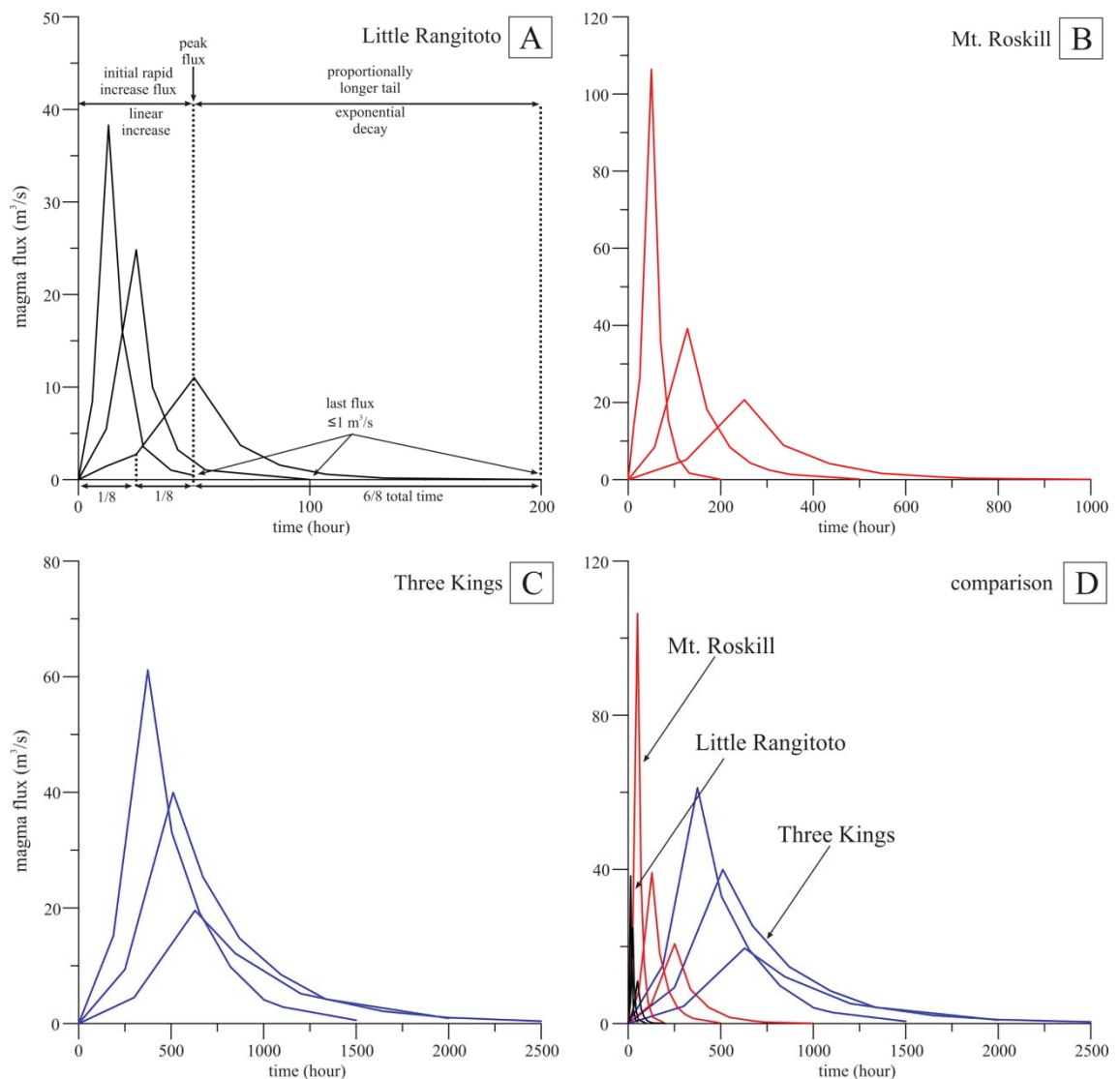


**Figure 7.2** Graph shows three effusion curves of Little Rangitoto (A), Mt. Roskill (B) and Three Kings (C) and their comparison (D).

The **pre-eruptive terrain** is represented by a DEM, in which the eruptive products, such as lava flows and scoria cones, have been removed. This DEM was created based on subtracting the volumes of each volcanic component (e.g. lava flows, ejecta rings, scoria cones etc.) from the present DSM. The final surface was smoothed with a moderately large ( $7 \times 7$ ) average moving window, before simulations. This removed any artificial “steps” that were created by stripping off the eruptive products from the present topography.

### 7.2.3. Matching lava flows with simulation results

Lava flow morphological properties, such as length ( $L$ ), thickness and its variability ( $t_{mean}$ ,  $t_{median}$ ), and area ( $A$ ), were calculated for actual and simulated lava flows. From each of these control parameters two types of error were calculated: (1) proportional error ( $\% = \text{simulated/observed} \times 100$ ), and (2) fitting function ( $\eta$ ). The fitting function is defined as (Rongo et al., 2008):

$$\eta = \sqrt{\frac{A_{sim} \cap A_{real}}{A_{sim} \cup A_{real}}} \quad (7.9)$$

where  $A_{sim}$  and  $A_{real}$  are the area of the simulated and real lava flows, respectively. The chosen scenarios have also the highest value of  $\eta$  (Table 7.3).

## 7.3. Results

Lava flows from eight volcanoes were simulated with the MAGFLOW code. In order of increasing eruptive volume, these examples were Little Rangitoto (0.001 km<sup>3</sup>), Mt. Hobson (0.007 km<sup>3</sup>), Mt. Roskill (0.015 km<sup>3</sup>), Mt. Albert (0.023 km<sup>3</sup>), Mt. St. John (0.036 km<sup>3</sup>), Three Kings (0.078 km<sup>3</sup>), Mt. Wellington (0.099 km<sup>3</sup>) and Mt. Eden (0.109 km<sup>3</sup>). These examples cover a wide volumetric range of the past eruptions of the field (ca. 96 % of the whole volcano population; Chapter 4).

For three examples, Mt. Hobson, Mt. Wellington and Mt. Eden, the pre-eruptive DSM was the most difficult to reconstruct. Thus, for these three the simulated flows did not agree well with the known lava flow thicknesses and outlines. For Mt. Albert and Mt. St. John the fit between the simulation and the actual outline was poor, with a fitting function,  $\eta$ , of  $\leq 0.5$ . These results were thus not used in the further validation procedures. The best simulation results ( $\eta = \geq 0.5$ ) were achieved at Little Rangitoto ( $\eta = 0.62$ ), Mt. Roskill ( $\eta = 0.84$ ) and Three Kings ( $\eta = 0.74$ ) (Figs. 7.3–5 and Table 7.3). In the case of Mt. Roskill and Three Kings volcanoes, longer effusive scenarios have higher  $\eta$  values. In these cases, the best fitting scenario selection was based on  $A_{sim} \cap A_{real} \%$ . These lava flows still cover 66–92% of the known extent, thus they can be used to provide the first estimate of the properties of effusive eruptions at the AVF.

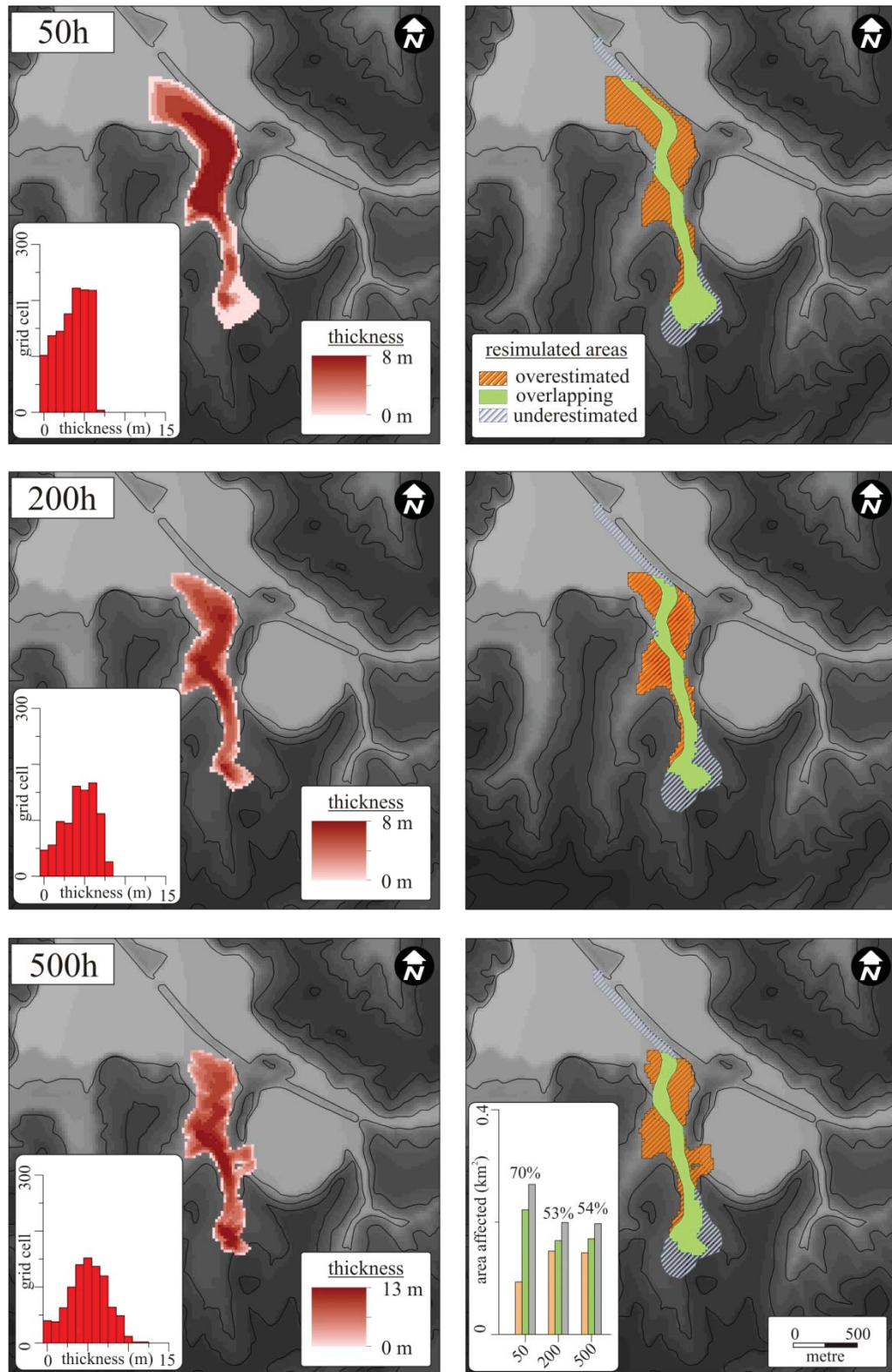


**Figure 7.3** Lava flow simulation results of Little Rangitoto (left-hand side) and comparison with the mapped extent of the flow (right-hand side). On the left-hand side, the histogram insets show the distribution of thickness values for the simulations.

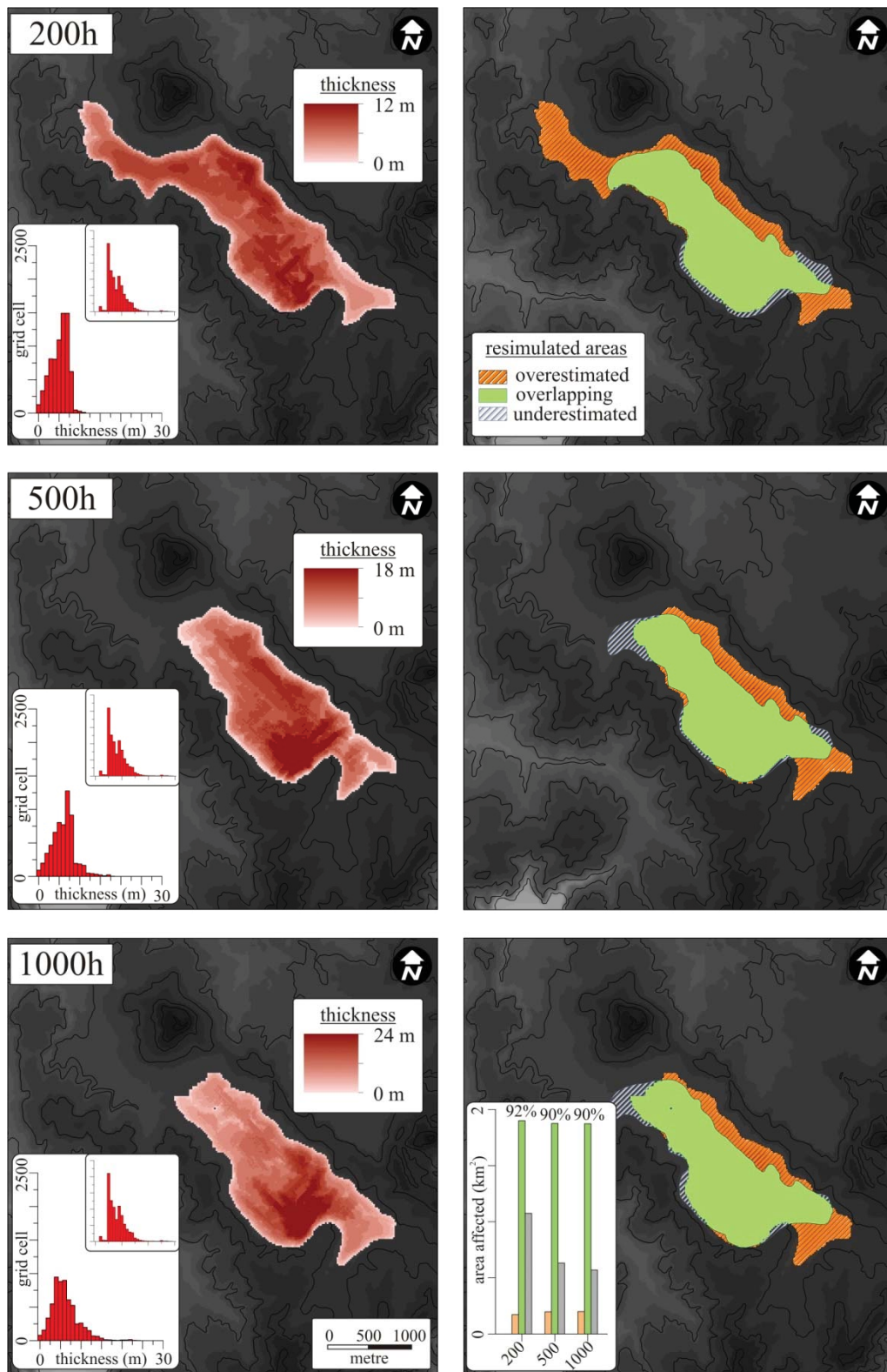


**Figure 7.4** Lava flow simulation results of Mt. Roskill (left-hand side) and comparison with the mapped extent of the flow (right-hand side). On the left-hand side, the histogram insets show the distribution of thickness values for the simulations; the smaller histograms are the original flow thickness distributions.

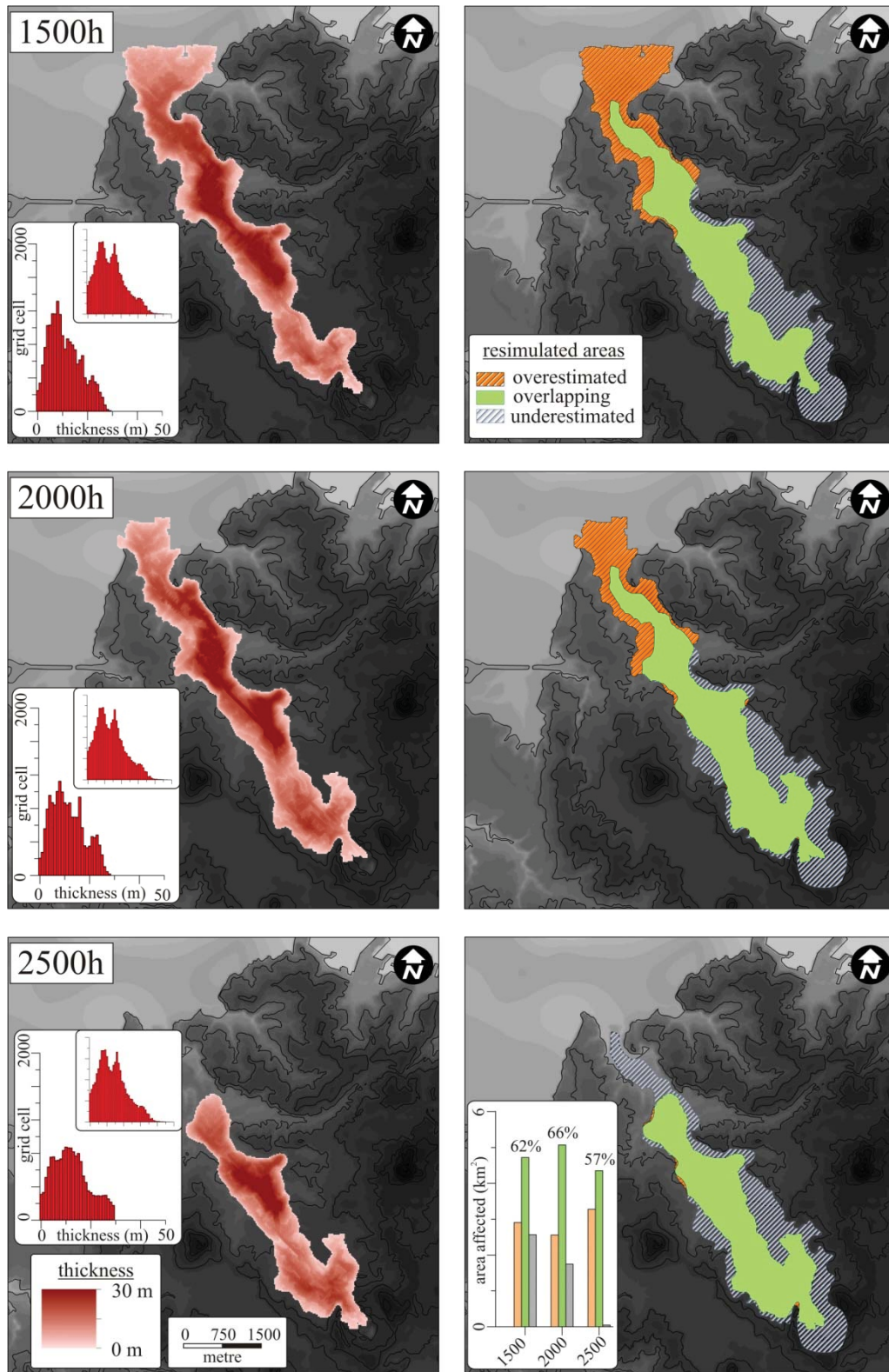


**Figure 7.5** Lava flow simulation results of Three Kings (left-hand side) and comparison with the mapped extent of the flow (right-hand side). On the left-hand side, the histogram insets show the distribution of thickness values for the simulations; the smaller histograms are the original flow thickness distributions.

**Table 7.3** Comparison of properties of simulated lava flow scenarios of Little Rangitoto, Mt. Roskill and Three Kings examples. The best-fit scenarios are highlighted in green.

Three Kings (0.078 km <sup>3</sup> )											
parameters	unit	real flow	1500h			2000h			2500h		
			simulated	$\eta$	%	simulated	$\eta$	%	simulated	$\eta$	%
<b>total area</b>	m <sup>2</sup>	7,628,358	7,288,408		95.5	6,815,685		89.3	4,398,481		57.7
underestimated	m <sup>2</sup>		2,906,898			2,558,471			3,275,821		
overlapping	m <sup>2</sup>	7,628,358	4,721,460	0.68	61.9	5,069,887	0.74	66.5	4,352,536	0.75	57.1
overestimated	m <sup>2</sup>		2,566,948			1,745,799			45,944		
<b>length</b>	m	6,729.13	7,915.30		117.6	7,523.63		111.8	5,180.21		77.0
<b>thickness mean</b>	m	13.8	11.1		80.5	11.4		82.9	11.1		80.9
<b>thickness median</b>	m	11.4	9.8		86.5	10.5		92.5	10.8		94.7

Mt. Roskill (0.015 km <sup>3</sup> )											
parameters	unit	real flow	200h			500h			1000h		
			simulated	$\eta$	%	simulated	$\eta$	%	simulated	$\eta$	%
<b>total area</b>	m <sup>2</sup>	2,073,084	2,975,513		143.5	2,507,990		121.0	2,443,200		117.9
underestimated	m <sup>2</sup>		172,851			197,614			200,114		
overlapping	m <sup>2</sup>	2,073,084	1,900,233	0.78	91.7	1,875,470	0.83	90.47	1,872,970	0.84	90.3
overestimated	m <sup>2</sup>		1,075,281			632,520			570,231		
<b>length</b>	m	2,463	3,697		150.1	2,189.33		88.9	2,058.20		83.6
<b>thickness mean</b>	m	8.3	5.1		61.4	6.1		72.9	6.1		73.9
<b>thickness median</b>	m	7.4	5.5		74.1	6.2		84.3	5.6		75.6

**Table 7.3** (continued)

Little Rangitoto (0.001 km <sup>3</sup> )											
parameters	unit	real flow	50h			200h			500h		
			simulated	$\eta$	%	simulated	$\eta$	%	simulated	$\eta$	%
<b>total area</b>	m <sup>2</sup>	315,550	489,120		155.0	366,340		116.1	367,540		116.5
underestimated	m <sup>2</sup>		93,586			148,579			145,234		
overlapping	m <sup>2</sup>	315,550	221,964	0.62	70.3	166,971	0.57	52.91	170,316	0.58	54.0
overestimated	m <sup>2</sup>		267,156			199,369			197,224		
<b>length</b>	m	2306.98	2,072.90		89.85	1,807.85		78.4	1,628.64		70.6
<b>thickness mean</b>	m	5.0	3.5		69.80	4.3		86.0	5.0		99.2
<b>thickness median</b>	m	5.0	3.8		75.36	4.5		90.0	5.0		99.3

The bulk volume was held constant, while eruption duration was varied in each model run. This resulted in shorter eruption durations (e.g. 50–500 hours) having larger maximum magma discharge rates (i.e. magma flux) than in those lava flows simulated over longer time (500–2500 hours). The most dramatic changes were shown by the maximum flow length. For example, the Three Kings simulated lava flows varied in length between 7900 and 5100 m, depending on rapid versus slow magma discharge rates. For long-lived scenarios, lava flow thickening (e.g. inflation) was observed (e.g. Mt. Roskill simulated flows went from 0–10 up to 0–23 m; Fig. 7.4).

## 7.4. Discussion

### 7.4.1. Volume-limited versus cooling-limited flow regimes

The best fitting lava flow simulations were obtained at a constant peak magma flux of  $\sim 40 \text{ m}^3/\text{s}$  in each case (e.g.  $38.3 \text{ m}^3/\text{s}$  for Little Rangitoto,  $39.1 \text{ m}^3/\text{s}$  for Mt. Roskill, and  $39.9 \text{ m}^3/\text{s}$  for Three Kings). All of the studied lava flows had, however, very contrasting eruptive volumes and lava flow lengths, showing that an empirical relationship between effusive rate and lava flow length (Walker, 1973) is not applicable. In the cooling-limited lava flow regime, flows attain their maximum length in accordance with the cooling rate, which is a function of the effusion rate (e.g. Harris and Rowland, 2009). This cooling-limited flow regime is a characteristic of some lava flows in Hawaii and Mt. Etna (e.g. Harris and Rowland, 2009). By contrast, the simulated lava flows from the AVF appear to have been emplaced in a volume-limited regime. In this case, the flow front and the body stop advancing before the maximum (i.e. cooling-limited) extent is reached, due to the magma supply shutting down (Harris and Rowland, 2009). The average effusion rates [i.e. total volume subdivided by the total duration (Harris and Rowland, 2009)] for the best-fitting scenarios are between 8.4 and  $10.8 \text{ m}^3/\text{s}$ . For a cooling-limited lava flow with an average rate of effusion of  $10 \text{ m}^3/\text{s}$ , maximum flow length is expected to be in the range of 8–12 km (Walker, 1973). The only flow that has reached this length in the AVF is that of Mt. St. John (Table 7.1). The majority of the lava flows in the AVF stopped well short of their cooling-limited ranges. This suggests a strong eruptive volume control (i.e. supply-control) on the evolution of past lava flows in the AVF. Volume-limited lava flow regimes are thus likely for any future effusive event in this volcanic field. To explain the similar peak magma flux

values at the AVF, other controls must have played an important role, such as differences in feeder-dyke geometries (e.g. number and length of source fissures) and ascent velocities.

#### 7.4.2. Constraints on magma ascent velocity

Magma ascent rate is an important control on eruption styles and conduit processes (Parfitt, 2004; Pioli et al., 2008; Valentine and Gregg, 2008). Due to the lack of direct observation of magma ascent, there are only indirect methods to estimate these, such as water contents within olivine crystals (e.g. Demouchy et al., 2006; Peslier and Luhr, 2006), band and zoning of olivine, pyroxene or spinel xenocrysts (e.g. Szabó and Bodnar, 1996; Jankovics et al., 2013) or mantle xenolith size (e.g. Sparks et al., 1977; Spera, 1984). These studies suggest that the ascent rates of basaltic magma that penetrate the crust lie between  $10^{-3}$  and  $10^1$  m/s.

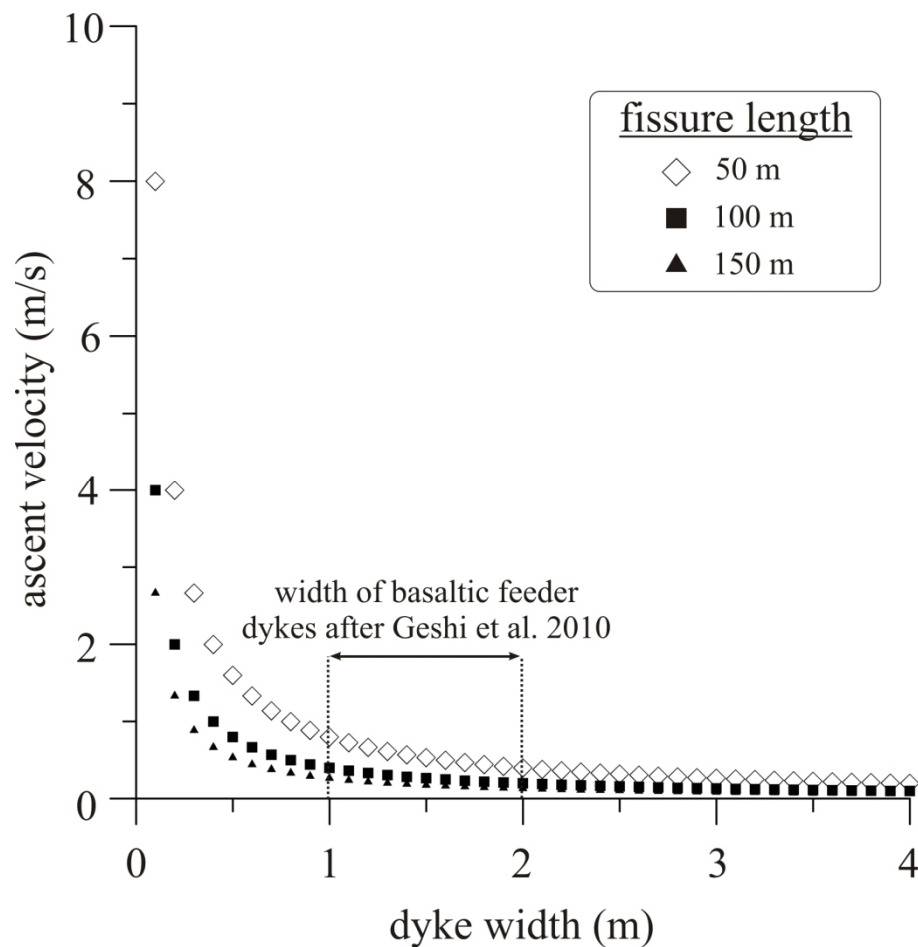


**Figure 7.6** Dyke widths as a function of ascent velocity for a fissure length of 50, 100 and 150 m. The magma flux is estimated at  $40 \text{ m}^3/\text{s}$ , in accordance with the value of best simulation.

In the AVF, there is limited information on ascent rates (e.g. Blake et al., 2006). The lava flow simulations may be used to calculate ascent velocity in a feeder dyke, if the dyke geometry is known (e.g. fissure length and dyke width). The minimum fissure lengths in the AVF can be estimated based on the size of the eruptive craters. These are usually  $\leq 200$  m in diameter for the larger eruptive centres (e.g. Rangitoto; Chapter 4). However, the majority of the scoria cones have many small craters with diameters of  $\leq 150$  m (Fig. 7.7). The peak discharge rate for all the best-fit results was  $\leq 40$  m<sup>3</sup>/s. Using dyke widths from 0.1 m to 4 m, increasing by 0.1 m, which is the accepted range of a small-volume ( $\leq 0.1$  km<sup>3</sup>) basaltic dykes (Geshi et al., 2010), the ascent velocity was modelled for fissure lengths of 50, 100 and 150 m (Fig. 7.6). The most likely width of a feeder dyke for scoria cone volcanoes is 1–2 m (e.g. Geshi et al., 2010; Galindo and Gudmundsson, 2012). This is equivalent to a magma ascent rate of 0.8–0.2 to 0.4–0.1 m/s (Fig. 7.6). This is consistent with a transitional eruption style, between Strombolian ( $\leq 0.1$  m/s) and Hawaiian eruption styles ( $\geq 0.1$  m/s) (Parfitt, 2004), which, in turn, matches several observed AVF volcanoes' facies architectures (Houghton et al., 1999).

Independent validation of this range of ascent velocities can be made from the settling of mantle-derived xenoliths. In Pupuke volcano, diameters of these mantle xenoliths reach up to 2 cm in diameter (e.g. Spargo, 2007). Based on these mantle xenolith sizes (Sparks et al., 1977), the calculated magma ascent rates range from 0.1 to maximum 1 m/s (Blake et al., 2006).

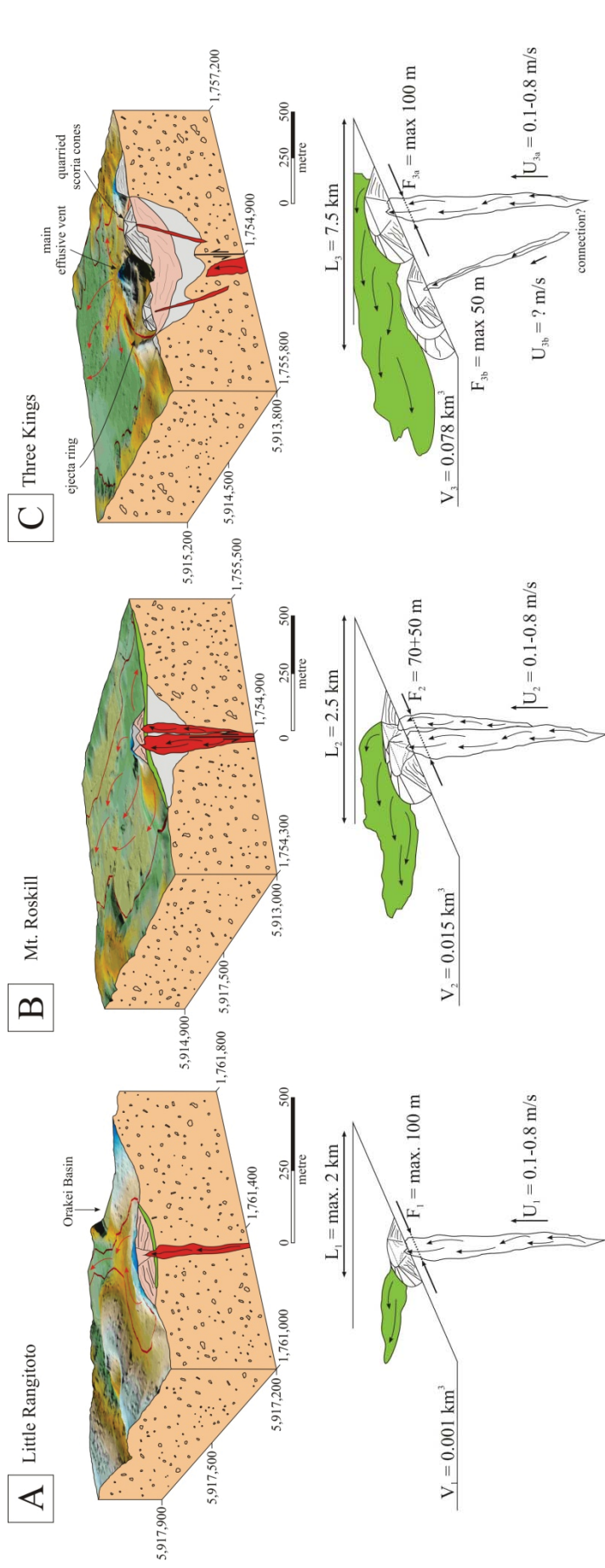


**Figure 7.7** Envisaged feeder dyke geometries of the three eruption centres. Abbreviated parameters are  $U$  – ascent velocity,  $L$  – flow length,  $F$  – fissure length, and  $V$  – bulk eruptive volume.

### 7.4.3. Volcanic hazard consequences

The magma ascent rates can be further used in approximating total rise time of a dyke from a high-pressure source to the surface. The likely source of these magmas is at a depth of  $\leq 2.5\text{--}3$  GPa, equivalent to 80–90 km, in the asthenosphere (e.g. McGee et al., 2013). Assuming a depth of 90 km and without crustal stalling (e.g. Smith et al., 2008), the total ascent of the magma would be over a maximum of 10.4 days, leaving little time for detecting seismic precursors or InSAR deformation, that are important for assessing the likely location of vent opening and preparing for an eruption in or near the densely populated City of Auckland. These rates are slightly lower than the range suggested by previous studies in the AVF (e.g. Sherburn et al., 2007). The effectiveness of detecting a rising pocket of magma lies in its volume. Rising magma in the AVF is capable of causing earthquakes up to a magnitude of  $\leq 5.5$  (Sherburn et al., 2007). The size of such ascending magma batch(es) also holds important information from hazard mitigation and management perspectives (e.g. influencing the duration of ongoing volcanic eruptions).

The durations of past eruptions are effectively unknown for the AVF. Durations for the lava flows simulations carried out here range from as little as 50 h (=2.1 days) for Little Rangitoto up to 500 to 1000 hours (=20.8 to 41.6 days) for medium-sized eruptions, such as Mt. Roskill. The largest simulated flow was from Three Kings, which may have lasted  $\geq 2000$  h (= 83.3 days). These confirm the first order approximations calculated in Chapter 4. These three examples of eruption durations cover almost the entire range (ca. 92%) of AVF volcanoes, and consequently, they can be used for hazard assessment purposes (e.g. lava flow hazard mapping using these confirmed and validated eruption durations and scenarios).

### 7.4.4. Creating eruption scenarios for lava flow hazard mapping

The best-fitting effusion curves and eruption scenarios discussed above could be used in further lava flow simulations. Given the small-volume of Little Rangitoto, and the present “wet”/interglacial environment, a replay of this eruption in the present day would be expected to be phreatomagmatic throughout a significant proportion of its

magma supply (Chapter 5). Lava flows are more likely with a larger magma supply, such as a Mt. Roskill and Three Kings event.

For lava flow hazard mapping by MAGFLOW and any other codes, there is a need to define vent locations. There are two approaches to this: (1) systematic, grid-fashioned, and (2) non-systematic distributions. In the grid-fashioned approach, the spacing between two vents should be defined in both  $X$  and  $Y$  principal directions. This has been applied at Mt. Etna (e.g. Favalli et al., 2009e; Cappello et al., 2011; 2012). For this technique the overall goal is to ensure as many simulations as possible for each grid cell location, building up a large database of complete scenarios. In the case of emergency, the stored data (e.g. simulation results) can be recalled quickly and be assessed further. The most popular technique is, however, the non-systematic vent position, which is usually based on the distribution of past volcanoes, on a composite volcano or within a monogenetic volcanic field (e.g. Connor et al., 2012; Favalli et al., 2012b). The spatial distribution of potential future vents is modelled by estimating spatial intensity with kernel techniques (Connor and Connor, 2009; Cappello et al., 2012; Becerril et al., 2013). In this case, volcanic eruptions are expected to be occurring in the area of high spatial intensity, if the magma release mechanism and its controls have not changed since the formation of the past eruption centres. This criterion is, however, not always fulfilled by a low-flux monogenetic volcanic field (Chapter 4), where the spatial distribution of eruption centres tends to be random (e.g. Le Corvec et al., 2013a). In the AVF, both techniques could be applied in future studies for better understanding of the hazard posed by lava flows. Given the contrasting susceptibility of the AVF, it is likely that the vent-spacing for the simulation is not uniform. In other words, vents in the simulation might be more largely-spaced in the predominantly flat Manukau Lowlands than in the valley-dominated Central Auckland and North Shore areas (Fig. 7.1). These different topographic conditions should be investigated in the future by applying lava flow simulation over sampling areas with different topographic conditions.

#### 7.4.5. Limits of lava flow simulations in volcanic field settings

In an intraplate volcanic field, the majority of the erupting volcanoes have had some degree of phreatomagmatic eruption during their eruptive histories. This is

controlled by the external environment, such as the type and distribution of surface- and ground-water and the hosting sediments (e.g. Sohn, 1996). A crater formed by a series of small-volume phreatomagmatic explosions can be a deposition centre for a subsequent lava flow, creating a scenario of overspill that cannot be accurately forecast. Consequently, the results of lava flow simulations have to be interpreted in accordance with the susceptibility to phreatomagmatism at the vent location of the simulated lava flow.

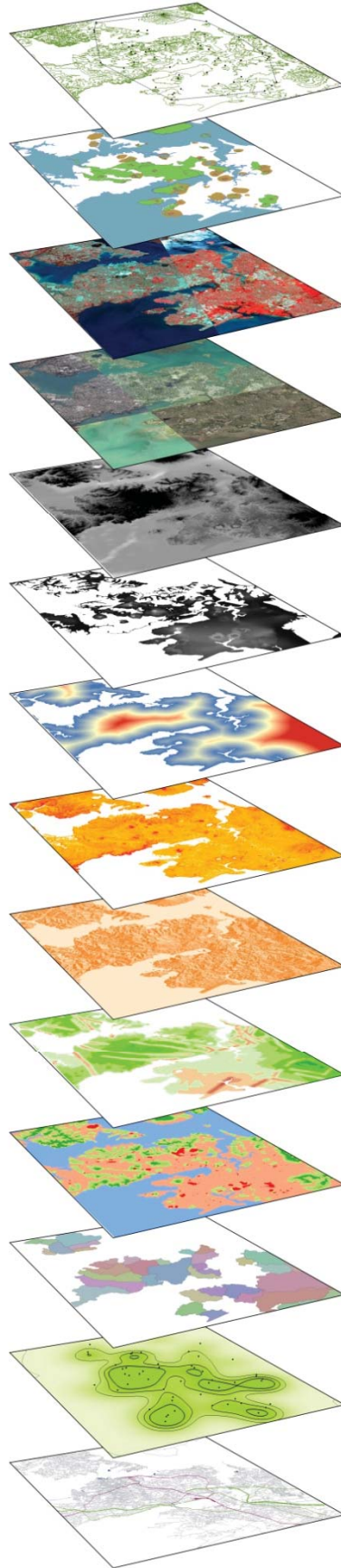
Another limitation can arise from the complexity of effusion curves that might vary from the theoretical norm of Fig 7.2. In light of geochemical studies, a monogenetic volcano might not be formed from a single batch of ascending magma, but compositionally multiple batches (e.g. Brenna et al., 2010). These subsequent magma batches can increase the magma flux temporally so that it is more susceptible to produce lava flows, such as has been recorded from Browns Island (e.g. McGee et al., 2012), or Pupuke (Spargo, 2007) volcanoes in the AVF. However, monogenetic volcanoes in the AVF include several chemically simpler examples, such as Crater Hill (Smith et al., 2008), Orakei Basin (Németh et al., 2012), Maungataketake (Agustín-Flores et al., 2014) or North Head (Agustín-Flores, pers. comm.). Geochemical diversity should be accounted for in the interpretation of lava flow simulations and hazard maps.

## 7.5. Conclusions

Applying lava flow simulation codes to an intraplate volcanic field is a promising method for estimating several controlling conditions that have an influence on the duration and impact of monogenetic eruptions. In this investigation, the lava flow simulation results suggested complex interactions occur between the magma supply volume, ascent velocity and feeder dyke geometry. These combine to influence the area and length of lava flows. Several well-modelled eruption scenarios of the AVF provide a wide range of magma supply scenarios that could be used for producing lava flow hazard and susceptibility maps. The necessity of such pre-eruption hazard mapping, planning and preparedness is justified in light of the extremely short rise time (about 10 days) of such small-volume magma batch(es) from the mantle to the surface. Such ascent eruptive scenarios and hazard planning could be applied for other potentially active monogenetic volcanic fields, such as Harrat Rahat, Saudi Arabia, or San

Francisco Volcanic Field in Arizona. In such as monogenetic settings, including the AVF is, pre-eruptive planning is critical, given the proximity of the metropolitan area to an active small-volume magmatic system.





Chapter 8  
Discussion  
and Conclusions

# 08 / discussion and conclusions

This Chapter summarises the major aspects of the geological and volcanological datasets and GIS data layers that were developed in this investigation, to provide a synthesis of our current understanding of volcanic hazard in the Auckland Volcanic Field (AVF), New Zealand. This Chapter goes on to propose conceptual models for analysing and mapping susceptibility and volcanic hazards in monogenetic volcanic fields. These can be used to interface with “standard” probabilistic techniques for identifying likelihoods of vent opening at a given location, such as kernel density methods. The Chapter describes how data integration into a GIS could be used to develop eruption style forecasts for the AVF and similar basaltic monogenetic volcanic fields.

Supplementary data for this Chapter are in Appendix B.

## Chapter contents

8.1. Discussion.....	217
8.2. A conceptual model for eruption style susceptibility mapping .....	218
8.3. A conceptual model for lava flow susceptibility mapping .....	227
8.4. Towards a GIS-based hazard assessment of monogenetic volcanic fields.....	231
8.5. Conclusions.....	233
8.5.1 Research objectives .....	233
8.5.2. Future directions of research.....	235
8.5.3. Concluding remarks .....	237

## Chapter Eight – Discussion and conclusions

### 8.1. Discussion

This investigation quantified the volumes of the volcanic edifices and component products formed during the 250 ky evolution of the Auckland Volcanic Field (AVF), New Zealand. These new data were derived from field observations and mapping, as well as remote sensing datasets, such as Light Detection And Ranging (LiDAR) derived Digital Surface Models (DSMs) (Chapter 3). The database for the AVF's volcanoes involved a systematic breakdown of the typical components of monogenetic volcanoes and a scheme to objectively calculate each component's Dense Rock Equivalent (DRE) eruptive volumes (Chapter 4). This was used to define magma supply scenarios for the AVF (Chapter 4). The database was expanded through analysing eruption sequences, particularly where changes in event styles were noted. Eruption styles, especially phreatomagmatism, were related to environmental factors, such as distances from past and present coastlines, distance from known fault lines, substrate and its thickness, as well as the inferred paleo-topography beneath volcanoes (Chapter 5). For larger magma supply eruptions, there was a greater occurrence of transitions in eruption styles from phreatomagmatic to magmatic explosive and effusive activity (Chapter 5). Products from effusive activity cover the largest area mapped in the AVF (with the exclusion of distal tephra, which has not been well mapped due to high levels of weathering and poor preservation). This highlights the necessity for lava flow hazard evaluation, which was carried out in Chapter 6 by a deterministic model using the current topography. In addition, Chapter 7 describes how a rheology-based numerical simulation code, MAGFLOW (Del Negro et al., 2005), could be used to evaluate past eruptions and to validate the used input parameters of for field-scale hazard mapping in the future.

This Chapter draws on the results from the whole study, and aims to provide new conceptual models for assessing susceptibility mapping for eruption styles in monogenetic volcanic fields (especially for phreatomagmatic eruptions), as well as for applying GIS-based techniques and numerical codes for lava flow susceptibility mapping in monogenetic volcanic fields, such as the AVF.

## 8.2. A conceptual model for eruption style susceptibility mapping

During the formation of a monogenetic volcano, phreatomagmatic vent-opening phases are common, as evidenced by volcanic edifices and/or macro and microscopic sedimentary features of basal pyroclastic deposits, such as matrix-dominated frameworks, dune- to cross-bedding, and blocky, stepped and irregular juvenile fragments (e.g. Sohn and Chough, 1989; Büttner et al., 1999; White and Ross, 2011). Such textural and sedimentological features are very common in the pyroclastic successions of many eruptive centres in the AVF (e.g. Allen et al., 1996; Houghton et al., 1999; Németh et al., 2012; Agustín-Flores et al., 2014). If eruptions have sufficient magma supply, this initial phase is followed by magmatic explosive and effusive activity, forming spatter-dominated scoria cones and lava flows. The hazard contrasts strongly between the two eruption types, with phreatomagmatic eruptions generally being more violent and a greater threat to life, but lava effusion can cover large areas ( $\geq 5 \text{ km}^2$ ), including at long distances from a vent area. Distinguishing between contrasting volcanic hazard types, especially on a spatial basis, has not been systematically carried out before in typical monogenetic fields.

Typical hazard assessment methods include the analysis of the spatial and temporal distribution of past volcanoes using kernel density and clustering methods (Connor and Hill, 1995; Condit and Connor, 1996; Magill et al., 2005b; Bebbington and Cronin, 2011; Bebbington, 2013; Cañón-Tapia, 2013). Evaluation of eruption types and event scenarios has been carried out using Bayesian Event Tree for Eruption Forecasting (BET\_EF), with the aid of expert-elicitation tools and pre-assigned probability distributions (Lindsay et al., 2010; Marzocchi et al., 2010; Sandri et al., 2011). Volcanic impact assessments are normally based on mapping of past deposits, as well as numerical simulations of tephra fall (Magill et al., 2005a; 2006; Selva et al., 2010), or lava flows (Connor et al., 2012). The most robust and complex model for hazard management and decision making is the BET\_EF, in terms of the amount of input data required. This tool calculates the probability of a broad range of volcanic hazard events on a short- and long-term basis at a volcano or volcanic field, based on as much geological/volcanological information and monitoring data as can be obtained (Marzocchi et al., 2008; 2010). The BET\_ET was refined to the AVF and tested in a full-scale eruption scenario “*Exercise Ruauumoko*” (Lindsay et al., 2010). For the AVF a

five node version of this modular code was applied (Lindsay et al., 2010), including node (1): unrest or not; node (2): magma or not; node (3): eruption or not; node (4): vent location; node (5): eruption style/size (Lindsay et al., 2010). The most relevant node to this investigation is the last one, which is based on the geological record of the AVF (e.g. Allen and Smith, 1994), expert elicitation and environmental constraints, such as present sea water coverage (Lindsay et al., 2010).

In this study, many spatial layers of information were used to construct a susceptibility map for the vent-opening phases of a future AVF eruption. Four partly related factors were considered in the assessment of susceptibility to phreatomagmatic vent-opening (Fig. 8.1): (1) thickness of post-Waitemata soft-sediments, (2) topographic position, (3) distance from present coastline, as well as (4) distance from known fault lines.

Post-Waitemata sediments in the AVF are water saturated and mostly unconsolidated. The presence of thick deposits of these units (Fig. 8.1A) led to the dominantly phreatomagmatic volcanism of the Manukau Lowlands area (e.g. Agustín-Flores et al., 2014). Scoria deposits and lava rocks (e.g. autobreccia zones at the foot of lava flows) can also yield substantial water along their fractures and contact zones with other deposits (e.g. Won et al., 2006), however, the potential role of such deposits/rocks in the AVF is not completely constrained. Thus, these geological units are not considered in this investigation.

The field's topography is represented by a 10 m resampled LiDAR-derived DSM (Fig. 8.1B), with the present day shoreline defined as 0 m a.s.l. (Fig. 8.1C). Lower topography slightly correlates with increased susceptibility to phreatomagmatism. Fault locations (Fig. 8.1D), also a potential factor in driving magma-water interactions, were taken from Kenny et al. (2012). Based on these external environmental factors, a susceptibility map for phreatomagmatic vent opening was created by a weighted overlay technique. For simplicity, each factor was weighted equally.

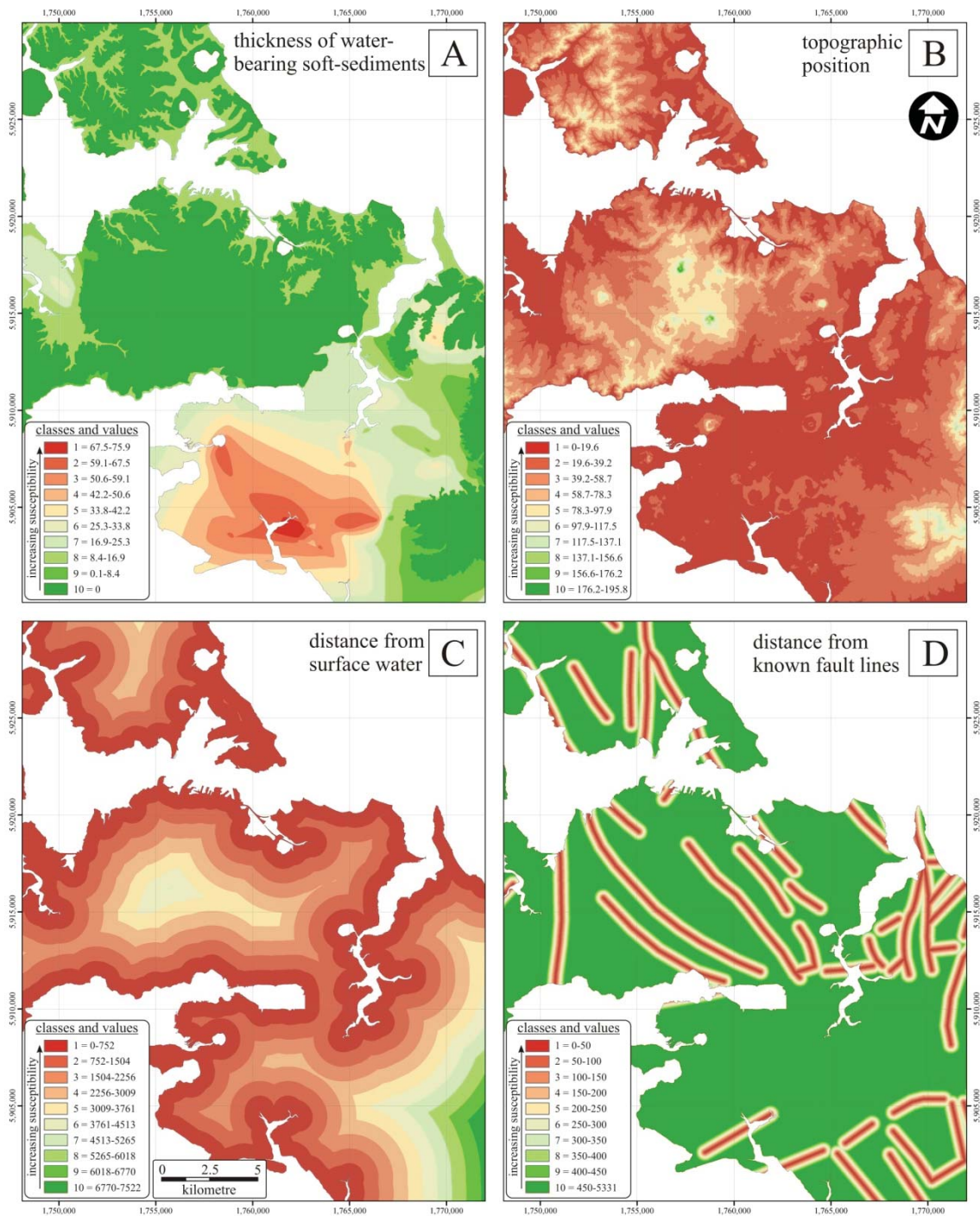


**Figure 8.1** Classified maps of features used for eruption style susceptibility mapping in the AVF. (A) Combined thickness map of post-Waitemata uncompacted non-volcanic sediments. (B) Topographic elevation. (C) Distance from the present shore line, (D) Distance from known faults.

The AVF was subdivided into high (class = 1–5) and low (class = 6–10) susceptibility areas for vent-opening phreatomagmatic eruptions. This first-order susceptibility map of the AVF (Fig. 8.2) highlights that the North Shore, Central Auckland and the Hunua Ranges share a similar susceptibility for phreatomagmatic eruptions, with the highest local susceptibilities along fault lines and/or where the

alluvium reaches  $\geq 20$  m thickness (Fig. 8.2). The Manukau Lowlands (except the Hunua Ranges) shows the highest susceptibility for phreatomagmatic vent opening (Fig. 8.2). The high susceptibility areas occupy about 205.3 km<sup>2</sup> (49.6% of the total mapped area), and nearly the same area is classed as having low susceptibilities (208.4 km<sup>2</sup>; 50.4% of the total mapped area). The geological record (e.g. 82% of the volcanoes had phreatomagmatic phases; Chapter 5) suggests most future AVF eruptions will have at least a phreatomagmatic vent-opening phase, but these would be most prevalent and also last longer in the high susceptibility areas (Fig. 8.2). Transition from phreatomagmatic to other eruption styles is also a function of magma supply volume (Chapter 5). For small-volume eruptions (e.g.  $\leq 0.01$  km<sup>3</sup>), the likelihood of a sustained or complete phreatomagmatic eruption is high in the Manukau Lowlands, and areas close to the current shoreline in other parts of the AVF. In these areas, the likely volcano that would be formed in a volcanic eruption is a maar surrounded by an ejecta ring capped by minimal (e.g. Maungataketake), or no (e.g. Pukaki) eruption products from magmatic explosive and effusive processes. Small-volume phreatomagmatic vent-opening phases are most likely in the low susceptibility areas of Central Auckland, North Shore and Hunua Range. Over these areas a spatter/scoria cone forming eruption is more likely, forming volcanoes similar to Mt. Roskill or Mt. Hobson. With larger magma volumes ( $\geq 0.05$  km<sup>3</sup>) magmatic dominated eruption sequences are more likely, with or without extensive vent opening phreatomagmatic phases. The former would create a volcano like Three Kings, whereas the latter would produce a volcano similar to Mt. Eden.

The AVF has demonstrably high (to moderately high) susceptibility for producing phreatomagmatic eruptions, especially in the initial phase. A few other volcanic fields, such as Bakony-Balaton Highland in Hungary (Martin and Németh, 2004; Kereszturi et al., 2011) or Hopi Buttes, Arizona, USA (White, 1991), have had similar high percentages of phreatomagmatic events, but most are far lower, with only 24% of vents being phreatomagmatic in the Pali Aike Volcanic Field (Mazzarini and D'Orazio, 2003), 13% in the Newer Volcanic Province, Australia (Boyce, 2013), 10% in the Cima Volcanic Field, California (Dohrenwend et al., 1986), 4% in Jeju Island, South Korea (Sohn, 1996), and  $\leq 1\%$  in the Llancanelo Volcanic Field, Argentina (Risso et al., 2008), or none at the Southwest Nevada Volcanic Field, Nevada (Valentine and Perry, 2007).

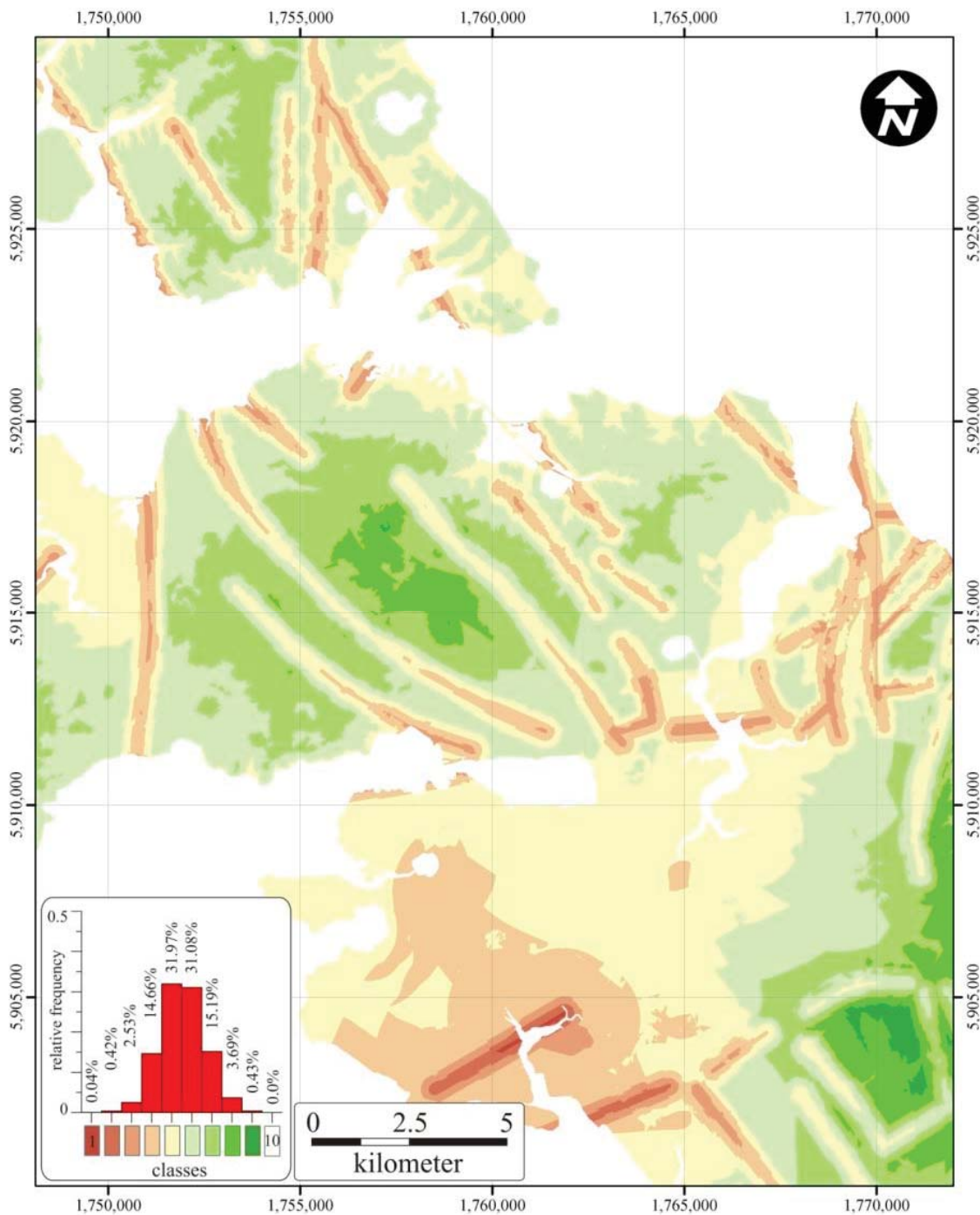


**Figure 8.2** Susceptibility map (red = high, green = low) for phreatomagmatic vent-opening phase in future eruptions in the AVF, based on combining the maps shown in Fig. 8.1. The inset shows the distribution of each susceptibility class. The areas below sea level (white) were not considered.

To develop the susceptibility map further, it is possible to link its classes with likely volumes of the phreatomagmatic phases of an eruption. This will create the opportunity to forecast certain eruption sequences for any location within a monogenetic volcanic field. The simplest way to link the susceptibility classes with a likely phreatomagmatic eruption volume is to construct a raster layer of the

phreatomagmatic volume through natural neighbour interpolation of data from each of the 52 AVF volcanoes. This interpolated surface can be compared with the susceptibility map using zonal statistics (Fig. 8.3). This shows that there is a strong correlation between the susceptibility map classes (Fig. 8.2) and the spatial distribution of phreatomagmatic volumes (Fig. 8.3). There is a decreasing trend of median phreatomagmatic tephra volume with decreasing susceptibility class. Based on the “volume-corrected” susceptibility map (Fig. 8.4), future phreatomagmatic phases and their volumes can be estimated for any spatial location within the AVF. Furthermore, a complete eruption sequence (e.g. Fig. 8.4) can be forecast using a user-specific magma supply volume (e.g. volumetric eruptive scenarios from Chapter 4), and the map produced for forecasting vent-opening phreatomagmatic eruption phases (Fig. 8.2).

While promising, this approach is limited by the sparse input data of AVF eruptions. This is difficult to improve in the AVF; however, this conceptual model could be tested at a volcanic field with more vents, such as the Newer Volcanic Province in Australia, Jeju Island in South Korea or San Francisco Volcanic Field, Arizona. Extending this approach to volcanic fields with other climatic and geological settings would also help to understand potential external and internal influences on monogenetic eruption styles, hence leading to improved forecasts.

A further limitation is that the past eruptive behaviour of the AVF may not be representative of the present environment (e.g. current sea level is higher, and the environment is “wetter”). This can be improved upon in the future by applying more direct forecasting methods. For eruption style forecasting, in particular for an initial phreatomagmatic phase, active monitoring of groundwater level and flow (e.g. flux, direction) is required. Given the extensive network of wells, hydrological exploration and groundwater extraction in the AVF, these two components (i.e. groundwater monitoring and phreatomagmatic susceptibility mapping) could easily be bridged in the future. Hazard evaluation can also be improved by better understanding physical influences on magma-water interaction (e.g. Agustín-Flores et al., 2014).

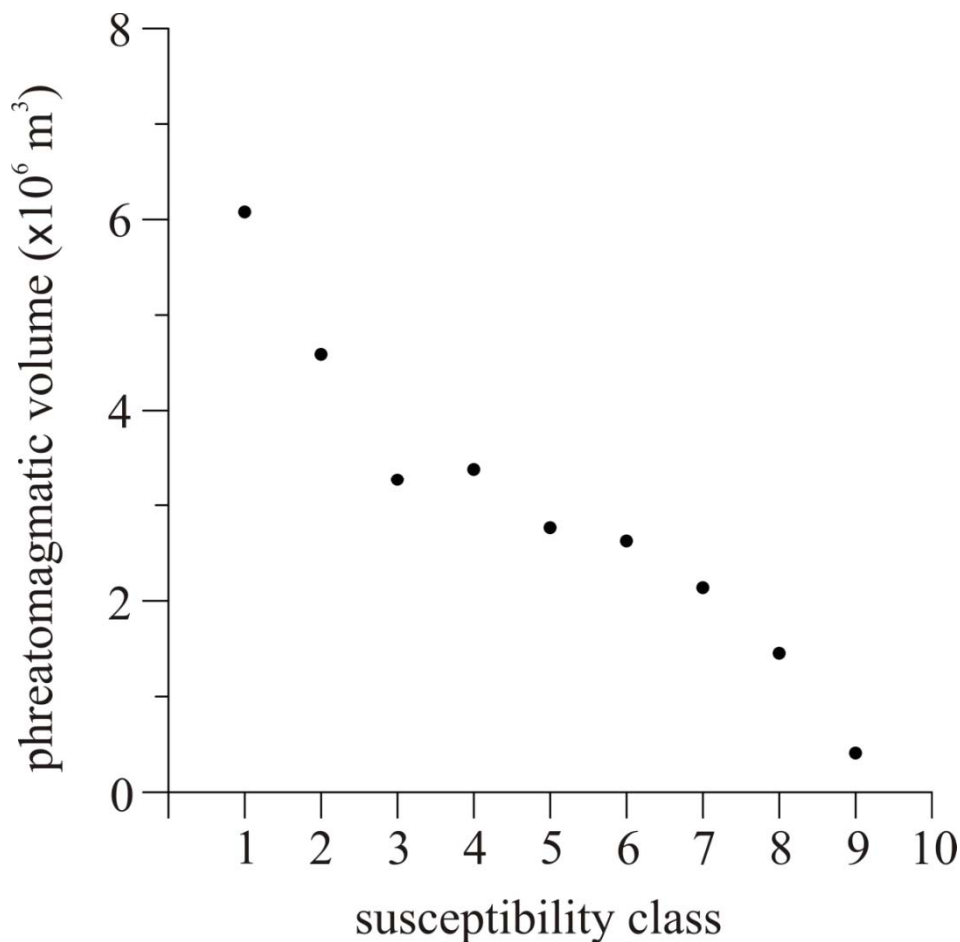


**Figure 8.3:** Scatter graph showing the relationship between susceptibility classes for phreatomagmatic eruptions (Fig. 8.2) and the median volume estimated from the interpolated raster of phreatomagmatic phases.

Geologically more appropriate eruption style forecasting can be carried out by applying hybrid approaches that combine deterministic (e.g. phreatomagmatic volume, total magma supply volume) and stochastic components (e.g. adding randomness). This approach can, for example, forecast eruption sequences by using the relationship between phreatomagmatic volumes and the thickness of post-Waitemata sediments (e.g. Chapter 5) in the Manukau Lowlands and other areas with thick soft-sediment cover (e.g. Fig. 8.1A), while the rest of the field can be modelled by a distribution based on past eruption properties using Monte Carlo simulations (e.g. sampling from an exponential distribution of the volume associated with the vent-opening phreatomagmatic phase).



The susceptibility map along with the eruption sequence forecasting method developed here does not indicate vent-location, and the next step could be to combine an assessment of the vent likelihood with susceptibility to phreatomagmatic eruptions. This eruption style susceptibility mapping technique can support decision making processes during volcanic unrest, such as within a BET\_EF approach (Marzocchi et al., 2010). The BET\_EF forecasting of eruption style in the AVF used simply the presence or absence of surface water to predict phreatomagmatic eruptions (Lindsay et al., 2010). However, phreatomagmatic eruptions occur irrespective of this in the AVF, because they result from interaction of magma with groundwater (e.g. Németh et al., 2012; Agustín-Flores et al., 2014). The eruption style susceptibility mapping described above can be directly integrated into the BET\_EF approach, providing a more detailed picture of potential volcanic hazards, based on multiple influencing factors (e.g. lithology, topography, faults and sea proximity; Fig. 8.2).

The conceptual model, quantifying external and internal influencing factors on eruption styles, combined with various deterministic (e.g. thickness and phreatomagmatic deposit volume relationship; Chapter 5) and probabilistic (e.g. distribution of phreatomagmatic volumes) input data, can be applied to any other potentially active monogenetic volcanic field (Table 8.1), where the location of an eruption may be critical for infrastructure or population.

**Table 8.1** List of cities and infrastructure located on or near monogenetic volcanic fields. In such settings susceptibility mapping could be useful to improve hazard assessment. Key: M – monogenetic; P – polygenetic; pop. – population (in million) in the metropolitan area; VF – volcanic field.

city/infrastructure	country	volcanic field	volcanism	pop.	last eruption	reference
Auckland	New Zealand	Auckland VF	m	1.4 m	505 yr BP	this study
Medina	Saudi Arabia	Harrat Rahat	m	1.2 m	1256 AD	Moufti et al. 2012
Uruapan and Morelia	Mexico	Michoacán-Guanajuato VF	m-p	ca. 1 m	1943-1952 AD	Guilbaud et al. 2011
Managua	Nicaragua	-	m	2.3 m	1245 yr BP	Pardo et al. 2009
Jeju Province	Korea	Jeju VF	m-p	0.6 m	1005 AD	Brenna et al. 2012
Mt. Gambier and its surroundings	Australia	Newer Volcanic Province	m	0.05 m	5 ka	van Otterloo and Cas 2013

Olot	Spain	Garrotxa VF	m	0.04 m	11 ka	Martí et al. 2011
Hagi	Japan	Abu VF	m	0.05 m	10 ka	Kiyosugi et al. 2010
Flagstaff	Arizona, USA	San Francisco VF	m	0.07 m	1050-1100 AD	Ort et al. 2009
Pozzuoli	Italy	Campi Flegrei	m-p	0.1 m	1538 AD	Marzocchi et al. 2010
radioactive waste repository Yucca Mountain	Nevada, USA	Southwest Nevada VF	m	-	80 ka	Connor et al. 2000
nuclear power plant at Aragat	Armenia	-	m-p	-	2090 yr BP	Karakhanian et al. 2003

### 8.3. A conceptual model for lava flow susceptibility mapping

The largest area affected by volcanism in the AVF was covered by lava flows (55% of the total area), in particular those associated with the larger-volume eruptions ( $\geq 0.05 \text{ km}^3$ ). Individual lava flows range between  $0.001 \text{ km}^3$  and  $0.7 \text{ km}^3$  (Chapter 4), and the most extensive ones emplaced in the young phase of volcanism of the AVF ( $\leq 40 \text{ ka}$ ). Based on the geological record, transitions from phreatomagmatic eruptions to Strombolian or fire-fountaining eruptions producing scoria cones and lava flows are most likely to occur in the elevated areas of the AVF (e.g. Central Auckland and North Shore).

The valley systems in the Central Auckland and North Shore areas are capable of channelising and containing an average-sized AVF lava flow, generally leading to longer flow lengths (e.g. Three Kings, Chapters 6 and 7). On the contrary, future lava flows in the Manukau Lowlands are more likely to spread radially and be shorter (e.g. Chapter 6). For this reason, analysis of topography, including the buildings and landscaping, is essential for hazard assessment in the AVF. In any hazard analysis, the varying lava flow properties on different topographies must be incorporated. In this investigation, lava flow susceptibility mapping was carried out using GIS-based tools. This approach is capable of identifying general trends in the topography in relation to a user-defined lava flow thickness, and the locally lowest elevation cells (e.g. Chapter 6). The limitation of such adaptive mapping approaches is the lack of knowledge on the dynamic processes involved in the emplacement of a lava flow (e.g. viscosity change,

cooling rate, pressure-driven spreading). Hence, this technique cannot always predict the total length of a lava flow based on a scenario volume. To fill this gap, deterministic lava flow simulation codes were applied (e.g. Chapter 7), such as MAGFLOW (Vicari et al., 2007; Del Negro et al., 2008). These physics/rheology-based simulation tools can solve complex emplacement mechanisms, but are essentially driven by the steepest descent path of a digital surface, and the changing rheological properties over time and distance from the source. In this way, such codes can be more effective at predicting run-out distances of future lava flows occurring in the AVF when specific eruption scenarios are well known.

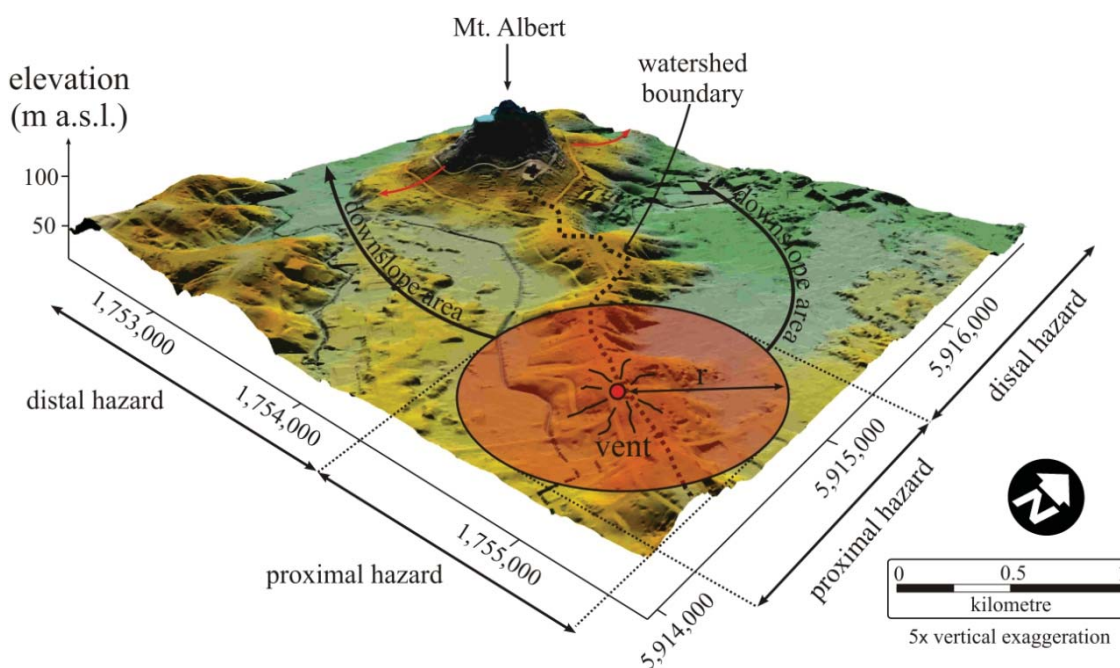


**Figure 8.5** A model of proximal and distal zones in lava flow simulations in a monogenetic volcanic field setting. A hypothetical vent (red dot) is characterised by a radius ( $r$ ), which is 1 km here. The circle with radius  $r$  shows the potential area that might be modified by initial cratering and ejecta ring formation during a phreatomagmatic eruption. This might be coupled with an eruption taking place on a watershed boundary (e.g. Mt. Albert). Lava flow modelling within proximal areas thus has a higher degree of uncertainty. Accuracy of prediction of potential lava flow path and length increases towards distal zones, where topographic modification from the eruption is not extensive.

Other stochastic codes, such as DOWNFLOW (Favalli et al., 2005), are solely based on the elevation change of the digital terrain and often do not allow the modelling of bifurcation and pressure-driven spreading of the flow as a rheological unit (Dragoni et al., 1986; Dragoni, 1989). However, for an emergency situation, they are quick to apply and require minimal input data [e.g. the DOWNFLOW code the needs number of iterations and the degree of topographic perturbation which is analogous to the flow

thickness (Favalli et al., 2005)]. Such slope-based codes describe the dispersion index of a digital surface well (Favalli et al., 2012a), which is analogous to the second-order derivatives of the surface, such as convexity-concavity (Moore et al., 1991; Jordan, 2007b).

In the early stages of many past AVF events, phreatomagmatic eruptions excavated broad dish-shaped craters, susceptible to lava ponding. This makes prediction of lava flow paths in proximal areas ( $\leq 2$  km) challenging. Therefore, the application of lava flow simulation codes requires a different conceptual model than, say, the simulation of lava flows during a flank eruption. To solve this, volcanic hazard was classified as a function of distance from the potential source vent (Fig. 8.5).

In this context, proximal areas are those impacted by surface modification from cratering and ejecta ring formation. In the AVF, the proximal area is estimated at  $\leq 2$  km in diameter, which is slightly larger than the diameter of the largest ejecta ring crater (Pupuke). This could vary in relation to the style and volumetric size of the early-onset eruption types, explosivity and spatial scale. Lava flow modelling results tend to be more reliable towards distal areas, where less syn-eruptive landscape modification occurs. This situation is especially important if the eruptions take place on a margin of a watershed. This was the case at Mt. Albert (Fig. 8.5), where two lava flow fields occurred on each side of a ridge and affected multiple watersheds. Due to uncertain and unknown proximal area modification at the stage of lava flow formation, any simple lava flow model would suffice for proximal lava flow simulations. Over the 'stable' distal zone, the lava flow will follow a path best predicted by the combined effects of topography and rheology.

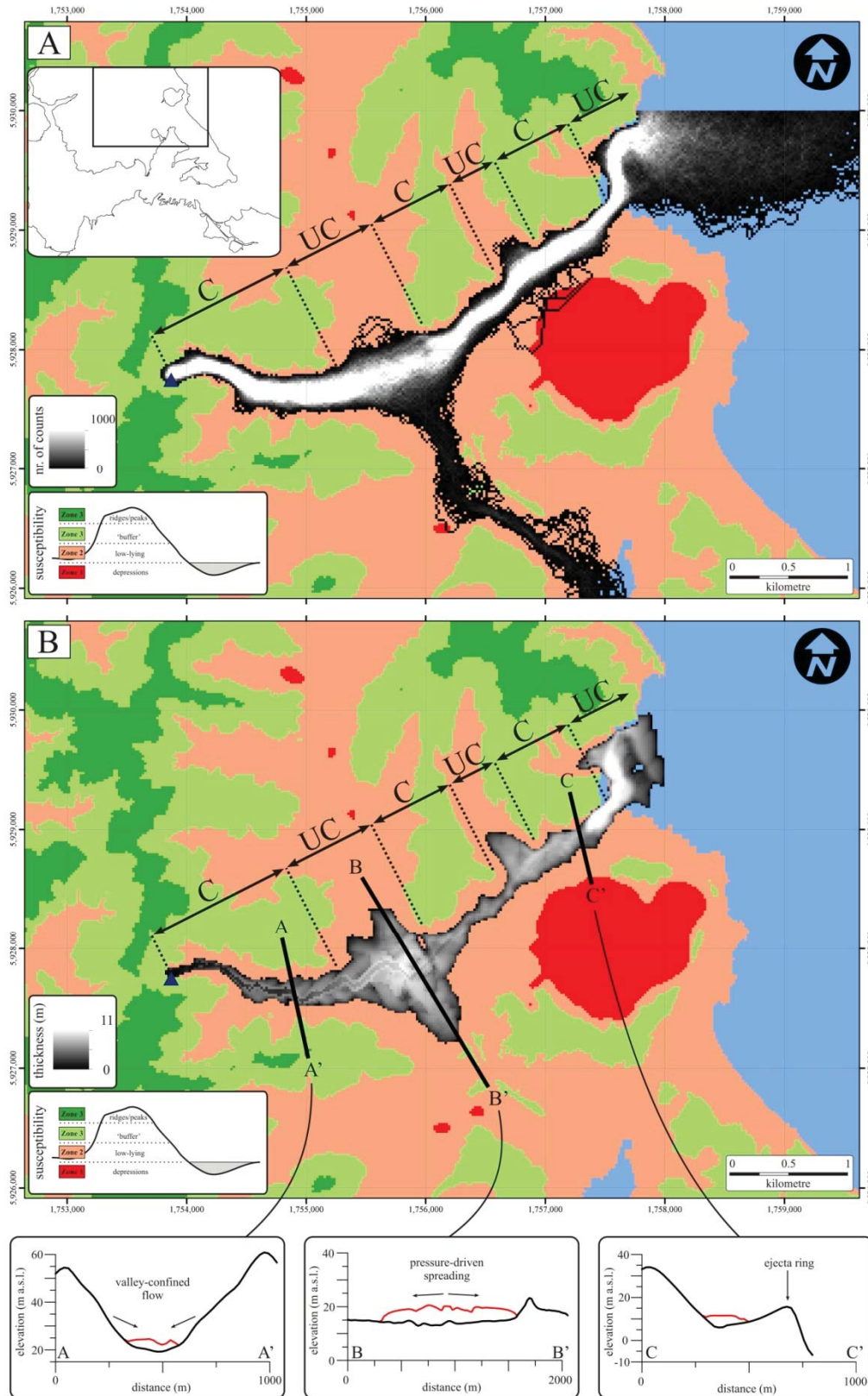


**Figure 8.6** Maps showing different methods of modelling lava flow susceptibility in the North Shore area, including (A) stochastic lava flow inundation map from a hypothesised vent (blue triangle), and (B) thickness map simulated by MAGFLOW using the Mt. Roskill effusive curve and magma supply volumes (e.g. Chapter 7). The insets shown in (B) are topographic profiles with the simulated lava flows (under red curve). The valley-confined (C) and unconfined (UC) flow zones of each simulation are marked.

To compare lava flow hazard mapping approaches, an example area from North Shore is shown with: (1) a ‘static’ susceptibility map based on the average thickness and current topography (Chapter 6), (2) deterministic, rheology-based simulations using MAGFLOW (Chapter 7), as well as (3) a stochastic code based on the current topography, similar to Favalli et al. (2005). The latter was included in this discussion to visualise a wider spectrum of numerical codes that have been designed to evaluate inundation hazard/susceptibility from lava flows. The results shown in Fig. 8.6 are from an adaptation of DOWNFLOW by modifying the LiDAR DSM by  $\pm 7.8$  m, which is the average thickness of lava flows in the AVF. Both the topography-based stochastic and the rheology-based MAGFLOW codes could resolve the topographic changes, such as valleys and flat areas, and the simulated flow is confined (“C” in Fig. 8.6) and unconfined (“UC” in Fig. 8.6), respectively. Furthermore, both results confirm the validity of the susceptibility zones mapped out in Chapter 6, and the “buffer” and “ridge” zones were not invaded by lava flows from the hypothetical vent (Fig. 8.6). Although the ejecta ring of Pupuke was mapped as part of the “low-lying” zone, numerical simulations by both codes predicted otherwise (Fig. 8.6B). This could be due to the static average lava flow thickness (i.e. 14.8 m) used in this susceptibility technique (Chapter 6). This was larger than the maximum thickness modelled by MAGFLOW (Fig. 8.6B). This highlights some of the limitations of the static method, but it remains one of the easiest and quickest methods for lava flow susceptibility mapping in monogenetic volcanic fields.

To forecast lava flow pathways in the complex terrain of a distributed volcanic field, results from all types of code should be incorporated. In the case of the AVF, many hypothetical vents should be used, because the site of the next eruptive centre is unknown. This field-scale hazard mapping could be carried out using randomly distributed vent locations, and/or systematically on a grid pattern.

#### 8.4. Towards a GIS-based hazard assessment of monogenetic volcanic fields

The importance of GIS lies in the efficient handling of the wide range of spatial data needed for volcanic hazard mapping and risk assessment (e.g. Pareschi et al., 2000; Renschler, 2005). Due to the spatial heterogeneity in eruption style susceptibility,

topography and external environmental factors, the spatial-dependence of volcanic processes and consequent hazards is high in the AVF and similar fields.

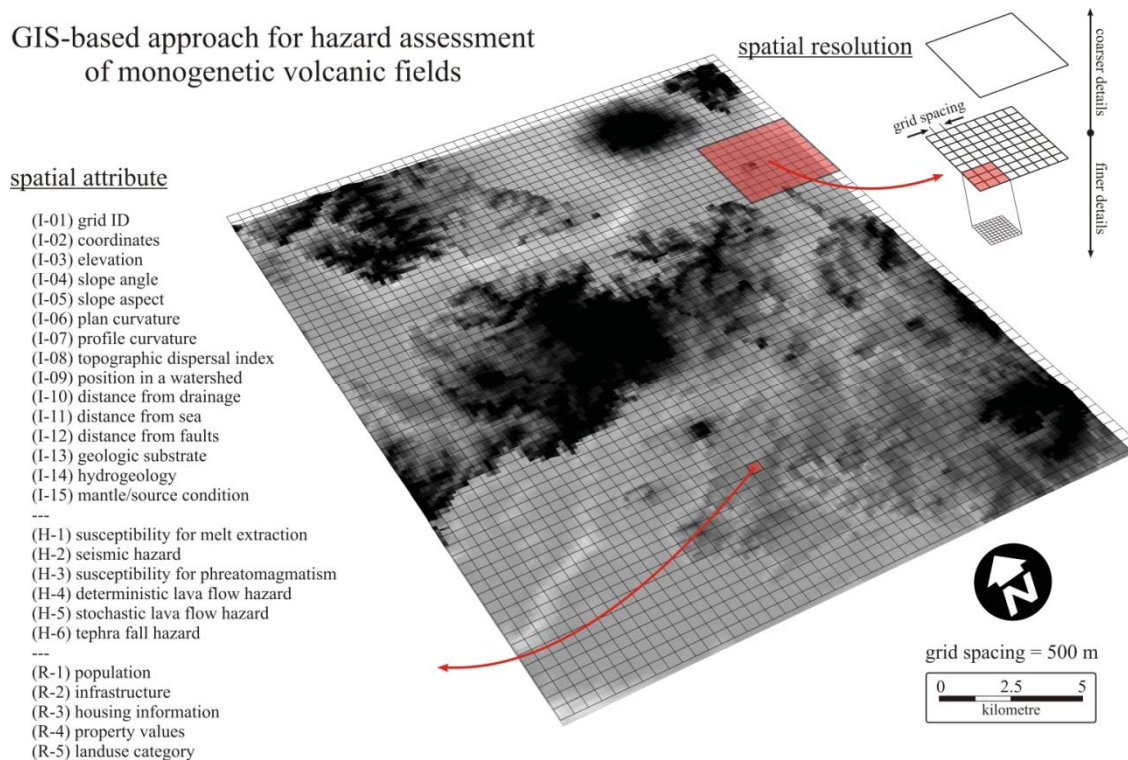


**Figure 8.7** Structure of spatial attribute based hazard assessment designed for the AVF. The layers of the database can be separated into input (I), hazard (H) and risk (R) components.

For the AVF, an effective GIS-based decision-making system can be developed based on the data currently available and created in this study. This approach is similar to susceptibility mapping of landslides (Chau et al., 2004; Gruber et al., 2008). A spatial attribute-based database (or data inventory) should be created, covering most of the AVF and a buffer zone around it. This could include the characteristics of past eruptive processes and volcanic structures, susceptibility and volcanic hazard maps of different volcanic phenomena, risk and vulnerability maps of the exposed assets and properties (Fig. 8.7). Other aspects could include a mantle/source depletion map (e.g. based on location and volumetric size of past eruptions), geological and structural/tectonic maps, distribution of past volcanoes, sea depth, hydrology, groundwater, drainage pattern, infrastructure, housing information etc. (Fig. 8.7). In this investigation, many of these input layers have been created, including Digital Surface Models (e.g. resampled LiDAR DSM), slope angles, slope aspects, watersheds, sea levels, drainage pattern, basic geological formations and their thicknesses, topographic susceptibility to lava

flow inundation, and susceptibility to vent opening phreatomagmatic eruptions. Any of the raster layers could be updated once any additional information becomes available. Furthermore, this approach could help in seeking correlations of factors involved in the formation and hazards of a monogenetic volcano. A further advantage is the potential to analyse neighbourhood relationships (i.e. proximity) from multiple input raster layers that can be incorporated into the hazard assessment with specific weightings.

Currently, the various raster layers have different spatial resolutions, between 2 and 20 m in accordance with their source data. The required resolution for analysis would depend on the scale of each area of interest. For example for a field-scale description of volcanic hazard, perhaps a 100 m to 1000 m spatial scale (i.e. resolution) would be appropriate, but finer scales would be needed around critical facilities and buildings. This is a further direction for research on how to make this GIS-based approach more sophisticated so that it could be applied to other monogenetic volcanic fields.

## 8.5. Conclusions

### 8.5.1 Research objectives

The main aim of this research was to investigate how numerical and systematic GIS methods and approaches could be used to better describe volcanic hazards in the AVF, using geological, and remote sensing data. This was split into the following research objectives:

- To investigate how systematic analysis of spatial location, area affected, edifice geometry, eruptive volume and eruptive sequences of the past eruptive centres of the AVF can be used to improve the understanding of the volcanic field's structure and hazard profile.

*Based on the eruptive volumes from Light Detection And Ranging (LiDAR) data, the volcanic edifice geometries and spatial locations were measured (Chapter 4), in order to understand the volume-time and the spatial-volume evolution of the field. The database created for the 52 volcanoes in the AVF is attached as Appendix B.*

- To quantify the typical combination of eruption styles and sequences during AVF eruptions, as well as exploring the range of external and internal factors that influence eruption styles in monogenetic volcanic fields.

*Based on the volume/eruption dataset created for the AVF, the distribution of past eruption styles and the sequences of the eruption phases in relation to their volumes were established (Chapter 5). The main feature identified was the common occurrence of phreatomagmatic explosive phases at the start of new eruptions. Four external/environmental factors were hypothesised to influence susceptibility to phreatomagmatism: water-bearing soft-sediment thickness, topographic position, and distance from the coastline and known faults. Due to the small sample size of eruptions in the AVF and the wide range in volume variability, there is no consistent correlation between phreatomagmatic phase volumes and the four external environmental influencing factors, except in the Manukau Lowlands. There are a different set of susceptibilities for phreatomagmatic eruptions in North Shore, Central Auckland and the Manukau Lowlands. In the latter area, large thicknesses of post-Waitemata loose, friable and saturated sediment lead to a predominance of phreatomagmatic eruptions, and those with the largest volumes.*

- To evaluate lava flow hazard and emplacement processes for a monogenetic field, via susceptibility mapping, and with a rheology-based lava flow simulation approach.

*Topography is a complex factor in lava hazard assessment in monogenetic volcanic fields, compared to steep-sided polygenetic volcanoes. Here, topography led to important differences in the elevated Central Auckland area, compared to the predominately flat Manukau Lowlands (Chapter 6). Using the present drainage pattern and the geometric parameters of past lava flows, a GIS-based susceptibility mapping technique was developed. This evaluated the lava-carrying capacity of catchments and sub-*

*catchments. This approach can be used with little input data, making it easily adoptable in other volcanic fields as a first approach to hazard assessment. Combining this with the application of rheology-based codes, such as MAGFLOW (Chapter 7), can provide constraints on the expected run-out-distance of future lava flows in the AVF and estimates on likely eruption durations. This combination of topography- and rheology-based approaches provides a robust approach for volcanic hazard mapping in monogenetic volcanic fields.*

- To use GIS to apply physical volcanological data, such as eruptive volumes, to the development of new hazard mapping techniques for monogenetic volcanic fields.

*Based on the input data created in Chapters 4 and 5 a weighted overlay technique was used to develop a susceptibility map for phreatomagmatic eruptions in the AVF. This vent-opening eruption style mapping technique could be applied to other monogenetic volcanic fields. With integration of forecasting of vent location probabilities, this tool contributes to a new type of hazard assessment for monogenetic volcanism.*

### 8.5.2. Future directions of research

Several possible directions for future research in the AVF and other similar volcanic fields have been identified during the course of this research.

- Using the eruptive volumes calculated in Chapter 4, along with the concept of magmatic footprint (Valentine and Perry, 2006) and geochemical data on the depth of magma extraction, mantle depletion mapping could be carried out for volcanic fields. This could highlight both the shape and character of various parts of the melt-yielding mantle. If an assumption of the melt yield could be developed, zones of depletion vs. untapped zones could be mapped and interpreted in terms of eruption site likelihoods.

- Further exploring the interplay between internal and external influencing factors in monogenetic volcanic fields could result in a better understanding of controls on the dominant eruption styles in the AVF and other similar fields. In the present investigation, for instance, the effect of direct sea water coverage was avoided, due to limited knowledge of the fine details of how magma would interact with shallow water: i.e., by a Molten Fuel Coolant Interaction (e.g. Zimanowski et al., 1997), or by bulk mixing and mingling, forming Surtseyan-type eruptions (e.g. Kokelaar, 1983).
- Geochemical variability, along with magma volume and extrusion rates, may also lead to variation in eruption styles and sequences. This could be investigated in an area with a large range in compositions and with large physical volcanology constraints on magma flux rates and magma fragmentation processes. This would help to test the degree of magmatic influencing factors on the observed fragmentation style changes in the course of an eruption in the AVF.
- The location and degree of faulting of the substrate in the AVF is unknown in the areas covered by post-Waitemata sediments or volcanic deposits (Kenny et al., 2012). Further research on fault locations across the whole region is needed to better investigate the relationships between vent locations, eruption types and faults.
- Active hydrogeology monitoring and developing a better understanding of the hydrologic behaviour of the range of substrates in the AVF (e.g. Agustín-Flores et al., 2014) will be an important step for more clearly classifying the potential likelihood of phreatomagmatic eruptions in the future. This research direction is vital for understanding how a future volcanic eruption could start and what hazards it may pose.

- The boundaries of the AVF are poorly defined, as they are in many volcanic fields. Typically a narrow area outside the current zone of vents is considered in hazard assessments; further research is needed to define clearer boundaries, or to explore the probabilities of the locus of volcanism moving outside the currently mapped “limits”.
- Further hybrid deterministic and probabilistic approaches could be developed based on the dataset provided in Chapters 4 and 5. This could provide a vast spectrum of techniques that could be exploited in susceptibility and volcanic hazard mapping.
- The mapping of susceptibility to phreatomagmatic eruptions presented here is a proof of concept. Further iterations of this, coupled with a forecast of the likely locations and volumes of future eruptions in the AVF, would provide the next generation of hazard maps.
- Lava flow emplacement is affected by various topographic (e.g. depression) and anthropogenic barriers (e.g. fences, houses). To improve hazard modelling in a heavily urbanised volcanic field, such as the AVF, a better understanding of lava flow/infrastructure interactions is needed, along with models and codes that are able to incorporate these effects.

### 8.5.3. Concluding remarks

Volcanism in the AVF is characterised by spatially isolated eruptions that exhibit a large range in volumes and styles. The total field eruptive volume was newly estimated at 1.704 km<sup>3</sup>. Larger volume eruptions produced the most complex eruption sequences with an array of styles. The largest and youngest volcano, Rangitoto, accounts for 41% of the total field’s magma output, but is only one of several outlier events in terms of volume. The time-averaged spatial and temporal magma flux was

estimated at  $0.005 \text{ km}^3/\text{km}^2$  and  $0.007 \text{ km}^3/\text{ky}$ , respectively. However, current age evidence suggests that eruption rates varied considerably over time.

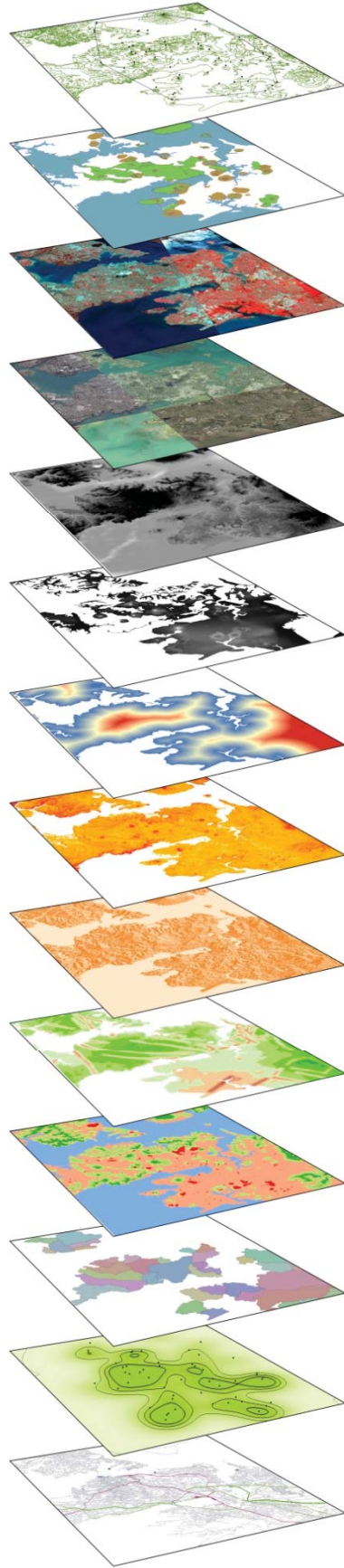
The substrate character, especially tens to a hundred metre of loose water-saturated sediments, low elevations, valley/alluvial settings, and fault lines lead to the largest chances of phreatomagmatic eruptions in the AVF. Thus the volcanism and eruption style were influenced by both internal (e.g. magma volume, eruption rate, composition) and external factors (e.g. lithology and its thickness, sea level, distance from fault lines, as well as topography). The latter environmental parameters can be used to develop a map of eruption site susceptibility to phreatomagmatic eruptions, or, conversely, for lava flow-producing events. An AVF susceptibility map constructed in this way has revealed that the Manukau Lowlands are most susceptible to producing phreatomagmatic eruptions and the higher-elevation areas of Central Auckland the least. This method needs to be developed further to integrate models of vent location and magma volume in order to better forecast future phreatomagmatic activity and complete eruption sequences numerically in the AVF. The AVF is highly susceptible to phreatomagmatic eruptions, which are likely to pose the largest hazard to populations in future eruptions. In the case of a future eruption in the AVF, rapid magma extraction and transport from source to surface means that a brief period (days to weeks) is available for preparation and coordination of an emergency response. As soon as the location of an eruption has been generally located by seismic monitoring and/or deformation, it can be mapped against susceptibility factors and a most-likely eruption scenario can be confirmed to authorities.

For eruptions with larger volume ( $\geq 0.05 \text{ km}^3$ ) in the AVF, even if they start with phreatomagmatism, they mostly transition into “dry” magmatic explosive and effusive phases, forming spatter/scoria cones and lava flows. It was found that with a combination of two methods, important features of lava hazard could be elucidated. Firstly, by analysing present topography, the susceptibility to channelisation and spread of lava flows can be represented in a GIS. This identifies catchment capacities for lava flows of a certain size, through a user-defined threshold value, such as average lava flow thickness. This locally adaptive method returned susceptibility maps that distinguished the low-lying (propensity to spread lava flows) and elevated, valley-dominated blocks (propensity to channelise lava flows). Lava flows are, however, not always directed solely by topography, in particular if slope gradients are low. To fill this

gap, a rheological lava simulation code, MAGFLOW, was applied to evaluate lava flow run-outs in the AVF and develop appropriate effusive eruption scenarios. Past lava flows with a range in eruptive volumes were successfully simulated, deriving likely eruption durations (e.g. 2 to 80 days) and effusion curves. By combining both susceptibility approaches and MAGFLOW or similar flow-modelling, a field-wide lava hazard evaluation can be best derived for a distributed volcanic field like the AVF.

The GIS tools and conceptual models, exemplified in this study on the AVF, are essential for volcanic hazard analysis in such broad and complex geological settings. This combination of geomorphic, hydrological and geological information, along with modelling and simulation tools, are needed for a comprehensive hazard and event type forecasting approach that meets the needs of both long-term land-use planning, and crisis/emergency response decision makers.





References cited



## References cited

- [1] Affleck, D.K., Cassidy, J. and Locke, C.A., 2001. Te Pouhawaiki Volcano and pre-volcanic topography in central Auckland: volcanological and hydrogeological implications. *New Zealand Journal of Geology and Geophysics*, 44: 313-321.
- [2] Aguilar, F.J., Agüera, F., Aguilar, M.A. and Carvajal, F., 2005. Effects of Terrain Morphology, Sampling Density, and Interpolation Methods on Grid DEM Accuracy. *Photogrammetric Engineering and Remote Sensing*, 71(7): 805-816.
- [3] Aguilar, F.J. and Mills, J.P., 2008. Accuracy Assessment of LiDAR-derived Digital Elevation Models. *The Photogrammetric Record*, 23(122): 148-169.
- [4] Agustín-Flores, J., Németh, K., Cronin, S.J., Lindsay, J.M., Kereszturi, G., Brand, B.D. and Smith, I.E.M., 2014. Phreatomagmatic eruptions through unconsolidated coastal plain sequences, Maungataketake, Auckland Volcanic Field (New Zealand). *Journal of Volcanology and Geothermal Research*, (accepted for publication).
- [5] Al-Salim, M.A., 2000. A geophysical and geological investigation of the Drury Fault and related block faulting, Southeast Auckland. MSc thesis, University of Auckland, New Zealand, pp. 1-236.
- [6] Allen, S.R., 2004. The Parnell Grit beds revisited: are they all the products of sector collapse of western subaerial volcanoes of the Northland Volcanic Arc? *New Zealand Journal of Geology and Geophysics*, 47: 509-524.
- [7] Allen, S.R., Bryner, V.F., Smith, I.E.M. and Ballance, P.F., 1996. Facies analysis of pyroclastic deposits within basaltic tuff-rings of the Auckland volcanic field, New Zealand. *New Zealand Journal of Geology and Geophysics*, 39: 309-327.
- [8] Allen, S.R. and Smith, I.E.M., 1991. The lava flows north of Takapuna beach. *Tane*, 33: 49-58.
- [9] Allen, S.R. and Smith, I.E.M., 1994. Eruption styles and volcanic hazard in the Auckland Volcanic Field, New Zealand. *Geoscience Reports of Shizuoka University*, 20: 5-14.
- [10] Alloway, B., Neall, V.E. and Vucetich, C.G., 1995. Late Quaternary (post 28,000 year B.P.) tephrostratigraphy of northeast and central Taranaki, New Zealand. *Journal of the Royal Society of New Zealand*, 25(4): 385-458.
- [11] Anderson, E.S., Thompson, J.A., Crouse, D.A. and Austin, R.E., 2006. Horizontal resolution and data density effects on remotely sensed LIDAR-based DEM. *Geoderma*, 132: 406-415.
- [12] Anderson, H.J., 1977. Gravity survey of north-west Manukau City, Auckland. BSc thesis, University of Auckland, New Zealand, pp. 1-46.
- [13] Andronico, D., Branca, S., Calvari, S., Burton, M., Caltabiano, T., Corsaro, R., Del Carlo, P., Garfi, G., Lodato, L., Miraglia, L., Murè, F., Neri, M., Pecora, E., Pompilio, M., Salerno, G. and Spampinato, L., 2005. A multi-disciplinary study of the 2002–03 Etna eruption: insights into a complex plumbing system. *Bulletin of Volcanology*, 67(4): 314-330.
- [14] Arana, V., Felpeto, A., Astiz, M., Garcia, A., Ortiz, R. and Abella, R., 2000. Zonation of the main volcanic hazards (lava flows and ash fall) in Tenerife, Canary Islands. A proposal for a surveillance network. *Journal of Volcanology and Geothermal Research*, 103: 377-391.

- [15] Aranda-Gómez, J.J. and Luhr, J.F., 1996. Origin of the Joya Honda maar, San Luis Potosí, Mexico. *Journal of Volcanology and Geothermal Research*, 74: 1-18.
- [16] Aranda-Gómez, J.J., Luhr, J.F., Housh, T.B., Connor, C.B., Becker, T. and Henry, C.D., 2003. Synextensional Pliocene–Pleistocene eruptive activity in the Camargo volcanic field, Chihuahua, México. *Geological Society of America Bulletin*, 115(3): 298-313.
- [17] Ashenden, C.L., Lindsay, J.M., Sherburn, S., Smith, I.E., Miller, C.A. and Malin, P.E., 2011. Some challenges of monitoring a potentially active volcanic field in a large urban area: Auckland volcanic field, New Zealand. *Natural Hazards*, 59(1): 507-528.
- [18] ASTER GDEM Validation Team, 2009. ASTER Global DEM Validation - Summary Report, pp. 1-28.
- [19] Auer, A., Martin, U. and Németh, K., 2007. The Fekete-hegy (Balaton Highland Hungary) "soft-substrate" and "hard-substrate" maar volcanoes in an aligned volcanic complex – Implications for vent geometry, subsurface stratigraphy and the paleoenvironmental setting. *Journal of Volcanology and Geothermal Research*, 159(1-3): 225-245.
- [20] Augustinus, P., Cochran, U., Kattel, G., D’Costa, D. and Shane, P., 2011. Late Quaternary paleolimnology of Onepoto maar, Auckland, New Zealand: Implications for the drivers of regional paleoclimate. *Quaternary International*, 253: 18-31.
- [21] Avolio, M.V., Crisci, G.M., Di Gregorio, S., Rongo, R., Spataro, W. and Trunfio, G.A., 2006. SCIARA  $\gamma$ 2: An improved cellular automata model for lava flows and applications to the 2002 Etnean crisis. *Computers & Geosciences*, 32(7): 876-889.
- [22] Axelsson, P., 1999. Processing of laser scanner data—algorithms and applications. *ISPRS Journal of Photogrammetry and Remote Sensing*, 54: 138-147.
- [23] Ayalew, L. and Yamagishi, H., 2005. The application of GIS-based logistic regression for landslide susceptibility mapping in the Kakuda-Yahiko Mountains, Central Japan. *Geomorphology*, 65(1–2): 15-31.
- [24] Bacon, C.R., 1982. Time-predictable bimodal volcanism in the Coso Range, California. *Geology*, 10(2): 65-69.
- [25] Ballance, P.F., 1964. The Sedimentology of the Waitemata Group in the Takapuna Section, Auckland. *New Zealand Journal of Geology and Geophysics*, 7: 466-499.
- [26] Ballance, P.F., 1974. An Inter-Arc Flysch Basin in Northern New Zealand: Waitemata Group (Upper Oligocene to Lower Miocene). *The Journal of Geology*, 82(4): 439-471.
- [27] Ballance, P.F., 1976. Stratigraphy and Bibliography of the Waitemata Group of Auckland, New Zealand. *New Zealand Journal of Geology and Geophysics*, 19(6): 897-932.
- [28] Baloga, S.M., Glaze, L.S. and Bruno, B.C., 2007. Nearest-neighbor analysis of small features on Mars: applications to tumuli and rootless cones. *Journal of Geophysical Research: Planets*, 112(E03002): DOI: 10.1029/2005JE002652.
- [29] Baltsavias, E.P., 1999a. Airborne laser scanning: basic relations and formulas. *ISPRS Journal of Photogrammetry and Remote Sensing*, 54(2–3): 199-214.
- [30] Baltsavias, E.P., 1999b. A comparison between photogrammetry and laser scanning. *ISPRS Journal of Photogrammetry and Remote Sensing*, 54(2–3): 83-94.

- [31] Bamler, R. and Hartl, P., 1998. Synthetic aperture radar interferometry. *Inverse Problems*, 14: 1-54.
- [32] Barberi, F., Carapezza, M.L., Valenza, M. and Villar, L., 1993. The control of lava flow during the 1991–1992 eruption of Mt. Etna *Journal of Volcanology and Geothermal Research*, 56(1-2): 1-34.
- [33] Barca, D., Crisci, G.M., Di Gregorio, S. and Nicoletta, F., 1994. Cellular automata methods for modelling lava flows: a method and examples of the Etnean eruptions. *Transport Theory and Statistical Physics*, 23: 195-232.
- [34] Barde-Cabusson, S., Bolós, X., Pedrazzi, D., Lovera, R., Serra, G., Martí, J. and Casas, A., 2013. Electrical resistivity tomography revealing the internal structure of monogenetic volcanoes. *Geophysical Research Letters*, 40(11): 2544-2549.
- [35] Barter, T.P., 1976. The Kaihu group (Plio-Quaternary) of the Awhitu Peninsula, South-West Auckland. PhD thesis, University of Auckland, New Zealand, pp. 1-299.
- [36] Bartolini, S., Cappello, A., Martí, J. and Del Negro, C., 2013. QVAST: a new Quantum GIS plugin for estimating volcanic susceptibility. *Natural Hazards and Earth System Sciences*, 13: 3031-3042.
- [37] Bater, C.W. and Coops, N.C., 2009. Evaluating error associated with lidar-derived DEM interpolation. *Computers & Geosciences*, 35(2): 289-300.
- [38] Bebbington, M. and Cronin, S.J., 2012. Paleomagnetic and geological updates to an event-order model for the Auckland Volcanic Field. *Proceedings of Fourth International Maar Conference - a multidisciplinary congress on monogenetic volcanism*, Auckland, New Zealand, Geoscience Society of New Zealand Miscellaneous Publication 131A: 5-6.
- [39] Bebbington, M.S., 2013. Assessing spatio-temporal eruption forecasts in a monogenetic volcanic field. *Journal of Volcanology and Geothermal Research*, 252: 14-28.
- [40] Bebbington, M.S. and Cronin, S.J., 2011. Spatio-temporal hazard estimation in the Auckland Volcanic Field, New Zealand, with a new event-order model. *Bulletin of Volcanology*, 73(1): 55-72.
- [41] Becerril, L., Cappello, A., Galindo, I., Neri, M. and Del Negro, C., 2013. Spatial probability distribution of future volcanic eruptions at El Hierro Island (Canary Islands, Spain). *Journal of Volcanology and Geothermal Research*, 257: 21-30.
- [42] Bellian, J.A., Kerans, C. and Jennette, D.C., 2005. Digital outcrop models; applications of terrestrial scanning lidar technology in stratigraphic modeling. *Journal of Sedimentary Research*, 75(2): 166-176.
- [43] Berry, K.A., 1986. Stratigraphic, structural and geophysical studies of Neogene sediments of the Manukau lowlands. MSc thesis, University of Auckland, New Zealand, pp. 1-178.
- [44] Berti, M., Corsini, A. and Daehne, A., 2013. Comparative analysis of surface roughness algorithms for the identification of active landslides. *Geomorphology*, 182: 1-18.
- [45] Bertotto, G.W., Bjerg, E.A. and Cingolani, C.A., 2006. Hawaiian and Strombolian style monogenetic volcanism in the extra-Andean domain of central-west Argentina. *Journal of Volcanology and Geothermal Research*, 158(3-4): 430-444.
- [46] Bilotta, G., Cappello, A., Hérault, A., Vicari, A., Russo, G. and Del Negro, C., 2012. Sensitivity analysis of the MAGFLOW Cellular Automaton model for lava flow simulation. *Environmental Modelling & Software*, 35: 122-131.

- [47] Bishop, M.A., 2007. Point pattern analysis of eruption points for the Mount Gambier volcanic sub-province: a quantitative geographical approach to the understanding of volcano distribution. *Area*, 39(2): 230-241.
- [48] Bishop, M.A., 2009. A generic classification for the morphological and spatial complexity of volcanic (and other) landforms. *Geomorphology*, 111(1-2): 104-109.
- [49] Bisson, M. and Del Carlo, P., 2013. A GIS-based application for volume estimation and spatial distribution analysis of tephra fallout: a case study of the 122 BC Etna eruption. *Annals of Geophysics*, 56(1): 1-12.
- [50] Bisson, M., Sulpizio, R., Zanchetta, G., Demi, F. and Santacroce, R., 2010. Rapid terrain-based mapping of some volcanoclastic flow hazard using GIS-based automated methods: a case study from southern Campania, Italy. *Natural Hazards*, 55(2): 371-387.
- [51] Blake, S., Wilson, C.J.N., Smith, I.E.M. and Leonard, G.S., 2006. Lead times and precursors of eruptions in the Auckland Volcanic Field, New Zealand: Indications from historical analogues and theoretical modelling. *GNS Science Report 2006/34*, pp. 1-22.
- [52] Boedihardi, R.M., 1990. Structural resistivity and temperature surveys of basement fracture zones in the greater Whitford area (South Auckland). MSc thesis, University of Auckland, New Zealand, pp. 1-186.
- [53] Bonin, O. and Rousseaux, F., 2005. Digital Terrain Model Computation from Contour Lines: How to Derive Quality Information from Artifact Analysis. *GeoInformatica*, 9(3): 253-268.
- [54] Bonne, K., Kervyn, M., Cascone, L., Njome, S., Van Ranst, E., Suh, E., Ayonghe, S., Jacobs, P. and Ernst, G., 2008. A new approach to assess long-term lava flow hazard and risk using GIS and low-cost remote sensing: the case of Mount Cameroon, West Africa. *International Journal of Remote Sensing*, 29(22): 6539-6564.
- [55] Borgefors, G., 1984. Distance transformations in arbitrary dimensions. *Computer Vision, Graphic, and Image Processing*, 27(3): 321-345.
- [56] Bowen, Z.H. and Waltermire, R.G., 2002. Evaluation of light detection and ranging (lidar) for measuring river corridor topography. *Journal of the American Water Resources Association*, 38(1): 33-41.
- [57] Boyce, J., 2013. The Newer Volcanics Province of southeastern Australia: a new classification scheme and distribution map for eruption centres. *Australian Journal of Earth Sciences*, 60(4): 449-462.
- [58] Brenna, M., Cronin, S.J., Németh, K., Smith, I.E.M. and Sohn, Y.K., 2011. The influence of magma plumbing complexity on monogenetic eruptions, Jeju Island, Korea. *Terra Nova*, 23: 70-75.
- [59] Brenna, M., Cronin, S.J., Smith, I.E.M., Maas, R. and Sohn, Y.K., 2012a. How Small-volume Basaltic Magmatic Systems Develop: a Case Study from the Jeju Island Volcanic Field, Korea. *Journal of Petrology*, 53(5): 985-1018.
- [60] Brenna, M., Cronin, S.J., Smith, I.E.M., Sohn, Y.K. and Maas, R., 2012b. Spatio-temporal evolution of a dispersed magmatic system and its implications for volcano growth, Jeju Island Volcanic Field, Korea. *Lithos*, 148: 337-352.
- [61] Brenna, M., Cronin, S.J., Smith, I.E.M., Sohn, Y.K. and Németh, K., 2010. Mechanisms driving polymagmatic activity at a monogenetic volcano, Udo, Jeju Island, South Korea. *Contributions to Mineralogy and Petrology*, 160: 931-950.
- [62] Briggs, R.M., Itaya, T., Lowe, D.J. and Keane, A.J., 1989. Ages of the Pliocene—Pleistocene Alexandra and Ngatutura Volcanics, western North Island, New

- Zealand, and some geological implications. *New Zealand Journal of Geology and Geophysics*, 32(4): 417-427.
- [63] Briggs, R.M., Okada, T., Itaya, T., Shibuya, H. and Smith, I.E.M., 1994. K-Ar ages, paleomagnetism, and geochemistry of the South Auckland volcanic field, North Island, New Zealand. *New Zealand Journal of Geology and Geophysics*, 37: 143-153.
- [64] Briggs, R.M., Utting, A.J. and Gibson, I.L., 1990. The origin of alkaline magmas in an intraplate setting near a subduction zone: the Ngatutura Basalts, North Island, New Zealand. *Journal of Volcanology and Geothermal Research*, 40: 55-70.
- [65] Brown, O.W. and Hugenholtz, C.H., 2013. Quantifying the effects of terrestrial laser scanner settings and survey configuration on land surface roughness measurement. *Geosphere*, 9(2): 367-377.
- [66] Brzank, A., Heipke, C., Goepfert, J. and Soergel, U., 2008. Aspects of generating precise digital terrain models in the Wadden Sea from lidar-water classification and structure line extraction. *ISPRS Journal of Photogrammetry and Remote Sensing*, 63(5): 510-528.
- [67] Büchel, G. and Lorenz, V., 1993. Syn- and post-eruptive mechanism of the Alaskan Ukinrek Maars in 1977. In: J. Negendank and B. Zolitschka (Editors), *Paleolimnology of European Maar Lakes. Lecture Notes in Earth Sciences*. Springer Berlin / Heidelberg, pp. 15-60.
- [68] Bulatović, V., Sušić, Z. and Ninkov, T., 2012. Estimate of the ASTER GDEM regional systematic errors and their removal. *International Journal of Remote Sensing*, 33(18): 5915-5926.
- [69] Burrough, P.A. and McDonnell, R.A., 1998. *Principles of Geographical Information Systems*. Oxford University Press, Oxford, United Kingdom, pp. 1-352.
- [70] Büttner, R., Dellino, P. and Zimanowski, B., 1999. Identifying modes of magma/water interaction from the surface features of ash particles. *Nature*, 401: 688-690.
- [71] Cabrera, A.P. and Caffè, P.J., 2009. The Cerro Morado Andesites: Volcanic history and eruptive styles of a mafic volcanic field from northern Puna, Argentina. *Journal of South American Earth Sciences*, 28(2): 113-131.
- [72] Calvari, S. and Pinkerton, H., 1999. Lava tube morphology on Etna and evidence for lava flow emplacement mechanisms. *Journal of Volcanology and Geothermal Research*, 90(3-4): 263-280.
- [73] Camp, V., Hooper, P., Roobol, M.J. and White, D.L., 1987. The Madinah eruption, Saudi Arabia: Magma mixing and simultaneous extrusion of three basaltic chemical types. *Bulletin of Volcanology*, 49(2): 489-508.
- [74] Campbell, B.A. and Shepard, M.K., 1996. Lava flow surface roughness and depolarized radar scattering. *Journal of Geophysical Research: Planets*, 101(E8): 18941-18951.
- [75] Cañón-Tapia, E., 2013. Volcano clustering determination: Bivariate Gauss vs. Fisher kernels. *Journal of Volcanology and Geothermal Research*, 258: 203-214.
- [76] Cappello, A., Neri, M., Acocella, V., Gallo, G., Vicari, A. and Del Negro, C., 2012. Spatial vent opening probability map of Etna volcano (Sicily, Italy). *Bulletin of Volcanology*, 74(9): 2083-2094.
- [77] Cappello, A., Vicari, A. and Del Negro, C., 2011. Retrospective validation of a lava-flow hazard map for Mount Etna volcano. *Annals of Geophysics*, 54(5): 634-640.

- [78] Carn, S.A., Krueger, A.J., Arellano, S., Krotkov, N.A. and Yang, K., 2008. Daily monitoring of Ecuadorian volcanic degassing from space. *Journal of Volcanology and Geothermal Research*, 176(1): 141-150.
- [79] Carter, L., 1971. Stratigraphy and Sedimentology of the Waitemata Group, Puketotara Peninsula, Northland. *New Zealand Journal of Geology and Geophysics*, 14(1): 169-191.
- [80] Cashman, K.V. and Kauahikaua, J.P., 1997. Reevaluation of vesicle distributions in basaltic lava flows. *Geology*, 25(5): 419-422.
- [81] Cashman, K.V., Mangan, M.T. and Newman, S., 1994. Surface degassing and modifications to vesicle size distributions in active basalt flows. *Journal of Volcanology and Geothermal Research*, 61(1-2): 45-68.
- [82] Cashman, K.V., Soule, S.A., Mackey, B.H., Deligne, N.I., Deardorff, N.D. and Dietterich, H.R., 2013. How lava flows: New insights from applications of lidar technologies to lava flow studies. *Geosphere*, DOI: 10.1130/GES00706.1
- [83] Cashman, K.V. and Sparks, R.S.J., 2013. How volcanoes work: A 25 year perspective. *Geological Society of America Bulletin*, DOI: 10.1130/B30720.1
- [84] Cashman, K.V., Sturtevant, B., Papale, P. and Navon, O., 2000. Magmatic Fragmentation. In: H. Sigurdsson, B.F. Houghton, S.R. McNutt, H. Rymer and J. Stix (Editors), *Encyclopedia of Volcanoes*. Academic Press, San Diego, California, pp. 421-429.
- [85] Cassata, W.S., Singer, B.S. and Cassidy, J., 2008. Laschamp and Mono Lake geomagnetic excursions recorded in New Zealand. *Earth and Planetary Science Letters*, 268: 76-88.
- [86] Cassidy, J., 1990. Seismic monitoring network [Auckland Volcanic field]. *New Zealand Volcanological Record*, 18: 14-15.
- [87] Cassidy, J., 2006. Geomagnetic excursion captured by multiple volcanoes in a monogenetic field. *Geophysical Research Letters*, 33(21): DOI: 10.1029/2006GL027284.
- [88] Cassidy, J. and Daly, M., 1995. Auckland Volcanic Field: seismic monitoring and seismicity, 1993. *New Zealand Volcanological Record*, 22: 20-21.
- [89] Cassidy, J., France, S.J. and Locke, C.A., 2007. Gravity and magnetic investigation of maar volcanoes, Auckland volcanic field, New Zealand. *Journal of Volcanology and Geothermal Research*, 159(1-3): 153-163.
- [90] Cassidy, J. and Locke, C.A., 2010. The Auckland volcanic field, New Zealand: Geophysical evidence for structural and spatio-temporal relationships. *Journal of Volcanology and Geothermal Research*, 195(2-4): 127-137.
- [91] Cassidy, J., Locke, C.A., Miller, C.A. and Rout, D.J., 1999. The Auckland Volcanic Field, New Zealand: geophysical evidence for its eruption history. *Geological Society, London, Special Publications*, 161: 1-10.
- [92] Cebriá, J.-M. and López-Ruiz, J., 1995. Alkali basalts and leucitites in an extensional intracontinental plate setting: The late Cenozoic Calatrava Volcanic Province (central Spain). *Lithos*, 35(1-2): 27-46.
- [93] Charlier, B.L.A. and Wilson, C.J.N., 2010. Chronology and Evolution of Caldera-forming and Post-caldera Magma Systems at Okataina Volcano, New Zealand from Zircon U–Th Model-age Spectra. *Journal of Petrology*, 51(5): 1121-1141.
- [94] Chau, K.T., Sze, Y.L., Fung, M.K., Wong, W.Y., Fong, E.L. and Chan, L.C.P., 2004. Landslide hazard analysis for Hong Kong using landslide inventory and GIS. *Computers & Geosciences*, 30(4): 429-443.

- [95] Chouet, B., Hamisevicz, N. and McGetchin, T.R., 1974. Photoballistics of Volcanic Jet Activity at Stromboli, Italy. *Journal of Geophysical Research*, 79(32): 4961-4976.
- [96] Chough, S.K. and Sohn, Y.K., 1990. Depositional mechanics and sequences of base surges, Songaksan tuff ring, Cheju Island, Korea. *Sedimentology*, 37(6): 1115-1135.
- [97] Condit, C.D. and Connor, C.B., 1996. Recurrence rates of volcanism in basaltic volcanic fields: An example from the Springerville volcanic field, Arizona. *Geological Society of America Bulletin*, 108(10): 1225-1241.
- [98] Connor, C.B., 1990. Cinder cone clustering in the TransMexican Volcanic Belt: Implications for structural and petrologic models. *Journal of Geophysical Research: Solid Earth* 95(B12): 19395-19405.
- [99] Connor, C.B. and Connor, L.J., 2009. 14 - Estimating spatial density with kernel methods. In: C.B. Connor, N.A. Chapman and L.J. Connor (Editors), *Volcanic and tectonic hazard assessment for nuclear facilities*. Cambridge University Press, Cambridge, United Kingdom, pp. 346-368.
- [100] Connor, C.B. and Conway, F.M., 2000. Basaltic volcanic fields. In: H. Sigurdsson, B.F. Houghton, S.R. McNutt, H. Rymer and J. Stix (Editors), *Encyclopedia of Volcanoes*. Academic Press, San Diego, California, pp. 331-343.
- [101] Connor, C.B. and Hill, B.E., 1995. Three nonhomogeneous Poisson models for the probability of basaltic volcanism: Application to the Yucca Mountain region, Nevada, U.S.A. *Journal of Geophysical Research: Solid Earth* 100(B6): 10107-10125.
- [102] Connor, C.B., Stamatakos, J.A., Ferrill, D.A., Hill, B.E., Ofoegbu, G., Conway, F.M., Sagar, B. and Trapp, J., 2000. Geologic factors controlling patterns of small-volume basaltic volcanism: Application to a volcanic hazards assessment at Yucca Mountain, Nevada. *Journal of Geophysical Research: Solid Earth* 105(1): 417-432.
- [103] Connor, L.J., Connor, C.B., Meliksetian, K. and Savov, I., 2012. Probabilistic approach to modeling lava flow inundation: a lava flow hazard assessment for a nuclear facility in Armenia. *Journal of Applied Volcanology*, 1:3.
- [104] Conoscenti, C., Di Maggio, C. and Rotigliano, E., 2008. GIS analysis to assess landslide susceptibility in a fluvial basin of NW Sicily (Italy). *Geomorphology*, 94(3-4): 325-339.
- [105] Conrad, C.P., Bianco, T.A., Smith, E.I. and Wessel, P., 2011. Patterns of intraplate volcanism controlled by asthenospheric shear. *Nature Geoscience*, 4: 317-321.
- [106] Conway, F.M., Connor, C.B., Hill, B.E., Condit, C.D., Mullaney, K. and Hall, C.M., 1998. Recurrence rates of basaltic volcanism in SP cluster, San Francisco volcanic field, Arizona. *Geology*, 26(7): 655-658.
- [107] Conybeer, M.A., 1995. Physical volcanology of Maungataketake Volcano. MSc thesis, University of Auckland, New Zealand, pp. 1-200.
- [108] Cook, C., Briggs, R.M., Smith, I.E.M. and Maas, R., 2005. Petrology and Geochemistry of Intraplate Basalts in the South Auckland Volcanic Field, New Zealand: Evidence for Two Coeval Magma Suites from Distinct Sources. *Journal of Petrology*, 46(3): 473-503.
- [109] Coombs, D.S., Landis, C.A., Norris, R.J., Sinton, J.M., Borns, D.J. and Craw, D., 1976. The Dun Mountain ophiolite belt, New Zealand, its tectonic setting,

- constitution, and origin, with special reference to the southern portion. *American Journal of Science*, 276(5): 561-603.
- [110] Costa-Cabral, M.C. and Burges, S.J., 1994. Digital Elevation Model Networks (DEMON): A Model of Flow Over Hillslopes for Computations of Contributing and Dispersal Areas. *Water Resources Research*, 30(6): 1681-1692.
- [111] Courtland, L., Kruse, S. and Connor, C., 2013. Violent Strombolian or not? Using ground-penetrating radar to distinguish deposits of low- and high-energy scoria cone eruptions. *Bulletin of Volcanology*, 75(12): 1-13.
- [112] Courtland, L.M., Kruse, S.E., Connor, C.B., Connor, L.J., Savov, I.P. and Martin, K.T., 2012. GPR investigation of tephra fallout, Cerro Negro volcano, Nicaragua: a method for constraining parameters used in tephra sedimentation models. *Bulletin of Volcanology*, 74(6): 1409-1424.
- [113] Crisci, G.M., Rongo, R., Di Gregorio, S. and Spataro, W., 2004. The simulation model SCIARA: the 1991 and 2001 lava flows at Mount Etna. *Journal of Volcanology and Geothermal Research*, 132: 253-267.
- [114] Cronin, S.J., Bebbington, M. and Lai, C.D., 2001. A probabilistic assessment of eruption recurrence on Taveuni volcano, Fiji. *Bulletin of Volcanology*, 63: 274-289.
- [115] Csatho, B., Schenk, T., Kyle, P., Wilson, T. and Krabill, W.B., 2008. Airborne laser swath mapping of the summit of Erebus volcano, Antarctica: Applications to geological mapping of a volcano. *Journal of Volcanology and Geothermal Research*, 177(3): 531-548.
- [116] Dahm, T., 2000. Numerical simulations of the propagation path and the arrest of fluid-filled fractures in the Earth. *Geophysical Journal International*, 141(3): 623-638.
- [117] Damiani, M.L., Groppelli, G., Norini, G., Bertino, E., Gigliuto, A. and Nucita, A., 2006. A lava flow simulation model for the development of volcanic hazard maps for Mount Etna (Italy). *Computers & Geosciences*, 32: 512-526.
- [118] Davidson, K.J. and Black, P.M., 1994. Diagenesis in Early Miocene Waitemata Group sediments, Upper Waitemata Harbour, Auckland, New Zealand. *Geoscience Report Shizuoka University*, 20: 135-142.
- [119] de la Cruz-Reyna, S. and Yokoyama, I., 2011. A geophysical characterization of monogenetic volcanism. *Geofisica Internacional*, 50(4): 465-484.
- [120] Deardorff, N. and Cashman, K., 2012. Emplacement conditions of the c. 1,600-year bp Collier Cone lava flow, Oregon: a LiDAR investigation. *Bulletin of Volcanology*, 74(9): 2051-2066.
- [121] Debella-Gilo, M. and Etzelmüller, B., 2009. Spatial prediction of soil classes using digital terrain analysis and multinomial logistic regression modeling integrated in GIS: Examples from Vestfold County, Norway. *Catena*, 77(1): 8-18.
- [122] Del Gaudio, V. and Wasowski, J., 2004. Time probabilistic evaluation of seismically induced landslide hazard in Irpinia (Southern Italy). *Soil Dynamics and Earthquake Engineering*, 24(12): 915-928.
- [123] Del Negro, C., Fortuna, L., Herault, A. and Vicari, A., 2008. Simulations of the 2004 lava flow at Etna volcano using the magflow cellular automata model. *Bulletin of Volcanology*, 70(7): 805-812.
- [124] Del Negro, C., Fortuna, L. and Vicari, A., 2005. Modelling lava flows by Cellular Nonlinear Networks (CNN): preliminary results. *Nonlinear Processes in Geophysics*, 12(4): 505-513.

- [125] Delaney, P.T., Pollard, D.D., Ziony, J.I. and McKee, E.H., 1986. Field Relations Between Dikes and Joints: Emplacement Processes and Paleostress Analysis. *Journal of Geophysical Research: Solid Earth* 91(B5): 4920-4938.
- [126] Demidjuk, Z., Turner, S., Sandiford, M., George, R., Foden, J. and Etheridge, M., 2007. U-series isotope and geodynamic constraints on mantle melting processes beneath the Newer Volcanic Province in South Australia. *Earth and Planetary Science Letters*, 261: 517-533.
- [127] Demouchy, S., Jacobsen, S.D., Gaillard, F. and Stern, C.R., 2006. Rapid magma ascent recorded by water diffusion profiles in mantle olivine. *Geology*, 34(6): 429-432.
- [128] Deng, Y., Wilson, J.P. and Bauer, B.O., 2007. DEM resolution dependencies of terrain attributes across a landscape. *International Journal of Geographical Information Science*, 21(2): 187-213.
- [129] Di Traglia, F., Cimarelli, C., de Rita, D. and Gimeno Torrente, D., 2009. Changing eruptive styles in basaltic explosive volcanism: Examples from Croscat complex scoria cone, Garrotxa Volcanic Field (NE Iberian Peninsula). *Journal of Volcanology and Geothermal Research*, 180(2-4): 89-109.
- [130] Dietterich, H.R., Poland, M.P., Schmidt, D.A., Cashman, K.V., Sherrod, D.R. and Espinosa, A.T., 2012. Tracking lava flow emplacement on the east rift zone of Kīlauea, Hawai‘i, with synthetic aperture radar coherence. *Geochemistry, Geophysics, Geosystems*, 13(5): Q05001.
- [131] Dohrenwend, J.C., Wells, S.G. and Turrin, B.D., 1986. Degradation of Quaternary cinder cones in the Cima volcanic field, Mojave Desert, California. *Geological Society of America Bulletin*, 97(4): 421-427.
- [132] Donoghue, S.L., Neall, V.E. and Palmer, A.S., 1995. Stratigraphy and chronology of late Quaternary andesitic tephra deposits, Tongariro Volcanic Centre, New Zealand. *Journal of the Royal Society of New Zealand*, 25(2): 115-206.
- [133] Douglas, D.H., 1986. Experiments to Locate Ridges and Channels to Create a New Type of Digital Elevation Models. *Cartographica*, 23(4): 29-61.
- [134] Dragoni, M., 1989. A dynamical model of lava flows cooling by radiation. *Bulletin of Volcanology*, 51: 88-95.
- [135] Dragoni, M., Bonafede, M. and Boschi, E., 1986. Downslope flow models of a Bingham liquid: implications for lava flows. *Journal of Volcanology and Geothermal Research*, 30: 305-325.
- [136] Dragoni, M. and Tallarico, A., 1994. The effect of crystallization on the rheology and dynamics of lava flows. *Journal of Volcanology and Geothermal Research*, 59: 241-252.
- [137] Dragut, L. and Eisank, C., 2011. Object representations at multiple scales from digital elevation models. *Geomorphology*, 129: 183-189.
- [138] Dragut, L., Eisank, C. and Strasser, T., 2011. Local variance for multi-scale analysis in geomorphometry. *Geomorphology*, 130: 162-172.
- [139] Dragut, L., Schauppenlehner, T., Muhar, A., Strobl, J. and Blaschke, T., 2009. Optimization of scale and parametrization for terrain segmentation: An application to soil-landscape modeling. *Computers & Geosciences*, 35: 1875-1883.
- [140] Dragut, L., Tiede, D. and Levick, S.R., 2010. ESP: a tool to estimate scale parameter for multiresolution image segmentation of remotely sensed data. *International Journal of Geographical Information Science*, 24(6): 859-871.

- [141] Dunning, S.A., Massey, C.I. and Rosser, N.J., 2009. Structural and geomorphological features of landslides in the Bhutan Himalaya derived from Terrestrial Laser Scanning. *Geomorphology*, 103(1): 17-29.
- [142] Duong, T., 2007. ks: Kernel Density Estimation and Kernel Discriminant Analysis for Multivariate Data in R. *Journal of Statistical Software*, 21(7): 1-16.
- [143] Eade, J., 2009. Petrology and correlation of lava flows from the central part of the Auckland Volcanic Field. MSC thesis, University of Auckland, New Zealand, pp. 1-88.
- [144] Eastman, J.R., 2009. IDRISI Taiga - Guide to GIS and Image Processing (Manual). Clark Lab & Clark University, Worcester, USA, pp. 1-342.
- [145] Eccles, J.D., Cassidy, J., Locke, C.A. and Spörli, K.B., 2005. Aeromagnetic imaging of the Dun Mountain Ophiolite Belt in New Zealand: insight into the fine structure of a major SW Pacific terrane suture. *Journal of the Geological Society of London*, 162: 723-735.
- [146] Edbrooke, S.W., 2001. Geology of the Auckland area. Scale 1:250,000. Institute of Geological & Nuclear Sciences geological maps 3. Institute of Geological & Nuclear Sciences, Lower Hutt, New Zealand, pp. 1-74.
- [147] Edbrooke, S.W., Crouch, E.M., Morgans, H.E.G. and Sykes, R., 1998. Late Eocene-Oligocene Te Kuiti Group at Mount Roskill, Auckland, New Zealand. *New Zealand Journal of Geology and Geophysics*, 41: 85-93.
- [148] Edbrooke, S.W., Mazengarb, C. and Stephenson, W., 2003. Geology and geological hazards of the Auckland urban area, *New Zealand Quaternary International*, 103(1): 3-21.
- [149] Evans, I.S., 1972. General geomorphometry, derivatives of altitude and descriptive statistics. In: R.J. Chorley (Editor), *Spatial Analysis in Geomorphology*. Methuen, London, United Kingdom, pp. 17-90.
- [150] Evans, J.P., Forster, C.B. and Goddard, J.V., 1997. Permeability of fault-related rocks, and implications for hydraulic structure of fault zones. *Journal of Structural Geology*, 19(11): 1393-1404.
- [151] Farr, T.G., 1992. Microtopographic evolution of lava flows at Cima Volcanic Field, Mojave Desert, California. *Journal of Geophysical Research: Solid Earth*, 97(B11): 15171-15179.
- [152] Farr, T.G., Rosen, P.A., Caro, E., Crippen, R., Duren, R., Hensley, S., Kobrick, M., Paller, M., Rodriguez, E., Roth, L., Seal, D., Shaffer, S., Shimada, J., Umland, J., Werner, M., Oskin, M., Burbank, D. and Alsdorf, D., 2007. The Shuttle Radar Topography Mission. *Reviews of Geophysics*, 45(2): RG2004.
- [153] Farrel, J.A. and Barth, M., 1998. The global positioning system & inertial navigation. McGraw-Hill Professional, pp. 1-340.
- [154] Favalli, M., Chirico, G.D., Papale, P., Pareschi, M.T. and Boschi, E., 2009a. Lava flow hazard at Nyiragongo Volcano, D.R.C. 1. Model calibration and hazard mapping. *Bulletin of Volcanology*, 71(4): 363-374.
- [155] Favalli, M., Fornaciai, A., Mazzarini, F., Harris, A., Neri, M., Behncke, B., Pareschi, M.T., Tarquini, S. and Boschi, E., 2010. Evolution of an active lava flow field using a multitemporal LIDAR acquisition. *Journal of Geophysical Research: Solid Earth*, 115(B11203): DOI: 10.1029/2010JB007463.
- [156] Favalli, M., Fornaciai, A. and Pareschi, M.T., 2009b. LIDAR strip adjustment: Application to volcanic areas. *Geomorphology*, 111(3-4): 123-135.
- [157] Favalli, M., Karátson, D., Mazzarini, F., Pareschi, M.T. and Boschi, E., 2009c. Morphometry of scoria cones located on a volcano flank: A case study from Mt.

- Etna (Italy), based on high-resolution LiDAR data. *Journal of Volcanology and Geothermal Research*, 186(3-4): 320-330.
- [158] Favalli, M., Mazzarini, F., Pareschi, M.T. and Boschi, E., 2009d. Topographic control on lava flow paths at Mount Etna, Italy: Implications for hazard assessment. *Journal of Geophysical Research: Earth Surface*, 114(F01019): DOI: 10.1029/2007JB000918.
- [159] Favalli, M., Pareschi, M.T., Neri, A. and Isola, I., 2005. Forecasting lava flow paths by a stochastic approach. *Geophysical Research Letters*, 32(3): DOI: 10.1029/2004GL021718.
- [160] Favalli, M., Tarquini, S., Fornaciai, A. and Boschi, E., 2009e. A new approach to risk assessment of lava flow at Mount Etna. *Geology*, 37(12): 1111-1114.
- [161] Favalli, M., Tarquini, S., Fornaciai, A. and Boschi, E., 2012a. Dispersion index of topographic surfaces. *Geomorphology*, 153–154: 169-178.
- [162] Favalli, M., Tarquini, S., Papale, P., Fornaciai, A. and Boschi, E., 2012b. Lava flow hazard and risk at Mt. Cameroon volcano. *Bulletin of Volcanology*, 74(2): 423-439.
- [163] Fell, R., Corominas, J., Bonnard, C., Cascini, L., Leroi, E. and Savage, W.Z., 2008. Guidelines for landslide susceptibility, hazard and risk zoning for land use planning. *Engineering Geology*, 102(3–4): 85-98.
- [164] Felpeto, A., Araña, V., Ortiz, R., Astiz, M. and García, A., 2001. Assessment and Modelling of Lava Flow Hazard on Lanzarote (Canary Islands). *Natural Hazards*, 23(2-3): 247-257.
- [165] Felpeto, A., Martí, J. and Ortiz, R., 2007. Automatic GIS-based system for volcanic hazard assessment. *Journal of Volcanology and Geothermal Research*, 166(1): 106-116.
- [166] Fernández, J., Tizzani, P., Manzo, M., Borgia, A., Gonzalez, P.J., Marti, J., Pepe, A., Camacho, A.G., Casu, F., Berardino, P., Prieto, J.F. and Lanari, R., 2009. Gravity-driven deformation of Tenerife measured by InSAR time series analysis. *Geophysical Research Letters*, 36(4): DOI: 10.1029/2008GL036920.
- [167] Fisher, P.F. and Tate, N.J., 2006. Causes and consequences of error in digital elevation models. *Progress in Physical Geography*, 30(4): 467-489.
- [168] Florinsky, I.V., 2009. Computation of the third-order partial derivatives from a digital elevation model. *International Journal of Geographical Information Science*, 23(2): 213-231.
- [169] Florinsky, I.V. and Kuryakova, G.A., 2000. Determination of grid size for digital terrain modelling in landscape investigations—exemplified by soil moisture distribution at a micro-scale. *International Journal of Geographical Information Science*, 14(8): 815-832.
- [170] Fornaciai, A., Bisson, M., Landi, P., Mazzarini, F. and Pareschi, M.T., 2010. A LiDAR survey of Stromboli volcano (Italy): Digital elevation model-based geomorphology and intensity analysis. *International Journal of Remote Sensing*, 31(12): 3177-3194.
- [171] Fornaciai, A., Favalli, M., Karátson, D., Tarquini, S. and Boschi, E., 2012. Morphometry of scoria cones, and their relation to geodynamic setting: A DEM-based analysis. *Journal of Volcanology and Geothermal Research*, 217–218: 56-72.
- [172] Fries, C.J., 1953. Volumes and weights of pyroclastic material, lava, and water erupted by Paricutin volcano, Michoacan, Mexico. *American Geophysical Union Transactions*, 34: 603-616.

- [173] Gaddis, L.R., Mougini-Mark, P.J. and Hayashi, I.N., 1990. Lava Flow Surface Textures: SIR-B Radar, Image Texture, Field Observations, and Terrain Measurements. *Photogrammetric Engineering and Remote Sensing*, 56(2): 211-224.
- [174] Gaffney, E.S. and Damjanac, B., 2006. Localization of volcanic activity: Topographic effects on dike propagation, eruption and conduit formation. *Geophysical Research Letters*, 33(14): DOI: 10.1029/2006GL026852.
- [175] Gaffney, E.S., Damjanac, B. and Valentine, G.A., 2007. Localization of volcanic activity: 2. Effects of pre-existing structure. *Earth and Planetary Science Letters*, 263: 323-338.
- [176] Galindo, I. and Gudmundsson, A., 2012. Basaltic feeder dykes in rift zones: geometry, emplacement, and effusion rates. *Natural Hazards and Earth System Sciences*, 12(12): 3683-3700.
- [177] Gallant, J.C. and Hutchinson, M.F., 1997. Scale dependence in terrain analysis. *Mathematics and Computers in Simulation*, 43(3-6): 313-321.
- [178] Gallay, M., 2013. Direct Acquisition of Data: Airborne laser scanning. *Geomorphological Techniques*, 2(1.4): 1-17.
- [179] Ganci, G., Vicari, A., Cappello, A. and Del Negro, C., 2012. An emergent strategy for volcano hazard assessment: From thermal satellite monitoring to lava flow modeling. *Remote Sensing of Environment*, 119: 197-207.
- [180] Gaonac'h, H., Stix, J. and Lovejoy, S., 1996. Scaling effects on vesicle shape, size and heterogeneity of lavas from Mount Etna. *Journal of Volcanology and Geothermal Research*, 74(1-2): 131-153.
- [181] Garbrecht, J. and Martz, L.W., 1994. Grid size dependency of parameters extracted from digital elevating models. *Computers & Geosciences*, 20(1): 85-87.
- [182] Garbrecht, J. and Martz, L.W., 1995. TOPAZ: An automated digital landscape analysis tool for topographic evaluation, drainage identification, watershed segmentation and subcatchment parameterisation: TOPAZ User Manual. U.S. Department of Agriculture, El Reno, Oklahoma, pp. 1-143.
- [183] Garbrecht, J. and Martz, L.W., 1997. The Assignment of Drainage Direction over Flat Surfaces in Raster Digital Elevation Models. *Journal of Hydrology*, 193: 204-213.
- [184] Garel, F., Kaminski, E., Tait, S. and Limare, A., 2013. The influence of wind on the estimation of lava effusion rate from thermal remote-sensing. *Journal of Volcanology and Geothermal Research*, 264: 223-230.
- [185] Garrido, M.S., Giménez, E., de Lacy, M.C. and Gil, A.J., 2011. Surveying at the limits of local RTK networks: Test results from the perspective of high accuracy users. *International Journal of Applied Earth Observation and Geoinformation*, 13(2): 256-264.
- [186] Gençalioglu-Kuşcu, G., Atilla, C., Cas, R.A.F. and Ilkay, K., 2007. Base surge deposits, eruption history, and depositional processes of a wet phreatomagmatic volcano in Central Anatolia (Cora Maar). *Journal of Volcanology and Geothermal Research*, 159(1-3): 198-209.
- [187] Germa, A., Quidelleur, X., Gillot, P.Y. and Tchilinguirian, P., 2010. Volcanic evolution of the back-arc Pleistocene Payun Matru volcanic field (Argentina). *Journal of South American Earth Sciences*, 29(3): 717-730.
- [188] Geshi, N., Kusumoto, S. and Gudmundsson, A., 2010. Geometric difference between non-feeder and feeder dikes. *Geology*, 38(3): 195-198.

- [189] Gevrek, A.I. and Kazanci, N., 2000. A Pleistocene, pyroclastic-poor maar from central Anatolia, Turkey: influence of a local fault on a phreatomagmatic eruption. *Journal of Volcanology and Geothermal Research*, 95(1-4): 309-317.
- [190] Geyer, A. and Martí, J., 2010. The distribution of basaltic volcanism on Tenerife, Canary Islands: Implications on the origin and dynamics of the rift systems. *Tectonophysics*, 483(3-4): 310-326.
- [191] Gili, J.A., Corominas, J. and Rius, J., 2000. Using Global Positioning System techniques in landslide monitoring. *Engineering Geology*, 55: 167-192.
- [192] Gilichinsky, M., Melnikov, D., Melekestsev, I., Zaretskaya, N. and Inbar, M., 2010. Morphometric measurements of cinder cones from digital elevation models of Tolbachik volcanic field, central Kamchatka. *Canadian Journal of Remote Sensing*, 36(4): 287-300.
- [193] Giordano, D. and Dingwell, D., 2003. Viscosity of hydrous Etna basalt: implications for Plinian-style basaltic eruptions. *Bulletin of Volcanology*, 65(1): 8-14.
- [194] Gomez-Fernandez, F., 2000. Application of a GIS algorithm to delimit the areas protected against basic lava flow invasion on Tenerife Island. *Journal of Volcanology and Geothermal Research*, 103: 409-423.
- [195] Goodchild, M.F., 2011. Scale in GIS: An overview. *Geomorphology*, 130(1-2): 5-9.
- [196] Gorokhovich, Y. and Voustianiouk, A., 2006. Accuracy assessment of the processed SRTM-based elevation data by CGIAR using field data from USA and Thailand and its relation to the terrain characteristics. *Remote Sensing of Environment*, 104: 409-415.
- [197] Gorte, B.G.H. and Koolhoven, W., 1990. Interpolation between isolines based on the Borgefors distance transform. *ITC Journals*, 1990-3: 245-247.
- [198] Gregg, T.K.P. and Fink, J.H., 2000. A laboratory investigation into the effects of slope on lava flow morphology. *Journal of Volcanology and Geothermal Research*, 96(3-4): 145-159.
- [199] Gregory, M.R., 1969. Sedimentary Features and Penecontemporaneous slumping in the Waitemata Group, Whangaparaoa Peninsula, North Auckland, New Zealand. *New Zealand Journal of Geology and Geophysics*, 12(1): 248-282.
- [200] Griffiths, R.W., 2000. The dynamics of lava flows. *Annual Review of Fluid Mechanics*, 32: 477-518.
- [201] Grohman, G., Kroenung, G. and Strebeck, J., 2006. Filling SRTM voids: The delta surface fill method. *Photogrammetric Engineering and Remote Sensing*, 72: 213-216.
- [202] Grosse, P., van Wyk de Vries, B., Petrinovic, I.A., Euillades, P.A. and Alvarado, G.E., 2009. Morphometry and evolution of arc volcanoes. *Geology*, 37(7): 651-654.
- [203] Gruber, A., Wessel, B., Huber, M. and Roth, A., 2012. Operational TanDEM-X DEM calibration and first validation results. *ISPRS Journal of Photogrammetry and Remote Sensing*, 73: 39-49.
- [204] Gruber, S., Huggel, C. and Pike, R., 2008. Modelling Mass Movements and Landslide Susceptibility. In: T. Hengl and H. Reuter (Editors), *Geomorphometry: Concepts, Software, Applications*. Elsevier B.V., pp. 527-550.
- [205] Guest, J.E., 1982. Styles of eruption and flow morphology in Mount Etna. In: R. Romano (Editor), *Mount Etna Volcano: A Review of the Recent Earth Science Studies*. *Memorie della Società Geologica Italiana*, 23, pp. 49-73.

- [206] Guest, J.E. and Murray, J.B., 1979. An analysis of hazard from Mount Etna volcano. *Journal of the Geological Society*, 136(3): 347-354.
- [207] Guilbaud, M.-N., Siebe, C. and Agustín-Flores, J., 2009. Eruptive style of the young high-Mg basaltic-andesite Pelagatos scoria cone, southeast of México City. *Bulletin of Volcanology*, 71(8): 859-880.
- [208] Guilbaud, M.-N., Siebe, C., Layer, P. and Salinas, S., 2012. Reconstruction of the volcanic history of the Tacámbaro-Puruarán area (Michoacán, México) reveals high frequency of Holocene monogenetic eruptions. *Bulletin of Volcanology*, 74(5): 1187-1211.
- [209] Gutmann, J.T., 1976. Geology of Crater Elegante, Sonora, Mexico. *Geological Society of America Bulletin*, 87(12): 1718-1729.
- [210] Guzzetti, F., Cardinali, M., Reichenbach, P., Cipolla, F., Sebastiani, C., Galli, M. and Salvati, P., 2004. Landslides triggered by the 23 November 2000 rainfall event in the Imperia Province, Western Liguria, Italy. *Engineering Geology*, 73(3-4): 229-245.
- [211] Guzzetti, F., Reichenbach, P., Cardinali, M., Galli, M. and Ardizzone, F., 2005. Probabilistic landslide hazard assessment at the basin scale. *Geomorphology*, 72(1-4): 272-299.
- [212] Hamilton, C.W., Fagents, S.A. and Thordarson, T., 2010. Explosive lava-water interactions II: self-organization processes among volcanic rootless eruption sites in the 1783-1784 Laki lava flow, Iceland. *Bulletin of Volcanology*, 72: 469-485.
- [213] Harding, B.C., Pattle A., Harris, M.G. and Twose, G., 2010. Groundwater response to dewatering of a volcanic vent. 11th IAEG Congress, New Zealand.
- [214] Harris, A., Favalli, M., Mazzarini, F. and Pareschi, M.T., 2007a. Best-fit results from application of a thermo-rheological model for channelized lava flow to high spatial resolution morphological data. *Geophysical Research Letters*, 34(1): DOI: 10.1029/2006gl028126.
- [215] Harris, A.J., Dehn, J. and Calvari, S., 2007b. Lava effusion rate definition and measurement: a review. *Bulletin of Volcanology*, 70(1): 1-22.
- [216] Harris, A.J.L. and Allen Iii, J.S., 2008. One-, two- and three-phase viscosity treatments for basaltic lava flows. *Journal of Geophysical Research: Solid Earth*, 113(9): DOI: 10.1029/2007jb005035.
- [217] Harris, A.J.L. and Baloga, S.M., 2009. Lava discharge rates from satellite-measured heat flux. *Geophysical Research Letters*, 36(19): DOI: 10.1029/2009GL039717.
- [218] Harris, A.J.L., Dehn, J., James, M.R., Hamilton, C., Herd, R., Lodato, L. and Steffke, A., 2007c. Pāhoehoe flow cooling, discharge, and coverage rates from thermal image chronometry. *Geophysical Research Letters*, 34(19): DOI: 10.1029/2007gl030791.
- [219] Harris, A.J.L., Favalli, M., Steffke, A., Fornaciai, A. and Boschi, E., 2010. A relation between lava discharge rate, thermal insulation, and flow area set using lidar data. *Geophysical Research Letters*, 37(20): DOI: 10.1029/2010GL044683.
- [220] Harris, A.J.L., Favalli, M., Wright, R. and Garbeil, H., 2011. Hazard assessment at Mount Etna using a hybrid lava flow inundation model and satellite-based land classification. *Natural Hazards*, 58(3): 1001-1027.
- [221] Harris, A.J.L., Flynn, L.P., Keszthelyi, L., Mouginiis-Mark, P.J., Rowland, S.K. and Resing, J.A., 1998. Calculation of lava effusion rates from LandsatTM data. *Bulletin of Volcanology*, 60: 52-71.

- [222] Harris, A.J.L., Murray, J.B., Aries, S.E., Davies, M.A., Flynn, L.P., Wooster, M.J., Wright, R. and Rothery, D.A., 2000. Effusion rate trends at Etna and Krafla and their implications for eruptive mechanisms. *Journal of Volcanology and Geothermal Research*, 102(3-4): 237-270.
- [223] Harris, A.J.L. and Rowland, S.K., 2001. FLOWGO: a kinematic thermorheological model for lava flowing in a channel. *Bulletin of Volcanology*, 63: 20-44.
- [224] Harris, A.J.L. and Rowland, S.K., 2009. Effusion Rate Controls on Lava Flow Length and the Role of Heat Loss: A Review. In: A. Hoskuldsson, T. Thordarson, G. Larsen, S. Self and S. Rowland (Editors), *The Legacy of George P.L. Walker*, Special Publications of IAVCEI 2. Geological Society of London, London, United Kingdom, pp. 33-51.
- [225] Hasenaka, T. and Carmichael, I.S.E., 1985. A compilation of location, size, and geomorphological parameters of volcanoes of the Michoacan-Guanajuato volcanic field, central Mexico. *Geofisica Internacional*, 24(4): 577-607.
- [226] Hayward, B., 1975. Lower Miocene geology of the Waitakere Hills, West Auckland, with emphasis on the paleontology. PhD thesis, University of Auckland, New Zealand, pp. 1-677.
- [227] Hayward, B., 1993. The tempestuous 10 million year life of a double arc and intra-arc basin--New Zealand's Northland Basin in the Early Miocene. In: P.F. Ballance (Editor), *South Pacific Sedimentary Basins*, *Sedimentary Basins of the World*. Elsevier, New York, pp. 113-142.
- [228] Hayward, B.W. and Brook, F.J., 1984. Lithostratigraphy of the basal Waitemata Group, Kawau Subgroup (new), Auckland, New Zealand. *New Zealand Journal of Geology and Geophysics*, 27: 101-123.
- [229] Hayward, B.W., Murdoch, G. and Maitland, G., 2011. *Volcanoes of Auckland*. Auckland University Press, Auckland, New Zealand, pp. 1-234.
- [230] Head, J.W., Bryan, W.B., Greeley, R., Guest, J.E., Schultz, P.H., Sparks, R.S.J., Walker, G.P.L., Whitford-Stark, J.L., Wood, C.A. and Carr, M.H., 1981. Distribution and morphology of basalt deposits on planets. In: B.V.S. Project (Editor), *Basaltic Volcanism on the Terrestrial Planets*. Pergamon Press, New York, pp. 701-800.
- [231] Head, J.W. and Wilson, L., 1989. Basaltic pyroclastic eruptions: Influence of gas-release patterns and volume fluxes on fountain structure, and the formation of cinder cones, spatter cones, rootless flows, lava ponds and lava flows. *Journal of Volcanology and Geothermal Research*, 37(3-4): 261-271.
- [232] Heming, R.F., 1980a. The Ngatatura diatreme. *New Zealand Journal of Geology and Geophysics*, 23(5-6): 569-573.
- [233] Heming, R.F., 1980b. Patterns of Quaternary basaltic volcanism in the northern North Island, New Zealand. *New Zealand Journal of Geology and Geophysics*, 23(3): 335-344.
- [234] Hengl, T., 2006. Finding the right pixel size. *Computers & Geosciences*, 32: 1283-1298.
- [235] Hengl, T. and Evans, I.S., 2008. Mathematical and Digital Models of the Land Surface. In: T. Hengl and H. Reuter (Editors), *Geomorphometry: Concepts, Software, Applications*. Elsevier B.V., pp. 31-63.
- [236] Hengl, T., Maathuis, B.H.P. and Wang, L., 2008. Geomorphometry in ILWIS. In: T. Hengl and H. Reuter (Editors), *Geomorphometry: Concepts, Software, Applications*. Elsevier B.V., pp. 309-331.

- [237] Herault, A., Vicari, A., Cirauda, A. and Del Negro, C., 2009. Forecasting lava flow hazard during the 2006 Etna eruption: Using the Magflow cellular automata model. *Computer & Geosciences*, 35(5): 1050-1060.
- [238] Hidaka, M., Goto, A., Susumu, U. and Fujita, E., 2005. VTFS project: Development of the lava flow simulation code LavaSIM with a model for three-dimensional convection, spreading, and solidification. *Geochemistry Geophysics Geosystems*, 6(7): Q07008.
- [239] Hill, B.E., Connor, C.B., Jarzempa, M.S., La Femina, P.C., Navarro, M. and Strauch, W., 1998. 1995 eruptions of Cerro Negro volcano, Nicaragua, and risk assessment for future eruptions. *Geological Society of America Bulletin*, 110(10): 1231-241.
- [240] Hintz, A.R. and Valentine, G.A., 2012. Complex plumbing of monogenetic scoria cones: New insights from the Lunar Crater Volcanic Field (Nevada, USA). *Journal of Volcanology and Geothermal Research*, 239–240: 19-32.
- [241] Hirano, A., Welch, R. and Lang, H., 2003. Mapping from ASTER stereo image data: DEM validation and accuracy assessment. *ISPRS Journal of Photogrammetry and Remote Sensing*, 57: 356-370.
- [242] Hirt, C., Filmer, M.S. and Featherstone, W.E., 2010. Comparison and validation of the recent freely available ASTER-GDEM ver1, SRTM ver4.1 and GEODATA DEM-9S ver3 digital elevation models over Australia. *Australian Journal of Earth Sciences*, 57(3): 337-347.
- [243] Hodgson, M.E. and Bresnahan, P., 2004. Accuracy of Airborne Lidar-Derived Elevation: Empirical Assessment and Error Budget. *Photogrammetric Engineering and Remote Sensing*, 70(3): 331-339.
- [244] Hofton, M., Dubayah, R., Blair, J.B. and Rabine, D., 2006. Validation of SRTM Elevations Over Vegetated and Non-vegetated Terrain Using Medium-Footprint Lidar. *Photogrammetric Engineering and Remote Sensing*, 72(3): 279-285.
- [245] Horrocks, M., Augustinus, P., Deng, Y., Shane, P. and Andersson, S., 2005. Holocene vegetation, environment, and tephra recorded from Lake Pupuke, Auckland, New Zealand. *New Zealand Journal of Geology and Geophysics*, 48: 85-94.
- [246] Horspool, N.A., Savage, M.K. and Bannister, S., 2006. Implications for intraplate volcanism and back-arc deformation in northwestern New Zealand, from joint inversion of receiver functions and surface waves. *Geophysical Journal International*, 166: 1466-1483.
- [247] Houghton, B.F., Bonadonna, C., Gregg, C.E., Johnston, D.M., Cousins, W.J., Cole, J.W. and Del Carlo, P., 2006. Proximal tephra hazards: Recent eruption studies applied to volcanic risk in the Auckland volcanic field, New Zealand. *Journal of Volcanology and Geothermal Research*, 155(1-2): 138-149.
- [248] Houghton, B.F. and Wilson, C.J.N., 1989. A vesicularity index for pyroclastic deposits. *Bulletin of Volcanology*, 51(6): 451-462.
- [249] Houghton, B.F., Wilson, C.J.N., Rosenberg, M.D., Smith, I.E.M. and Parker, R.J., 1996. Mixed deposits of complex magmatic and phreatomagmatic volcanism: an example from Crater Hill, Auckland, New Zealand. *Bulletin of Volcanology*, 58: 59-66.
- [250] Houghton, B.F., Wilson, C.J.N. and Smith, I.E.M., 1999. Shallow-seated controls on styles of explosive basaltic volcanism: a case study from New Zealand. *Journal of Volcanology and Geothermal Research*, 91: 97-120.

- [251] Houghton, B.F., Wilson, C.J.N., Smith, I.E.M. and Parker, R.J., 1991. A mixed deposit of simultaneously erupting fissure vents: Crater Hill, Auckland, New Zealand. *New Zealand Geological Survey Record*, 43: 45-50.
- [252] Huang, Y., Hawkesworth, C., Smith, I., van Calsteren, P. and Black, P., 2000. Geochemistry of late Cenozoic basaltic volcanism in Northland and Coromandel, New Zealand: implications for mantle enrichment processes. *Chemical Geology*, 164: 219-238.
- [253] Huang, Y., Hawkesworth, C., van Calsteren, P., Smith, I. and Black, P., 1997. Melt generation models for the Auckland volcanic field, New Zealand: constraints from U-Th isotopes. *Earth and Planetary Science Letters*, 149(1-4): 67-84.
- [254] Hulme, G., 1974. The Interpretation of Lava Flow Morphology. *Geophysical Journal of the Royal Astronomical Society*, 39(2): 361-383.
- [255] Hutton, C. and Brazier, R., 2012. Quantifying riparian zone structure from airborne LiDAR: Vegetation filtering, anisotropic interpolation, and uncertainty propagation. *Journal of Hydrology*, 442-443: 36-45.
- [256] ILWIS, 2001. ILWIS 3.0 Academic - User's Guide. Unit Geo Software Development, Sector Remote Sensing & GIS, IT Department, International Institute for Aerospace Survey and Earth Sciences (ITC), Enschede, The Netherlands, pp. 1-520.
- [257] Irwin, M., 2009. Synthesis of existing structural data for the Auckland Volcanic Field. IESE Report 1-2009.01. Institute of Earth Science and Engineering, Auckland, New Zealand, pp. 1-213.
- [258] Isaac, M.J., Herzer, R.J., Brook, F.J. and Hayward, B.W., 1994. Cretaceous and Cenozoic sedimentary basins of Northland, New Zealand. Institute of Geological and Nuclear Sciences monograph 8. GNS, Gracefield Research Center, Lower Hutt, New Zealand, pp. 137-149.
- [259] Ishihara, K., Iguchi, M. and Kamo, K., 1990. Numerical Simulation of Lava Flows on Some Volcanoes in Japan. In: J.H. Fink (Editor), *Lava Flows and Domes*. IAVCEI Proceedings in Volcanology. Springer Berlin Heidelberg, pp. 174-207.
- [260] Jankovics, M.É., Dobosi, G., Embey-Isztin, A., Kiss, B., Sági, T., Harangi, S. and Ntaflos, T., 2013. Origin and ascent history of unusually crystal-rich alkaline basaltic magmas from the western Pannonian Basin. *Bulletin of Volcanology*, 75(9): 1-23.
- [261] Jankovics, M.É., Harangi, S., Kiss, B. and Ntaflos, T., 2012. Open-system evolution of the Fűzes-tó alkaline basaltic magma, western Pannonian Basin: Constraints from mineral textures and compositions. *Lithos*, 140-141: 25-37.
- [262] Jenson, S.K. and Domingue, J.O., 1988. Extracting topographic structure from digital elevation data for geographic information system analysis. *Photogrammetric Engineering and Remote Sensing*, 54(11): 1593-1600.
- [263] Johnston, D.M., Nairn, I.A., Thordarson, T. and Daly, M., 1997. Volcanic Impact Assessment for the Auckland Volcanic Field. Auckland Regional Council Technical Publication, 79, pp. 1-208.
- [264] Jones, K.H., 1998. A comparison of algorithms used to compute hill slope as a property of the DEM. *Computers & Geosciences*, 24(4): 315-323.
- [265] Jordan, G., 2003. Morphometric analysis and tectonic interpretation of digital terrain data: a case study. *Earth Surface Processes and Landforms*, 28(8): 807-822.

- [266] Jordan, G., 2007a. Adaptive smoothing of valleys in DEMs using TIN interpolation from ridgeline elevations: An application to morphotectonic aspect analysis. *Computers & Geosciences*, 33(4): 573-585.
- [267] Jordan, G., 2007b. Digital Terrain Analysis in a GIS Environment. Concepts and Development. In: R. Peckham and G. Jordan (Editors), *Digital Terrain Modelling. Lecture Notes in Geoinformation and Cartography*. Springer Berlin-Heidelberg, Germany, pp. 1-43.
- [268] Jordan, G., Meijninger, B.M.L., van Hinsbergen, D.J.J., Meulenkamp, J.E. and van Dijk, P.M., 2005. Extraction of morphotectonic features from DEMs : Development and applications for study areas in Hungary and NW Greece. *International Journal of Applied Earth Observation and Geoinformation*, 7(3): 163-182.
- [269] Jordan, G. and Schott, B., 2005. Application of wavelet analysis to the study of spatial pattern of morphotectonic lineaments in digital terrain models. A case study. *Remote Sensing of Environment*, 93: 31-38.
- [270] Joyce, K.E., Samsonov, S., Manville, V., Jongens, R., Graettinger, A. and Cronin, S.J., 2009. Remote sensing data types and techniques for lahar path detection: A case study at Mt Ruapehu, New Zealand. *Remote Sensing of Environment*, 113: 1778-1786.
- [271] Jurado-Chichay, Z., Rowland, S.K. and Walker, G.P.L., 1996. The formation of circular littoral cone from tube-fed pahoehoe: Mauna Loa, Hawaii. *Bulletin of Volcanology*, 57(7): 471-482.
- [272] Karakhanian, A., Jrbashyan, R., Trifonov, V., Philip, H., Arakelian, S., Avagyan, A., Baghdassaryan, H., Davtian, V. and Ghoukassyan, Y., 2003. Volcanic hazards in the region of the Armenian Nuclear Power Plant. *Journal of Volcanology and Geothermal Research*, 126(1-2): 31-62.
- [273] Karátson, D., Telbisz, T. and Wörner, G., 2012. Erosion rates and erosion patterns of Neogene to Quaternary stratovolcanoes in the Western Cordillera of the Central Andes: An SRTM DEM based analysis. *Geomorphology*, 139-140: 122-135.
- [274] Katz, R.F., Spiegelman, M. and Holtzman, B., 2006. The dynamics of melt and shear localization in partially molten aggregates. *Nature*, 442: 676-679.
- [275] Kauahikaua, J., Margriter, S., Lockwood, J. and Trusdell, F., 1995a. Applications of GIS to the Estimation of Lava Flow Hazards on Mauna Loa Volcano, Hawai'i. In: J.M. Rhodes and J.P. Lockwood (Editors), *Mauna Loa Revealed: Structure, Composition, History, and Hazards*. American Geophysical Union, pp. 315-325.
- [276] Kauahikaua, J., Margriter, S. and Moore, R., 1995b. GIS-Aided Volcanic Activity Hazard Analysis for the Hawaii Geothermal Project Environmental Impact Statement. In: A. Carrara and F. Guzzetti (Editors), *Geographical Information Systems in Assessing Natural Hazards. Advances in Natural and Technological Hazards Research*. Springer Netherlands, pp. 235-257.
- [277] Kear, D. and Schofield, J.C., 1959. Te Kuiti group. *New Zealand Journal of Geology and Geophysics*, 2(4): 685-717.
- [278] Kear, D. and Thompson, B.N., 1964. Volcanic risk in Northland. *New Zealand Journal of Geology and Geophysics*, 7(1): 87-93.
- [279] Keating, G.N., Valentine, G.A., Krier, D.J. and Perry, F.V., 2008. Shallow plumbing systems for small-volume basaltic volcanoes. *Bulletin of Volcanology*, 70: 563-582.

- [280] Kenny, F., Matthews, B. and Todd, K., 2008. Routing overland flow through sinks and flats in interpolated raster terrain surfaces. *Computers & Geosciences*, 34(11): 1417-1430.
- [281] Kenny, J.A., Lindsay, J. and Howe, T.M., 2011. Large-Scale Faulting in the Auckland Region. IESE Report 1-2011.04, University of Auckland, New Zealand: 1-98.
- [282] Kenny, J.A., Lindsay, J.M. and Howe, T.M., 2012. Post-Miocene faults in Auckland: insights from borehole and topographic analysis. *New Zealand Journal of Geology and Geophysics*, 55(4): 323-343.
- [283] Kereszturi, G., Csillag, G., Németh, K., Sebe, K., Balogh, K. and Jáger, V., 2010. Volcanic architecture, eruption mechanism and landform evolution of a Pliocene intracontinental basaltic polycyclic monogenetic volcano from the Bakony-Balaton Highland Volcanic Field, Hungary. *Central European Journal of Geosciences*, 2(3): 362-384.
- [284] Kereszturi, G., Geyer, A., Martí, J., Németh, K. and Dóniz-Páez, F.J., 2013a. Evaluation of morphometry-based dating of monogenetic volcanoes—a case study from Bandas del Sur, Tenerife (Canary Islands). *Bulletin of Volcanology*, 75(7): 1-19.
- [285] Kereszturi, G., Jordan, G., Németh, K. and Dóniz-Páez, J.F., 2012a. Syn-eruptive morphometric variability of monogenetic scoria cones. *Bulletin of Volcanology*, 74(9): 2171-2185.
- [286] Kereszturi, G. and Németh, K., 2011. Shallow-seated controls on the evolution of the Upper Pliocene Kopasz-hegy nested monogenetic volcanic chain in the Western Pannonian Basin, Hungary. *Geologica Carpathica*, 62(6): 535-546.
- [287] Kereszturi, G. and Németh, K., 2012a. Monogenetic basaltic volcanoes: genetic classification, growth, geomorphology and degradation. In: K. Németh (Editor), *Updates in Volcanology - New Advances in Understanding Volcanic Systems*, ISBN: 978-953-51-0915-0. InTech, pp. 3-88, DOI: 10.5772/51387.
- [288] Kereszturi, G. and Németh, K., 2012b. Structural and morphometric irregularities of eroded Pliocene scoria cones at the Bakony–Balaton Highland Volcanic Field, Hungary. *Geomorphology*, 136(1): 45-58.
- [289] Kereszturi, G., Németh, K., Cronin, J.S., Agustin-Flores, J., Smith, I.E.M. and Lindsay, J., 2013b. A model for calculating eruptive volumes for monogenetic volcanoes – Implication for the Quaternary Auckland Volcanic Field, New Zealand. *Journal of Volcanology and Geothermal Research*, 266: 16-33.
- [290] Kereszturi, G., Németh, K., Csillag, G., Balogh, K. and Kovács, J., 2011. The role of external environmental factors in changing eruption styles of monogenetic volcanoes in a Mio/Pleistocene continental volcanic field in western Hungary. *Journal of Volcanology and Geothermal Research*, 201(1-4): 227-240.
- [291] Kereszturi, G., Procter, J., Cronin, J.S., Németh, K., Bebbington, M. and Lindsay, J., 2012b. LiDAR-based quantification of lava flow susceptibility in the City of Auckland (New Zealand). *Remote Sensing of Environment*, 125: 198-213.
- [292] Kermodé, L., 1992. Geology of the Auckland urban area. Scale 1 : 50,000. Institute of Geological and Nuclear Sciences geological maps 2. Institute of Geological and Nuclear Sciences, Lower Hutt, New Zealand, pp. 1-63.
- [293] Kervyn, M., Ernst, G.G.J., Goossens, R. and Jacobs, P., 2008. Mapping volcano topography with remote sensing: ASTER vs. SRTM. *International Journal of Remote Sensing*, 29(22): 6515-6538.

- [294] Kilburn, C.R.J., 2000. Lava Flows and Flow Fields. In: H. Sigurdsson, B.F. Houghton, S.R. McNutt, H. Rymer and J. Stix (Editors), *Encyclopedia of Volcanoes*. Academic Press, San Diego, California, pp. 291-305.
- [295] Kiyosugi, K., Connor, C.B., Wetmore, P.H., Ferwerda, B.P., Germa, A.M., Connor, L.J. and Hintz, A.R., 2012. Relationship between dike and volcanic conduit distribution in a highly eroded monogenetic volcanic field: San Rafael, Utah, USA. *Geology*, 40(8): 695-698.
- [296] Kiyosugi, K., Connor, C.B., Zhao, D., Connor, L.J. and Tanaka, K., 2010. Relationships between volcano distribution, crustal structure, and P-wave tomography: an example from the Abu Monogenetic Volcano Group, SW Japan. *Bulletin of Volcanology*, 72(3): 331-340.
- [297] Kiyosugi, K., Horikawa, Y., Nagao, T., Itaya, T., Connor, C. and Tanaka, K., 2013. Scoria cone formation through a violent Strombolian eruption: Irao Volcano, SW Japan. *Bulletin of Volcanology*, 76(1): 1-14.
- [298] Kokelaar, B.P., 1983. The mechanism of Surtseyan volcanism. *Journal of the Geological Society*, 140: 939-944.
- [299] Kon Joon, B., Schwartz, F.W. and Braun, A., 2007. Verification of the Vertical Error in C-Band SRTM DEM Using ICESat and Landsat-7, Otter Tail County, MN. *IEEE Transactions on Geoscience and Remote Sensing*, 45(1): 36-44.
- [300] Konecny, V., Kovac, M., Lexa, J. and Sefara, J., 2002. Neogene evolution of the Carpatho-Pannonian region: an interplay of subduction and back-arc diapiric uprising in the mantle. *EGU Stephan Mueller Special Publication Series 1*: 105-123.
- [301] Kuntz, M.A., Champion, D.E., Spiker, E.C. and Lefebvre, R.H., 1986. Contrasting magma types and steady-state, volume-predictable, basaltic volcanism along the Great Rift, Idaho. *Geological Society of America Bulletin*, 97(5): 579-594.
- [302] Latimer, C., Samsonov, S., Tiampo, K. and Manville, V., 2010. Inverting for source parameters using a genetic algorithm applied to deformation signals observed at the Auckland Volcanic Field. *Canadian Journal of Remote Sensing*, 36(S2): S266-S273.
- [303] Le Corvec, N., Bebbington, M.S., Lindsay, J.M. and McGee, L.E., 2013a. Age, distance and geochemical evolution within a monogenetic volcanic field: Analyzing patterns in the Auckland volcanic field eruption sequence. *Geochemistry, Geophysics, Geosystems*, 14(9): 3648-3665.
- [304] Le Corvec, N., Menand, T. and Lindsay, J., 2013b. Interaction of ascending magma with pre-existing crustal fractures in monogenetic basaltic volcanism: an experimental approach. *Journal of Geophysical Research: Solid Earth*, 118(3): 968-984.
- [305] Le Corvec, N., Spörli, K.B., Rowland, J. and Lindsay, J., 2013c. Spatial distribution and alignments of volcanic centers: Clues to the formation of monogenetic volcanic fields? *Earth-Science Reviews*, 124: 96-114.
- [306] Lefebvre, N.S., White, J.D.L. and Kjarsgaard, B.A., 2012. Spatter-dike reveals subterranean magma diversions: Consequences for small multivalent basaltic eruptions. *Geology*, 40(5): 423-426.
- [307] Lefebvre, N.S., White, J.D.L. and Kjarsgaard, B.A., 2013. Unbedded diatreme deposits reveal maar-diatreme-forming eruptive processes: Standing Rocks West, Hopi Buttes, Navajo Nation, USA. *Bulletin of Volcanology*, 75(8): 1-17.
- [308] Li, Z., Zhu, Q. and Gold, C., 2005. *Digital Terrain Modeling: Principles and Methodology*. CRC Press, Boca Raton, Florida, pp. 1-318.

- [309] Lindsay, J., Marzocchi, W., Jolly, G., Constantinescu, R., Selva, J. and Sandri, L., 2010. Towards real-time eruption forecasting in the Auckland Volcanic Field: application of BET\_EF during the New Zealand National Disaster Exercise 'Ruamoko'. *Bulletin of Volcanology*, 72(2): 185-204.
- [310] Lindsay, J.M., Leonard, G.S., Smid, E.R. and Hayward, B.W., 2011. Age of the Auckland Volcanic Field: a review of existing data. *New Zealand Journal of Geology and Geophysics*, 54(4): 379-401.
- [311] LINZ, 2010. Manukau Harbour – NZTopo50 - BB31 (1:50,000). Land Information New Zealand.
- [312] LINZ, 2012a. Auckland – NZTopo50 - BA32 (1:50,000). Land Information New Zealand.
- [313] LINZ, 2012b. Papatoetoe – NZTopo50 - BB32 (1:50,000). Land Information New Zealand.
- [314] LINZ, 2012c. Waitemata Harbour – NZTopo50 - BA31 (1:50,000). Land Information New Zealand.
- [315] Lister, J.R. and Kerr, R.C., 1991. Fluid-Mechanical Models of Crack Propagation and Their Application to Magma Transport in Dykes. *Journal of Geophysical Research: Solid Earth* 96(B6): 10049-10077.
- [316] Liu, X., 2008. Airborne LiDAR for DEM generation: some critical issues. *Progress in Physical Geography*, 32(1): 31-49.
- [317] Lombardo, V. and Buongiorno, M.F., 2006. Lava flow thermal analysis using three infrared bands of remote-sensing imagery: A study case from Mount Etna 2001 eruption. *Remote Sensing of Environment*, 101: 141-149.
- [318] Lombardo, V., Harris, A.J.L., Calvari, S. and Buongiorno, M.F., 2009. Spatial variations in lava flow field thermal structure and effusion rate derived from very high spatial resolution hyperspectral (MIVIS) data. *Journal of Geophysical Research: Solid Earth*, 114(B02208): DOI: 10.1029/2008jb005648.
- [319] Lorenz, V., 1986. On the growth of maar and diatremes and its relevance to the formation of tuff rings. *Bulletin of Volcanology*, 48(5): 265-274.
- [320] Lorenz, V., 2003. Maar-Diatreme Volcanoes, their Formation, and their Setting in Hard-rock or Soft-rock environments. *Geolines*, 15: 72-83.
- [321] Lorenz, V., 2007. Syn- and posteruptive hazards of maar–diatreme volcanoes. *Journal of Volcanology and Geothermal Research*, 159: 285-312.
- [322] Lorenz, V. and Kurszlaukis, S., 2007. Root zone processes in the phreatomagmatic pipe emplacement model and consequences for the evolution of maar–diatreme volcanoes. *Journal of Volcanology and Geothermal Research*, 159: 4-32.
- [323] Lowry, A.R., Hamburger, M.W., Meertens, C.M. and Ramos, E.G., 2001. GPS monitoring of crustal deformation at Taal Volcano, Philippines. *Journal of Volcanology and Geothermal Research*, 105(1–2): 35-47.
- [324] Luhr, J.F. and Simkin, T., 1993. Parícutin: the volcano born in a Mexican cornfield. *Geoscience Press, U.S.*, pp. 1-427.
- [325] Lutz, T.M. and Gutmann, J.T., 1995. An improved method of determining alignments of point-like features and its implications for the Pinacate volcanic field, Mexico. *Journal of Geophysical Research: Solid Earth* 100(B9): 17659-17670.
- [326] Lynch, D.J., Musselman, T.E., Gutmann, J.T. and Patchett, P.J., 1993. Isotopic evidence for the origin of Cenozoic volcanic rocks in the Pinacate volcanic field, northwestern Mexico. *Lithos*, 29(3–4): 295-302.

- [327] Maas, H.-G. and Vosselman, G., 1999. Two algorithms for extracting building models from raw laser altimetry data. *ISPRS Journal of Photogrammetry and Remote Sensing*, 54: 153-163.
- [328] Maathuis, B.H.P. and Wang, L., 2006. Digital Elevation Model Based Hydro-processing. *Geocarto International*, 21(1): 21-26.
- [329] MacMillan, R.A. and Shary, P.A., 2008. Landforms and Landform Elements in Geomorphometry. In: T. Hengl and H. Reuter (Editors), *Geomorphometry: Concepts, Software, Applications*. Elsevier B.V., pp. 227-254.
- [330] Magill, C. and Blong, R., 2005a. Volcanic risk ranking for Auckland, New Zealand. I: Methodology and hazard investigation. *Bulletin of Volcanology*, 67(4): 331-339.
- [331] Magill, C. and Blong, R., 2005b. Volcanic risk ranking for Auckland, New Zealand. II: Hazard consequences and risk calculation. *Bulletin of Volcanology*, 67(4): 340-349.
- [332] Magill, C., Blong, R. and McAneney, J., 2005a. VolcaNZ—A volcanic loss model for Auckland, New Zealand. *Journal of Volcanology and Geothermal Research*, 149(3-4): 329-345.
- [333] Magill, C., McAneney, K. and Smith, I., 2005b. Probabilistic Assessment of Vent Locations for the Next Auckland Volcanic Field Event. *Mathematical Geology*, 37(3): 227-242.
- [334] Magill, C.R., Hurst, A.W., Hunter, L.J. and Blong, R.J., 2006. Probabilistic tephra fall simulation for the Auckland Region, New Zealand. *Journal of Volcanology and Geothermal Research*, 153: 370-386.
- [335] Malet, J.P., Maquaire, O. and Calais, E., 2002. The use of Global Positioning System techniques for the continuous monitoring of landslides: application to the Super-Sauze earthflow (Alpes-de-Haute-Provence, France). *Geomorphology*, 43: 33-54.
- [336] Mangan, M.T. and Cashman, K.V., 1996. The structure of basaltic scoria and reticulite and inferences for vesiculation, foam formation, and fragmentation in lava fountains. *Journal of Volcanology and Geothermal Research*, 73: 1-18.
- [337] Manville, V., Németh, K. and Kano, K., 2009. Source to sink: A review of three decades of progress in the understanding of volcanoclastic processes, deposits, and hazards. *Sedimentary Geology*, 220(3-4): 136-161.
- [338] Mark, D.M., 1984. Automatic Detection of Drainage Networks from Digital Elevation Models. *Cartographica*, 21(2-3): 168-178.
- [339] Marra, M.J., Alloway, B.V. and Newnham, R.M., 2006. Paleoenvironmental reconstruction of a well-preserved Stage 7 forest sequence catastrophically buried by basaltic eruptive deposits, northern New Zealand. *Quaternary Science Reviews*, 25: 2143-2161.
- [340] Marsella, M., Scifoni, S., Coltelli, M. and Proietti, C., 2011. Quantitative analysis of the 1981 and 2001 Etna flank eruptions: a contribution for future hazard evaluation and mitigation. *Annals of Geophysics*, 54(5): 492-498.
- [341] Martí, J., Planagumà, L., Geyer, A., Canal, E. and Pedrazzi, D., 2011. Complex interaction between Strombolian and phreatomagmatic eruptions in the Quaternary monogenetic volcanism of the Catalan Volcanic Zone (NE of Spain) *Journal of Volcanology and Geothermal Research*, 201(1-4): 178-193.
- [342] Martin, U. and Németh, K., 2004. Mio/Pliocene Phreatomagmatic Volcanism in the Western Pannonian Basin. *Geologica Hungarica Series Geologica*, 26, Budapest, Hungary, pp. 1-192.

- [343] Martin, U. and Németh, K., 2006. How Strombolian is a "Strombolian" scoria cone? Some irregularities in scoria cone architecture from the Transmexican Volcanic Belt, near Volcán Ceboruco (Mexico), and Al Haruj (Libya). *Journal of Volcanology and Geothermal Research*, 155(1-2): 104-118.
- [344] Martínez, J., Soria-Medina, A., Arias, P. and Buffara-Antunes, A.F., 2012. Automatic processing of Terrestrial Laser Scanning data of building facades. *Automation in Construction*, 22: 298-305.
- [345] Martz, L.W. and Garbrecht, J., 1992. Numerical definition of drainage networks and subcatchment areas from digital elevation models. *Computers & Geosciences*, 18: 747-761.
- [346] Martz, L.W. and Garbrecht, J., 1998. The Treatment of Flat Areas and Depressions in Automated Drainage Analysis of Raster Digital Elevation Models. *Hydrological Processes*, 12: 843-855.
- [347] Martz, L.W. and Garbrecht, J., 1999. An outlet breaching algorithm for the treatment of closed depressions in a raster DEM. *Computers & Geosciences*, 25(7): 835-844.
- [348] Marzocchi, W., Sandri, L. and Selva, J., 2008. BET\_EF: a probabilistic tool for long- and short-term eruption forecasting. *Bulletin of Volcanology*, 70(5): 623-632.
- [349] Marzocchi, W., Sandri, L. and Selva, J., 2010. BET\_VH: a probabilistic tool for long-term volcanic hazard assessment. *Bulletin of Volcanology*, 72(6): 705-716.
- [350] Mattox, T.N. and Mangan, M.T., 1997. Littoral hydrovolcanic explosions: a case study of lava-seawater interaction at Kilauea volcano. *Journal of Volcanology and Geothermal Research*, 75(1-2): 1-17.
- [351] Mazot, A., Smid, E., Schwendenmann, L., Delgado-Granados, H. and Lindsay, J., 2013. Soil CO<sub>2</sub> flux baseline in an urban monogenetic volcanic field: the Auckland Volcanic Field, New Zealand. *Bulletin of Volcanology*, 75(11): 1-9.
- [352] Mazzarini, F., 2004. Volcanic vent self-similar clustering and crustal thickness in the northern Main Ethiopian Rift. *Geophysical Research Letters*, 31(4): DOI: 10.1029/2003GL018574.
- [353] Mazzarini, F. and Armienti, P., 2001. Flank Cones at Mount Etna Volcano: Do they have a power-law distribution? *Bulletin of Volcanology*, 62(6-7): 420-430.
- [354] Mazzarini, F. and D'Orazio, M., 2003. Spatial distribution of cones and satellite-detected lineaments in the Pali Aike Volcanic Field (southernmost Patagonia): insights into the tectonic settings of a Neogene rift system. *Journal of Volcanology and Geothermal Research*, 125: 291-305.
- [355] Mazzarini, F., Favalli, M., Isola, I., Neri, M. and Pareschi, M.T., 2008. Surface roughness of pyroclastic deposits at Mt. Etna by 3D laser scanning. *Annals of Geophysics*, 51(5-6): 813-822.
- [356] Mazzarini, F., Pareschi, M.T., Favalli, M., Isola, I., Tarquini, S. and Boschi, E., 2005. Morphology of basaltic lava channels during the Mt. Etna September 2004 eruption from airborne laser altimeter data. *Geophysical Research Letters*, 32(4): DOI: 10.1029/2004GL021815.
- [357] Mazzarini, F., Pareschi, M.T., Favalli, M., Isola, I., Tarquini, S. and Boschi, E., 2007. Lava flow identification and aging by means of lidar intensity: Mount Etna case. *Journal of Geophysical Research: Solid Earth* 112(B02201): DOI: 10.1029/2005JB004166
- [358] McGee, L., Smith, I., Millet, M.-A., Handley, H. and Lindsay, J., 2013. Asthenospheric control of melting processes in a monogenetic basaltic system:

- A case study of the Auckland Volcanic Field, New Zealand. *Journal of Petrology*, 54(10): 2125-2153.
- [359] McGee, L.E., Beier, C., Smith, I.E.M. and Turner, S.P., 2011. Dynamics of melting beneath a small-scale basaltic system: a U-Th–Ra study from Rangitoto volcano, Auckland volcanic field, New Zealand. *Contributions to Mineralogy and Petrology*, 162(3): 547-563.
- [360] McGee, L.E., Millet, M.-A., Smith, I.E.M., Németh, K. and Lindsay, J.M., 2012. The inception and progression of melting in a monogenetic eruption: Motukorea Volcano, the Auckland Volcanic Field, New Zealand. *Lithos*, 155: 360-374.
- [361] Meng, X., Wang, L., Silván-Cárdenas, J.L. and Currit, N., 2009. A multi-directional ground filtering algorithm for airborne LIDAR. *ISPRS Journal of Photogrammetry and Remote Sensing*, 64(1): 117-124.
- [362] Milligan, J.A., 1977. A geophysical study of Rangitoto volcano. MSc thesis, University of Auckland, New Zealand, pp. 1-296.
- [363] Minár, J. and Evans, I.S., 2008. Elementary forms for land surface segmentation: The theoretical basis of terrain analysis and geomorphological mapping. *Geomorphology*, 95: 236-259.
- [364] Minár, J., Jenčo, M., Evans, I.S., Kadlec, M., Krcho, J., Pacina, J., Burian, L. and Benová, A., 2013. Third-order geomorphometric variables (derivatives): definition, computation and utilization of changes of curvatures. *International Journal of Geographical Information Science*, 27(7 ): 1381-1402.
- [365] Miyamoto, H. and Sasaki, S., 1997. Simulating lava flows by an improved cellular automata method. *Computers & Geosciences*, 23(3): 283-292.
- [366] Molloy, C., Shane, P. and Augustinus, P., 2009. Eruption recurrence rates in a basaltic volcanic field based on tephra layers in maar sediments: Implications for hazards in the Auckland volcanic field. *Geological Society of America Bulletin*, 121(11-12): 1666-1677.
- [367] Moore, I.D., Grayson, R.B. and Landson, A.R., 1991. Digital Terrain Modelling: A Review of Hydrological, Geomorphological, and Biological Applications. *Hydrological Processes*, 5(1): 3-30.
- [368] Morris, A.R., Anderson, F.S., Mouginiis-Mark, P.J., Haldemann, A.F.C., Brooks, B.A. and Foster, J., 2008. Roughness of Hawaiian volcanic terrains. *Journal of Geophysical Research: Planets*, 113(E12007): DOI: 10.1029/2008je003079.
- [369] Morris, D.G. and Heerdegen, R.G., 1988. Automatically Derived Catchment Boundary and Channel Networks and Their Hydrological Applications. *Geomorphology*, 1(2): 131-141.
- [370] Moufti, M.R., Moghazi, A.M. and Ali, K.A., 2012. Geochemistry and Sr–Nd–Pb isotopic composition of the Harrat Al-Madinah Volcanic Field, Saudi Arabia. *Gondwana Research*, 21(2–3): 670-689.
- [371] Mouginiis-Mark, P.J. and Garbeil, H., 2005. Quality of TOPSAR topographic data for volcanology studies at Kilauea Volcano, Hawaii: An assessment using airborne lidar data. *Remote Sensing of Environment*, 96(2): 149-164.
- [372] Mrlina, J., Kämpf, H., Kroner, C., Mingram, J., Stebich, M., Brauer, A., Geissler, W.H., Kallmeyer, J., Matthes, H. and Seidl, M., 2009. Discovery of the first Quaternary maar in the Bohemian Massif, Central Europe, based on combined geophysical and geological surveys. *Journal of Volcanology and Geothermal Research*, 182(1-2): 97-112.
- [373] Nakamura, K., 1977. Volcanoes as possible indicators of tectonic stress orientation—principal and proposal. *Journal of Volcanology and Geothermal Research*, 2(1): 1-16.

- [374] Needham, A.J., Lindsay, J.M., Smith, I.E.M., Augustinus, P. and Shane, P.A., 2011. Sequential Eruption of Alkaline and Sub-Alkaline Magmas from a small Monogenetic volcano in The Auckland Volcanic Field, New Zealand. *Journal of Volcanology and Geothermal Research*, 201(1-4): 126-142
- [375] Nelson, A., Reuter, H.I. and Gessler, P., 2008. DEM Production Methods and Sources. In: T. Hengl and H. Reuter (Editors), *Geomorphometry: Concepts, Software, Applications*. Elsevier B.V., pp. 65-85.
- [376] Nelson, C.S., 1978. Stratigraphy and paleontology of the Oligocene Te Kuiti Group, Waitomo County, South Auckland, New Zealand. *New Zealand Journal of Geology and Geophysics*, 21(5): 553-594.
- [377] Nelson, C.S. and Hume, T.M., 1987. Paleoenvironmental controls on mineral assemblages in a shelf sequence: Te Kuiti Group, South Auckland, New Zealand. *New Zealand Journal of Geology and Geophysics*, 30: 343-362.
- [378] Németh, K., 2004. The morphology and origin of wide craters at Al Haruj al Abyad, Libya: maars and phreatomagmatism in a large intracontinental flood lava field? *Zeitschrift für Geomorphologie*, 48(4): 417-439.
- [379] Németh, K., 2010. Monogenetic volcanic fields: Origin, sedimentary record, and relationship with polygenetic volcanism. *The Geological Society of America Special Paper*, 470: 43-66.
- [380] Németh, K., Cronin, S., Smith, I.M. and Agustin Flores, J., 2012. Amplified hazard of small-volume monogenetic eruptions due to environmental controls, Orakei Basin, Auckland Volcanic Field, New Zealand. *Bulletin of Volcanology*, 74(9): 2121-2137.
- [381] Németh, K., Cronin, S.J., Haller, M.J., Brenna, M. and Csillag, G., 2010. Modern analogues for Miocene to Pleistocene alkali basaltic phreatomagmatic fields in the Pannonian Basin: "soft-substrate" to "combined" aquifer controlled phreatomagmatism in intraplate volcanic fields. *Central European Journal of Geosciences* 2(3): 339-361.
- [382] Németh, K., Goth, K., Martin, U., Csillag, G. and Suhr, P., 2008. Reconstructing paleoenvironment, eruption mechanism and paleomorphology of the Pliocene Pula maar, (Hungary). *Journal of Volcanology and Geothermal Research*, 177(2): 441-456.
- [383] Németh, K., Martin, U. and Harangi, S., 2001. Miocene phreatomagmatic volcanism at Tihany (Pannonian Basin, Hungary). *Journal of Volcanology and Geothermal Research*, 111(1-4): 111-135.
- [384] Németh, K., Risso, C., Nullo, F. and Kereszturi, G., 2011. The role of collapsing and rafting of scoria cones on eruption style changes and final cone morphology: Los Morados scoria cone, Mendoza, Argentina. *Central European Journal of Geosciences*, 3(2): 102-118.
- [385] Németh, K., White, J.D.L., Reay, A. and Martin, U., 2003. Compositional variation during monogenetic volcano growth and its implication for magma supply to continental volcanic fields. *Journal of the Geological Society of London*, 160: 523-530.
- [386] Nitzsche, T., Rolf, C. and de Wall, H., 2006. Origin of magnetic anomalies in volcaniclastic units of the Messel maar-diatreme (Germany). *Zeitschrift der Deutschen Gesellschaft für Geowissenschaften*, 157(3): 373-385.
- [387] Nowak, J.F., 1995. Lava flow structures of a basalt volcano, Rangitoto Island, Auckland, New Zealand. MSc thesis, University of Auckland, New Zealand, pp. 1-224.

- [388] O'Neill, C. and Spiegelman, M., 2010. Formulations for Simulating the Multiscale Physics of Magma Ascent. In: A. Dosseto, S.P. Turner and J.A. van Orman (Editors), *Timescales of Magmatic Processes: From Core to Atmosphere*. John Wiley & Sons, Ltd., Chichester, United Kingdom pp. 87-101.
- [389] Oky Dicky Ardiansyah, P. and Yokoyama, R., 2002. DEM generation method from contour lines based on the steepest slope segment chain and a monotone interpolation function. *ISPRS Journal of Photogrammetry and Remote Sensing*, 57(1-2): 86-101.
- [390] Ort, M.H. and Carrasco-Núñez, G., 2009. Lateral vent migration during phreatomagmatic and magmatic eruptions at Tecuitlapa Maar, east-central Mexico. *Journal of Volcanology and Geothermal Research*, 181(1-2): 67-77.
- [391] Pardo, N., Cronin, S., Palmer, A., Procter, J. and Smith, I., 2012. Andesitic Plinian eruptions at Mt. Ruapehu: quantifying the uppermost limits of eruptive parameters. *Bulletin of Volcanology*, 74(5): 1161-1185.
- [392] Pardo, N., Macias, J.L., Giordano, G., Cianfarra, P., Avellán, D.R. and Bellatreccia, F., 2009. The ~1245 yr BP Asososca maar eruption: The youngest event along the Nejapa–Mirafleres volcanic fault, Western Managua, Nicaragua. *Journal of Volcanology and Geothermal Research*, 184(3-4): 292-312.
- [393] Pareschi, M.T., Cavarra, L., Favalli, M., Giannini, F. and Meriggi, A., 2000. GIS and Volcanic Risk Management. In: G.A. Papadopoulos, T. Murty, S. Venkatesh and R. Blong (Editors), *Natural Hazards*. Springer Netherlands, pp. 361-379.
- [394] Parfitt, E.A., 1998. A study of clast size distribution, ash deposition and fragmentation in a Hawaiian-style volcanic eruption *Journal of Volcanology and Geothermal Research*, 84: 197-208.
- [395] Parfitt, E.A., 2004. A discussion of the mechanisms of explosive basaltic eruptions. *Journal of Volcanology and Geothermal Research*, 134(1-2): 77-107.
- [396] Parfitt, E.A. and Wilson, L., 1995. Explosive volcanic eruptions - IX. The transition between Hawaiian-style lava fountaining and Strombolian explosive activity. *Geophysical Journal International*, 121(1): 226-232.
- [397] Parkinson, B.W. and Spilker, J.J. (Editors), 1996. *Global Positioning System: Theory & Applications*. Progress in Astronautics and Aeronautics Series, 163. The American Institute of Aeronautics and Astronautics, pp. 1-793.
- [398] Paton, D., Johnston, D., Gough, J., Dowrick, D., Manville, V., Batistich, T. and Baddon, L., 1999. Auckland Volcanic Risk Project: Stage 2. Technical Publication No. 126, Auckland Regional Council, pp. 1-99.
- [399] Payn, T.W., Hill, R.B., Höck, B.K., Skinner, M.F., Thorn, A.J. and Rijkse, W.C., 1999. Potential for the use of GIS and spatial analysis techniques as tools for monitoring changes in forest productivity and nutrition, a New Zealand example. *Forest Ecology and Management*, 122(1-2): 187-196.
- [400] Pedrazzi, D., Bolós, X. and Martí, J., 2014. Phreatomagmatic volcanism in complex hydrogeological environments: La Crosa de Sant Dalmai maar (Catalan Volcanic Zone, NE Spain). *Geosphere*: DOI: 10.1130/ges00959.1.
- [401] Perugini, D., Speziali, A., Caricchi, L. and Kueppers, U., 2011. Application of fractal fragmentation theory to natural pyroclastic deposits: Insights into volcanic explosivity of the Valentano scoria cone (Italy). *Journal of Volcanology and Geothermal Research*, 202(3-4): 200-210.
- [402] Peslier, A.H. and Luhr, J.F., 2006. Hydrogen loss from olivines in mantle xenoliths from Simcoe (USA) and Mexico: Mafic alkalic magma ascent rates and water budget of the sub-continental lithosphere. *Earth and Planetary Science Letters*, 242(3-4): 302-319.

- [403] Pieri, D. and Abrams, M., 2005. ASTER observations of thermal anomalies preceding the April 2003 eruption of Chikurachki volcano, Kurile Islands, Russia. *Remote Sensing of Environment*, 99: 84-94.
- [404] Pinkerton, H., 1987. Factors affecting the morphology of lava flows. *Endeavour*, 11(2): 73-79.
- [405] Pinkerton, H. and Norton, G., 1995. Rheological properties of basaltic lavas at sub-liquidus temperatures: laboratory and field measurements on lavas from Mount Etna. *Journal of Volcanology and Geothermal Research*, 68(4): 307-323.
- [406] Pinkerton, H. and Stevenson, R.J., 1992. Methods of determining the rheological properties of magmas at sub-liquidus temperatures. *Journal of Volcanology and Geothermal Research*, 53(1-4): 47-66.
- [407] Pioli, L., Azzopardi, B.J. and Cashman, K.V., 2009. Controls on the explosivity of scoria cone eruptions: Magma segregation at conduit junctions. *Journal of Volcanology and Geothermal Research*, 186(3-4): 407-415.
- [408] Pioli, L., Erlund, E., Johnson, E., Cashman, N., K., , Wallace, P., Rosi, M. and Delgado Granados, H., 2008. Explosive dynamics of violent Strombolian eruptions: The eruption of Parícutin Volcano 1943–1952 (Mexico). *Earth and Planetary Science Letters*, 271(1-4): 359-368.
- [409] Planchon, O. and Darboux, F., 2002. A fast, simple and versatile algorithm to fill the depressions of digital elevation models. *Catena*, 46(2-3): 159-176.
- [410] Pollyea, R.M. and Fairley, J.P., 2012. Experimental evaluation of terrestrial LiDAR-based surface roughness estimates. *Geosphere*, 8(1): 1-7.
- [411] Praharaj, T., Swain, S.P., Powell, M.A., Hart, B.R. and Tripathy, S., 2002. Delineation of groundwater contamination around an ash pond: Geochemical and GIS approach. *Environment International*, 27(8): 631-638.
- [412] Prewitt, J., 1970. Object Enhancement and Extraction. In: Lipkin, B.S. and A. Rosenfeld (Editors), *Picture processing and Psychopictorics*. Academic Press, Orlando, USA pp. 75-149.
- [413] Procter, J., Cronin, S.J., Fuller, I.C., Lube, G. and Manville, V., 2010. Quantifying the geomorphic impacts of a lake-breakout lahar, Mount Ruapehu, New Zealand. *Geology*, 38(1): 67-70.
- [414] Proietti, C., Coltelli, M., Marsella, M. and Fujita, E., 2009. A quantitative approach for evaluating lava flow simulation reliability: LavaSIM code applied to the 2001 Etna eruption. *Geochemistry, Geophysics, Geosystems*, 10(9): Q09003.
- [415] Raaflaub, L.D. and Collins, M.J., 2006. The effect of error in gridded digital elevation models on the estimation of topographic parameters. *Environmental Modelling & Software*, 21: 710-732.
- [416] Rabus, B., Eineder, M., Roth, A. and Bamler, R., 2003. The shuttle radar topography mission—a new class of digital elevation models acquired by spaceborne radar. *ISPRS Journal of Photogrammetry and Remote Sensing*, 57: 241-262.
- [417] Rafferty, W.J. and Heming, R.F., 1979. Quaternary alkalic and sub-alkalic volcanism in South Auckland, New Zealand. *Contributions to Mineralogy and Petrology*, 71: 139-150.
- [418] Rapprich, V., Cajz, V., Kostak, M., Pécskay, Z., Ridkosil, T., Raska, P. and Radon, M., 2007. Reconstruction of eroded monogenetic Strombolian cones of Miocene age: A case study on character of volcanic activity of the Jicin Volcanic Field (NE Bohemia) and subsequent erosional rates estimation. *Journal of Geosciences*, 52(3-4): 169-180.

- [419] Raza, A., Brown, R.W., Ballance, P.F., Hill, K.C. and Kamp, P.J.J., 1999. Thermal history of the early Miocene Waitemata Basin and adjacent Waipapa Group, North Island, New Zealand. *New Zealand Journal of Geology and Geophysics*, 42: 169-188.
- [420] Renschler, C.S., 2005. Scales and uncertainties in using models and GIS for volcano hazard prediction. *Journal of Volcanology and Geothermal Research*, 139(1-2): 73-87.
- [421] Reuter, H.I., Hengl, T., Gessler, R. and Soille, P., 2008. Preparation of DEMs for Geomorphometric Analysis. In: T. Hengl and H. Reuter (Editors), *Geomorphometry: Concepts, Software, Applications*. Elsevier B.V., pp. 87-120.
- [422] Reuter, H.I., Nelson, A. and Jarvis, A., 2007. An evaluation of void filling interpolation methods for SRTM data. *International Journal of Geographical Information Science*, 21(9): 983-1008.
- [423] Ricketts, B.D., Ballance, P.F., Hayward, B.W. and Mayer, W., 1989. Basal Waitemata Group lithofacies: rapid subsidence in an early Miocene interarc basin, New Zealand. *Sedimentology*, 36: 559-580.
- [424] Riedel, C., Ernst, G.G.J. and Riley, M., 2003. Controls on the growth and geometry of pyroclastic constructs. *Journal of Volcanology and Geothermal Research*, 127(1-2): 121-152.
- [425] Risso, C., Németh, K., Combina, A.M., Nullo, F. and Drosina, M., 2008. The role of phreatomagmatism in a Plio-Pleistocene high-density scoria cone field: Llanquahué Volcanic Field, Argentina. *Journal of Volcanology and Geothermal Research*, 168: 61-86.
- [426] Robinson, G.J., 1994. The accuracy of digital elevation models derived from digitized contour data. *Photogrammetric Record*, 14: 805-814.
- [427] Robinson, J.E. and Eakins, B.W., 2006. Calculated volumes of individual shield volcanoes at the young end of the Hawaiian Ridge. *Journal of Volcanology and Geothermal Research*, 151(1-3): 309-317.
- [428] Rodríguez-González, A., Fernández-Turiel, J.L., Pérez-Torrado, F.J., Aulinas, M., Carracedo, J.C., Gimeno, D., Guillou, H. and Paris, R., 2011. GIS methods applied to the degradation of monogenetic volcanic fields: A case study of the Holocene volcanism of Gran Canaria (Canary Islands, Spain). *Geomorphology*, 134(3-4): 249-259.
- [429] Rodríguez-González, A., Fernández-Turiel, J.L., Pérez-Torrado, F.J., Gimeno, D. and Aulinas, M., 2009a. Geomorphological reconstruction and morphometric modelling applied to past volcanism. *International Journal of Earth Sciences*, 99(3): 645-660.
- [430] Rodríguez-González, A., Fernández-Turiel, J.L., Pérez-Torrado, F.J., Hansen, A., Aulinas, M., Carracedo, J.C., Gimeno, D., Guillou, H., Paris, R. and Paterne, M., 2009b. The Holocene volcanic history of Gran Canaria island: implications for volcanic hazards. *Journal of Quaternary Science*, 24(7): 697-709.
- [431] Rodríguez, E., Morris, C.S., Belz, J.E., Chapin, E.C., Martin, J.M., Daffer, W. and Hensley, S., 2005. An Assessment of the SRTM Topographic Products. Technical Report Jet Propulsion Laboratory D-31639, Pasadena, California, pp. 1-143.
- [432] Rongo, R., Spataro, W., D'Ambrosio, D., Vittoria Avolio, M., Trunfio, G.A. and Di Gregorio, S., 2008. Lava Flow Hazard Evaluation Through Cellular Automata and Genetic Algorithms: an Application to Mt Etna Volcano. *Fundamenta Informaticae*, 87(2): 247-267.

- [433] Rosenberg, M.D., 1991. The nature and mechanisms of phreatomagmatic volcanism in the South Auckland volcanic field. MSc thesis, University of Waikato, pp. 1-464.
- [434] Ross, P.-S., Delpit, S., Haller, M.J., Németh, K. and Corbella, H., 2011. Influence of the substrate on maar-diatreme volcanoes – an example of a mixed setting from the Pali Aike volcanic field, Argentina. *Journal of Volcanology and Geothermal Research*, 201(1-4): 253-271
- [435] Ross, P.-S. and White, J.D.L., 2012. Quantification of vesicle characteristics in some diatreme-filling deposits, and the explosivity levels of magma–water interactions within diatremes. *Journal of Volcanology and Geothermal Research*, 245–246: 55-67.
- [436] Ross, P.S., White, J.D.L., Valentine, G.A., Taddeucci, J., Sonder, I. and Andrews, R.G., 2013. Experimental birth of a maar–diatreme volcano. *Journal of Volcanology and Geothermal Research*, 260: 1-12.
- [437] Rossi, M.J., 1997. Morphology of the 1984 open-channel lava flow at Krafla volcano, northern Iceland. *Geomorphology*, 20(1-2): 95-112.
- [438] Rossi, M.J. and Gudmundsson, A., 1996. The morphology and formation of flow-lobe tumuli on Icelandic shield volcanoes. *Journal of Volcanology and Geothermal Research*, 72(3-4): 291-308.
- [439] Rout, D.J., Cassidy, J., Locke, C.A. and Smith, I.E.M., 1993. Geophysical evidence for temporal and structural relationships within the monogenetic basalt volcanoes of the Auckland volcanic field, northern New Zealand. *Journal of Volcanology and Geothermal Research*, 57(1-2): 71-83.
- [440] Rowland, S., Garbeil, H. and Harris, A., 2005. Lengths and hazards from channel-fed lava flows on Mauna Loa, Hawai'i, determined from thermal and downslope modeling with FLOWGO. *Bulletin of Volcanology*, 67: 634-647.
- [441] Rowland, S.K., Jurado-Chichay, Z. and Ernst, G.J., 2009. Pyroclastic deposits and lava flows from the 1759–1774 eruption of El Jorullo, México: Aspects of “violent strombolian” activity and comparison with Parícutin. In: A. Hoskuldsson, T. Thordarson, G. Larsen, S. Self and S. Rowland (Editors), *The Legacy of George P.L. Walker*, Special Publications of IAVCEI 2. Geological Society of London, London, United Kingdom, pp. 105-128.
- [442] Rubin, A.M., 1995. Propagation of Magma-Filled Cracks. *Annual Review Of Earth And Planetary Sciences*, 23: 287-336.
- [443] Rust, A.C. and Cashman, K.V., 2011. Permeability controls on expansion and size distributions of pyroclasts. *Journal of Geophysical Research: Solid Earth*, 116(B11202): DOI: 10.1029/2011jb008494.
- [444] Samsonov, S., Tiampo, K., Gonzalez, P.J., Manville, V. and Jolly, G., 2010. Ground deformation occurring in the city of Auckland, New Zealand, and observed by Envisat interferometric synthetic aperture radar during 2003-2007. *Journal of Geophysical Research: Solid Earth*, 115(B08410): DOI: 10.1029/2009jb006806.
- [445] Sandiford, A., Alloway, B. and Shane, P., 2001. A 28,000-6,600 cal yr record of local and distal volcanism preserved in a paleolake, Auckland, New Zealand. *New Zealand Journal of Geology and Geophysics*, 44: 323-336.
- [446] Sandiford, A., Newnham, R.M., Alloway, B.V. and Ogden, J., 2003. A 28 000-7600 cal yr BP pollen record of vegetation and climate change from Pukaki Crater, northern New Zealand. *Palaeogeography, Palaeoclimatology, Palaeoecology*, 201(3-4): 235-247.

- [447] Sandri, L., Jolly, G., Lindsay, J., Howe, T. and Marzocchi, W., 2011. Combining long- and short-term probabilistic volcanic hazard assessment with cost-benefit analysis to support decision making in a volcanic crisis from the Auckland Volcanic Field, New Zealand. *Bulletin of Volcanology*, 74(3): 705-723.
- [448] Sandri, L., Marzocchi, W. and Gasperini, P., 2005. Some insights on the occurrence of recent volcanic eruptions of Mount Etna volcano (Sicily, Italy). *Geophysical Journal International*, 163(3): 1203-1218.
- [449] Sano, T., 1991. Map of Rangitoto Island showing lava flows and sample locations. Shinznoka University.
- [450] Sano, T., 1994. Geological and petrological study of Rangitoto Island, Auckland Volcanic Field. *Geoscience reports of Shizuoka University*, 20: 25-32.
- [451] Sato, H. and Taniguchi, H., 1997. Relationship between crater size and ejecta volume of recent magmatic and phreato-magmatic eruptions: Implications for energy partitioning. *Geophysical Research Letters*, 24(3): 205-208.
- [452] Schulz, R., Buness, H., Gabriel, G., Pucher, R., Rolf, C., Wiederhold, H. and Wonik, T., 2005. Detailed investigation of preserved maar structures by combined geophysical surveys. *Bulletin of Volcanology*, 68: 95-106.
- [453] Schumann, G., Matgen, P., Cutler, M.E.J., Black, A., Hoffmann, L. and Pfister, L., 2008. Comparison of remotely sensed water stages from LiDAR, topographic contours and SRTM. *ISPRS Journal of Photogrammetry and Remote Sensing*, 63(3): 283-296.
- [454] Scifoni, S., Coltelli, M., Marsella, M., Proietti, C., Napoleoni, Q., Vicari, A. and Del Negro, C., 2010. Mitigation of lava flow invasion hazard through optimized barrier configuration aided by numerical simulation: The case of the 2001 Etna eruption. *Journal of Volcanology and Geothermal Research*, 192(1-2): 16-26.
- [455] Searle, E.J., 1962. The Volcanoes of Auckland City. *New Zealand Journal of Geology and Geophysics*, 5(2): 193-227.
- [456] Searle, E.J., 1964. Volcanic Risk in the Auckland metropolitan area. *New Zealand Journal of Geology and Geophysics*, 7(1): 94-100.
- [457] Searle, E.J., 1981. *City of Volcanoes: a geology of Auckland*. Longman Paul, Auckland, New Zealand, pp. 1-195.
- [458] Segerstrom, K., 1950. Erosion Studies at Paricutin, State of Michoacán, Mexico *Geological Survey Bulletin*, 965-A: 1-163.
- [459] Self, S., Keszthelyi, L. and Thordarson, T., 1998. The importance of pahoehoe. *Annual Review of Earth and Planetary Sciences*, 26: 81-110.
- [460] Self, S., Kienle, J. and Hout, J.-P., 1980. Ukinrek maar, Alaska, II Deposits and formation of the 1977 craters. *Journal of Volcanology and Geothermal Research*, 7: 39-65.
- [461] Selva, J., Costa, A., Marzocchi, W. and Laura Sandri, L., 2010. BET\_VH: exploring the influence of natural uncertainties on long-term hazard from tephra fallout at Campi Flegrei (Italy). *Bulletin of Volcanology*, 72(6): 717-733.
- [462] Settle, M., 1979. The structure and emplacement of cinder cone fields. *American Journal of Science*, 279(10): 1089-1107.
- [463] Shakoor, A. and Smithmyer, A.J., 2005. An analysis of storm-induced landslides in colluvial soils overlying mudrock sequences, southeastern Ohio, USA. *Engineering Geology*, 78(3-4): 257-274.
- [464] Shane, P., Gehrels, M., Zawalna-Geer, A., Augustinus, P., Lindsay, J. and Chaillou, I., 2013. Longevity of a small shield volcano revealed by crypto-tephra studies (Rangitoto volcano, New Zealand): Change in eruptive behavior of a basaltic field. *Journal of Volcanology and Geothermal Research*, 257: 174-183.

- [465] Shane, P. and Hoverd, J., 2002. Distal record of multi-sourced tephra in Onepoto Basin, Auckland, New Zealand: implications for volcanic chronology, frequency and hazards. *Bulletin of Volcanology*, 64(7): 441-454.
- [466] Shane, P. and Sandiford, A., 2003. Paleovegetation of marine isotope stages 4 and 3 in Northern New Zealand and the age of the widespread Rotoehu tephra. *Quaternary Research*, 59: 420-429.
- [467] Shane, P. and Smith, I., 2000. Geochemical fingerprinting of basaltic tephra deposits in the Auckland Volcanic Field. *New Zealand Journal of Geology and Geophysics*, 43: 569-577.
- [468] Shane, P., Strachan, L.J. and Smith, I., 2010. Redefining the Waitemata Basin, New Zealand: A new tectonic, magmatic, and basin evolution model at a subduction terminus in the SW Pacific. *Geochemistry Geophysics Geosystems*, 11(4): Q04008.
- [469] Shane, P. and Zawalna-Geer, A., 2011. Correlation of basaltic tephra from Mt Wellington volcano: Implications for the penultimate eruption from the Auckland Volcanic Field. *Quaternary International*, 246: 374-381.
- [470] Sharpnack, D.A. and Akin, G., 1969. An algorithm for computing slope and aspect from elevation. *Photogrammetric Survey*, 35: 247-248.
- [471] Shary, P.A., Sharaya, L.S. and Mitusov, A.V., 2002. Fundamental quantitative methods of land surface analysis. *Geoderma*, 107(1-2): 1-32.
- [472] Shaw, C. and Woodland, A., 2012. The role of magma mixing in the petrogenesis of mafic alkaline lavas, Rockeskyllerkopf Volcanic Complex, West Eifel, Germany. *Bulletin of Volcanology*, 74(2): 359-376.
- [473] Shaw, C.S.J., 2004. The temporal evolution of three magmatic systems in the West Eifel volcanic field, Germany. *Journal of Volcanology and Geothermal Research*, 131: 213-240.
- [474] Shaw, S.J., Woodland, A.B., Hopp, J. and Trenholm, N.D., 2010. Structure and evolution of the Rockeskyllerkopf Volcanic Complex, West Eifel Volcanic Field, Germany. *Bulletin of Volcanology*, 72: 971-990.
- [475] Shea, T., Houghton, B.F., Gurioli, L., Cashman, K.V., Hammer, J.E. and Hobden, B.J., 2010. Textural studies of vesicles in volcanic rocks: An integrated methodology. *Journal of Volcanology and Geothermal Research*, 190(3-4): 271-289.
- [476] Shepard, M.K., Campbell, B.A., Bulmer, M.H., Farr, T.G., Gaddis, L.R. and Plaut, J.J., 2001. The roughness of natural terrain: A planetary and remote sensing perspective. *Journal of Geophysical Research: Planets*, 106(E12): 32777-32795.
- [477] Sherburn, S., Scott, B.J., Olsen, J. and Miller, C., 2007. Monitoring seismic precursors to an eruption from the Auckland Volcanic Field, New Zealand. *New Zealand Journal of Geology and Geophysics*, 50: 1-11.
- [478] Sheridan, M.F. and Wohletz, K.H., 1981. Hydrovolcanic Explosions: The Systematics of Water-Pyroclast Equilibration. *Science*, 212: 1387-1389.
- [479] Sibson, R., 1981. A Brief Description of Natural Neighbour Interpolation. In: V. Barnett (Editor), *In Interpreting multivariate data*, pp. 21-36.
- [480] Siebe, C., Rodriguez-Lara, V., Schaaf, P. and Abrams, M., 2004. Radiocarbon ages of Holocene Pelado, Guespalapa, and Chichinautzin scoria cones, south of Mexico City: implications for archaeology and future hazards. *Bulletin of Volcanology*, 66: 203-225.
- [481] Skácelová, Z., Rapprich, V., Valenta, J., Hartvich, F., Šrámek, J., Radon, M., Gazdová, R., Nováková, L., Kolínský, P. and Pécskay, Z., 2010. Geophysical

- research on structure of partly eroded maar volcanoes: Miocene Hnojnice and Oligocene Rychnov volcanoes (northern Czech Republic). *Journal of Geosciences*, 55: 333-345.
- [482] Slater, J.A., Garvey, G., Johnston, C., Haase, J., Heady, B., Kroenung, G. and Little, J., 2006. The SRTM Data Finishing Process and Products. *Photogrammetric Engineering and Remote Sensing*, 72(3): 237-247.
- [483] Smith, I.A.M., Okada, T., Itaya, T. and Black, P.M., 1993. Age relationships and tectonic implications of late Cenozoic basaltic volcanism in Northland, New Zealand. *New Zealand Journal of Geology and Geophysics*, 36: 385-393.
- [484] Smith, I.E.M. and Allen, S.R., 1993. Volcanic Hazards at the Auckland Volcanic Field. Volcanic Hazards Information Series, 5. New Zealand Ministry of Civil Defence, pp. 1-34.
- [485] Smith, I.E.M., Blake, S., Wilson, C.J.N. and Houghton, B.F., 2008. Deep-seated fractionation during the rise of a small-volume basalt magma batch: Crater Hill, Auckland, New Zealand. *Contributions to Mineralogy and Petrology*, 155(4): 511-527.
- [486] Smith, I.E.M., McGee, L. and Lindsay, J.M., 2009. Review of the Petrology of the Auckland Volcanic Field. IESE Report 1-2009.03. Institute of Earth Science and Engineering, Auckland, New Zealand, pp. 1-39.
- [487] Sohn, Y.K., 1996. Hydrovolcanic processes forming basaltic tuff rings and cones on Cheju Island, Korea. *Geological Society of America Bulletin*, 108(10): 1199-1211.
- [488] Sohn, Y.K. and Chough, S.K., 1989. Depositional processes of the Suwolbong tuff ring, Cheju Island (Korea). *Sedimentology*, 36: 837-855.
- [489] Sohn, Y.K., Cronin, S.J., Brenna, M., Smith, I.E.M., Németh, K., White, J.D.L., Murtagh, R.M., Jeon, Y.M. and Kwon, C.W., 2012. Ilchulbong tuff cone, Jeju Island, Korea, revisited: A compound monogenetic volcano involving multiple magma pulses, shifting vents, and discrete eruptive phases. *Geological Society of America Bulletin*, 124(3-4): 259-274.
- [490] Sohn, Y.K. and Yoon, S.-H., 2010. Shallow-marine records of pyroclastic surges and fallouts over water in Jeju Island, Korea, and their stratigraphic implications. *Geology*, 38(8): 763-766.
- [491] Son, M., Kim, J.S., Jung, S., Ki, J.S., Kim, M.-C. and Sohn, Y.K., 2012. Tectonically controlled vent migration during maar–diatreme formation: An example from a Miocene half-graben basin in SE Korea. *Journal of Volcanology and Geothermal Research*, 223–224: 29-46.
- [492] Spargo, S., 2007. The Pupuke volcanic centre: polygenic magmas in a monogenetic field. MSc thesis, University of Auckland, New Zealand, pp. 1-286.
- [493] Sparks, R.S.J., Pinkerton, H. and Macdonald, R., 1977. The transport of xenoliths in magmas. *Earth and Planetary Science Letters*, 35(2): 234-238.
- [494] Speight, J.G., 1974. A parametric approach to landform regions. *Special Publication of the Institute of British Geographers*, 7: 213-230.
- [495] Spera, F., 1984. Carbon dioxide in petrogenesis III: role of volatiles in the ascent of alkaline magma with special reference to xenolith-bearing mafic lavas. *Contributions to Mineralogy and Petrology*, 88(3): 217-232.
- [496] Spera, F.J., Fowler, S.J., Spera, F.J. and Fowler, S.J., 2009. Conceptual model for small-volume alkali basalt petrogenesis: implications for volcanic hazards at the proposed Yucca Mountain nuclear waste repository. In: C.B. Connor, N.A. Chapman and L.J. Connor (Editors), *Volcanic and Tectonic Hazard Assessment*

- for Nuclear Facilities. Cambridge University Press, Cambridge, United Kingdom, pp. 195-227.
- [497] Spörli, K.B., 1978. Mesozoic tectonics, North Island, New Zealand. *Geological Society of America Bulletin*, 89: 415-425.
- [498] Spörli, K.B., 1989. Exceptional structural complexity in turbidite deposits of the piggy-back Waitemata Basin, Miocene, Auckland/Northland, New Zealand. In: K.B. Spörli and K. , D., (Editors), *Geology of Northland - Accretion, Allochthons and Arcs at the Edge of the New Zealand Micro-continent*. The Royal Society of New Zealand, Wellington, New Zealand, pp. 183-194.
- [499] Spörli, K.B. and Browne, G.H., 1982. Structure in a Miocene interarc basin; Waitemata Group at White Bluff, Auckland, New Zealand. *Journal of The Royal Society of New Zealand*, 11(2): 87-92.
- [500] Spörli, K.B. and Eastwood, V.R., 1997. Elliptical boundary of an intraplate volcanic field, Auckland, New Zealand *Journal of Volcanology and Geothermal Research*, 79(3-4): 169-179.
- [501] Spörli, K.B. and Rowland, J.V., 2007. Superposed deformation in turbidites and syn-sedimentary slides of the tectonically active Miocene Waitemata Basin, northern New Zealand. *Basin Research*, 19: 199-216.
- [502] Sprung, P., Schuth, S., Münker, C. and Hoke, L., 2007. Intraplate volcanism in New Zealand: the role of fossil plume material and variable lithospheric properties. *Contributions to Mineralogy and Petrology*, 153(6): 669-687.
- [503] Stasiuk, M.V. and Jaupart, C., 1997. Lava flow shapes and dimensions as reflections of magma system conditions. *Journal of Volcanology and Geothermal Research*, 78(1-2): 31-50.
- [504] Stern, T., Smith, E.G.C., Davey, F.J. and Muirhead, K.J., 1987. Crustal and upper mantle structure of the northwestern North Island, New Zealand, from seismic refraction data. *Geophysical Journal of the Royal Astronomical Society*, 91: 913-936.
- [505] Stern, T., Stratford, W., Seward, A., Henderson, M., Savage, M., Smith, E., Benson, A., Greve, S. and Salmon, M., 2010. Crust–mantle structure of the central North Island, New Zealand, based on seismological observations. *Journal of Volcanology and Geothermal Research*, 190(1–2): 58-74.
- [506] Stevens, N.F., Garbeil, H. and Mouginiis-Mark, P.J., 2004. NASA EOS Terra ASTER: Volcanic topographic mapping and capability. *Remote Sensing of Environment*, 90: 405-414.
- [507] Su, J. and Bork, E., 2006. Influence of vegetation, slope, and lidar sampling angle on DEM accuracy. *Photogrammetric Engineering and Remote Sensing*, 72(11): 1265-1274.
- [508] Suhr, P., Goth, K., Lorenz, V. and Suhr, S., 2006. Long lasting subsidence and deformation in and above maar-diatreme volcanoes - a never ending story *Zeitschrift der Deutschen Gesellschaft für Geowissenschaften*, 157(3): 491-511.
- [509] Suiting, I. and Schmincke, H.-U., 2009. Internal vs. external forcing in shallow marine diatreme formation: A case study from the Iblean Mountains (SE-Sicily, Central Mediterranean). *Journal of Volcanology and Geothermal Research*, 186(3–4): 361-378.
- [510] Sumner, J., Blake, S., Matela, R. and Wolff, J., 2005. Spatter. *Journal of Volcanology and Geothermal Research*, 142: 49-65.
- [511] Szabó, C. and Bodnar, R.J., 1996. Changing magma ascent rates in the Nógrád–Gömör volcanic field, Northern Hungary/Southern Slovakia: evidence from

- CO<sub>2</sub>-rich fluid inclusions in metasomatized upper mantle xenoliths. *Petrology*, 4(3): 221-230.
- [512] Székely, B. and Karátson, D., 2004. DEM-based morphometry as a tool for reconstructing primary volcanic landforms: examples from the Börzsöny Mountains, Hungary. *Geomorphology*, 63(1-2): 25-37.
- [513] Szilassi, P., Jordan, G., van Rompaey, A. and Csillag, G., 2006. Impacts of historical land use changes on erosion and agricultural soil properties in the Kali Basin at Lake Balaton, Hungary. *Catena*, 68(2-3): 96-108.
- [514] Taddeucci, J., Scarlato, P., Capponi, A., Del Bello, E., Cimarelli, C., Palladino, D.M. and Kueppers, U., 2012. High-speed imaging of Strombolian explosions: The ejection velocity of pyroclasts. *Geophysical Research Letters*, 39(2): DOI: 10.1029/2011gl050404.
- [515] Taddeucci, J., Sottili, G., Palladino, D.M., Ventura, G. and Scarlato, P., 2009. A note on maar eruption energetics: current models and their application. *Bulletin of Volcanology*, 72(1): 75-83.
- [516] Taisne, B. and Jaupart, C., 2009. Dike propagation through layered rocks. *Journal of Geophysical Research: Solid Earth*, 114(B09203): DOI: 10.1029/2008jb006228.
- [517] Takada, A., 1994. The influence of regional stress and magmatic input on styles of monogenetic and polygenetic volcanism. *Journal of Geophysical Research: Solid Earth*, 99(B7): 13563-13573.
- [518] Tanaka, K.L., Shoemaker, E.M., Ulrich, G.E. and Wolfe, E.W., 1986. Migration of volcanism in the San Francisco volcanic field, Arizona. *Geological Society of America Bulletin*, 97(2): 129-141.
- [519] Tarquini, S. and Favalli, M., 2011. Mapping and DOWNFLOW simulation of recent lava flow fields at Mount Etna. *Journal of Volcanology and Geothermal Research*, 204(1-4): 27-39.
- [520] Tarquini, S. and Favalli, M., 2013. Uncertainties in lava flow hazard maps derived from numerical simulations: The case study of Mount Etna. *Journal of Volcanology and Geothermal Research*, 260: 90-102.
- [521] Tarquini, S., Favalli, M., Mazzarini, F., Isola, I. and Fornaciai, A., 2012. Morphometric analysis of lava flow units: Case study over LIDAR-derived topography at Mount Etna, Italy. *Journal of Volcanology and Geothermal Research*, 235–236: 11-22.
- [522] Taud, H., Parrot, J.-F. and Alvarez, R., 1999. DEM generation by contour line dilation. *Computers & Geosciences*, 25(7): 775-783.
- [523] Temme, A.J.A.M., Schoorl, J.M. and Veldkamp, A., 2006. Algorithm for dealing with depressions in dynamic landscape evolution models. *Computers & Geosciences*, 32(4): 452-461.
- [524] Thorarinsson, S., 1966. The surtsey eruption course of events and the development of Surtsey and other new islands. *Surtsey Research Progress Report II.*: 117-123.
- [525] Thordarson, T. and Self, S., 1993. The Laki (Skaftar Fires) and Grimsvotn eruptions in 1783–85. *Bulletin of Volcanology*, 55: 233-263.
- [526] Tokarev, P.I., 1983. Calculation of the magma discharge, growth in the height of the cone and dimensions of the feeder channel of Crater I in the Great Tolbachik Fissure Eruption, July 1975. In: S.A. Fedotov and Y.K. Markhinin (Editors), *The Great Tolbachik Fissure Eruption: Geological and Geophysical Data, 1975-1976.* . Cambridge University Press, Cambridge, pp. 27-35.

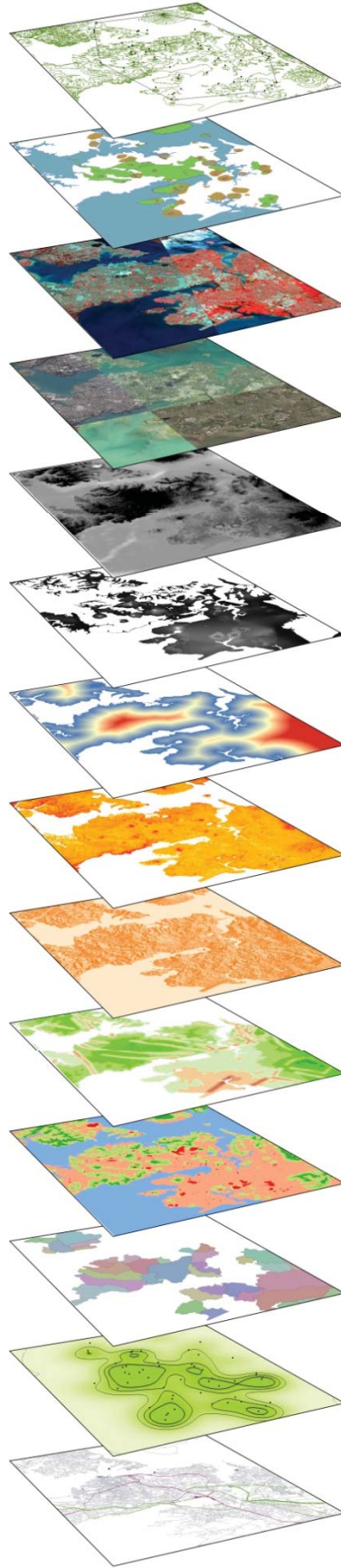
- [527] Tsai, V.J.D., 1993. Delaunay Triangulations in TIN creation: an overview and a linear-time algorithm. *International Journal of Geographic Information Systems*, 6: 501-512.
- [528] Tucker, D.S. and Scott, K.M., 2009. Structures and facies associated with the flow of subaerial basaltic lava into a deep freshwater lake: The Sulphur Creek lava flow, North Cascades, Washington. *Journal of Volcanology and Geothermal Research*, 185(4): 311-322.
- [529] Valentine, G.A., 2012. Shallow plumbing systems for small-volume basaltic volcanoes, 2: Evidence from crustal xenoliths at scoria cones and maars. *Journal of Volcanology and Geothermal Research*, 223–224: 47-63.
- [530] Valentine, G.A. and Gregg, T.K.P., 2008. Continental basaltic volcanoes - Processes and problems. *Journal of Volcanology and Geothermal Research*, 177(4): 857-873.
- [531] Valentine, G.A. and Hirano, N., 2010. Mechanisms of low-flux intraplate volcanic fields—Basin and Range (North America) and northwest Pacific Ocean. *Geology*, 38(1): 55-58.
- [532] Valentine, G.A. and Keating, G.N., 2007. Eruptive styles and inferences about plumbing systems at Hidden Cone and Little Black Peak scoria cone volcanoes (Nevada, U.S.A.). *Bulletin of Volcanology*, 70(1): 105-113.
- [533] Valentine, G.A., Krier, D.J., Perry, F.V. and Heiken, G., 2007. Eruptive and geomorphic processes at the Lathrop Wells scoria cone volcano. *Journal of Volcanology and Geothermal Research*, 161(1-2): 57-80.
- [534] Valentine, G.A. and Krogh, K.E.C., 2006. Emplacement of shallow dikes and sills beneath a small basaltic volcanic center – The role of pre-existing structure (Paiute Ridge, southern Nevada, USA). *Earth and Planetary Science Letters*, 246(3-4): 217-230.
- [535] Valentine, G.A. and Perry, F.V., 2006. Decreasing magmatic footprints of individual volcanoes in a waning basaltic field. *Geophysical Research Letters*, 33(14): DOI: 10.1029/2006GL026743.
- [536] Valentine, G.A. and Perry, F.V., 2007. Tectonically controlled, time-predictable basaltic volcanism from a lithospheric mantle source (central Basin and Range Province, USA). *Earth and Planetary Science Letters*, 261(1-2): 201-216.
- [537] Valentine, G.A. and White, J.D.L., 2012. Revised conceptual model for maar-diatremes: Subsurface processes, energetics, and eruptive products. *Geology*: doi: 10.1130/G33411.1
- [538] van Otterloo, J. and Cas, R.F., 2013. Reconstructing the eruption magnitude and energy budgets for the pre-historic eruption of the monogenetic 5 ka Mt. Gambier Volcanic Complex, south-eastern Australia. *Bulletin of Volcanology*, 75(12): 1-18.
- [539] Vazquez, J.A. and Ort, M.H., 2006. Facies variation of eruption units produced by the passage of single pyroclastic surge currents, Hopi Buttes volcanic field, USA. *Journal of Volcanology and Geothermal Research*, 154(3-4): 222-236.
- [540] Vespermann, D. and Schmincke, H.-U., 2000. Scoria cones and tuff rings. In: H. Sigurdsson, B.F. Houghton, S.R. McNutt, H. Rymer and J. Stix (Editors), *Encyclopedia of Volcanoes*. Academic Press, San Diego, California, pp. 683-694.
- [541] Vicari, A., Cirauda, A., Del Negro, C., Herault, A. and Fortuna, L., 2009. Lava flow simulations using discharge rates from thermal infrared satellite imagery during the 2006 Etna eruption. *Natural Hazards*, 50(3): 539-550.

- [542] Vicari, A., Ganci, G., Behncke, B., Cappello, A., Neri, M. and Del Negro, C., 2011. Near-real-time forecasting of lava flow hazards during the 12–13 January 2011 Etna eruption. *Geophysical Research Letters*, 38(13): DOI: 10.1029/2011gl047545.
- [543] Vicari, A., Herault, A., Del Negro, C., Coltelli, M., Marsella, M. and Proietti, C., 2007. Simulations of the 2001 lava flow at Etna volcano by the Magflow Cellular Automata model. *Environmental Modelling & Software*, 22(10): 1465-1471.
- [544] Von Neumann, J., 1966. *Theory of Self-Reproducing Automata*. University of Illinois Press, pp. 1-388.
- [545] von Veh, M.W. and Németh, K., 2009. An assessment of the alignments of vents on geostatistical analysis in the Auckland Volcanic Field, New Zealand. *Geomorphologie*, 3: 175-186.
- [546] Vosselman, G. and Maas, H.G., 2001. Adjustment and filtering of raw laser altimetry data. *OEEPE Workshop on Airborne Laser Systems and Interferometric SAR for Detailed Digital Elevation Models*, 40: 62-72.
- [547] Wadge, G., 1981. The variation of magma discharge during basaltic eruptions. *Journal of Volcanology and Geothermal Research*, 11(2–4): 139-168.
- [548] Wadge, G., Young, P.A.V. and McKendrick, I.J., 1994. Mapping lava flow hazards using computer simulation. *Journal of Geophysical Research: Solid Earth*, 99(B1): 489-504.
- [549] Walker, G.P.L., 1973. Lengths of lava flows. *Philosophical Transactions of the Royal Society of London. Series A, Mathematical and Physical Sciences*, 274: 107-118.
- [550] Wantim, M., Kervyn, M., Ernst, G., Marmol, M., Suh, C. and Jacobs, P., 2013. Morpho-Structure of the 1982 Lava Flow Field at Mount Cameroon Volcano, West-Central Africa. *International Journal of Geosciences*, 4(3): 564-583.
- [551] Wantim, M.N., Suh, C.E., Ernst, G.G.J., Kervyn, M. and Jacobs, P., 2011. Characteristics of the 2000 fissure eruption and lava flow fields at Mount Cameroon volcano, West Africa: a combined field mapping and remote sensing approach. *Geological Journal*, 46: 344-363.
- [552] Watanabe, T., Koyaguchi, T. and Seno, T., 1999. Tectonic stress controls on ascent and emplacement of magmas. *Journal of Volcanology and Geothermal Research*, 91(1): 65-78.
- [553] Wehr, A. and Lohr, U., 1999. Airborne laser scanning—an introduction and overview. *ISPRS Journal of Photogrammetry and Remote Sensing*, 54(2–3): 68-82.
- [554] Weller, J.N., Martin, A.J., Connor, C.B., Connor, L.J. and Karakhanian, A., 2009. Modelling the Spatial Distribution of Volcanoes: An Example From Armenia. In: H.M. Mader, S.G. Coles, C.B. Connor and L.J. Connor (Editors), *Statistics in Volcanology*. The Geological Society, London, pp. 77-87.
- [555] White, J.D.L., 1991. Maar-diatreme phreatomagmatism at Hopi Buttes, Navajo Nation (Arizona), USA. *Bulletin of Volcanology*, 53: 239-258.
- [556] White, J.D.L., 1996. Impure coolants and interaction dynamics of phreatomagmatic eruptions. *Journal of Volcanology and Geothermal Research*, 74(3-4): 155-170.
- [557] White, J.D.L. and Ross, P.-S., 2011. Maar-diatreme volcanoes: A review. *Journal of Volcanology and Geothermal Research*, 201(1-4): 1-29.
- [558] Wijbrans, J., Németh, K., Martin, U. and Balogh, K., 2007.  $^{40}\text{Ar}/^{39}\text{Ar}$  geochronology of Neogene phreatomagmatic volcanism in the western

- Pannonian Basin, Hungary. *Journal of Volcanology and Geothermal Research*, 164(4): 193-204.
- [559] Wilson, C.J.N., Houghton, B.F., McWilliams, M.O., Lanphere, M.A., Weaver, S.D. and Briggs, R.M., 1995. Volcanic and structural evolution of Taupo Volcanic Zone, New Zealand: a review. *Journal of Volcanology and Geothermal Research*, 68(1-3): 1-28.
- [560] Wise, D.J., Cassidy, J. and Locke, C.A., 2003. Geophysical imaging of the Quaternary Wairoa North Fault, New Zealand: a case study. *Journal of Applied Geophysics*, 53: 1-16.
- [561] Wise, S., 2000. Assessing the quality for hydrological applications of digital elevation models derived from contours. *Hydrological Processes*, 14: 1909-1929.
- [562] Wise, S., 2007. Effect of differing DEM creation methods on the results from a hydrological model. *Computers & Geosciences*, 33(10): 1351-1365.
- [563] Wise, S., 2011. Cross-validation as a means of investigating DEM interpolation error. *Computers & Geosciences*, 37: 978-991.
- [564] Wohletz, K.H., 1986. Explosive magma-water interactions: Thermodynamics, explosion mechanism and field studies. *Bulletin of Volcanology*, 48(5): 245-264.
- [565] Wohletz, K.H. and Sheridan, M.F., 1983. Hydrovolcanic explosions II. Evolution of basaltic tuff rings and tuff cones. *American Journal of Science*, 283: 385-413.
- [566] Won, J.-H., Lee, J.-Y., Kim, J.-W. and Koh, G.-W., 2006. Groundwater occurrence on Jeju Island, Korea. *Hydrogeology Journal*, 14(4): 532-547.
- [567] Wood, C.A., 1979. Monogenetic volcanoes in terrestrial planets, *Proceedings of the 10th Lunar and Planetary Science Conference*: 2815-2840.
- [568] Wood, J., 1996. The geomorphological characterization of Digital Elevation Models. University of Leicester, United Kingdom, pp. 1-185.
- [569] Wood, J.D. and Fisher, P.F., 1993. Assessing interpolation accuracy in elevation models. *Computer Graphics and Applications*, 13(2): 48-56.
- [570] Woodcock, C.E. and Strahler, A.H., 1987. The Factor of Scale in Remote Sensing. *Remote Sensing of Environment*, 21: 311-332.
- [571] Woollaston, M., 1996. The Junction Magnetic Anomaly in the Auckland region. BSc thesis, University of Auckland, New Zealand, pp. 1-62.
- [572] Wright, R., Flynn, L.P., Garbeil, H., Harris, A.J.L. and Pilger, E., 2004. MODVOLC: near-real time thermal monitoring of global volcanism. *Journal of Volcanology and Geothermal Research*, 135: 29-49.
- [573] Wright, R., Flynn, L.P. and Harris, A.J.L., 2001. Evolution of lava flow-fields at Mount Etna, 27-28 October 1999, observed by Landsat 7 ETM+. *Bulletin of Volcanology*, 63(1): 1-7.
- [574] Wright, R., Garbeil, H., Baloga, S.M. and Mouginiis-Mark, P.J., 2006. An assessment of shuttle radar topography mission digital elevation data for studies of volcano morphology. *Remote Sensing of Environment*, 105(1): 41-53.
- [575] Wright, R., Garbeil, H. and Harris, A.J.L., 2008. Using infrared satellite data to drive a thermo-rheological/stochastic lava flow emplacement model: A method for near real-time volcanic hazard assessment. *Geophysical Research Letters*, 35(19): DOI: 10.1029/2008GL035228.
- [576] Wu, S., Jonathan Li, J. and Huang, G.H., 2008. A study on DEM-derived primary topographic attributes for hydrologic applications: Sensitivity to elevation data resolution. *Applied Geography*, 28: 210-223.

- [577] Yilmaz, H.M., 2007. The effect of interpolation methods in surface definition: an experimental study. *Earth Surface Processes and Landforms*, 32(9): 1346-1361.
- [578] Young, P. and Wadge, G., 1990. FLOWFRONT: simulation of a lava flow. *Computers & Geosciences*, 16: 1171-1191.
- [579] Zevenbergen, L.W. and Thorne, C.R., 1987. Quantitative analysis of land surface topography. *Earth Surface Processes and Landforms*, 12: 47-56.
- [580] Zhang, K. and Whitman, D., 2005. Comparison of Three Algorithms for Filtering Airborne Lidar Data. *Photogrammetric Engineering and Remote Sensing*, 71(3): 313-324.
- [581] Zhang, W. and Montgomery, D.R., 1994. Digital elevation model grid size, landscape representation, and hydrologic simulations. *Water Resources Research*, 30(4): 1019-1028.
- [582] Zhao, S., Cheng, W., Zhou, C., Chen, X., Zhang, S., Zhou, Z., Liu, H. and Chai, H., 2011. Accuracy assessment of the ASTER GDEM and SRTM3 DEM: an example in the Loess Plateau and North China Plain of China. *International Journal of Remote Sensing*, 32(23): 8081-8093.
- [583] Zhou, Q. and Liu, X., 2004. Analysis of errors of derived slope and aspect related to DEM data properties. *Computers & Geosciences*, 30(4): 369-378.
- [584] Ziadat, F.M., 2007. Effect of Contour Intervals and Grid Cell Size on the Accuracy of DEMs and Slope Derivatives. *Transactions in GIS*, 11(1): 67-81.
- [585] Zimanowski, B., 1998. Phreatomagmatic explosions. In: A. Freundt and M. Rosi (Editors), *From Magma to Tephra: Developments in Volcanology 4*. Elsevier, Amsterdam, pp. 25-54.
- [586] Zimanowski, B., Büttner, R. and Lorenz, V., 1997. Premixing of magma and water in MFCI experiments. *Bulletin of Volcanology*, 58(6): 491-495.





Appendices





## Appendix A – Pullout map

This Appendix is a geological and topographic map of the Auckland volcanic field, New Zealand with the location of the volcanic centres and geographical names mentioned in this thesis.



## Appendix B – Supplementary data (DVD)

This Appendix contains the input files, intermediate data-processing files and output files, tables and data created in this research. The data on the DVD are organised into folders by Chapter.



## DVD content

### Appendix for Chapter 3

#### 01 – INPUT DATA

- auckland\_aster\_30m.tif – ASTER GDEM (30 m resolution) covering Auckland. Downloaded from [www.gdem.ersdac.jspacesystems.or.jp](http://www.gdem.ersdac.jspacesystems.or.jp).
- auckland\_cont\_topo50\_Z.shp – Contour lines based on the topographic maps with scale of 1:50,000. Downloaded from [www.linz.govt.nz](http://www.linz.govt.nz).
- auckland\_srtm\_90m.tif – SRTM DTM (90 m resolution) covering Auckland. Downloaded from [www.srtm.usgs.gov](http://www.srtm.usgs.gov).
- browns\_GPS.shp – High accuracy ground control data surveyed by Real Time Kinematic GPS on the Browns Island.
- NZmarks\_auckland\_ALL.shp – High accuracy ground control data based on the geodetic network. Downloaded from [www.linz.govt.nz](http://www.linz.govt.nz).
- pukaki\_GPS.shp – High accuracy ground control data surveyed by Real Time Kinematic GPS on the Pukaki.
- rangitoto\_GPS.shp – High accuracy ground control data surveyed by Real Time Kinematic GPS on the Rangitoto.
- rangitoto\_TLS\_point\_05m.shp – High accuracy ground control data surveyed by Terrestrial Laser Scanning GPS on the Browns Island.

#### 02 – PROCESSED DATA

- whole\_tin05m (folder) – This folder contains the TIN created from rangitoto\_TLS\_point\_05m.shp file.
- aster\_minus\_tls\_corr.tif – Elevation difference between ASTER GDEM and the TLS DSM on the Rangitoto.
- lidar\_minus\_tls\_corr.tif – Elevation difference between LiDAR DSM and the TLS DSM on the Rangitoto.
- nzmarks\_auckland\_all\_ASTERerror.shp – Elevation difference between the geodetic survey marks and ASTER GDEM.
- nzmarks\_auckland\_all\_LIDARerror.shp – Elevation difference between the geodetic survey marks and LiDAR DSM.
- nzmarks\_auckland\_all\_SRTMerror.shp – Elevation difference between the geodetic survey marks and SRTM DTM.
- nzmarks\_auckland\_all\_TOPO50error.shp – Elevation difference between the geodetic survey marks and topo50 DEM.

- `srtm_minus_tls_corr.tif` – Elevation difference between SRTM DTM and the TLS DSM on the Rangitoto.
- `topo50_minus_tls_corr.tif` – Elevation difference between topo50 DEM and the TLS DSM on the Rangitoto.
- `tsl_05m_nn05m_corr.tif` – Gridded TLS DSM with 0.5 m horizontal resolution, used as a reference surface.

### 03 – OUTPUT DATA

- `auckland_aster_30m_land.tif` – ASTER GDEM coverage for Auckland with 30 m horizontal resolution (on-shore only).
- `auckland_cont_topo50_z_edited_dem_4m_peak_depression_land.tif` – DEM based on topo50 contour lines for Auckland with 4 m horizontal resolution (on-shore only).
- `auckland_lidar_2m_f.tif` – LiDAR DSM with 2 m horizontal resolution for Auckland (on-shore only).
- `auckland_lidar_2m_f_nn10m_land.tif` – Resampled LiDAR DSM with 10 m horizontal resolution for Auckland (on-shore only).
- `auckland_lidar_bathy_merged_nn10m_undef.tif` – Resampled LiDAR DSM with 10 m horizontal resolution and merged with the contour-based bathymetric data available for Auckland. The bathymetric data were downloaded from [www.linz.govt.nz](http://www.linz.govt.nz).
- `auckland_lidar_bathy_merged_nn10m_undef_nn20m_a3.tif` – Resampled LiDAR DSM with 20 m horizontal resolution and merged with the contour-based bathymetric data available for Auckland. The bathymetric data were downloaded from [www.linz.govt.nz](http://www.linz.govt.nz).
- `auckland_srtm_90m_land.tif` – SRTM DTM coverage for Auckland with 90 m horizontal resolution (on-shore only).

## Appendix for Chapter 4

### 01 – INPUT DATA

- `auckland_vents.shp` – Location of 52 vents in Auckland.
- `PETLAB_drill_cores_waitemata.shp` – Location of those drill cores that reached the Waitemata country rocks.
- `PETLAB_drill_cores.shp` – Drill core location in Auckland. Downloaded from [www.pet.gns.cri.nz](http://www.pet.gns.cri.nz).

- PETLAB\_drill\_cores\_lava.shp – Location of those drill cores that reached the the bottom of lava flows.

## 02 – MAPPING DATA

- auckland\_lava.shp – Mapped boundaries of lava rocks.
- auckland\_lava\_thickness.shp – Input points used to interpolate lava flow thickness map (auckland\_lava\_thickness.tif) based on drill core data and additional point in which the Waitemata country rocks are on surface.
- auckland\_lava\_thickness.tif – Interpolated map by natural neighbour method (Sibson, 1981) for the lava flow and scoria cone thickness in the Central Auckland area.
- auckland\_lidar\_0masl.shp – Polygon of onshore areas based on the LiDAR DSM ( $\geq 0$  m a.s.l.).
- auckland\_scoria.shp – Mapped boundaries of scoriaceous deposits.
- auckland\_tuff.shp – Mapped boundaries of phreatomagmatic tuff deposits.
- auckland\_vents\_convex\_hull.shp – Convex hull of the area encompassed by the 52 vents.
- spot\_height\_waitemata.shp – Input points used to interpolate top surface of the Waitemata country rocks based on drill core data and additional point in which the Waitemata country rocks are on surface.

## 03 – OUTPUT DATA

- 2013\_kereszturi\_et\_al\_JVGR.pdf – Published paper on the eruptive volumes of the Auckland volcanic field.
- SM1\_blank.xls – Blank copy of eruptive volume scheme used in Auckland.
- SM2\_volumes.xls – Summary of the eruptive volumes in Auckland.

# Appendix for Chapter 5

## 01 – INPUT DATA

- auckland\_lidar\_land.shp – Onshore areas defined from the LiDAR DSM ( $\geq 0$  m a.s.l.).
- auckland\_lidar\_sea.shp – Offshore areas defined from the LiDAR DSM ( $\leq 0$  m a.s.l.).
- faults\_kenny2012.shp – Location known faults in Auckland based on Kenny et al. (2012).
- auckland\_lidar\_bathy\_merged\_nn10m\_undef.tif – Resampled LiDAR DSM with 10 m horizontal resolution and merged with the contour-based bathymetric

data available for Auckland. The bathymetric data were downloaded from [www.linz.govt.nz](http://www.linz.govt.nz).

## 02 – PROCESSED DATA

- auckland\_post\_waitemata\_soft\_sediment1.shp – Mapped boundaries of thin ( $\leq 20$  m) post-Waitemata non-volcanic sediment (mostly in North Shore and Central Auckland areas).
- auckland\_post\_waitemata\_soft\_sediment2.shp – Mapped boundaries of thick ( $\geq 20$  m) post-Waitemata non-volcanic sediment (mostly in Manukau Lowlands).
- PETLAB\_drill\_crosssection.shp – Drill cores used to establish cross-section through Manukau Lowlands in Fig. 5.3.
- PETLAB\_MANUKAU\_profileA\_3D.shp – Profile line A–A' through Manukau Lowlands used in Fig. 5.3.
- PETLAB\_MANUKAU\_profileB\_3D.shp – Profile line B–B' through Manukau Lowlands used in Fig. 5.3.

## 03 – OUTPUT DATA

- auckland\_faults\_DIST.tif – Distance map from known fault lines (faults\_kenny2012.shp).
- auckland\_faults\_DIST\_RECLASS.tif – Classified distance map from the present shore line.
- auckland\_lidar\_bathy\_merged\_nn10m\_TOPO.tif – Elevation map based on the LiDAR DSM with bathymetric data. This map was resampled to 10 m resolution.
- auckland\_lidar\_bathy\_merged\_nn10m\_TOPO\_RECLASS.tif – Classified distance map.
- auckland\_lidar\_bathy\_merged\_nn10m\_undef\_0\_SEA.tif – Map of onshore areas at the present day sea level.
- auckland\_lidar\_bathy\_merged\_nn10m\_undef\_0\_SEA\_poly.shp – Polygon of onshore areas at the present day sea level.
- auckland\_lidar\_bathy\_merged\_nn10m\_undef\_0\_SEA\_poly\_VENT.shp – Distance between vent locations and present day coastline.
- auckland\_lidar\_bathy\_merged\_nn10m\_undef\_m5\_SEA.tif – Map of onshore areas in the case of a sea level scenario of present level minus 5 m.
- auckland\_lidar\_bathy\_merged\_nn10m\_undef\_m5\_SEA\_poly.shp – Polygon of onshore areas in the case of a sea level scenario of present level minus 5 m.
- auckland\_lidar\_bathy\_merged\_nn10m\_undef\_m5\_SEA\_poly\_VENT.shp – Distance between vent locations and present sea level minus 5 m.
- auckland\_lidar\_bathy\_merged\_nn10m\_undef\_m10\_SEA.tif – Map of onshore areas in the case of a sea level scenario of present level minus 10 m.
- auckland\_lidar\_bathy\_merged\_nn10m\_undef\_m10\_SEA\_poly.shp – Polygon of onshore areas in the case of a sea level scenario of present level minus 10m.

- auckland\_lidar\_bathy\_merged\_nn10m\_undef\_m10\_SEA\_poly\_VENT.shp – Distance between vent locations and present sea level minus 10 m.
- auckland\_lidar\_bathy\_merged\_nn10m\_undef\_p5\_SEA.tif – Map of onshore areas in the case of a sea level scenario of present level plus 5 m.
- auckland\_lidar\_bathy\_merged\_nn10m\_undef\_p5\_SEA\_poly.shp – Polygon of onshore areas in the case of a sea level scenario of present level plus 5 m.
- auckland\_lidar\_bathy\_merged\_nn10m\_undef\_p5\_SEA\_poly\_VENT.shp – Distance between vent locations and present sea level plus 5 m.
- auckland\_lidar\_bathy\_merged\_nn10m\_undef\_p10\_SEA.tif – Map of onshore areas in the case of a sea level scenario of present level plus 10 m.
- auckland\_lidar\_bathy\_merged\_nn10m\_undef\_p10\_SEA\_poly.shp – Polygon of onshore areas in the case of a sea level scenario of present level plus 10m.
- auckland\_lidar\_bathy\_merged\_nn10m\_undef\_p10\_SEA\_poly\_VENT.shp – Distance between vent locations and present sea level plus 10 m.
- auckland\_lidar\_sea\_DIST.tif – Distance map from the present shore line (auckland\_lidar\_sea.shp).
- auckland\_lidar\_sea\_DIST\_RECLASS.tif – Classified distance map from the present shore line.
- auckland\_soft\_sediment\_thickness.tif – Thickness map of the post-Waitemata non-volcanic, soft-sediments based on drill core data (spot\_height\_waitemata.shp), and mapping.
- auckland\_soft\_sediment\_thickness\_RECLASS.tif – Classified thickness map of the post-Waitemata non-volcanic, soft-sediments.

## Appendix for Chapter 6

### 01 – INPUT DATA

- auckland\_lava\_thickness.shp – Input points used to interpolate lava flow thickness map (auckland\_lava\_thickness.tif) based on drill core data and additional point in which the Waitemata country rocks are on surface.
- auckland\_lava\_thickness.tif – Interpolated map by natural neighbour method (Sibson, 1981) for the lava flow and scoria cone thickness in the Central Auckland area.
- auckland\_powerline\_BORDER.shp – Polyline map of the main power lines in Auckland. Downloaded from [www.linz.govt.nz](http://www.linz.govt.nz).
- auckland\_railway\_BORDER.shp – Polyline map of the railway network of Auckland. Downloaded from [www.linz.govt.nz](http://www.linz.govt.nz).
- auckland\_road\_BORDER.shp – Polyline map of the road network of Auckland. Downloaded from [www.linz.govt.nz](http://www.linz.govt.nz).
- auckland\_wharf\_BORDER.shp – Polyline map of the wharfs in Auckland. Downloaded from [www.linz.govt.nz](http://www.linz.govt.nz).

- bridge\_BORDER.shp – Polyline map of the bridges in Auckland. Downloaded from [www.linz.govt.nz](http://www.linz.govt.nz).

## 02 – PROCESSED DATA

- auckland\_channel\_intersections\_ras\_values\_point.shp – Intersection points of the present drainage system.
- auckland\_channel\_intersections\_ras\_values\_point\_OUTLET.shp – Outlet point of the present drainage to the sea.
- auckland\_drainage\_msc11000.tif – Map of the extracted drainage network using TOPAZ.
- auckland\_watersheds\_BORDER.shp – Analysed watersheds in Auckland.

## 03 – OUTPUT DATA

- 2012\_kereszturi\_et\_al\_RSoE.pdf – Published paper on the lava flow susceptibility map of the Auckland volcanic field.
- auckland\_kernel\_density\_all\_2420m.tif – Spatial intensity map created by a symmetric, Gaussian kernel with a bandwidth of 2420 m based on the past vent locations.
- auckland\_kernel\_density\_all\_2420m\_25perc.shp – Percentage contours of the input data (25%).
- auckland\_kernel\_density\_all\_2420m\_50perc.shp – Percentage contours of the input data (50%).
- auckland\_kernel\_density\_all\_2420m\_75perc.shp – Percentage contours of the input data (75%).
- auckland\_kernel\_density\_all\_2420m\_100perc.shp – Percentage contours of the input data (100%).
- auckland\_lava\_flow\_susceptibility\_scenario1.tif – Lava flow susceptibility maps of Auckland (scenario 1).
- auckland\_lava\_flow\_susceptibility\_scenario2.tif – Lava flow susceptibility maps of Auckland (scenario 2).

## Appendix for Chapter 7

### 01 – INPUT DATA

/Albert:

- auckland\_lava\_albert.shp – Mapped extent of the lava flow.
- paleo\_albert\_final\_a11\_a5\_USED.tif – Reconstructed pre-eruptive DSM for Mt. Albert.

- vent\_500h.txt – Effusion curve for 500h scenario.
- vent\_1000h.txt – Effusion curve for 1000h scenario.
- vent\_1500h.txt – Effusion curve for 1500h scenario.

/Eden:

- auckland\_lava\_eden.shp – Mapped extent of the lava flow.
- paleo\_eden\_final\_a11\_a5.tif – Reconstructed pre-eruptive DSM for Mt. Eden.
- vent\_2500h.txt – Effusion curve for 2000h scenario.
- vent\_5000h.txt – Effusion curve for 2500h scenario.

/Hobson:

- auckland\_lava\_hobson.shp – Mapped extent of the lava flow.
- paleo\_hobson\_final\_a11\_a5.tif – Reconstructed pre-eruptive DSM for Mt. Hobson.
- vent\_100h.txt – Effusion curve for 100h scenario.
- vent\_200h.txt – Effusion curve for 200h scenario.
- vent\_500h.txt – Effusion curve for 500h scenario.

/Little Rangitoto:

- auckland\_lava\_little\_rangitoto.shp – Mapped extent of the lava flow.
- paleo\_little\_rangitoto\_a3\_final\_a5.tif – Reconstructed pre-eruptive DSM for Little Rangitoto.
- vent\_50h.txt – Effusion curve for 50h scenario.
- vent\_200h.txt – Effusion curve for 200h scenario.
- vent\_500h.txt – Effusion curve for 500h scenario.

/Roskill:

- auckland\_lava\_roskill.shp – Mapped extent of the lava flow.
- paleo\_roskill\_edited\_final\_edited\_a11\_a5\_sink.tif – Reconstructed pre-eruptive DSM for Mt. Roskill.
- vent\_200h.txt – Effusion curve for 200h scenario.
- vent\_500h.txt – Effusion curve for 500h scenario.
- vent\_1000h.txt – Effusion curve for 1000h scenario.

/St John:

- auckland\_lava\_ST\_JOHN.shp – Mapped extent of the lava flow.
- paleo\_st\_john\_sink\_a5\_a7.tif – Reconstructed pre-eruptive DSM for Mt. St. John.
- vent\_200h.txt – Effusion curve for 200h scenario.

- vent\_500h.txt – Effusion curve for 500h scenario.
- vent\_1000h.txt – Effusion curve for 1000h scenario.

/Three Kings:

- auckland\_lava\_three\_kings.shp – Mapped extent of the lava flow.
- paleo\_three\_king\_final\_edited\_a11\_a5\_sink.tif – Reconstructed pre-eruptive DSM for Three Kings.
- vent\_1500h.txt – Effusion curve for 1500h scenario.
- vent\_2000h.txt – Effusion curve for 2000h scenario.
- vent\_2500h.txt – Effusion curve for 2500h scenario.

/Wellington:

- auckland\_lava\_wellington.shp – Mapped extent of the lava flow.
- paleo\_wellington\_final\_a11\_a5\_sink.tif – Reconstructed pre-eruptive DSM for Mt. Wellington.
- vent\_1500h.txt – Effusion curve for 1500h scenario.
- vent\_2000h.txt – Effusion curve for 2000h scenario.

SETTINGS.docx – Input setting file for the MAGFLOW used in this study.

UTM\_vents\_simulations.xls – List of coordinates of the vent for the simulated lava flows.

## 02 – OUTPUT DATA

/Albert:

- albert\_500\_ESRI.asc – Thickness map of the simulated lava flow by MAGFLOW (scenario duration = 500 h).
- albert\_1000\_ESRI.asc – Thickness map of the simulated lava flow by MAGFLOW (scenario duration = 1000 h).
- albert\_1500\_ESRI.asc – Thickness map of the simulated lava flow by MAGFLOW (scenario duration = 1500 h).

/Eden:

- eden\_2500\_ESRI.asc – Thickness map of the simulated lava flow by MAGFLOW (scenario duration = 2500 h).
- eden\_5000\_ESRI.asc – Thickness map of the simulated lava flow by MAGFLOW (scenario duration = 5000 h).

/Little Rangitoto:

- little\_rangitoto\_50h\_ESRI.asc – Thickness map of the simulated lava flow by MAGFLOW (scenario duration = 50 h).
- little\_rangitoto\_50h\_poly.shp – Boundary of the simulated lava flow (scenario duration = 50 h).

- little\_rangitoto\_50h\_poly\_OVER.shp – Overestimated areas (scenario duration = 50 h).
- little\_rangitoto\_50h\_poly\_RESIM.shp – Matching areas of the simulated flow and the actual outline (scenario duration = 50 h).
- little\_rangitoto\_50h\_poly\_UNDER.shp – Underestimated areas (scenario duration = 50 h).
- little\_rangitoto\_200h\_ESRI.asc – Thickness map of the simulated lava flow by MAGFLOW (scenario duration = 200 h).
- little\_rangitoto\_200h\_poly.shp – Boundary of the simulated lava flow (scenario duration = 200 h).
- little\_rangitoto\_200h\_poly\_OVER.shp – Overestimated areas (scenario duration = 200 h).
- little\_rangitoto\_200h\_poly\_RESIM.shp – Matching areas of the simulated flow and the actual outline (scenario duration = 200 h).
- little\_rangitoto\_200h\_poly\_UNDER.shp – Underestimated areas (scenario duration = 200 h).
- little\_rangitoto\_500h\_ESRI.asc – Thickness map of the simulated lava flow by MAGFLOW (scenario duration = 500 h).
- little\_rangitoto\_500h\_poly.shp – Boundary of the simulated lava flow (scenario duration = 500 h).
- little\_rangitoto\_500h\_poly\_OVER.shp – Overestimated areas (scenario duration = 500 h).
- little\_rangitoto\_500h\_poly\_RESIM.shp – Matching areas of the simulated flow and the actual outline (scenario duration = 500 h).
- little\_rangitoto\_500h\_poly\_UNDER.shp – Underestimated areas (scenario duration = 500 h).

/Roskill:

- roskill\_200h\_ESRI.asc – Thickness map of the simulated lava flow by MAGFLOW (scenario duration = 200 h).
- roskill\_200h\_poly.shp – Boundary of the simulated lava flow (scenario duration = 200 h).
- roskill\_200h\_poly\_OVER.shp – Overestimated areas (scenario duration = 200 h).
- roskill\_200h\_poly\_RESIM.shp – Matching areas of the simulated flow and the actual outline (scenario duration = 200 h).
- roskill\_200h\_poly\_UNDER.shp – Underestimated areas (scenario duration = 200 h).
- roskill\_500h\_ESRI.asc – Thickness map of the simulated lava flow by MAGFLOW (scenario duration = 500 h).

- roskill\_500h\_poly.shp – Boundary of the simulated lava flow (scenario duration = 500 h).
- roskill\_500h\_poly\_OVER.shp – Overestimated areas (scenario duration = 500 h).
- roskill\_500h\_poly\_RESIM.shp – Matching areas of the simulated flow and the actual outline (scenario duration = 500 h).
- roskill\_500h\_poly\_UNDER.shp – Underestimated areas (scenario duration = 500 h).
- roskill\_1000h\_ESRI.asc – Thickness map of the simulated lava flow by MAGFLOW (scenario duration = 1000 h).
- roskill\_1000h\_poly.shp – Boundary of the simulated lava flow (scenario duration = 1000 h).
- roskill\_1000h\_poly\_OVER.shp – Overestimated areas (scenario duration = 1000 h).
- roskill\_1000h\_poly\_RESIM.shp – Matching areas of the simulated flow and the actual outline (scenario duration = 1000 h).
- roskill\_1000h\_poly\_UNDER.shp – Underestimated areas (scenario duration = 1000 h).

/St John:

- st\_john\_200\_ESRI.asc – Thickness map of the simulated lava flow by MAGFLOW (scenario duration = 200 h).
- st\_john\_500\_ESRI.asc – Thickness map of the simulated lava flow by MAGFLOW (scenario duration = 500 h).
- st\_john\_1000\_ESRI.asc – Thickness map of the simulated lava flow by MAGFLOW (scenario duration = 1000 h).

/Three Kings:

- three\_kings\_1500h\_ESRI.asc – Thickness map of the simulated lava flow by MAGFLOW (scenario duration = 1500 h).
- three\_kings\_150h\_poly.shp – Boundary of the simulated lava flow (scenario duration = 1500 h).
- three\_kings\_1500h\_poly\_OVER.shp – Overestimated areas (scenario duration = 1500 h).
- three\_kings\_1500h\_poly\_RESIM.shp – Matching areas of the simulated flow and the actual outline (scenario duration = 1500 h).
- three\_kings\_1500h\_poly\_UNDER.shp – Underestimated areas (scenario duration = 1500 h).
- three\_kings\_2000h\_ESRI.asc – Thickness map of the simulated lava flow by MAGFLOW (scenario duration = 2000 h).

- three\_kings\_2000h\_poly.shp – Boundary of the simulated lava flow (scenario duration = 2000 h).
- three\_kings\_2000h\_poly\_OVER.shp – Overestimated areas (scenario duration = 2000 h).
- three\_kings\_2000h\_poly\_RESIM.shp – Matching areas of the simulated flow and the actual outline (scenario duration = 2000 h).
- three\_kings\_2000h\_poly\_UNDER.shp – Underestimated areas (scenario duration = 2000 h).
- three\_kings\_2500h\_ESRI.asc – Thickness map of the simulated lava flow by MAGFLOW (scenario duration = 2500 h).
- three\_kings\_2500h\_poly.shp – Boundary of the simulated lava flow (scenario duration = 2500 h).
- three\_kings\_2500h\_poly\_OVER.shp – Overestimated areas (scenario duration = 2500 h).
- three\_kings\_2500h\_poly\_RESIM.shp – Matching areas of the simulated flow and the actual outline (scenario duration = 2500 h).
- three\_kings\_2500h\_poly\_UNDER.shp – Underestimated areas (scenario duration = 2500 h).

/Wellington:

- wellington\_1500\_ESRI.asc – Thickness map of the simulated lava flow by MAGFLOW (scenario duration = 1500 h).
- wellington\_2000\_ESRI.asc – Thickness map of the simulated lava flow by MAGFLOW (scenario duration = 2000 h).

## Appendix for Chapter 8

- auckland\_faults\_DIST.tif – Distance map from known fault lines (faults\_kenny2012.shp).
- auckland\_faults\_DIST\_RECLASS.tif – Classified distance map from the present shore line.
- auckland\_lidar\_bathy\_merged\_nn10m\_TOPO.tif – Elevation map based on the LiDAR DSM with bathymetric data. This map was resampled to 10 m resolution.
- auckland\_lidar\_bathy\_merged\_nn10m\_TOPO\_RECLASS.tif – Classified distance map.
- auckland\_lidar\_sea\_DIST.tif – Distance map from the present shore line (auckland\_lidar\_sea.shp).
- auckland\_lidar\_sea\_DIST\_RECLASS.tif – Classified distance map from the present shore line.

- auckland\_soft\_sediment\_thickness.tif – Thickness map of the post-Waitemata non-volcanic, soft-sediments based on drill core data (spot\_height\_waitemata.shp), and mapping.
- auckland\_soft\_sediment\_thickness\_RECLASS.tif – Classified thickness map of the post-Waitemata non-volcanic, soft-sediments.
- auckland\_vents\_TRANS\_ALL\_nn10m\_INT\_CLIP\_ZONAL\_MEDIAN.tif – Zonal statistics for the susceptibility classes. The values show the expected vent opening phase volume based on the past behaviour.
- auckland\_vents\_TRANS\_ALL\_nn10m.tif – Interpolated raster based on the AVF volcanoes phreatomagmatic phase volumes
- auckland\_vent\_WEIGHTS.shp – Extracted susceptibility classes at past eruptive centres of the AVF.
- auckland\_susceptibility\_map\_weights.tif – Susceptibility map of the AVF for phreatomagmatic vent opening eruptions.
- auckland\_susceptibility\_map\_weights\_HIGH.tif – High susceptibility areas for phreatomagmatic vent opening (class = 1–5)
- auckland\_susceptibility\_map\_weights\_LOW.tif – Low susceptibility areas for phreatomagmatic vent opening (class = 6–10)





## Appendix C – Statement of contribution

This thesis contains Chapters that were published as journal articles. This Appendix contains the “Statement of contribution to doctoral thesis containing publications” form (DCR 16).

